From the holdings of the Department of Special Collections , Princeton University Library, Princeton, NJ

These documents are either in the public domain, or can only be used for educational and research purposes (Fair use) as per U.S. Copyright law (text below). By accessing this file, all users agree that their use falls in the public domain or within fair use as defined by the copyrightlaw. We do not charge any permission or usage fees for the publication of images of material inour collections, including those provided by Princeton University Library, via our website, catalog, or directly from staff.For more information regarding copyright, credit, and citation please review the information onthe Copyright, Credit and Citation Guidelines page of our website.
https://library.princeton.edu/special-collections/policies/copyright-credit-and-citation-guidelines. If you have any questions, including how to order higher-quality images from the collection, contact Special Collections Public Services via our Ask Us! Form. https://library.princeton.edu/special-collections/ask-us

---

Doctoral Dissertations, 2011-2026

Astrophysical Sciences

2022

Small Galaxies in a Wide-Field Era: On the Interplay Between the Structure of Low-Mass Galaxies and the Processes that Shape Them

Kado-Fong, Erin

Princeton, NJ : Princeton University

---

http://arks.princeton.edu/ark:/88435/dsp01b8515r60c

U.S. Copyright law: The copyright law of the United States (Title 17, §108, United States Code) governs the making of photocopies or other reproductions of copyrighted material. Under certain conditions specified in the law, libraries and archives are authorized to furnish a photocopy or other reproduction. One of these specified conditions is that the photocopy or reproduction is not to be used for any purpose other than private study, scholarship, or research. If a user makes a request for, or later uses, a photocopy or reproduction for purposes in excess of fair use that user may be liable for copyright infringement. This institution reserves the right to refuse to accept a copying order if, in its judgment, fulfillment of the order would involve a violation of copyright law. https://www.copyright.gov/title17/title17.pdf

Small Galaxies in a Wide-Field Era: On the Interplay Between the Structure of Low-Mass Galaxies and the Processes that Shape Them

Erin Kado-Fong

A Dissertation
Presented to the Faculty
of Princeton University
in Candidacy for the Degree
of Doctor of Philosophy

Recommended for Acceptance
by the Department of
Astrophysical Sciences
Adviser: Jenny Greene

September 2022

© Copyright by Erin Kado-Fong, 2022.

All Rights Reserved

Abstract

Low-mass "dwarf" galaxies, galaxies with stellar masses less than $M_\star \sim 10^9 M_\odot$, are key testbeds for many contemporary problems in astrophysics. The shallow potential wells of these low-mass systems make their structure particularly sensitive to physical processes at both sub-galactic and super-galactic scales; dwarfs in the mass range of $10^7 \lesssim M_\star/M_\odot \lesssim 10^9$ are key testbeds for our understanding of star formation physics, galaxy interactions, and dark matter. However, due to their low luminosities, it is only recently that wide-field surveys have reached the requisite depth and spatial resolution to probe the dwarf population at distances beyond a few tens of Mpc. In this thesis, I develop new data analysis methods to fill the gaps in our knowledge of low-mass galaxies using modern wide-field surveys, focusing particularly on the interconnected nature of star formation, galaxy interactions, and their respective impacts on galaxy structure.

I first provide an abbreviated introduction to the history of the observation and cataloging of dwarf galaxies in Chapter 1. Chapter 2 and Chapter 3 center around the detection and classification of extragalactic tidal debris – the first focuses on high mass-ratio encounters between low-mass and massive galaxies, while the second focuses on roughly equal mass mergers between dwarfs. Chapter 4 and Chapter 5 develop and deploy statistical tools to measure the three dimensional shape of dwarf galaxies for both a spectroscopic sample of high surface brightness dwarfs and a sample of Low Surface Brightness Galaxies. Chapter 6 goes on to compare the three dimensional structure of these observed dwarf galaxies to that of the simulated dwarfs in the FIRE-2 cosmological zoom suite. Chapter 7 maps out the star formation rate and star formation efficiency of a sample of Ultra Diffuse Galaxies and "normal" dwarfs, while Chapter 8 considers the physical picture of star formation in these galaxies in the model of pressure-regulated, feedback-modulated star formation. Finally, Chapter 9 gives a short overview of the current and upcoming observational campaigns of which I am a part that will further expand our view of the low-mass galaxy population.

Acknowledgements

I have been extremely fortunate to have spent the last five years in the company of people who have made this time both a scientifically fruitful and a personally wonderful experience.

First, I thank my advisor Jenny Greene, without whose expertise and support this would never have been possible. Her tireless scientific and professional guidance has built the foundation of my own scientific outlook. I am deeply grateful for all of the time she has spent reading my drafts, revising proposals, and dispensing invaluable advice on every facet of academic life. Jenny was the first person to reach out to me from Princeton; it has been an honor to work with her for these past five years, and to have seen her daughter Ada go from an infant sleeping in the office during meetings to being an avid listener of history podcasts.

I would also like to thank Jim Gunn, Robert Lupton, Eve Ostriker, Jeong-Gyu Kim, and Chang-Goo Kim, with whom I worked on semester projects. Their guidance, expertise, and patience with an observer working in the realms of instrumentation and simulations was so very appreciated and invaluable in developing my abilities as an astronomer.

I thank my undergraduate advisor, Danilo Marchesini, for encouraging me to start doing research in astronomy and his continued support and guidance. I thank my REU advisors, Peter KG Williams and Edo Berger, for their guidance in writing my first ever paper, and for setting a high water mark in terms of LaTeX organization.

I am grateful to my many collaborators and to the wonderful graduate student community in the department at Princeton. I am in particular grateful to Lachlan Lancaster, Johnny Greco, and Scott Carlsten, who are fall under both categories. I would also like to thank the other members of Jenny's group for their indispensable scientific advice and expertise over the years, including Rachael Beaton, Shany Danieli, Andy Goulding, and Song Huang.

The other graduate students in the department are a huge part of the reason why I have enjoyed my time at Princeton so much. I would like to thank all of them for the joy of their presence and friendship both during and after their time as PhD students, including Avery Bailey, Luke Bouma, Erin Flowers, Goni Halevi, Cole Holcomb, Brianna Lacy, Zack Li, Alwin Mao, Mackenzie Moody, Eric Moseley, Kris Pardo, Heather Prince, Amy Secunda, Vassilis Tsiolis, Rui Xu, and Wenrui Xu.

I would also like to thank all of the friends I've made over the past five years in both the Princeton and New York areas. Their kindness, support, and good-natured ribbing has made me feel right at home here. Thank you in particular to all of the friends who literally catch me when I fall – as in all aspects of life, it is much easier to try hard when someone you can trust is holding onto the other end of the rope.

I am forever grateful to my mom Helen, my dad Steven, and the rest of my family for their endless love and support over the years. I also thank my grandparents Jean, Edwin, Alice, and York for making all of this possible.

Finally, I thank Francesco Lin for his support and encouragement throughout this journey. Thank you for thinking that I'm funny, and for being my go-to resource for all things LaTeX math mode.

Preface

This dissertation consists of nine chapters; the first chapter is an introduction to the current state of our knowledge of the population and structure of low-mass galaxies, and the following eight chapters are published or ongoing studies. The second through eighth chapters are self-contained studies which have been published in or submitted to peer-reviewed journals. The final chapter presents ongoing work and an outlook on the prospects of future surveys. For the convenience of the reader, I list the published works below, along with a list of presentations in which I have discussed work contained within this dissertation..

Publications

1. Tidal Features at $0.05 < z < 0.45$ in the Hyper Suprime-Cam Subaru Strategic Program: Properties and Formation Channels
   Erin Kado-Fong, Jenny E. Greene, David Hendel, Adrian M. Price-Whelan, Johnny P. Greco, Andy D. Goulding, Song Huang, Kathryn V. Johnston, Yutaka Komiyama, Chien-Hsiu Lee, Nate B. Lust, Michael A. Strauss, Masayuki Tanaka
   (ApJ 866, 103)

2. Star Formation in Isolated Dwarf Galaxies Hosting Tidal Debris: Extending the Dwarf-Dwarf Merger Sequence
   Erin Kado-Fong, Jenny E. Greene, Johnny P. Greco, Rachael Beaton, Andy D. Goulding, Sean D. Johnson, Yutaka Komiyama
   (ApJ 159, 103)

3. Tracing the Intrinsic Shapes of Dwarf Galaxies Out to Four Effective Radii: Clues to Low-mass Stellar Halo Formation
   Erin Kado-Fong, Jenny E. Greene, Song Huang, Rachael Beaton, Andy D. Goulding, Yutaka Komiyama
   (ApJ 897, 143)

4. The Intrinsic Shapes of Low Surface Brightness Galaxies (LSBGs): A Discriminant of LSBG

Galaxy Formation Mechanisms

Erin Kado-Fong, Mihai Petrescu, Majid Mohammad, Johnny P. Greco, Jenny E. Greene, Elizabeth A. K. Adams, Song Huang, Lukas Leisman, Ferah Munshi, Dimitrios Tanoglidis, Jordan Van Nest

(ApJ 920, 72)

5. The In-situ Origins of Dwarf Stellar Outskirts in FIRE-2

   Erin Kado-Fong, Robyn E. Sanderson, Jenny E. Greene, Emily C. Cunningham, Coral Wheeler, T. K. Chan, Kareem El-Badry, Philip F. Hopkins, Andrew Wetzel, Michael Boylan-Kolchin, Claude-André Faucher-Giguère, Song Huang, Eliot Quataert, Tjitske Starkenburg

   (ApJ 931, 152)

Presentations

1. (conference) Stellar Halos Across the Cosmos *[Heidelberg, Germany. 2018/07]*
2. (conference) UC Santa Cruz Galaxy Workshop *[Santa Cruz, USA. 2018/08]*
3. (conference) Light in the Suburbs: Structure and Chemodynamics of Galaxy Halos *[Sesto, Italy. 2019/06]*
4. (conference) Subaru 20th Anniversary Conference *[Waikōloa ,USA. 2019/11]*
5. (conference) Local "Local Group" Group Meeting *[New York, USA. 2020/12]*
6. (seminar) Tufts Astronomy Seminar *[Medford, USA. 2021/04]*
7. (seminar) UC Santa Cruz FLASH Seminar *[Santa Cruz, USA. 2021/09]*
8. (seminar) Stanford University Tea Talk *[Stanford, USA. 2021/09]*
9. (seminar) University of Arizona Galaxy Group Seminar *[Tucson, USA. 2021/09]*
10. (colloquium) Yale University Astronomy *[New Haven, USA. 2021/10]*
11. (colloquium) Center for Computational Astrophysics *[New York, USA. 2021/10]*

12. (seminar) NYU Informal Seminar *[New York, USA. 2021/11]*

13. (seminar) University of Pennsylvania Astronomy Seminar *[Philadelphia, USA. 2021/12]*

14. (seminar) The Ohio State Price Prize Seminar *[Columbus, USA. 2021/12]*

Data Acknowledgements

Based in part on data collected at the Subaru Telescope and retrieved from the HSC data archive system, which is operated by Subaru Telescope and Astronomy Data Center at National Astronomical Observatory of Japan.

The Hyper Suprime-Cam (HSC) collaboration includes the astronomical communities of Japan and Taiwan, and Princeton University. The HSC instrumentation and software were developed by the National Astronomical Observatory of Japan (NAOJ), the Kavli Institute for the Physics and Mathematics of the Universe (Kavli IPMU), the University of Tokyo, the High Energy Accelerator Research Organization (KEK), the Academia Sinica Institute for Astronomy and Astrophysics in Taiwan (ASIAA), and Princeton University. Funding was contributed by the FIRST program from Japanese Cabinet Office, the Ministry of Education, Culture, Sports, Science and Technology (MEXT), the Japan Society for the Promotion of Science (JSPS), Japan Science and Technology Agency (JST), the Toray Science Foundation, NAOJ, Kavli IPMU, KEK, ASIAA, and Princeton University.

This paper makes use of software developed for the Large Synoptic Survey Telescope. We thank the LSST Project for making their code available as free software at http://dm.lsst.org

The Pan-STARRS1 Surveys (PS1) have been made possible through contributions of the Institute for Astronomy, the University of Hawaii, the Pan-STARRS Project Office, the Max-Planck Society and its participating institutes, the Max Planck Institute for Astronomy, Heidelberg and the Max Planck Institute for Extraterrestrial Physics, Garching, The Johns Hopkins University, Durham University, the University of Edinburgh, Queens University Belfast, the Harvard-Smithsonian Center for Astrophysics, the Las Cumbres Observatory Global Telescope Network Incorporated, the National Central University of Taiwan, the Space Telescope Science Institute, the National Aeronautics and Space Administration under Grant No. NNX08AR22G issued through the Planetary

Science Division of the NASA Science Mission Directorate, the National Science Foundation under Grant No. AST-1238877, the University of Maryland, and Eotvos Lorand University (ELTE) and the Los Alamos National Laboratory.

Some of the data presented in this paper were obtained from the Mikulski Archive for Space Telescopes (MAST). STScI is operated by the Association of Universities for Research in Astronomy, Inc., under NASA contract NAS5-26555. Support for MAST for non-HST data is provided by the NASA Office of Space Science via grant NNX13AC07G and by other grants and contracts.

Simulations used in this work were run using XSEDE supported by NSF grant ACI-1548562, Blue Waters via allocation PRAC NSF.1713353 supported by the NSF, and NASA HEC Program through the NAS Division at Ames Research Center.

The authors also would like to thank the Flatiron Institute Scientific Computing Core for providing computing resources that made this research possible, and especially for their hard work facilitating remote work during the pandemic. Analysis for this paper was carried out on the Flatiron Institute's computing cluster `rusty`, which is supported by the Simons Foundation.

Based on observations made with the NASA Galaxy Evolution Explorer. GALEX is operated for NASA by the California Institute of Technology under NASA contract NAS5-98034.

This research has made use of the NASA/IPAC Infrared Science Archive, which is operated by the Jet Propulsion Laboratory, California Institute of Technology, under contract with the National Aeronautics and Space Administration.

This research has made use of the VizieR catalogue access tool, CDS, Strasbourg, France.

For my family.

Contents

Abstract 3

Acknowledgements 4

Preface 6

1 The Low-Mass Galaxy Population **34**

1.1 An Abbreviated History of the Imaging and Cataloging of Dwarf Galaxies 35

1.2 Dwarfs in the Modern Era of Wide-Field Surveys 37

2 Tidal Debris Around Massive Galaxies **38**

2.1 Introduction 38

2.2 Sample selection 43

2.2.1 HSC-SSP 43

2.2.2 SDSS spectra 44

2.3 Identification and characterization of tidal features 45

2.3.1 Detection 45

2.3.2 Contaminant removal 47

2.3.3 Visual Morphological Classification 50

2.3.4 Detection recovery efficiency 52

2.3.5 Measuring tidal feature color 55

2.4 Results 58

2.4.1 Observed tidal feature occurrence fractions 58

2.4.2 Host galaxy properties . . . 63
2.4.3 Tidal feature colors . . . 65
2.5 Discussion . . . 69
2.5.1 The mass ratio of shell-forming events . . . 71
2.5.2 Star formation in tidal features . . . 75
2.5.3 Host galaxy morphologies . . . 75
2.6 Summary and conclusions . . . 77
2.7 Appendix: Image decomposition . . . 78
2.8 Appendix: Surface brightness limits . . . 81

3 Mergers Between Dwarf Galaxies 84

3.1 Introduction . . . 84
3.2 Sample Selection . . . 86
3.2.1 Spectroscopic sample . . . 86
3.2.2 HSC-SSP Imaging . . . 89
3.3 Tidal Feature Detection . . . 89
3.3.1 Updates to the method of Kado-Fong et al. 2018 . . . 91
3.3.2 Construction of the visual sample . . . 93
3.4 Results . . . 94
3.4.1 The automated and visual samples . . . 94
3.4.2 Detection fraction and star formation . . . 96
3.4.3 Host color vs. stellar mass . . . 97
3.4.4 Tidal Feature and Host Morphology . . . 98
3.5 Discussion . . . 99
3.5.1 The dwarf-dwarf merger sequence . . . 99
3.5.2 Evidence for a merger pathway for BCD formation . . . 101
3.5.3 The origin of non-interacting dwarf starbursts . . . 101
3.6 Conclusions and Future Direction . . . 102

3.7 Appendix: Isolation and sample selection: robustness tests . . . 104
3.7.1 Isolation Criteria . . . 104
3.7.2 The GAMA and SDSS samples . . . 105
3.8 Appendix: Updates to the detection algorithm . . . 106

4 Three-Dimensional Structure of Low-Mass Galaxies 109

4.1 Introduction . . . 109
4.2 Observations and Data Processing . . . 112
4.2.1 HSC-SSP Imaging . . . 112
4.2.2 Initial Sample Selection . . . 113
4.2.3 Volume Corrections . . . 114
4.3 1D Surface Brightness Profile Measurement . . . 117
4.3.1 Single Sérsic fits . . . 117
4.3.2 Non-parametric Surface Brightness Profiles . . . 118
4.3.3 Profile Measurement Validation . . . 122
4.4 3D Shape Inference . . . 124
4.4.1 Validation: Comparison to Sérsic Populations . . . 128
4.4.2 Validation: Comparison to Padilla et al. 2008 . . . 129
4.5 Results . . . 131
4.5.1 3D Shape as a function of Stellar Mass and Radius . . . 132
4.5.2 3D Shape and Galaxy Color . . . 133
4.5.3 3D Shape and Environment . . . 134
4.6 Discussion . . . 136
4.6.1 The Emergence of Round Outskirts Around Low-Mass Galaxies . . . 136
4.6.2 Morphological Transformation and Quenching . . . 138
4.6.3 Comparison with Simulations . . . 139
4.7 Conclusions . . . 139
4.8 Appendix: Tests of the Background Subtraction . . . 141

4.9 Appendix: Tabulation of Inferred Parameters . . . 145
4.10 Appendix: Allowing for Shape-Size Covariance . . . 145
4.11 Appendix: Parameter Recovery and Sample Size . . . 146

5 Three-Dimensional Structure of Low Surface Brightness Galaxies 148

5.1 Introduction . . . 148
5.2 Sample Construction . . . 152
5.2.1 The HSC-SSP Sample . . . 153
5.2.2 The DES Sample . . . 154
5.2.3 The ALFALFA/Legacy Sample . . . 156
5.2.4 The Coma Cluster Sample . . . 157
5.2.5 Physical and Observed Properties of the Samples . . . 157
5.3 Intrinsic Shape Inference . . . 160
5.4 Results . . . 169
5.4.1 Intrinsic Shape versus Color and Environment . . . 170
5.5 Discussion . . . 171
5.5.1 Comparison to Observations . . . 171
5.5.2 Comparison to Simulations . . . 173
5.6 Conclusions . . . 176
5.7 Appendix: Mock Recovery Tests . . . 177

6 Low-Mass Galaxy Shapes in the FIRE Simulations 179

6.1 Introduction . . . 179
6.2 Methods . . . 182
6.2.1 The FIRE Simulations . . . 183
6.2.2 Intrinsic Shape Measurements . . . 189
6.3 Results . . . 193
6.3.1 The Intrinsic Shapes of the FIRE-2 Dwarf Galaxies . . . 193
6.3.2 The Origin of Dwarf Halo Stars . . . 197

6.3.3 The Observability of the FIRE-2 Dwarf Stellar Halos . . . 204
6.3.4 Properties of the Disky and Non-Disky Dwarfs . . . 205
6.4 Discussion . . . 206
6.4.1 Comparison to Other Simulations . . . 207
6.4.2 A Divergent Path of Low-mass Stellar Halo Formation . . . 208
6.4.3 The Non-Disky Dwarfs . . . 210
6.5 Conclusions . . . 213
6.6 Appendix: Placing Limits on the Presence of a Non-Disky Minority Population . . . 215
6.7 Appendix: A comparison between direct cumulative and inferred differential shape measurements . . . 217
6.8 Appendix: Projection Gallery of Disky and non-Disky Dwarfs . . . 220

7 Observational Constraints on the Star Formation Efficiency of Ultra-Diffuse Galaxies 223

7.1 Introduction . . . 223
7.2 Datasets . . . 226
7.2.1 Sample Overview . . . 227
7.2.2 UV-Optical Imaging . . . 230
7.2.3 HI Measurements . . . 231
7.3 SED Fitting . . . 235
7.3.1 Stellar Population Models . . . 235
7.3.2 Defining Global, Regional, and Cluster SEDs . . . 236
7.3.3 SED Fitting . . . 238
7.4 Method Validation . . . 241
7.4.1 Intra-sample Comparisons . . . 242
7.4.2 Inter-sample Comparisons to the Literature . . . 244
7.5 Results . . . 245
7.5.1 The Efficiency and Distribution of Star Formation in UDGs . . . 246

7.5.2 The HI Properties of the UDG Sample . . . 247
7.5.3 The Color-Mass Relation of UDGs . . . 248
7.6 Discussion . . . 250
7.6.1 Implications for UDG Formation . . . 250
7.6.2 The Stellar Structure of Dwarfs at fixed M_{HI} . . . 252
7.7 Conclusions . . . 253
7.8 Fitting Gallery . . . 255

8 Star Formation of Dwarfs in the Pressure-Regulated, Feedback-Modulated Theory of Star Formation 258

8.1 Introduction . . . 258
8.2 Datasets . . . 260
8.3 Background on PRFM theory . . . 262
8.4 Results . . . 266
8.4.1 The validity of PRFM assumptions in the present sample . . . 266
8.4.2 Estimating ρ_{sd} . . . 267
8.4.3 P_{DE} Estimates . . . 270
8.4.4 PRFM predictions . . . 271
8.4.5 Empirical estimates of Υ_{tot} . . . 272
8.5 Discussion . . . 274
8.5.1 Star Formation Efficiency in UDGs . . . 274
8.5.2 Molecular Hydrogen in UDGs . . . 276
8.5.3 If UDGs Live in Special Halos . . . 281
8.6 Conclusions . . . 282

9 Towards a Census of Star-Forming Dwarfs 284

9.1 The Merian Survey . . . 285
9.2 The Prime Focus Spectrograph Subaru Strategic Program . . . 288

List of Figures

1.1 A visual demonstration of the progress made in the capability of wide-field surveys to study the detailed structure of dwarf galaxies over the past three decades. Here we show imaging of the Low Surface Brightness Galaxy LSBG766 [Greco et al., 2018c]. Each cutout is 0.02 deg on a side, or $\sim$ 8.3 kpc at the distance of the galaxy (24 Mpc). In the top row, we show from left the (digitized) photographic survey DSS2-red [Lasker et al., 1990, Djorgovski et al., 1998], the g-band image from the Sloan Digital Sky Survey [SDSS, York et al., 2000], and the g-band image from the most recent data release of the Hyper Suprime-Cam Subaru Strategic Program [HSC-SSP, Aihara et al., 2018a]. In the bottom row we show gri-composite RGB images from SDSS and HSC-SSP. 36

2.1 A schematic diagram of our algorithm to detect tidal features in HSC-SSP data. From left to right, the flow chart shows the convolution step, generation of high spatial frequency images, and detection image creation. 41

2.2 An illustration of the filtering algorithm as applied to the sum of a non-interacting HSC galaxy and a simulated shell system from Hendel and Johnston [2015] with a mean surface brightness of $\bar{\mu}_i = 25.4$ mag arcsec^{-2}. *Left:* $\mathbf{I_0}$, the sum of the non-interacting HSC galaxy cutout and simulated, PSF-convolved tidal feature system. *Middle:* The detection map, $\mathbf{C}$, generated from the left panel. The two brightest caustics in the shell system are clearly visible (yellow-green regions, left of panel), along with a background galaxy. *Right:* The simulated tidal feature from Hendel and Johnston [2015]. The orange outlines show the boundaries of the region that our method identifies as a tidal feature candidate. All panels are shown with a logarithmic stretch. 44

2.3 Redshift v. stellar mass for the galaxies in the parent spectroscopic sample (small grey points), the tidal feature sample (black) and the neighbor contaminant sample (orange). The one-dimensional histograms over redshift and stellar mass are shown in the top and right panels, respectively. In each case, the black bars show the distribution of the final, visually classified sample. In these panels, the orange bars show the neighbor contaminant sample, while the black bars show the tidal feature sample. The neighbor contaminants are not offset from the main tidal feature population, indicating that removing candidates via visual inspection does not introduce significant bias into the characteristics of our final tidal feature sample. 48

2.4 *Top row:* Pixel recovery fractions ($f_{\rm rec}$, see Equation 2.5) for simulated streams (left) and shells (right). Each box shows the fraction of pixels associated with the simulated tidal feature that are recovered by the algorithm for a given tidal feature mean $i_{\rm HSC}$ band surface brightness and radial extent, as measured in units of the host effective radius. Generally, a higher fraction of pixels is recovered for the simulated streams; this is expected due to the number of particles occupying diffuse stellar fans in the shells. *Bottom row:* Detection fractions for streams (left) and shells (right). Here, the values at each grid point show the percent of simulated tidal feature systems in which at least 5% of the area covered by the tidal feature is flagged as a detection. In all panels, the drop in completeness at very high surface brightnesses ($\bar{\mu}_i \lesssim 25.$ mag arcsec^{-2}) is due to cases in which a part of the tidal feature is bright enough to be flagged as central galaxy substructure (e.g. spiral arms). 49

2.5 A sample of $i_{\rm HSC}$ band imaging of shells (left column), streams (middle column) and non-interacting galaxies (right) in our sample. The orange outlines show the boundaries of the detected regions found by our filtering algorithm. The horizontal black line in the bottom right of each panel spans 30 kpc at the redshift of the central galaxy. In all panels, a logarithmic stretch is used to emphasize low surface brightness features. 57

2.6 Tidal feature occurrence fractions as a function of stellar mass (y-axis) and redshift (x-axis) for the visually identified stream (top) and shell (bottom) samples. Each bin in the top (bottom) panel is annotated with the fraction of galaxies tagged as a stream (shell) host from the full spectroscopic sample. Blank regions indicate bins for which no tidal feature systems were identified. 58

2.7 Properties of the stream (blue) and shell (red) host galaxies. The small grey points show the full spectroscopic sample within our target redshift range. *Left:* redshift versus stellar mass for the tidal feature sample. *Center:* redshift versus $(g-i)$ color for the sample. At all redshifts, shell hosts tend to be redder and more massive than their counterparts that host streams. *Right:* $(g-i)$ color versus concentration for the $z < 0.15$ galaxies in our sample. The shell host galaxies have, on average, higher concentration than the stream hosts, indicating that the shell sample contains a larger fraction of ETGs than does the stream host galaxy sample. 62

2.8 *Top: gri*-composite images [Lupton et al., 2004] of the three disc galaxies that host shells in our sample. Both caustics and diffuse stellar fans are visible in all cases. In the middle panel, two umbrella-like shell structures are visible to the left of the galaxy. *Bottom:* The same galaxies in the $i_{\rm HSC}$ band, with the features detected by the algorithm shown in orange. A diffuse trail is also visible in the top right of the rightmost panels, which is not detected due to its overlap with the cutout edge. . . 66

2.9 Stellar mass versus the fraction of tidal features that are shells for the $z < 0.15$ galaxies in our final tidal feature sample. Shells are found more frequently around more massive galaxies, growing from $\approx 20\%$ at $\log(M_\star/M_\odot) = 10.5$ to $\approx 50\%$ at $\log(M_\star/M_\odot) = 11.5$. A larger shell fraction around massive galaxies is expected due to an increase in the number of radially-biased satellite infall trajectories around such galaxies [Jiang et al., 2015, Hendel and Johnston, 2015]. 67

2.10 Scaled kernel density estimates of the difference between the color of the tidal features and the core of the host galaxy (measured within a radius of $1R_{\rm e,host}$) for the shells (top panel, red) and the streams (bottom panel, blue) via a kernel density estimate (using an Epanechnikov kernel with a width of $\Delta(g-i) = 0.15$). In each panel, the solid lines show the color distribution of the full sample. The dashed lines show the $\Delta(g-i)$ distribution for our high-concentration ETG sample ($C > 3.1$), normalized to the number of high-concentration galaxies in the sample. In the top panel, the grey solid line shows the distribution of $\Delta(g-i)$ for the shells that we would have derived if we did not remove features with measured $\Delta(g-i) < -0.5$ as neighbors. The grey shaded region in the top panel shows the color cut that we implement on the color measurements of individual tidal features to remove neighbors in the shell sample. 68

2.11 The distribution of $(g-i)$ restframe colors for our stream sample, using the K-correction computed for a 0.5 Gyr (purple), 5 Gyr (green), and 12 Gyr (red) SSP from Bruzual and Charlot 2003. The dashed vertical lines show the restframe colors for, from left to right, the 0.5 Gyr (purple), 5 Gyr (green) and 12 Gyr (red) populations. The existence of streams with rest-frame colors bluer than the youngest SSP considered implies that a subset of the streams are not on the red sequence, and host star formation. 69

2.12 *Left:* $i_{\rm HSC}$ band imaging of a sample of shells where the color of the shell caustics (boundaries defined by the orange outlines) is consistent with the color of the host galaxy within $1R_{\rm e,host}$. *Right:* a sample of shells for which the color of the shell caustics is bluer ($\Delta m < -0.25$ mag) than the color of the host galaxy within $1R_{\rm e,host}$. All panels use a logarithmic stretch to increase contrast at low surface brightness. The shells that are as red as their host galaxy cores display a higher incidence of type I shells ($86^{+14}_{-35}\%$) than their blue counterparts ($30 \pm 14\%$). 70

2.13 Example decompositions following the algorithm presented in Section 2.3.1. *Top row:* From left: the $r_{\rm HSC}$ band input image, the $\mathbf{c^{(5)}}$ component, and the $\mathbf{c^{(31)}}$ component. *Second row:* the same for $i_{\rm HSC}$. *Third row:* the same for $z_{\rm HSC}$. *Bottom row:* From left, the initial detection image ($\mathbf{C}$) for the $i_{\rm HSC}$ band, the cleaned detection image (wherein the cores of sources and spiral arms are removed), and the detection map (red) overlaid on the $i_{\rm HSC}$ band input image. 80

2.14 An example of $i_{\rm HSC}$ band imaging of a non-interacting galaxy from the parent sample stacked with a simulated stream from [Hendel and Johnston, 2015]. *Top left:* The original $i_{\rm HSC}$ band image. *Top right:* the galaxy with a simulated stream injected into the image, where $\bar{\mu}_i = 23.5$ mag arcsec^{-2}. *Bottom left:* the same stream with $\bar{\mu}_i = 26.375$ mag arcsec^{-2}, the surface brightness at which our completeness for extended ($d > 5R_{\rm e,host}$) is at $\approx 75\%$ (see Section 2.3.4 for details). *Bottom right:* the same stream with $\bar{\mu}_i = 28.4$ mag arcsec^{-2}, the surface brightness limit derived using the method from [Morales et al., 2018]. The stream is not detectable in either case. 82

3.1 The distribution of our sample in redshift (top panel) and stellar mass (bottom panel). In both panels, the red filled histogram shows the GAMA dwarfs and the green filled histogram shows the SDSS dwarfs. The unfilled black and dashed grey histograms show the distribution of the full isolated dwarf sample and a random subset of 6683 galaxies from the full dwarf sample. This is to guide the eye and show that show that there is no significant difference between the distributions of the full and isolated dwarf samples. 88

3.2 An illustration of the multiscale detection method used to find tidal debris around dwarf galaxies. *Top left:* the *gri* composite image of the target galaxy. To guide the eye, the maximal area contour of the detecion map is shown as a contour in red in all panels. *From top middle:* the starlet coefficients in order of increasing spatial scale. The intensity of the images are scaled logarithmically. We note that certain tidal features are only seen in certain coefficients. For example, the inner shell is strongly detected in the second and third coefficients, while the outer shells are detected with high significance in the third and fourth coefficients. *Bottom right:* the $gri_{\rm HSC}$ composite image of the target galaxy with the full detection map overlaid as a contour. The contours show regions of increasing detection significance (i.e. detected in more coefficients). 90

3.3 Examples of galaxies with no tidal feature detection (top row), ambiguous tidal feature detections (middle row), and unambiguous tidal feature detections (bottom row). For the examples in which candidate tidal feature systems are detected, the lowest significance level detection map is plotted as a red outline. We note that although there are some clear cases of spiral arm contamination (e.g. the far right middle panel), we do not remove these cases from the sample, and show that they do not statistically affect our conclusions. 91

3.4 Tidal feature detection percentage for our sample of dwarfs in bins of redshift and host stellar mass (main panel). The color and numbers reflect the percentage of dwarf galaxies that host tidal features in each bin. The top auxiliary panels show the projection of the detection fraction distribution onto redshift, while the righthand auxiliary panels show the projection as a function of host stellar mass. In each auxiliary panel, the unfilled grey histogram shows the normalized distribution of the parent sample. The left panels in blue show the automated sample, while the right panels in orange show the visual sample. 92

3.5 The fraction of dwarfs around which tidal debris is detected for the automated sample (left) and visual sample (right). The top row shows detection fraction as a function of Hα equivalent width, while the bottom row shows detection fraction as a function of host $(g-i)$ color as measured by SDSS. In each panel, the unfilled grey histogram shows the normalized distribution of the parent sample. 95

3.6 *Top:* $(g-i)$ color from SDSS versus stellar mass for non-interacting field dwarfs (grey) and tidal feature host centers (blue). The dashed black line is fit to the non-interacting dwarf galaxy sample. *Bottom:* the deviation of host (g − i) color from the linear fit shown in the top panel for the non-interacting hosts (grey histogram) and tidal feature hosts (blue unfilled histogram). The dashed grey and blue vertical lines show the median deviation for the non-interacting and tidal feature hosts, respectively. 97

3.7 *gri*-composite images for 16 of the starbursting dwarfs with detected tidal debris in our sample. The dashed cyan contours show the maximal outline of the tidal feature detection map produced from our algorithm. 99

3.8 The same as the analysis of the auotmated sample in Figure 3.5, but where the isolation criterion of Paudel et al. [2018] is used to construct an isolated dwarf sample. The pink errorbars show the detection fraction as a function of Hα equivalent width for dwarf galaxies separated by at least 700 kpc in projected distance and $\Delta v > 700$ km s^{-1} from their nearest massive neighbor. For clarity, these points are offset horizontally. The blue shaded region shows the results for the full sample (i.e. the same data as Figure 3.5). The black errorbars show the isolated dwarf sample created from the intersection of the two isolation criteria (i.e. those galaxies considered to be isolated by both criteria). All three samples produce statistically consistent results. 105

3.9 The same as Figure 3.5, but showing the results from the galaxies observed by GAMA (red) and SDSS (green) separately. The blue shaded region shows the results for the full sample (i.e. the same data as Figure 3.5). The left column shows the results for the automated sample, while the right column shows the results for the visual sample. In all cases, the results derived when analyzing the SDSS and GAMA samples separately are in good agreement with each other and with the results obtained from the combined sample. 106

4.1 *Top:* we show the normalized stellar mass function (SMF), $\tilde{\phi}(\log_{10}(M_\star/M_\odot))$, for each magnitude-limited subset of our sample with dash-connected scatter. The normalized SMF for the full sample is shown by the solid blue curve. For reference, the Schechter fit of Panter et al. [2007] and the double Schechter fit of Wright et al. [2017] are normalized to our stellar mass range and shown in the dashed and solid lines, respectively. The raw distribution in stellar mass (i.e. without $1/\mathrm{V_{max}}$ weights) is shown by the grey filled histogram. We find that our normalized SMF matches that of Wright et al. [2017] well. *Middle:* the maximum observable redshift, z_{max}, for each galaxy in the sample as a function of stellar mass. As at top, points are colored by the magnitude limit of the source spectroscopic program. The mean z_{max} as a function of stellar mass is also shown for each program by the large scatter points. *Bottom:* the redshift distribution, colored by source survey. 112

4.2 *Top*: The distribution of Sérsic indices over the dwarf sample. The majority of the dwarfs are well-described by an exponential ($n = 1$) profile. *Bottom*: The distribution of effective radii in the sample, as measured from the Sérsic fits. 114

4.3 Example 1D surface brightness profiles for galaxies that span the range of stellar mass and redshift in our sample. The lefthand (righthand) columns show galaxies at the low (high) redshift end of the sample, while the rows are ordered in decreasing stellar mass. Each pair of panels shows the $i_{\rm HSC}$-band image with the measurements at $1R_{\rm eff}$ (blue), $2R_{\rm eff}$ (orange), $3R_{\rm eff}$ (green), and $4R_{\rm eff}$ (red) overplotted as ellipses. The $gri_{\rm HSC}$-composite RGB image is also shown in the inset panel to more clearly show the morphology of the galaxy. The right panel shows the 1D surface brightness profile of the galaxy; vertical lines show the physical extent at 1-$4R_{\rm eff}$ (same colors as left). We also show the surface brightness of the PSF by the grey curve, and the nominal surface brightness limit of $\mu_i = 28.5$ mag arcsec^{-2} by the grey horizontal line. 115

4.4 *Top:* the distribution of surface brightness measured at $1 - 4R_{\rm eff}$, as labeled. *Bottom:* surface brightness versus projected axis ratio, again colored by measurement radius. Though some measurements are below our nominal surface brightness limit of $\mu_i = 28.5$ mag arcsec^{-2}, these comprise only $\sim 7\%$ of ellipticity measurements, and their inclusion does not have a statistically significant effect on the overall ellipticity distribution. 117

4.5 The distribution of errors in recovered effective radius (left), ellipticity at $1R_{\rm eff}$ (middle), and ellipticity at $3R_{\rm eff}$ (right) for an injected population of disk ($[A, B, C] = [1., 0.9, 0.1]$, blue), spheroid ($[A, B, C] = [1., 0.9, 0.9]$, red), and prolate ($[A, B, C] = [1., 0.1, 0.1]$, green) galaxies. Each mock galaxy is assigned a viewing angle drawn isotropically over the sphere, injected into the HSC data with an $n = 1$ Sérsic profile, and recovered with our pipeline. In each panel, the text shows the $5^{\rm th}$, $25^{\rm th}$, $50^{\rm th}$, $75^{\rm th}$, and $95^{\rm th}$ percentile of the distribution. 118

4.6 *Left:* the observed distribution of projected axis ratio, $q = b/a$, for the HSC non-parametric measurements (filled teal histogram), HSC Sérsic measurements (green histogram), and SDSS catalog measurements (derived from exponential fits, brown histogram). All three measurements are in good agreement; we find that the mean difference in measured q ($\langle \Delta q \rangle$) and the standard deviation of this difference ($\sigma_{\Delta q}$) are $(\langle \Delta q \rangle, \sigma_{\Delta q}) = (0.017, 0.71)$ and $(\langle \Delta q \rangle, \sigma_{\Delta q}) = (-0.01, 0.10)$ for the HSC Sérsic measurements and SDSS catalog exponential measurements, respectively. In the middle panel we plot the non-parametric measurements at $1\mathrm{R_{eff}}$ against the HSC Sérsic measurements, while in the right panel we show the same non-parametric measurements at $1\mathrm{R_{eff}}$ against the SDSS exponential measurements, for galaxies in the SDSS catalog. 119

4.7 For the injected ellipsoid populations described in Figure 4.5, we infer the 3D shape distribution of the population from the recovered projected axis ratios. In each column, we show the inference results for our injected populations of disk ($[A, B, C] = [1., 0.9, 0.1]$, left), spheroid ($[A, B, C] = [1., 0.9, 0.9]$, middle), and prolate ($[A, B, C] = [1., 0.1, 0.1]$, right) galaxies. The top row shows the recovered b/a distribution as filled histograms and the posterior b/a sample as unfilled black histograms. The bottom row shows the distribution of the posterior sample over the intrinsic axes (B and C). The black circle shows the true position of the intrinsic axes. For physical context, we show the C/A values measured for the Milky Way disk-halo system as measured by Schönrich and Binney [2009] and Iorio and Belokurov [2019]. The dashed black line shows the definitional boundary of $B = C$. 124

4.8 Inferred 3D shape distributions as a function of stellar mass (increasing towards top) and morphology (spirals at top, ellipticals at bottom), using SDSS catalog measurements following the morphology criterion of Padilla and Strauss [2008]. In each panel, the filled contours show the inferred 3D shape distribution using our method, while the blue errorbars show the mean and standard deviation of the 3D shape distribution from Padilla and Strauss [2008] in roughly analogous bins of $r_{\rm SDSS}$-band absolute magnitude. Our inferred shape distributions are in general agreement with those of Padilla and Strauss [2008], taking into account that the absolute magnitude cuts are not equivalent to our cuts in stellar mass. In particular, the highest luminosity bin of Padilla and Strauss [2008], where our inference is in significant disagreement, extends to $M_\star \sim 10^{12} M_\odot$. We also show the same contours for the pure disk, prolate, and spheroid Sérsic population presented in Figure 4.7 by the dashed blue, green, and red curves. 127

4.9 For bins in increasing stellar mass (rows) and measurement radius (columns), the distribution of inferred axis ratios B/A and C/A for the dwarf sample. Each panel shows the distribution of intrinsic axis ratios in orange. The black ellipses show the 1σ region of the maximum a posteriori estimate, $\max_{P(\vec{\alpha}|\{b/a\})} \vec{\alpha}$. We also show the same contours for the pure disk, prolate, and spheroid Sérsic population presented in Figure 4.7 by the dashed blue, green, and red curves. The black line shows the B/A=C/A definitional boundary. Each inset panel shows the observed axis ratio, b/a= $1-\epsilon$, distribution as the solid teal histogram. The distribution of b/a produced by the posterior sample in B/A and C/A is shown by the orange unfilled histogram; individual samples from the posterior are shown by the grey unfilled histograms. . . 128

4.10 For dwarfs with $M_\star > 10^{8.5} M_\odot$, the inferred shape distribution for blue ($g-i < 0.90$) and red ($g-i > 0.90$) galaxies as a function of radius. Similar to the trend we see in the analogous mass bin of Figure 4.8, the 3D distribution of blue galaxies is diskier than the red galaxies at $R = 1\mathrm{R_{eff}}$. At large radii, both blue and red galaxies move towards spheroid shapes. As in Figure 4.9, we show the 50th percentile regions of the pure disk, prolate, and spheroid Sérsic population presented in Figure 4.7 by the dashed blue, green, and red curves. 131

4.11 For dwarfs with stellar masses $M_\star > 10^{8.5} M_\odot$, the inferred shape distribution for field (distance to nearest neighbor $\mathrm{d_{NN}} > 1$Mpc) and satellite ($\mathrm{d_{NN}} \leq 1$Mpc) galaxies. We see negligible difference between satellite and field galaxies; both are consistent with thick discs at $1\mathrm{R_{eff}}$, and C/A increases towards spheroid shapes at larger distances from the galaxy center. As in Figure 4.9, we show the analogous contours of the pure disk, prolate, and spheroid Sérsic population presented in Figure 4.7 by the dashed blue, green, and red curves. 132

4.12 The change in galaxy thickness (C/A) as a function of radius for $10^9 < M_\star/M_\odot < 10^{9.6}$ (top) and $10^{8.5} < M_\star/M_\odot < 10^9$ (bottom). In both cases, the dwarfs become systematically more spheroidal (C$\sim$A, $B/A \gtrsim 0.8$ for all cases) at large radii. For physical context, we also show the C/A axis ratio of the Milky Way thin disk & thick disk [Schönrich and Binney, 2009], and the stellar halo at $R = 0$ & $R = 6\mathrm{R_{eff}}$ [Iorio and Belokurov, 2019]. The MW axis ratios are shown by vertical black lines, as labeled in the bottom panel. 135

4.13 The residual sky in the HSC-i band near our sample as measured from nearby Sky Objects in the vicinity of our target galaxies. The sky background is measured as a function of Sky Object aperture size for Sky Objects within 100" (green, 43149 Sky Objects) and 200" (purple, 172974 Sky Objects) of our target galaxy sample. At left, we give the sky background in counts/pixel. At right, we show the change in surface brightness expected for an object with surface brightness 28.5 mag arcsec^{-2}. The solid curves show the median sky residual, while the shaded regions show the 25$^{\rm th}$ and 75$^{\rm th}$ percentiles. We find that the residual background has a negligible impact ($\lesssim$ 0.02 mag arcsec^{-2}) on the surface brightness measured at our nominal surface brightness limit of 28.5 mag arcsec^{-2}. 143

4.14 *Left:* the distribution of effective radius and projected axis ratio for a sample drawn from the posterior distribution for a model where we allow for a non-zero covariance between C/A and $\mathrm{R_{eff}}$. *Middle:* the distribution over $\mathrm{R_{eff}}$ and projected axis ratio (b/a) for the observed galaxies. *Right:* the inferred distribution over intrinsic axis ratios for the fiducial model (orange filled contours) and the model at left (green unfilled contours). 146

4.15 For a population of mock disk galaxies described by $\vec{\alpha} = \{\mu_B, \mu_C, \sigma_B, \sigma_C\} = \{0.9, 0.1, 0., 0.\}$, we investigate the precision at which the model parameters $\vec{\alpha}$ may be recovered as a function of sample size N. The top row shows, in each panel, the true distribution of the projected axis ratio b/a in teal and the posterior sample in orange. Individual draws from the posterior are shown in grey. The bottom row shows the distribution of intrinsic axis ratios (B/A and C/A) from the posterior sample in orange. The maximum a posteriori estimate is shown by the black ellipse. The pure disk, prolate, and spheroidal populations are shown by dashed contours (see Figure 4.7). A successful recovery is one in which the orange contours of the posterior samples coincides with the dashed blue contours of the pure disk population. 147

5.1 Example grz RGB cutouts from the three imaging sets considered in this work. The top row shows an example from the red end of the sample ($(g-r) > \langle(g-r)\rangle_{75}$, where $\langle\rangle_{XX}$ indicates the $XX^{\rm th}$ percentile), while the bottom shows an example from the blue end ($(g-r) < \langle(g-r)\rangle_{25}$). Note that because the Legacy Survey UDG sample was originally selected to have HI, the red end of the distribution is still relatively blue in absolute terms. Each example in the figure is chosen to have approximately the same mean effective g-band surface brightness of $\langle\mu\rangle_{\rm R_{eff}} \sim 25$ mag arcsec^{-2}. The cutouts of the HSC and DES imaging are 20" on a side, while the Legacy Survey cutout is 40" on a side. The galaxies shown for each sample are (top panel, bottom panel): HSC (LSBG-325, LSBG-211), DES (ID224789651, ID214498053), and Legacy (AGC114754, AGC336397). 149

5.2 Surface brightness distributions of the red ($(g-i) > 0.64$) galaxies in the DES [Tanoglidis et al., 2021, red] and HSC-SSP [Greco et al., 2018c, , black] LSBG samples. The $\langle\mu\rangle_{\rm R_{eff}} = 26.5$ mag arcsec^{-2} 80% completeness limit for the HSC-SSP LSBG sample (Greco et al., in preparation) is shown by the dotted black vertical line. We empirically measure the completeness limit of the DES sample as the $\langle\mu\rangle_{\rm R_{eff}}$ at which the surface brightness distribution diverges from that of the deeper HSC-SSP sample. . 151

5.3 We compare the distribution in absolute r-band magnitude and physical effective radius for the samples examined in this work. We show in green a contextualization of the Greco et al. [2018c] HSC-SSP LSBG sample M_r and effective radius distribution as computed by assuming that all galaxies in the LSBG sample are at the cross-correlation median distance of 60 Mpc (Greco et al., in prep.). We show the same quantities computed for the HI-selected sample using the HI redshifts measured by Leisman et al. [2017] and Janowiecki et al. [2019] by the unfilled blue histogram. Finally, we show the Coma Cluster UDGs of Alabi et al. [2020] by the unfilled orange histogram (dashed lines). Though the DES sample is not shown in this figure, we expect that the DES sample is similar in mass and size to the HSC sample. 152

5.4 Ellipticity versus surface brightness for the four samples considered in this work, as labeled. We use these diagnostic plots to demonstrate that the distribution of ellipticity does not change over the range of surface brightnesses considered in this work, supporting our assumption that the full sample can be characterized by a single distribution in three-dimensional shape, and to visually illustrate the different depths of the four samples. 155

5.5 A schematic diagram to illustrate movement in the B/A vs. C/A plane. The red, green, and blue points show the position of an archetypal spheroidal, prolate, and disky ellipsoid, respectively. The axis ratios are (B/A,C/A) = (0.9,0.9), (0.1,0.1), and (0.9, 0.1) for the three cases. At right, we show a three-dimensional representation of the ellipsoid that corresponds to each case in the corresponding color. We additionally show the principal axes A, B, and C as grey, gold, and magenta lines in each panel. 159

5.6 The distribution of Sérsic indices for the red ($g - i > 0.64$) and blue ($g - i < 0.64$) HSC LSBGs [Greco et al., 2018c, filled histograms] and DES LSBGs [Tanoglidis et al., 2021, unfilled histograms]. Though there is a an offset between the HSC and DES measurements, there is no significant difference between the red and blue subsets of each sample. We also show the HI-selected (dot-dashed green) and Coma (dotted orange) UDGs, which are also consistent with the LSBG distribution of Sérsic indices. 160

5.7 The inferred intrinsic axis ratios for the galaxy samples considered in this work: from the top left, the HSC-SSP, the DES sample, the HI-selected galaxies, the red galaxies of the DES sample ($g - i < 0.64$), the blue galaxies of the DES sample ($g - i \geq 0.64$), and the Coma UDGs. The filled contours show the inference results when only ellipticity is fit, while the unfilled turquoise contours in the DES panels show the inference results when both surface brightness and ellipticity are fit. The unfilled dashed contours show the results of recovery tests for a disky (blue), prolate (green), and spheroidal (red) population via ellipticity-only inference. The bottom panel shows the distribution over projected axis ratio ($\mathrm{b/a} = 1 - \epsilon$) for each sample. There is no signficant difference between the inferred shapes of the joint models and ellipticity-only models, indicating that incompleteness due to surface brightness limits does not induce a significant bias in the observed ellipticity distributions of the LSBGs. 161

5.8 Recovery results for joint inference of the samples; from left to right: the full DES sample, red DES LSBGs, and blue DES LSBGs. *Top row:* The surface brightness distribution for each population. The thick orange curve shows our posterior sample (thin orange curves show individual pulls from the posterior). The solid teal histograms show the observed population. Unfilled black histograms show model projections which fall outside of the sample surface brightness limits. *Middle row:* the same for the ellipticity distributions. *Bottom row:* we show the intrinsic axis ratio distribution of the posterior sample as filled orange contours. The maximum a posteriori results are shown by black ellipses. We note that the joint inference does not converge for the HSC-SSP and HI-selected samples due to the low number of objects; we thus use only the ellipticity-only inference for these samples. 162

5.9 *Left:* A comparison between the results presented in this work (filled orange contours) and observational results from the literature. Our results are in good agreement with the group/cluster UDG samples of Burkert [2017] (who assumes a non-triaxial model where B/A=C/A) and Rong et al. [2020], indicating that the intrinsic shape distribution of LSBGs is not strongly affected by their environment. We also compare our results to those of the "normal" high surface brightness dwarf populations at $1R_{eff}$ presented in Kado-Fong et al. [2020b]. We find that the LSBG sample is significantly rounder (higher C/A) than the massive dwarfs of Kado-Fong et al. [2020b]. Errorbars on the HSB points show the inferred 1σ dispersion of the HSB sample, not the error on the mean values. *Right:* A comparison between the inferred intrinsic shapes of red and blue LSBGs (unfilled red and blue contours, respectively) presented in this work and theoretical predictions from the literature. For visual clarity, we show only the contours that contain 68% of our inferred LSBG shapes in order to be consistent to the plotted errorbars of the Romulus and NIHAO simulations, for which the errorbars span the 16th to 84th percentiles. We find that the intrinsic shape distributions vary significantly between the simulations considered. In particular, Auriga [Liao et al., 2019] predicts a strong shape divergence between blue and red UDGs, while NIHAO [Jiang et al., 2019, Cardona-Barrero et al., 2020] predicts significantly more triaxial (for dispersion-dominated UDGs) or flatter (for rotation-supported UDGs) shapes than those inferred from observed LSBGs. Romulus appears to well-produce the shape distribution of blue LSBGs, but overpredicts the shape evolution between blue and red LSBGs. 163

5.10 Recovery results for joint inference of the three extreme mock populations presented in Kado-Fong et al. [2020b]. Each column shows a different mock population; from left to right, we show the disk, spheroid, and prolate mock populations. *Top row:* The surface brightness distribution for each population. The thick orange curve show our posterior sample (thin orange curves show individual pulls from the posterior). The solid teal histograms show the observed population. *Middle row:* the same for the ellipticity distributions. *Bottom row:* we show the intrinsic axis ratio distribution of the posterior sample as filled orange contours. The analogous results from ellipticity-only inferences are shown by the dashed contours. 178

6.1 The surface density of young stars (left column, star particles with ages less than 2 Gyr), old stars (middle column, star particles with ages greater than 12 Gyr), and HI (right column) for an example dwarf with a disk-halo structure, m11h (MHD+). The rows show the projection along the y-axis, x-axis, and z-axis, such that the z-axis is aligned with the disk minor axis. 182

6.2 The intrinsic shape of the young and old stellar populations for the three subsets of the sample we consider in this work. In each panel, the green filled circles show the intrinsic shape of the young (ages less than 2 Gyr) stellar population and the orange squares show the intrinsic shape of the old stellar population (ages older than 12 Gyr). Lines connect the measurements for each individual galaxy. The blue and red ellipses show the observed 1σ distribution of the dwarf sample of Kado-Fong et al. [2020b] at $1R_{eff}$ and $4R_{eff}$, respectively. At left a comparison sample of high-mass ($M_\star > 10^{10} M_\odot$) galaxies is shown; these galaxies host a clear disk-halo transition between their young and old stellar populations, where the youngest stars are assembled in a thin disk and the oldest populate a spheroidal stellar halo. The center panel shows the sample of dwarf galaxies that host a disk halo system; the disks in these dwarfs are thicker (higher C/A) than those of the higher mass galaxies, while the old stellar components are less round (lower C/A). Finally, at right, we show the non-disky dwarfs in the sample, which are characterized by the lack of a young stellar disk, as well as the lack of a monotonic increase in C/A and the presence as a significant change in B/A function of age. 183

6.3 *At left:* the change in minor-to-major intrinsic axis ratio C/A as a function of stellar age, in bins of 2 Gyr. We show the change in C/A over the minimum C/A across all age bins (because of the monotonic increase in C/A as a function of age for these galaxies, this is equivalent to the change in C/A over the youngest age bin). Dwarf disks are shown in purple, while high-mass disks are shown in grey. Not only are the old stellar populations of the dwarf disks less spheroidal than their high-mass counterparts, d(C/A)/d(age) is markedly smaller in the dwarfs than the high-mass galaxies. *At right:* the stellar surface density of an example dwarf (top two rows) and massive galaxy (bottom two rows) in bins of 2 Gyr. As at left, while the dwarf stellar population thickens gradually with increasing age, there is a sharp transition between the thin disk and round stellar halo in the more massive galaxy – this contrast is consistent with the differing origin of the dwarf and massive stellar outskirts, wherein dwarf stellar halos are produced via in-situ migration of star particles rather than the accretion of satellites. 197

6.4 *Left:* particle distance from host galaxy center versus time for two high-mass galaxies (m11f (MHD+) and m11g (MHD+), grey-outlined panels) and two disky dwarfs (m11h (MHD+) and m11b , purple-outlined panels), colored by particle age at $z = 0$. The dashed (dotted) black lines show the 3D radius that contains 90% (50%) the stellar mass at $z = 0$. *Right:* distribution over maximum distance from host achieved for star particles younger than 2 Gyr (blue), between 6 and 8 Gyr (orange), and older than 12 Gyr (red). Median values for $R_{\rm max}$ for each age component are shown by the colored vertical lines. The oldest stars in the massive galaxies are dominated by accreted star particles that remain on large-apocenter orbits to $z = 0$. 198

6.5 *Lefthand panels:* To diagnose the origin of the star particles that populate the stellar halo for the galaxies in this work, we plot the maximum distance between the youngest (ages < 2 Gyr) and oldest (ages > 12 Gyr) star particles and the host center against their $z = 0$ distance. These populations are good tracers of the disk and halo structures, if such structures exist. Star particles with an in-situ origin should flare from the 1:1 line (the dashed black line and physical minimum), while accreted particles populate horizontal bands due to a shared maximum distance that corresponds with the original distance between the main host and progenitor system. As a visual aid, we show a maximum offset of 15 kpc as the dotted grey line. In this space, it is clear that while the massive galaxy (m11f, MHD+), is dominated by an accreted stellar halo (bottom right panel), the dwarf galaxy (m11h, MHD+), old stellar populations are largely in-situ structures. The x-axis and y-axis limits are set at $2/3\mathrm{R_{vir}}$ and $\mathrm{R_{vir}}$, respectively. *Right panel:* For the full sample of disky dwarfs (m11v (MHD+) is excluded due to a central halo tracking issue at high redshift resulting from an ongoing interaction at $z = 0$) and massive galaxies ($\mathrm{M_\star} > 10^{10}\mathrm{M_\odot}$), the fraction of star particles with a lifetime radial displacement of greater than 15 comoving kpc ($\Delta\mathrm{R} = \mathrm{max_R\,R(z) - R(z = 0)}$), $\mathrm{f_{\Delta R>15kpc}}$. We show this quantity both for the old star particles (filled circles, ages greater than 12 Gyr) and the star particles with large $z = 0$ distances from host halo center (unfilled circles, $\mathrm{R} > 15$ kpc). Both the old stars and stars in the outskirts show an increasing fraction of high-displacement (likely ex-situ) stars as a function of stellar mass, in agreement with the picture of an increasingly in-situ-dominated stellar halo for dwarf galaxies. 199

6.6 For a massive (grey, $M_{halo} \sim 10^{12} M_\odot$) and dwarf (purple, $M_{halo} \sim 10^{11} M_\odot$) disk galaxy, we show the change in the exponential stellar scale height h_z as a function of age. For the star particles with a given age, the solid curves show the current, z = 0 scale height of those star particles, while the dashed curves show the scale height of the same single-aged population at $z = z_{form} = z(t_{lb} = \text{age})$. We exclude stars older than 10 Gyr, as in the massive galaxy they are likely to be dominated by ex-situ stars which should not be well-described by an exponential distribution at birth. Whereas the stars in the massive galaxy show a negligible change in vertical scale, the dwarf stars are consistently more extended at current times than they were at their formation time. This is consistent with the picture in which the dwarf stellar outskirts are populated by stars that have been heated to larger radii after their formation. In contrast, the massive galaxy FIRE-2 thick disks are formed due to an overall change in the configuration of star formation as a function of cosmic time (see Yu et al. 2021). 200

6.7 Mock HSC-i band surface brightness maps (top row) and HSC-i light-weighted age maps (bottom row) for an example set of galaxies which span the mass and morphologies studied in this work. From left to right, we show: m11h (CR+), a disky dwarf at the high end of the dwarf stellar mass range ($M_{\star,90} = 3 \times 10^9 M_\odot$), m11b (MHD+), a disky dwarf at the low end of the dwarf stellar mass range ($M_{\star,90} = 7 \times 10^7 M_\odot$), m11c (Hydro+, no MD), a non-disky dwarf, and m11g (MHD+), a massive galaxy ($M_{\star,90} = 5 \times 10^{10} M_\odot$). The lime contour in each panel is an isophote at $\mu_i = 28.5$ mag arcsec^{-2}, the approximate surface brightness limit of the HSC-SSP i-band for galaxy outskirts. The values written in lime at the bottom of the top row of panels show the approximate maximum radius that HSC-SSP observations would be able to reach for each galaxy, as a function of the i-band effective radius of the galaxy (as determined by a single two-dimensional Sérsic fit). 201

6.8 The HI gas fraction $M_{\rm HI}/(M_\star + M_{\rm HI})$ versus stellar mass for the simulated FIRE-2 galaxies (marked as crosses) and the observed sample of [Bradford et al., 2015, light grey scatter]. The FIRE-2 galaxies are colored by morphology, as indicated. The FIRE-2 dwarfs tend to be overly HI-depleted compared to observed galaxies [see also El-Badry et al., 2018a], so the gas rich end of the FIRE-2 dwarfs are the most consistent with observations. In particular, the galaxies that successfully form disks have HI gas fractions consistent with the observed relation, while the non-disky dwarfs are systematically gas depleted relative to the Bradford et al. [2015] sample. 202

6.9 At left, the fraction of stellar mass built up in bursts (defined as time periods where $\langle {\rm SFR} \rangle_{\rm 10Myr}/\langle {\rm SFR} \rangle_{\rm Gyr} > 1.5$) versus stellar mass for the sample of FIRE-2 dwarfs. The purple points show disky dwarfs, while the green points show the non-disky dwarfs, and the grey points show the non-dwarfs. The low-mass dwarfs that have HI gas fractions of greater than $(M_{\rm HI}/(M_\star + M_{\rm HI}) = 0.7$ are shown with a dashed outline. We find that the dwarfs that are able to form a young stellar disk have either particularly quiescent (non-bursty) recent star formation histories, or are particularly gas rich relative to the other simulated galaxies. At right we show the star formation history for a non-disky dwarf (top, m11d (Hydro+, MD)) and a disky dwarf (bottom, m11h (Hydro+, MD)). In each panel we show the 10 Myr-averaged and Gyr-averaged star formation rates as the light and dark curves, respectively. We also show vertical lines at $t_{\rm lb} = 2$ Gyr, the time period over which the burst mass fraction is computed. 203

6.10 The maximum a posteriori (solid curves) and standard deviation (shaded regions) estimates of the observational intrinsic shape parameters as a function of the fraction of the mock sample that is drawn from the non-disky galaxy distribution. The solid black line (region) in each panel shows the maximum a posteriori estimate (standard deviation) of the $f_{non-disky} = 0$ sample. Clockwise from top left, we show: μ_B, the mean axis ratio B/A, μ_C, the mean axis ratio C/A, σ_B, the standard deviation of B/A, and σ_C, the standard deviation of C/A. As the non-disky fraction increases, the mean B/A decreases and mean C/A increases, consistent with a more non-disky shape overall. 216

6.11 The L2-norm, ℓ_2, calculated between the inferred shape parameters of the mock observational sample as a function of the mock sample that is drawn from the non-disky galaxy distribution. The errors reflect the propagation of errors using the standard deviation of the MCMC chains as the uncertainty on the inferred shape parameters. 218

6.12 *Left:* the results of the mock observational inference for m11h (CR+) at one effective radius. The inset panel shows the distribution of the projected axis ratio b/a for 1000 instances of random projections of the FIRE-2 dwarf in green; the orange curve shows the model output from the inference machinery (600 steps with 300 burn-in; walker convergence is checked manually). Light grey curves show individual draws from the posterior. The main panel shows the same model in intrinsic axis ratio space; the direct cumulative measurement for the young (age $<$ 2 Gyr) star particles is shown by the black X. The colored, dashed contours show results for toy models of a disk (blue), spheroid (red) and prolate (green) galaxy under HSC wide imaging conditions. *Right:* the same, but for differential measurements at four effective radii and cumulative measurements of old (age $>$ 12 Gyr) star particles. In both cases, the differential and cumulative shape measurements well-trace each other. 219

6.13 Projections of young stars (left), old stars (middle), and HI gas (right) for the disky dwarf m11b (Hydro+, no MD) in the same format as Figure 6.1. 221

6.14 Projections of young stars (left), old stars (middle), and HI gas (right) for the non-disky dwarf m11c (Hydro+, no MD) in the same format as Figure 6.1. 222

7.1 A comparison of the integrated properties of the samples derived in this work against the directly measured result of Leroy et al. [2008] (beige points). In all panels, the red points show UDGs and the purple points show NSA dwarfs. From left, we show the relationship between stellar mass and HI mass, the relationship between HI mass and SFR, and the star-forming main sequence (SFMS). In the SFMS panel, we also show the results of the SDSS DR7 MPA-JHU added-value catalogs in greyscale [Kauffmann et al., 2003, Brinchmann et al., 2004, Salim et al., 2007]. We find a good agreement between our results and those from the literature. Although the UDGs have high HI masses for their stellar mass (left panel), they have relatively little SFR for their HI mass (middle panel). 224

7.2 *Top:* 21 cm line flux (S_{21}) versus redshift for the NSA (purple) and UDG (red) samples. The nominal ALFALFA flux limit is shown by the dashed black line, while the minimum S_{21} of the UDG sample is shown in red. The unfilled symbols show the expected S_{21} of each of the galaxies in the UDG sample *if* we assume that the distribution over HI fraction of the underlying UDG population is identical to that of the NSA dwarfs. *Bottom:* the distribution over observed HI fractions for the NSA (filled purple histogram) and UDG (unfilled red histogram) samples. The hatched red histogram shows the distribution of HI fractions that we would *expect* to see from the UDG sample if the distribution over HI fractions is identical between the UDG population and NSA sample. We thus conclude that the UDG sample is inconsistent with having the same distribution over f_{HI} as the NSA sample. 225

7.3 Estimates of the SFR, stellar mass, and HI surface densities in a globally averaged sense; i.e., the ratio between the integrated measurement and the isophotal size of the galaxy. UDGs are shown in red and NSA dwarfs in purple for all cases. In this figure, we exclude all NSA dwarfs with stellar masses exceeding $M_\star = 10^9 M_\odot$. . . . 227

7.4 A comparison between our estimates of the HI surface density radial profiles for the UDG (red solid curves) and NSA (purple solid curves) samples against spatially resolved HI measurements of dwarfs from the literature. We show the direct radial profiles of Leroy et al. [2008] in green, and Sérsic fits inferred for a sample of HI-rich UDGs from the HI spatial distribution metrics provided by Gault et al. [2021] in orange. We find that our radial profile estimates are in good agreement with these direct literature measurements. 230

7.5 A schematic layout of the fitting technique used in this work. At left, we represent the high-resolution optical data and low-resolution UV data (panels *a* and *c*, respectively). Panels *b* and *d* represent the global fit between the optical and UV data; in this step, the apertures are matched between the optical and UV data. Panel *e* shows the spatial division of the optical data into regions in which regional SEDs are measured. Panel *f* shows the clustering of these spatial regions into three representative clusters; these cluster SEDs will be fit jointly with the global UV photometry (panel *d*). 233

7.6 An example of the fitting process for one of the NSA galaxies (NSA ID 5449). *Top row:* from left, the HSC *gri*-composite image, the SED cluster map (analogous to panel *f* of Figure 7.5), and the joint UV-optical SED fit. The joint model SED is the result of fitting the spatially resolved (cluster) optical photometry and global UV photometry. The black curves show the model spectra, while the orange points show the model photometry for each filter. The red points show the global UV-optical photometry. The model fitting and figure fluxes are computed as HSC counts. *Middle row:* optical-only results for the individual cluster SEDs. The color of the title text corresponds to the color of the region in the top middle panel; the format is equivalent to the joint SED fit (top right), with the addition of the SEDs measured in individual spatial regions as blue points. *Bottom row:* the resultant stellar mass (left) and SFR (right) maps. 234

7.7 *Top:* a comparison between the best-fit stellar masses of the NSA (purple) and UDG (red) samples using the global photometry (y-axis) and the spatially-resolved optical photometry (x-axis). *Bottom:* the same as above, but for SFR. 239

7.8 *Left:* a comparison between the stellar masses of the galaxies in this work (x-axis) and their catalog NSA stellar masses. The dashed line and shaded regions show the median, and range between the $16^{\rm th}$ and $84^{\rm th}$ percentiles of the deviation $\log_{10}(M_\star/M_\odot) - \log_{10}(M_{\star,\rm NSA}/M_\odot)$. *Middle:* the same, but for SED fitting-derived SFRs and FUV-only SFRs as computed from the catalog *GALEX* measurements using the SFR(FUV) prescription of Kennicutt [1998]. *Right:* a comparison between SFRs derived from the Hα fluxes measured from SDSS 3" fiber fibers (x-axis) and the total SFR within the central 3" of our SED fits (y-axis, red). The dashed black line denotes a 1:1 relation. As in the left panel, the dashed purple line and shaded purple regions show the median, and range between the $16^{\rm th}$ and $84^{\rm th}$ percentiles. SFRs derived from Hα measure star formation over a shorter timescale ($\sim$ 10 Myr) than our SED fits (100 Myr), and some physical scatter is expected as a result; we show the standard deviation (in logarithmic space) of the difference between Hα-derived and FUV-derived SFRs for a set of Local Volume dwarfs from Karachentsev et al. [2021] as a visual aid to the reader in gauging the scatter. 240

7.9 A comparison between radial profiles in stellar mass surface density (left) and star formation rate surface density (right) from our SED fitting method (solid curves) as compared to direct measurements from [Leroy et al., 2008, dashed curves]. The color of the curves show the integrated stellar mass of the galaxy in all cases. We find that there is good agreement between our radial profiles and the directly measured profiles in both amplitude and extent. 242

7.10 A comparison between HI surface density estimates and SFR surface density measurements averaged over 500 pc, 1 kpc, and global scales. In all panels, we only show NSA galaxies that are within the stellar mass range of the UDG sample (i.e. $M_\star < 3 \times 10^8$ $M_\odot$). For visual clarify, we show a random subset of (at most) 70 points for each sample with individual errorbars and colored by sample source; we show the full sample as the underlying grey scatter. Here, we demonstrate that the low SFE(HI) that characterizes the globally averaged properties of the UDGs persists down to sub-kpc scales. 244

7.11 A comparison between various measures of galaxy mass and galaxy size; the top row shows size as a function of HI mass, while the bottom row shows size as a function of stellar mass. The left column shows size as measured by the HSC-g band half-light radius, while the right column shows size as measured by the half stellar mass radius. In each panel, the purple dashed line shows the least squares power law fit to the NSA galaxies. The red dashed line shows the least squares fit to the UDG sample when the index of the power law is held fixed to that of the NSA dwarf fit. The shaded regions span the 16th to 84th percentiles as estimated from bootstrap resampling. As one expects, the UDG sample is large in size for their stellar masses. However, their half-stellar mass radii are unremarkable for their HI masses. 245

7.12 Optical color versus stellar mass-to-light ratios in the HSC-g band computed for our UDG (red) and NSA (purple) samples. We find no significant difference in the color-mass relation between the two samples, and additionally find the samples to be reasonably well-described by color-mass relations from the literature (Into and Portinari 2013 as the dashed line, Bell et al. 2003 as the dotted line). 246

7.13 A sample of three example galaxies from the NSA sample, as labeled. From left, we show the HSC-SSP gri-composite RGB image, the median star formation rate surface density map, and the median stellar mass surface density map. These galaxies are chosen to span the range of morphologies present in the sample. 256

7.14 A sample of three example galaxies from the UDG sample, as labeled. From left, we show the HSC-SSP gri-composite RGB image, the median star formation rate surface density map, and the median stellar mass surface density map. These galaxies are chosen to span the range of morphologies present in the sample. 257

8.1 The distribution over ρ_{sd} for our fiducial dark matter halo assumptions (see text) for the NSA dwarfs (purple) and UDGs (red) at 500 pc, 1 kpc, and global scales from left to right. The shaded regions are bounded by the $16^{\rm th}$ to $84^{\rm th}$ percentiles of the distribution. The NSA dwarfs are characterized by systematically higher stellar+dark matter densities, which is unsurprising given that the UDGs are characterized by low stellar surface densities. 262

8.2 The distribution over $P_{\rm DE}$ for the NSA dwarfs (purple) and UDGs (red) at 500 pc, 1 kpc, and global scales from left to right. The shaded regions at 500 pc and 1 kpc are bounded by the $16^{\rm th}$ to $84^{\rm th}$ percentiles of the distribution. We find no significant variation in $P_{\rm DE}$ as a function of spatial scale, but find that the NSA dwarfs have systematically higher dynamical equilibrium pressures than the UDG dwarfs. 266

8.3 The contribution of self-gravity to the total midplane weight ($\mathcal{W}_{\rm gas}/\mathcal{W}$) as a function of dynamical equilibrium pressure ($P_{\rm DE}$) as a function of spatial scale (500 pc to global average, from left to right). We show individual errorbars for a random sample of regions from the UDG sample (red) and the NSA sample (purple); the full sample is shown in grey. Note that the tracks visible in the left and middle panels are a result of the median assumed HI profiles; the uncertainty in the HI profiles result in a larger dispersion in $\mathcal{W}_{\rm gas}/\mathcal{W}$ than is implied by the tracks alone (as is shown by the errorbars of the colored points). We find that the external weight ($\mathcal{W}_{\rm ext}$) is relatively less important in the UDGs as compared to the NSA dwarfs. 269

8.4 *Top Row:* a comparison between HI surface density estimates and SFR surface density measurements at 500 pc (left column), 1 kpc (middle column), and global scales (right column). In all panels, we only show NSA galaxies that are within the stellar mass range of the UDG sample. For visual clarity, we show a random subset of (at most) 70 points for each sample with individual errorbars and colored by sample source; we show the full sample as the underlying grey scatter. *Bottom row:* a comparison between the observed SFR surface densities and the PRFM predictions. Again, red points show UDGs while purple points show NSA dwarfs. 274

8.5 *Left:* an estimate of the dynamical equilibrium pressure (P_{DE}) for our sample. We overplot the theoretical (Equation 8.6) and numerical (Equation 8.7) predictions of Ostriker & Kim (2022, in preparation) as the dashed and solid lines, respectively. *Right:* an empirical estimate of $\Upsilon_{\rm tot}$ as a function of $P_{\rm DE}$. We compare to kpc-scale observations from PHANGS [orange dot-dashed, Sun et al., 2020], EDGE-CALIFA [blue dot-dashed, Barrera-Ballesteros et al., 2021], and KINGFISH [green dot-dashed, Herrera-Camus et al., 2017], as well as to the predictions of Ostriker & Kim (2022, in preparation). 275

8.6 The estimated H_2 fraction (where $f_{H_2} = \Sigma_{H_2}/[\Sigma_{H_2} + \Sigma_{\rm HI}]$) for the regions in our sample at 500 pc (left), 1 kpc (middle), and global scales (right) when we assume a constant H_2 depletion time of $\tau_{\rm dep} = \Sigma_{H_2}/\Sigma_{\rm SFR} = 1.8$ Gyr. The red histograms shows the UDGs, while the purple histograms show the NSA dwarfs. We find that while the distribution in f_{H_2} peaks at $f_{H_2} < 0.2$ for both the UDGs and NSA galaxies, the NSA dwarfs are characterized by a tail to high molecular gas fractions. This finding is consistent with the under-prediction of the HI-only PRFM estimate for the highly star-forming regions of the NSA galaxies (as shown in Figure 8.4). 277

8.7 A comparison between the expected CO (1-0) luminosities of our NSA (purple) and UDG (red) dwarf samples and real measurements from the literature. We estimate L_{CO1-0} by assuming a constant H_2 depletion time of $\tau_{dep} = 1.8$ Gyr and bounding our estimates from α_{CO} measurements of the LMC and SMC [Schruba et al., 2011]. We find that the expected CO luminosities of the galaxies in the present sample are comparable to measurements made of galaxies at lower distances, but lie well below literature measurements of galaxies at similar distances. 277

8.8 *Left:* The observed versus estimated Σ_{SFR} for our UDGs under our fiducial assumptions about their dark matter halos (blue filled contour) and for low concentration halos (unfilled red contour). For this demonstration, we hold the halo mass constant between the fiducial and low-concentration predictions. *Right:* A comparison between our fiducial and low concentration results in the dynamical pressure versus empirical Υ_{tot} plane. We show the Ostriker & Kim (2022, in preparation) theoretical and simulation-driven predictions by the dashed and solid black lines. 278

9.1 A preliminary demonstration of the continuum subtraction for the Merian survey for a $M_\star \sim 10^8$ $M_\odot$ galaxy at $z_{spec} = 0.092$. The top row shows the subtraction for the Hα filter (N708), while the bottom shows the same for the [OIII]+Hβ filter (N540). In each row, the left panel shows the average of the nearest two broad-bands (r_{HSC} and i_{HSC} at top, g_{HSC} and r_{HSC} at bottom), the middle panel shows the medium-band image, and the right panel shows the difference between the medium-band and composite broad-band images. This figure is intended for visualization purposes only, and does not include a correction between the HSC and DECam point spread functions. 287

9.2 The predicted, volume-scaled mass-size relation predicted by the Merian survey (blue points) as compared to the GAMA survey (red). Merian non-detections are shown in grey points. Merian reaches lower stellar masses than GAMA over a larger volume (GAMA is mass-complete to $M_\star = 10^9 M_\odot$ at $z = 0.05$, roughly 5.5% of the Merian volume). 288

Chapter 1

The Low-Mass Galaxy Population

Dwarf galaxies are, by number, the most common type of galaxy in the Universe at all redshifts. Due to their intrinsic faintness, however, our understanding of the low-mass galaxy population has historically lagged behind our knowledge of their more massive counterparts. Indeed, their low stellar masses ($M_\star \lesssim 10^9 M_\odot$) renders difficult a complete census of the low-mass galaxy population in both the realm of observations, where their low luminosities make collecting complete samples difficult beyond the Local Universe, and in the realm of cosmological simulations, where their low masses demand high spatial and mass resolution. Nevertheless, these dwarf galaxies are crucial testing grounds for our understanding of dark matter, star formation, and cosmology.

Dwarf galaxies have long been key players in controversies surrounding our understanding of the nature of dark matter and the problems of the ΛCDM (cold dark matter) cosmological paradigm [the "core-cusp" problem, the "too big to fail" problem, the "missing satellites" problem, the "plane of satellites" problem, Bullock and Boylan-Kolchin, 2017]. It is only recently that simulations have begun to produce more realistic models of dwarf galaxies [Peñarrubia et al., 2012, Fritz et al., 2018]; these advancements have come largely from improvements in modeling the effect of baryons. Star formation feedback is, in particular, a strong driver of dwarf galaxy assembly and evolution; due to their shallow potential wells, dwarf galaxies are keenly sensitive to the details of star formation feedback [El-Badry et al., 2016, Kado-Fong et al., 2020b, Smith et al., 2020]. However, our under-

standing of the physics of star formation still falls far short of fully explaining the properties of the low-mass galaxy population [El-Badry et al., 2018a, Kado-Fong et al., 2022c]. Indeed, dwarf galaxies are the observable key to solving long-established and fundamental questions across a wide array of fields, from cosmology to star formation physics. This thesis centers around the exploration of dwarf galaxy structure for large samples of massive dwarfs beyond the Local Universe ($N \gtrsim \mathcal{O}(100)$, $10^7 \lesssim \mathrm{M}_\star/\mathrm{M}_\odot \lesssim 10^9$, $d \gtrsim 10$ Mpc), and the interplay between this structure and the astrophysical processes that shape the dwarf population.

1.1 An Abbreviated History of the Imaging and Cataloging of Dwarf Galaxies

Before we consider the astrophysical importance of dwarf galaxies, it is of interest to consider the history of the study of these low-mass galaxies. The Large Magellanic Cloud (LMC) and Small Magellanic Cloud (SMC), at $\mathrm{M}_\star \sim 3{\times}10^9\mathrm{M}_\odot$ [van der Marel, 2006, Besla, 2015] and $\mathrm{M}_\star \sim 3{\times}10^8\mathrm{M}_\odot$ [Besla, 2015], are the closest and best-known examples of dwarf galaxies. The LMC and SMC are naked eye objects and large on the sky, with apparent diameters of $11^\circ.8$ and $4^\circ.2$. Both the LMC and SMC are readily visible in a dark southern sky, and are known to be part of Aboriginal Australian legend as the camping sites of an elderly couple known as Jukara [Filipovic et al., 1996, Haynes et al., 2010]. The LMC may have additionally appeared in astronomical catalogs as early as 964 via the work of the Persian astronomer Al-Sûfi, though the names "Large Magellanic Cloud" and "Small Magellanic Cloud" are derived from observations made during the voyage lead by Ferdinand Magellan (Fernão de Magalhães) circa 1520 [Filipovic et al., 1996].

Dwarf galaxies are thus almost certainly the first known class of external galaxies, though their status as external galaxies (or indeed the existence of a Universe beyond the Milky Way) was established only about one hundred years ago [Hubble, 1926], due in great part to work done to calibrate period-luminosity relations in the SMC [Leavitt and Pickering, 1912].

Despite being among the first type of galaxy to be discovered, however, the low mass of dwarf galaxies has hindered statistical studies of the dwarf population in wide-field surveys. Even at

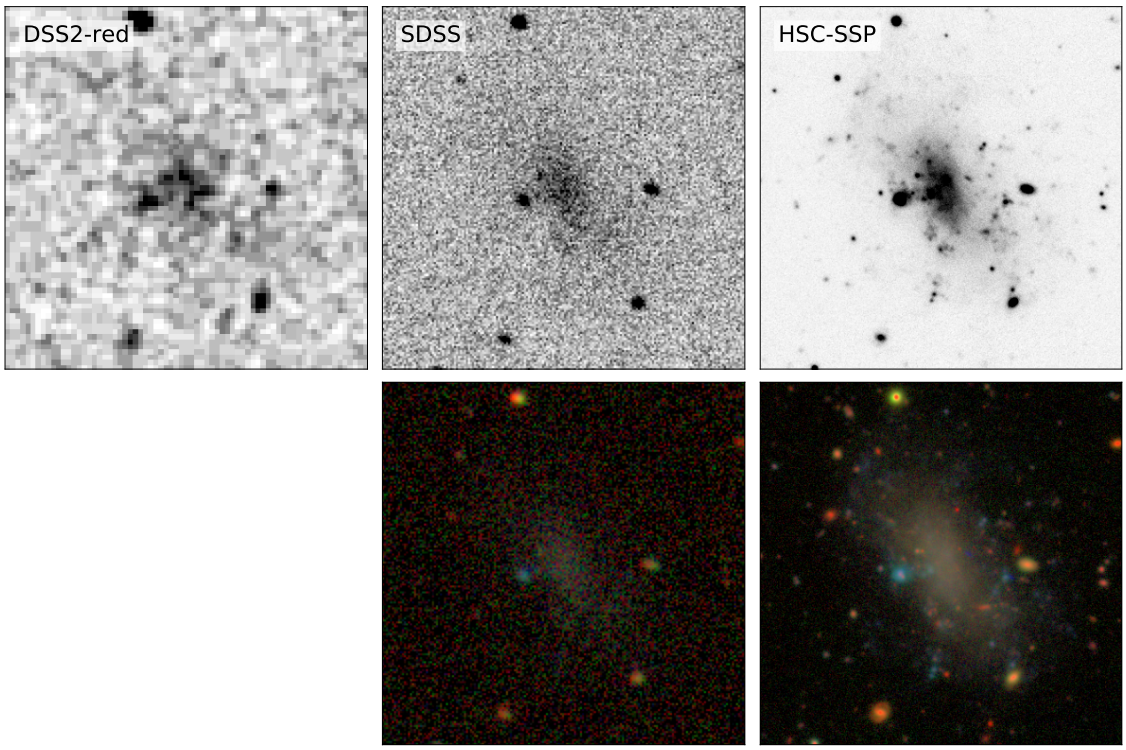

Figure 1.1 A visual demonstration of the progress made in the capability of wide-field surveys to study the detailed structure of dwarf galaxies over the past three decades. Here we show imaging of the Low Surface Brightness Galaxy LSBG766 [Greco et al., 2018c]. Each cutout is 0.02 deg on a side, or ~ 8.3 kpc at the distance of the galaxy (24 Mpc). In the top row, we show from left the (digitized) photographic survey DSS2-red [Lasker et al., 1990, Djorgovski et al., 1998], the g-band image from the Sloan Digital Sky Survey [SDSS, York et al., 2000], and the g-band image from the most recent data release of the Hyper Suprime-Cam Subaru Strategic Program [HSC-SSP, Aihara et al., 2018a]. In the bottom row we show *gri*-composite RGB images from SDSS and HSC-SSP.

modest distances, our view of the dwarf population has been historically fragmented into observational pockets (blueberries, blue compact dwarfs, ultra diffuse galaxies, etc.); this fragmentation has been driven in large part by the mass and surface brightness incompleteness of previous surveys. Now, however, wide-field surveys have reached the depth and spatial resolution necessary to make possible the idea of a census of the low-mass galaxy population at $z > 0$.

We show a visual representation of the progress made by wide-field surveys over the past ~ 3 decades in Figure 1.1. Here, we show the digitized photographic survey DSS2-red at left ($\sim$1995),

the Sloan Digital Sky Survey at center (SDSS, 1998-2009), and the Hyper Suprime-Cam Subaru Strategic Program at right (HSC-SSP, 2014-2022). The top row shows single band images, while the bottom shows *gri*-composite RGB images for SDSS and HSC-SSP. The galaxy in Figure 1.1 is a Low Surface Brightness Galaxy at 24 Mpc from the catalog of Greco et al. [2018c]; these dwarfs are characterized by their low surface brightnesses and large on-sky sizes.

As is readily apparent from the images themselves, wide-field surveys have made tremendous progress in both spatial resolution and sensitivity over the past few decades. Although it has long been possible to study the detailed structure of more massive galaxies using these wide-field surveys, studies of dwarf structure have only become accessible in recent years.

1.2 Dwarfs in the Modern Era of Wide-Field Surveys

The work contained within this dissertation focuses largely on quantifying the physical processes that control the assembly and structure of dwarf galaxies in large, statistical samples – this statistical approach to studies of dwarf galaxies has been made possible by the advent of current era wide-field surveys such as those discussed above. As shown in Figure 1.1, modern imaging surveys now capture low-mass galaxies sufficiently well to go beyond studies of their integrated characteristics towards detailed evaluations of their structural properties, and the physical processes which govern the emergence of such structure.

In the following chapters, I will discuss a series self-contained studies that leverage modern imaging surveys to explore the structural properties of dwarf galaxies in new detail. These studies will approach the formation of dwarf galaxy structure from several different angles, from their role in galaxy-galaxy interactions (Chapter 2 and Chapter 3), the assembly of their own stellar outskirts (Chapter 4, Chapter 5, and Chapter 6), as well as the interplay between their structure and star formation (Chapter 7 and Chapter 8). Finally, in Chapter 9, I will consider the possibilities that next generation surveys – especially spectroscopic surveys, which will establish distances to larger samples of low-mass galaxies in heretofore largely unexplored areas of parameter space – will open up for the study of these low-mass systems.

Chapter 2

Tidal Debris Around Massive Galaxies

2.1 Introduction

In the hierarchical merging model of galaxy formation, galaxy mergers are a crucial mechanism through which galaxies grow in size and mass [Toomre, 1977, White and Rees, 1978, White and Frenk, 1991]. This picture of galaxy formation has received strong support from modern cosmological simulations and semi-analytical models. A general consensus has emerged that for the highest masses, the growth of galaxies is dominated by matter accreted from other systems, with the *ex situ* (accreted) stellar mass fraction reaching ~ 0.80 [Oser et al., 2010, Lee and Yi, 2013, Rodriguez-Gomez et al., 2016], suggesting that mergers are necessary to produce galaxies of $\log(M_\star/M_\odot) \gtrsim 11.0$ [Lee and Yi, 2017].

The idea that mergers can generate extended features is well-established, having been shown first by Pfleiderer [1963] and Toomre and Toomre [1972] for on-going mergers between two equal-mass discs. It is now also widely accepted that the extended, low surface brightness features found around low redshift galaxies are the product of past merging events [Malin and Carter, 1983, Quinn,

1983, Dupraz and Combes, 1986, Fort et al., 1986, Mihos et al., 1998, Bartošková et al., 2011, Pop et al., 2017b], and that the structure and characteristics of these features hold a substantial amount of information regarding the dynamics and assembly history of their hosts [e.g. Johnston et al., 2008, Belokurov et al., 2017].

These tidal features can be separated into two broad classes: "shells", which are characterized by umbrella-like fans and caustics of stars whose radius of curvature points towards the host galaxy, and "streams", which are extended ribbon-like structures near the host galaxy. The boundary between these two classes is intrinsically soft, as stream-like features can, due to line-of-sight projection effects, appear shell-like [Foster et al., 2014, Greco et al., 2018a] and have been shown to evolve into shell-like systems [Hendel and Johnston, 2015]. Nevertheless, the ensemble characteristics of these shells and streams are distinct – shells tend to be found around massive ellipticals and do not appear to host significant star formation [Malin and Carter, 1983, Tal et al., 2009, Atkinson et al., 2013], while streams can be quite blue, and often appear around disc galaxies [Adamo et al., 2012, Knierman et al., 2012, Atkinson et al., 2013, Higdon et al., 2014].

The nature of the mergers that formed these tidal features, however, is still debated. In the minor merger picture of shell formation, a low mass satellite falls radially into the potential of a more massive host and the stars of the satellite form the resultant tidal feature [see, e.g., Johnston et al., 2001, Kawata et al., 2006, Sanderson and Helmi, 2013, Hendel and Johnston, 2015]. This mechanism of tidal feature formation has been successfully used to model many nearby systems (e.g. the Umbrella galaxy by Foster et al. 2014, the Ophiuchus Stream by Price-Whelan et al. 2016, Sumo Puff by Greco et al. 2018a), and the inferred merger mass ratios for most known tidal features that have been modeled are in agreement with this picture [Kawata et al., 2006, Feldmann et al., 2008, Gu et al., 2013, Foster et al., 2014].

However, a separate formation channel has been proposed wherein the shells are formed by major mergers. Following Hernquist and Spergel [1992], it was recently reported by Pop et al. [2017b] that the shells found around the most massive galaxies in the *Illustris* simulation [Vogelsberger et al., 2014] are generated by major mergers, with the distribution of shell-forming events peaking at mergers between galaxies of approximately equal stellar mass. Observations of three dwarf galaxies

in the Virgo Cluster [Paudel et al., 2017], and of nine nearby early-type galaxies (ETGs) taken from the Malin and Carter [1983] sample [Carlsten et al., 2017] show signs of shells that are thought to be generated by major mergers. Unlike tidal features formed from minor mergers between a quiescent host and quiescent satellite, where the tidal feature is bluer than the core of its host galaxy due to the color-mass relation along the red sequence, these major merger shells should show metallicities close to those at the core of the galaxy [Pop et al., 2017a], implying colors close to that of the core of the host [see, e.g. Gallazzi et al., 2006]. This provides an observationally accessible difference between the minor and major merger scenarios.

The picture for stream formation is somewhat clearer: they are generally accepted to originate from infalling satellites with relatively high angular momentum, although there is a smooth transition from stream to shell in the minor merger picture [see, e.g. Hernquist and Quinn, 1988, Hendel and Johnston, 2015]. Blue, low surface brightness tidal streams can, however, be caused by both recent minor [Knierman et al., 2012, 2013] and older major mergers [Rodruck et al., 2016]. We additionally observe red, quiescent streams which show no active star formation. These could be either the result of a dry merger or from quenching of a gas-rich satellite upon infall [Feldmann et al., 2008].

The majority of observational work on tidal features in external galaxies to date has been based upon targeted observations of a relatively small number of galaxies [see, e.g. Schweizer and Seitzer, 1988, Martínez-Delgado et al., 2009, 2010, Kim et al., 2012, Knierman et al., 2012, 2013, Beaton et al., 2014, Martínez-Delgado et al., 2015, Rodruck et al., 2016, Greco et al., 2018a]. Amongst those works that are able to derive tidal feature occurrence fractions, where $f_{\rm tidal}$ is the fraction of all galaxies that host tidal features, inferred values of $f_{\rm tidal}$ vary by a factor of 7, from $f_{\rm tidal}< 0.10$ to $f_{\rm tidal}> 0.70$ [Malin and Carter, 1983, van Dokkum, 2005, Tal et al., 2009, Nair and Abraham, 2010, Atkinson et al., 2013, Hood et al., 2018]. This is due in part to variations in targeting strategy and detection methods, as well as from differences in imaging depth. Moreover, the vast majority of the existing samples of tidal features are created via visual inspection.

Large variations in $f_{\rm tidal}$ as a function of survey depth are expected due to a steep dependence of tidal feature number density on peak surface brightness. Simulations predict that the majority

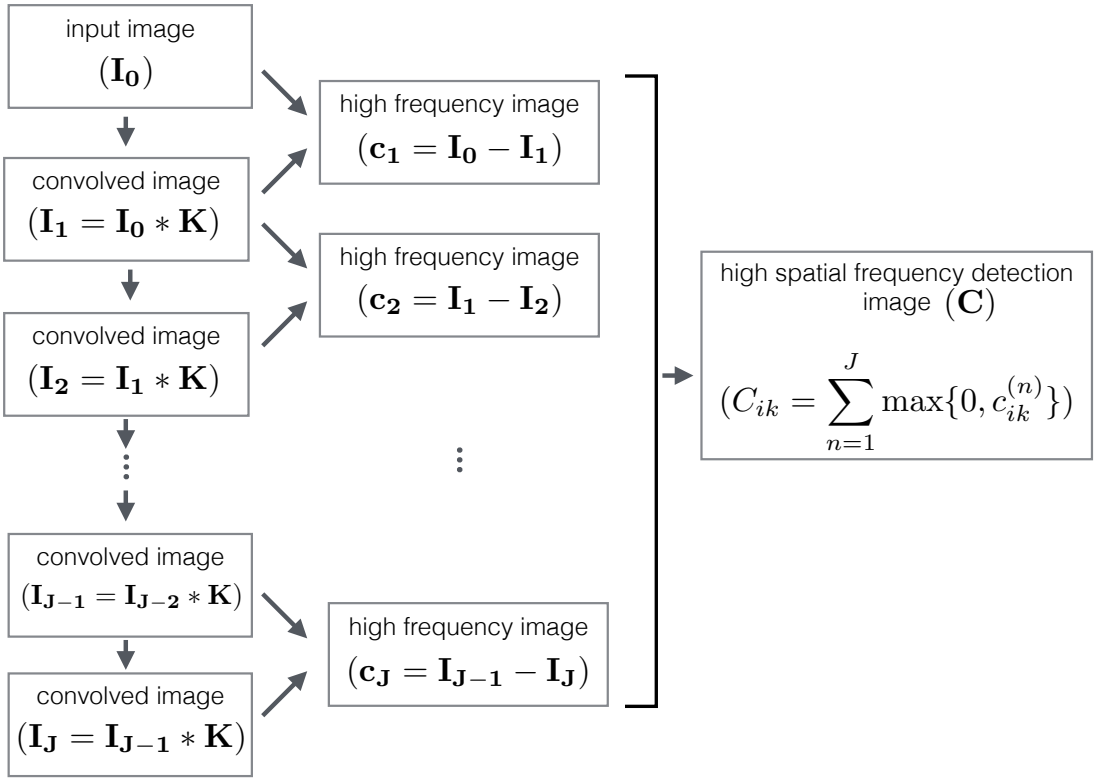

Figure 2.1 A schematic diagram of our algorithm to detect tidal features in HSC-SSP data. From left to right, the flow chart shows the convolution step, generation of high spatial frequency images, and detection image creation.

of tidal features, having been formed from minor accretion events, have a peak surface brightness of $\gtrsim 30$ mag arcsec^{-2} [Johnston et al., 2008]. We note that although wide field imaging campaigns do not yet routinely reach these surface brightnesses, such campaigns continue to characterize the observable tidal feature population at progressively lower surface brightnesses.

The Hyper Suprime Cam Subaru Strategic Program (hereafter HSC-SSP) is an ongoing wide-field survey executed by the Hyper Suprime Cam mounted on the 8.2 meter Subaru telescope [Miyazaki et al., 2012, Furusawa et al., 2018, Komiyama et al., 2018, Miyazaki et al., 2018, Kawanomoto et al. 2018, in prep.]. HSC-SSP is planning to cover over 1400 deg^2 of the sky in five bands ($grizy$) to $i_{\rm HSC} \sim 26$ [5σ point source depth, see Aihara et al., 2018b,a]. The survey boasts a median $0.56''$ seeing in the $i_{\rm HSC}$ band [Aihara et al., 2018a], making it an optimal imaging campaign in which to detect extended, low surface brightness features around galaxies out to intermediate redshifts [see Greco et al., 2018c,a, Huang et al., 2018a,b]. Such a survey will be able to search for low surface brightness tidal features across a much larger area of the sky than previous campaigns at similar depths [e.g. Atkinson et al., 2013], and to much lower surface brightnesses than previous surveys such as SDSS.

In this paper, we consider 21,208 galaxies with spectroscopic observations from the Sloan Digital Sky Survey DR12 [Alam et al., 2015] in the footprint of the Hyper Suprime-Cam Subaru Strategic Program (HSC-SSP) Wide layer [Aihara et al., 2018a]. The HSC Wide layer covers the largest on-sky area at a relatively shallow depth ($i \sim 26$) relative to the Deep and UltraDeep Layers ($i \sim 27$ and $i \sim 28$, respectively). We describe the survey and sample selection in Section 2.2. Our aims are as follows. First, for a survey as large as HSC-SSP, it is necessary to construct an algorithm which is capable of producing a homogeneously selected sample of galaxies with tidal features. In Section 2.3, we create an algorithm for automatic detection and, because there does not exist a suitable training set, we classify the morphologies of detected tidal features through visual inspection. In Section 2.4, we compare the results of our method to previous, purely visual samples , and compare the nature of the stream and shell host galaxies to each other, as well as to the non-interacting galaxies in our sample. We present the results of measurements of the color of the tidal features in Section 2.4.3. Finally, we discuss the demographics of the tidal feature hosts, and typical origins of the features

in our sample.

In this work, we adopt a cosmology of $\Omega_m = 0.3$, $\Omega_\Lambda = 0.7$, and $H_0 = 70$ km s^{-1} Mpc^{-1}.

2.2 Sample selection

2.2.1 HSC-SSP

In this work, we use the coadded images produced by the HSC software pipeline hscPipe [Bosch et al., 2018]. For extended, low surface brightness structure, accurate sky subtraction is crucial. hscPipe performs sky subtraction via fitting a sixth-order 2D Chebyshev polynomial to a binned average of the image (with a bin size of 128×128 pixels, or $21.5'' \times 21.5''$). Sky subtraction is performed prior to source detection, after initial source detection, and after final (per-visit) source detection during CCD processing. During coaddition, a constant background is measured and subtracted from the images. For a detailed description of the HSC-SSP data reduction process, see Bosch et al. [2018]. Because the $i_{\rm HSC}$ band has the best seeing on average across HSC-SSP, we use the $i_{\rm HSC}$ band images as our detection images.

We set our redshift limits at $0.05 < z < 0.45$, selecting from cross matches between the HSC Wide catalog from hscPipe (internal data release S16A, ~ 200 deg^2) and the SDSS spectroscopic surveys. At the lowest redshifts, we are currently unable to accurately detect tidal features. This is due to issues in background subtraction around very extended galaxies that become important when the size of the target galaxy becomes comparable to the area over which the background is subtracted (however, we note that the background subtraction has been improved for future data releases). At the high redshift cut of our window, we lose the ability to detect tidal features due to cosmological surface brightness dimming and a loss of spatial resolution; a negligible number of galaxies at $z > 0.45$ have automatically detected tidal features using our algorithm (see Figure 2.6 and Section 2.3.4 for details regarding our surface brightness limits and sample completeness). In Section 2.3.4, we investigate our surface brightness limits by injecting simulated tidal features at various spatial extents into non-interacting galaxies from our sample.

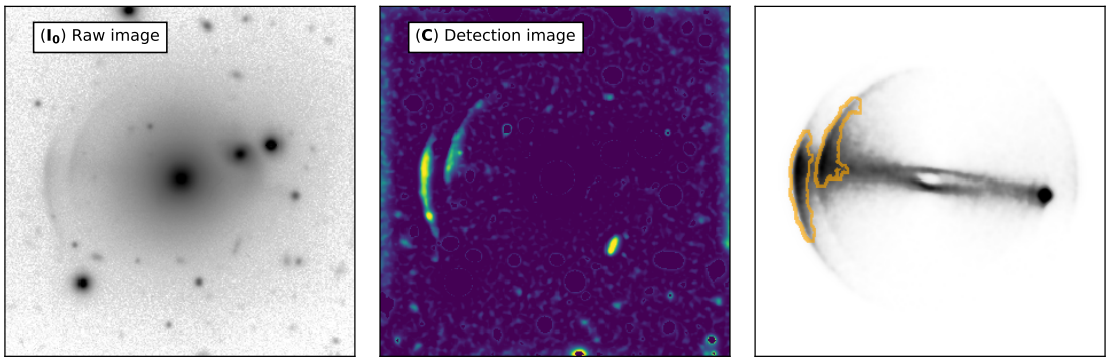

Figure 2.2 An illustration of the filtering algorithm as applied to the sum of a non-interacting HSC galaxy and a simulated shell system from Hendel and Johnston [2015] with a mean surface brightness of $\bar{\mu}_i = 25.4$ mag arcsec^{-2}. *Left:* $\mathbf{I_0}$, the sum of the non-interacting HSC galaxy cutout and simulated, PSF-convolved tidal feature system. *Middle:* The detection map, $\mathbf{C}$, generated from the left panel. The two brightest caustics in the shell system are clearly visible (yellow-green regions, left of panel), along with a background galaxy. *Right:* The simulated tidal feature from Hendel and Johnston [2015]. The orange outlines show the boundaries of the region that our method identifies as a tidal feature candidate. All panels are shown with a logarithmic stretch.

2.2.2 SDSS spectra

All of the galaxies in the present sample are selected to have spectra from SDSS DR12, and thus have known spectroscopic redshifts [Alam et al., 2015]. We additionally use stellar masses derived by Chen et al. [2012] by fitting the SDSS spectra to principal components constructed from the models of Bruzual and Charlot [2003]. We use the stellar masses calculated by Kauffmann et al. [2003] when a stellar mass measurement from Chen et al. [2012] is not available, where an offset calibrated from the galaxies where a stellar mass was available from both methods is applied to the stellar masses from Kauffmann et al. [2003]. Both stellar mass estimates adopt a Kroupa [2001] initial mass function.

We include galaxies from both the SDSS Legacy catalog [complete to $r < 17.77$ mag, Strauss et al., 2002] and the Baryon Oscillation Spectroscopic Survey of SDSS-III [BOSS, color-selected and roughly stellar mass complete, Dawson et al., 2013, Reid et al., 2016]. This generates a sample composed primarily of massive, low-z galaxies with a bias towards elliptical galaxies. To avoid

concerns about inhomogeneity of the SDSS samples, we consider our sample in bins of stellar mass and redshift. We additionally note that for $z < 0.15$ (which we will consider as a low-z subset of the full spectroscopic sample), the sample is dominated by galaxies from the SDSS Legacy catalog. We use the HSC catalog associated with the internal data release S16A to cross match HSC objects to their SDSS spectroscopic counterparts, resulting in 21,208 galaxies.

2.3 Identification and characterization of tidal features

2.3.1 Detection

Visually classifying every nearby galaxy in the HSC footprint is neither scalable nor feasible. It is therefore of interest to use this initial spectroscopic sample to develop a more automated detection method that can be applied to the full HSC-SSP survey area. However, an automated method for detecting tidal features should be:

1. Able to operate in a single band (both to maximize the area over which the algorithm can function, and so that the algorithm can be applied to any arbitrary bandpass).
2. Agnostic to the global morphological characteristics of both the tidal features and host.
3. Functional in the low surface brightness regime.

To this end, we have developed a method that separates high spatial frequency features (e.g. streams, shell caustics) from low spatial frequency features (e.g. host galaxy light) in a single band image.

Our algorithm is represented schematically in Figure 2.1. We iteratively separate low and high spatial frequency features, using the $i_{\rm HSC}$ band image output by hscPipe. We take our initial image as a 512×512 pixel cutout (approximately $86''$ on a side) around a galaxy of interest in our parent sample ($\mathbf{I_0}$). The $n^{\rm th}$ image is then given by the convolution of the previous image and the kernel, $\mathbf{K}$ (leftmost column, Figure 2.1):

$$\mathbf{I_n} = \mathbf{I_{n-1}} * \mathbf{K}, \tag{2.1}$$

where $\mathbf{K}(x,y) = \mathbf{h_{1D}}\mathbf{h_{1D}}^T$. We choose ϕ to be the one-dimensional B3-spline

$$\phi(x) = \frac{1}{12}(|x-2|^3 - 4|x-1|^3 + 6|x|^3 - 4|x+1|^3 + |x+2|^3), \tag{2.2}$$

which results in the convolution mask $\mathbf{h_{1D}}^T = (\frac{1}{16}\ \frac{1}{4}\ \frac{3}{8}\ \frac{1}{4}\ \frac{1}{16})$ pixels (where each pixel spans 0.168 arcsec), following Starck et al. [2007]. We then isolate the high spatial frequency features in the image by constructing a high spatial frequency image, $\mathbf{c^{(n)}}$, from the difference of the smoothed and un-smoothed images. This is shown in the middle column of Figure 2.1 as

$$\mathbf{c^{(n)}} = \mathbf{I_{n-1}} - \mathbf{I_n}. \tag{2.3}$$

Thus, those features that have spatial frequencies which are present in $\mathbf{I_{n-1}}$ but removed in $\mathbf{I_n}$ have positive values in $\mathbf{c^{(n)}}$; $\mathbf{c^{(n)}}$ is essentially the output of the well-known unsharp masking algorithm on image $\mathbf{I_{n-1}}$ [for astronomical applications, see, e.g. Malin, 1977, Meaburn, 1980].

We then construct a detection image of the high spatial frequency components in the image by stacking the positive components of each $\mathbf{c^{(n)}}$:

$$C_{ik} = \sum_{n=2}^{J} \max\{0, c_{ik}^{(n)}\}, \tag{2.4}$$

where C_{ik} is the pixel at (i,k) in the stacked image, $c_{ik}^{(n)}$ is the pixel at (i,k) in $\mathbf{c^{(n)}}$, and J is the number of layers in the filter bank (rightmost column, Figure 2.1). We exclude the first component, $\mathbf{c}^{(1)}$, as it is dominated by noise features.

For high J, the spatial frequencies probed by $c^{(J)}$ become low and can encompass the host galaxy. Similarly, the spatial frequencies associated with the host galaxy are strongly dependent on the physical size and redshift of the galaxy. The value of J is therefore tuned to the sample at hand. The range of on-sky sizes for the galaxies in our sample, which tend to be massive and low redshift (our sample has a mean redshift of $z = 0.260$, and a mean stellar mass of $\log(M_\star/M_\odot) = 11.19$), allows us to adopt a static value for J. Here, we set $J = 36$ (i.e. where the signal from one pixel can spread over at most a square with sides of 145 pixels).

2.3.2 Contaminant removal

This method to produce the detection image **C** generates high pixel values at the locations of tidal features, the cores of sources, spiral arms, and imaging artifacts. To remove contaminants from imaging artifacts, we reject detections where a saturated star is located within the image cutout, when greater than 20% of the pixels in the cutout are flagged as missing data, or when greater than 95% of the pixels in the cutout are flagged as being near a bright star. These cuts are tuned to the pipeline used to process the HSC SSP S16A imaging data, removing imaging artifacts that produce high spatial frequency features.

We take the following approach to remove contamination from spiral arms and neighboring galaxies. First, a flux threshold is applied to identify the cores of the brightest objects. The core of the target galaxy is excluded from this flux thresholding. The threshold is then iteratively lowered: at each iteration, the detected regions (i.e., a group of contiguous pixels) that are either connected to a previously detected source or are considered circular ($|\pi R_{\rm obj}^2 - A_{\rm obj}| < 0.25$, where $R_{\rm obj}$ and $A_{\rm obj}$ are half the extent of the object and the area of the object in pixels, respectively) are flagged as non-target objects. This cut is designed to remove faint point source-like objects, which are circular in the detection image due to the axisymmetric and monotonically decreasing radial profile of the convolution mask used. For an application of this technique to low surface brightness galaxies see Greco et al. [2018c]. To remove detections from imaging artifacts and noise, we require that candidate detections cover at least 250 pixels (approximately 7.05 arcsec^2). This removes detections that originate from the random fluctuations in the background or unmasked imaging artifacts. Though the threshold is set heuristically, reasonable changes to this threshold do not affect our results. For a visualization of our decomposition, cleaning, and detection process, see Section 2.7.

In total, we detect candidate tidal features around 1561 of the galaxies in our sample. For this initial application, we take the additional step of visually classifying the morphology of the tidal features in the automated sample (i.e. the 1561 galaxies around which tidal features have been detected), as well as removing contamination from tidal features that are likely associated with

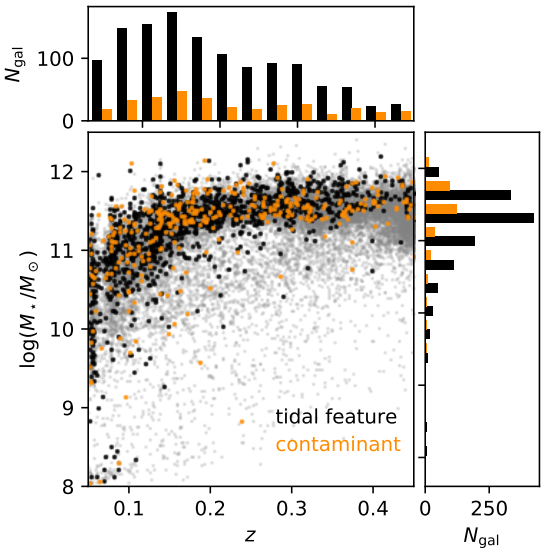

Figure 2.3 Redshift v. stellar mass for the galaxies in the parent spectroscopic sample (small grey points), the tidal feature sample (black) and the neighbor contaminant sample (orange). The one-dimensional histograms over redshift and stellar mass are shown in the top and right panels, respectively. In each case, the black bars show the distribution of the final, visually classified sample. In these panels, the orange bars show the neighbor contaminant sample, while the black bars show the tidal feature sample. The neighbor contaminants are not offset from the main tidal feature population, indicating that removing candidates via visual inspection does not introduce significant bias into the characteristics of our final tidal feature sample.

projected neighbors.

In Figure 2.2, we show the result of the algorithm on a synthetic case. Here, the signal which we wish to isolate is a simulated shell system from Hendel and Johnston 2015 with a mean surface brightness of $\bar{\mu}_i = 25.4$ mag arcsec^{-2}, where the mean is taken over pixels which have at least one count after the simulation is convolved with the HSC PSF (see Section 2.3.4). We add this signal to an $i_{\rm HSC}$ band image of a non-interacting galaxy from the parent sample (left panel). The detection image, $\mathbf{C}$, that we derive for the raw image, $\mathbf{I_0}$, is shown in the middle panel; the two bright caustics in the system are visible in the middle of the detection image. The detected tidal features output by the algorithm are shown by the orange outline in the rightmost panel.

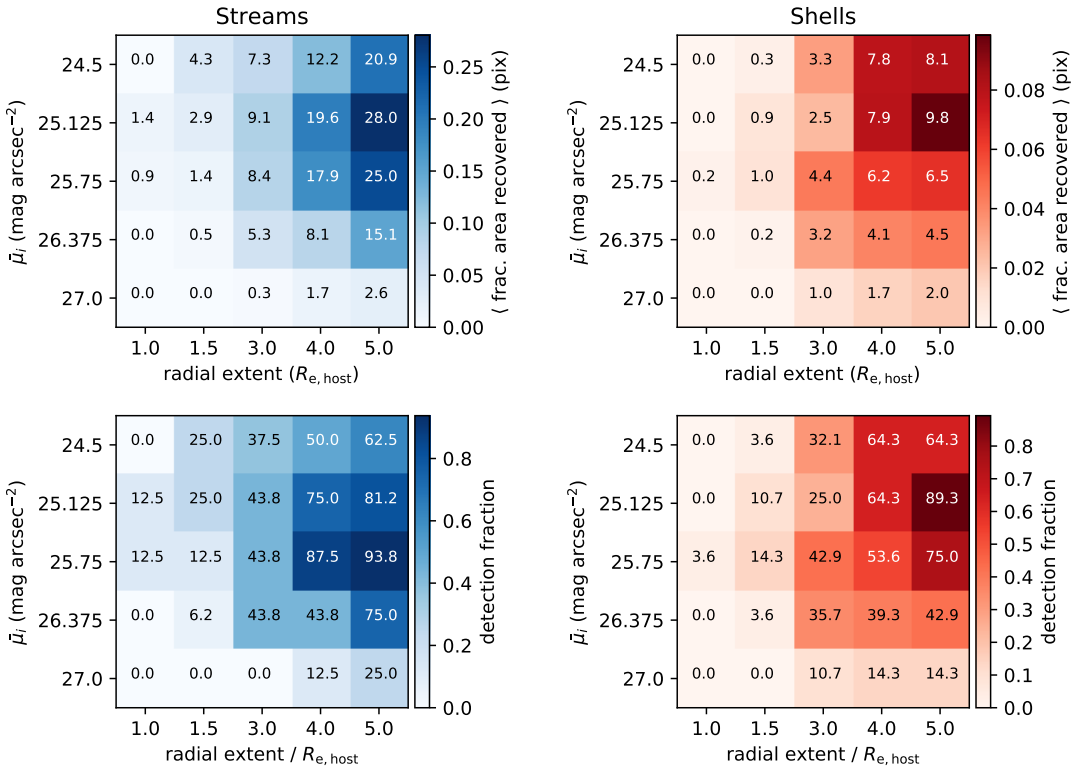

Figure 2.4 *Top row:* Pixel recovery fractions (f_{rec}, see Equation 2.5) for simulated streams (left) and shells (right). Each box shows the fraction of pixels associated with the simulated tidal feature that are recovered by the algorithm for a given tidal feature mean i_{HSC} band surface brightness and radial extent, as measured in units of the host effective radius. Generally, a higher fraction of pixels is recovered for the simulated streams; this is expected due to the number of particles occupying diffuse stellar fans in the shells. *Bottom row:* Detection fractions for streams (left) and shells (right). Here, the values at each grid point show the percent of simulated tidal feature systems in which at least 5% of the area covered by the tidal feature is flagged as a detection. In all panels, the drop in completeness at very high surface brightnesses ($\bar{\mu}_i \lesssim 25.$ mag arcsec^{-2}) is due to cases in which a part of the tidal feature is bright enough to be flagged as central galaxy substructure (e.g. spiral arms).

2.3.3 Visual Morphological Classification

While all of the tidal features in our sample were detected in an automated fashion, using the methodology described in above, we additionally visually classified tidal-feature morphologies and removed neighbors from the automated sample. In order to build a classification algorithm that can differentiate shells from streams, it is necessary to have a sufficiently representative sample of known shells and streams from which an algorithm can be trained. A possible approach is to employ a supervised learning algorithm where some known set of tidal features is used as the training set. There do exist simulated tidal features from which mock observations could be created for training [e.g. Kawata et al., 2006, Johnston et al., 2008, Hendel and Johnston, 2015, Amorisco, 2017, Pop et al., 2017b] and tidal feature catalogs that overlap with the HSC Wide footprint [e.g. Nair and Abraham, 2010, Atkinson et al., 2013]. However, training solely from simulations would risk propagating biases due to the parameter space explored by the simulation. The latter approach, training from known tidal feature hosts, is likely to yield large numbers of false negatives in the training set where HSC-SSP data reveal tidal features around a galaxy that was not identified previously, as HSC-SSP data reaches significantly lower surface brightnesses than previous surveys at similar areas. A training set from only those works that reach significantly lower surface brightnesses than HSC-SSP [e.g. van Dokkum, 2005, Martínez-Delgado et al., 2009, Tal et al., 2009] would have neither the necessary size nor be representative of the distribution of host galaxies in the sample at hand.

Additionally, identifying the host of a tidal feature is in some cases a non-trivial problem [see, e.g., Greco et al., 2018a]. For nearby galaxies with extended tidal features, the host galaxy is often not the source that is closest to the tidal feature. Future work will address automatic classification of such cases; for the sample at hand, we identify these cases visually.

We visually classify each galaxy in the automated sample using three possible classes: stream, shell, and neighbor contaminant. Shells are characterized by their caustics, and the center of curvature is located near the center of the host galaxy. Streams are long, thin features wherein the curvature is not globally oriented towards the center of the host galaxy (though streams are not

necessarily radial features). Neighbor contaminants are classified either as background galaxies (an example can be seen in the bottom right panel of Figure 2.5) or tidal features that are associated with a neighboring galaxy, rather than the target. A small number of imaging artifacts from HSC (e.g. missing data, satellite trails, and imaging defects around saturated stars) also passed our automatic cuts, and were removed at this stage.

In cases where the detected tidal features are not visible to the human classifier, our visual classification is primarily governed by the shape of the detected regions (see, for example, the bottom lefthand panel of Figure 2.5). The visual classification produces a final sample of 214 shell hosts and 987 stream hosts between $0.05 < z < 0.45$.

We also consider the effect of astrophysical contaminants that could have passed both automatic and visual cuts on our sample selection. First, strong lenses could be mistaken for shell caustics and propagated to the final sample. However, from a comparison between the redshift distribution of our final tidal feature sample galaxies and the the redshift distribution of known HSC strong lenses from Sonnenfeld et al. [2018], it is highly unlikely that strong lenses are a significant contaminant. Second, it is possible that some identified tidal features are in fact low surface-brightness galaxies (hereafter LSBGs) that are not associated with the target galaxy. There are some notably ambiguous cases [see Merritt et al., 2016, Greco et al., 2018a], and it is possible that there are LSBGs misidentified as tidal features in our final sample due to chance alignment. However, because of the low on-sky density of LSBGs, we expect < 3 chance-aligned LSBGs in our final sample (here we define chance-aligned as a LSBG anywhere within the 512×512 cutout made around each galaxy, so this contamination rate should also be seen as an upper limit). We estimate this contamination based on the detection 781 of LSBGs in $\sim$200 deg^2 of HSC Wide data by Greco et al. [2018c].

In Figure 2.3, we compare the redshift versus stellar mass distribution of our visually classified tidal feature sample (black) and visually identified contaminant sample (orange). We note that there is no apparent bias in the distribution of the visually classified neighbor contaminants with respect to our final sample.

We summarize the number of galaxies in our sample in Table 2.1. In particular, we note that the automatic detection step removes $\approx 93\%$ of the parent sample from consideration during visual

Table 2.1. Galaxy sample creation summary

Cut type	N_{gal}	Frac. of initial sample
Initial SDSS sample	21208	1.00
After automatic cut	1561	0.073
After visual classification	1201	0.057

Note. — The number of galaxies surviving each stage of sample selection. Note that the automatic detection step removes $\approx 93\%$ of the parent sample from consideration for the visual morphological classification.

inspection, such that the main function of the visual classification is to differentiate shells from streams in our sample, and to remove 23% of objects as contaminants. We further note that because the false positives are driven by imaging artifacts and background sources, the analysis herein would not be strongly affected by including the visually identified contaminants.

2.3.4 Detection recovery efficiency

In previous work, the surface brightness limits of tidal feature searches have normally been estimated from the variations in fluxes from random sky apertures [Atkinson et al., 2013, Hood et al., 2018, Morales et al., 2018]. If we were to use the methods described in Atkinson et al. [2013] and Morales et al. [2018], we would derive nominal surface brightness limits for the Wide layer of HSC-SSP of $\mu_i \sim 27.9$ mag arcsec^{-2} and $\mu_i \sim 28.4$ mag arcsec^{-2} from each method, respectively.

However, the detection of tidal features is also strongly dependent on the apparent size and morphology of the tidal feature. We find that the surface brightness limits derived from the methods from prior work are significantly deeper than practical limits for both automatic and visual inspection (for more details, see Section 2.8). Moreover, our automated algorithm allows us to run through the detection process many times without a proportionate increase in the required human time. Thus, in order to understand the surface brightness and angular size limits of our detection method as applied to the HSC wide layer, we use the simulated tidal features of Hendel and Johnston [2015] to create mock HSC-like tidal feature systems.

Taking $i_{\rm HSC}$ band cutouts of six galaxies (4 elliptical, and 2 disc galaxies) in which no candidate tidal features were originally detected, we insert nine mock tidal features into each galaxy. We inject all tidal features such that the line of sight runs perpendicular to the orbital plane; the recovery fractions should therefore be taken as upper limits with respect to tidal feature orientation. The tidal features are scaled to a grid of mean surface brightnesses and sizes (normalized to the effective radius of the host) over $24.5 < \bar{\mu}_i < 27.0$ mag arcsec^{-2}and $1 < d/R_{\rm e,host} < 5$, and convolved with the local HSC PSF. Here, d refers to the maximum radial extent of the tidal feature, and $\bar{\mu}_i$ refers to the mean surface brightness of the convolved tidal feature system, averaged over the pixels in the cutout which have at least one count after convolution with the HSC PSF. Simulations of four streams and five shells are used for this test.

For each simulated system, we define the recovery fraction as:

$$f_{\rm rec} = \frac{N_{\rm pix,rec}}{N_{\rm pix,sim}}, \tag{2.5}$$

where $N_{\rm pix,rec}$ is the total number of pixels flagged as part of a detected tidal feature, and $N_{\rm pix,sim}$ is the total number of pixels in the PSF-convolved simulation that have at least one count. Although the detection algorithm is never successful in recovering 100% of the pixels with some flux associated with the simulated tidal feature, the value of $f_{\rm rec}$ is a useful measure of the algorithm performance. The definition of $N_{\rm pix,sim}$ is a convenient normalization which excludes pixels that, while technically associated with the simulated tidal feature, are at surface brightnesses much fainter than what would be feasibly detectable.

The results of these tests are shown in Figure 2.4. The lefthand column (blue) shows the results for the simulated stream systems, while the righthand column (red) shows the results for the simulated shell systems. The top row shows, for a given radial extent and mean surface brightness, the average $f_{\rm rec}$ of the simulated systems. The lower row shows, again for a given radial extent and mean surface brightness, the fraction of systems wherein $f_{\rm rec} > 0.05$ (approximately the threshold at which a visual morphological classification can be made).

As expected, tidal features which extend farther from the center of the host galaxy are more

easily detectable due to reduced host light contamination. For a given surface brightness and tidal feature extent, the simulated streams have a higher $f_{\rm rec}$ than shells (upper row) and are more likely to be detected at visually classifiable levels than shells (lower row); this is a product of the fact that a significant number of the particles in the simulated shells are contained within diffuse stellar fans (for reference, see the low surface brightness fans in the right panel of Figure 2.2).

There is also a drop in detection recovery at very high mean surface brightnesses; the detection fraction of both streams and shells drops from $> 80\%$ to $< 65\%$ between injected features with a mean surface brightness of 25.125 mag arcsec^{-2} and 24.5 mag arcsec^{-2}. This occurs when the tidal feature enters a regime in which its associated signal in the detection map become comparable to that of spiral arms and neighboring sources. These tidal features are therefore removed as a likely contaminant (i.e. misidentified as a neighboring source or spiral arm). However, such features are in practice typically associated with ongoing major mergers with mass ratios close to 1:1, which are are not the focus of this work. In these cases, the material in the tidal features can be from the disruption of either the host or interloper; here, we focus on those cases in which the material in the tidal features is drawn primarily from the satellite. We note that there are more effective means for finding merger samples with HSC [Goulding et al., 2018], and ultimately it will be productive to think about both types of samples together. Ongoing major mergers are also significantly less common than tidal features, and are therefore not a significant contaminant in our sample. It should also be noted that the parameters that we choose in the detection step are tuned to our primarily low-z, massive sample. If applied to a different set of galaxies (e.g. higher redshift), it is likely that the thresholds used would need to be adjusted.

As shown in Figure 2.4, the algorithm can identify tidal features down to ≈ 27 mag/arcsec^2 at an extent of $d \gtrsim 4R_{\rm e,host}$. We note, however, that we are significantly incomplete at these surface brightnesses (for example, although we detect, on average, 2.6% of the pixels of our simulated streams at 27 mag/arcsec^2 with an extent of $d = 5R_{\rm e,host}$, only 25% of simulated cases yield a detection). Our approximate 50% completeness for tidal features with $d \geq 3R_{\rm e,host}$ is $\bar{\mu}_i \approx 26.4$ mag arcsec^{-2}.

2.3.5 Measuring tidal feature color

For a subset of the galaxies with detected tidal features, the features are sufficiently far from the galaxy to allow for a clean measurement of color. We rerun our detection algorithm in the $g_{\rm HSC}$ band, and measure the color of the detected tidal features by using the union of the detected regions in $g_{\rm HSC}$ and $i_{\rm HSC}$ as the apertures (for example, in Figure 2.2 the orange outlines in the rightmost panel would be used as an aperture).

To determine where the color of the tidal feature will be significantly impacted by flux from the host galaxy, we measure the tidal feature contrast ratio, $c_{\rm tf}$, as the observed flux of the system and expected flux from the host via surface brightness profiles where the tidal features have been masked from the image, i.e. $c_{\rm tf} = f_{\rm observed}/\hat{f}_{\rm host}$. We measure $f_{\rm observed}$ by simple aperture photometry, where the aperture is the detected region associated with the tidal feature. We estimate $\hat{f}_{\rm host}$ by measuring the surface brightness profiles of our sample in the $g_{\rm HSC}$ and $i_{\rm HSC}$ bands in elliptical annuli. Here, the position angle and ellipticity are obtained from fits to the host galaxy using imfit [Erwin, 2015], where neighboring galaxies and the tidal feature system are masked from the fit. $\hat{f}_{\rm host}$ is then the flux expected in the region of the tidal feature as estimated by the surface brightness profile in that region.

To calibrate and test the ability of $c_{\rm tf}$ to trace the accuracy in measurements of colors for extended tidal features, we inject tidal feature simulations (presented in Section 2.3.4) of known colors into non-interacting HSC galaxies. The data from the N-body simulations of Hendel and Johnston [2015] are also convolved with the HSC PSFs in each band. The simulated systems are then run through our full detection and color measurement algorithm. We find that a $c_{\rm tf}$ threshold of 2.5 produces tidal feature colors which are accurate to 0.06 mag, which includes the effect from band-dependent PSF size.

For a given tidal feature system, it is possible that a number of the detected regions are contaminants that have been detected along with the true tidal features; see Section 2.3.3 for a description of the expected types of contaminants. At this stage, we only flag contaminated regions within a tidal feature system, and do not remove galaxies from the sample. However, when we estimate the

average color of the tidal feature system, we use color as a filter to remove regions that are unlikely to be associated with the target galaxy.

The color of the candidate tidal feature with respect to the host also acts as a flag for potential neighbor contamination for individual detected regions. When comparing tidal feature color to host color, we consider $\Delta(g-i)$, where $\Delta(g-i)$ is defined as the difference between the $(g-i)$ color of the tidal feature and the host (i.e. larger values correspond to a tidal feature that is redder with respect to its host). In the case of shells, we keep only those tidal feature candidates with $-0.5 < \Delta(g-i) < 0.2$ mag. For this initial sample, we verify visually that this color cut does not remove potentially interesting tidal features from the sample. Streams have been observed to host significant star formation [Knierman et al., 2012, Higdon et al., 2014], and so we impose only the red cut, i.e. we keep those color measurements for which $\Delta(g-i) < 0.2$ mag.

After removing likely neighbors (i.e. those detected regions that are removed due to the cuts in color), we estimate an average color of the tidal feature system by taking the mean of the colors measured for the individual detected regions. We estimate the uncertainty on the measurement of the average color ($\sigma_{\overline{\rm TF}}$) as follows:

$$\sigma_{\overline{\rm TF}} = (\sum_{i}^{N} \sigma_{{\rm TF},i}^2 + \sigma_{\rm sim})^{1/2}, \tag{2.6}$$

where $\sigma_{{\rm TF},i}$ is the uncertainty on the color of the $i^{\rm th}$ detected tidal feature region (as propagated from the variance maps output by hscPipe) in a system of N tidal feature regions (defined as a group of contiguous pixels that are flagged by the detection algorithm; for example, Figure 2.2 shows a $N = 2$ system), and $\sigma_{\rm sim}$ is the uncertainty due to PSF differences and host galaxy contamination ($\sigma_{\rm sim} \sim 0.06$, from above).

Finally, we estimate the color of the host galaxy core from simple aperture photometry with an aperture diameter of $2R_{\rm e,host}$. We do not perform PSF matching for this measurement, as the impact of doing so is negligible.

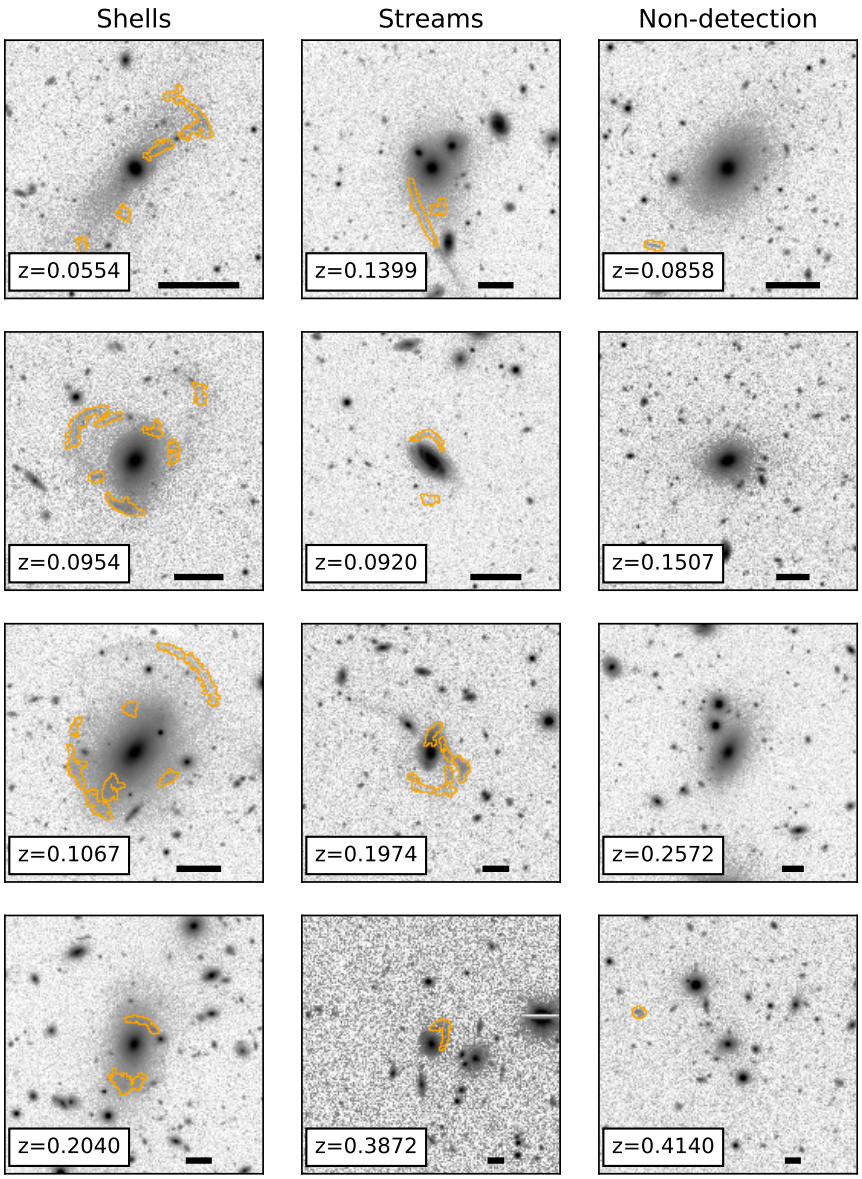

Figure 2.5 A sample of $i_{\rm HSC}$ band imaging of shells (left column), streams (middle column) and non-interacting galaxies (right) in our sample. The orange outlines show the boundaries of the detected regions found by our filtering algorithm. The horizontal black line in the bottom right of each panel spans 30 kpc at the redshift of the central galaxy. In all panels, a logarithmic stretch is used to emphasize low surface brightness features.

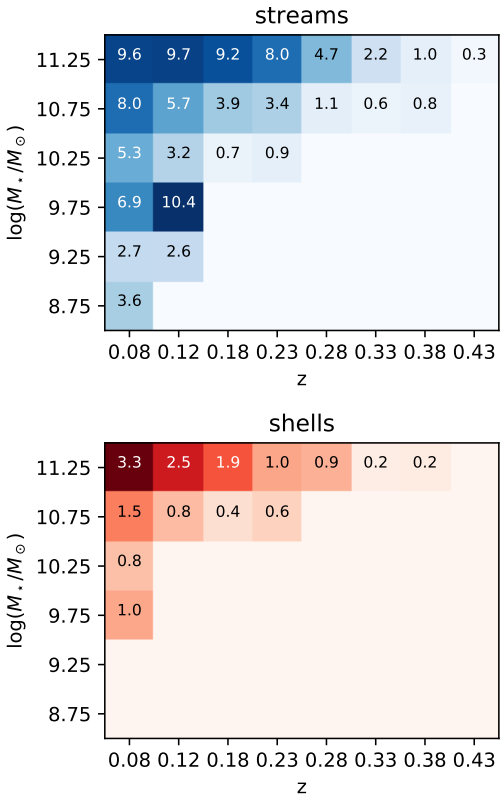

Figure 2.6 Tidal feature occurrence fractions as a function of stellar mass (y-axis) and redshift (x-axis) for the visually identified stream (top) and shell (bottom) samples. Each bin in the top (bottom) panel is annotated with the fraction of galaxies tagged as a stream (shell) host from the full spectroscopic sample. Blank regions indicate bins for which no tidal feature systems were identified.

2.4 Results

Here, we present a sample of 214 shells and 987 streams found semi-automatically in the S16A internal release of the HSC-SSP Wide layer (covering $\sim$200 deg^2). The tidal feature morphologies are visually classified as either streams or shells, and cover a redshift range of $0.05 < z < 0.45$. In Figure 2.5, we show a sample of shell (left) and stream (middle) galaxies, and galaxies without tidal features (right) as identified by this method.

2.4.1 Observed tidal feature occurrence fractions

We first consider the tidal feature occurrence fractions for our sample, which we define to be the fraction of galaxies in the sample within a given range of redshift and stellar mass in which a stream or shell was detected, divided by the total number of galaxies in the sample that occupy that area

of parameter space. As shown in Section 2.3.4, the observed occurrence fraction will reflect both the astrophysical occurrence fraction and our ability to recover the tidal feature signal from HSC data.

Many factors affect the observed surface brightness of a tidal feature system. The tidal feature grows increasingly faint with time since its creation due to phase mixing [Hendel and Johnston, 2015] and stellar population fading [e.g. Conroy et al., 2009a], while the orbital parameters of the encounter influence the morphology of the resultant tidal feature [see, e.g. Johnston et al., 2008, Sanderson and Helmi, 2013, Hendel and Johnston, 2015, Pop et al., 2017b]. The surface brightness and angular size of the tidal feature are also dependent on the redshift of the source due to changes in the angular diameter distance and surface brightness dimming. Lower mass galaxies should also host tidal features from lower mass satellites, which produce tidal features of lower surface brightnesses. Figure 2.6 shows our observed occurrence fractions as a function of host redshift and stellar mass. As expected, our observed occurrence fractions fall as redshift is increased or stellar mass is decreased. The observed occurrence fractions of shells falls more steeply as a function of redshift than that of streams, which we expect from our lower recovery fractions for simulated shells in Figure 2.4. At low redshift ($z < 0.15$), we find a number of low mass systems with $\log(M_\star/M_\odot) < 9.7$ that are apparent stream hosts. From a visual inspection of these objects, we find that these systems are either dwarf galaxies undergoing major mergers (due to the mass of the galaxies involved, the surface brightness of the extended features is low enough to avoid being thrown out as spiral arms), or close neighbors of larger galaxies that host tidal features. Though ongoing major mergers in dwarf galaxies are not the focus of this paper, we note that our method could also generate samples of such ongoing mergers if a different parent sample were used [see, e.g. Paudel et al., 2018].

The fraction of galaxies which host observable tidal features has been measured by many authors who find a wide range of values, from 7% as derived from SDSS [Nair and Abraham, 2010] to 71% from a deep imaging campaign of local ETGs [van Dokkum, 2005]. It is likely that a majority of faint substructures have peak surface brightnesses of > 30 mag arcsec^{-2} [Johnston et al., 2008], and that the occurrence and morphology of tidal features is dependent on the mass and merging history

of the host [Wang et al., 2005, Jiang et al., 2015, Hendel and Johnston, 2015]. Thus, tidal feature detection is highly sensitive to the type of host galaxy examined and to the surface brightness limits of the relevant observations, leading to a large variance in the observed tidal feature occurrence fractions.

In campaigns where a smaller area on the sky is observed to large depths, the limiting surface brightness is significantly deeper than that which is accessible from the HSC wide layer [e.g. van Dokkum, 2005, Tal et al., 2009, Martínez-Delgado et al., 2010]. Although we are unable to construct a matching sample against which to compare our observations, we note that the systematically higher occurrence fractions that are often found by such studies point to the minor merger picture, in which increasingly more numerous and minor mergers leave behind increasingly fainter tidal features [Johnston et al., 2008].

Other studies present samples that we have no clean method of emulating. For example, Schweizer and Seitzer [1988] consider S0, S0/Sa, and Sa NGC galaxies and derives an occurrence fraction of 16%, while Adams et al. [2012] observe a 3% tidal feature occurrence fraction for cluster ETGs.

However, it is valuable to consider whether the tidal feature occurrence rate that we observe from our semi-automatic method is consistent with those samples derived from visual classification alone. Here, we compare our observed occurrence fractions to literature results where it is possible to account for differences in sample selection.

Comparison to Atkinson et al. [2013]

The catalog of tidal feature hosts in the Canada-France-Hawaii Telescope Legacy Survey (hereafter CFHTLS) assembled by Atkinson et al. [2013] is perhaps the clearest benchmark against which we can evaluate our observed tidal feature occurrence fractions. The CFHTLS data are similar to the HSC Wide layer in terms of depth and spatial resolution; the deepest band that Atkinson et al. [2013] considers, the CFHT g band, has a roughly equivalent 5σ point source depth as $i_{\rm HSC}$ in the Wide layer of HSC-SSP [Boulade et al., 2003, Aihara et al., 2018a]. The catalog was constructed entirely from visual inspection, and thus serves to test the efficiency of our method against pure

visual inspection.

To compare our tidal feature detection fractions to those of Atkinson et al. [2013], we consider the 2113 galaxies in our sample for which $15.5 < r_{\rm SDSS} < 17$ mag, $M_r < -19.3$ [derived from SDSS, Alam et al., 2015] and $0.05 < z < 0.2$, following the sample selection cuts used by Atkinson et al. [2013]. We find a tidal feature occurrence fraction of $13.30 \pm 0.79\%$, where the uncertainty reflects only counting uncertainty assuming a Poisson distribution. This fraction is significantly higher than those in Figure 2.6 because of the additional cuts for bright galaxies imposed in the Atkinson et al. 2013 sample.

Within the Atkinson et al. [2013] sample (hereafter the CFHTLS sample), we consider only the galaxies for which the authors were able to make a morphological classification of the tidal feature. We furthermore exclude any galaxies for which the only feature morphology tags belong to the classes "diffuse" and "fan", which are observed in 4.6% of their galaxies, as the nature of our method biases us significantly against the detection of tidal features which are diffuse (i.e. of similar or lower spatial frequency than their host galaxy).

Given these cuts, the fraction of galaxies that host morphologically classifiable tidal features of Atkinson et al. [2013] is, at $12.98 \pm 0.85\%$, in agreement with our observed tidal feature occurrence fraction.

Given that the Atkinson et al. [2013] sample was constructed via purely visual classification from a dataset with a similar limiting depth and spatial resolution as HSC-SSP, this agreement is encouraging, and implies that our detection method is able to detect tidal features as well as visual inspection methods can for tidal features with high spatial frequency features.

Comparison to Malin and Carter [1983]

As one of the earliest papers to report the occurrence rates of shells around elliptical galaxies, it is informative to compare our shell occurrence fraction to that of Malin and Carter [1983]. However, we caution that it is not straightforward to compare the data of Malin and Carter [1983], taken with photographic plates, to HSC SSP data; we use this comparison only as an order of magnitude estimate. The authors consider a sample of NGC ellipticals from the ESO/SRC (IIIa-J) Southern

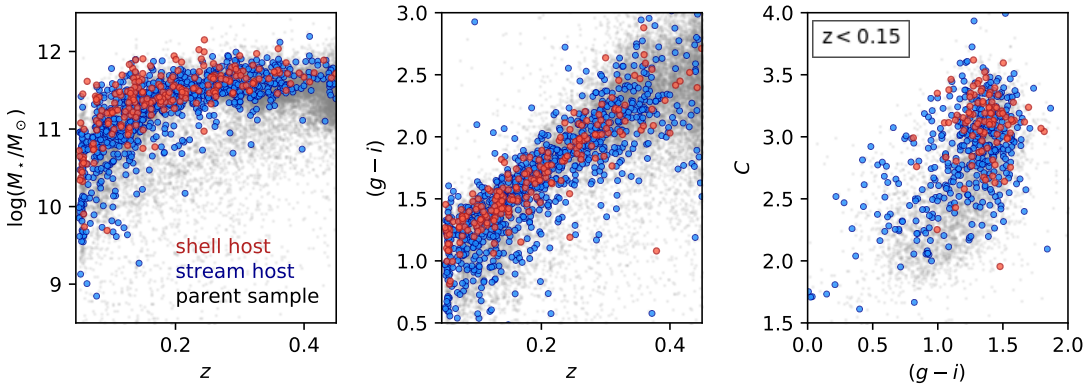

Figure 2.7 Properties of the stream (blue) and shell (red) host galaxies. The small grey points show the full spectroscopic sample within our target redshift range. *Left:* redshift versus stellar mass for the tidal feature sample. *Center:* redshift versus $(g-i)$ color for the sample. At all redshifts, shell hosts tend to be redder and more massive than their counterparts that host streams. *Right:* $(g-i)$ color versus concentration for the $z < 0.15$ galaxies in our sample. The shell host galaxies have, on average, higher concentration than the stream hosts, indicating that the shell sample contains a larger fraction of ETGs than does the stream host galaxy sample.

Sky Survey, and find that 5.8% of the galaxies therein show signs of stellar shells. The authors cite their surface brightness limit as $B = 26.5$ mag arcsec^{-2} on photographic plates.

Although the galaxies considered by Malin and Carter [1983] are at significantly lower redshifts, we do not expect the true shell occurrence fraction to change significantly out to $z \lesssim 0.1$ [Pop et al., 2017b]. We use concentration as a proxy for morphology, wherein high-concentration galaxies are likely ellipticals, and low-concentration galaxies are likely discs. C is defined as the ratio between the the radii containing 90% and 50% of the Petrosian i-band luminosity as measured in SDSS. We consider only high-concentration ($C > 3.1$) galaxies at the lowest redshifts that we can probe ($0.05 < z < 0.1$). We set the cut in concentration following Strateva et al. [2001] and D'Souza et al. [2014], but increase our threshold to obtain a more pure sample of ellipticals. This subset of our sample gives a shell occurrence fraction of 6.13 ± 1.23%, which is in agreement with that of the Malin and Carter [1983] sample.

2.4.2 Host galaxy properties

We first review the properties of the galaxies that host shells and streams in the context of the full SDSS spectroscopic sample. Relative to the non-interacting sample (i.e. galaxies for which no tidal features were detected), shell hosts tend to have higher stellar masses and redder $(g-i)$ colors at a given redshift (left and middle panels, Figure 2.7). Stream hosts span the full range of stellar masses and colors present in the non-interacting sample at a given redshift.

At $z < 0.15$, stream host galaxies in our sample have higher concentrations on average than do the non-interacting sample. The shell host galaxies have higher average concentrations than do either the stream hosts or the non-interacting sample (Figure 2.7, right panel). These offsets imply that the shell hosts tend to be massive, red ETGs (since high concentration is correlated with an elliptical morphology).

We find no significant differences between the color gradients of the tidal feature host galaxies and a non-interacting sample matched in mass, redshift, and color – this implies either that the average tidal feature is generated by a minor merger that does not significantly alter the color gradient of the host, or that the tidal feature was created sufficiently long ago that the host is fully relaxed. This is in agreement with the findings of Kim et al. [2012], who find that the bulk structural properties of tidal feature hosts are not significantly different than those of non-interacting galaxies.

A dearth of low-concentration galaxies hosting shells

From a visual inspection of our sample, we find only three instances in which a low-concentration (disc) galaxy hosts a shell (these three cases are shown in Figure 2.8). Here, we investigate possible selection or completeness effects that could produce this dearth of observed low-concentration galaxies that host shells at a fixed stellar mass.

In a paradigm where satellites falling into more massive hosts tend to be on more radial infall trajectories [see, e.g. Benson, 2005, Jiang et al., 2015], we expect somewhat fewer spiral galaxies to host shells due to the differences in the stellar mass range occupied by elliptical and spiral galaxies. To gauge whether the low number of shells observed around discs is purely a mass effect, Figure 2.9

shows the fraction of tidal features that are identified as shells in our sample as a function of stellar mass at $z < 0.15$.

To estimate the effect of differential completeness in shell and stream detection on the trend apparent in Figure 2.9, we take the naive null hypothesis that shells and streams appear equally often, independent of stellar mass, and have radial extents that are distributed uniformly from $3R_{\rm e,host}$ to $5R_{\rm e,host}$. We here disregard the effect of passive stellar population fading, and assume that the shells and streams have the same distribution in time since interaction. We also assume that the events all have the same mass ratio. Using the simulations presented in Section 2.3.4, this scenario would predict that the fraction of observed shells would remain roughly constant as a function of host stellar mass, and rise at low masses ($\log(M_\star/M_\odot) \lesssim 10.5$). Thus, we expect that the trend seen in Figure 2.9 is not a completeness effect.

As a second experiment, if we take the naive assumption that the morphology of the tidal feature is independent of the morphology of the host, we would expect $\approx 15\%$ of detectable tidal features around low-concentration galaxies to be shell-like at $\log(M_\star/M_\odot) \sim 10.5$, near the peak of the distribution of stellar mass for a sample of low-concentration galaxies in our sample. However, we find that only $4\% \pm 3\%$ ($6\% \pm 4\%$) of the tidal features around $C < 2.8$ ($C < 2.6$) galaxies at $10.2 < \log(M_\star/M_\odot) < 10.7$ are shell-like.

We repeat this exercise using morphological classifications from the citizen science project Galaxy Zoo [Lintott et al., 2011]. Here, we consider only those galaxies where one class accounts for $> 80\%$ of the votes. Here, we again find a dearth of late-type galaxies hosting shells. We thus conclude that indeed there is a significant deficit of shells around late-type galaxies.

We now consider whether this deficit is due to our detection method, which may be biased against finding shells around face-on discs, where bright substructure (e.g. spiral arms) may obscure tidal features. Broadly speaking, contamination by spiral arms should affect the detection of shells and streams equally, rather than preferentially affecting the fraction of observed shells. We used the method outlined in Section 2.3.4 to compare the detection recovery efficiency of shell-like tidal features around a face-on spiral to that of an elliptical host with similar on-sky size. We did not find significant differences in detection recovery for the automatic stage in these two cases.

However, it is probable that human classifiers are biased against shell-like tidal features around face-on disc galaxies, as the curvature of shell caustics is similar to that of spiral arms. To test whether a human bias could account for the difference in shell fraction at fixed stellar mass, we consider only shells which are substantially separated from their host galaxy (i.e. where contamination by host light is low, or high values of $c_{\rm tf}$, see Section 2.3.5), and find that we again observe relatively more ellipticals that host shell systems at fixed stellar mass. We therefore conclude that the relative dearth of shell systems around disc galaxies in our sample is not due to a bias in our sample selection method. We return to interpret this result in Section 2.5.3.

2.4.3 Tidal feature colors

We are able to measure colors for 78 shell systems and 497 stream systems in our sample. Below, we present the average $(g-i)$ colors of tidal feature systems. Here, we specifically consider the difference in the average color of the tidal feature system and the core of its host galaxy (hereafter $\Delta(g-i)$). In the case of a non-star-forming satellite, $\Delta(g-i)$ is a probe of the mass ratio of the merging event that formed the shells: if one assumes that the tidal feature progenitor satellites sat on the red sequence during their infall, the mass of the satellite may be estimated by finding the mass on the red sequence that corresponds to the measured satellite color [Gu et al., 2013, Huang et al., 2016]. We find this assumption to be reasonable, as the red colors measured for the shells are too red to plausibly host significant star formation. In the case of blue tidal features, $\Delta(g-i)$ does not yield mass information.

Shell colors

We find that the shells are, on average, slightly bluer than their hosts, with a mean color offset of -0.15 ± 0.02 mag (see top panel of Figure 2.10). The observed $\Delta(g-i)$ does not have a strong dependence on the mass of the host galaxy. This finding is in agreement with the majority of individual systems in the literature for which the color of the shells have been measured [Quinn, 1983, Gu et al., 2013, Foster et al., 2014]. The color difference between the shells and their hosts then suggests that our sample is dominated by mergers where the infalling satellite is significantly

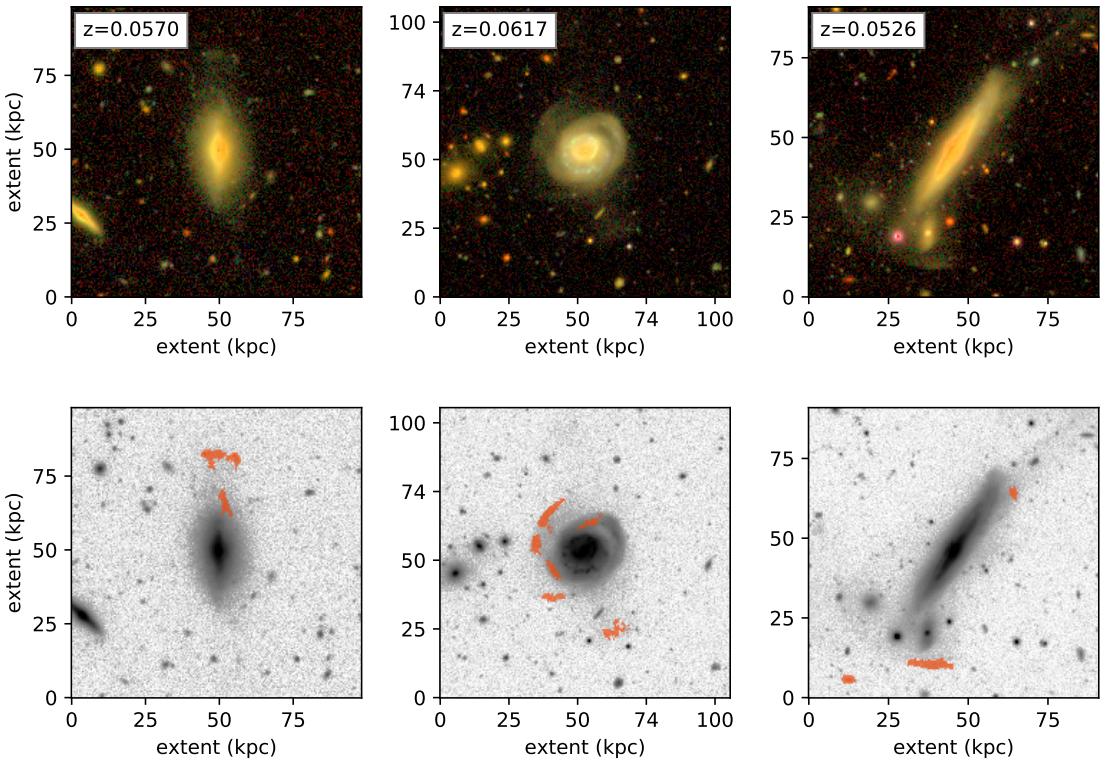

Figure 2.8 *Top: gri*-composite images [Lupton et al., 2004] of the three disc galaxies that host shells in our sample. Both caustics and diffuse stellar fans are visible in all cases. In the middle panel, two umbrella-like shell structures are visible to the left of the galaxy. *Bottom:* The same galaxies in the i_{HSC} band, with the features detected by the algorithm shown in orange. A diffuse trail is also visible in the top right of the rightmost panels, which is not detected due to its overlap with the cutout edge.

less massive than the host.

However, we also find that for $15\% \pm 4.4\%$ of shell galaxies, the colors of the shells are consistent, within errors, with those of the core of their host galaxy. We will hereafter refer to these galaxies as "red shell" galaxies. This lack of a color difference has been suggested by Pop et al. [2017a] to be a signature of shells produced by major mergers, wherein the shell caustics of the system within ≈ 50 kpc from the host center approach the metallicity of the core of the host galaxy. Though the

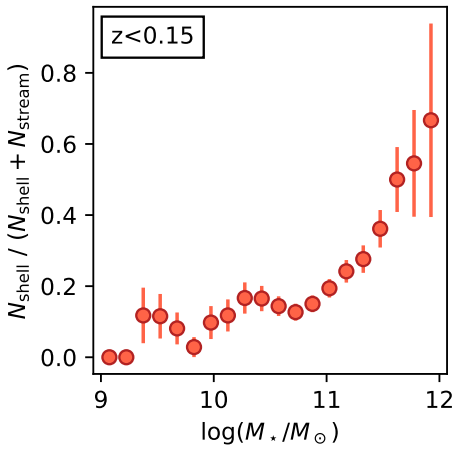

Figure 2.9 Stellar mass versus the fraction of tidal features that are shells for the $z < 0.15$ galaxies in our final tidal feature sample. Shells are found more frequently around more massive galaxies, growing from $\approx$ 20% at $\log(M_\star/M_\odot) = 10.5$ to $\approx$ 50% at $\log(M_\star/M_\odot) = 11.5$. A larger shell fraction around massive galaxies is expected due to an increase in the number of radially-biased satellite infall trajectories around such galaxies [Jiang et al., 2015, Hendel and Johnston, 2015].

shell caustics in Pop et al. [2017a] have slightly lower metallicities than the host core, we estimate that their optical colors will be consistent within the errors to the core of the host within $1R_{\rm e,host}$.

Though there are relatively few "red shell" galaxies, we find there to be a morphological difference between these shells and the bulk of the shell population. Relative to the other galaxies that host shells, "red shell" galaxies tend to host more Type I shells, wherein the axis of symmetry of the shells is aligned with the major axis of the galaxies (see the leftmost panel of the second row in Figure 2.12 for an example). The caustics of Type II shells, on the other hand, are arranged randomly around the galaxy (see the middle panel of the bottom row in Figure 2.12 for an example). The Type I shell occurrence fraction in our "red shell" sample is 86^{+14}_{-35}%, significantly higher than the Type I shell occurrence fraction for the rest of the shell hosts, 30 ± 14%. Considering both the "red shell" galaxies and minor merger-like shell hosts together gives a Type I host fraction of 43 ± 12%. This is in agreement with the same quantity estimated by Prieur [1990] for the catalog of Malin and Carter [1983]. The uncertainties listed are those derived from counting statistics only, and reflect the significant uncertainty that we face due to low numbers of "red shell" galaxies present in the sample.

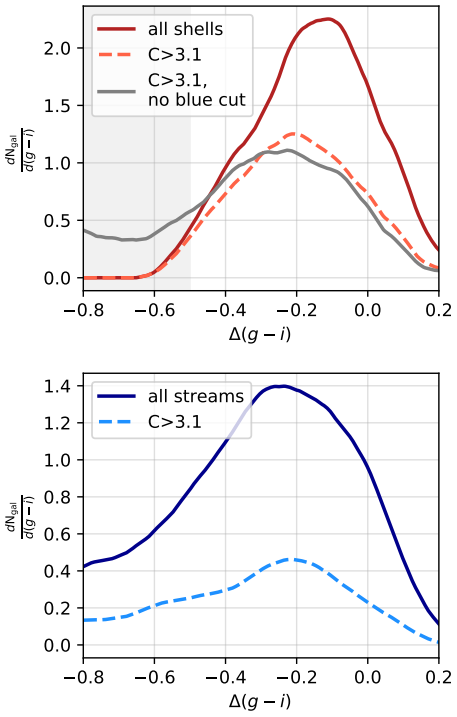

Figure 2.10 Scaled kernel density estimates of the difference between the color of the tidal features and the core of the host galaxy (measured within a radius of $1R_{\rm e,host}$) for the shells (top panel, red) and the streams (bottom panel, blue) via a kernel density estimate (using an Epanechnikov kernel with a width of $\Delta(g-i) = 0.15$). In each panel, the solid lines show the color distribution of the full sample. The dashed lines show the $\Delta(g-i)$ distribution for our high-concentration ETG sample ($C > 3.1$), normalized to the number of high-concentration galaxies in the sample. In the top panel, the grey solid line shows the distribution of $\Delta(g-i)$ for the shells that we would have derived if we did not remove features with measured $\Delta(g-i)< -0.5$ as neighbors. The grey shaded region in the top panel shows the color cut that we implement on the color measurements of individual tidal features to remove neighbors in the shell sample.

Stream colors

The streams in our sample are bluer with respect to their hosts than the shells are, with a mean offset of -0.38 ± 0.02 mag (see bottom row of Figure 2.10). There are also a number of very blue streams around less massive galaxies. We bound the restframe colors of these streams by calculating K-corrections for three SSPs from Bruzual and Charlot 2003 with a Chabrier [2003a] initial mass function for a young (0.5 Gyr), intermediate-aged (5 Gyr), and old (12 Gyr) population (see Figure 2.11). The $(g-i)$ rest-frame colors of the SSPs are shown by the dashed vertical lines. Based on the rest-frame $(g-i)$ colors of the streams relative to those of the SSPs, a subset of streams in our sample are blue enough to suggest that they likely host active star formation.

We do a visual search for UV counterparts to our stream sample in Galaxy Evolution Explorer [*GALEX*, Martin et al., 2005, Morrissey et al., 2007] imaging surveys (i.e. the All-Sky Imaging, Medium Imaging, Deep Imaging, and Nearby Galaxy Surveys, as well as the Guest Investigator Program). There are 8 systems in our sample (of the 280 cases where imaging was available) that

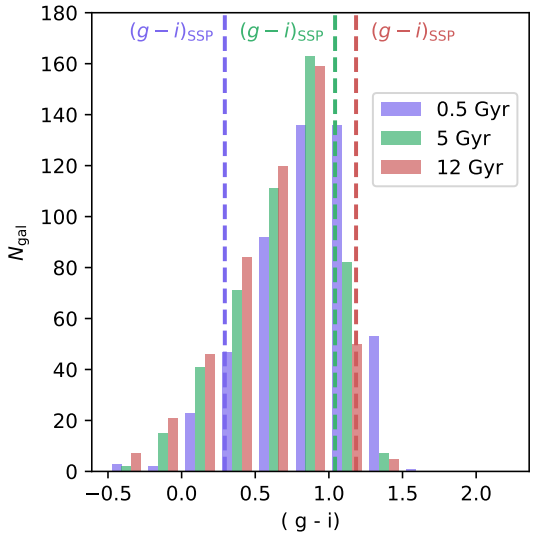

Figure 2.11 The distribution of $(g-i)$ restframe colors for our stream sample, using the K-correction computed for a 0.5 Gyr (purple), 5 Gyr (green), and 12 Gyr (red) SSP from Bruzual and Charlot 2003. The dashed vertical lines show the restframe colors for, from left to right, the 0.5 Gyr (purple), 5 Gyr (green) and 12 Gyr (red) populations. The existence of streams with rest-frame colors bluer than the youngest SSP considered implies that a subset of the streams are not on the red sequence, and host star formation.

show obvious bright *GALEX* counterparts associated with detected streams (though 2 of these cases were tidal debris created by an ongoing major merger), and it is likely that there are more *GALEX*-detected streams that would be found as a result of more careful photometry; we leave a more detailed examination of UV stream counterparts to future work.

2.5 Discussion

For decades, astronomers have used tidal features to probe the merger histories and potentials of the Milky Way and external galaxies [Quinn, 1983, 1984, Dupraz and Combes, 1986, Hernquist and Quinn, 1987, 1988, 1989, Hernquist and Spergel, 1992, van Dokkum, 2005, Kawata et al., 2006, Johnston et al., 2008, Sanderson and Helmi, 2013, Hendel and Johnston, 2015, Price-Whelan et al., 2016]. But disentangling the relative importance of merger mass ratio, orbital angular momentum,

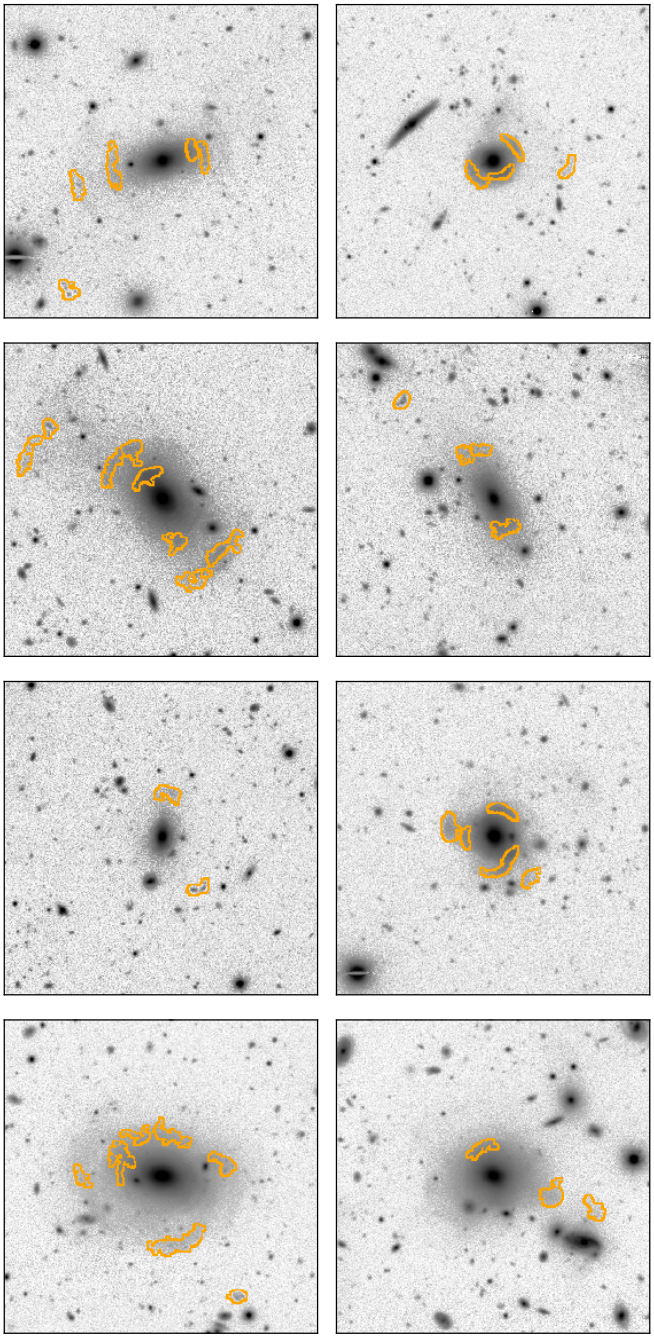

Figure 2.12 *Left:* $i_{\rm HSC}$ band imaging of a sample of shells where the color of the shell caustics (boundaries defined by the orange outlines) is consistent with the color of the host galaxy within $1R_{\rm e,host}$. *Right:* a sample of shells for which the color of the shell caustics is bluer ($\Delta m < -0.25$ mag) than the color of the host galaxy within $1R_{\rm e,host}$. All panels use a logarithmic stretch to increase contrast at low surface brightness. The shells that are as red as their host galaxy cores display a higher incidence of type I shells ($86^{+14}_{-35}\%$) than their blue counterparts ($30 \pm 14\%$).

and galaxy potential shape is non-trivial from both an observational and theoretical standpoint.

HSC-SSP provides the on-sky area and surface brightness sensitivity to generate an unprecedentedly large sample of shells and streams around external galaxies, giving us the numbers necessary to consider, on a statistical level, the questions of tidal feature formation. With a sample of 1,201 tidal feature hosts from the on-going survey, we are able to compare the characteristics of the observed shell and stream samples. We find that shells are more commonly associated with massive, high-concentration galaxies (see Figure 2.7); although streams are more common (214 shell and 987 stream hosts), the fraction of tidal features that are classified as shells rises steeply with host stellar mass (see Figure 2.9). We additionally measure the colors of a subset of extended tidal features; this allows us to estimate the mass ratio of the merger event in the case of the red sequence progenitors (see Figure 2.10), and gives insight into the prevalence of star formation in tidal features for non-quiescent progenitors (see Figure 2.11). Here, we consider probable formation scenarios and physical characteristics of a typical tidal feature system in our sample.

2.5.1 The mass ratio of shell-forming events

First we consider the mass ratios of the mergers that formed the shells in our sample. We have observed a bias in host galaxies towards massive ellipticals (see Figure 2.9 and Figure 2.7). In the canonical theoretical picture of tidal feature formation, streams and shells are created from the stars in a satellite galaxy as it falls into a more massive halo; shells are formed from satellites on orbits with low angular momentum, and the debris morphology gradual transitions from "shell-like" to "stream-like" with increasing angular momentum [Johnston et al., 2008, Sanderson and Helmi, 2013, Amorisco, 2015, Hendel and Johnston, 2015]. The idea that shells could form from major mergers was introduced several decades ago [Hernquist and Spergel, 1992], and recent theoretical work using cosmological simulations has suggested that the shell population is dominated by mergers more major than 10:1 (and that the distribution peaks at ≈1:1, Pop et al. 2017b,a).

In the minor merger picture of tidal feature formation, as host mass rises, the fraction of red sequence satellites also rises [Hansen et al., 2009, Skelton et al., 2009, Wetzel et al., 2012, Wang et al., 2014, Sales et al., 2015]. In the two-stage model of galaxy formation [Oser et al., 2010], such

hosts are have built up the outskirts of the galaxy since $z \lesssim 2$ via dry mergers of, on average, mass ratios of ≈5:1 [Gabor and Davé, 2012, Oser et al., 2012, Hilz et al., 2013]. Observations of such galaxies in SDSS also indicate that the satellite population is dominated by red sequence galaxies in both the field [Wang et al., 2014] and in high-density environments [Hansen et al., 2009].

The dominance of red sequence satellites is generally understood to originate from interactions between the host and satellite. Cold gas reservoirs in infalling satellites are thought to be drained via environmental effects: the satellites' gas reservoirs experience ram-pressure stripping [Gunn and Gott, 1972, Simpson et al., 2018], are unable to accrete new gas, and, in halos with $M_{\rm halo} > 10^{12} M_{\odot}$, undergo shock heating [Dekel and Birnboim, 2006]. At lower host masses, these effects are expected to be significantly weaker, allowing the blue satellite fraction to rise as the host mass decreases [Prescott et al., 2011, Wang et al., 2014, Sales et al., 2015]. The characteristics of the observed tidal feature population are then intrinsically linked to the progenitor population from which they were formed.

For shells with a major merger origin, where the observed host light contains a significant contribution from the interloper, the shells should be at similar metallicities to the host galaxy core [Pop et al., 2017a]. This leads to shell colors that are consistent to that of the host core, to within our measurement error. Thus, we expect that the majority of shell-forming progenitors are red sequence galaxies for which $\Delta(g-i)$ provides a probe of the merger mass ratio.

Signatures of major and minor shell-forming mergers

We find that the majority of shell galaxies have colors which are consistent with a minor merger origin; from our measured mean value of $\Delta(g-i) = -0.15 \pm 0.02$, we place an upper limit on our mean mass ratio of $\approx 4:1$ via the stellar mass-$(g-i)_{\rm HSC}$ relation for our SDSS parent sample, though the spread and flattening in the mass-color relation prevents us from inferring a precise mass ratio from the colors of any given individual tidal feature system. It should be noted that this procedure has large error bars, especially at high host masses due to the flattening of the color-mass relation – previous studies that find color differences close to our mean color difference cite mass ratios as small as $90:1$ for a host galaxy of $M_{\rm I} \approx -18.7$ mag [Gu et al., 2013].

The detection of shells that are as red as their hosts is suggestive of a major merger origin for some of the shell systems. The observed correlation between shell morphology and shell color (and therefore mass ratio) in Section 2.4.3 is in good agreement with predictions from Amorisco [2017], who shows that progressively larger satellites (in terms of merger mass ratio) are dragged into more radial orbits via dynamical friction. This morphology-color relation is also in agreement with the visual morphology of the shells presented in Pop et al. [2017b]. In the picture presented by Amorisco [2017], the more major shell-forming mergers in our sample should form the classical Type I shells; indeed, we observed that $86^{+14}_{-35}\%$ of our "red shell" galaxies are Type I shells. Meanwhile, the shells formed from more minor mergers may retain increasingly more angular momentum at the point at which the stars were stripped. This results in shell morphologies suggestive of higher angular momenta where the shell caustics are distributed randomly in azimuth about the host core [Sanderson and Helmi, 2013, Hendel and Johnston, 2015] and a lower fraction of Type I shells ($30 \pm 14\%$). Cosmological studies also suggest that more major mergers are preferentially accreted along the major axis of the galaxy [Wang et al., 2005]; major merger shells are also expected to form preferentially as Type I shells [Hernquist and Spergel, 1992].

We therefore suggest that the majority of observable shells are generated from intermediate and minor mergers, while major mergers play an important but subdominant role in shell formation. This picture is in agreement with the current state of the literature, in which the majority of observations point to a minor merger origin [Malin et al., 1983, Quinn, 1983, Fort et al., 1986, Gu et al., 2013, Foster et al., 2014], but there exists some evidence for shells with a major merger origin [see, e.g. Carlsten et al., 2017, Paudel et al., 2017]. Our main tension with the results of Pop et al. [2017b] is in the mass ratio distribution of shell-forming events; whereas Pop et al. [2017b] find a distribution dominated by relatively major mergers that peaks at ≈1:1 mergers, we find that shells are primarily formed by mergers with mass ratios more minor than ≈4:1, with a tail towards major mergers.

Both our sample and the results of Pop et al. [2017a], however, indicate that major mergers tend to form Type I shells. Our observations are also in agreement with the predictions of Hendel and Johnston [2015] and Pop et al. [2017b], which predict that the expected number of shell galaxies

should increase with the mass of the host. Further work is necessary to explore possible technical, observational, or physical explanations for the discrepancies in the nature of HSC and *Illustris* shell galaxies of Pop et al. [2017b]. In particular, the appearance and characteristics of specific shell morphologies should be compared across theoretical and observational work.

Other influences on shell morphology and color

It has also been proposed that, for minor mergers, the morphology of the resulting shell system is governed by the shape of the dark matter halo. Using N-body simulations of shell-forming mergers, Dupraz and Combes [1986] propose that prolate halos preferentially form Type I shells, and that oblate halos preferentially form Type II shells. The authors furthermore state that shells around prolate halos are more common. However, it has also been argued by Hernquist and Quinn [1989] that other characteristics of the merging event (such as orbital parameters, satellite mass, etc.) play a significant role in the morphology of the resultant tidal feature, and thus obfuscate any relationship between the form of the host potential and the tidal feature morphology.

In the minor merger picture of shell formation, the outskirts of the satellite are the first material to be stripped from the infalling satellite and form the outermost shells [Hernquist and Quinn, 1987]. The color of these shells is then expected to be bluer than that of the host core. To consider whether this effect poses a significant problem for our analysis, we refer to the color gradients measured by D'Souza et al. [2014] for ellipticals. We consider here whether the color difference caused by stripping material from the outskirts of the infalling satellite is of similar magnitude to the color difference caused by the luminosity-color relation of ellipticals. Material stripped from the half-light radius of an elliptical satellite would be $\sim 0.05 - 0.1$ mag bluer in $(g-r)_{\rm SDSS}$ than at the core of the satellite. Using the same color gradients to compare a host galaxy of $11 < \log(M_\star/M_\odot) < 11.4$ and a satellite of $10.2 < \log(M_\star/M_\odot) < 10.4$, D'Souza et al. 2014 yields a color difference of $\Delta(g-r)_{\rm SDSS} \sim 0.19$. The color difference between this hypothetical host and satellite is almost a factor of 4 larger than the color difference between the satellite host and outskirts. Therefore, we conclude that the color gradient of the satellite galaxies cannot mimic the full color difference originating from the mass ratio between the satellite and host galaxy.

2.5.2 Star formation in tidal features

We now consider the characteristics of streams in our sample, which occur across the full host stellar mass range of our smaple. In particular, we consider the evidence for star formation in the streams in our samples.

At $\log(M_\star/M_\odot) \lesssim 11$, the majority of infalling satellites are blue [Wang et al., 2014, Sales et al., 2015]. Thus, we expect some tidal features that host star formation around such galaxies. As expected, we find no evidence for tidal features that host star formation around massive early-type galaxies (see previous section). Outside of our high mass, high-concentration sample, however, there are a significant number of streams with colors suggestive of active star formation (see Figure 2.11). The detection of UV emission in a subset of streams in *GALEX* imaging also suggests that the streams are capable of hosting star formation. Such star-forming streams have previously been observed [see, e.g. Adamo et al., 2012, Knierman et al., 2012, Atkinson et al., 2013], and are thought to represent star-forming environments that are significantly different from star formation in the disc of a galaxy. It is thus of interest to further study the star-forming properties of these extended features, though a more detailed analysis of their composition and star forming history is inaccessible from optical imaging alone.

2.5.3 Host galaxy morphologies

Finally, we consider the connection between host galaxy morphology and tidal feature morphology. In Section 2.4.2, we showed that the dearth of observed shells around low-concentration galaxies is not an effect of our detection methods. Here, we consider possible astrophysical origins of this phenomenon. At fixed stellar mass, ellipticals are far more likely to host observable shells than disc galaxies; we find that out of the 214 shell hosts, only 3 are late-type galaxies.

Both early-type and late-type galaxies should undergo a significant number of minor mergers throughout their assembly history. However, at fixed stellar mass, late-type galaxies generally possess a lower fraction of *ex situ* stellar mass (i.e., stars that were formed external to the galaxy and accreted after formation), as shown in Rodriguez-Gomez et al. [2016], D'Souza et al. [2014].

If it is assumed that there is no correlation between the morphology of the host galaxy and the morphology of the tidal features, we should be able to see a significantly higher number of shells around disc galaxies than are presently identified in the sample. We exclude the possibility that this is a manifestation of morphology-dependent completeness effects in Section 2.4.2, and here consider astrophysical explanations for the lack of shells around low concentration galaxies in our sample.

Two possible explanations for this phenomenon are as follows. First, the tidal feature morphology is likely more sensitive to the total mass of the system than the stellar mass alone. Mandelbaum et al. [2006] showed that for more massive galaxies ($\log(M_\star/M_\odot) \gtrsim 11.0$), elliptical galaxies tend to have larger halo masses than do disc galaxies at a fixed stellar mass. Because shells also preferentially form in more massive systems (see Figure 2.9), this picture would lead to a smaller fraction of disc galaxies with shells. The interpretation is complicated, however, by the fact that more massive ellipticals are also more likely than a massive disc to be at the center of a group or cluster; in this case, the derived halo mass would reflect the total group or cluster halo, rather than the halo of the individual galaxy alone. Furthermore, the detectable lifetime of a shell system as a function of environment is not well known, though there is evidence that the tidal feature occurrence fraction is suppressed in clusters [Adams et al., 2012, Sheen et al., 2012].

Additionally, it is probable that elliptical galaxies can host shells generated by more major mergers than can a disc galaxy. We have shown that there is a subset of shells which appear to have been created during a major merger; such events would not be able to form shells around a disc galaxy without disrupting the disc of the host [Hernquist and Spergel, 1992].

It is also likely that the most minor mass ratio at which we can detect streams is higher than for shells. Based on the analysis in Section 2.3.4, we are able to recover streams at lower mean surface brightnesses than we are able to recover shells. Holding the time of satellite infall fixed to control for passive stellar population fading, which also affects surface brightness [see, e.g., Conroy et al., 2009a], and using the surface brightness of the feature as a crude proxy for the mass ratio of the event, we would be able to detect stream-forming events at more extreme mass ratios than shell-forming events because of the difference in our completeness in streams and shells (see Figure 2.4). If the disc galaxies are unable to host a shell-forming major merger (while maintaining their disc),

and if streams are more easily detectable in more minor mergers, we would expect a lower number of shells around disc galaxies relative to ellipticals and a lower number of shells relative to streams around disc galaxies, as observed. This interpretation is also supported by the detections of shells in a small sample of disc galaxies observed at surface brightness significantly fainter than what is attainable in the Wide Layer of HSC-SSP ($\mu_V \sim 28.5$ mag arcsec^{-2}) by Martínez-Delgado et al. [2010].

Aside from the observed dearth of shells around spirals, we also note an apparent bias for shells around disc galaxies to be oriented such that the axis of symmetry of the shell lies in the plane of the disc (see Figure 2.8). Though this observation hinges on extremely small numbers (face-on discs cannot be considered in this analysis, as shells oriented perpendicular to the disc would lie on top of the disc), it is of interest to note that the disc galaxies that host shells in Morales et al. [2018], NGC 681 and NGC 4762, are aligned in the same manner as those in our sample.

However, because this sample targeted primarily massive, red galaxies, it would be informative to explore this morphological difference further using a sample that includes more late-type galaxies.

2.6 Summary and conclusions

In this work, we have presented observations of 1,201 systems that host tidal features in the redshift range $0.05 < z < 0.45$ in the HSC-SSP Wide Layer with accompanying spectroscopic observations from SDSS. Of these systems, we find that 214 host shells, and 987 host streams. For 78 shell systems and 497 stream systems, we are additionally able to measure the average $(g - i)$ color of the tidal features.

In our sample, streams appear around galaxies with a range of masses, colors, and concentrations. We find evidence for star formation in streams around low mass host galaxies, but no evidence for star formation around massive ETGs, suggesting that satellites are quickly quenched upon infall into a massive elliptical. Shells appear to form preferentially around massive, red, ETGs, with only 3 examples of shell systems around disc galaxies in our sample.

Although the majority of the shells in our sample appear to be generated from a minor merger,

there exist a non-negligible number of shells which appear to have originated from a major merger. These "red shell" galaxies are furthermore predominantly Type I, wherein the shell caustics are roughly symmetric about the major axis of the galaxy; this morphological dependence has been predicted in simulations [Hernquist and Spergel, 1992, Pop et al., 2017b].

Based on the performance of the automatic detection method presented in this work, future investigations will focus on fully automating the detection and morphological classification of tidal features such that the technique may be autonomously applied to the full HSC dataset and future wide field imaging campaigns (e.g. *LSST*, *Euclid*), as well as extending our analysis to existing datasets. Because the majority of tidal features are expected to lie at $\gtrsim 30$ mag arcsec^{-2} [Johnston et al., 2008], efforts using future generations of deep wide-field imaging will greatly increase the number of detected tidal features around galaxies, and provide a new window into the impact of minor mergers upon galaxy growth.

2.7 Appendix: Image decomposition

To illustrate our method of image decomposition, we consider the case of a galaxy hosting a stream in Figure 2.13. The top three rows show the $n = 5$ and $n = 31$ components of the decomposition (middle and right columns, respectively) and the input image (left column). As can be seen from the size of the bright objects' cores, the spatial frequencies that the nth coefficient probes decrease as n grows large. The stream itself has red observed colors, detected clearly in the i_{HSC} and z_{HSC} bands and less so in r_{HSC}. We show multiband observations of this stream in order to show the change in algorithm performance as a function of the contrast in surface brightness between the tidal feature and the host galaxy. In practice, to cover the largest amount of area possible while keeping the application of our method consistent, we consider only the i_{HSC} band during detection.

The effect of noise on our decomposition is also visible in the middle column of Figure 2.13. The z_{HSC} band imaging has significantly more noise than the i_{HSC} image, which corresponds to higher noise in the $\mathbf{c^{(5)}}$ image. Because the noise is largely uncorrelated on large scales, however, there is relatively little difference between the $\mathbf{c^{(31)}}$ image of the i_{HSC} band and that of its counterpart in

the z_{HSC} band.

Finally, we show the effect of cleaning the detection image in the bottom row of Figure 2.13. The left panel shows the initial detection image, $\mathbf{C}$, as obtained from Equation 2.4. The middle panel shows the detection image after the cleaning steps outlined in Section 2.3.1 are applied. The right panel shows the output of the detection algorithm on the i_{HSC} band image. As noted in Section 2.3.1, features in the detection map that overlap significantly with neighboring sources are not included in the final detection.

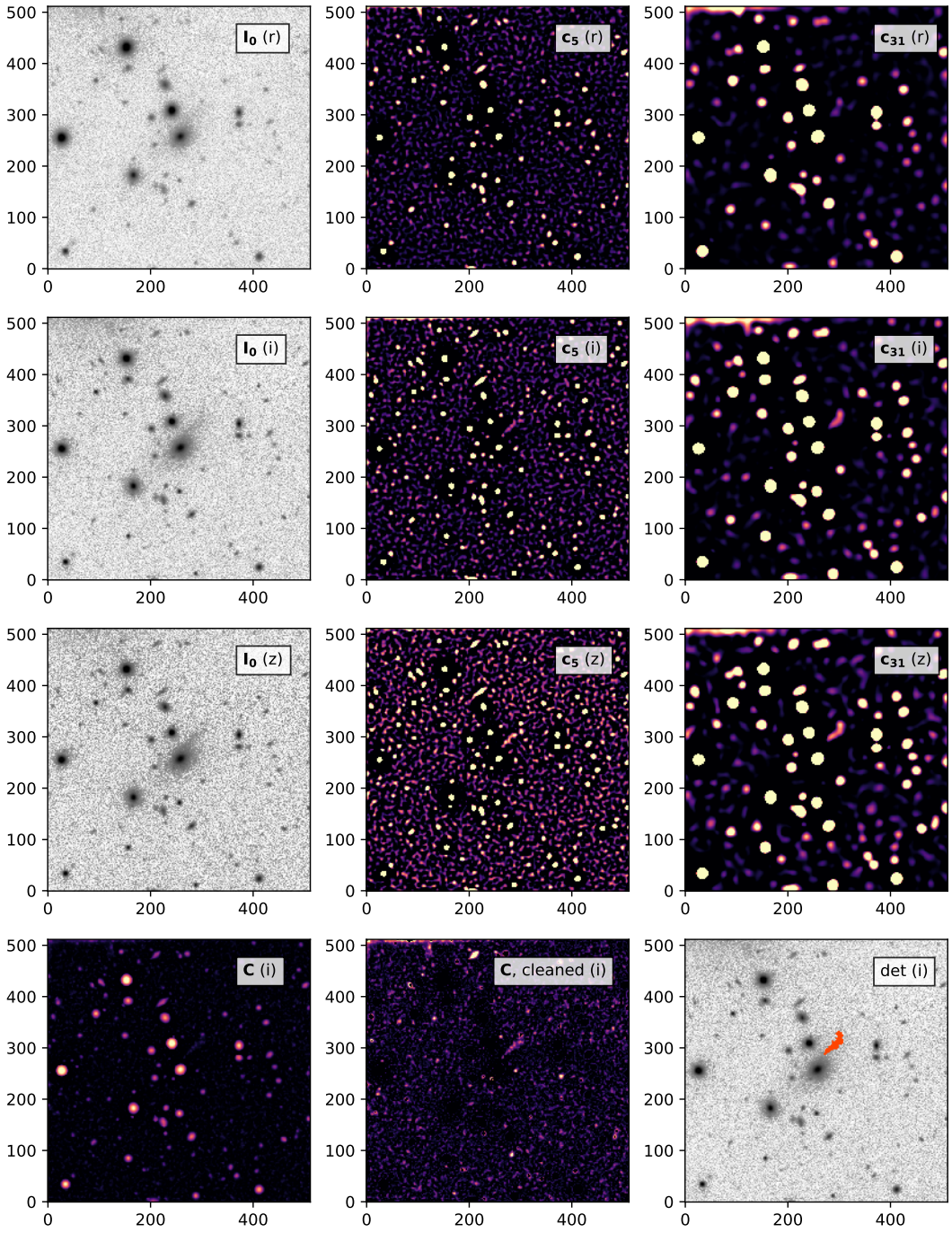

Figure 2.13 Example decompositions following the algorithm presented in Section 2.3.1. *Top row:* From left: the $r_{\rm HSC}$ band input image, the $\mathbf{c}^{(5)}$ component, and the $\mathbf{c}^{(31)}$ component. *Second row:* the same for $i_{\rm HSC}$. *Third row:* the same for $z_{\rm HSC}$. *Bottom row:* From left, the initial detection image ($\mathbf{C}$) for the $i_{\rm HSC}$ band, the cleaned detection image (wherein the cores of sources and spiral arms are removed), and the detection map (red) overlaid on the $i_{\rm HSC}$ band input image.

2.8 Appendix: Surface brightness limits

Here, we consider the surface brightness limits that we would have derived following examples in the literature. The nominal surface brightness limits that we calculate from the methods in Atkinson et al. [2013] and Morales et al. [2018] are comparable to the values generated for the Atkinson et al. [2013] and Morales et al. [2018] datasets, who give surface brightness limits of $\mu \sim 27.7$ mag arcsec^{-2} (stacked *gri* images) and $\mu \sim 28.1$ mag arcsec^{-2} ($r_{\rm SDSS}$ imaging). However, our tidal feature injections indicate that we are highly incomplete at these surface brightnesses (see Figure 2.4).

Figure 2.14 shows the result of injecting a simulated stream at the HSC nominal surface brightness limits (not including the bound remnant visible in the upper right panel) of 26.375 mag arcsec^{-2}, where we measure a completeness of $\approx 75\%$ (bottom left), and 28.4 mag arcsec^{-2} (bottom right). Though 28.4 mag arcsec^{-2} is the nominal surface brightness of the HSC i-band when derived in the same way as estimates for other surveys in the literature [Atkinson et al., 2013, Hood et al., 2018, Morales et al., 2018], a stream at this surface brightness is not detectable through either human or automatic means. We do note that Huang et al. 2018b measured surface brightness profiles of massive galaxies down to $\mu_i \sim 28.5$ mag arcsec^{-2} – this measurement was performed by leveraging the information provided by the shape and location of the galaxy isophotes at smaller radii. In our case, in order to assess the completeness of our automated search, it is necessary to run the full suite of injected simulations as detailed in Section 2.3.4.

Furthermore, the surface brightness limit of a tidal feature search is an intrinsically difficult quantity to measure, as the detectability of a tidal feature is dependent on both its surface brightness and the area of the feature, which is naturally different for each system. One may consider the limiting case in which there are two tidal features with the same peak surface brightness μ_0. The first tidal feature has only one pixel with a value corresponding to μ_0, while the second has many pixels with values approximately μ_0. Though the two tidal features have the same peak surface brightness, the second instance will be significantly easier to detect. In visual inspection methods, the human hours needed to quantify completeness as a function of these factors is prohibitive. In

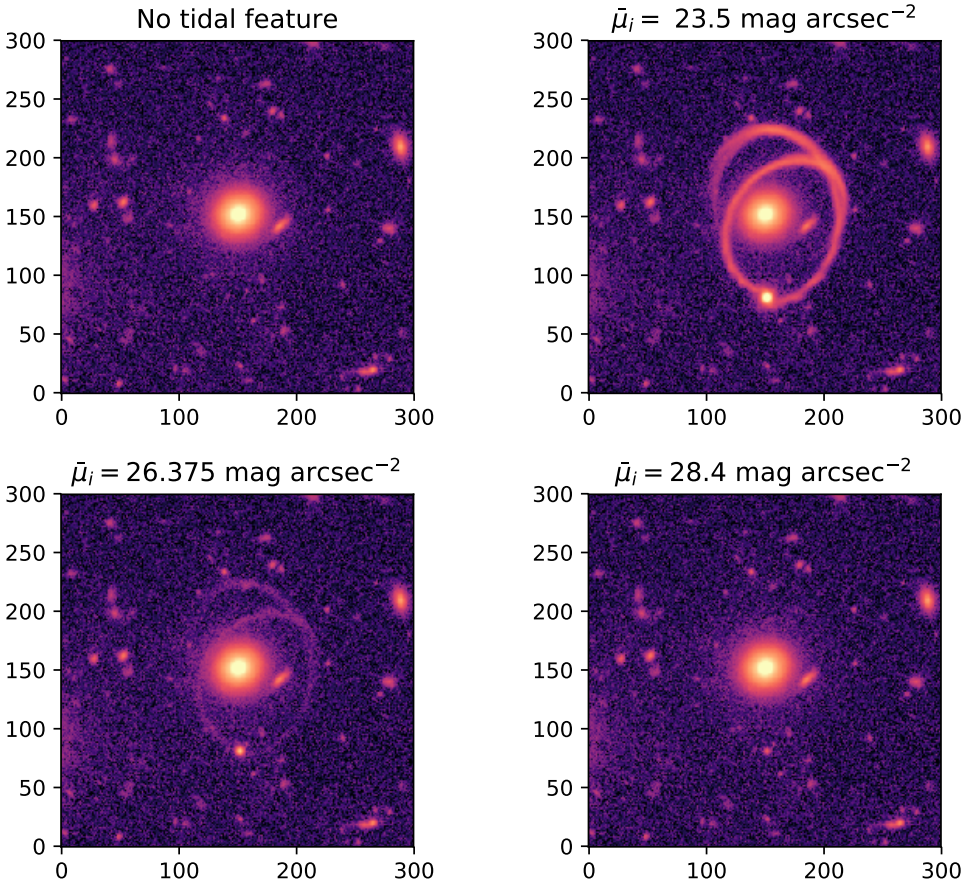

Figure 2.14 An example of $i_{\rm HSC}$ band imaging of a non-interacting galaxy from the parent sample stacked with a simulated stream from [Hendel and Johnston, 2015]. *Top left:* The original $i_{\rm HSC}$ band image. *Top right:* the galaxy with a simulated stream injected into the image, where $\bar{\mu}_i = 23.5$ mag arcsec^{-2}. *Bottom left:* the same stream with $\bar{\mu}_i = 26.375$ mag arcsec^{-2}, the surface brightness at which our completeness for extended ($d > 5R_{\rm e,host}$) is at $\approx 75\%$ (see Section 2.3.4 for details). *Bottom right:* the same stream with $\bar{\mu}_i = 28.4$ mag arcsec^{-2}, the surface brightness limit derived using the method from [Morales et al., 2018]. The stream is not detectable in either case.

our automatic detection method, however, simulations can be run easily. Thus, in Section 2.3.4, we consider both the mean surface brightness and the extendedness of the tidal feature in describing our completeness.

Chapter 3

Mergers Between Dwarf Galaxies

3.1 Introduction

Dwarf galaxies are the most abundant subset of galaxies in the universe [Binggeli et al., 1988]. Though hierarchical structure formation should also proceed for these systems, there are very few examples of extragalactic dwarf-dwarf mergers in the literature. A number of individual cases have been examined in great detail [Martinez-Delgado et al., 2012, Annibali et al., 2016, Privon et al., 2017], and a small number of systematic searches for dwarfs undergoing interactions with other low-mass systems have been performed either by searching for dwarf companions [Stierwalt et al., 2017], or by searching for low surface brightness (LSB) merger signatures [Paudel et al., 2018].

Such studies show evidence for hierarchical merging at low galaxy mass – Annibali et al. [2019] finds evidence for ongoing accretion events around the dwarf galaxy DD0 68 with mass ratios of 10:1 and 100:1. Though these focused studies reveal in great detail the accretion histories of individual systems, the question of the commonality of merger features around dwarf galaxies is still poorly understood.

From matching SDSS to Millenium-II, $\approx 3\%$ of dwarf galaxies ($\log(M_\star/M_\odot) < 9.6$) should have a companion of at least $\sim 30\%$ its mass. Moreover, $\sim 10\%$ of dwarf galaxies are expected to have undergone a major merger since $z \sim 1$ [Sales et al., 2013]. It is thus of interest to characterize the

frequency and characteristics of dwarf galaxies that show signs of a recent dwarf-dwarf merger.

The star formation activity during and after the merger of two dwarf galaxies is also a largely unconstrained realm. Less than 2% of dwarf galaxies in the field are observed to be quiescent [Geha et al., 2012]. If dwarf galaxies are indeed undergoing major mergers, this suggests that mergers between dwarfs do not succeed in quenching star formation, in contrast to the expectation of major merger outcomes for more massive galaxies [Bekki, 1998, Hopkins et al., 2008, Ellison et al., 2018].

Furthermore, such dwarf-dwarf mergers have been proposed as a mechanism to create Blue Compact Dwarfs (hereafter BCDs). These starbursting dwarfs are at $M_B \geq -18$, have physical sizes of less than 1 kpc, and show a strongly starbursting spectrum [Bekki, 2008a]. BCDs tend to show a more centrally concentrated mass profile than a typical dwarf irregular galaxy, as well as higher central surface brightnesses [Janowiecki and Salzer, 2014]. However, some BCDs also host old stellar populations of $\gtrsim 1$ Gyr [Aloisi et al., 2007, Annibali et al., 2013].

Previous searches for tidal features around low mass galaxies have found a depressed tidal feature detection fraction relative to samples of more massive galaxies. A study of SDSS and CFHT Legacy Survey data found that approximately 0.68% of the low mass galaxies in their sample host tidal features [Paudel et al., 2018]. Though the tidal feature fraction should increase as the effective surface brightness limit improves [see, e.g. Annibali et al., 2019], it is possible that tidal features around dwarf galaxies at low-z are intrinsically rare features. Thus, in this work we search for LSB tidal debris around a sample of isolated dwarf galaxies identified in the GAMA and SDSS spectroscopic surveys at $z < 0.12$ in imaging from the Wide layer of the Hyper Suprime-Cam Subaru Strategic Program (HSC-SSP) imaging.

In Section 3.2 we establish the parent sample of spectroscopically confirmed dwarfs with imaging in HSC-SSP. In Section 3.3 we outline the automated detection algorithm employed to search for tidal debris around dwarf galaxies. We present the dependence of the frequency of detectable features around a host galaxy as a function of the host properties and star formation activity in Section 3.4. Finally, we discuss the implications for the observational dwarf galaxy merging sequence in Section 3.5.

Throughout this paper we adopt a standard flat ΛCDM model in which $H_0 = 70$ km s^{-1} Mpc^{-1}

and $\Omega_m = 0.3$.

3.2 Sample Selection

For the purposes of this study, we follow [Stierwalt et al., 2015] in defining a dwarf galaxy as a galaxy with stellar mass of $\log(M_\star/M_\odot) < 9.6$. We note that this is somewhat lower than the value used by other studies (for example, Paudel et al. [2018] uses a cutoff of $\log(M_\star/M_\odot) < 10.0$).

We additionally exclude galaxies at $z > 0.13$, as we are in practice unable to find LSB tidal debris around galaxies at this mass range above this redshift cutoff (for a discussion of the completeness of our tidal feature detection method, see Figure 3.4).

3.2.1 Spectroscopic sample

To generate a sample of isolated dwarfs, we consider only galaxies with spectra from either the Sloan Digital Sky Survey (SDSS) spectroscopic surveys [both legacy and BOSS surveys, Strauss et al., 2002, Dawson et al., 2013, Reid et al., 2016] or from the Galaxy and Mass Assembly (GAMA) spectroscopic survey [Baldry et al., 2018].

These cuts leave a parent sample of 8412 dwarf galaxies. 3733 of the target galaxies have spectra from the SDSS surveys, while 5001 galaxies have spectra from GAMA (678 galaxies have spectra from both GAMA and SDSS).

For galaxies with GAMA spectra, we adopt the stellar masses provided by the GAMA team [Taylor et al., 2011]. These stellar masses are measured assuming a Chabrier initial mass function [Chabrier, 2003b]. For galaxies with SDSS spectra, we adopt stellar masses derived using the Conroy et al. [2009b] flexible stellar population synthesis (FSPS) models assuming a Kroupa initial mass function [Kroupa, 2001]. For galaxies in our sample that have spectroscopy from both GAMA and SDSS, we find that the FSPS stellar masses are higher than the equivalent measurement in the GAMA catalog by a median of 0.08 dex and a median absolute deviation of 0.35 dex. To reconcile this systematic shift, we reduce the masses derived from SDSS observations by 0.08 dex, but note that including or excluding this shift does not affect the results presented in this work.

Because we want to study the star formation properties of these dwarfs, we also use the Hα line measurements provided by the GAMA and SDSS spectroscopic databases.

Finally, because we are interested only in interactions between two dwarf galaxies, we require that the target galaxies have a 3D physical separation of at least 1 Mpc from the nearest massive galaxy ($\log(M_\star/M_\odot) > 10.0$) in the NASA Sloan Atlas [Blanton et al., 2011], as measured from the angular diameter distances using the spectroscopic redshifts of the target catalog and the NSA. In this work, we use NSA version 1.0.1, which was released with SDSS DR13 and reaches $z \sim 0.15$.

Though the NSA is nominally complete only to $z = 0.055$, we note that the fraction of galaxies that are flagged as satellites is independent of redshift. To confirm that we are not misclassifying satellite dwarfs, we compare the satellite fraction as function of redshift for the sample as constructed above and the satellite fraction of the dwarfs with GAMA spectra when isolation was evaluated by matching to the GAMA spectroscopic catalog. We find no significant differences in the satellite fraction. We therefore conclude that we are not misclassifying a significant number of satellite galaxies as field dwarfs.

We also remove galaxies that are projected closer than 0.01 deg to a massive galaxy, regardless of physical association. This cut aims to remove those cases in which a dwarf galaxy overlaps significantly with high surface brightness light from a more massive projected neighbor.

The isolation criterion that we adopt here is somewhat different than isolation criteria adopted in the literature in that we make a cut in angular diameter distance rather than directly in velocity space [Geha et al., 2012, Paudel et al., 2018]. Because the isolation of the galaxies in question is important to the interpretation of this work, we additionally verify that the choice of isolation criterion does not affect our results; we refer the reader to Section 3.7 for a discussion therein.

These distance cuts leave a final sample of 6683 galaxies; 3169 of these galaxies have spectra from SDSS, and 4034 have spectra from GAMA. 520 galaxies have spectra from both SDSS and GAMA. In Figure 3.1, we show the distribution of the GAMA and SDSS dwarfs as a function of redshift (top) and stellar mass (bottom). We also show the distribution of the isolated dwarf sample in black. To show that the isolation cut does not introduce a shift in the redshift or stellar mass of the parent sample, we also show a random subset of 6683 galaxies from the full dwarf sample as

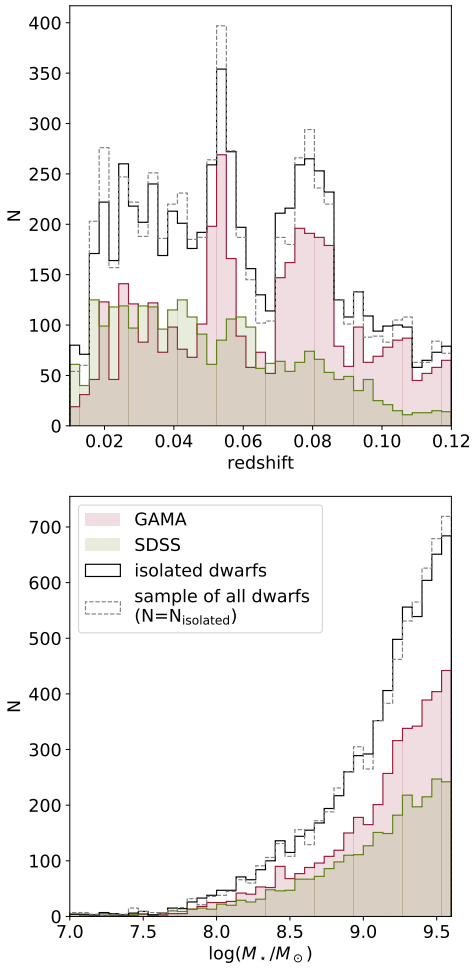

Figure 3.1 The distribution of our sample in redshift (top panel) and stellar mass (bottom panel). In both panels, the red filled histogram shows the GAMA dwarfs and the green filled histogram shows the SDSS dwarfs. The unfilled black and dashed grey histograms show the distribution of the full isolated dwarf sample and a random subset of 6683 galaxies from the full dwarf sample. This is to guide the eye and show that show that there is no significant difference between the distributions of the full and isolated dwarf samples.

the dashed grey histogram.

Though the distribution of the SDSS and GAMA galaxy samples are markedly different in redshift and stellar mass, we will show that we reach the same conclusions when considering only the SDSS or only the GAMA sample. In cases where spectra from both SDSS and GAMA are available, we prioritize measurements from GAMA because the spectra are deeper. This will be discussed more fully in Section 3.3 and Section 3.7.

3.2.2 HSC-SSP Imaging

The detection of tidal debris resulting from low mass mergers requires imaging that covers a large enough area to find a sizable number of galaxies that host such features while simultaneously probing the relevant low surface brightness universe. HSC-SSP is particularly well-suited towards this aim; HSC-SSP will cover over 1400 square degrees on the sky to a limiting magnitude of $i_{\rm HSC} \sim 26$ for point sources [Bosch et al., 2018]. Detection of low surface brightness features is a function of both the detection algorithm and the imaging sensitivity. We find that HSC-SSP reaches surface brightness limit of $\sim$27 mag arcsec^{-2} when detecting isolated LSB structure [Greco et al., 2018c, Kado-Fong et al., 2018], and > 28.5 mag arcsec^{-2} when probing LSB structure of known morphology [e.g. the smooth halo of massive ellipticals, Huang et al., 2018e].

For this work, we use the HSC S18A data release, which covers over 300 square degrees on the sky in $g_{\rm HSC}$, $r_{\rm HSC}$, and $i_{\rm HSC}$. We do not use $z_{\rm HSC}$ and $y_{\rm HSC}$ imaging because the surface brightness limits and seeing of these bands are significantly worse than the bluer bands, and including these bands would decrease the usable area of this work without contributing significantly to the detection of LSB structure. This data release is equivalent to the second public data release (hereafter PDR2) presented in [Aihara et al., 2019]. The area covered by our search is somewhat smaller than the total area released in PDR2, as we require imaging in $g_{\rm HSC}$, $r_{\rm HSC}$, and $i_{\rm HSC}$ bands for each target galaxy. We also briefly note that the background subtraction method implemented in this release has been updated from that which was used for the first HSC-SSP public data release. This new background subtraction method reduces oversubtraction of the haloes around bright galaxies, allowing us to target galaxies at lower redshifts than were possible in Kado-Fong et al. [2018].

3.3 Tidal Feature Detection

From previous work, the fraction of dwarf galaxies that host tidal features detectable in HSC-SSP is likely on the order of a few percent [Paudel et al., 2018]; though it is possible to select tidal feature hosts via visual inspection, constructing an automatic detection algorithm is a significantly more scalable approach. Towards this end, we use an updated version of the tidal feature detection

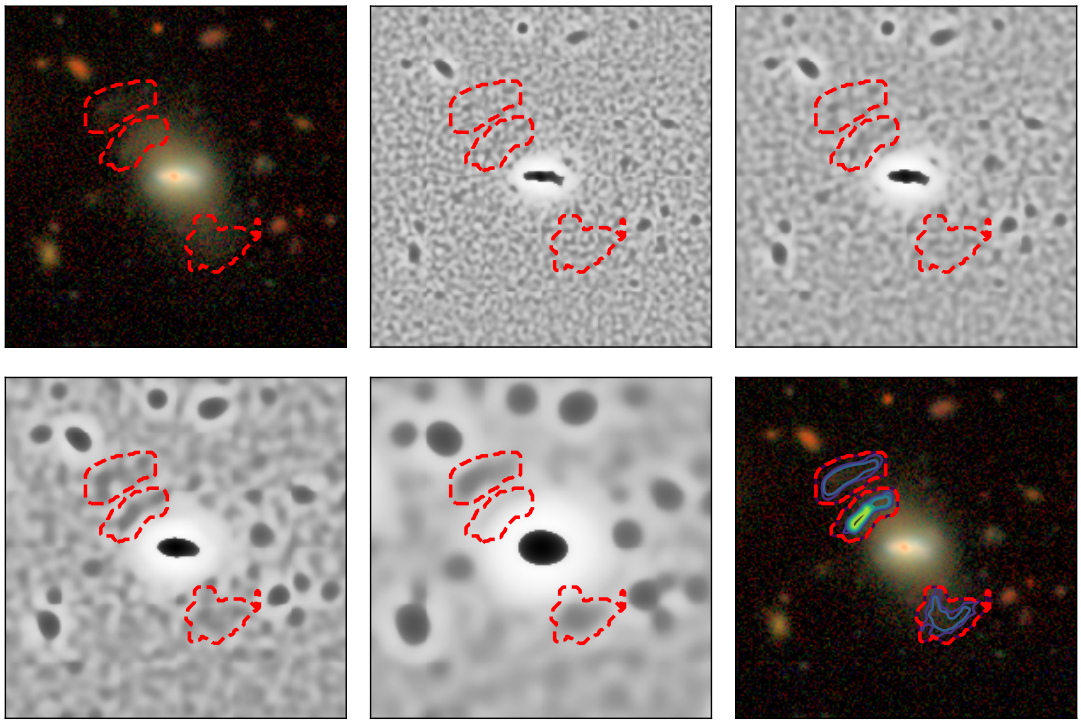

Figure 3.2 An illustration of the multiscale detection method used to find tidal debris around dwarf galaxies. *Top left:* the *gri* composite image of the target galaxy. To guide the eye, the maximal area contour of the detecion map is shown as a contour in red in all panels. *From top middle:* the starlet coefficients in order of increasing spatial scale. The intensity of the images are scaled logarithmically. We note that certain tidal features are only seen in certain coefficients. For example, the inner shell is strongly detected in the second and third coefficients, while the outer shells are detected with high significance in the third and fourth coefficients. *Bottom right:* the gri_{HSC} composite image of the target galaxy with the full detection map overlaid as a contour. The contours show regions of increasing detection significance (i.e. detected in more coefficients).

algorithm presented in Kado-Fong et al. [2018] to automatically identify tidal features around dwarf galaxies.

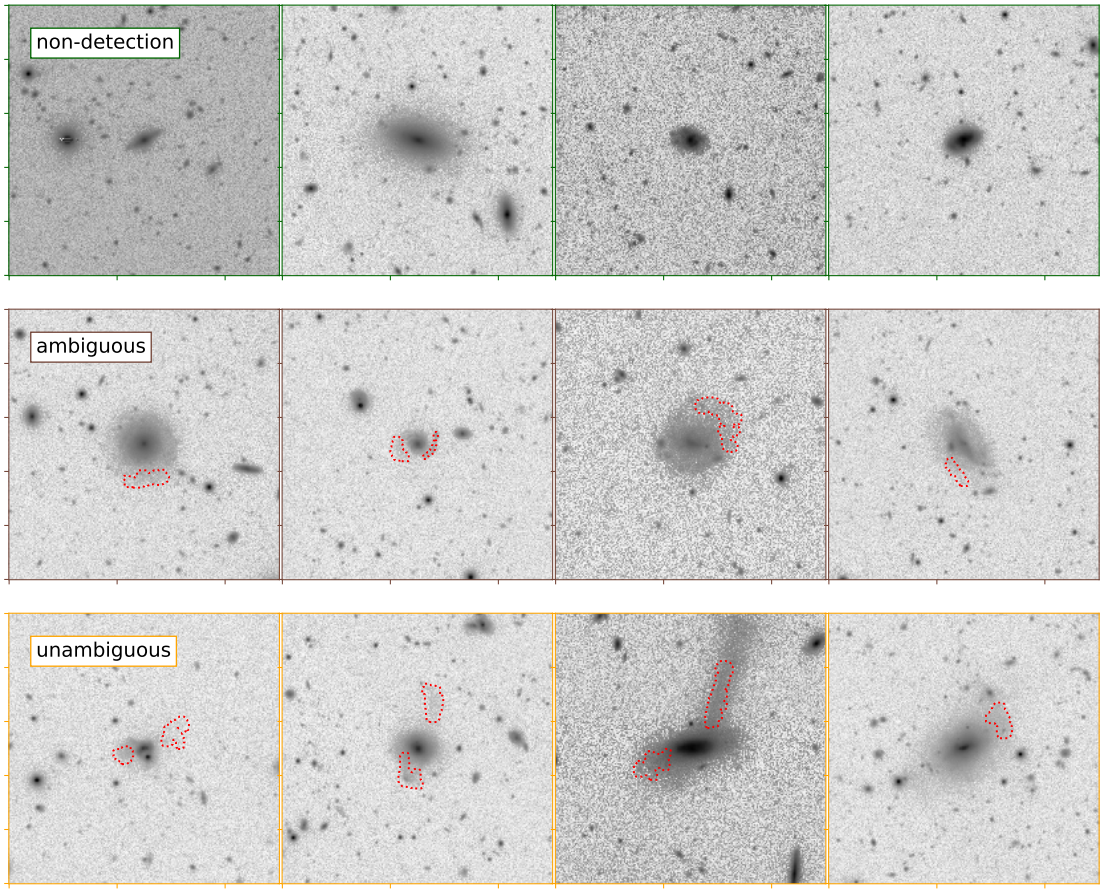

Figure 3.3 Examples of galaxies with no tidal feature detection (top row), ambiguous tidal feature detections (middle row), and unambiguous tidal feature detections (bottom row). For the examples in which candidate tidal feature systems are detected, the lowest significance level detection map is plotted as a red outline. We note that although there are some clear cases of spiral arm contamination (e.g. the far right middle panel), we do not remove these cases from the sample, and show that they do not statistically affect our conclusions.

3.3.1 Updates to the method of Kado-Fong et al. 2018

The main purpose of the algorithm presented in Kado-Fong et al. [2018] is to detect tidal features against the smooth background of a host galaxy by leveraging the contrasting spatial scales of the

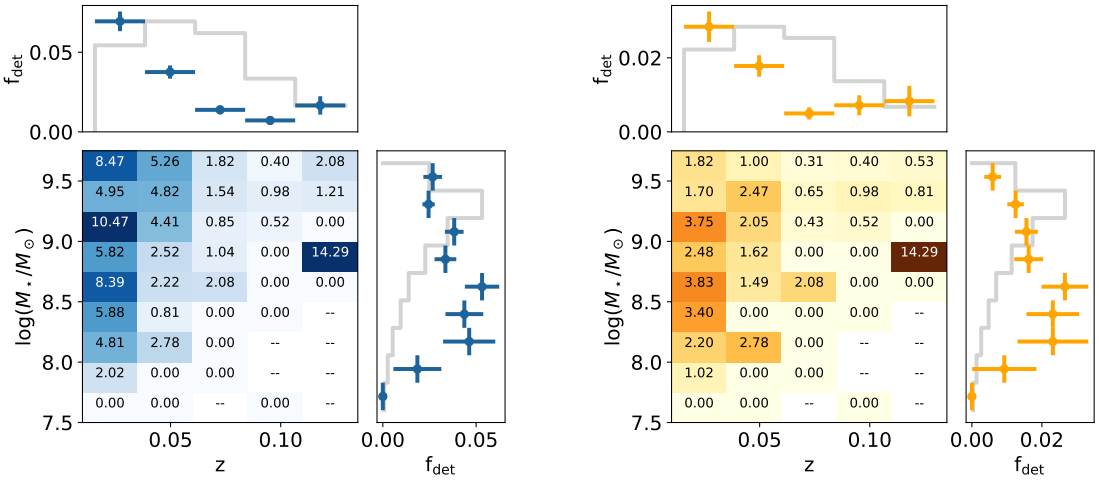

Figure 3.4 Tidal feature detection percentage for our sample of dwarfs in bins of redshift and host stellar mass (main panel). The color and numbers reflect the percentage of dwarf galaxies that host tidal features in each bin. The top auxiliary panels show the projection of the detection fraction distribution onto redshift, while the righthand auxiliary panels show the projection as a function of host stellar mass. In each auxiliary panel, the unfilled grey histogram shows the normalized distribution of the parent sample. The left panels in blue show the automated sample, while the right panels in orange show the visual sample.

tidal feature and the host halo. To do so in a way that is independent of the morphology of the host, we decompose the image into coefficients of increasing spatial scale. Tidal debris candidates are then identified as contiguous structures in the spatial decomposition.

Here, we summarize the updated detection algorithm. For the full details of the updates made to the method, see Section 3.8.

In order to detect tidal features on a variety of spatial scales, we decompose the image of the target galaxy into wavelet coefficients of increasing characteristic length; specifically, we use the starlet transform of Starck et al. [2015]. Low surface brightness features are detected in each coefficient independently and assigned to the most probable host galaxy (as determined by flux-weighted distance). Tidal features are detected independently in the g_{HSC}, r_{HSC}, and i_{HSC} band images; tidal features must be detected in at least two bands in order to be accepted as part of the

final detection map.

In Figure 3.2 we illustrate the detection method of a galaxy in our sample. The RGB images show the *gri* composite image of the galaxy, while the grey scale images show the wavelet coefficients (the first wavelet coefficient is not shown) of the $i_{\rm HSC}$ band image. The full detection map is shown in the bottom right panel of the figure.

3.3.2 Construction of the visual sample

The main purpose of the algorithm described above is to avoid the need to visually classify the full sample. However, because the morphology of many dwarf galaxies are irregular, there exist ambiguous cases in which the origin of a possible tidal feature is unclear. To ensure that the inclusion of such ambiguous cases does not bias our results, we visually inspect the automated sample and construct a subset visual sample that consists of only tidal feature systems that are unambiguously the result of a merger with another dwarf galaxy. We follow the benchmarks set forward in Paudel et al. [2018], and generally look for the morphology of the detected LSB feature to be inconsistent with extended irregular structure or flocculent spiral arms. Figure 3.3 shows a selection of example galaxies with no tidal feature detection (top row, green outlines), with an ambiguous detection (middle row, brown outlines), and with an unambiguous detection (bottom row, orange outlines).

We will use this visual sample to demonstrate that when considering trends with respect to the presence of tidal features, our results are unchanged whether or not ambiguous cases are included. When considering an individual galaxy or when asking a question that requires tidal features that are photometric quality, we recommend using the visual sample to determine whether there are unambiguous signs of merging between dwarf galaxies. As we will show below, however, we find no statistical differences in the population properties of interest between the automated sample and visual sample. In Table 3.3.2 we provide a summary of the total, field, and interacting dwarf samples.

	N	$N_{detection}$
all dwarfs	8412	284
field dwarfs	6683	224
visual sample	–	101

Table 3.1 Summary of the merging dwarf sample presented in this work. The first row gives the total number of dwarfs and number of tidal feature hosts for all dwarfs with spectroscopic confirmation and HSC imaging (i.e. including dwarfs that are non-isolated). The second row gives the same numbers, but for only those dwarfs that satisfy the isolation criterion described in Section 3.2.1. The final row gives the number of tidal feature hosts whose LSB features are unambiguously the result of a merger with a companion.

3.4 Results

In total, our automated sample consists of 224 galaxies; 101 of galaxies these galaxies make up the visual sample (i.e. are visually confirmed to be unambiguous merger debris).

We therefore find a total tidal feature detection fraction of 3.40% in the automated sample and 1.61% in the visual sample. When considering only those host galaxies at $z < 0.05$, we find a tidal feature detection fraction of 6.14% in the automated sample and 2.73% in the visual sample. We consider a more detailed analysis of our completeness as a function of host stellar mass and redshift in Section 3.4.1.

3.4.1 The automated and visual samples

In Figure 3.4 and Figure 3.5 we show the statistical properties of the automated and visual sample in blue and orange, respectively. In particular, we note that although the absolute fraction of galaxies with tidal features is shifted down for the visual sample, there is no significant shift in the relative tidal feature detection fraction as a function of any of the host galaxy properties that we examine.

In particular, Figure 3.4 shows the detection fraction for the automated sample and visual sample as a function of host galaxy mass and redshift. The main panels show the tidal feature detection fraction at a given redshift and host stellar mass, while the framing panels show the detection fraction projected along stellar mass (right) and redshift (top).

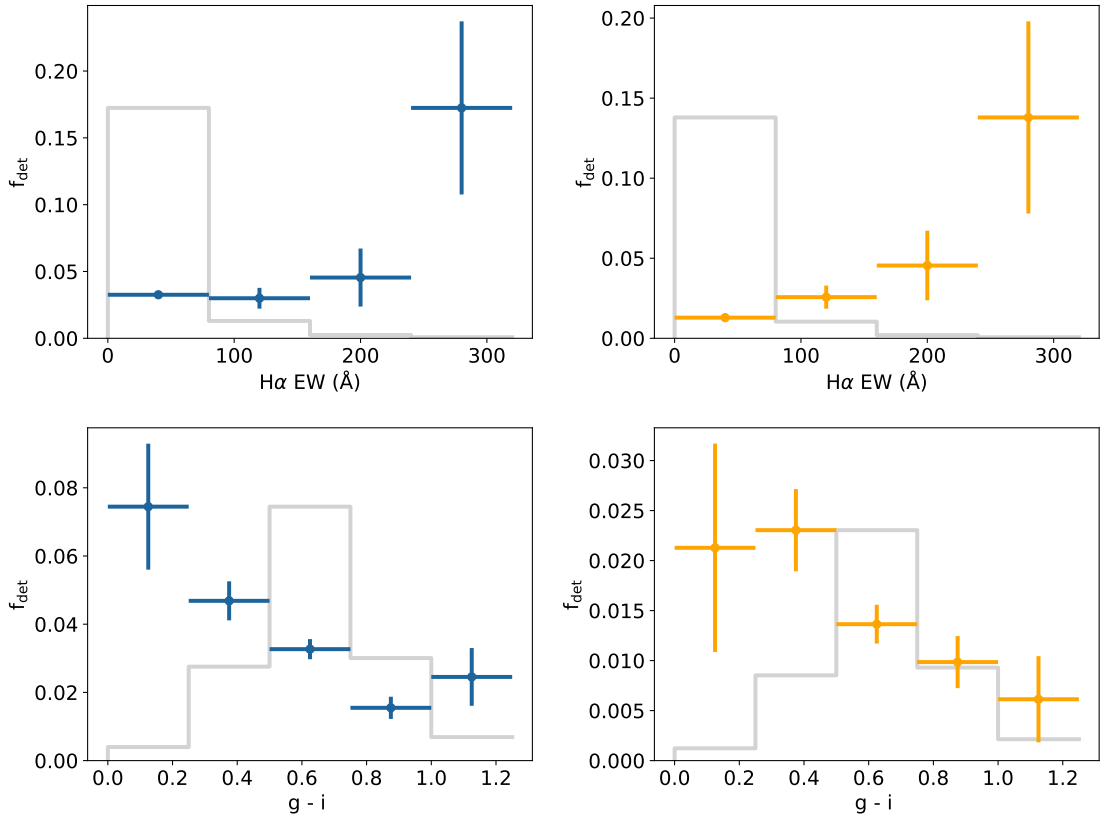

Figure 3.5 The fraction of dwarfs around which tidal debris is detected for the automated sample (left) and visual sample (right). The top row shows detection fraction as a function of Hα equivalent width, while the bottom row shows detection fraction as a function of host $(g-i)$ color as measured by SDSS. In each panel, the unfilled grey histogram shows the normalized distribution of the parent sample.

Both when considering host stellar mass and host redshift, we see that the distribution of host galaxy properties does not change significantly between the automated sample and the visual sample. In particular, we find that the redshift of 50% relative completeness is approximately $z = 0.05$ for both samples. We note that although our absolute completeness is unknown, we can measure our relative completeness by comparing to the tidal feature detection fraction at the low redshift end of our sample (6.14% and 2.73% at $z < 0.05$) in our sample and making the assumption

that there is no astrophysical change in true tidal feature occurrence fraction within the redshift range considered.

Similarly, we see that at the lowest redshift bin, where we are most complete, the tidal feature detection fraction decreases as host stellar mass decreases at stellar masses $\log(M_\star/M_\odot) \lesssim 8.5$). This can be understood by noting that as the host stellar mass decreases, the stellar surface density of tidal debris generated from a merger at a given mass ratio decreases.

Because the difference in the distribution of tidal feature detection fractions for the automated and visual sample is not statistically significant, we conclude that astrophysical contamination by features that are not related to recent accretion events does not significantly affect the outcome of our results. We furthermore conclude that some of the visually ambiguous features in the sample are indeed tidal in nature.

3.4.2 Detection fraction and star formation

In order to probe the effect of host star formation rate on the tidal feature incidence rate, we show the tidal feature detection fraction as a function of host Hα equivalent width and of host (g - i) color from SDSS in Figure 3.5. Here, we use host colors from SDSS because the centers of a subset of the brighter galaxies in our sample are saturated in HSC imaging. Again, we find no significant difference between the distribution of the automated and visual sample when considering tracers of star formation.

We find that the tidal feature detection fraction decreases monotonically as a function of host (g - i) color, with the detection fraction of the bluest host galaxies ($(g-i) < 0.3$) a factor of ~ 4 higher than that of the reddest hosts ($(g-i) > 0.9$) for both the automated and visual sample.

To show that star formation rate does indeed drive this color dependence, we also show the tidal feature detection fraction as a function of Hα equivalent width. As can be seen in Figure 3.5, we find that the fraction of galaxies that host detectable tidal features increases as a function of Hα equivalent width.

Figure 3.5 shows the results when considering the galaxies observed in the GAMA and SDSS spectroscopic surveys together. To confirm that the dependence of tidal feature detection fraction

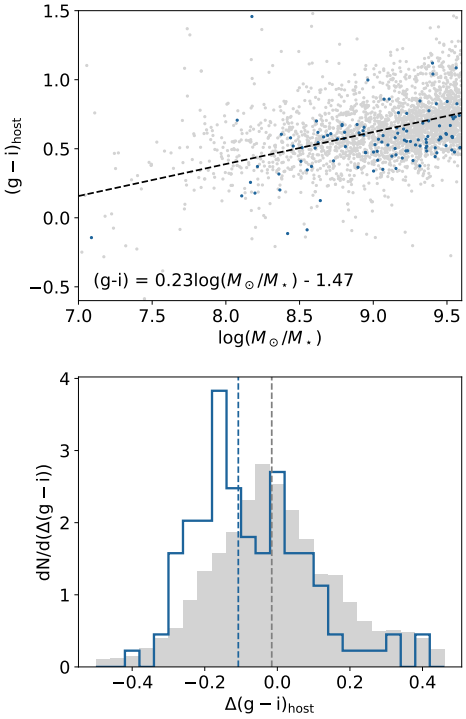

Figure 3.6 *Top:* $(g-i)$ color from SDSS versus stellar mass for non-interacting field dwarfs (grey) and tidal feature host centers (blue). The dashed black line is fit to the non-interacting dwarf galaxy sample. *Bottom:* the deviation of host (g − i) color from the linear fit shown in the top panel for the non-interacting hosts (grey histogram) and tidal feature hosts (blue unfilled histogram). The dashed grey and blue vertical lines show the median deviation for the non-interacting and tidal feature hosts, respectively.

on SFR is not a manifestation of the nature of the parent sample, in Section 3.7 we show that we find the same result when considering the GAMA and SDSS galaxies separately.

If we define the starbursting sample as those hosts with Hα equivalent widths greater than 100Å [Lee et al., 2009, Stierwalt et al., 2015], we find that 4.8% of the starbursts host detectable tidal features. In the highest Hα equivalent width bin (240<EW$_{\mathrm{H}\alpha}$ <320Å), the fraction of galaxies that host tidal features grows to 17%, albeit with large uncertainty as there are only 29 dwarfs in this bin, 5 of which show signs of a merger.

3.4.3 Host color vs. stellar mass

In the top panel of Figure 3.6, we show $(g-i)$ as a function of host galaxy mass for the tidal feature hosts in blue and the centers of apparently non-interacting field dwarfs (selected using the same nearest neighbor cut as for the tidal feature hosts) in grey. The top panel scatter points show values for individual systems, while the bottom panel shows the deviation of the central color from

a fit to the $(g-i)$ colors of the non-interacting hosts.

This illustrates that for their stellar mass, the central SDSS color of the visual sample tidal features hosts are slightly bluer than the isolated dwarfs in which we detect no tidal features, with the median $\Delta(g-i)$ values differing by $\mathcal{S} = \langle \Delta(g-i)_{\rm host,TF} \rangle_{50} - \langle \Delta(g-i)_{\rm host,noTF} \rangle_{50} = -0.086$ (where $\langle \rangle_{50}$ refers to the median).

Because this analysis is sensitive to host stellar mass, we verify that the results do not change under the following modifications: neglecting the shift in stellar mass applied to the SDSS-derived quantities in Section 3.2.1 ($\mathcal{S} = -0.086$), using only masses from SDSS measurements ($\mathcal{S} = -0.097$), and using only masses from GAMA measurements ($\mathcal{S} = -0.082$). In all cases, the tidal feature hosts remain bluer than their non-interacting counterparts and the deviation from the fiducial value of $\mathcal{S}$ is small ($\max(|\delta\mathcal{S}/\mathcal{S}|) = 0.12$).

3.4.4 Tidal Feature and Host Morphology

Though we do not visually classify the morphology in the full sample, we make a brief points on the tidal feature morphology present in the sample.

In particular, we note that there exists a significant population of dwarf galaxies that host stellar shells, similar to those observed in higher mass galaxies [Atkinson et al., 2013, Carlsten et al., 2017, Hood et al., 2018, Kado-Fong et al., 2018].

In the literature, the formation of shells around galaxies is centered largely on the formation of shells around massive ellipticals. However, as observed in this sample, shells can also be formed around low-mass galaxies.

We also note that the starbursting galaxies in our sample that host tidal features have morphologies consistent with those of blue compact dwarfs (hereafter BCDs). Figure 3.7 shows *gri* composite images for the set of starbursting dwarfs with detected tidal features in the sample.

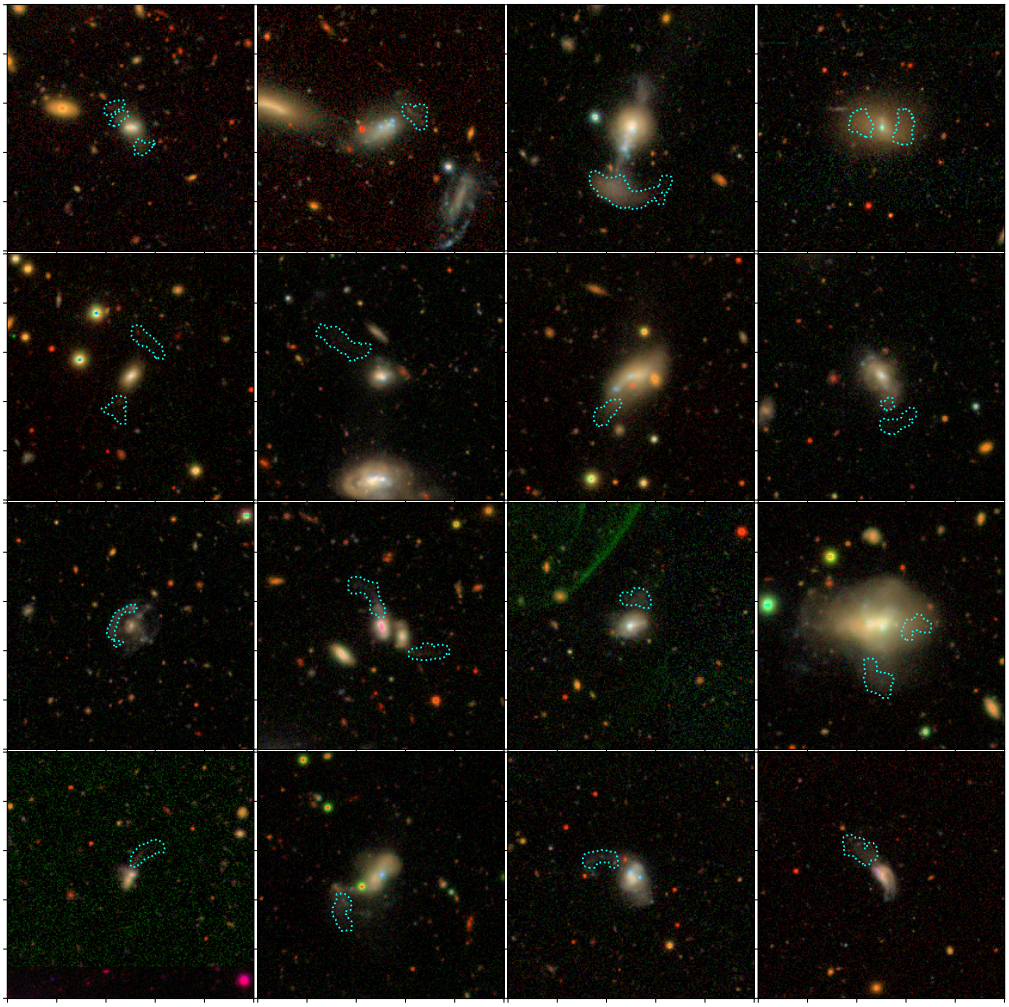

Figure 3.7 *gri*-composite images for 16 of the starbursting dwarfs with detected tidal debris in our sample. The dashed cyan contours show the maximal outline of the tidal feature detection map produced from our algorithm.

3.5 Discussion

3.5.1 The dwarf-dwarf merger sequence

The observed increase in the fraction of galaxies that host tidal features as a function of Hα equivalent width (see Figure 3.5) is consistent with the picture in which some fraction of starbursting

dwarfs are undergoing a period of triggered star formation as the result of a merger with another dwarf galaxy.

We also find that dwarfs which host tidal features are systematically bluer than those that do not host detectable tidal features, as shown in Figure 3.6. This offset can be interpreted either as an increase in the star formation efficiency (here we define the star formation efficiency to be $\mathrm{SFE} = \mathrm{SFR}/M_{\mathrm{H_2}}$) or the molecular gas fraction ($f_{\mathrm{H_2}} = M_{\mathrm{H_2}}/M_\star$) in the post-merger galaxy (i.e. a movement down and to the right in $(\mathrm{g}-\mathrm{i})$-$\log_{10}(M_\star/M_\odot)$ space), or as an increase in stellar mass while maintaining the same specific star formation rate ($\mathrm{sSFR} = \mathrm{SFR}/M_\star$, such that $\mathrm{sSFR} = f_{\mathrm{H_2}}\mathrm{SFE}$) and central host color (i.e. a shift purely rightwards). We find that the median offset in host color can nominally be reproduced by assuming that all mergers are the result of an equal mass merger with no net change in the central host color. However, this interpretation cannot explain the increase in the tidal feature detection rate as a function of star formation activity. We therefore conclude that the shift in host central color is connected to star formation triggered during the merger, rather than stellar mass build-up alone.

This picture of a merger-driven starburst is in good agreement with the results of Stierwalt et al. [2015], who find that dwarf galaxy pairs in the TiNy Titans sample have a significantly higher starburst fraction than unpaired dwarfs. We also extend the results of Pustilnik et al. [2001], Östlin et al. [2001], and Lelli et al. [2014], who find high dwarf pair and interaction fractions for samples of galaxies known to be BCDs, to a larger sample of dwarf galaxies that span a range of morphologies and star formation rates.

This result can be interpreted in analog to the triggered starbursts observed in mergers between more massive galaxies [see, e.g. Hopkins et al., 2008, Ellison et al., 2018]. However, to our knowledge there has not yet been an observational sample of merging dwarf galaxies that span a range of star formation activity in the field.

Though it is widely expected from simulations that mergers will quench star formation in massive post-merger systems, the nature of the quenching mechanism is still unclear. Quenching has been proposed to operate via gas ejection by galaxy-scale winds [see, for example, Hopkins et al., 2008], gas reservoir exhaustion via triggered star formation [e.g. Bekki, 1998], or by a highly turbulent post-

merger ISM [Ellison et al., 2018]. The observations of merger-driven starbursts in dwarf galaxies without the presence of a signficant quiescent population in the field may then help to constrain the physical mechanism behind quenching in the high-mass regime.

3.5.2 Evidence for a merger pathway for BCD formation

We furthermore note that the morphologies of the most vigorously starforming galaxies are consistent with that of blue compact dwarfs (BCDs). BCDs are characterized by the presence of a small number of vigorously star forming regions that have a spectrum similar to that of HII regions [Bekki, 2008a]. Figure 3.7 shows our sample of starbursting dwarfs that host tidal features – though the low surface brightness outskirts of the galaxies increase the size of the galaxy, in shallower imaging only the compact star forming core regions would be observable.

It has been proposed by Bekki [2008a] that a possible avenue of BCD formation is the merger between two field dwarf galaxies – the increase in the detection fraction for starburst galaxies is in good agreement with this formation mechanism. This formation mechanism also predicts that older stellar populations will be distributed preferentially towards the outskirts of the galaxy, in agreement with our observations.

3.5.3 The origin of non-interacting dwarf starbursts

A remaining open question is that of the chronological link between triggered star formation and tidal feature observability. Though the tidal feature detection fraction is significantly higher for high Hα EW galaxies than for the full sample, we do not see signatures of interaction around all starbursting dwarfs. Even when including the results from Stierwalt et al. [2015], who find an increase in the starburst fraction for dwarfs in pairs, currently detectable dwarf-dwarf interactions cannot account for the observed fraction of dwarfs that are currently in a starburst phase.

We consider three possibilities to explain the apparently non-interacting starbursting dwarfs: that the timescale of tidal feature observability is less than the timescale of elevated star formation, that starbursts can be triggered by mergers more minor than we are able to probe in this study, and that some fraction of dwarf starbursts are instigated by secular processes.

The first possibility, that the timescale of tidal feature observability is short relative to the timescale of elevated star formation rate, appears to be unlikely due to the long dynamical times in the outskirts of dwarf galaxies. Though the surface brightness of a tidal stream is expected to decay quickly in the first 2 Gyr [Johnston et al., 2001], we expect the starburst phase to be short relative to this timescale [Bekki, 2008a].

The second possibility, that some starbursts are triggered by mergers more minor than those to which we are currently privy, almost certainly accounts for some fraction of dwarf starbursts. Though the connection between accretion event and starburst trigger is not easily made for individual objects, we note that the nearby starbursting dwarf NGC 4449 hosts a disrupting satellite with a stellar mass ratio near 50:1 [Rich et al., 2012, Martinez-Delgado et al., 2012]. We are likely only sensitive to recent major mergers, where both progenitor galaxies carry significant gas reservoirs; however, Starkenburg et al. [2016a] showed that significant triggered star formation can occur in a 5:1 mass ratio merger, even when the incoming satellite is a dark halo.

Finally, secular mechanisms have long been considered as an explanation for dwarf starbursts. Elmegreen et al. [2012] suggests that the inspiral of massive gas clumps (on the order of a few percent of the total galaxy mass) can power starbursts in dwarf galaxies. Similarly, Noguchi [2001] suggests an explanation for BCD formation using a viscosity-driven mass transport and density threshold for star formation to explain to compact starforming clumps that characterize BCDs.

Because we are only sensitive to relatively major mergers between dwarf galaxies, we are not yet able to distinguish between the picture of a fully merger driven or partially secular explanation for such starbursts. However, deeper imaging will be able to more strongly constrain the contribution of minor mergers to the population of starbursting dwarfs.

3.6 Conclusions and Future Direction

In this work, we have presented a sample of 224 isolated dwarf galaxies with automatically detected signatures of recent merger activity selected from 6683 spectroscopically confirmed dwarfs in the SDSS and GAMA spectroscopic surveys.

We find that the fraction of galaxies that host detectable tidal features increases strongly as a function of star formation activity, reaching a tidal feature detection of fraction of 15-20% at the highest Hα EW considered (EW $>$ 250Å), and that galaxies that host tidal features are systematically bluer than apparently non-interacting field dwarfs at the same stellar mass.

Because the origin of irregular LSB structure around dwarf galaxies can be ambiguous, we construct a visual sample of 101 galaxies that host unambiguous merger debris (see the bottom row of Figure 3.3). We find no evidence for a difference in the distribution of tidal feature detection fraction between the automated sample and visual sample as a function of Hα equivalent width, host $(g-i)$ color, host stellar mass, or host redshift. This implies that the automated sample is dominated by mergers between dwarf galaxies and that contamination (from secular irregular morphology, spiral arms, etc.) does not change the results presented in this study.

The dependence of tidal feature detection fraction on star formation activity supports claims that mergers between dwarf galaxies are able to trigger starbursts and form blue compact dwarfs [Bekki, 2008a]. Observations of dwarf galaxies in pairs also show an elevated starburst fraction [Stierwalt et al., 2015]. However, it is not yet clear whether merger-driven starbursts can explain the entirety of the starbursting dwarf population.

These findings extend observations of star formation in the dwarf-dwarf merger sequence and show for the first time in a large sample that merger-driven star formation continues after coalescence, building upon the evidence for interaction-driven star formation seen in dwarf pairs [Stierwalt et al., 2015, Besla et al., 2018] and spatially resolved measurements of star formation in individual post-merger dwarf systems [Paudel et al., 2018, Annibali et al., 2019].

In order to compare these observations of dwarf-dwarf mergers to expectations of hierarchical structure formation in ΛCDM and to predictions of star formation activity in low-mass systems, it is now necessary to compare observations and simulations of mergers between isolated dwarfs in an equivalent manner. Such studies have already been executed for minor mergers with dark halos [Starkenburg and Helmi, 2015, Starkenburg et al., 2016a,b], but expanded work concerning the expected population of observable tidal features around dwarf galaxies will provide a valuable point of comparison to simulations.

3.7 Appendix: Isolation and sample selection: robustness tests

3.7.1 Isolation Criteria

It is necessary for this work to create a sample of isolated dwarfs. However, there exist cases in which different isolation criteria disagree on whether a dwarf can be considered isolated. To ensure that our results are not influenced by these cases, we re-analyze our automated sample with an additional isolation criterion.

We adopt the isolation criterion of Paudel et al. [2018] because the scope of the work was to identify mergers between dwarf galaxies. Paudel et al. [2018] required that the dwarf be separated by at least 700 kpc in projection and 700 km s^{-1} from its nearest massive neighbor, where we adopt a mass cut of $M_\star > 4 \times 10^{10} M_\odot$ such that the median stellar mass of the massive neighbors coincides with that reported by Paudel et al. [2018]. This method produces a sample of 231 isolated dwarfs, as compared to 224 in the original isolated sample. There are 191 dwarfs that are classified as isolated by both samples; there are 20 dwarfs that are classified as isolated by the original criterion and not by the secondary criterion, and 40 dwarfs that are classified as isolated by the secondary and not the original criterion.

We compare this new isolated dwarf sample and the intersection of the two isolated samples to the original isolated dwarf sample in Figure 3.8. The left panel shows the detection fraction as a function of Hα equivalent width, while the right panel shows the same as a function of SDSS (g - i) color. The blue shaded regions show the results for the original sample, the pink errorbars for the new isolated dwarf sample, and the black errorbars for the intersection of the two samples. Each case produces statistically consistent results, from which we conclude that our results are not driven by contamination by non-isolated dwarf galaxies.

3.7.2 The GAMA and SDSS samples

Given the heterogeneous characteristics of a sample constructed by combining dwarf galaxies observed by the GAMA and SDSS campaigns, we would like to confirm that we retrieve the same results when considering the two samples separately.

Figure 3.9 is a variation of Figure 3.5, which presents the tidal feature detection fraction as a function of indications of star formation activity. In Figure 3.9, the results from the GAMA survey (red) and the SDSS survey (green) are shown separately, while the grey shaded region shows the results for the combined sample. The results obtained from the separated samples are in good agreement with each other and with the results of the combined sample. We thus conclude that the dependence on star formation activity that we observe is not driven by the effective selection function of the parent sample.

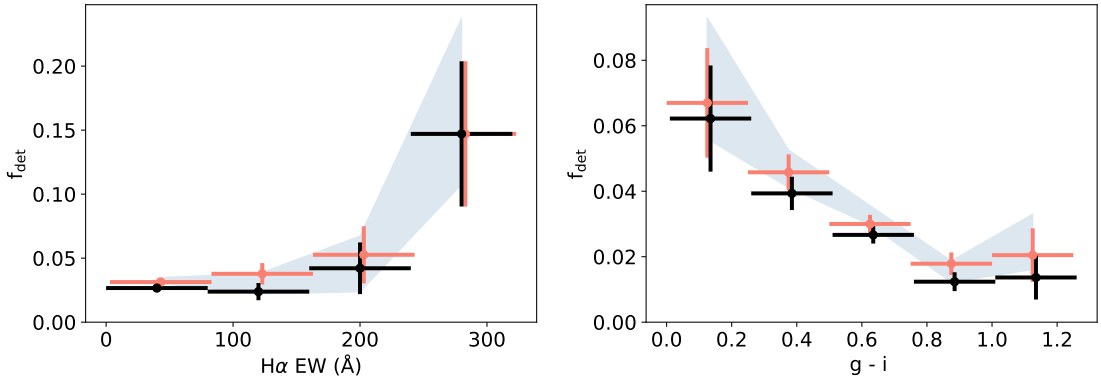

Figure 3.8 The same as the analysis of the auotmated sample in Figure 3.5, but where the isolation criterion of Paudel et al. [2018] is used to construct an isolated dwarf sample. The pink errorbars show the detection fraction as a function of Hα equivalent width for dwarf galaxies separated by at least 700 kpc in projected distance and $\Delta v > 700$ km s^{-1} from their nearest massive neighbor. For clarity, these points are offset horizontally. The blue shaded region shows the results for the full sample (i.e. the same data as Figure 3.5). The black errorbars show the isolated dwarf sample created from the intersection of the two isolation criteria (i.e. those galaxies considered to be isolated by both criteria). All three samples produce statistically consistent results.

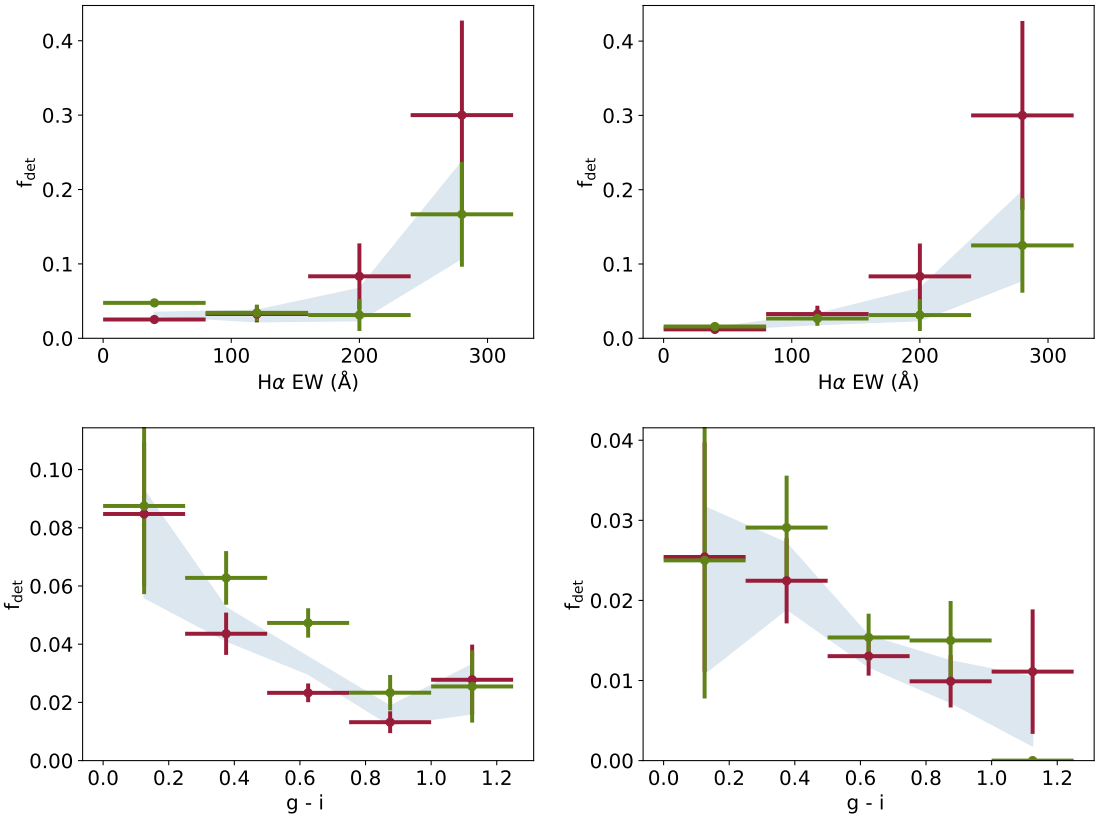

Figure 3.9 The same as Figure 3.5, but showing the results from the galaxies observed by GAMA (red) and SDSS (green) separately. The blue shaded region shows the results for the full sample (i.e. the same data as Figure 3.5). The left column shows the results for the automated sample, while the right column shows the results for the visual sample. In all cases, the results derived when analyzing the SDSS and GAMA samples separately are in good agreement with each other and with the results obtained from the combined sample.

3.8 Appendix: Updates to the detection algorithm

The updated tidal feature detection algorithm that we employ in this work differs from the original method in several points. First, we now use the starlet wavelet transform [Starck et al., 2015] to decompose the input image into starlet coefficients that probe a specific spatial scale (previously, we used a modification of the starlet transform that did not probe as large a range of spatial scales).

Next, we now use the Python package `sep` [Barbary, 2016], an implementation of the detection algorithm developed in Bertin and Arnouts [1996], to detect faint features in each difference image

individually, and construct a final detection map from the features detected at each spatial scale. We detect features at greater than 2σ significance in the logarithmic image. This change makes it possible to detect more extended LSB features that overlap with a large number of foreground and/or background sources; because compact sources have power only at small spatial scales, detecting features at each starlet coefficient separately allows for "deblending" as a function of characteristic spatial extent. To ensure that this change does not characterize the halos of faint sources as tidal features around bright sources, we require that the flux-weighted center of each tidal feature be separated from the flux-weighted center of any source by at least 10 pix, set to be approximately twice the PSF FWHM of the worst seeing band ($g_{\rm HSC}$).

Finally, we wish to limit contamination from spiral arms and faint neighbors. To do so, we consider the asymmetry and clumpiness of the detected candidate tidal feature system. We follow the historical definition of asymmetry, using

$$\mathcal{A} = \frac{\sqrt{(\sum_i f_i - \tilde{f}_i)^2}}{2\sum_i f_i}, \tag{3.1}$$

where f_i and $\tilde{f}_i$ are the flux at position i and the flux at position i when the image is rotated by 180 degrees, respectively. We additionally define the clumpiness of the light in the detected LSB debris to be

$$\mathcal{C} = \sqrt{\frac{\langle f_i^2 \rangle}{\langle f_i \rangle^2}}. \tag{3.2}$$

In a forthcoming work, we will optimize the values of $\mathcal{A}$ and $\mathcal{C}$ with respect to a visually labeled sample of massive galaxies (Kado-Fong et al. in prep.). For this work, however, we choose relatively liberal thresholds that may decrease the purity of our sample ($\mathcal{A} > 0.005$ and $\mathcal{C} < 20.0$), and instead show that our results are unchanged whether we consider the automated detection sample or the systems that show unambiguous merger debris.

Finally, we consider that not all low surface brightness debris in the image cutout is necessarily associated with our target galaxy. We first remove from the detection all features less than 10 pixels from the edge of the cutout. Then, we perform a flux-weighted nearest neighbor clustering in which

each contiguous low surface brightness feature is assigned to its most probable host. To do so, we detect the host galaxies via `sep` in the original image and assign a weight inversely proportional to the host flux $w_i = f_i^{-1}/(\sum_j f_j^{-1})$.

Each contiguous region of the candidate tidal feature system is then assigned to its most probable host by minimizing the weighted distance between the center of light of the contiguous region and those of the potential host galaxies. That is to say, the most probable host j minimizes $w_i(\mathbf{x_i} - \mathbf{x_j^h})$.

The full detection process is performed independently for the $g_{\rm HSC}$, $r_{\rm HSC}$, and $i_{\rm HSC}$ bands. Only detected regions that are present in at least two of bands are retained. This decision is in contrast to that of Kado-Fong et al. [2018], in which only the band with the best average seeing (the $i_{\rm HSC}$ band) was considered. This change was made because in contrast to Kado-Fong et al. [2018], we do not visually inspect the full sample, and therefore remove artifacts via their non-astrophysical colors.

Chapter 4

Three-Dimensional Structure of Low-Mass Galaxies

4.1 Introduction

The existence of a smooth stellar component in the outskirts of local dwarfs is a common, but puzzling, phenomenon [Lin and Faber, 1983, Minniti and Zijlstra, 1996, Grebel, 1999, Minniti et al., 1999, Roychowdhury et al., 2013]. Round stellar halos are a near-ubiquitous component of more massive galaxies – thought to be assembled largely through the accretion of satellite galaxies, the stars that populate these outskirts provide key insights into the galaxy's assembly history [see, e.g. Bullock and Johnston, 2005, Abadi et al., 2006]. Due to a decreasing stellar mass to halo mass ratio, satellite accretion by dwarf centrals deposits fewer stars per unit halo mass than analogous events around more massive systems [Purcell et al., 2007, Brook et al., 2014]. It is thus considered unlikely that minor mergers are able to fuel the formation of a stellar halo in dwarf galaxies.

Instead, it has been suggested that the stellar outskirts of dwarfs are an in-situ structure. In the field, dwarf galaxies sit in shallow potential wells; their structure is therefore more sensitive to the details of star formation feedback than more massive galaxies. Supernovae-driven winds

[Hu, 2019], cosmic ray feedback [Dashyan and Dubois, 2020], stellar winds, radiation pressure, and photoionization [Muratov et al., 2015, El-Badry et al., 2016] are all expected to more efficiently displace gas in dwarfs than in more massive hosts (both in moving gas to large radii and in removing it from the system entirely). In particular, hydrodynamical simulations have predicted that star formation feedback can induce significant size fluctuations in the stellar content of dwarf galaxies, driving the formation of a round stellar halo by inducing radial migration via potential fluctuations, as well as forming stars in outflowing and inflowing gas [Stinson et al., 2009, Maxwell et al., 2012, El-Badry et al., 2016].

Not all theories of dwarf stellar halo formation are purely in-situ, however; Bekki [2008b] suggested that round stellar outskirts around dwarfs may be formed as a product of dwarf-dwarf major mergers (a merger wherein the mass of the secondary is at most a factor of ~ 3 less than that of the primary). Such major mergers are expected to occur for about 75% of galaxies in this stellar mass range, but are expected to proceed far more often in the early universe – only 30% of these galaxies are expected to have undergone a major merger in the last 10 Gyr [Deason et al., 2014, Besla et al., 2018]. Stellar outskirts formed in this manner would tend to be comprised of ancient stellar populations; using the surface brightness profile given by Bekki [2008b] directly after the outskirts are formed and taking into account surface brightness dimming due to passive evolution [Conroy et al., 2009b], in the major merger scenario we would not expect to detect an extended round stellar component around the majority of dwarfs.

Moreover, the dwarfs that have been found to host extended, smooth intermediate-old age stellar populations are nearby systems in the Local Volume [and mostly in the Local Group, see Zaritsky et al., 2000, Aparicio and Tikhonov, 2000, Aparicio et al., 2000, Hidalgo et al., 2003, Demers et al., 2006, Bernard et al., 2007, Stinson et al., 2009, Strader et al., 2012, Nidever et al., 2019, Pucha et al., 2019]. It remains unclear whether such a structure is a generic feature of dwarfs (pointing to an in-situ origin), or a result of the influence of the more massive galaxies in the Local Group.

Understanding the intrinsic shape of dwarf galaxies is thus of interest in understanding the stellar assembly of these low-mass systems, and for constraining recipes for star formation feedback. However, it has historically been challenging to construct a sample of dwarfs with sufficient numbers

whose imaging is deep enough to measure stable ellipticity profiles. Previous works have been confined to the Local Volume [Roychowdhury et al., 2013], or to the most massive dwarfs [$M_\star > 10^9 M_\odot$, Padilla and Strauss, 2008, van der Wel et al., 2014, Zhang et al., 2019]. Moreover, there has not been an effort previously to measure the intrinsic shapes of dwarf outskirts, due largely to the aforementioned technical hurdles.

In this work, we combine the large sample of spectroscopically confirmed dwarfs observed by the Sloan Digital Sky Survey spectroscopic surveys [both legacy and BOSS surveys, Strauss et al., 2002, Dawson et al., 2013, Reid et al., 2016] and the Galaxy and Mass Assembly (GAMA) spectroscopic survey [Baldry et al., 2012] with the wide and deep imaging of the Hyper Suprime-Cam Subaru Strategic Program [HSC-SSP; Aihara et al., 2018b,a, Miyazaki et al., 2018, Komiyama et al., 2018, Kawanomoto et al., 2018, Furusawa et al., 2018, Bosch et al., 2018, Huang et al., 2018c, Coupon et al., 2018] to quantify the 3D shape distribution of dwarf galaxies as a function of radius.

The wide area covered by the HSC-SSP in conjunction with the surface brightness sensitivity and high resolution of its imaging allows us to map stable ellipticity profiles of the dwarfs out to four times the half-light radius ($R = 4\mathrm{R_{eff}}$, where $\mathrm{R_{eff}}$ is defined by a single Sérsic fit, as described in Section 4.3) at $0.005 < z < 0.2$ and $7.0 \leq \log_{10}(M_\star/M_\odot) \leq 9.6$. This allows us to construct a sufficiently large sample of dwarfs to infer the distribution of their intrinsic shapes from observations of their projected 2D shapes at fixed radius. In Section 4.2, we detail the sample selection and volume corrections implemented for the sample. We detail the methodology and validation of the 1D surface brightness profiles and the 3D shape inference separately, in Section 4.3 and Section 4.4, respectively. We then examine the change in dwarf 3D shape as a function of radius and dwarf properties in Section 4.5, and consider the implications of the observed shape evolution to proposed dwarf stellar halo formation mechanisms in Section 4.6.

Throughout this paper we adopt a standard flat ΛCDM model in which $\mathrm{H_0} = 70$ km s^{-1} Mpc^{-1} and $\Omega_m = 0.3$.

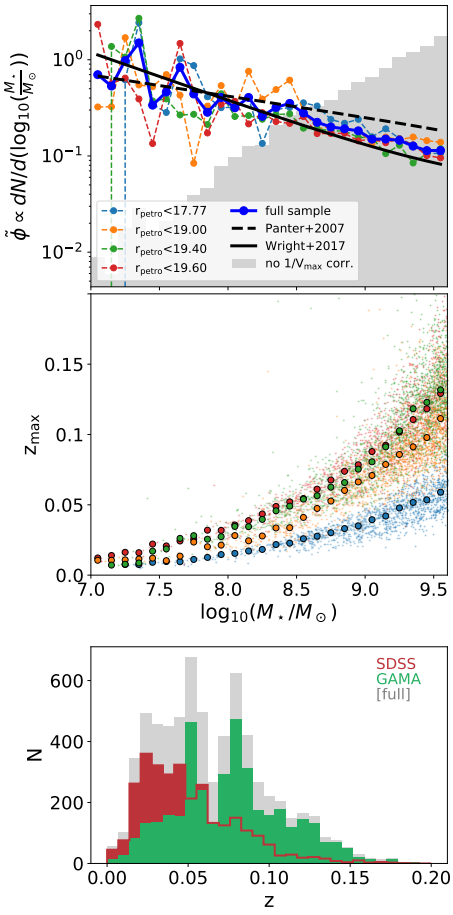

Figure 4.1 *Top:* we show the normalized stellar mass function (SMF), $\tilde{\phi}(\log_{10}(M_\star/M_\odot))$, for each magnitude-limited subset of our sample with dash-connected scatter. The normalized SMF for the full sample is shown by the solid blue curve. For reference, the Schechter fit of Panter et al. [2007] and the double Schechter fit of Wright et al. [2017] are normalized to our stellar mass range and shown in the dashed and solid lines, respectively. The raw distribution in stellar mass (i.e. without $1/V_{max}$ weights) is shown by the grey filled histogram. We find that our normalized SMF matches that of Wright et al. [2017] well. *Middle:* the maximum observable redshift, z_{max}, for each galaxy in the sample as a function of stellar mass. As at top, points are colored by the magnitude limit of the source spectroscopic program. The mean z_{max} as a function of stellar mass is also shown for each program by the large scatter points. *Bottom:* the redshift distribution, colored by source survey.

4.2 Observations and Data Processing

4.2.1 HSC-SSP Imaging

As noted above, the HSC-SSP imaging boasts wide, deep, and high resolution imaging, making it well-suited for an exploration of the low surface brightness outskirts of low-mass galaxies. Upon completion, HSC-SSP will provide imaging with a median seeing of $\sim 0.6''$ in the $i_{\rm HSC}$ over ~ 1400 square degrees to a point source depth of $i_{\rm HSC} \sim 26$ in its shallowest "Wide" layer [Aihara et al., 2019]. The data have been shown to reach surface brightness limits of $i_{\rm HSC} \sim 28.5$ mag arcsec^{-2} for measurements around a known target [Huang et al., 2018e]. We test the surface brightness limit of the HSC-SSP data in the vicinity of our sample in Section 4.8, and find that $\mu_i = 28.5$ mag arcsec^{-2}

is a conservative choice of limiting surface brightness. Indeed, with an empirical correction to the background, it has been shown that HSC-SSP reaches depths of $\mu_r \sim 29.5$ mag arcsec^{-2}. However, because we allow several parameters to drift during our surface brightness profile measurements, we adopt the fiducial surface brightness limit of $\mu_i = 28.5$ mag arcsec^{-2}.

For this work, we use the internal HSC-SSP S18A data release, which covers the same area as the second public data release of Aihara et al. [2019] and is processed with a very similar data reduction pipeline. Though are there some minor differences between the data reduction pipeline used for S18A and PDR2, these changes do not affect the parts of the pipeline discussed in this work. We require only coverage in the $i_{\rm HSC}$ band, resulting in an area of ~ 796 deg^2 with a point source depth of $i = 26.2^{+0.2}_{-0.4}$. The $i_{\rm HSC}$ band is best choice to study the overall shape of the stellar distribution for two main reasons. First, the $i_{\rm HSC}$ bands has best seeing out of the five HSC bands. Second, it is less sensitive to dust extinction and star forming regions relative to the bluer $g_{\rm HSC}$ and $r_{\rm HSC}$ bands, and deeper than the redder $z_{\rm HSC}$ and $y_{\rm HSC}$ are significantly shallower.

4.2.2 Initial Sample Selection

All dwarfs in the present sample have been spectroscopically observed by either the SDSS or GAMA spectroscopic surveys. We limit our sample to dwarfs at $0.005 < z < 0.2$; the redshift distribution of the sample peaks at $z \lesssim 0.05$, as shown in the bottom panel of Figure 4.1. Due to the intrinsic faintness of low-mass galaxies, the majority of our sample is at $z \lesssim 0.1$.

This selection yields a sample of 11338 dwarfs. In 3128 cases, there is a bright star (or related imaging artifact) within $5{\rm R}_{\rm eff}$ of the target galaxy; because our goal is to measure ellipticity profiles out to the outskirts of the dwarfs, we remove these galaxies from the final sample. An additional 548 galaxies are too close to neighbors to measure a reliable surface brightness profile, or are coincident with an imaging artifact.

We adopt stellar masses measured by the SDSS and GAMA teams. The stellar masses measured by the GAMA team use a Chabrier initial mass function [Chabrier, 2003b] by Taylor et al. [2011]. The stellar masses measured by the SDSS team are derived using the Conroy et al. [2009b] Flexible Stellar Population Synthesis (FSPS) models with a Kroupa initial mass function [Kroupa, 2001]. In

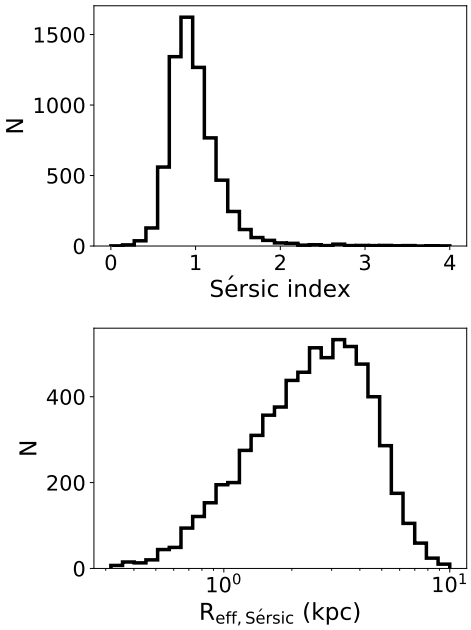

Figure 4.2 *Top*: The distribution of Sérsic indices over the dwarf sample. The majority of the dwarfs are well-described by an exponential ($n = 1$) profile. *Bottom*: The distribution of effective radii in the sample, as measured from the Sérsic fits.

Kado-Fong et al. [2020a], we found that, for galaxies with both SDSS and GAMA spectroscopy, the SDSS stellar masses are higher than the GAMA stellar masses by a median of 0.08 dex and a median absolute deviation of 0.35 dex. We therefore reduce the masses derived from SDSS observations by 0.08 dex; it is however important to note that due to the width of our mass bins, including or excluding this shift does not impact this work.

4.2.3 Volume Corrections

Our sample is drawn from the SDSS and GAMA spectroscopic surveys, both of which comprise several subsets with different magnitude limits. The sample is composed of observations from the SDSS Legacy Survey [$r_{\rm petro} < 17.77$, Strauss et al., 2002], the low redshift component of SDSS BOSS [$r_{\rm petro} < 19.6$, Dawson et al., 2013], and the GAMA second public release [$r_{\rm petro} < 19.4$ or $r_{\rm petro} < 19.0$, depending on the region; see Liske et al., 2015]. To convert this sample from magnitude-limited to volume-limited, we adopt the classical $1/\mathrm{V}_{\rm max}$ correction to simulate a volume-limited sample.

As all of the galaxies in our sample are low mass, none have maximum observable redshifts for

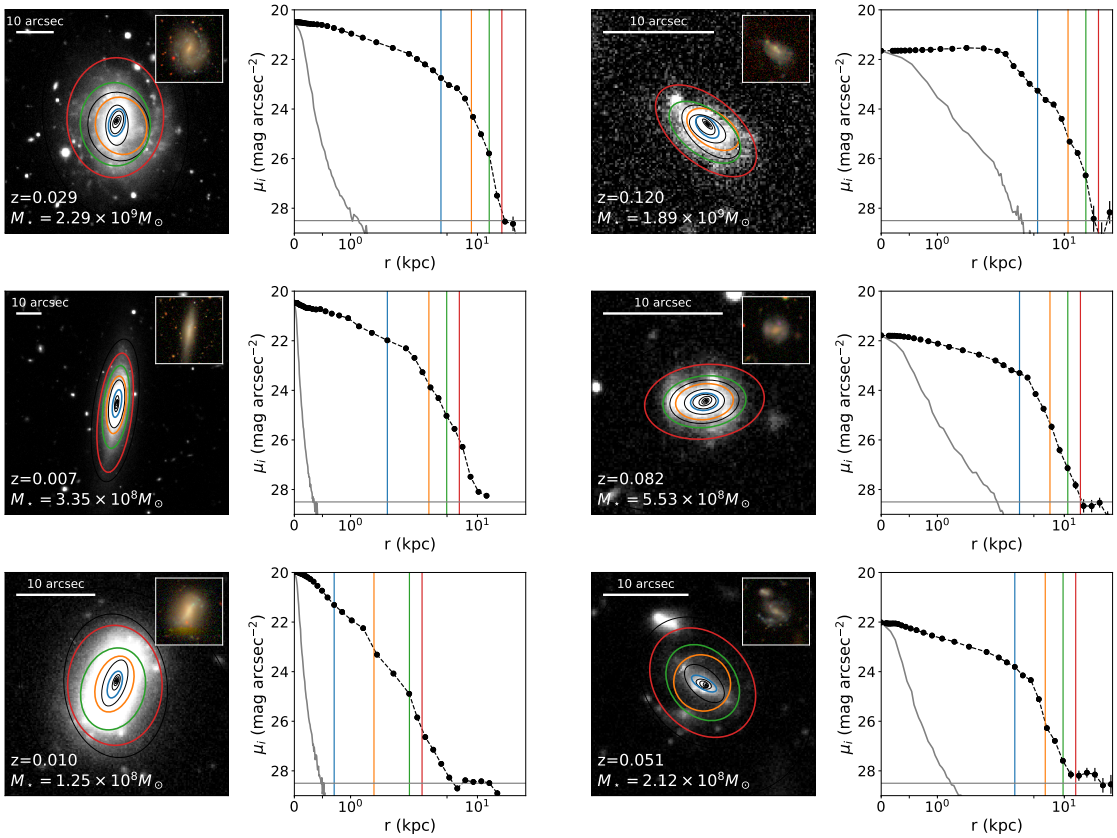

Figure 4.3 Example 1D surface brightness profiles for galaxies that span the range of stellar mass and redshift in our sample. The lefthand (righthand) columns show galaxies at the low (high) redshift end of the sample, while the rows are ordered in decreasing stellar mass. Each pair of panels shows the $i_{\rm HSC}$-band image with the measurements at $1R_{\rm eff}$ (blue), $2R_{\rm eff}$ (orange), $3R_{\rm eff}$ (green), and $4R_{\rm eff}$ (red) overplotted as ellipses. The $gri_{\rm HSC}$-composite RGB image is also shown in the inset panel to more clearly show the morphology of the galaxy. The right panel shows the 1D surface brightness profile of the galaxy; vertical lines show the physical extent at 1-4$R_{\rm eff}$ (same colors as left). We also show the surface brightness of the PSF by the grey curve, and the nominal surface brightness limit of $\mu_i = 28.5$ mag arcsec^{-2} by the grey horizontal line.

which the observed-frame r-band lies outside of the wavelength range of the (SDSS or GAMA) optical spectrograph. We are thus able to compute the maximum redshift at which the observed $r_{\rm SDSS}$ Petrosian magnitude lies within the spectroscopic selection, $z_{\rm max}$, directly from the spectra using the public filter response curves measured for SDSS in 2001[1]. We use the catalog SDSS and

[1]http://www.sdss3.org/instruments/camera.php

GAMA r_{SDSS} Petrosian magnitudes to compute z_{max}. Though the spectroscopic observations span a considerable range in time, it has been shown that the SDSS r-band filter transmission curve has evolved by less than 0.01 mag [Doi et al., 2010]. We therefore use the fiducial SDSS transmission curve for all galaxies.

We remove galaxies for which $z \geq z_{max} + 0.005$ or $z_{max} < 0.005$ (recall that our minimum redshift cut is $z = 0.005$), as these conditions suggest that there is a problem with the catalog photometry or spectroscopy. From inspection, these are largely comprised of cases where a large galaxy has been erroneously divided into several "low-mass galaxies" during image segmentation [i.e. shredding, see Blanton et al., 2011]. These cuts produce a final sample of 6758 galaxies.

To validate our directly computed z_{max} values, we compare the distribution of stellar masses in our sample, as weighted by $1/V_{max}$, to published stellar mass functions in the literature. We report the stellar mass function normalized over our sample mass range; that is, $\tilde{\phi}(\log_{10}(M_\star/M_\odot)) \equiv C_0 dN/d(\log_{10}(M_\star/M_\odot))$ where C_0 is a constant defined such that $\int_{7.0}^{9.6} \tilde{\phi}(x)dx = 1$.

The top panel of Figure 4.1 shows this normalized stellar mass function of each magnitude-limited subset in our sample as dashed-line curves. The distribution over the full sample is shown by the thick blue lines, while the original unweighted stellar mass distribution of the sample is shown by the filled grey histogram. The double Schechter fit of Wright et al. [2017, from GAMA] is shown by the solid black line, and the Schechter fit of Panter et al. [2007, from SDSS] by the dashed black line. In both cases, the parametric fits are normalized over the stellar mass range of our sample.

Our $1/V_{max}$-corrected stellar mass distribution is in good agreement with the results of Wright et al. [2017], and is somewhat steeper than the mass function of Panter et al. [2007]. This is expected, as Wright et al. [2017] includes significantly more galaxies at the stellar mass range of the present sample; the agreement between our normalized stellar mass function and that of Wright et al. [2017] indicates that the $1/V_{max}$ weights we implement are well-behaved.

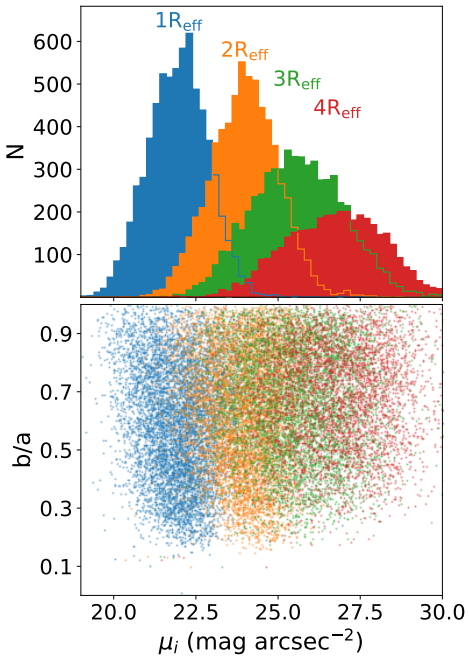

Figure 4.4 *Top:* the distribution of surface brightness measured at $1 - 4R_{\rm eff}$, as labeled. *Bottom:* surface brightness versus projected axis ratio, again colored by measurement radius. Though some measurements are below our nominal surface brightness limit of $\mu_i = 28.5$ mag arcsec^{-2}, these comprise only $\sim 7\%$ of ellipticity measurements, and their inclusion does not have a statistically significant effect on the overall ellipticity distribution.

4.3 1D Surface Brightness Profile Measurement

With a volume-corrected sample in hand, we now turn to the main objective of this work. The measurement of a 3D shape distribution requires both careful measurements of the projected 1D surface brightness profiles and a framework with which the 3D shape distribution may be inferred from these projected profiles.

We first address our adopted 1D profile measurement scheme. To establish a reasonable initial guess for the centroid position, mean ellipticity, and position angle of the source, we first fit each galaxy with a single Sérsic profile. We also use the Sérsic profile fit to measure an effective radius ($R_{\rm eff}$) for each source. We then extract a 1D ellipticity profile from each galaxy by allowing the isophotal shape to vary with radius.

4.3.1 Single Sérsic fits

Though a single Sérsic model is not flexible enough to fully describe the structure of dwarf galaxies, it provides a stable and robust model to extract basic flux-weighted structural parameters.

The position angle, ellipticity, centroid from this single Sérsic fit are used to initialize the non-parametric surface brightness profile measurement at R_{eff}. Because dwarf galaxies are often characterized by irregular, off-center star forming regions [Binney and Tremaine, 2008], an inflexible and monotonically decreasing model is necessary to establish a reliable galaxy centroid. We additionally adopt the Sérsic-derived effective radius as R_{eff} throughout the paper. In Figure 4.2, we show the distribution over Sérsic index (top) and effective radius (bottom) for our sample. The dwarfs tend to be well-described by an exponential ($n = 1$) profile, with a median [25th, 75th percentile] Sérsic index of 0.94 [0.79,1.1]. Their effective radii are typically a few kpc, with a median [25th, 75th percentile] value of 2.5 kpc [1.6, 3.7 kpc], though we note that there is a strong relationship between stellar mass and effective radius.

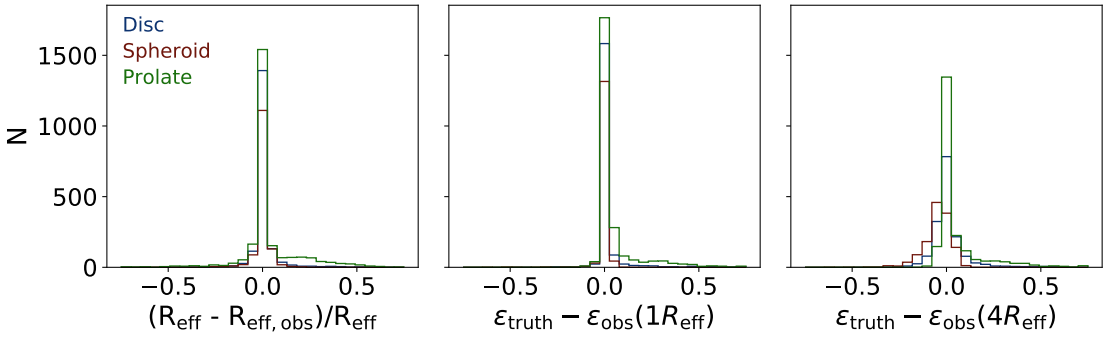

Figure 4.5 The distribution of errors in recovered effective radius (left), ellipticity at $1R_{eff}$ (middle), and ellipticity at $3R_{eff}$ (right) for an injected population of disk ($[A, B, C] = [1., 0.9, 0.1]$, blue), spheroid ($[A, B, C] = [1., 0.9, 0.9]$, red), and prolate ($[A, B, C] = [1., 0.1, 0.1]$, green) galaxies. Each mock galaxy is assigned a viewing angle drawn isotropically over the sphere, injected into the HSC data with an $n = 1$ Sérsic profile, and recovered with our pipeline. In each panel, the text shows the 5th, 25th, 50th, 75th, and 95th percentile of the distribution.

4.3.2 Non-parametric Surface Brightness Profiles

Though a single Sérsic fit provides a reasonable initial guess for their surface brightness profiles, dwarf galaxies are rich in substructure, and not well-described by a single Sérsic profile. Single Sérsic profiles are also unable to trace changes in ellipticity as a function of radius, by definition.

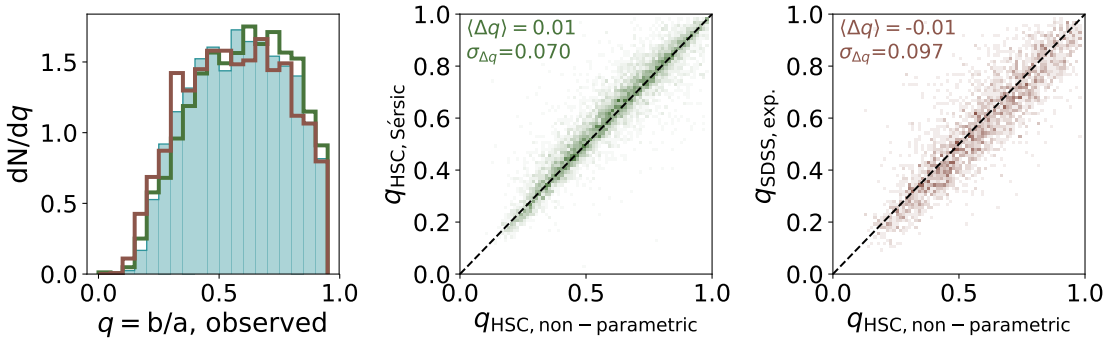

Figure 4.6 *Left:* the observed distribution of projected axis ratio, $q = b/a$, for the HSC non-parametric measurements (filled teal histogram), HSC Sérsic measurements (green histogram), and SDSS catalog measurements (derived from exponential fits, brown histogram). All three measurements are in good agreement; we find that the mean difference in measured q ($\langle \Delta q \rangle$) and the standard deviation of this difference ($\sigma_{\Delta q}$) are $(\langle \Delta q \rangle, \sigma_{\Delta q}) = (0.017, 0.71)$ and $(\langle \Delta q \rangle, \sigma_{\Delta q}) = (-0.01, 0.10)$ for the HSC Sérsic measurements and SDSS catalog exponential measurements, respectively. In the middle panel we plot the non-parametric measurements at $1\mathrm{R_{eff}}$ against the HSC Sérsic measurements, while in the right panel we show the same non-parametric measurements at $1\mathrm{R_{eff}}$ against the SDSS exponential measurements, for galaxies in the SDSS catalog.

In order to better describe the complex structure of low mass galaxies, and to test whether ellipticity changes as a function of radius, we adopt a more flexible non-parametric method to measure the 1D surface brightness profiles of the galaxies in our sample. We use the method introduced by Huang et al. [2018e], which is based on the IRAF Ellipse algorithm (Jedrzejewski 1987), and allows ellipticity ϵ, central position (x_c, y_c)[2], and position angle PA to vary as a function of semi-major axis a. The exceptional depth of the HSC-SSP imaging allows us to fit profiles with these parameters free without the fit becoming unstable. To further safeguard against an unstable fit, if the centroid shifts by more than $0.5\mathrm{R_{eff}}$ at $r = \mathrm{R_{shift}}$, we disregard the surface brightness profile at $r > \mathrm{R_{shift}}$.

To generate reliable surface brightness profiles, we must first mask out galaxies that are near the target. To do so, we use the method introduced in Kado-Fong et al. [2020a, Appendix B] to detect and mask background sources by detecting sources at spatial frequencies that are high

[2]We allow the centroid to drift in order to accommodate the presence of off-center starforming regions that may dominate the light near the center of the galaxy. At the radii we consider for this work, the ellipticity distribution does not change significantly when the centroid is held constant or left free.

relative to the smooth light of the target outskirts. This approach allows us to remove background galaxies that are at small projected distances from the target galaxy, where they are most likely to contaminate measurements of the galaxy outskirts. We also apply a 3σ clipping to the pixel values along each isophote to reduce the impact from other objects. Huang et al. [2018e] and Ardila et al. (in prep.) have shown that this method works well even for massive galaxies with extended stellar halos. We also adopt a moderately large multiplicative step size of $(a_{n+1} - a_n)/a_n = 0.2$ to help stabilize the ellipticity measurement in the outskirts of the galaxy. In Figure 4.3, we show example 1D profiles that span the stellar mass and redshift range of our sample. The left panel of each pair shows the isophote at $1 - 4\mathrm{R_{eff}}$ plotted over the i_{HSC}-band image. The gri_{HSC}-composite RGB image is also shown by the inset panel. The right panel shows the 1D surface brightness profile for each example. The examples decrease in stellar mass from top to bottom, and increase in redshift from left to right. In addition, we show the overall distribution of surface brightness at 1-4$\mathrm{R_{eff}}$ for our 1D profile fits in the top panel of Figure 4.4, and the surface brightness versus ellipticity in the bottom panel. Though we use effective radii (and multiples thereof) in this work, we have also verified that using fixed physical radii does not change our results.

At $4\mathrm{R_{eff}}$, the farthest extent to which we measure ellipticity profiles, the median surface brightness is $\langle \mu_i \rangle = 26.8$ mag arcsec^{-2}, significantly brighter than our surface brightness limit. Seven percent of galaxies have a surface brightness of > 28.5 mag arcsec^{-2} at $4\mathrm{R_{eff}}$; we do not remove them from the sample, as their inclusion or exclusion from this analysis does not have a statistically significant impact on the overall ellipticity distribution of the overall sample or subsamples considered in this work. To ensure that we are able to reach this nominal surface brightness limit, we examine the residual sky background near our dwarf sample in Section 4.8, and find that the sky is slightly uniformly undersubtracted near our dwarfs, corresponding to a surface brightness difference of $\Delta\mu_i \lesssim 0.02$ mag arcsec^{-2} at $\mu_i = 28.5$ mag arcsec^{-2}. We thus confirm that the profiles are well-recovered down to our nominal surface brightness limit, and that the residual sky does not affect the shape measurements made in the outskirts of the galaxies.

The Impact of the Point Spread Function

In many situations, it is important to correct for the effects of the point spread function (PSF) in order to probe the outskirts of galaxies [see, e.g. Trujillo and Fliri, 2016]. In this work, we expect that the effect of the PSF does not significantly affect our results for the following reasons.

First, due to the high resolution of the HSC imaging, the region of interest for our sample ($r > \mathrm{R_{eff}}$) is not strongly affected by the smearing effect of the finite seeing (the median seeing is $i_{\mathrm{HSC}} \sim 0.6$, Aihara et al. 2019), even at the high redshift end of our sample. To visually demonstrate the size of the PSF with respect to the scale of the profile measurements, in Figure 4.3 we plot the profile of the PSF in grey. Second, it is important to note that because the cores of dwarfs are intrinsically fainter than those of their more massive analogs, the effect of scattered light is smaller for a fixed surface brightness limit. The theoretical HSC PSF model of Coupon et al. [2018], which was derived via optical tracing of the instrumental and atmospheric PSF, also shows that the large angular-scale wing of the HSC PSF should not affect measurements made in the outskirts for a sample such as the one considered in this work.

To affirm the above statements quantitatively, we apply a series of tests to the sample. First, we find that the ellipticity distribution (at all radii) does not change significantly as a function of redshift; one expects that the effect of the PSF would become more pronounced for higher redshift targets. Second, we re-fit our galaxies with the single Sérsic model described in Section 4.3.3 convolved with the PSF produced from the HSC-SSP data reduction pipeline. This is a standard technique used to account for the effect of the PSF when using a parametric model [for a review, see Knapen and Trujillo, 2017]. We find that the ellipticity as measured with this convolved Sérsic model and the non-parametric ellipticity measurements at $1\mathrm{R_{eff}}$ are offset by $\mu_{\Delta\epsilon} = -0.030 \pm 0.001$, where $\Delta\epsilon = \epsilon_{1\mathrm{R_{eff}}} - \epsilon_{\mathrm{conv}}$. This shift is statistically significant, but not large enough to impact our results.

This is not to say that the effect of the PSF is generically unimportant for low surface brightness science in HSC images – at $r \gtrsim 30$ kpc and $z \sim 0.1$, Wang et al. [2019] found that the extended HSC PSF can account for up to 40% of the flux in the stacked profile of galaxies at $10^{9.2} < M_\star/M_\odot <$

$10^{9.9}$ in HSC-SSP. At $r \lesssim 20$kpc with the bulk of the sample sitting at $z < 0.1$, however, the PSF has a much less significant effect. In particular, Figure 9 in Wang et al. [2019] shows that the impact of the PSF, which depends both on the central surface brightness and concentration of the galaxy, should be small for our sample, which is populated by dwarf galaxies with low central surface brightnesses (relative to massive galaxies) and exponential profiles. For a dwarf with an exponential profile and a central surface brightness of $\mu_i \sim 20$ mag arcsec^{-2}, the extended wings of the HSC PSF appear at around a scale of 2 arcsec and a surface brightness of 27 mag arcsec^{-2}. At scales comparable to $4R_{\rm eff}$, this effect will be even smaller. We thus do not expect that the PSF will affect the results presented in this work.

4.3.3 Profile Measurement Validation

In order to test the validity of our inferred size and ellipticity profiles, we perform several mock galaxy injection tests. In particular, we first confirm that we can recover the ellipticity of Sérsic profiles injected at low surface brightness without significant bias. Then, we compare our non-parameteric measurements of ellipticity at $1R_{\rm eff}$ to both the parametric measurements of our Sérsic fits to the HSC data and published ellipticity measurements from SDSS imaging to verify that there is no systematic shift between the parametric and non-parametric measurements.

Recovery of Injected Sérsics

First, we inject mock galaxies composed of a single Sérsic profile, the parameters of which (effective surface brightness, effective radius, and intrinsic axis ratios) are drawn from a known distribution, into the HSC co-adds. The surface brightness of the mock galaxies is set to cover the same range as the real galaxies, and the Sérsic index is fixed at $n = 1$ (exponential) for all galaxies. The position of the mock galaxies are selected to be empty locations where there are no detections in any of the five HSC bands, but no other constraints are made on the galaxy placement. These mock galaxies should therefore be affected by imaging artifacts, background galaxies, and residual astrophysical fore/background (e.g. galactic cirrus) in the same way as are the real galaxies in our sample.

Figure 4.5 shows the injected and recovered distributions of the galaxy structural parameters.

We find that the properties of the injected galaxies in this simple test are well-recovered: at $4R_{\rm eff}$, for 75% of cases the ellipticity of the mock galaxy is recovered to better than $|\epsilon_{\rm truth} - \epsilon_{\rm obs}| \leq 0.065$. Crucially, decreasing surface brightness does not significantly bias the our ellipticity measurement. In Figure 4.4, we show the surface brightness distribution of the real galaxy 1D profiles measured at 1-4 $R_{\rm eff}$. The lower envelope of the projected axis ratio distribution clearly increases with increasing radius (and therefore decreasing surface brightness). We do not find such a trend for the injected disk population, which samples b/a uniformly, over the same range in surface brightness.

While we do not test for the impact of asymmetric features that are not captured by a single Sérsic model, this test verifies that the ellipticity profile is well-recovered in HSC imaging conditions across a range of different injected distributions.

Comparison to parametric b/a measurements

In order to capture the often irregular and asymmetric structure of dwarf galaxies, our non-parametric profile fits allow many parameters to vary as a function of semi-major axis. Thus, it is important to compare our non-parametric measurements of ellipticity to measurements of the same quantity using a more rigid model.

In the left panel of Figure 4.6, we show the distribution over the observed axis ratio, $q = {\rm b/a} = 1 - \epsilon$, as measured from the non-parametric ellipticity profiles at $R_{\rm eff}$ (filled teal histogram), from Sérsic fits to the HSC-SSP imaging (green, unfilled), and from exponential fits to SDSS imaging of the same galaxies. We find that our non-parametric measurements are in good agreement with both the Sérsic profile fits ($\sigma_{\Delta q} = 0.07$) and the SDSS exponential profile fits ($\sigma_{\Delta q} = 0.101$). The increase in scatter with respect to the SDSS measurements is not unexpected, as the SDSS imaging is significantly shallower and fit with a less flexible model (i.e. where the Sérsic index is fixed to $n = 1$). The lack of bias as a function of projected axis ratio, however, is a good indication that our non-parametric measurements obtain reasonable results despite their flexibility.

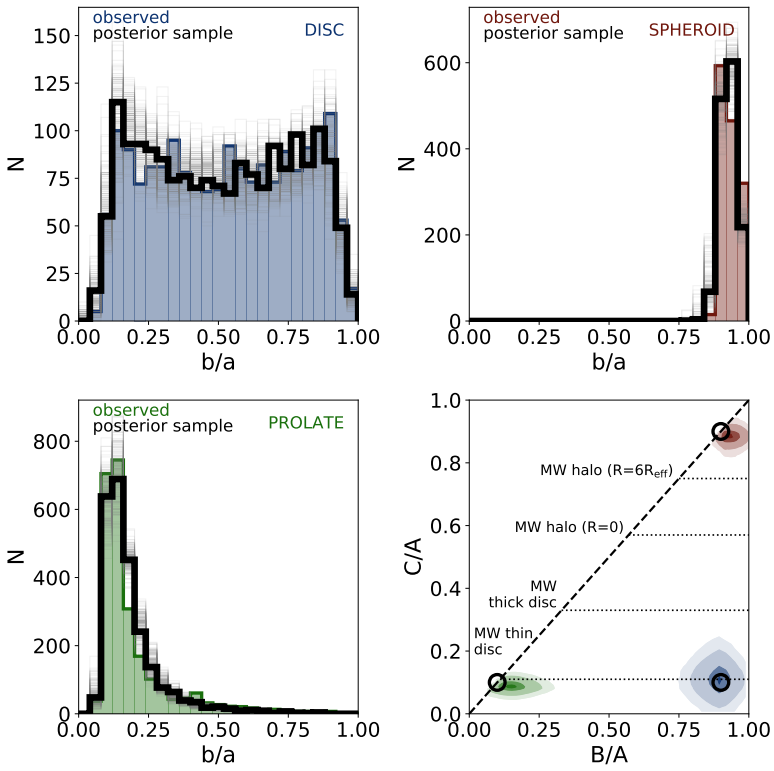

Figure 4.7 For the injected ellipsoid populations described in Figure 4.5, we infer the 3D shape distribution of the population from the recovered projected axis ratios. In each column, we show the inference results for our injected populations of disk ($[A, B, C] = [1., 0.9, 0.1]$, left), spheroid ($[A, B, C] = [1., 0.9, 0.9]$, middle), and prolate ($[A, B, C] = [1., 0.1, 0.1]$, right) galaxies. The top row shows the recovered b/a distribution as filled histograms and the posterior b/a sample as unfilled black histograms. The bottom row shows the distribution of the posterior sample over the intrinsic axes (B and C). The black circle shows the true position of the intrinsic axes. For physical context, we show the C/A values measured for the Milky Way disk-halo system as measured by Schönrich and Binney [2009] and Iorio and Belokurov [2019]. The dashed black line shows the definitional boundary of $B = C$.

4.4 3D Shape Inference

Let us assume that the 3D shapes of each galaxy in our sample (or subsample) are drawn from a single distribution over the intrinsic axis ratios B/A and C/A, given by $\mathrm{P}(\vec{\alpha})$ where $\vec{\alpha}$ is some set of parameters that describes the distribution of B/A and C/A. The projected axis ratio, q, for any given ellipsoid is determined solely by the observer's viewing angle, (θ, ϕ). That is to say, the

projected axis ratio q can be written as $q = \mathcal{F}(B/A, C/A, \theta, \phi)$.

The analytic expression for $\mathcal{F}$ was presented by Simonneau et al. [1998], and is reproduced below. First, $(ab)^2$ and $(a^2 + b^2)$ can be rewritten as follows:

$$a^2b^2 = f^2 = (C\sin\theta\cos\phi)^2 + (BC\sin\theta\sin\phi)^2 + (B\cos\theta)^2, \tag{4.1}$$

$$a^2 + b^2 = g = \cos^2\phi + \cos^2\theta\sin^2\phi + B^2(\sin^2\phi + \cos^2\theta\cos^2\phi) + (C\sin\theta)^2 \tag{4.2}$$

We now define the quantity h to be

$$h \equiv \sqrt{\frac{g - 2f}{g + 2f}}, \tag{4.3}$$

such that it may be shown that

$$\frac{b}{a} = \frac{1 - h}{1 + h} \tag{4.4}$$

Because the distribution of viewing angles is known to be isotropic on the surface of the sphere, we can predict the projected distribution of q given a choice of intrinsic shape distribution characterized by $\vec{\alpha}$ by sampling ϕ and θ as follows:

$$\begin{aligned} \phi &\sim \mathcal{U}[0, 2\pi] \\ \nu &\sim \mathcal{U}[0, 1] \\ \theta &= \cos^{-1}(2\nu - 1) \end{aligned} \tag{4.5}$$

For simplicity, we first consider a normal distribution over both B and C, such that the 3D shape distribution can be described by the parameters $\vec{\alpha} = \{\mu_B, \mu_C, \sigma_B, \sigma_C\}$. We find that the data are well-described by this relatively simple model, and that the fit is not significantly changed or improved by a more complex model [as motivated by Zhang et al., 2019, see Section 4.10].

Armed with this framework, we are able to quickly estimate the distribution of projected axis ratios for a given choice of $\vec{\alpha}$. This can then be compared cheaply to the observed distribution of q by adopting a Poisson likelihood,

$$\ln p(q|\mu_B, \mu_C, \sigma_B, \sigma_C) = \sum_i n_i \ln m_i - m_i - \ln n_i!, \tag{4.6}$$

where n_i is the observed count where $0.04i < q \leq 0.04(i+1)$ and m_i is the predicted count in the same range. Though this likelihood is in principle sensitive to the adopted bin size, for our sample we find that the results are not significantly affected by reasonable choices for the bin width. For each step, we choose the binsize from a uniform distribution bounded by [0.03,0.1]. The minimum width is chosen such that for the minimum sample size that we consider ($N = 700$, see Section 4.5.1), for a uniform distribution of projected axis ratio the standard deviation of the counts in a given bin is expected to be $\sim 20\%$ of the mean bin count.

We adopt a flat prior for all model parameters. The prior over μ_B and μ_C is set purely by the physical boundaries:

$$p(\mu_B) = \begin{cases} 1 & \text{if} \quad 0 < \mu_B < 1 \\ 0 & \text{otherwise} \end{cases} \tag{4.7}$$

we additionally constrain $\mu_C \leq \mu_B$ to maintain the order of axes,

$$p(\mu_C) = \begin{cases} 1 & \text{if} \quad (0 < \mu_C < 1) \quad (\mu_C \leq \mu_B) \\ 0 & \text{otherwise,} \end{cases} \tag{4.8}$$

additionally, when sampling from a given α, we disregard cases where $C > B$.

We implement the same flat prior over σ_B and σ_C:

$$p(\sigma_X) = \begin{cases} q0 & \text{otherwise} \end{cases} \tag{4.9}$$

where $X \in (B, C)$. Here, the upper limit is set so that the distribution is contained largely within

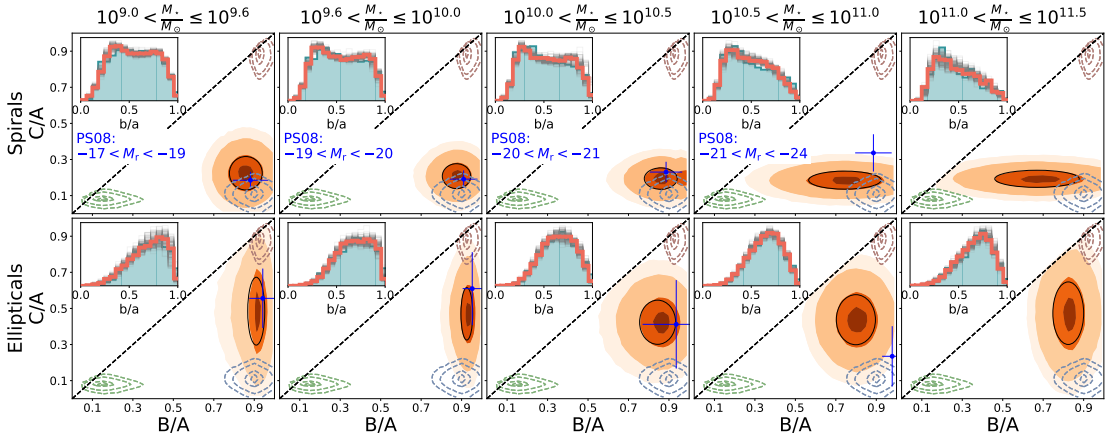

Figure 4.8 Inferred 3D shape distributions as a function of stellar mass (increasing towards top) and morphology (spirals at top, ellipticals at bottom), using SDSS catalog measurements following the morphology criterion of Padilla and Strauss [2008]. In each panel, the filled contours show the inferred 3D shape distribution using our method, while the blue errorbars show the mean and standard deviation of the 3D shape distribution from Padilla and Strauss [2008] in roughly analogous bins of $r_{\rm SDSS}$-band absolute magnitude. Our inferred shape distributions are in general agreement with those of Padilla and Strauss [2008], taking into account that the absolute magnitude cuts are not equivalent to our cuts in stellar mass. In particular, the highest luminosity bin of Padilla and Strauss [2008], where our inference is in significant disagreement, extends to $M_\star \sim 10^{12} M_\odot$. We also show the same contours for the pure disk, prolate, and spheroid Sérsic population presented in Figure 4.7 by the dashed blue, green, and red curves.

the physically admissible region.[3]

We can then write the posterior probability distribution as $p(\vec{\alpha}|q_{\rm obs}) \propto p(q_{\rm obs}|\vec{\alpha}) p(\mu_B) p(\mu_C) p(\sigma_B) p(\sigma_C)$. To sample efficiently from this distribution, we use the Markov Chain Monte Carlo ensemble sampler implemented in emcee [Foreman-Mackey et al., 2013]. For each case discussed in the work, we run the sampler with 32 walkers and 3000 moves. We verify that the walkers have converged and discard the first 150 moves of each.

[3] We furthermore find that none of our data suggest σ_X near 0.5, indicating that this choice of boundary does not affect our results.

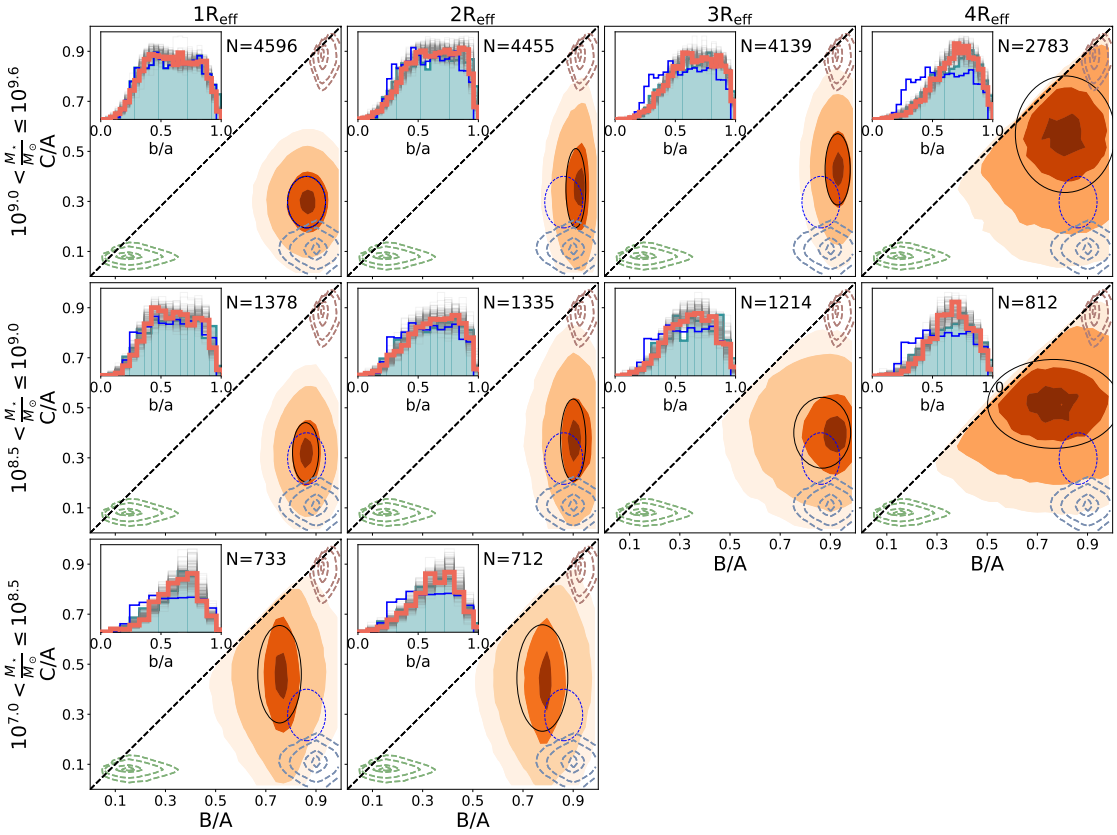

Figure 4.9 For bins in increasing stellar mass (rows) and measurement radius (columns), the distribution of inferred axis ratios B/A and C/A for the dwarf sample. Each panel shows the distribution of intrinsic axis ratios in orange. The black ellipses show the 1σ region of the maximum a posteriori estimate, $\max_{P(\vec{\alpha}|\{b/a\})} \vec{\alpha}$. We also show the same contours for the pure disk, prolate, and spheroid Sérsic population presented in Figure 4.7 by the dashed blue, green, and red curves. The black line shows the B/A=C/A definitional boundary. Each inset panel shows the observed axis ratio, b/a= $1-\epsilon$, distribution as the solid teal histogram. The distribution of b/a produced by the posterior sample in B/A and C/A is shown by the orange unfilled histogram; individual samples from the posterior are shown by the grey unfilled histograms.

4.4.1 Validation: Comparison to Sérsic Populations

In order to test our 3D inference framework, we return to the injected Sérsic populations of Section 4.3.3. These tests have the advantage of incorporating both major sources of uncertainty in the final 3D shape inference: the uncertainty in the 1D profile measurement (due to, e.g., neighboring

galaxies, residual sky background) and in the 3D shape inversion problem.

In Figure 4.7, we show the recovered distribution of projected axis ratios by the colored histograms: blue for the disk population, red for spheroidal, and green for prolate. The distribution of projected axis ratios generated by sampling the posterior is shown by the thick black stepped curve in each (the thin black lines show individual draws from the posterior). The lower right panel of Figure 4.7 shows the distribution of this posterior sample in the intrinsic B-C axis space; the colored contours show the regions that contain 0.34^2, 0.68^2, 0.95^2, and 0.99^2 of the distribution (corresponding to the 0.5σ, 1σ, 2σ, and 3σ regions for a multivariate normal distribution). The black circles show the true value of μ_B and μ_C.

When the true value of μ_B and μ_C are sufficiently distant from the boundary, we find that we are able to recover their values very well, as seen for the disk population in blue. However, we find that our inferred values are biased when the true value is close to the imposed boundary (B/A=C/A) of the problem, as is the case for the spheroidal and prolate populations. Based on the shape distributions inferred by studies at higher masses [see,e.g. Padilla and Strauss, 2008, van der Wel et al., 2014] and by studies of ultra diffuse galaxies in clusters [Burkert, 2017, Rong et al., 2020], as well as the shape distributions measured from cosmological simulations [Pillepich et al., 2019], it is unlikely that real galaxies are characterized by extreme distributions at the B=C boundary.

All of our injected Sérsic galaxies are drawn from a 3D shape distribution where $\sigma_B = 0$ and $\sigma_C = 0$; the inferred σ_B and σ_C in these test cases should then provide a lower limit on the intrinsic dispersion to which we are sensitive.[4]

4.4.2 Validation: Comparison to Padilla et al. 2008

Before applying this shape inference framework to our sample of HSC dwarfs, we want to confirm that our method can reproduce published 3D shape distributions of higher mass galaxies. Towards this end, we use SDSS catalog shape measurements to infer 3D shape distributions from data that are analogous to those of Padilla and Strauss [2008], who use SDSS catalog measurements to

[4]Because the Sérsic profiles are quite different from real galaxies, we do not attempt to deconvolve the error in σ_B and σ_C for the real sample using these test cases in this work.

estimate the 3D shape distribution of galaxies with stellar masses of $M_\star \gtrsim 10^9 M_\odot$.

For a linear combination of an exponential profile (i.e., a Sérsic profile with index $n = 1$) and a deVaucouleurs profiles (i.e., a Sérsic profile with index $n = 4$), the SDSS photometric catalog provides the weight assigned to the $n = 4$ component as $f_{\rm deV}$ [Abazajian et al., 2004]. Padilla and Strauss [2008] separate their sample into a subset of spiral galaxies, wherein $f_{\rm deV} < 0.8$, and elliptical galaxies, wherein $f_{\rm deV} > 0.8$, and evaluate their 3D shape distributions independently. Using the SDSS DR16 catalog, we divide the sample of galaxies with $z < 0.05$ and $M_\star \gtrsim 10^9 M_\odot$ in the same manner [Ahumada et al., 2019].

We then use the 3D shape inference method described above to estimate the distribution over intrinsic axes B and C for bins of approximately 0.5 dex in stellar mass (the first mass cut is set at $\log_{10}(M_\star/M_\odot) = 9.6$ so that the lowest mass bin considered is equivalent to the highest mass bin of our sample).

The results of this inference, with the roughly equivalent $r_{\rm SDSS}$-band absolute magnitude bins of Padilla and Strauss [2008] overlaid, are shown in Figure 4.8. Each panel inset shows both the observed distribution of b/a, measured via the non-parametric profile construction described in Section 4.3, by filled teal histograms. We then overplot the distribution of projected b/a generated from sampling the MCMC chain in grey, i.e. $\vec{\alpha}_i \sim P(\mu_B, \mu_C, \sigma_B, \sigma_C|\text{b/a})$. The distribution of b/a over all of these samples is then shown by the thick orange curve. In the main panel, we show the analogous distribution in the intrinsic axes (B-C) plane. Here, the same samples from the posterior are shown by the orange filled contour. The dashed colored curves are the contours of the pure disk, spheroid, and prolate Sérsic populations shown in the lower right panel of Figure 4.7.

Due to the differences in data used and the imperfect mapping between stellar mass and absolute magnitude, we do not expect that the inferences will be statistically identical. However, we find good agreement between our results and those of Padilla and Strauss [2008] for all but their brightest bin at $-21 < M_r < -24$, which includes a significantly wider mass range than our most similar bin. Having reproduced the 3D shape distribution of this literature sample, and of the mock galaxies injected into HSC imaging, we proceed to apply the shape inference technique to the dwarf sample at hand.

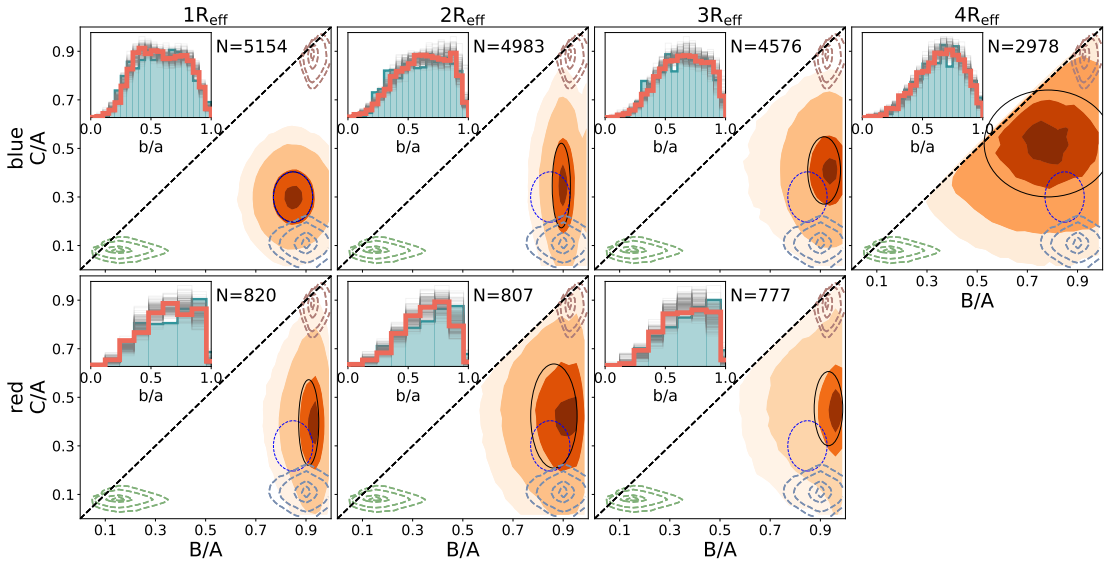

Figure 4.10 For dwarfs with $M_\star > 10^{8.5} M_\odot$, the inferred shape distribution for blue ($g-i < 0.90$) and red ($g-i > 0.90$) galaxies as a function of radius. Similar to the trend we see in the analogous mass bin of Figure 4.8, the 3D distribution of blue galaxies is diskier than the red galaxies at $R = 1\mathrm{R_{eff}}$. At large radii, both blue and red galaxies move towards spheroid shapes. As in Figure 4.9, we show the 50th percentile regions of the pure disk, prolate, and spheroid Sérsic population presented in Figure 4.7 by the dashed blue, green, and red curves.

4.5 Results

The HSC-SSP imaging has both the surface brightness sensitivity to reliably measure the ellipticity profile of individual galaxies out to $3\mathrm{R_{eff}}$ and the on-sky area necessary to build a sample large enough to infer the 3D shape distribution.

Before proceeding, we note that the transition from thin disk to thick disk to spheroid does not have a well-defined boundary. To put our results into context, we provide the intrinsic axis ratios of the Milky Way disk and halo system. Assuming an exponentially declining disk, the Milky Way has a disk scale length of 2.5 kpc, a thin disk scale height of 270 pc, and a thick disk scale height of 820 pc. This corresponds to an axis ratio of $C/A = 0.11$ for the MW thin disk, and $C/A = 0.33$ for the MW thick disk [Schönrich and Binney, 2009]. The MW stellar halo becomes increasing spheroidal as a function of radius in the range of $0.57 \leq C/A \leq 0.75$ [Iorio and Belokurov, 2019].

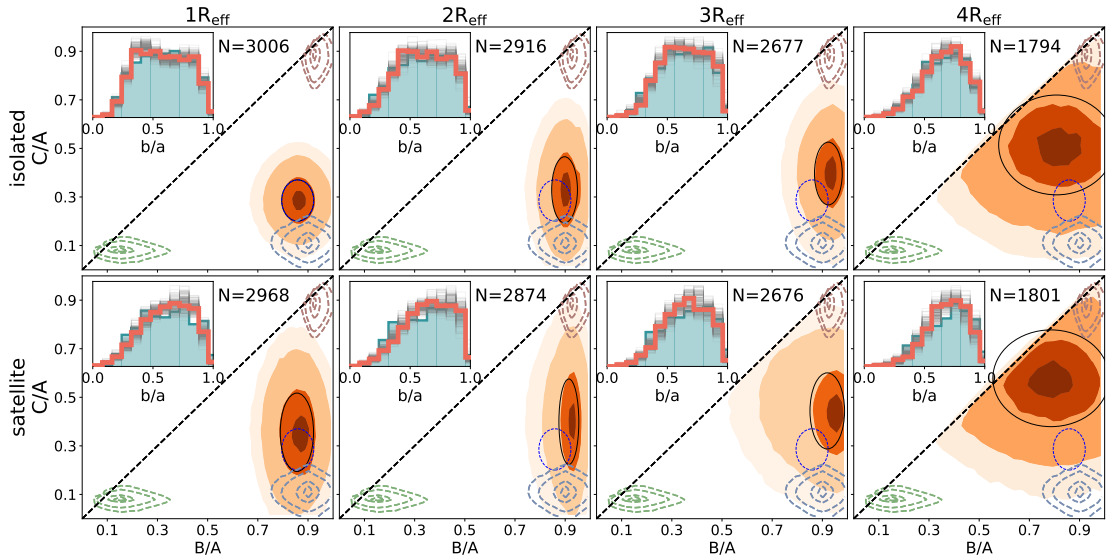

Figure 4.11 For dwarfs with stellar masses $M_\star > 10^{8.5} M_\odot$, the inferred shape distribution for field (distance to nearest neighbor $d_{NN} > 1$Mpc) and satellite ($d_{NN} \leq 1$Mpc) galaxies. We see negligible difference between satellite and field galaxies; both are consistent with thick discs at $1R_{eff}$, and C/A increases towards spheroid shapes at larger distances from the galaxy center. As in Figure 4.9, we show the analogous contours of the pure disk, prolate, and spheroid Sérsic population presented in Figure 4.7 by the dashed blue, green, and red curves.

4.5.1 3D Shape as a function of Stellar Mass and Radius

We first consider the change in the galaxy 3D shape as a function of stellar mass and radius. Previous studies have found that the high mass end of our sample ($10^9 < M_\star/M_\odot < 10^{9.6}$) are composed largely of (thick) discs [Padilla and Strauss, 2008, Sánchez-Janssen et al., 2010, van der Wel et al., 2014]; 3D shapes beyond $1R_{eff}$ or at lower masses have not been measured for general dwarf samples.

First, we consider the distribution of observed b/a as measured at $1R_{eff}$, $2R_{eff}$, $3R_{eff}$, and $4R_{eff}$ for bins of stellar mass in Figure 4.9. Each panel shows the number of measurements made for each slice in radius and stellar mass. From tests with Sérsic populations, we find that the recovered values of σ_B and σ_C increase significantly at $N \lesssim 700$; we therefore do not consider subsets where $N < 700$ (see Section 4.11).

From the observed distribution alone, we see first that the distribution of projected axis ratios becomes increasingly more concentrated at large values of b/a as we consider larger radii. This is consistent with a shift towards more spheroidal shapes; indeed, in Figure 4.9, we see that the high-mass dwarfs are consistent with a thick disk at $1R_{\rm eff}$, and shift towards the spheroidal extreme at $3R_{\rm eff}$ and $4R_{\rm eff}$. We note that a minority of the galaxies in the sample have bars at $1R_{\rm eff}$ – though these bars clearly do not dominate the signal (bars are intrinsically prolate, with $\mu_B \sim \mu_C \sim 0.3$ Compère et al. [2014], Méndez-Abreu et al. [2018]), it is likely that they contribute to the recovered triaxiality of the sample. Indeed, though the dwarfs are only slightly triaxial ($\mu_B \sim 0.75$ at all masses and radii), we find that a purely oblate model is a significantly worse fit to the data.

We see relatively little change in the intrinsic shape distribution of galaxies at $10^{8.5} < M_\star/M_\odot \leq 10^{9.0}$ and those at $10^{9.0} < M_\star/M_\odot \leq 10^{9.6}$. Both show $\mu_C(1R_{\rm eff}) \sim 0.3$, and shift towards progressively larger μ_C with increasing radius. In our lowest mass bin, we see a hint that the shape distribution shifts dramatically, towards lower μ_B and μ_C (i.e. away from the pure disk region). Though this behavior is not unexpected, as lower mass galaxies are expected to be increasingly dispersion dominated [see, e.g. Wheeler et al., 2017, Pillepich et al., 2019], and consistent with a previous study of Virgo dwarfs at somewhat lower stellar masses by Sánchez-Janssen et al. [2016], we caution that we are not complete at this mass bin, and that the number of galaxies in our lowest mass bin is significantly lower (N$\sim$ 700), which may lead to an overestimation of σ_B and/or σ_C (see Section 4.11).

4.5.2 3D Shape and Galaxy Color

At higher masses, we reproduce in Figure 4.8 the divergence in 3D shape distribution of spiral and elliptical galaxies seen in Padilla and Strauss [2008]. One can then reasonably expect to see a similar trend at $\approx 1R_{\rm eff}$ when our sample is divided between red and blue galaxies. We divide our sample at $(g-i)_{\rm SDSS} = 0.9$, chosen as the midpoint between the blue sequence and red cloud for this choice of color and stellar mass range[5].

[5]Because the red sequence is relatively unpopulated at this mass range, we choose the division using the SDSS catalog and a somewhat broader range in stellar mass $M_\star \lesssim 10^{10.5} M_\odot$

We show the 3D shape distribution for the highest mass bin in Figure 4.10 as a function of radius, again at $1R_{\rm eff}$, $2R_{\rm eff}$, and $3R_{\rm eff}$ from left to right. The left column shows the results at $1R_{\rm eff}$. Indeed, in the leftmost column we see that the red galaxies are at preferentially larger C/A with respect to blue galaxies, similar to Figure 4.8 when the sample is split between spiral and elliptical galaxies.

At larger radii, however, we find that the blue and red galaxies occupy the same region in the B-C plane. While the red galaxies show little shape change with radius, the distribution of blue galaxies increases in σ_C and shifts towards the spheroidal corner (red dashed curve) of parameter space.

4.5.3 3D Shape and Environment

Star formation in dwarfs is thought to be quenched by almost entirely environmental means [Geha et al., 2012]; it is of interest, then to ask whether populations of field and satellite dwarfs display the same change in 3D shapes as do blue and red dwarfs. For this exercise, we search massive companions ($M_\star > 10^{10} M_\odot$) in the NASA Sloan Atlas (NSA) within $\Delta v < 1000$ km s^{-1} and 1 Mpc projected distance. We choose the projected distance cut $d_{\rm NN} > 1$Mpc to coincide with the distance at which the dwarf quenched fraction, $f_{\rm quench}(d_{\rm NN})$, approaches its field limit $f_{\rm quench}(d_{\rm NN} \to \infty)$ for the mass range considered in Geha et al. [2012, see Figure 4]. We additionally consider only galaxies at $z < 0.10$. Though the NSA contains galaxies up to $z = 0.15$, at $z > 0.1$ the satellite fraction begins to drop, indicating that the massive galaxy sample is not sufficiently complete to characterize the environment of the dwarfs in our sample. In Figure 4.11, we show the 3D shape distribution for field (top row) and satellite (bottom row) dwarfs at $M_\star > 10^9 M_\odot$. Unlike the dwarfs separated by color, the satellite and field dwarf samples show roughly the same 3D shape distribution as a function of radius. It is important to note that the difference in σ_B at large radius between the field and satellite dwarfs is likely unphysical, as the inferred σ_B for these populations is close to or below the estimated σ_B for our zero-scatter disk and spheroid populations (shown in Figure 4.11 by the dashed contours).

We find that at $1R_{\rm eff}$, the satellite galaxies scatter towards marginally more spheroidal shapes

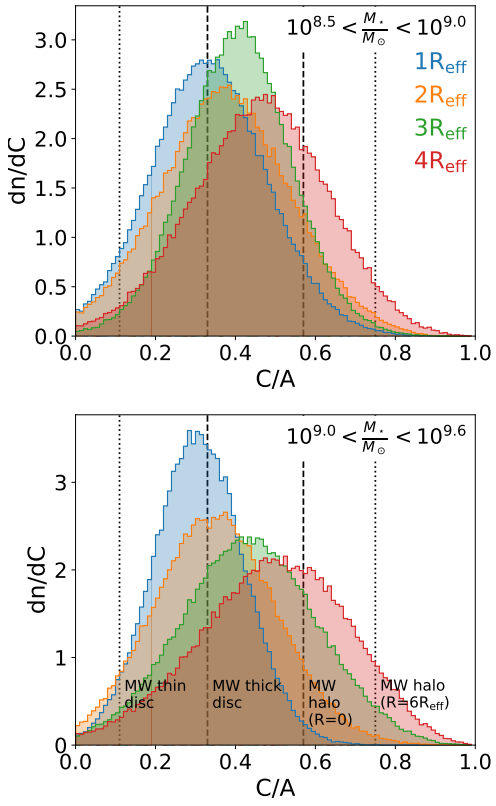

Figure 4.12 The change in galaxy thickness (C/A) as a function of radius for $10^9 < M_\star/M_\odot < 10^{9.6}$ (top) and $10^{8.5} < M_\star/M_\odot < 10^9$ (bottom). In both cases, the dwarfs become systematically more spheroidal (C$\sim$A, $B/A \gtrsim 0.8$ for all cases) at large radii. For physical context, we also show the C/A axis ratio of the Milky Way thin disk & thick disk [Schönrich and Binney, 2009], and the stellar halo at $R = 0$ & $R = 6\mathrm{R_{eff}}$ [Iorio and Belokurov, 2019]. The MW axis ratios are shown by vertical black lines, as labeled in the bottom panel.

than do the field galaxies. This effect is similar to the trend seen in Section 4.5.2 between red and blue dwarfs, but the separation between field and satellite galaxies is relatively small. Though the projected axis ratio distribution of field galaxies and satellite galaxies is significantly different (Kolmogorov-Smirnov p-value$\approx$ 0.001), we do not see a significant difference between the b/a distribution of field galaxies and blue satellites (KS p-value$\approx$ 0.29). This is likely due to fact that, for our sample, nearly all red galaxies are satellites of more massive galaxies [Geha et al., 2012]. Blue galaxies, on the other hand, are found both as satellites and in the field. It is likely that making a cut on color produces, in effect, a selection of satellite galaxies that have been more processed by the host central.

Finally, to facilitate an easier comparison to future worsk, we note that maximum a posteriori estimates and 1σ standard deviations for all the subsamples considered in this section are tabulated in Section 4.9.

4.6 Discussion

4.6.1 The Emergence of Round Outskirts Around Low-Mass Galaxies

At higher masses, stellar halos are generally thought to be the product of a series of minor mergers, which deposit stars at large radii [Amorisco, 2017]. However, because the stellar-to-halo mass ratio tends to increase as galaxy mass decreases, the dwarfs in our sample are unlikely to accrete a sufficient mass in stars to build a stellar halo via minor mergers alone [Purcell et al., 2007, Moster et al., 2013].

Even though it appears unlikely that dwarfs can accrete a stellar halo via conventional means, it has long been known that dwarfs in the Local Group and M81 Group host a smooth intermediate/old stellar population in their outskirts [see Stinson et al., 2009, Hargis et al., 2020, and references therein]. These observations hint at the existence of an in-situ halo formation mechanism at low masses, but this conclusion is obfuscated for two reasons:, first the sample is comprised almost entirely of galaxies that are interacting with a more massive companion. Second, such stellar halos have been confirmed for only a few tens of galaxies. In this work, we have presented the first large sample where a clear transition to a round stellar component is detected in the outskirts of dwarfs that are not Local Group members.

In Section 4.5.1, we presented a set of inferred 3D shapes for a sample of dwarf galaxies as a function of stellar mass and radius. Due to the depth of the HSC-SSP imaging, we are able to measure ellipticity profiles out to $4R_{\rm eff}$ for the most massive dwarfs in our sample. Indeed, we see that the structure of the dwarfs are characterized by thick discs at $1R_{\rm eff}$ and become increasingly spheroidal at large radii, as shown in the top row of Figure 4.9. For clarity we also show the C/A distribution as a function of radius for the $10^9 M_\odot < M_\star < 10^{9.6} M_\odot$ and $10^{8.5} M_\odot < M_\star < 10^9 M_\odot$ stellar mass bins in Figure 4.12. At $1R_{\rm eff}$, the dwarfs have C/A axis ratios consistent with the Milky Way thick disk, and significantly thicker than the MW thin disk [Schönrich and Binney, 2009]. This thick disk morphology is in rough agreement with previous measurements for dwarfs in SDSS and the Local Group [Padilla and Strauss, 2008, Sánchez-Janssen et al., 2010, Roychowdhury et al., 2013]. At $4R_{\rm eff}$, the dwarfs shapes are of comparable thickness to the inner stellar halo of the

MW as measured by Iorio and Belokurov [2019]. These results indicate that the dwarf disk-halo interface is similar in structure, if not origin, to more massive galaxies.

Though they are not expected to form through minor mergers, the existence of round stellar outskirts around dwarfs is not unexpected theoretically. Dwarf galaxies sit in shallow potential wells, and are thus more sensitive to the effects of star formation feedback than their more massive analogs. Stinson et al. [2009] proposed that dwarf galaxies would generically form stellar halos through stellar radial migration, star formation in outflows, and a contraction of the central star-forming region. Similarly, Maxwell et al. [2012] found that stellar feedback could drive sufficient quantities of dense gas to produce a fluctuation in the overall potential and thus build a stellar spheroid through migration [see also El-Badry et al., 2016]. The concordance in 3D shape at large radii for blue and red dwarfs, as shown in Figure 4.10, and at all measured radii in field and satellite dwarfs, as shown in Figure 4.11, also suggests that the creation of round outskirts is not driven by an interaction with a more massive halo.

It has also been suggested that dwarf halos could be formed as a result of major mergers between dwarfs [Bekki, 2008b]. However, the detection of an increasingly spheroidal component in the outskirts of our dwarf sample is at odds with this formation mechanism; the major merger rate of dwarfs is likely not high enough to generate enough stellar halos to produce such a population. Simulations suggest that approximately 30% of dwarfs in our stellar mass range outside of the Virial radius of a MW-like object have undergone a dwarf-dwarf major merger in the past 10 Gyr [Deason et al., 2014]. Though dwarf-dwarf major mergers were more common in the early universe, due to fading via passive evolution it is unlikely that we would be able to detect such ancient halos. Though the $z = 0$ surface brightness of any given merger-driven stellar halo is dependent on its assembly history, Bekki [2008b] finds that their simulated stellar halo reaches ~ 30 mag arcsec^{-2} at $R \sim 2$ kpc. If the stellar halo population had a uniform age of 1 Gyr at the time of halo creation, and was created at a lookback time of 10 Gyr, the stellar halo will have dimmed by 1-2 mag arcsec^{-2} by $z = 0$ from the evolution of the mass-to-light ratio alone (as computed from the FSPS models of Conroy et al. 2009b), well below the surface brightness sensitivity of our imaging. Moreover, the intermediate age stellar component often observed at large radii in resolved star

studies requires a relatively recent deposition of stars in the outskirts [see, e.g. Zaritsky et al., 2000, Stinson et al., 2009, and citations therein]. We thus find it unlikely that major mergers are the sole formation mechanism of low-mass stellar halo formation, though we note that some individual cases are consistent with both star formation feedback and accretion driving stellar halo formation [Pucha et al., 2019]. The apparent ubiquity of round stellar outskirts in this work is instead consistent with the proposal that stellar outskirts are formed primarily through in-situ processes.

4.6.2 Morphological Transformation and Quenching

It has long been observed that the cessation of star formation in dwarfs, their morphological transformation from a disk-dominated to a dispersion-dominated structure, and their proximity to more massive galaxies are all strongly correlated [see, for example, Dressler, 1980, Lin and Faber, 1983, Postman and Geller, 1984, Weinmann et al., 2006, Geha et al., 2012, Kormendy and Bender, 2012, Ann, 2017].

As shown in the leftmost column of Figure 4.10, we find that the blue dwarfs in our sample tend towards lower values of C/A than red dwarfs – that is, the blue dwarfs are more consistent with a thick disk, while red dwarfs scatter towards more spheroidal shapes. This is in concordance with the familiar morphology-color dichotomy, and follows the same trend seen in intrinsic shape studies of satellite dwarfs in the nearby Universe [Sánchez-Janssen et al., 2019] and at higher masses [see, e.g. Padilla and Strauss, 2008, Rodríguez et al., 2016, and Figure 4.8]. We see a similar trend when separating dwarfs by the projected nearest neighbor distance (within 1000 km s^{-1}), though the shift between satellite and field galaxies is relatively marginal (see leftmost column of Figure 4.11). This finding is in good agreement with the results of Sánchez-Janssen et al. 2019, who find that for a sample of quiescent satellite dwarfs, intrinsic shape correlates strongly with galaxy morphology and luminosity, but is largely insensitive to the specific environment of the dwarf.

We do not detect a significant difference in the intrinsic shapes of blue satellites and dwarfs in the field. This is in contrast with the shift towards rounder shapes seen in the red galaxy subset (Figure 4.10) and satellite galaxies (without a color cut, Figure 4.11). This suggests that morphological transformation operates on a longer timescale than star formation quenching, or

that quenching is a prerequisite to the morphological transformation. However, it is important to note our choice of model (a singly-peaked multivariate Gaussian) will necessarily only recover the dominant shape population.

4.6.3 Comparison with Simulations

Due again to their increased sensitivity to star formation feedback, the 3D shapes of dwarfs are a strong constraint on the feedback prescription of cosmological simulations.

Pillepich et al. [2019] give the distribution of dwarf 3D shapes as measured at twice the stellar half-mass radius. First, we note that our results are in broad agreement with those of Pillepich et al. [2019] in that our 3D shapes are in the disky/spheroidal regime, with essentially no galaxies in the prolate regime (defined by van der Wel et al. [2014] as $B/A < 1 - C/A$). At $\mathrm{R_{eff}}$, the change in our 3D shape distribution is also qualitatively similar to that of Pillepich et al. [2019]; as stellar mass decreases, σ_C increases and the distribution shifts towards more spheroidal shapes (as shown in the leftmost column of Figure 4.9).

However, under the assumption of centrally concentrated star formation, we would expect the half-mass radius to be larger than the half-light radius, implying that a comparison at the same physical radius should occur at $> 2\mathrm{R_{eff}}$. Moreover, the conversion between the i_{HSC}-band surface brightness and the stellar mass distribution is a function of the galaxy's stellar populations.

Clearly, to make a quantitative comparison, it will require significant effort to put the simulations and observations on equal footing. Nevertheless, the broad agreement in the shape distribution of dwarfs and its evolution with stellar mass is a promising step.

4.7 Conclusions

In this work we have measured the surface brightness and ellipticity profiles of a sample of spectroscopically confirmed dwarfs using imaging from the Hyper Suprime-Cam Subaru Strategic Program (Section 4.3). We then extended the framework commonly used to infer 3D galaxy shapes [see, e.g., Padilla and Strauss, 2008, Roychowdhury et al., 2013, van der Wel et al., 2014, Zhang et al., 2019,

Putko et al., 2019] to measure the change in dwarf galaxy shape as a function of radius.

We show that the population of dwarfs in our sample tend to host thick, disk-like structures at $1R_{eff}$, and evolve towards more spheroidal shapes in their outskirts (see Figure 4.9). This finding is in agreement with the predicted quasi-spherical shapes of in-situ stellar halos [Stinson et al., 2009].

At $M_\star > 10^{8.5} M_\odot$, blue dwarfs tend to be diskier than red dwarfs near their centers (i.e. at R=$1R_{eff}$, left panel of Figure 4.10). This divergence as a function of color mirrors the same dichotomy seen at higher masses, where blue galaxies are preferentially diskier and red galaxies relatively thicker and spheroidal (see Figure 4.8). However, the outskirts of both red and blue dwarfs move towards more spheroidal shapes, suggestive of an in-situ formation mechanism for the extended stellar outskirts. This interpretation is also supported by a uniform trend towards more spheroidal outskirts in both field and satellite galaxies (see Figure 4.11).

The sample considered in this work is based on spectroscopic surveys; we are thus missing low surface brightness and ultra diffuse galaxies (UDGs). In particular, simulations suggest that the effective surface brightness cuts implemented in the SDSS and GAMA spectroscopic surveys bias dwarf samples towards more compact objects [Wright et al., 2021]. Previous works have focused on samples of cluster UDGs: Burkert [2017] find that, for a sample of Coma UDGs, $\mu_B = \mu_C \sim 0.67$ (for a model with the assumption $C = B \leq A$). Similarly, Rong et al. [2020] find that for a triaxial model, $\mu_B = 0.86$ and $\mu_C = 0.49$. These results imply that cluster UDGs are typically rounder than high surface brightness dwarfs, with an intrinsic minor axis ratio (C/A) comparable to the outskirts of dwarfs in our sample.

However, samples of cluster UDGs are in highly overdense environments compared to the typical dwarf galaxy in our sample. To more fairly compare the structural composition of low surface brightness and high surface brightness dwarfs, and better understand the nature of the relationship between these two populations, we must instead look to build a sufficiently large sample of UDGs in the field [e.g., Bellazzini et al., 2017, Leisman et al., 2017, Román and Trujillo, 2017, Greco et al., 2018a, Tanoglidis et al., 2021] such that the deprojection problem is tractable.

Our analysis also suggests that at $M_\star < 10^{8.5} M_\odot$, dwarfs become increasingly round (larger μ_C). However, our spectroscopic sample is far from mass-complete at $M_\star < 10^8 M_\odot$. In order to more

comprehensively understand the properties of the dwarf population, it is necessary to construct a large and mass-complete sample of dwarfs at stellar masses lower than what is accessible with spectroscopic surveys currently in hand. As has been shown theoretically, star formation feedback is expected to play an increasingly dramatic role in the stellar structure of increasingly low mass dwarfs; extending the observational lever arm to lower stellar masses will provide a important constraint on prescriptions for star formation feedback, and provide novel insights into the stellar structure of such systems.

4.8 Appendix: Tests of the Background Subtraction

The fidelity of the background subtraction is of key importance for two aspects of our analysis. First, background subtraction schemes that measure the sky background on scales comparable to the size of the target galaxies are liable to attribute diffuse light in the target outskirts to the sky background. This causes oversubtracted "dark rings" around galaxies that are large on the sky. Second, a uniform under- or oversubtraction of the background could affect our measurement of $R_{\rm eff}$, as well as the estimate of our surface brightness limit.

Dark rings were a significant problem for nearby massive galaxies in the first data release of the HSC-SSP, prompting a change in the background estimation algorithm used for S18A (and the second data release). The updated algorithm is described in detail in Section 4.1 of Aihara et al. [2019]; here we summarize the changes that most strongly affect performance for our sample.

The most pertinent change to the sky subtraction algorithm of S18A (or equivalently, PDR2) is that the sky is now estimated over the full focal plane, rather than over individual CCDs. In both cases, the sky is estimated by fitting a sixth-order two-dimensional Chebyshev polynomial to "superpixels", which are themselves defined as the clipped mean of non-detection pixels within an $N \times N$ pixel grid. However, because the S18A pipeline fits a sky background over the entire focal plane of HSC, the superpixels can be much larger ($N = 1024$ pixels, $2'.8$ deg) than is possible with individual CCD sky estimation ($N = 256$ pixels, $43''$). The maximum radial range at which we

measure the 1D surface brightness profiles in this work is 500 pixels (84"), significantly smaller than the S18A superpixels. Oversubtracted dark rings should thus not occur around our target galaxies in S18A – indeed, the galaxies are sufficiently small on the sky that the dark ring oversubtraction was not likely to be present even in the PDR1 pipeline.

To quantitatively test this statement, as well as to estimate the overall residual sky background in the vicinity of our targets, we follow the approach of Li et al. 2020, in prep., who test the performance of the surface brightness sensitivity and S18A background subtraction for a set of low-z ($z \sim 0.02$) and intermediate-z ($z \sim 0.40$) massive galaxies in HSC. From tests on mock galaxies and comparisons to imaging from the Dragonfly Wide Field Survey [Danieli et al., 2020] and the Dark Energy Camera Legacy Survey [DECaLS, Dey et al., 2019], they conclude that the intermediate-redshift massive galaxies are slightly uniformly undersubtracted, while the low-redshift massive galaxies are slightly uniformly oversubtracted. They moreover find that nearby 'Sky Objects' (SkyObj), can be used to estimate and correct for the residual over- or undersubtraction of the sky background to reach surface brightness sensitivities of $\mu_r \sim 29.5$ mag arcsec^{-2}. These Sky Objects are identified by the HSC data reduction pipeline (see Section 6.6.8 of Aihara et al. 2019) to be locations in which no objects are detected. Sky Object photometry is measured in apertures ranging from 20 arcsec to 118 arcsec in diameter.

We estimate the residual background around our dwarf sample by taking the mean flux in sky objects in the vicinity of our sample, as is done by Li et al. 2020, in prep for their more massive galaxy sample. We expect that the sky around our dwarf galaxies will be better estimated than the sky around the low-z massive galaxy for two reasons. First, our sample is characterized by nearly exponential profiles (Sérsic indices close to $n = 1$), meaning that their surface brightness profiles drop more steeply with distance than do the higher n massive galaxies in Li et al. 2020, in prep. Second, the massive galaxies are much more physically extended than our sample, and thus appear larger on-sky at fixed redshift.

Indeed, we find that the background around our galaxies tends to be slightly undersubtracted to a similar degree as the intermediate-redshift sample of Li et al. 2020, in prep. In Figure 4.13 we show the estimate of the sky background as a function of Sky Object aperture size for Sky

Objects within 100 arcsec (green) and 200 arcsec (purple) of our target galaxies. For context, we reiterate that the maximum distance at which we measure profiles is 84 arcsec. We note that the two largest Sky Objects (of size 84 arcsec and 118 arcsec) are as large or larger than the extent over which we measure 1D profiles. Sky Objects with increasingly large apertures are more likely to include contributions from background objects; The increase in the background level as a function of aperture size can be partially attributed to this effect. Regardless, we find that in all cases the additive background residual is $\lesssim 0.004$ counts per pixel. This corresponds to a change in surface brightness of $\lesssim 0.02$ mag arcsec^{-2} for an object with surface brightness 28.5 mag arcsec^{-2}. The impact of the sky residual is small down to our nominal surface brightness limit of 28.5 mag arcsec^{-2}.

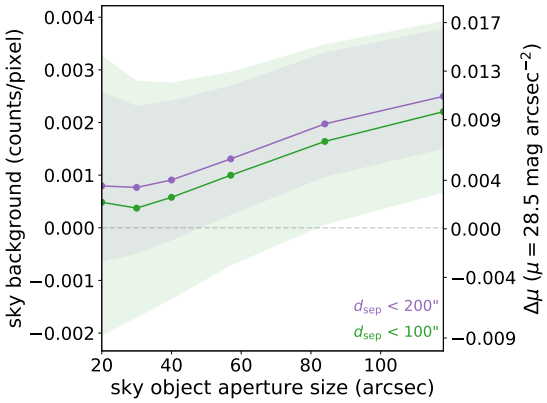

Figure 4.13 The residual sky in the HSC-i band near our sample as measured from nearby Sky Objects in the vicinity of our target galaxies. The sky background is measured as a function of Sky Object aperture size for Sky Objects within 100" (green, 43149 Sky Objects) and 200" (purple, 172974 Sky Objects) of our target galaxy sample. At left, we give the sky background in counts/pixel. At right, we show the change in surface brightness expected for an object with surface brightness 28.5 mag arcsec^{-2}. The solid curves show the median sky residual, while the shaded regions show the 25th and 75th percentiles. We find that the residual background has a negligible impact ($\lesssim 0.02$ mag arcsec^{-2}) on the surface brightness measured at our nominal surface brightness limit of 28.5 mag arcsec^{-2}.

Table 4.1. Maximum a Posteriori Estimates and 1σ Standard Deviations of Inferred Parameters

Figure	Selection	R	μ_B	μ_C	σ_B	μ_C
Figure 4.9	$[10^{9.0}, 10^{9.6}]M_\odot$	$1R_{\rm eff}$	0.84 ± 0.01	0.30 ± 0.01	0.09 ± 0.01	0.11 ± 0.01
		$2R_{\rm eff}$	0.93 ± 0.02	0.35 ± 0.02	0.04 ± 0.02	0.15 ± 0.02
		$3R_{\rm eff}$	0.94 ± 0.01	0.43 ± 0.01	0.05 ± 0.01	0.14 ± 0.01
		$4R_{\rm eff}$	0.82 ± 0.04	0.56 ± 0.02	0.21 ± 0.02	0.19 ± 0.03
	$[10^{8.5}, 10^{9.0}]M_\odot$	$1R_{\rm eff}$	0.75 ± 0.03	0.47 ± 0.03	0.02 ± 0.04	0.19 ± 0.02
		$2R_{\rm eff}$	0.79 ± 0.03	0.46 ± 0.03	0.05 ± 0.04	0.20 ± 0.05
		$3R_{\rm eff}$	0.81 ± 0.05	0.47 ± 0.03	0.18 ± 0.03	0.17 ± 0.03
		$4R_{\rm eff}$	0.80 ± 0.10	0.44 ± 0.04	0.30 ± 0.06	0.10 ± 0.05
	$[10^{7.0}, 10^{8.5}]M_\odot$	$1R_{\rm eff}$	0.86 ± 0.02	0.32 ± 0.02	0.02 ± 0.02	0.11 ± 0.02
		$2R_{\rm eff}$	0.91 ± 0.03	0.38 ± 0.02	0.05 ± 0.02	0.17 ± 0.02
		$3R_{\rm eff}$	0.93 ± 0.06	0.41 ± 0.02	0.06 ± 0.05	0.11 ± 0.04
		$4R_{\rm eff}$	0.79 ± 0.07	0.50 ± 0.03	0.27 ± 0.03	0.18 ± 0.03
Figure 4.10	$(g-i) < 0.90$	$1R_{\rm eff}$	0.84 ± 0.01	0.30 ± 0.01	0.08 ± 0.01	0.10 ± 0.01
		$2R_{\rm eff}$	0.90 ± 0.02	0.34 ± 0.01	0.02 ± 0.02	0.14 ± 0.02
		$3R_{\rm eff}$	0.94 ± 0.04	0.42 ± 0.01	0.04 ± 0.03	0.12 ± 0.02
		$4R_{\rm eff}$	0.77 ± 0.04	0.54 ± 0.02	0.26 ± 0.02	0.20 ± 0.02
	$(g-i) > 0.90$	$1R_{\rm eff}$	0.93 ± 0.03	0.40 ± 0.02	0.01 ± 0.03	0.17 ± 0.03
		$2R_{\rm eff}$	0.89 ± 0.05	0.43 ± 0.03	0.07 ± 0.04	0.17 ± 0.04
		$3R_{\rm eff}$	0.96 ± 0.07	0.46 ± 0.04	0.04 ± 0.05	0.12 ± 0.06
Figure 4.11	$d_{\rm NN} > 1$Mpc	$1R_{\rm eff}$	0.89 ± 0.01	0.29 ± 0.01	0.04 ± 0.01	0.08 ± 0.01
		$2R_{\rm eff}$	0.90 ± 0.02	0.35 ± 0.01	0.05 ± 0.02	0.11 ± 0.02
		$3R_{\rm eff}$	0.93 ± 0.03	0.39 ± 0.01	0.05 ± 0.02	0.13 ± 0.02

Table 4.1 (cont'd)

Figure	Selection	R	μ_B	μ_C	σ_B	μ_C
		$4R_{\rm eff}$	0.85 ± 0.05	0.48 ± 0.03	0.23 ± 0.02	0.20 ± 0.03
	$d_{\rm NN} \leq 1$Mpc	$1R_{\rm eff}$	0.86 ± 0.03	0.36 ± 0.02	0.04 ± 0.02	0.17 ± 0.02
		$2R_{\rm eff}$	0.91 ± 0.03	0.40 ± 0.02	0.06 ± 0.02	0.16 ± 0.02
		$3R_{\rm eff}$	0.95 ± 0.06	0.44 ± 0.03	0.04 ± 0.05	0.14 ± 0.04
		$4R_{\rm eff}$	0.76 ± 0.04	0.59 ± 0.04	0.25 ± 0.04	0.17 ± 0.04

Note. — For inferred parameters associated with Figure 4.10 and Figure 4.11, only galaxies with stellar masses $> 10^{8.5} M_{\odot}$ are considered.

4.9 Appendix: Tabulation of Inferred Parameters

For ease of comparison to future studies, in Table 4.1 we provide the maximum a posteriori estimates and 1σ standard deviations of the intrinsic shape parameters inferred for the samples presented in Figure 4.9, Figure 4.10, and Figure 4.11. In each row, we list the figure, sample selection criterion, and measurement radius associated with the inferred parameters.

4.10 Appendix: Allowing for Shape-Size Covariance

For a sample of galaxies at higher stellar mass and redshift, Zhang et al. [2019] showed that the inferred 3D shape distribution changes significantly when allowing a non-zero covariance between galaxy size and ellipticity.

To test whether this model is necessary for our sample of dwarfs, we fit a multivariate normal described by $\vec{\alpha} = \{\mu_A, \mu_B, \mu_C, \sigma_{AA}, \sigma_{BB}, \sigma_{CC}, \sigma_{AC}\}$[6]. As in Zhang et al. [2019], we only allow for a non-zero covariance between A and C. In order to understand whether the ($R_{\rm eff}$, b/a) data demand a non-zero shape-size covariance, we initiate walkers normally distributed about the best-fit values inferred for the fiducial models. For each parameter X, initial values for the walkers are drawn from a normal distribution $\mathcal{N}(\tilde{X}, 0.25\tilde{X})$ where $\tilde{X}$ is the best-fit value from the fiducial model.

[6]here, A is in kpc, whereas B and C are defined as normalized lengths relative to A

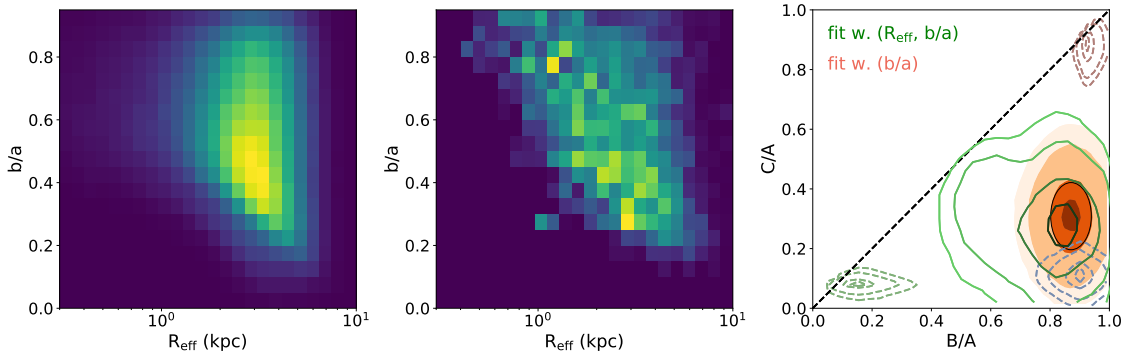

Figure 4.14 *Left:* the distribution of effective radius and projected axis ratio for a sample drawn from the posterior distribution for a model where we allow for a non-zero covariance between C/A and R_{eff}. *Middle:* the distribution over R_{eff} and projected axis ratio (b/a) for the observed galaxies. *Right:* the inferred distribution over intrinsic axis ratios for the fiducial model (orange filled contours) and the model at left (green unfilled contours).

The results of this test are shown in Figure 4.14. Though the data are well-described by a slightly negative shape-size covariance $\sigma_{AC} \sim -0.16$, we find that this model yields a small shift towards lower B/A, and a negligible shift in C/A. Therefore, because the model of [Zhang et al., 2019] adds three additional degrees of freedom to the model (μ_A, σ_A, and σ_{AC}), we choose to fit the marginalized b/a distribution, rather than (R_{eff},b/a).

4.11 Appendix: Parameter Recovery and Sample Size

As sample size decreases, the precision of our inferred model parameters $\vec{\alpha} = \{\mu_B, \mu_C, \sigma_B, \sigma_C\}$ decreases in kind. In Figure 4.15, we show the distribution of intrinsic axis ratios inferred for a sample of N={100,200,1500,2500} galaxies. We find that at N$\sim$ 200 galaxies, though μ_B and μ_C are well-recovered, σ_B and σ_C are increasingly overestimated[7]. We thus choose to only consider subsets of galaxies where N$>$ 700.

[7]We note that σ_B and σ_C are always overestimated when $\sigma_B = \sigma_C = 0$ due to the uncertainty in measuring 1D surface brightness profiles

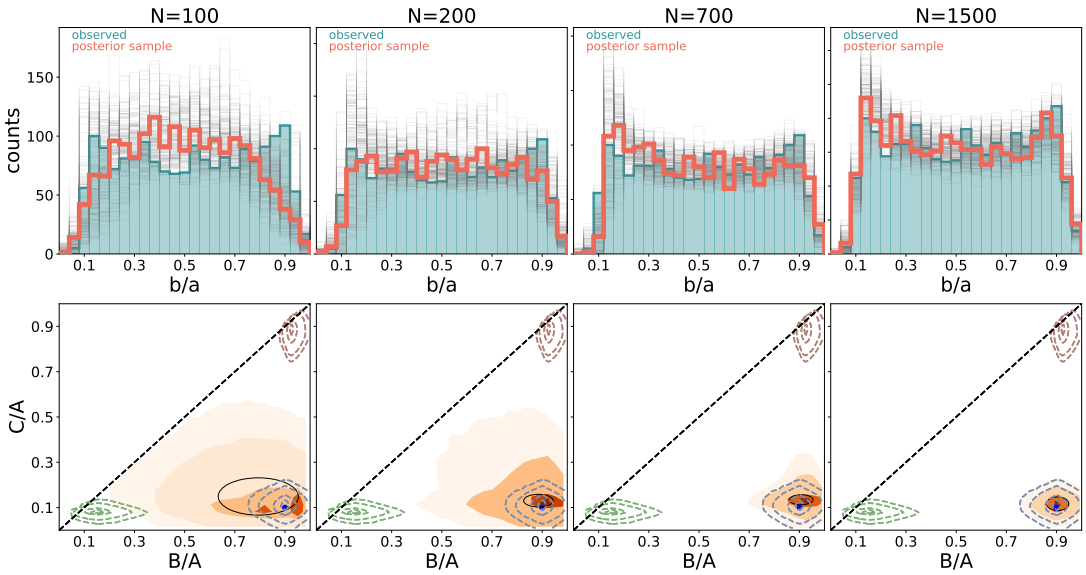

Figure 4.15 For a population of mock disk galaxies described by $\vec{\alpha} = \{\mu_B, \mu_C, \sigma_B, \sigma_C\} = \{0.9, 0.1, 0., 0.\}$, we investigate the precision at which the model parameters $\vec{\alpha}$ may be recovered as a function of sample size N. The top row shows, in each panel, the true distribution of the projected axis ratio b/a in teal and the posterior sample in orange. Individual draws from the posterior are shown in grey. The bottom row shows the distribution of intrinsic axis ratios (B/A and C/A) from the posterior sample in orange. The maximum a posteriori estimate is shown by the black ellipse. The pure disk, prolate, and spheroidal populations are shown by dashed contours (see Figure 4.7). A successful recovery is one in which the orange contours of the posterior samples coincides with the dashed blue contours of the pure disk population.

Chapter 5

Three-Dimensional Structure of Low Surface Brightness Galaxies

5.1 Introduction

Low surface brightness galaxies, or LSBGs, are an observationally defined galaxy population characterized by a low average surface brightness and large on-sky sizes [e.g. $\langle\mu\rangle_{\mathrm{R_{eff}}} > 24.3$ mag arcsec^{-2} and $\mathrm{R_{eff}} > 2.5''$ Greco et al., 2018c, Tanoglidis et al., 2021, though specific surface brightness and size cuts vary]; ultra-diffuse galaxies (UDGs) are LSBGs with large physical effective radii [e.g. $\mathrm{R_{eff}} > 1.5$ kpc, van Dokkum et al., 2015, – UDG identification thus requires a distance measurement]. The origin and physical properties of this extreme tail of the dwarf population is still a matter of debate – the formation path of low surface brightness galaxies (LSBGs) and their relationship with the general galaxy population has been a topic of sustained interest since their discovery [Sandage and Binggeli, 1984, McGaugh et al., 1995, Dalcanton et al., 1997].

Present day simulations have proposed several pathways for the formation of LSBGs and UDGs. It has been proposed that UDGs populate the high-spin tail of dwarf-mass dark matter halos [Amorisco and Loeb, 2016, Rong et al., 2017, Liao et al., 2019], are formed via vigorous star

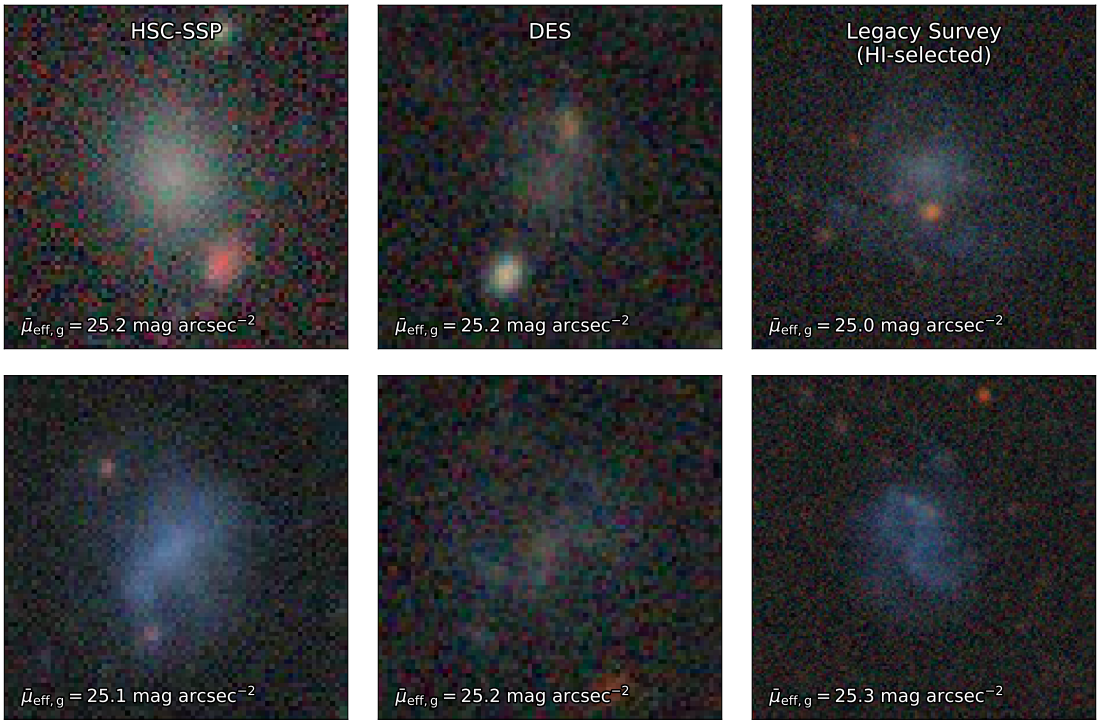

Figure 5.1 Example grz RGB cutouts from the three imaging sets considered in this work. The top row shows an example from the red end of the sample ($(g-r) > \langle(g-r)\rangle_{75}$, where $\langle\rangle_{XX}$ indicates the XXth percentile), while the bottom shows an example from the blue end ($(g-r) < \langle(g-r)\rangle_{25}$). Note that because the Legacy Survey UDG sample was originally selected to have HI, the red end of the distribution is still relatively blue in absolute terms. Each example in the figure is chosen to have approximately the same mean effective g-band surface brightness of $\langle\mu\rangle_{\mathrm{R_{eff}}} \sim 25$ mag arcsec^{-2}. The cutouts of the HSC and DES imaging are 20" on a side, while the Legacy Survey cutout is 40" on a side. The galaxies shown for each sample are (top panel, bottom panel): HSC (LSBG-325, LSBG-211), DES (ID224789651, ID214498053), and Legacy (AGC114754, AGC336397).

formation feedback and outflows [Di Cintio et al., 2017, Chan et al., 2018, Jiang et al., 2019], are formed via effects induced by high-density environments [Jiang et al., 2019, Tremmel et al., 2020] or are the product of early major mergers which trigger the radial migration of star formation [Wright et al., 2021]. Given the significant array of formation scenarios for this class of galaxies, it is of interest to identify observable quantities which may discriminate between the proposed formation mechanisms.

The current generation of deep wide-field surveys have enabled a new generation of systematic studies of thousands of LSBGs over a range of environments [Danieli et al., 2018, Greco et al., 2018c, Tanoglidis et al., 2021]. However, due to the uncertainty in the distances of LSBG samples, much of the work on the inherent physical properties of these low surface brightness galaxies has been focused on the UDG populations in groups and clusters wherein the cluster distance may be assumed [van Dokkum et al., 2015, Martínez-Delgado et al., 2016, van der Burg et al., 2016, Yagi et al., 2016, Lee et al., 2017, Román and Trujillo, 2017, Danieli and van Dokkum, 2019, Mancera Piña et al., 2019a, Román et al., 2019, Rong et al., 2020, Zaritsky et al., 2019, Barbosa et al., 2020, Prole et al., 2021].

The intrinsic, three-dimensional shapes of galaxies provide key insights into the formation and evolution of galaxy structure [see, e.g. Padilla and Strauss, 2008, Sánchez-Janssen et al., 2010, Costantin et al., 2018, Méndez-Abreu et al., 2018, Kado-Fong et al., 2020b, Carlsten et al., 2021]. Indeed, the morphology and intrinsic shape distribution of LSBGs are key properties that may be explored, even when individual distances are not known. For "normal" high surface brightness galaxies, the three-dimensional shape of a galaxy population changes starkly as a function of both mass and color, producing the familiar color-morphology bimodality [see, e.g. Padilla and Strauss, 2008]. In the dwarf mass regime, there is evidence for a transition in stellar intrinsic shape from thick disk to oblate spheroid as a function of stellar mass [Sánchez-Janssen et al., 2010, Kado-Fong et al., 2020b]. Studies in nearby groups and clusters suggest that UDGs in high density environments are generally oblate spheroids, though the impact of the environment itself is difficult to ascertain without an analogous sample in less crowded environments. How the structure of the general LSBG population relates to that of high surface brightness galaxies remains largely unexplored.

In this work we combine three LSBG samples to infer the distribution of three-dimensional shapes of the wide-field selected LSBG population: the sample of Tanoglidis et al. [2021] detected from the Dark Energy Survey (DES), the sample of Greco et al. [2018c] detected from the Hyper Suprime-Cam Subaru Strategic Program (HSC-SSP), and the HI-selected sample of Janowiecki et al. [2019] selected from the Arecibo Legacy Fast ALFA (ALFALFA) survey and reprocessed using Legacy Survey imaging. These three samples provide complementary views of the LSBG

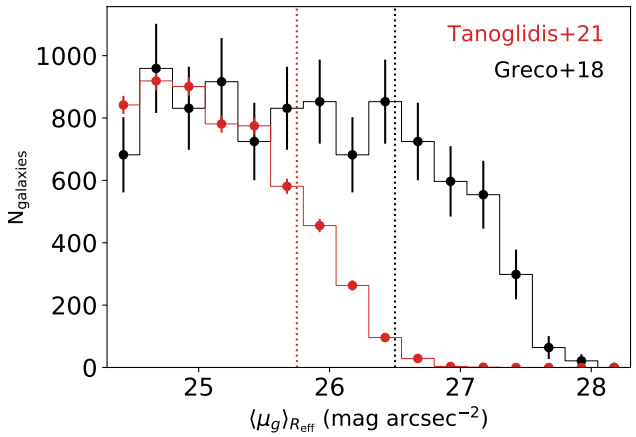

Figure 5.2 Surface brightness distributions of the red ($(g-i) > 0.64$) galaxies in the DES [Tanoglidis et al., 2021, red] and HSC-SSP [Greco et al., 2018c, , black] LSBG samples. The $\langle\mu\rangle_{\mathrm{R_{eff}}} = 26.5$ mag arcsec^{-2} 80% completeness limit for the HSC-SSP LSBG sample (Greco et al., in preparation) is shown by the dotted black vertical line. We empirically measure the completeness limit of the DES sample as the $\langle\mu\rangle_{\mathrm{R_{eff}}}$ at which the surface brightness distribution diverges from that of the deeper HSC-SSP sample.

population. The DES and HSC-SSP samples are constructed using very similar methods, and while the DES sample includes a larger number of galaxies, the HSC-SSP sample is drawn from deeper imaging data. The HI-selected sample, meanwhile, is selected using a markedly different approach and has associated distances to each object. In Section 5.2 we detail the samples, as well as the collation and homogenization of the DES and HSC-SSP samples, In Section 5.3, we extend the methodology of Kado-Fong et al. [2020b] to include the effect of intrinsic shape on both ellipticity and surface brightness and provide an overview of the inference machinery used to determine the three-dimensional shape distribution. We present our main findings for the samples and for color subsets of the DES sample in Section 5.4, and contextualize our findings with previous observational and theoretical work in Section 5.5. Throughout this paper we adopt a standard flat ΛCDM model in which $\mathrm{H_0} = 70$ km s^{-1} Mpc^{-1} and $\Omega_m = 0.3$.

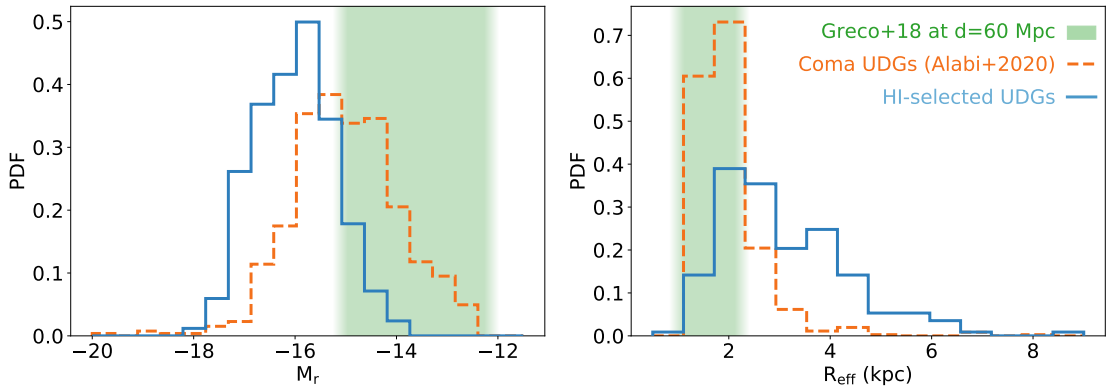

Figure 5.3 We compare the distribution in absolute r-band magnitude and physical effective radius for the samples examined in this work. We show in green a contextualization of the Greco et al. [2018c] HSC-SSP LSBG sample M_r and effective radius distribution as computed by assuming that all galaxies in the LSBG sample are at the cross-correlation median distance of 60 Mpc (Greco et al., in prep.). We show the same quantities computed for the HI-selected sample using the HI redshifts measured by Leisman et al. [2017] and Janowiecki et al. [2019] by the unfilled blue histogram. Finally, we show the Coma Cluster UDGs of Alabi et al. [2020] by the unfilled orange histogram (dashed lines). Though the DES sample is not shown in this figure, we expect that the DES sample is similar in mass and size to the HSC sample.

5.2 Sample Construction

In this work we use the LSBG catalogs created by Tanoglidis et al. [2021] and Greco et al. [2018c]. These catalogs are created using very similar methods, though the surface brightness limit of the DES imaging is significantly brighter than the deeper HSC-SSP imaging. We additionally re-analyse the galaxies of Janowiecki et al. [2019] using imaging from the eighth data release of the Legacy Survey [Dey et al., 2019], both in order to take advantage of the deeper Legacy Survey imaging and to process the HI-selected sample using a method consistent with that of Greco et al. [2018c] and Tanoglidis et al. [2021]. In Figure 5.1 we show examples cutouts from each imaging set used in this work. Examples are drawn to span the range of colors represented by the sample, and are chosen to have approximately the same mean effective surface brightness.

For all surface brightnesses in this work we refer to the mean surface brightness within one

circularized effective radius, i.e.

$$\langle\mu\rangle_{\mathrm{R_{eff,circ}}} = \mathrm{m}(< \mathrm{R_{eff,circ}}) - 2.5\log_{10}(\pi \mathrm{R_{eff}^2}), \tag{5.1}$$

as derived from single Sérsic fits, where $\mathrm{R_{eff,circ}}$ referes to the circularized effective radius ($\mathrm{R_{eff,circ}} = a\sqrt{b/a}$, where a and b are the observed semi-major and semi-minor axes, respectively).

5.2.1 The HSC-SSP Sample

The Hyper Suprime-Cam Subaru Strategic Program, hereafter HSC-SSP, is an ongoing widefield survey conducted on the 8.2 m Subaru Hyper Suprime-Cam set to cover around 1400 square degrees to a 5σ point source depth of $\mathrm{g_{HSC}} = 26.6$ mag with a seeing of 0.77" [Aihara et al., 2019]. The exceptional depth and coverage of this survey make it a powerful tool for the discovery of low surface brightness structures [see, e.g. Greco et al., 2018c, Huang et al., 2018d, Kado-Fong et al., 2018, Wang et al., 2019, Kado-Fong et al., 2020a]. In this work, we use the catalog of 781 LSBGs found by Greco et al. [2018c] in the first ~ 200 deg^2 of the survey.

This LSBG sample was constructed using a specialized pipeline detailed in Greco et al. [2018c]; for the reader's convenience, we summarize the main points of the method here. The main aim of the pipeline is to detect contiguous and extended low surface brightness sources. There are two main contaminants to this goal: low surface brightness structures associated with bright galaxies (i.e. tidal features or extended stellar halos), and faint background galaxies. To remove the former, an iterative thresholding is applied wherein objects with at least 15% of their pixels elevated above 28σ over the global background are discarded from the sample. To remove the latter, each detection is required to contain at least 100 contiguous pixels. Single component Sérsic models are then fit to each remaining source using the software imfit[1] [Erwin, 2015] and visually inspected. This visual inspection removes spurious detections due to low surface brightness contaminants; these are most typically galactic cirrus, tidal features from massive galaxies, and wings of bright stars. Finally, each galaxy is required to have an effective radius of $\mathrm{R_{eff}} > 2.5$ arcsec, a $\mathrm{g_{HSC}}$-band mean effective

[1] https://github.com/perwin/imfit

surface brightness (measured within the circularized effective radius) of $24.3 < \langle\mu\rangle_{\mathrm{R_{eff}}} < 28.8$ mag arcsec^{-2}, and an ellipticity ($\epsilon = 1 - \mathrm{b/a}$, where b/a is the ratio of the semi-minor to semi-major axis) of $\epsilon < 0.7$.

The selection function of the Greco et al. [2018c] sample has been explored in detail [Greco, 2018, chapter 5] via the injection of mock LSBGs (characterized by single Sérsic profiles) into HSC-SSP imaging. These mock galaxies are processed through the same HSCPipe [Bosch et al., 2018] data reduction pipeline that was employed for the reduction of the imaging used for the Greco et al. [2018c] analysis. These tests in particular explore detection efficiency as a function of angular size, surface brightness, and Sérsic index. They find that the detection efficiency of the Greco et al. [2018c] pipeline as a function of surface brightness is largely independent of angular size, though at surface brightnesses below the 80% completeness limit ($\mu_{\mathrm{eff}} = 26.5$ mag arcsec^{-2}), detection efficiency is higher for galaxies with larger angular sizes. Similarly, detection efficiency as a function of angular size is independent of Sérsic index for galaxies with angular sizes greater than $\mathrm{R_{eff}} \gtrsim 4$". Detection efficiency is higher for low Sérsic indices below this angular size. We thus conclude that for the purpose of our work, which does not focus on galaxies below this 80% completeness limit, the dependence of detection efficiency on size and Sérsic index should not greatly affect our results. Indeed, we have performed the analysis detailed in this work using both the full [Greco et al., 2018c] sample and a surface brightness limited sample ($\langle\mu\rangle_{\mathrm{R_{eff}}} < 26.5$ mag arcsec^{-2}), and find that our results do not change at statistically significant levels.

5.2.2 The DES Sample

Though the depth of HSC-SSP allows for the discovery of very faint LSBGs, the restricted area of the Greco et al. [2018c] catalog makes the 3D shape inversion problem intractable for subsets of the catalog sample. To overcome this limitation, we will also utilize a sample of 20,977 LSBGs selected from ~ 5000 deg^2 in the first three years of the Dark Energy Survey (hereafter DES). The published version of Tanoglidis et al. [2021] contains 23,790 LSBGs with a mean effective surface brightness cut of $\langle\mu\rangle_{\mathrm{R_{eff}}} > 24.2$ mag arcsec^{-2}. We use an earlier version of the catalog with a mean effective surface brightness cut of $\langle\mu\rangle_{\mathrm{R_{eff}}} > 24.3$ mag arcsec^{-2}, consistent with Greco et al. [2018c],

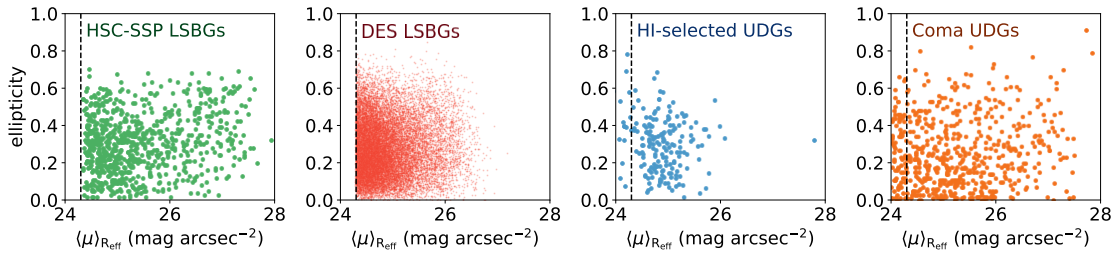

Figure 5.4 Ellipticity versus surface brightness for the four samples considered in this work, as labeled. We use these diagnostic plots to demonstrate that the distribution of ellipticity does not change over the range of surface brightnesses considered in this work, supporting our assumption that the full sample can be characterized by a single distribution in three-dimensional shape, and to visually illustrate the different depths of the four samples.

as measured by SExtractor. Both versions of the catalog have been made publicly available by the DES team[2].

The sample construction of the Tanoglidis et al. [2021] sample is, by design, quite similar to that of the Greco et al. [2018c] sample. However, there are a number of significant differences, which we will enumerate here for convenience. First, the DES sample selection was performed on the DES Y3 Gold coadd object catalog (v2.2; Sevilla-Noarbe et al. 2020, in preparation). Second, they employed a support vector machine (SVM) classifier trained from an initial visual classification in order to remove contaminant objects. Remaining false positives were then removed via visual inspection. Like the Greco et al. [2018c] sample, this visual inspection removes common low surface brightness contaminants from the final sample. Finally, the size and average surface brightness cuts were made on the SExtractor measurements, not on the single component Sérsic model fits.

Though a direct measurement of the completeness of this catalog has not yet been made, we can make an empirical estimate using the surface brightness distribution of the Greco et al. [2018c] sample, which is drawn from a deeper survey, as a benchmark. In particular, the surface brightness distribution of the red ($g - i > 0.64$) LSBGs in the Greco et al. [2018c] sample is consistent with being flat down to their 80% completeness limit in surface brightness. We therefore estimate the 80% completeness limit of the DES LSBG sample to be at the point where the surface brightness

[2] `https://des.ncsa.illinois.edu/releases/other/y3-lsbg`

distribution of red galaxies in the DES sample diverges significantly from that of the HSC-SSP sample. Because the surface brightness completeness of the HSC sample has been extensively tested via mock injections, we base our completeness estimate of the DES sample on the divergence in surface brightness limit from the HSC sample. The red LSBG surface brightness distribution for the two samples are shown in Figure 5.2; using this approach, we find a completeness limit of $\langle\mu\rangle_{\mathrm{R_{eff}}} \sim 25.75$ mag arcsec^{-2} for the DES LSBG sample.

Though the initial LSBG sample of Tanoglidis et al. [2021] is based on surface brightnesses measured with SExtractor, the final sample selection is made using surface brightness measurements from galfit.

5.2.3 The ALFALFA/Legacy Sample

Finally, we include in our analysis the HI-selected UDG sample of Janowiecki et al. [2019]. The sample is an environment-blind sample originally selected UDGs in HI from the ALFALFA survey [Giovanelli et al., 2005, Haynes et al., 2011] and measured the optical properties of the associated galaxies using imaging from the Sloan Digital Sky Survey [SDSS, York et al., 2000] using the same methods as Leisman et al. [2017], who selected an analogous sample of isolated HI-bearing UDGs. Because of the relatively shallow depth of SDSS, Leisman et al. [2017] and Janowiecki et al. [2019] assumed an exponential surface brightness distribution and an ellipticity of $\epsilon = 0$. For this work, we use imaging from the deeper Legacy Survey [Dey et al., 2019, point source 5σ limiting magnitude of g = 24] for the 188 galaxies in the Janowiecki et al. [2019] sample covered by Legacy Survey imaging to model the surface brightness distributions as single Sérsic functions where the Sérsic index and ellipticity are allowed to vary.

Using the $\mathrm{R_{eff}}$ measurements provided by Janowiecki et al. [2019], we obtained centered cutouts of the galaxies from the Legacy survey's Data Release 8 of size $20\mathrm{R_{eff}}$ on a side. The Sérsic fits were carried out using the same methodology as Greco et al. [2018c], as summarized in Section 5.2.1, though we used sep [Barbary, 2016] to obtain the initial object segmentations maps. Due to the irregularity of the galaxies and large amount of interfering background sources and/or bright star formation knots, ∼40% of the object masks were manually adjusted. Measurements from sep were

also used to provide initial size and ellipticity guesses to imfit. The new measurements made for this paper will made be public in a forthcoming work (Petrescu, M. et al. in prep.).

5.2.4 The Coma Cluster Sample

In order to expand the range of environments probed in this study, we further include the Coma cluster sample of Alabi et al. [2020], who construct a catalog of Coma Cluster galaxies with a specific focus on extending the set of known LSBGs in the Coma Cluster. They perform an initial selection using SEXtractor and refine the sample via visual inspection and structural parameter inference via GALFIT. We use the catalog measurements of Alabi et al. [2020] for this analysis, and thus caution that the methods used for the structural measurements of this sample differ significantly than those used for the HSC-SSP, DES, and HI-selected samples, which are all based on the methodology of Greco et al. [2018c]. We provide an abbreviated description of the catalog construction method of Alabi et al. [2020] for completeness. First, they perform an initial object detection using SEXtractor to remove stars and compact (FWHM$\lesssim$ 0.5 kpc) objects. Next, they use a cut in the R-band magnitude-surface brightness plane to identify a sample of galaxies to model. All the remaining galaxies are modelled with one-component Sérsic profiles using GALFIT [Peng et al., 2010]. Finally, the Sérsic fits are evaluated, and they remove high ($n > 2$) Sérsic index galaxies that are redder than 1σ from the red sequence at the distance of Coma. We use the structural parameters measured from a single Sérsic fit to the Subaru SuprimeCam R band data of Alabi et al. [2020]. We consider only galaxies in the catalog that are UDGs, with effective radii exceeding 1.5 kpc and mean effective surface brightnesses fainter than 24 mag arcsec^{-2}.

5.2.5 Physical and Observed Properties of the Samples

As this work centers around the analysis of three similarly processed but heterogeneously selected samples, it is informative to compare the physical and observed properties of the three samples. As the derivation of many physical properties hinges on a measure of galaxy distance, we first address existing redshift measurements for the samples.

A forthcoming analysis of the HSC-SSP catalog estimates a median source distance of $\sim$60 Mpc

(Greco et al., in preparation); we adopt this value in this analysis. We show the soft boundaries of the absolute r-band magnitude and effective radius distributions over the LSBG sample if we assume a fixed distance of 60 Mpc in blue with Figure 5.3. We show the analogous metrics for the Coma cluster UDG sample of Alabi et al. [2020] by the orange dashed histogram. We stress that the sample range over these physical properties is provided only to contextualize the general nature of the sample, and should not be interpreted as estimates of the absolute magnitude or effective radius of the LSBGs. This approach will not, for example, populate the tails of the absolute magnitude and effective radius distribution. We note that even if all galaxies were assumed to be at a distance of 100 Mpc, the median absolute r-band magnitude would still be $\langle M_r \rangle = -14.8$ ($\langle M_r \rangle = -13.7$ at d = 60 Mpc).

We do not have a distance estimate for the Tanoglidis et al. [2021] sample; because the sample selection is modeled after that of Greco et al. [2018c], we assume that the distribution over absolute magnitude and effective radius is similar. Due to the difference in the surface brightness limits of DES and HSC-SSP (see Figure 5.2), this assumption is likely incorrect in the details, but should hold as an order of magnitude estimate.

Finally, due to the initial HI selection of the ALFALFA/Legacy sample, HI redshifts have been measured for each galaxy; details of these meaurements can be found in Leisman et al. [2017] and Janowiecki et al. [2019]. The r-band absolute magnitude and effective radius distributions for the HI-selected sample are shown in Figure 5.3 by unfilled orange histograms. We find that the HI-selected sample tends to be more luminous and larger than both the HSC and Yagi et al. [2016] samples. This is likely because the HI selection was sensitive only to the most massive HI disks, as well as because the selection employed a more stringent physical size requirement than that of Greco et al. [2018c] (when assuming the median source distance of d = 60 Mpc). We also note that the HI-selected sample is significantly more distant than the HSC sample, which is consistent with the HI-selected sample being more luminous.

In Figure 5.4, we show the distribution of mean effective surface brightness versus ellipticity for the four samples considered in this work. These panels show first that there is no global trend in ellipticity as a function of surface brightness, supporting the assumption that each sample can be

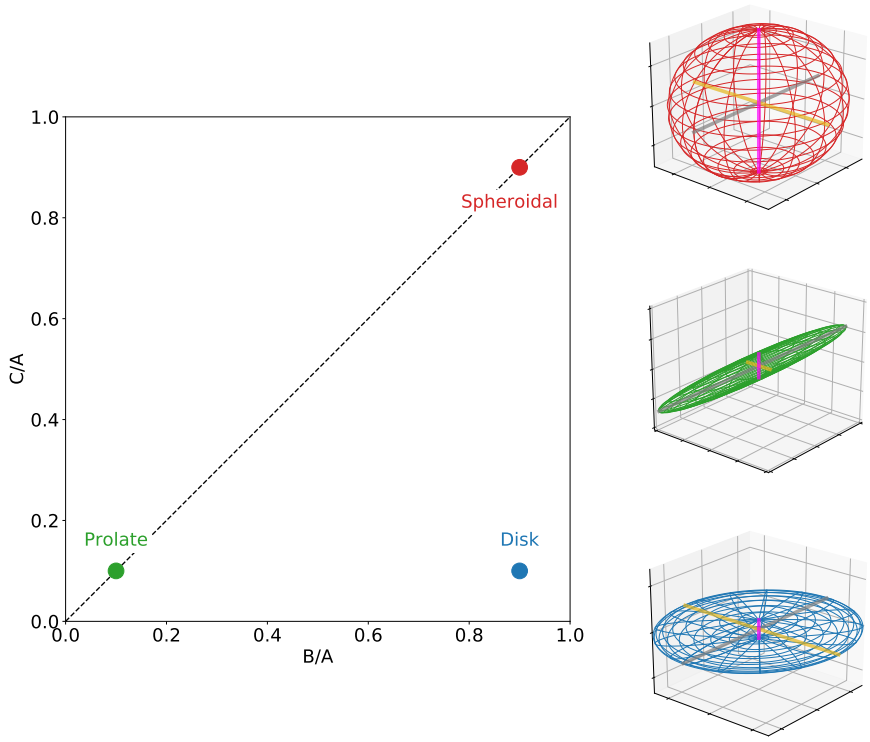

Figure 5.5 A schematic diagram to illustrate movement in the B/A vs. C/A plane. The red, green, and blue points show the position of an archetypal spheroidal, prolate, and disky ellipsoid, respectively. The axis ratios are $(B/A,C/A) = (0.9,0.9)$, $(0.1,0.1)$, and $(0.9, 0.1)$ for the three cases. At right, we show a three-dimensional representation of the ellipsoid that corresponds to each case in the corresponding color. We additionally show the principal axes A, B, and C as grey, gold, and magenta lines in each panel.

characterized by a singular unified distribution over three-dimensional shape. Indeed, the covariance between the surface brightness and ellipticity within our surface brightness limits is minimal or consistent with zero for all four samples: $\mathrm{Cov}(\langle\mu\rangle_{\mathrm{R_{eff}}}, \epsilon)_{\mathrm{HSC}} = 2.80^{+3.06}_{-3.37} \times 10^{-3}$ mag arcsec^{-2}, $\mathrm{Cov}(\langle\mu\rangle_{\mathrm{R_{eff}}}, \epsilon)_{\mathrm{DES}} = -1.10^{+0.35}_{-0.34} \times 10^{-3}$ mag arcsec^{-2}, $\mathrm{Cov}(\langle\mu\rangle_{\mathrm{R_{eff}}}, \epsilon)_{\mathrm{HI}} = -2.74^{+3.65}_{-3.77} \times 10^{-3}$ mag arcsec^{-2}, and $\mathrm{Cov}(\langle\mu\rangle_{\mathrm{R_{eff}}}, \epsilon)_{\mathrm{Coma}} = 1.32^{+0.70}_{-0.69} \times 10^{-2}$ mag arcsec^{-2}.

We note that the r band photometry of the HSC sample is from the HSC r band, the photometry of the Yagi et al. [2016] sample is from the Suprime R band, and the photometry of the HI sample is from the Legacy Survey r band. To gauge the effect of the differences between these bands,

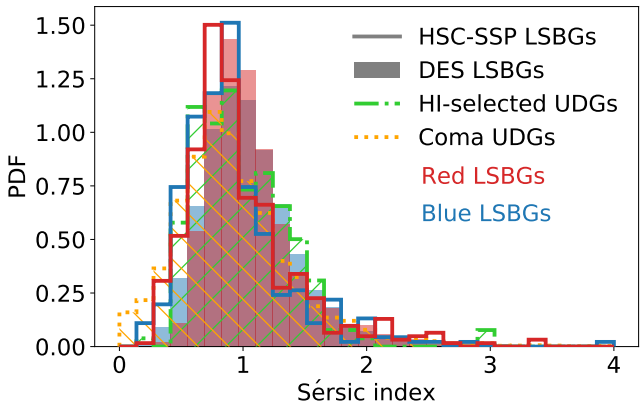

Figure 5.6 The distribution of Sérsic indices for the red ($g-i>0.64$) and blue ($g-i<0.64$) HSC LSBGs [Greco et al., 2018c, filled histograms] and DES LSBGs [Tanoglidis et al., 2021, unfilled histograms]. Though there is a an offset between the HSC and DES measurements, there is no significant difference between the red and blue subsets of each sample. We also show the HI-selected (dot-dashed green) and Coma (dotted orange) UDGs, which are also consistent with the LSBG distribution of Sérsic indices.

we compute synthetic photometry through each bandpass for a set of model dwarf spectra taken from dwarfs in the catalog of Muzzin et al. [2013]. We find that the difference between the bands is minimal, with an average difference between the HSC and Suprime r bands of $(\langle\Delta m\rangle, \sigma_{\Delta m}) = 0.00 \pm 0.03$ and an average difference between the HSC and DECam r bands of $(\langle\Delta m\rangle, \sigma_{\Delta m}) = -0.01 \pm 0.04$.

5.3 Intrinsic Shape Inference

The distribution of intrinsic shapes may be inferred from the observed ellipticity distribution of a galaxy population by assuming that the galaxies can, at fixed radius, be described by ellipsoids with semi-principal axis diameters A, B, and C where C $\leq$ B $\leq$ A. In Figure 5.5, we show the positions in B/A-C/A space and 3D renderings of three archetypical examples: a disk (blue), prolate (green), and spheroid (red). We also assume that the LSBG samples can be described by a single multivariate normal distribution over the principal axis ratios B/A and C/A. This method

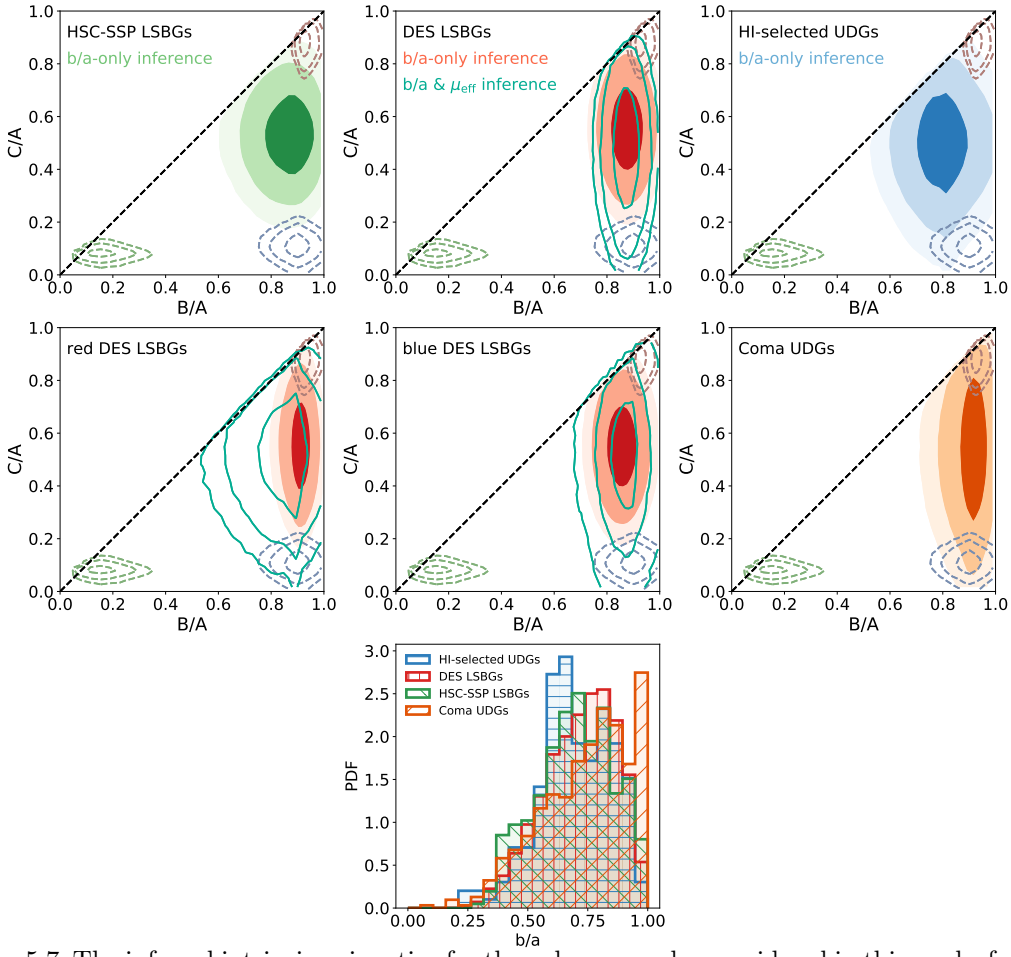

Figure 5.7 The inferred intrinsic axis ratios for the galaxy samples considered in this work: from the top left, the HSC-SSP, the DES sample, the HI-selected galaxies, the red galaxies of the DES sample ($g-i<0.64$), the blue galaxies of the DES sample ($g-i\geq 0.64$), and the Coma UDGs. The filled contours show the inference results when only ellipticity is fit, while the unfilled turquoise contours in the DES panels show the inference results when both surface brightness and ellipticity are fit. The unfilled dashed contours show the results of recovery tests for a disky (blue), prolate (green), and spheroidal (red) population via ellipticity-only inference. The bottom panel shows the distribution over projected axis ratio (b/a $= 1-\epsilon$) for each sample. There is no signficant difference between the inferred shapes of the joint models and ellipticity-only models, indicating that incompleteness due to surface brightness limits does not induce a significant bias in the observed ellipticity distributions of the LSBGs.

is detailed in Kado-Fong et al. [2020b]; we summarize the salient points below.

The projected axis ratio, $q=$ b/a where b and a are respectively the semi-minor and semi-major

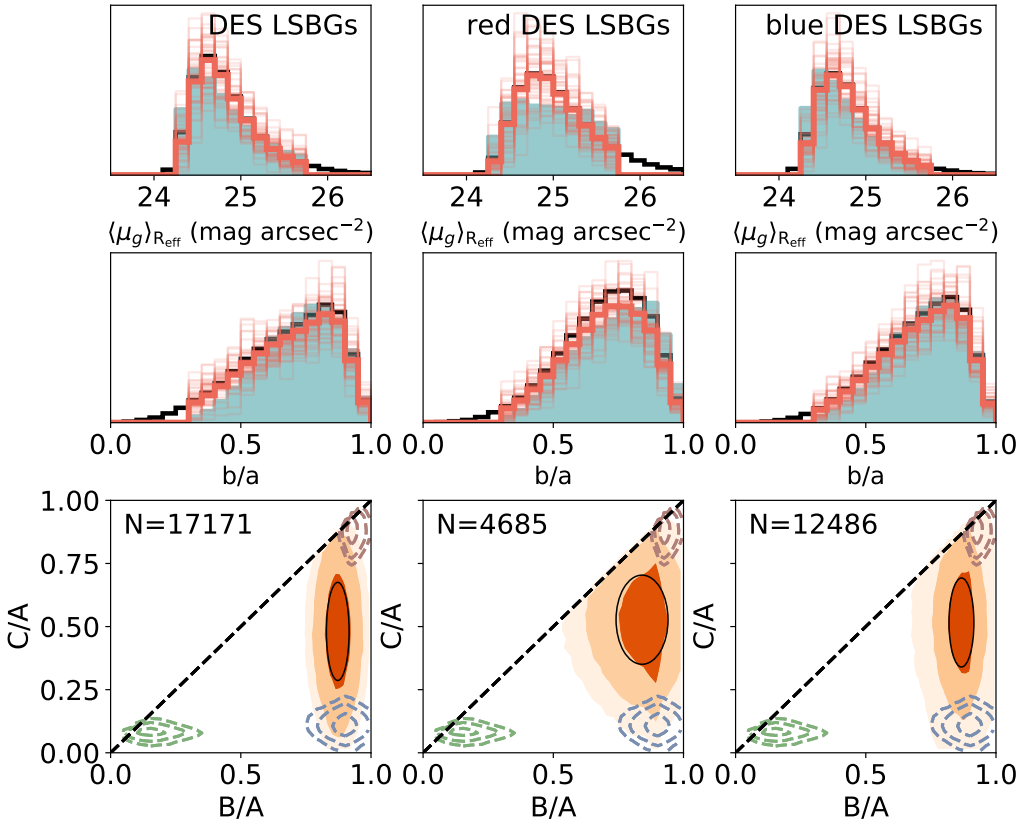

Figure 5.8 Recovery results for joint inference of the samples; from left to right: the full DES sample, red DES LSBGs, and blue DES LSBGs. *Top row:* The surface brightness distribution for each population. The thick orange curve shows our posterior sample (thin orange curves show individual pulls from the posterior). The solid teal histograms show the observed population. Unfilled black histograms show model projections which fall outside of the sample surface brightness limits. *Middle row:* the same for the ellipticity distributions. *Bottom row:* we show the intrinsic axis ratio distribution of the posterior sample as filled orange contours. The maximum a posteriori results are shown by black ellipses. We note that the joint inference does not converge for the HSC-SSP and HI-selected samples due to the low number of objects; we thus use only the ellipticity-only inference for these samples.

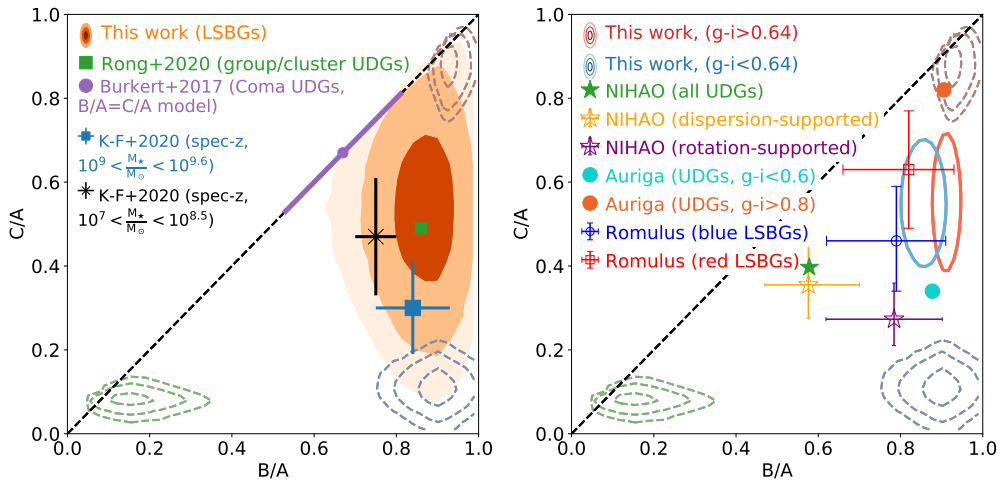

Figure 5.9 *Left:* A comparison between the results presented in this work (filled orange contours) and observational results from the literature. Our results are in good agreement with the group/cluster UDG samples of Burkert [2017] (who assumes a non-triaxial model where B/A=C/A) and Rong et al. [2020], indicating that the intrinsic shape distribution of LSBGs is not strongly affected by their environment. We also compare our results to those of the "normal" high surface brightness dwarf populations at $1R_{\rm eff}$ presented in Kado-Fong et al. [2020b]. We find that the LSBG sample is significantly rounder (higher C/A) than the massive dwarfs of Kado-Fong et al. [2020b]. Errorbars on the HSB points show the inferred 1σ dispersion of the HSB sample, not the error on the mean values. *Right:* A comparison between the inferred intrinsic shapes of red and blue LSBGs (unfilled red and blue contours, respectively) presented in this work and theoretical predictions from the literature. For visual clarity, we show only the contours that contain 68% of our inferred LSBG shapes in order to be consistent to the plotted errorbars of the Romulus and NIHAO simulations, for which the errorbars span the $16^{\rm th}$ to $84^{\rm th}$ percentiles. We find that the intrinsic shape distributions vary significantly between the simulations considered. In particular, Auriga [Liao et al., 2019] predicts a strong shape divergence between blue and red UDGs, while NIHAO [Jiang et al., 2019, Cardona-Barrero et al., 2020] predicts significantly more triaxial (for dispersion-dominated UDGs) or flatter (for rotation-supported UDGs) shapes than those inferred from observed LSBGs. Romulus appears to well-produce the shape distribution of blue LSBGs, but overpredicts the shape evolution between blue and red LSBGs.

axes of the projected ellipse, for a given ellipsoid is determined solely by the observer's viewing angle, (θ, ϕ), i.e. $\mathrm{q} = \mathcal{F}(\mathrm{B/A}, \mathrm{C/A}, \theta, \phi)$. The analytic expression for $\mathcal{F}$ was presented by Simonneau et al.

[1998], and is reproduced below. First, $(ab)^2$ and $(a^2 + b^2)$ can be rewritten as follows:

$$a^2b^2 = f^2 = (C\sin\theta\cos\phi)^2 + (BC\sin\theta\sin\phi)^2 + (B\cos\theta)^2, \tag{5.2}$$

$$a^2 + b^2 = g = \cos^2\phi + \cos^2\theta\sin^2\phi + B^2(\sin^2\phi + \cos^2\theta\cos^2\phi) + (C\sin\theta)^2 \tag{5.3}$$

We now define the quantity h to be

$$h \equiv \sqrt{\frac{g-2f}{g+2f}}, \tag{5.4}$$

such that it may be shown that

$$\frac{b}{a} = \frac{1-h}{1+h} \tag{5.5}$$

Because the distribution of viewing angles is known to be isotropic on the surface of the sphere, we can predict the projected distribution of q given a choice of intrinsic shape distribution characterized by $\vec{\alpha}$ by sampling ϕ and θ as follows:

$$\begin{aligned} \phi &\sim \mathcal{U}[0, 2\pi] \\ \nu &\sim \mathcal{U}[0, 1] \\ \theta &= \cos^{-1}(2\nu - 1) \end{aligned} \tag{5.6}$$

However, we must also consider the bias imposed by surface brightness selection inherent in the selection method of LSBG samples. To create a low surface brightness galaxy sample, one must necessarily make a cut in surface brightness. Because galaxies are three-dimensional objects, it is possible that some galaxies will be considered "low surface brightness" only at certain viewing angles. This effect is maximized for disky (C < B $\sim$ A) galaxies, wherein the observed surface brightness will be systematically lower for face-on views than for edge-on views. An attempt to

invert the 3D shape of such a sample without accounting for this potential incompleteness could then result in severely biased results.

If one assumes that the LSBGs are well-described by a Sérsic profile with $n = 1$, the observed surface brightness of an object as a function of viewing angle is exactly prescribed by the intrinsic shape of the object and its intrinsic stellar density. We find that this assumption is well-supported by the data (see Figure 5.6), and adopt a fixed profile with $n = 1$ for this work. We neglect the effect of dust on the observed shape in this framework – due to the low masses, large effective radii, and low surface densities of the objects in question, it is unlikely that dust will significantly impact the observed shape at $1\mathrm{R_{eff}}$. With these assumptions in hand, by including additional parameters to describe the distribution of intrinsic density of the LSBGs, we can take into account this potential surface brightness incompleteness when inferring the intrinsic 3D shapes of the LSBG samples.

To do so, we compute the projected surface brightness within $\mathrm{R_{eff}}$ for a given choice of shape (B/A,C/A), viewing angle (θ, ϕ) and intrinsic density ρ_0. We find that using three-dimensional $\mathrm{R_{eff,3D}}$ (as opposed to the projected $\mathrm{R_{eff}}$) does not strongly affect our results, and considerably reduces computation time, so choose to use the three-dimensional $\mathrm{R_{eff,3D}}$ in this calculation. We first compute the three-dimensional density using the analytic approximation for the three-dimensional Sérsic density profile of Prugniel and Simien [1997]:

$$\rho(\frac{r}{\mathrm{R_{eff,3D}}}) = \rho_0(\frac{r}{\mathrm{R_{eff,3D}}})^{-p_n} \exp[-b_n(\frac{r}{\mathrm{R_{eff,3D}}})^{1/n}] \tag{5.7}$$

where

$$p_n = 1 - \frac{0.549}{n} + \frac{0.055}{n^2} \tag{5.8}$$

and $\Gamma(2n) = 2\gamma(2n, b_n)$. We rotate this grid to align with the line of sight defined by (θ, ϕ) using the rotation matrix

$$\mathbb{A} = \begin{bmatrix} \cos\phi & \cos\theta\sin\phi & \sin\theta\sin\phi \\ -\sin\phi & \cos\theta\cos\phi & \sin\theta\cos\phi \\ 0 & -\sin\theta & \cos\theta \end{bmatrix}$$

such that the rotated coordinates $\vec{r}_r = \mathbb{A}\vec{r}$ align with the line of sight along the $\vec{z}$ axis. We

then measure the mean surface brightness within $1R_{\mathrm{eff},3D}$. To reduce computation time, we pre-compute the surface brightness as a function of shape (B/A, C/A) and viewing angle (θ, ϕ), sampling uniformly over parameter space in a grid of size 30^4. We then linearly interpolate over this grid during inference; we find that our results are not significantly affected by the adoption of this approximation scheme.

In order to jointly fit the ellipticity and mean surface brightness distribution of our galaxy samples, we modify the Poisson likelihood used in Kado-Fong et al. [2020b] to include the surface brightness distribution:

$$\begin{aligned} \ln p(\vec{q}_{\mathrm{obs}}, \langle\vec{\mu}\rangle_{\mathrm{R_{eff},obs}}|\vec{\alpha}) &= \sum_i n_i \ln m_i - m_i - \ln n_i! \\ \vec{\alpha} &= (\mathrm{Q}_0, \mathrm{S}_0, \mu_{\rho_0}, \sigma_{\mathrm{Q}_0}, \sigma_{\mathrm{S}_0}, \sigma_{\rho_0}) \end{aligned} \tag{5.9}$$

where $\mathrm{Q} = \mathrm{B/A}$ and $\mathrm{S} = \mathrm{C/A}$. In our notation, Q_0 and σ_{Q_0} (S_0 and σ_{S_0}) correspond to the mean and standard deviation of the axis ratio B/A (C/A) assuming a bivariate Gaussian as the functional form for the underlying intrinsic shape distribution. We find that the ellipticity distributions of our LSBG samples (as well as the high surface brightness dwarf samples of Kado-Fong et al. [2020b]) are able to be well-reproduced by the relatively simple bivariate Gaussian model. We thus do not consider more complex functional forms in this work, though we have explored a model that includes size-shape covariance in Kado-Fong et al. [2020b] and the effect of a bimodal ground truth distribution on our bivariate and unimodal Gaussian modeling in an upcoming work (Kado-Fong et al., submitted). The observed count in bins of axis ratio is given as n_i, and m_i is the predicted count in the same range. We do not consider draws that lie outside of the observable boundaries ($\epsilon > 0.7$ for the HSC and DES samples or below the surface brightness limit) – that is, the imposed absence of high surface brightness or low q sources does not impact the likelihood computation. We adopt axis ratio bins of $dq = 0.05$ and mean surface brightness bins of $d\langle\mu\rangle_{\mathrm{R_{eff}}} = 0.5$ for all inferences in this work[3].

We use the Markov Chain Monte Carlo ensemble sampler implemented in emcee [Foreman-

[3]We previously found in Kado-Fong et al. [2020b] that the choice of bin size does not strongly affect inference results

Mackey et al., 2013] to sample efficiently from the posterior $\ln p(\vec{\alpha}, \vec{q}_{\rm obs}, \langle\vec{\mu}\rangle_{\rm R_{eff},obs})$. We implement a flat prior over the physical range of all our fitted parameters; that is:

$$p(\mathrm{Q}_0) = \begin{cases} 1 & \text{if} \quad 0 < \mathrm{Q}_0 < 1 \\ 0 & \text{otherwise} \end{cases} \tag{5.10}$$

We additionally constrain $\mathrm{S}_0 \leq \mathrm{Q}_0$ to maintain the order of axes,

$$p(\mathrm{S}_0) = \begin{cases} 1 & \text{if} \quad (0 < \mathrm{S}_0 < 1) \wedge (\mathrm{S}_0 \leq \mathrm{Q}_0) \\ 0 & \text{otherwise,} \end{cases} \tag{5.11}$$

When sampling from a given α, we disregard ellipsoids where $C > B$. We only require that the mean surface brightness is a positive value, i.e.

$$p(\rho_0) = \begin{cases} 1 & \text{if} \quad \mu_{\rho_0} > 0 \\ 0 & \text{otherwise.} \end{cases} \tag{5.12}$$

Similarly, we require the standard deviations of B/A and C/A are a positive value less than $\sigma = 0.5$:

$$p(\sigma_X) = \begin{cases} 1 & \text{if} \quad 0 < \sigma_X < 0.5 \\ 0 & \text{otherwise} \end{cases} \tag{5.13}$$

for $X \in \{B, C\}$. We only require σ_{ρ_0} to be positive:

$$p(\sigma_{\rho_0}) = \begin{cases} 1 & \text{if} \quad 0 < \sigma_{\rho_0} \\ 0 & \text{otherwise.} \end{cases} \tag{5.14}$$

We run all inferences for at least 500 steps over 32 walkers, and discard the first 250 steps of each walker. We manually confirm that the chains have converged. We also extend the mock recovery tests of Kado-Fong et al. [2020b] to include this joint inference scheme – we present the results of

Table 5.1. Median values and 95% credible intervals of inferred intrinsic shape parameters; ellipticity-only inference

Sample	Q_0 (B/A)	σ_{Q_0}	S_0 (C/A)	σ_{S_0}	T_0
HSC-SSP	$0.85^{+0.09}_{-0.07}$	$0.07^{+0.07}_{-0.07}$	$0.53^{+0.04}_{-0.04}$	$0.13^{+0.04}_{-0.03}$	$0.38^{+0.18}_{-0.24}$
DES	$0.88^{+0.01}_{-0.02}$	$0.05^{+0.02}_{-0.01}$	$0.55^{+0.01}_{-0.01}$	$0.14^{+0.01}_{-0.01}$	$0.34^{+0.07}_{-0.05}$
HI-selected	$0.80^{+0.10}_{-0.06}$	$0.09^{+0.05}_{-0.08}$	$0.50^{+0.08}_{-0.06}$	$0.16^{+0.14}_{-0.06}$	$0.50^{+0.14}_{-0.24}$
red DES	$0.91^{+0.03}_{-0.03}$	$0.03^{+0.02}_{-0.03}$	$0.55^{+0.02}_{-0.02}$	$0.14^{+0.01}_{-0.02}$	$0.25^{+0.08}_{-0.08}$
blue DES	$0.85^{+0.02}_{-0.03}$	$0.05^{+0.02}_{-0.02}$	$0.55^{+0.01}_{-0.01}$	$0.14^{+0.01}_{-0.01}$	$0.39^{+0.07}_{-0.06}$
Coma	$0.90^{+0.07}_{-0.07}$	$0.04^{+0.06}_{-0.04}$	$0.54^{+0.06}_{-0.06}$	$0.23^{+0.05}_{-0.05}$	$0.26^{+0.18}_{-0.18}$

Note. — In all cases, the first 250 steps of each walker are discarded. For ease of comparison with literature results, we also report T_0, the median triaxiality ($T = (1-(B/A)^2)/(1-(C/A)^2)$), as calculated by sampling the inferred shape distributions.

Table 5.2. Median values and 95% credible intervals of inferred intrinsic shape parameters; surface brightness and ellipticity inference

Sample	Q_0 (B/A)	σ_{Q_0}	S_0 (C/A)	σ_{S_0}	T_0	ρ_0	σ_{ρ_0}
DES	$0.87^{+0.02}_{-0.49}$	$0.05^{+0.03}_{-0.04}$	$0.48^{+0.04}_{-0.03}$	$0.19^{+0.02}_{-0.12}$	$0.31^{+0.10}_{-0.08}$	$0.67^{+0.11}_{-0.50}$	$0.40^{+0.05}_{-0.21}$
red DES	$0.83^{+0.06}_{-0.42}$	$0.11^{+0.11}_{-0.10}$	$0.53^{+0.45}_{-0.08}$	$0.17^{+0.05}_{-0.06}$	$0.43^{+0.26}_{-0.19}$	$0.20^{+0.10}_{-0.08}$	$0.50^{+0.08}_{-0.28}$
blue DES	$0.86^{+0.03}_{-0.05}$	$0.05^{+0.03}_{-0.03}$	$0.52^{+0.04}_{-0.04}$	$0.18^{+0.03}_{-0.05}$	$0.35^{+0.10}_{-0.09}$	$0.60^{+0.16}_{-0.21}$	$0.47^{+0.13}_{-0.08}$

Note. — The same as Table 5.3 for Figure 5.8. In all cases, the first 250 steps of each walker are discarded. For ease of comparison with literature results, we also report T_0, the median triaxiality ($T = (1-(B/A)^2)/(1-(C/A)^2)$), as calculated by sampling the inferred shape distributions.

these tests in Section 5.7. We find that the joint inference reduces the inference precision for the spheroid and prolate populations, where the surface brightness changes little with viewing angle, but increases the inference precision for the disk population, where the surface brightness changes strongly with viewing angle.

5.4 Results

We show the results of the intrinsic shape inference in Figure 5.7. From top left, we show the inference for the HSC-SSP LSBG sample of Greco et al. [2018c], the full DES sample of Tanoglidis et al. [2021], the HI-selected sample originally constructed by Leisman et al. [2017] and Janowiecki et al. [2019], the blue ($g - i < 0.64$) DES LSBGs, and the red ($g - i \geq 0.64$) DES LSBGs. For the DES sample and subsamples, we show the inference results when surface brightness and ellipticity are jointly fit (unfilled turquoise contours) and when only ellipticity is considered (filled orange histogram). We find that the joint fit does not converge for the HSC-SSP and HI-selected samples due to the relatively small sample sizes (a result that is expected based on the tests that we ran with mock galaxy populations, see Section 5.7 and Kado-Fong et al. 2020b); we thus only show the results of the ellipticity-only inference. In all cases, the joint maximum a posteriori (MAP) estimate and ellipticity-only MAP estimates are within very good agreement, indicating that the observed surface brightness cut does not significantly bias the observed ellipticity distribution. To rephrase this point, we find that because the intrinsic shapes of the LSBGs are relatively round, the observed surface brightness does not correlate strongly with the ellipticity. We additionally show the distribution of model surface brightnesses and ellipticities (along with their observational counterparts) for the DES samples in Figure 5.8. We find that the surface brightness distribution of the red LSBGs is not as well-fit in our inference – this likely indicates that the underlying surface brightness distribution is not well-described by a Gaussian. However, through tests with a uniform surface brightness distribution we find that our results are robust against a change in the assumed parametric form of the underlying surface brightness distribution. Furthermore, disky shapes are required to produce a strong correlation between surface brightness and ellipticity, and it is highly

unlikely based on previous studies of dwarfs [Sánchez-Janssen et al., 2010, Burkert, 2017, Rong et al., 2020, Kado-Fong et al., 2020b, Carlsten et al., 2021] and higher mass galaxies [see, e.g. Padilla and Strauss, 2008] that the red LSBGs would be diskier than the blue LSBGs. We present the maximum a posteriori estimates, along with associated uncertainties, for all inference results in Table 5.3.

Though the numbers of the HSC-SSP and HI-selected samples preclude a division as a function of galaxy color, we can use these samples to confirm that our method returns consistent results for both samples. For the HSC sample, this is a simple confidence check with a deeper sample – assuming that the shapes measured in DES are not significantly impacted by the depth of the imaging, the samples should return a consistent result, as they are selected using similar methods. The concordance of HI-selected UDG intrinsic shape distribution is somewhat more intriguing, as the sample is more luminous and selected to have significant stores of cold gas and is likely a more luminous sample (see Figure 5.3) – we defer a more complete discussion of this result to Section 5.5.1.

5.4.1 Intrinsic Shape versus Color and Environment

The correlated bimodality of morphology and color is a well-established facet of the galaxy population for massive galaxies [see, e.g. Padilla and Strauss, 2008] At dwarf masses, there is evidence that the bimodality persists in massive dwarfs [Kado-Fong et al., 2020b], with some evidence that the structural properties may begin to converge at lower masses [Carlsten et al., 2021]. Blue galaxies are typically also disk galaxies, while red galaxies are ellipticals. It is thus of interest to ask whether the same bimodality is observed in the DES LSBG sample (the HSC-SSP sample is not large enough to split into two samples).

As shown in Figure 5.7, we find no evidence for a significant difference in intrinsic shape distribution of the red and blue LSBGs of the DES sample. This result is not unexpected; as shown in Figure 5.6, the Sérsic index distribution of red and blue LSBGs are also remarkably similar for both the DES and HSC-SSP samples, as well as the HI-selected sample. This is in strong contrast to more massive galaxies, wherein the Sérsic index distributions are markedly different between the

red and blue galaxy populations.

We also find that the three-dimensional shapes of the UDGs are largely unchanged as a function of environment, as shown by contrasting the Coma UDGs (rightmost panel, second row in Figure 5.9) to the blue LSBGs and HI-selected galaxies, both of which are unlikely to be dominated by dwarfs in cluster environments. Indeed, this result is in agreement with previous measurements of cluster UDG shapes, as will be further discussed in Section 5.5.1.

5.5 Discussion

Although the existence of LSBGs has been known observationally for some time, the path through which this tail of the galaxy population is formed remains unclear. UDGs in the field have been proposed to form via a variety of processes, including that they may populate high spin halos [Dalcanton et al., 1997, Amorisco and Loeb, 2016, Liao et al., 2019], that they are formed via star formation feedback [Jiang et al., 2019, Chan et al., 2018], or that they are the end products of early mergers that cause star formation to migrate to large radii [Wright et al., 2021]. High density environments provide potential alternate pathways to UDG formation via environmental effects such as ram pressure stripping and tidal heating [Jiang et al., 2019, Tremmel et al., 2020]. Here, we consider the implications of the inferred intrinsic shapes of our LSBG samples both in conjunction with previous observational works and in comparison to contemporary theoretical predictions.

5.5.1 Comparison to Observations

We first compare our inferred LSBG shape distribution to results from the literature. We probe both the potential influence of environment by comparing to the inferences of cluster and group UDG shapes from Burkert [2017] and Rong et al. [2020] and the potential influence of surface density by comparing to the "normal" dwarf (meaning higher surface brightness) spectroscopic sample of Kado-Fong et al. [2020b], as shown in Figure 5.9.

We find remarkably good agreement between our results and those of Rong et al. [2020], who infer the shape distribution of UDGs in high density group and cluster environments. We also see

good agreement with the results of Burkert [2017], when it is considered that this work did not allow for triaxiality (i.e. enforced B/A=C/A). Though the environments of the DES and HSC-SSP samples are not known on the level of individual systems, the spatial distribution of the red and blue LSBGs of both samples suggest that the red LSBGs are more clustered than the blue LSBGs, which have a nearly homogeneous distribution on the sky [Greco et al., 2018c, Tanoglidis et al., 2021]. This indicates that red LSBGs are relatively more likely to live in high density environments, while blue LSBGs are relatively more likely to live in the field. We can thus say that, on average, the blue LSBGs live in lower density environments than the samples of Burkert [2017] and Rong et al. [2020]. Because these literature samples are focused on large groups and clusters, it is also likely the case that the typical red LSBG lives in a lower density environment than Burkert [2017] and Rong et al. [2020], but in a higher density environment than the typical blue LSBG. The concordance of shapes between all these samples then indicates that the local environment does not play a key role in determining the intrinsic shape of low surface brightness galaxies.

Next, we compare the results of the LSBG galaxy sample to those of the spectroscopic "normal" dwarf sample of Kado-Fong et al. [2020b]. These dwarfs are drawn from the Sloan Digital Sky Survey (SDSS) and Galaxy And Mass Assembly (GAMA) spectroscopic surveys. GAMA, the deeper of these surveys, has an effective surface brightness limit of $\mu_{\mathrm{r,eff}} \sim 24$ mag arcsec^{-2} [Baldry et al., 2012], meaning that the spectroscopic dwarf sample is nearly disjoint in surface brightness with the LSBG samples. Kado-Fong et al. [2020b] finds evidence that the intrinsic shape of dwarf galaxies changes as a function of mass – in particular, that dwarfs at $M_\star \lesssim 10^{8.5}$ are relatively more spheroidal than their higher mass analogs. To make a rough estimate of the stellar masses of our LSBG samples, we adopt a singular distance of 60 Mpc for the HSC-SSP sample (as informed by the cross-correlation analysis in Greco et al., in prep.), and estimate the mass-to-light ratio $(M/L)_i$ from the $(g-i)$ colors presented in Greco et al. [2018c] and the color relations of Bell et al. [2003]. We find that, for this rough approximation, the mean stellar mass of the HSC-SSP sample is roughly $\log(M_\star/M_\odot) \sim 7.5$. Our HSC and DES LSBG samples are thus most similar in stellar mass to the lowest mass bin of $7.5 < \log_{10}(\mathrm{M}_\star/\mathrm{M}_\odot) < 8.5$ in Kado-Fong et al. [2020b]. Indeed, we find that these low mass, high surface brightness dwarfs are relatively oblate and spheroidal, similar

to the LSBG samples However, despite being likely more luminous than the HSC and DES samples (see Figure 5.3), the HI-selected sample is also characterized by oblate spheroidal shapes. This is in contrast to the observed mass evolution of normal dwarfs, wherein the higher mass dwarfs maintain well-formed, albeit thick, disks. We thus suggest that the LSBGs may be thicker (in C/A) than the equivalent HSB galaxy sample – this effect is most distinct when considering that the more luminous HI-selected sample is also characterized by oblate spheroidal shapes. However, the incompleteness of the HSB sample at low ($M_\star \lesssim 10^8 M_\odot$) masses and the uncertainties in the stellar mass distribution of the HSC and DES samples suggest that more complete samples of HSB dwarfs, along with more distance determinations for LSBG dwarfs, are needed to secure this result.

Taken all together, the results presented in this work in conjunction with literature results from group/cluster UDGs and normal dwarfs shed new light onto the structure formation of LSBGs. First, the concordance of shapes between LSBGs as a function of environment implies that the formation mechanism of cluster and field LSBGs does not produce drastically different intrinsic shapes. Second, we suggest that LSBGs and UDGs may be rounder than their HSB counterparts, and possibly unable to support well-formed stellar disks where HSB dwarfs succeed in maintaining them.

5.5.2 Comparison to Simulations

Having contextualized our results with previous observational results from the literature, we now compare our findings to predictions from the UDG populations produced in cosmological simulations. There are several paths to UDG formation proposed by various simulations; we focus here on the Auriga simulation [Liao et al., 2019], the NIHAO simulation [Jiang et al., 2019], and the Romulus simulations [Tremmel et al., 2020, Wright et al., 2021].

The UDG formation path of the simulations differ significantly, and those differences manifest in the predicted intrinsic shape distribution of each simulation. The Auriga field UDGs form in high spin halos (see also Dalcanton et al. 1997, Amorisco and Loeb 2016 who also form UDGs in the high spin tail the halo population), while satellite UDGs form via a mixture of tidal effects and field UDG capture by massive halos. This results in a pronounced difference in the intrinsic shape

distributions of the red and blue UDGs, wherein the blue Auriga UDGs are thick disks (turquoise point, right panel of Figure 5.9) and the red Auriga UDGs are spheroidal (orange point). This shape contrast is in disagreement with our results, which do not point to a significant bimodality in shape as a function of color or a significant population of disky UDGs at any mass. Furthermore, our results indicate that the HI-selected LSBG sample is puffier (higher C/A) than the HSB sample of Kado-Fong et al. [2020b] at similar stellar masses – this finding is also at odds with the theory that LSBGs form in the high angular momentum tail of the halo distribution function.

The NIHAO simulations, meanwhile, predict that UDGs are formed in the field via supernovae feedback. These UDGs are characterized by particularly bursty star formation histories relative to the more compact galaxies in NIHAO [Di Cintio et al., 2017]. Satellite UDGs are formed from infalling field UDGs and created from tidal effects. Though Jiang et al. [2019] do not compute the intrinsic shape distributions of satellite and field (or red and blue) UDGs separately, they do report the overall mean intrinsic principal axis ratios. We find that the NIHAO results are significantly more triaxial than our observed results. This excessive triaxiality is also seen in a subset of the FIRE galaxies which are also characterized by particularly bursty star formation histories [Chan et al., 2018, Kado-Fong et al., in prep]. Cardona-Barrero et al. [2020] further analyze the shape distribution of the NIHAO UDGs as a function of their stellar kinematics. They find in particular that the rotationally supported UDGs are characterized by more oblate ($B/A_{\rm rotation} > B/A_{\rm dispersion}$) and flatter disks. We find that these rotationally supported UDGs are, on average, flatter than our observed LSBG and UDG samples, similar to those found in the Auriga simulations.

The formation mechanisms for UDGs in the Romulus simulations stand in contrast to those presented in NIHAO and Auriga. Since Romulus cannot resolve high-density star formation and thus large outflows in dwarfs, feedback cannot drive their formation. However, upcoming comparison work between the Romulus simulations and the Marvel-ous Dwarfs, a zoom suite that succeeds in forming cored dwarf profiles via feedback with a force resolution of 60 pc and a DM [stellar] mass resolution of 6650 $M_\odot$ [420 $M_\odot$] [Munshi et al., 2021], does indicate that the UDG shapes of Romulus and Marvel-ous are broadly consistent (Munshi et al., in prep.). Thus, we do not expect that the intrinsic shapes of the LSBGs in Romulus are simply an effect of resolution. The Romulus

simulations furthermore do not find halo spin as a primary mechanism for UDG formation, as is the case in Auriga.

Both Wright et al. [2021] and Tremmel et al. [2020] explore alternative formation mechanisms in isolation and in a cluster environment. In particular, Tremmel et al. [2020] suggest that cluster UDGs are formed primarily through the dual effects of passive fading following quenching via ram pressure after early cluster infall and size evolution in the cluster environment. In the field, Wright et al. [2021] find that Romulus UDGs are formed via early major mergers that redistribute star formation to larger radii. Van Nest, J. et al., in prep will explore the shape evolution of UDGs in comparison to dwarfs in Romulus. We select LSBGs from Romulus25 [Tremmel et al., 2017] and RomulusC [Tremmel et al., 2019] on their central surface brightness and effective radius in a method similar to that in Tremmel et al. [2020], Wright et al. [2021]. To best match the properties of the LSBG sample in this work, we impose a size cut of $R_{\rm eff} > 1$ kpc and a surface brightness cut of $\langle\mu\rangle_{\rm R_{eff}} > 24.3$ mag arcsec^{-2}. They are divided into blue and red populations based on their $g-i$ color using the same dividing value of $(g-i) = 0.64$ as the observational sample. The values shown in Figure 5.9 correspond to the median of each population with the error bars representing the 16th to 84th percentile ranges. Although the Romulus LSBGs show slightly more intrinsic shape evolution as a function of their $(g-i)$ color, both the red and blue simulated LSBG populations are in reasonable agreement with our observed samples. We expect that the color-shape evolution seen in Romulus is partially driven by resolution effects: dwarfs are overquenched in the cluster environment of RomulusC [Tremmel et al., 2017], leading to overly red colors and an over-representation of cluster LSBGs at the red end of the color distribution. We thus conclude that the Romulus LSBGs are in the best agreement with the inferred observational shapes out of the simulation results considered here. The intrinsic shapes of the blue LSBGs, whose formation path is not tied to being in a high-density environment, are in particularly good agreement with the inferred shapes of the observational samples, which also sample a wide range of environments.

5.6 Conclusions

In this work we have presented the first three-dimensional shape inference of the wide-field samples of LSBGs selected in DES, HSC-SSP, and ALFALFA. We find that all three samples are well-characterized by oblate spheroids, with minor principal axis ratios (C/A) significantly higher than the thick disks observed in high mass, high surface brightness dwarfs. We also find no significant difference in the shape distribution of red and blue LSBGs, an inference bolstered by the analogous concordance in the distribution of Sérsic indices over red and blue LSBGs.

Our inferred shape distributions are in good agreement with the shape distributions inferred for cluster UDGs [Burkert, 2017, Rong et al., 2020]. These results suggest that the intrinsic shapes of LSBGs are not greatly affected by their environments. We also find some evidence that LSBGs are unable to maintain stellar disks at stellar masses where normal, high surface brightness dwarfs regularly maintain thick disks. Intriguingly, we do note that there is evidence that these UDGs are still able to support gaseous disks [Mancera Piña et al., 2019b, 2020, Gault et al., 2021]. However, more work is needed to address both the mass incompleteness of HSB dwarf samples below $M_\star \sim 10^8 M_\odot$ and the large uncertainties in the distance estimate of the LSBG samples.

The different formation mechanisms proposed by cosmological simulations for UDGs and LSBGs manifest strongly in their intrinsic shape distributions. We find that our results are in some conflict with simulated UDGs that form in high spin halos and those that are puffed up through vigorous star formation feedback. However, we do find that our observed intrinsic shape distribution is in good agreement with simulated UDGs from the Romulus simulation suite, wherein field UDGs are formed by early major mergers that cause star formation to migrate outwards [Wright et al., 2021] and cluster UDGs are formed via environmental quenching and tidal heating [Tremmel et al., 2020].

These results show that intrinsic shape distributions are able to provide promising constraints on the formation path of the extreme low surface brightness end of the dwarf galaxy population. The results in this work suggest that the intrinsic shapes of the LSB and HSB galaxy populations may begin to converge at low masses. However, future observational efforts to contextualize the LSBG population face two substantial technical challenges: linking LSBG and HSB samples in

order to systematically characterize dwarf properties across the spectrum of surface brightnesses, and establishing distance measures to LSBGs in the field. Upcoming survey instruments (e.g. Rubin/LSST, PFS, DESI, WALLABY, SKA,) will provide the necessary sensitivity and survey power to make significant strides in the former. Work on the latter is an ongoing area of development (Greco, J. et al., in prep.), and will allow analyses such as the one presented in this work to provide a truly comprehensive view of the diversity in dwarf structure.

5.7 Appendix: Mock Recovery Tests

We extend the mock recovery tests of Kado-Fong et al. [2020b] to include the relation between surface brightness and intrinsic shape in our mock recovery tests. We implement this relation by computing the expected surface brightness of each synthetic population given the intrinsic shape and viewing angle of each mock galaxy. We do not impose surface brightness limits for these mock tests. Because the mock galaxies projected structural parameters are not remeasured from mock HSC imaging, the absolute value of the surface brightnesses in this test are not consequential to the results. Rather, the test is designed to evaluate our ability to recover the shape of the surface brightness distribution. In Figure 5.10 we show the inferred intrinsic shape distribution of the posterior sample, as well as the distribution of the model population in average surface brightness (top row) and ellipticity (middle row). We find that the joint inference, on average, makes the inference more uncertain. However, the inference actually becomes more precise for the disky mock population. This can be understood by considering that the correlation between surface brightness, ellipticity, and viewing angle is maximized for a disky object. The inference becomes more precise due to the additional information provided by this covariance. For the spheroidal and prolate populations, however, the surface brightness distributions are very narrow. Thus, although two extra parameters must now be fitted, the surface brightness provides relatively little extra information.

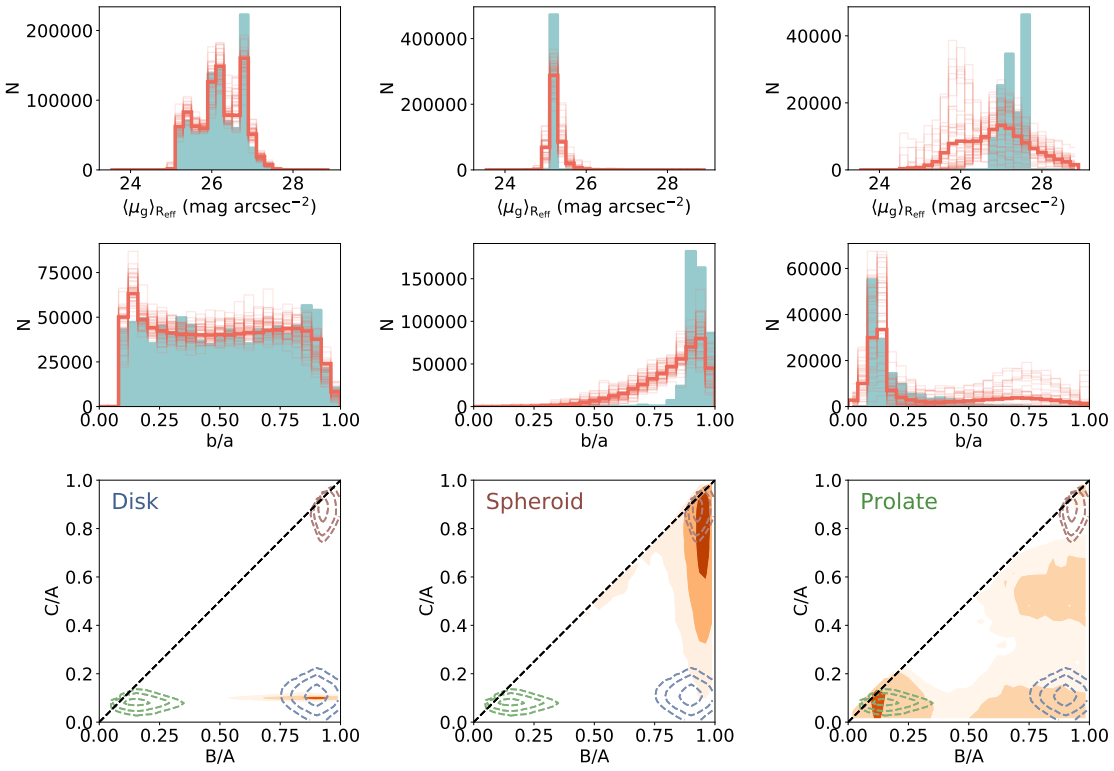

Figure 5.10 Recovery results for joint inference of the three extreme mock populations presented in Kado-Fong et al. [2020b]. Each column shows a different mock population; from left to right, we show the disk, spheroid, and prolate mock populations. *Top row:* The surface brightness distribution for each population. The thick orange curve show our posterior sample (thin orange curves show individual pulls from the posterior). The solid teal histograms show the observed population. *Middle row:* the same for the ellipticity distributions. *Bottom row:* we show the intrinsic axis ratio distribution of the posterior sample as filled orange contours. The analogous results from ellipticity-only inferences are shown by the dashed contours.

Chapter 6

Low-Mass Galaxy Shapes in the FIRE Simulations

6.1 Introduction

It has long been observed that dwarf galaxies host extended, round old stellar populations reminiscent in structure to the stellar halos of massive galaxies [Lin and Faber, 1983, Minniti and Zijlstra, 1996, Minniti et al., 1999, Zaritsky et al., 2000, Aparicio and Tikhonov, 2000, Aparicio et al., 2000, Hidalgo et al., 2003, Demers et al., 2006, Bernard et al., 2007, Stinson et al., 2009, Strader et al., 2012, Nidever et al., 2019, Pucha et al., 2019, Kado-Fong et al., 2020b]. Recently, it has been shown that high-mass dwarfs ($10^{8.5} < M_\star < 10^{9.6} M_\odot$) can form a thick stellar & HI disk [Roychowdhury et al., 2013, van der Wel et al., 2014, Nath Patra, 2020] in conjunction with a round stellar halo [Kado-Fong et al., 2020b].

In massive ($\mathrm{M}_\star > 10^{10}\mathrm{M}_\odot$) galaxies, stellar halos are thought to form primarily from the accretion of less massive satellite galaxies [see, e.g. Bullock and Johnston, 2005]. However, dwarf galaxies do not typically accrete enough stellar mass via minor mergers to form a stellar halo in the same way as their massive counterparts [Read et al., 2006, Purcell et al., 2007, Brook et al., 2014,

Anglés-Alcázar et al., 2017, Fitts et al., 2018], and major mergers are too rare to form dwarf stellar halos that are observable in wide-field imaging [Kado-Fong et al., 2020b]. Observed dwarf stellar halos also differ from massive stellar halos in that they host intermediate-age stellar populations [see, e.g., Zaritsky et al., 2000, Aparicio and Tikhonov, 2000, Aparicio et al., 2000, Hidalgo et al., 2003, Demers et al., 2006, Bernard et al., 2007, Stinson et al., 2009, Strader et al., 2012, Nidever et al., 2019, Pucha et al., 2019]. These observational results suggest that in-situ processes might be responsible for the apparent ubiquity of their round and old stellar outskirts. Mechanisms that have been proposed include the star formation-driven radial migration of stars [Stinson et al., 2009, El-Badry et al., 2016], and dynamical heating from interactions with dark subhalos [Starkenburg and Helmi, 2015, Starkenburg et al., 2016a]. Due to their shallow potential wells (relative to more massive galaxies), energy and momentum injected into the interstellar medium (ISM) from star formation feedback can drive galactic outflows that displace a significant fraction of gas to large radii, thus causing fluctuations in the gravitational potential. The effect on the distribution of dark matter by these baryon-driven fluctuations has been often cited as a potential resolution for the "core-cusp" problem [see, e.g. Navarro et al., 1996, Read and Gilmore, 2005, Pontzen and Governato, 2012, Chan et al., 2015], but the same effect has also been shown to induce stellar migration in previous studies. Notably, Stinson et al. [2009] named stellar radial migration as a potential formation pathway for stellar halos in dwarfs, and El-Badry et al. [2016] showed, using FIRE-1 simulations, that this radial migration operates most efficiently for dwarfs of stellar mass $M_\star \sim 10^9 M_\odot$. It is thus reasonable to say that a plausible formation pathway exists for in-situ stellar halo assembly at low masses ($M\star \lesssim 10^9 M_\odot$), and certainly that a mechanism to perturb star particles to large radii operates in the FIRE-2 simulations.

Observational studies also indicate that dwarf stellar halos may be primarily in-situ structures. First, observations of resolved stellar populations in the extended stellar outskirts of many local dwarfs galaxies show a population of both old and intermediate age stars [see Stinson et al., 2009, Vansevičius et al., 2004, Hargis et al., 2020, and references therein], in significant contrast to the ancient stellar halos of higher mass galaxies. This indicates that the movement of stars into the extended envelope is an ongoing process. Moreover, Kado-Fong et al. [2020b] show that,

for a sample of 5974 dwarf galaxies at $z \lesssim 0.15$, low-mass galaxies ($10^{8.5} < M_\star < 10^{9.6} M_\odot$) are generically rounder at larger radius regardless of environment. They further show that the majority of isolated dwarfs host thick disks near their centers, while red satellite dwarfs are more spheroidal (following the familiar color-morphology bimodality seen at higher masses). Because dwarfs do not typically accrete sufficient stellar mass to form an ex-situ stellar halo that would be detectable in current-generation widefield imaging [e.g. Purcell et al., 2007], both the dominance of this disk to halo structure in the isolated dwarf sample and the presence of spheroidal stellar outskirts regardless of environment suggest that the formation of low-mass stellar outskirts is a primarily in-situ process. Thus, in order to match observations, simulated dwarfs should have both a young stellar disk and an old, round stellar halo. This requirement is especially relevant for a stellar halo produced largely by star formation feedback, as under-regulated or over-active star formation feedback has been shown to be capable of disrupting the disk in dwarf galaxies [El-Badry et al., 2018b,c, Smith et al., 2020]. The requirement to match galaxy structure places a new constraint on the feedback physics implemented in simulations – there must be sufficient energy to heat the old stellar population, producing a round stellar halo, while simultaneously maintaining a young stellar disk.

The FIRE[1] project combines both the resolution needed to study the detailed structure of dwarf galaxies and the cosmological context necessary to understand the formation of that structure. In this work, we examine the three-dimensional stellar structure of a set of isolated dwarf galaxies ($10^8 \lesssim M_\star/M_\odot \lesssim 10^{10}$) in the FIRE-2 simulation suite [Hopkins et al., 2018]. We first determine whether or not the FIRE-2 simulations reproduce the disk-halo systems observed to be the dominant population in observations, and then we examine the origin of these stellar halos. In Section 6.2, we summarize the basic properties of the FIRE-2 simulations (Section 6.2.1) and our intrinsic shape measurement method (Section 6.2.2). We present our main findings in Section 6.3, then discuss those results in Section 6.4. In particular, a comparison of this study to previous theoretical works can be found in Section 6.4.1, while a discussion of the origin of stellar halos in the FIRE-2 dwarfs and the context of non-disky dwarfs is found in Section 6.4.2 and Section 6.4.3, respectively.

[1] `http://fire.northwestern.edu`

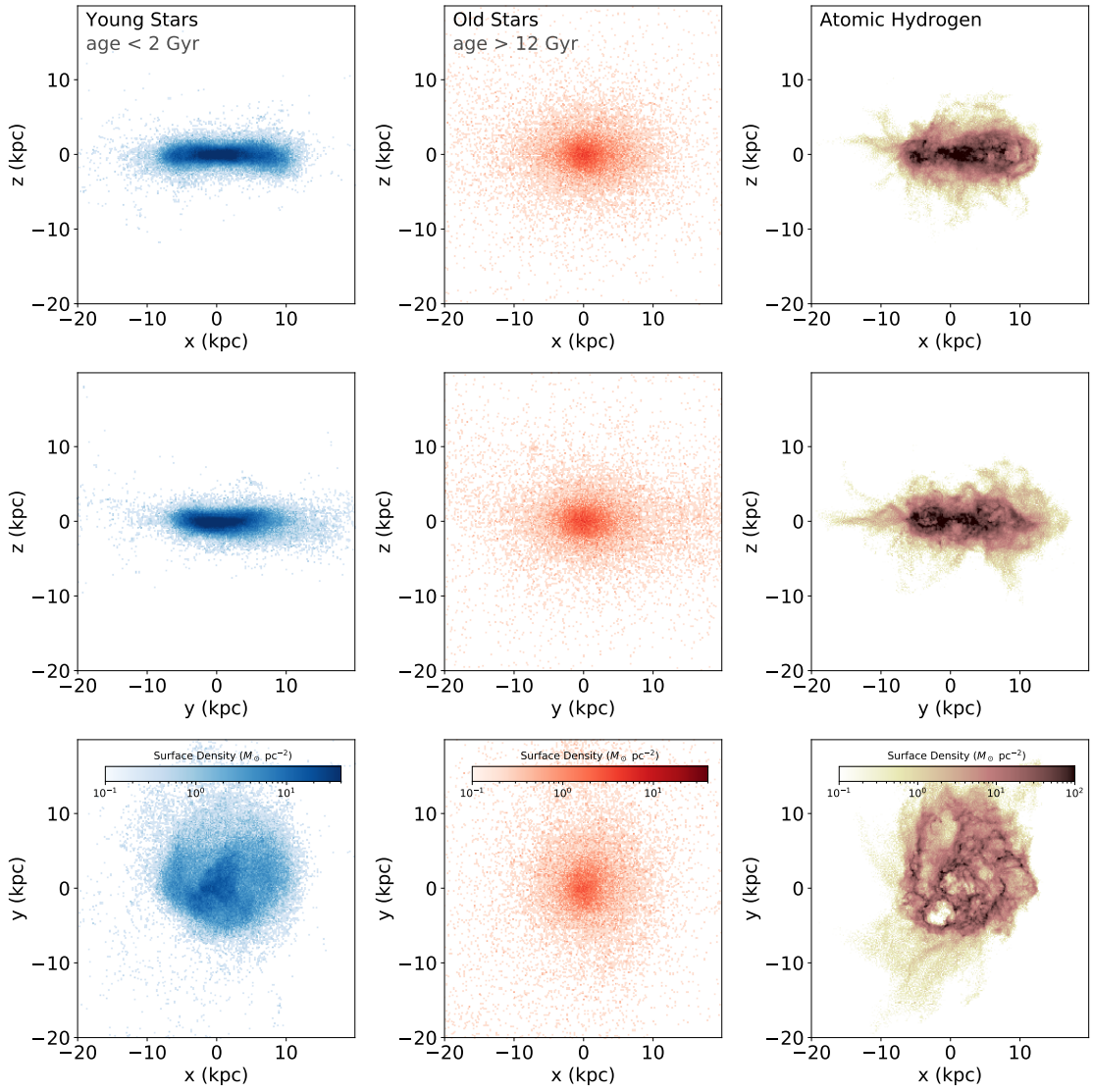

Figure 6.1 The surface density of young stars (left column, star particles with ages less than 2 Gyr), old stars (middle column, star particles with ages greater than 12 Gyr), and HI (right column) for an example dwarf with a disk-halo structure, m11h (MHD+). The rows show the projection along the y-axis, x-axis, and z-axis, such that the z-axis is aligned with the disk minor axis.

6.2 Methods

Here we give a brief overview of the FIRE-2 simulation suite and the sample of FIRE-2 galaxies included in this work. We then detail the method used to compute the intrinsic shape of the

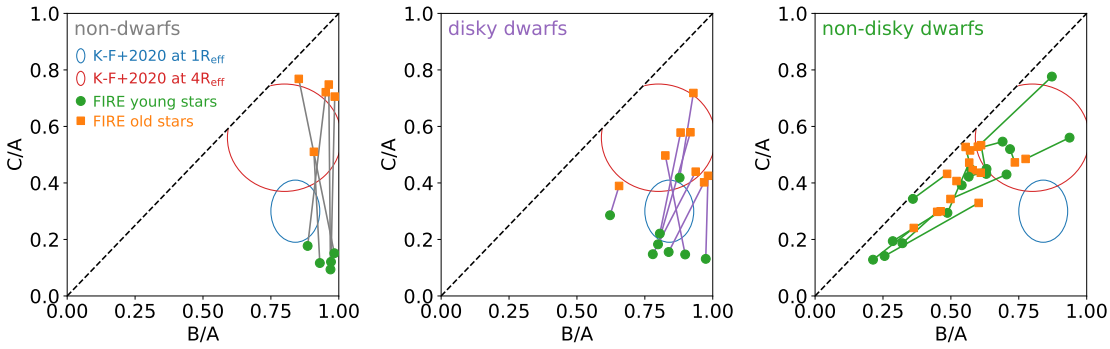

Figure 6.2 The intrinsic shape of the young and old stellar populations for the three subsets of the sample we consider in this work. In each panel, the green filled circles show the intrinsic shape of the young (ages less than 2 Gyr) stellar population and the orange squares show the intrinsic shape of the old stellar population (ages older than 12 Gyr). Lines connect the measurements for each individual galaxy. The blue and red ellipses show the observed 1σ distribution of the dwarf sample of Kado-Fong et al. [2020b] at $1R_{\rm eff}$ and $4R_{\rm eff}$, respectively. At left a comparison sample of high-mass ($M_\star > 10^{10} M_\odot$) galaxies is shown; these galaxies host a clear disk-halo transition between their young and old stellar populations, where the youngest stars are assembled in a thin disk and the oldest populate a spheroidal stellar halo. The center panel shows the sample of dwarf galaxies that host a disk halo system; the disks in these dwarfs are thicker (higher C/A) than those of the higher mass galaxies, while the old stellar components are less round (lower C/A). Finally, at right, we show the non-disky dwarfs in the sample, which are characterized by the lack of a young stellar disk, as well as the lack of a monotonic increase in C/A and the presence as a significant change in B/A function of age.

simulations.

6.2.1 The FIRE Simulations

Due to the low masses and small sizes of dwarf galaxies, studying their detailed structure requires high resolution simulations. Moreover, their shallow potential wells make the structure of dwarf galaxies relatively more sensitive to the details of the implementation of feedback from star formation, such as stellar winds and supernovae, than the structure of more massive galaxies. Thus, while realistic feedback prescriptions are crucial to understanding the structural properties of low mass galaxies, such galaxies are also among the most sensitive tests of these same feedback prescriptions [e.g. Brooks and Zolotov, 2014, Hu et al., 2016, Wheeler et al., 2017, Hu, 2019, Wheeler

et al., 2019, Dashyan and Dubois, 2020, Smith et al., 2020]. Furthermore, *cosmological* simulations are necessary to properly capture the significant effect of reionization on these small galaxies [e.g. Bovill and Ricotti, 2009, Boylan-Kolchin et al., 2015, Weisz and Boylan-Kolchin, 2017, Fitts et al., 2017, Graus et al., 2019]. Cosmological simulations also supply the variety of environments [e.g. Garrison-Kimmel et al., 2019, Jahn et al., 2019] and assembly histories [e.g. Fitts et al., 2017] needed to study the dwarf population, especially given the relatively large impact that interactions even with purely dark subhalos can have on the star formation histories of dwarfs [Starkenburg et al., 2016a].

We use simulations from the FIRE project, specifically the suite of cosmological-baryonic zoom-in simulations run with the FIRE-2 feedback models [Hopkins et al., 2018] along with some variations described below. The FIRE project contains a suite of simulated dwarf galaxies that are uniquely well-suited for the structural study at hand – as we have argued above, assessing the origin of dwarf stellar structure formation requires simulations that are both cosmological in nature and high resolution. The baryonic particle mass of the dwarf simulations at hand range between 2100-7100 $M_\odot$, with a minimum gravitational force softening of ~ 2 pc. Though there are a relatively low number of initial conditions (we study nine in this work), the resolution of the FIRE-2 simulations is critical for robust studies of the stellar structure of low-mass galaxies [Ludlow et al., 2021]. Indeed, it has been shown that the stellar structure of FIRE-2 dwarfs at even lower masses remain robust to resolution effects [Wheeler et al., 2019]. Thus, we expect the structure of these relatively more massive galaxies to be robust to resolution effects due to the high resolution of the FIRE-2 simulations – moreover, as a small forward reference, we note that we find no evidence for a dependence between resolution and the dwarf properties we measure in this work.

All simulations use the Meshless-Finite-Mass (hereafter MFM) mode of the GIZMO[2] gravity+magnetohydrodynamic code [Hopkins, 2015], which provides adaptive spatial resolution, conservation of mass, energy, and momentum, and excellent shock-capturing and conservation of angular momentum, reproducing advantages of both smoothed-particle hydrodynamics (SPH) and Eulerian adaptive mesh refinement (AMR) schemes. Gravity is solved with an improved version of the

[2] `http://www.tapir.caltech.edu/~phopkins/Site/GIZMO.html`

Tree-PM solver from GADGET-3 [Springel, 2005], with fully-adaptive (and fully-conservative) gravitational force softenings for gas (so hydrodynamic and force softenings are always self-consistently matched), following Price and Monaghan [2007].

Table 6.1 lists the simulations included in this study. All are simulations of isolated galaxies (the main halo being simulated is the highest-mass object in the zoomed box). The names of the simulations follow a convention: (1) in the prefix "mXX," the number XX denotes the order of magnitude of the halo mass of the most massive halo in the zoomed region, in solar masses; (2) the letter following the prefix is a label representing the simulation's unique initial conditions; (3) the parenthetical after the resolution indicator is a shorthand reference to the physics included in the run (described further below).

We select the $z = 0$ snapshots of the set of isolated dwarf galaxy simulations with stellar masses $10^8 \lesssim M_\star/M_\odot < 10^{10}$, along with a set of three higher mass galaxies ($M_\star > 10^{10} M_\odot$) that we use as a reference sample. We will show in this work that the stellar halos of the high-mass reference set are built largely from accreted particles, as expected for $L_\star$ galaxies, and use this high-mass sample as a benchmark for classical stellar halo assembly.

We use simulations run with three different variations of the FIRE physics engine, denoted in the "Run Type" column of Table 6.1 as (Hydro+, no MD), (Hydro+, MD), (MHD+), and (CR+) to explore the sensitivity of our conclusions to small changes in the baryonic physics implemented in the simulations. Runs marked (Hydro+, no MD) and (Hydro+, MD) use the core FIRE-2 physics described in full in Hopkins et al. [2018] with and without metal diffusion (MD), respectively. Runs marked (Hydro+, MD) in Table 6.1 use the physics described above, but also include the numerical implementation of turbulent metal diffusion described in Escala et al. [2018]. Including a model for turbulent metal diffusion allows neighboring gas cells to exchange gas as it is enriched, as we presume happens in nature. This has the main effect of narrowing the distribution of abundances of different metals in the gas and stars, bringing the width of the abundance distributions in line with observations from dwarf galaxies without changing the structural properties of the galaxies themselves [Escala et al., 2018]. Since we do not expect metal diffusion to affect the properties studied in this work, both (Hydro+) designations may be treated interchangeably, as separate

realizations of similar dwarfs from the same initial conditions that differ only in the stochastic variation induced by a different pattern of stellar feedback—we propagate the presence of metal diffusion in the naming scheme for completeness.

In brief, radiative heating and cooling is treated from $10 - 10^{10}\,\mathrm{K}$, including free-free, photo-ionization/recombination, Compton, photoelectric & dust collisional, cosmic ray, molecular, and metal-line & fine-structure processes (following each of 11 tracked species independently), and accounting for photo-heating both by a UV background [Faucher-Giguère et al., 2009] and local sources, as well as self-shielding. In the UV background model used for the simulations in this work, reionization occurs at $z \sim 10$, significantly earlier than current empirical constraints [see, e.g. Planck Collaboration et al., 2020].The early reionization onset mainly affects the star formation histories of ultra-faint galaxies (up to around $M_* \sim 10^5\ M_\odot$; Wheeler et al. 2019) with far less stellar mass than the simulated galaxies studied here.

Star formation occurs only in gas identified as self-gravitating according to the Hopkins et al. [2013] criterion, which is also molecular and self-shielding (following Krumholz and Gnedin 2011), Jeans unstable, and exceeds a minimum density threshold $n_{\rm min} = 1000\,\mathrm{cm}^{-3}$. Once a star particle forms, the simulations explicitly follow several different stellar feedback mechanisms, including (1) local and long-range momentum flux from radiation pressure (in the initial UV/optical single-scattering, and re-radiated light in the IR), (2) energy, momentum, mass and metal injection from SNe (Types Ia and II) and stellar mass loss (both OB and AGB), and (3) photo-ionization and photo-electric heating. Every star particle is treated as a single stellar population with known mass, age, and metallicity from which all feedback event rates, luminosities, energies, mass-loss rates, and other relevant quantities are tabulated directly from stellar evolution models (STARBURST99; Leitherer et al. 1999), assuming a Kroupa [2001] IMF.

Runs marked (MHD+) again use the same physics as the (Hydro+) runs but solve the equations of ideal magneto-hydrodynamics (MHD) as described and tested in Hopkins and Raives [2016] and Hopkins [2016], with anisotropic Spitzer-Braginskii conduction and viscosity as described in Hopkins [2017], Su et al. [2017], and Hopkins et al. [2020a]. Runs marked (CR+) include all of the physics implemented in the (MHD+) runs, with the addition of the magnetohydrodynamic treatment of

cosmic rays described in Chan et al. [2019], Hopkins et al. [2020a], and Ji et al. [2020]. Magnetic fields, conduction, and viscosity have only small effects on bulk galaxy properties at any mass scale [Hopkins et al., 2020a], but cosmic rays can can suppress SF and total stellar masses by factors $\sim 2-4$ for galaxies with $M_{\rm vir} \gtrsim 10^{11} M_{\odot}$ at late times ($z \lesssim 1-2$) by building up hot gas in the galaxy halo that suppresses the galactic fountain [Hopkins et al., 2020a]. This only occurs in halos massive enough to confine the hot ($T \sim 10^{6} K$) gas, and the set of dwarfs we consider here are right on the boundary of this effect, which is more pronounced in the more massive systems used for comparison (last five rows of Table 6.1. However, we do not see any systematic difference in the shapes of the galaxies produced in the (CR+) runs relative to the (MHD+) and (Hydro+) runs.

These simulations are uniquely well-suited to study the connection between the formation of dwarf galaxies and their structure. The combination of physics implementations in the (Hydro+) runs have already been shown to reproduce the mass-size relation of observed galaxies across $\gtrsim 5$ orders of magnitude in stellar mass [El-Badry et al., 2016, Chan et al., 2018]. The sample includes a large range of different assembly histories (9 in total for the dwarf sample) that give rise to a wide variety of present-day galaxy morphologies, from thin disks to highly diffuse structures [El-Badry et al., 2018a]. With the FIRE-2 feedback model, the resolved ISM produces star formation histories that are generically bursty for dwarf galaxies [e.g. Sparre et al., 2017, Faucher-Giguère, 2018, Flores Velázquez et al., 2021], an effect which can be suppressed in lower-resolution simulations that do not resolve the multiphase ISM. On the other hand, the burstiness of the star formation in these simulations is slightly enhanced relative to models that explicitly include local radiative feedback, which has the effect of warming the gas and disrupting some GMCs before collapse, leading to a smoother SFH in massive dwarfs [Hopkins et al., 2020b].

Because these simulations resolve individual large GMCs [Benincasa et al., 2020] where the star formation occurs, the star formation has a very high spatial granularity across the galaxy; clustering of starforming clouds is thus naturally taken into account down to ∼pc scales. The granularity of the resulting stellar feedback in both space and time is also very high, since the mass of the individual star particles (2100-7100 $M_{\odot}$ per particle) is sufficiently small to support the assumption that each represents a single-age, single-metallicity stellar population while still

Table 6.1. Basic Properties of the FIRE-2 Galaxies Included in this Work

Run Name	M_{vir} $[10^{11} M_\odot]$	R_{vir} [kpc]	$M_{\star,90}$ $[10^{9} M_\odot]$	$R_{50,\star}$ [kpc]	class	m_{bary} $[10^{3} M_\odot]$	Reference
m11a (Hydro+, no MD)	0.39	0.89	0.11	2.79	non-disky	2.1	[1]
m11a (CR+)	0.39	0.89	0.05	1.27	non-disky	2.1	[2]
m11b (CR+)	0.40	0.90	0.09	2.20	disky	2.1	[1]
m11b (MHD+)	0.40	0.90	0.07	2.29	disky	2.1	[2]
m11b (Hydro+, no MD)	0.40	0.90	0.11	2.54	disky	2.1	[3]
m11c (CR+)	1.37	1.35	0.78	2.79	non-disky	2.1	[2]
m11c (MHD+)	1.41	1.36	1.16	3.21	non-disky	2.1	[4]
m11c (Hydro+, no MD)	1.37	1.35	0.84	3.00	non-disky	2.1	[4]
m11d (CR+)	2.71	1.70	1.55	4.12	non-disky	7	[2]
m11d (MHD+)	2.75	1.71	5.03	5.71	non-disky	7	[2]
m11d (Hydro+, MD)	2.72	1.70	4.06	6.97	non-disky	7.1	[2]
m11e (Hydro+, MD)	1.43	1.38	1.46	3.84	non-disky	7.1	[2]
m11e (CR+)	1.40	1.36	0.65	3.28	non-disky	7.1	[4]
m11e (MHD+)	1.45	1.38	1.25	4.55	non-disky	7.1	[4]
m11h (CR+)	1.76	1.47	2.87	3.60	disky	7	[5]
m11h (MHD+)	1.81	1.49	4.44	3.46	disky	7	[2]

being large enough to fully sample the IMF at the high-mass end [Sanderson et al., 2020]. The inclusion of turbulent metal diffusion additionally reproduces the observed dependence of the width of abundance spreads on stellar mass in dwarfs [Escala et al., 2018]. Comparing runs with additional physics to the (Hydro+) runs for identical initial conditions allows us to both confirm that these variations do not strongly influence the structure of dwarfs, and set a bound on the degree of scatter due to stochastic supernova feedback for a fixed assembly history.

6.2.2 Intrinsic Shape Measurements

We parameterize the three dimensional shapes of the sample using the ratio of the semi-principal axis diameters A, B, and C where A $\geq$ B $\geq$ C. The ratios of these axes, B/A and C/A, give a quantitative description of the intrinsic shape of each galaxy; in Figure 5.5, we show three extreme cases in both B/A vs. C/A space at left and as wireframe renderings at right. In particular, we show a prolate galaxy in green (C/A $\sim$ B/A $\ll$ 1), a disky galaxy in blue (C/A $\ll$ B/A $\sim$ 1), and a spheroidal galaxy in red (C/A $\sim$ B/A $\sim$ 1). For context, we also show the 1σ contours of the observed dwarfs sample of Kado-Fong et al. [2020b] in blue (measurements at 1$R_{\rm eff}$) and red (measurements at 4$R_{\rm eff}$).

Making structural measurements for age-separated stellar components of low-mass halos requires simulations of sufficiently high resolution. Even at the mass resolution of the FIRE-2 simulations studied in this work, we use cumulative (i.e. the shape of the stars within a given radius), rather than differential (the shape of the stars at a given radius), intrinsic shape measurements in order to overcome instability due to low stellar densities in the outskirts of the dwarfs, though we note that the radial density profile remains stable. This is a qualitatively different approach than what is used in integrated light measurements of intrinsic shape, where the galaxy intrinsic shape distribution is inferred at fixed radius [Padilla and Strauss, 2008, van der Wel et al., 2014, Kado-Fong et al., 2020b]. The need for a cumulative measure of the intrinsic shape will also lead us to measure intrinsic shapes as a function of stellar age instead of galactocentric radius, comparing in particular the young (ages $<$ 2 Gyr) and old (ages $>$ 12 Gyr) stellar populations (see Section 6.3.1). Based on observations of nearby dwarfs, this age separation is expected to correlate with the observational differential shapes [see, e.g. Zaritsky et al., 2000, Aparicio and Tikhonov, 2000, Aparicio et al., 2000, Hidalgo et al., 2003, Demers et al., 2006, Bernard et al., 2007, Stinson et al., 2009, Strader et al., 2012, Nidever et al., 2019, Pucha et al., 2019]. However, we note that the age-separated populations that we use in this work are not the exact equivalent to the radially-separated stellar populations of Kado-Fong et al. [2020b]. The simulated and observed measurements also differ in that the observed measurements of the galaxy projected shapes are used to infer the intrinsic shape distribution of

Table 6.1 (cont'd)

Run Name	M_{vir} $[10^{11} M_\odot]$	R_{vir} [kpc]	$M_{\star,90}$ $[10^{9} M_\odot]$	$R_{50,\star}$ [kpc]	class	m_{bary} $[10^{3} M_\odot]$	Reference
m11h (Hydro+, MD)	1.80	1.48	3.62	4.13	disky	7.1	[2]
m11i (Hydro+, MD)	0.69	1.08	0.93	3.79	non-disky	7.1	[2]
m11i (CR+)	0.63	1.05	0.22	2.88	non-disky	7.1	[2]
m11i (MHD+)	0.68	1.07	0.58	3.68	disky	7.1	[2]
m11q (MHD+)	1.45	1.38	1.87	3.04	non-disky	7	[2]
m11q (Hydro+, MD)	1.41	1.36	0.63	2.62	non-disky	7.1	[2]
m11v (CR+)	2.95	1.74	2.59	8.27	non-disky	7.1	[2]
m11v (MHD+)	2.20	1.58	2.51	3.52	disky	7.1	[2]
m11f (CR+)	4.30	1.98	12.02	3.56	non-dwarf	12	[2]
m11f (MHD+)	4.75	2.04	31.74	2.57	non-dwarf	12	[2]
m11g (CR+)	5.35	2.13	11.00	4.80	non-dwarf	12	[3]
m11g (MHD+)	6.05	2.21	49.02	2.78	non-dwarf	12	[2]
m12i (Hydro+, no MD)	10.46	2.66	70.60	2.89	non-dwarf	7.1	[2]

Note. — Virial mass (M_{Vir}) is measured within the Bryan and Norman [1998] virial radius of the halo at $z = 0$. $M_{\star,90}$ and $R_{\star,50}$ are the stellar mass and radius enclosing 90% and 50% of the stellar mass within 30 kpc of the galaxy center, respectively. "Baryonic particle mass" denotes the initial mass of gas & star particles in the simulation. "Hydro+" indicates runs with the core physics suite with and without metal diffusion ("MD"), while "MHD+" indicates runs that also include treatment for magnetic fields and fully anisotropic conduction and viscosity. "CR+" indicates runs that also include treatment of cosmic rays (in addition to the physics described by MHD+). Morphological classifications are discussed in Section 6.3.1. References: (1) Chan et al. 2018, (2) Hopkins et al. 2020a, (3) Hopkins et al. 2018, (4) El-Badry et al. 2018a, (5) Wetzel et al. 2016.

the galaxy population (whereas the simulated values are direct intrinsic shape measurements of individual galaxies), and that the simulated measurements are mass-weighted in bins of stellar age (whereas the observed measurements are light-weighted at fixed radii). Thus, the emphasis of this work will be on the change in galaxy structure within the simulations and observations as a function of galaxy properties, rather than a direct quantitative comparison between the observed and simulated measurements. However, in Section 6.7, we also demonstrate that these cumulative measurements well-trace mock measurements made using the observational inference machinery of Kado-Fong et al. [2020b].

As mentioned above, unlike in observations, in simulations we are able to directly measure the intrinsic shape of the galaxies in our sample. To do so, we compute the reduced moment of inertia tensor $\mathbf{I}$ from the set of star particles at distances less than $R_{\rm max} = 50$ kpc for the simulated galaxies with $\mathrm{M_{halo}} \sim 10^{11}\mathrm{M_\odot}$ and $R_{\rm max} = 70$ kpc for the galaxy with $\mathrm{M_{halo}} \sim 10^{12}\mathrm{M_\odot}$. The reduced moment of inertia tensor $\mathbf{I}$ is given by

$$\mathbf{I} = \begin{bmatrix} I_{xx} & I_{xy} & I_{xz} \\ I_{yx} & I_{yy} & I_{yz} \\ I_{zx} & I_{zy} & I_{zz} \end{bmatrix} \tag{6.1}$$

where each element is computed from the star particles (of mass m_k) as

$$I_{ij} = \frac{\sum_{r_k < R_{\rm max}} m_k q_{i,k} q_{j,k} / r_k}{\sum_{r_n < R_{\rm max}} m_n}, \tag{6.2}$$

for $i, j \in (x, y, z)$ and where $\mathbf{r_k} = (q_x^k, q_y^k, q_z^k)$ is the distance from the principal halo center. The principle axes calculated from the reduced moment of inertia may overweight star particles at large distances relative to the unreduced moment of inertia tensor; for our sample, however, we find a median fractional difference in the principal axis ratios of 5%, and conclude that our choice of moment of inertia tensor does not significantly affect our results. The eigenvalues λ_1, λ_2 and λ_3 of this matrix are the inverse squares of the semi-principal axis diameters A, B, and C of the Poinsot ellipsoid that corresponds to the moment of inertia tensor:

$$\frac{B}{A} = \sqrt{\frac{\lambda_1}{\lambda_2}}$$
$$\frac{C}{A} = \sqrt{\frac{\lambda_1}{\lambda_3}}. \tag{6.3}$$

This method is, in principle, sensitive to the choice of $R_{\rm max}$ and emphasizes the contribution of particles at large r (see Equation 6.2). We test the effect of our choice of intrinsic shape measurement method as follows. First, though we choose a larger $R_{\rm max}$ for the higher mass halo, we would derive the same shape parameters B/A and C/A to within $\Delta(B/A) \sim \Delta(C/A) \sim 0.01$ at $R_{\rm max} = 50$ kpc. Furthermore, although we adopt a fixed value of $R_{\rm max} = 50$ kpc for the dwarf galaxies considered in this work, we find that varying $R_{\rm max}$ does not qualitatively affect our results down to $R_{\rm max} \sim 10$ kpc. Finally, we fit two dimensional Sérsic profiles to projections of each galaxy along its principal axes, and find no evidence for a systematic offset between the Sérsic fits and moment of inertia-derived axis ratios. Thus, although the moment of inertia method potentially overemphasizes star particles at large distances, we find that our results are not impacted by this bias in practice.

Observational works indicate that dwarfs in this mass range should host a central thick disk [see, e.g. van der Wel et al., 2014] with a round extended stellar component [Kado-Fong et al., 2020b] that is populated by intermediate/old stars [see Stinson et al., 2009, and citations therein]. If a disk-halo system is indeed present in the FIRE-2 dwarfs, we should be able to detect the same transition from disk to halo when computing the intrinsic shape in bins of stellar age – we demonstrate that this transition is indeed detectable in mock HSC data in Section 6.3.2. We visualize an example of such a divide in Figure 6.1, which shows the projected density of the dwarf galaxy m11h (MHD+) in young stars (left column, blue) old stars (middle column, red) and neutral hydrogen (right column).

Table 6.2. Mean Intrinsic Shape Ratios of the FIRE-2 Dwarf Sample

	$\langle \frac{B}{A} \rangle_{\rm young}$	$\langle \frac{C}{A} \rangle_{\rm young}$	$\langle {\rm N} \rangle_{\rm young}$	$\langle \frac{B}{A} \rangle_{\rm old}$	$\langle \frac{C}{A} \rangle_{\rm old}$	$\langle {\rm N} \rangle_{\rm old}$
Non-dwarfs	0.95 ± 0.02	0.13 ± 0.01	9.6×10^5	0.93 ± 0.02	0.69 ± 0.04	9.2×10^5
Disky Dwarfs	0.82 ± 0.03	0.21 ± 0.03	6.3×10^4	0.89 ± 0.04	0.50 ± 0.04	8.6×10^4
Non-Disky Dwarfs	0.55 ± 0.05	0.39 ± 0.04	9.9×10^4	0.56 ± 0.02	0.42 ± 0.02	9.6×10^4

Note. — Mean intrinsic shape measurements (denoted by $\langle\rangle$) and the associated error on the mean for the sample considered in this work, divided by morphology. $\langle {\rm N} \rangle$ refers to the number of star particles used in the shape computation for the old (ages greater than 12 Gyr) and young (ages less than 2 Gyr) stellar populations.

6.3 Results

6.3.1 The Intrinsic Shapes of the FIRE-2 Dwarf Galaxies

We present the main results of this section in Figure 6.2. In each panel, we show the intrinsic axis ratios of the simulated galaxies, B/A and C/A, where C $\leq$ B $\leq$ A. At left, for reference, we show the well-defined stellar disk and halo systems of the high-mass ($M_\odot > 10^{10} M_\star$) reference sample (m11f, m11g, and m12i, see Table 6.1). The intrinsic shapes of young star particles (youngest $25^{\rm th}$ percentile) and old star particles (oldest $25^{\rm th}$ percentile) are shown in blue and red, respectively. In this panel, the young stars clearly are assembled in a well-formed disk (C < B $\sim$ A), and the old stars occupy a round stellar halo (A $\sim$ B $\sim$ C). Similarly, in the middle panel, we show the dwarf galaxies in our sample that have a clear disk-halo system. These galaxies are characterized by substantial increases in C/A as a function of age along with relatively little evolution in B/A compared to C/A over the same comparison, and were categorized by visual inspection of the galaxies' stellar components. Although the oldest (ages greater than 12 Gyr) stars may not dominate the light in the outskirts of the FIRE-2 dwarfs, we see the same trend towards a more spheroidal shape when comparing the young (ages less than 2 Gyr) and intermediate (ages between 2 and 12 Gyr) star particles.

We note that the young stellar disks in these dwarfs tend to be thicker (higher C/A) than the

disks in the higher mass galaxies – this phenomenon is in good agreement with previous observational findings [Padilla and Strauss, 2008, Sánchez-Janssen et al., 2010, Kado-Fong et al., 2020b]. Both the high-mass and dwarf disks are largely axisymmetric, maintaining a B/A ~ 1 in both their young and old stellar populations. Though the old stellar population is significantly rounder than the young stellar disks of these dwarfs, the dwarf stellar halos are not as round (meaning C/A approaching unity) as those of the old stellar population in the high-mass comparison sample. This is again consistent with the observations of Kado-Fong et al. [2020b], who find that dwarfs have an average minor-to-major axis ratio $\langle C/A \rangle \sim 0.5$ at $4\mathrm{R_{eff}}$, significantly flatter than the outer stellar halo of the Milky Way [$C/A \gtrsim 0.8$, Das and Binney, 2016, Iorio et al., 2018]. This may be due to a difference in the formation mechanism of dwarf stellar halos and massive galaxy stellar halos, which we will explore in later sections.

The evolution of C/A as a function of age is also markedly different between the disky dwarfs and high-mass reference sample. In Figure 6.3, we show the change in C/A from the minimum C/A for each disky dwarf (purple) and high-mass galaxy (grey). Because C/A increases monotonically as a function of age for both these groups, this is equivalent to showing the change in C/A from the C/A of the youngest (t < 2 Gyr) star particles. The $x - z$ projections as a function of age for one such disky dwarf (top) and one high-mass galaxy (bottom) are shown at right. The figure serves to illustrate two main points: first, the overall change in C/A is systematically smaller for the disky dwarf sample. Second, the high-mass galaxies approach their maximum C/A values more rapidly as a function of age, with a sharp increase in C/A at $5 \lesssim t_{\mathrm{age}} \lesssim 8$ Gyr and relatively little change beyond that. This can also be seen qualitatively in the stark change in shape between the [4,6] Gyr and [6,8] Gyr surface densities of the high-mass galaxy. The dwarf galaxies, meanwhile, increase in C/A gradually as a function of age.

This difference in the three-dimensional shape as a function of age between the massive and dwarf disk galaxies can be understand when one considers the origins of the star particles that constitute these age-binned groups. In Figure 6.4, we show the histories of a random subset of star particles in two massive disks (top two rows, grey panels) and two disky dwarfs (bottom two rows, purple panels). In the left panels, we show particle distance from the galaxy center as a

function of time, while on the right we show the distribution of the maximum distance attained by these particles in three age bins (ages < 2 Gyr in blue, between 6 and 8 Gyr in orange, and > 12 Gyr in red). The particle tracks on the left are colored by age, as are the histograms at right. We find in particular that the old, spheroidal components of the massive galaxies (the red tracks and histograms show particles with ages > 12 Gyr) correspond to accreted components on orbits characterized by large apocenters that persist down to $z = 0$. The young (ages < 2 Gyr) components are formed in-situ close to the host center, and the intermediate (ages between 6-8 Gyr) components represent a transition between the ex-situ and in-situ-dominated stellar populations.

The disky dwarfs, meanwhile, are dominated by stars formed in-situ (though some accreted particles are present) at all ages – in the right panels, we show that although the majority of old stars in the massive disks attain a maximum distance greater than the radius containing 90% of the star particles at $z = 0$ ($R_{\star,90}(z = 0)$), the star particles in dwarf disks are characterized by maximum distances less than $R_{\star,90}(z = 0)$ at all ages. That is, the difference in the evolution of three-dimensional shapes as a function of age between the massive and dwarf disks is driven by a difference in the origin of the stars that populate each age group. The spheroidal old component of the massive disks are driven by an accreted population that fall in on relatively circular orbits compared to the flatter, in-situ population that dominates the old stellar component of the disky dwarfs. We will further examine the origin and shape evolution of the disky dwarfs in Section 6.3.2 by examining the role of accreted star particles in building the stellar outskirts of the full sample (Figure 6.5).

Finally, in the right panel of Figure 6.2, we show the intrinsic shapes of the non-disky dwarfs in our sample. Although we refer to these galaxies as "non-disky" dwarfs, this morphological class refers to galaxies that lack a young stellar disk and do not show a monotonic increase in C/A as a function of stellar age. These dwarfs do not have a well-defined disk-halo structure, and appear to be significantly different in intrinsic shape to the population of observed galaxies from Kado-Fong et al. [2020b][3]. The lack of a well-defined disk in particular may point to an overly vigorous or bursty star formation history, preventing the formation of a rotationally supported disk at low redshift.

[3]We quantify the possibility of an existent but minority non-disky dwarf population in the observations of Kado-Fong et al. [2020b] in Section 6.6 and discuss this idea further in Section 6.4.3

El-Badry et al. [2018c] found in particular that the ability of FIRE-2 galaxies to form a gaseous disk and maintain a fairly quiescent (less bursty) star formation history is linked to the accretion of high angular momentum gas at low redshifts, wherein low-mass FIRE-2 galaxies struggle to build up stores of this high angular momentum gas due to both efficient gas removal via star formation feedback and inefficient cooling of high angular gas in the circumgalactic medium.

While the star formation feedback and/or cooling prescription may lead to a lack of a disk-halo structure in some dwarfs, those same prescriptions are capable of creating dwarf stellar disk-halo systems that are remarkably similar in structure to the observed population. Thus, in this work we will examine the two facets of the sample separately, examining first the dwarf stellar halo (in the simulated galaxies that do form disks) and then the origin of the non-disky dwarfs.

As a final note, we find that there is no change in the morphological classification of the galaxy as a function of the physics implementation for the majority of the dwarfs in the sample. That is, it appears that the $z = 0$ stellar intrinsic structure is largely unaffected by the additional physics implemented in the (MHD+) and (CR+) runs as described in Section 6.2.1. However, we do find that two galaxies, m11i and m11v, are disky in their (MHD+) runs and non-disky in their (CR+) or (Hydro+) runs. We find that the change in morphological classification in m11i is due to its proximity to the boundary between our disky and non-disky classifications – indeed, in the middle panel of Figure 6.2, the disky m11i (MHD+) galaxy is shown by the pair of points at the lowest B/A value of the dwarf sample. Thus, we conclude that the change in morphological class of m11i is due to the rigid nature of the binary classification that we use in this work. Though the disky and non-disky dwarfs are generally well-separated morphological classes, there do exist edge cases such as m11i in which the classification can change as a result of relatively small perturbations in intrinsic axes space. m11v does undergo a significant shape change between the MHD+ ($B/A = 0.90$ and $C/A = 0.46$ for $t < 2$ Gyr stars) and CR+ ($B/A = 0.25$ and $C/A = 0.13$) runs. However, m11v is also experiencing an ongoing interaction that is the likely cause of this shape variation.

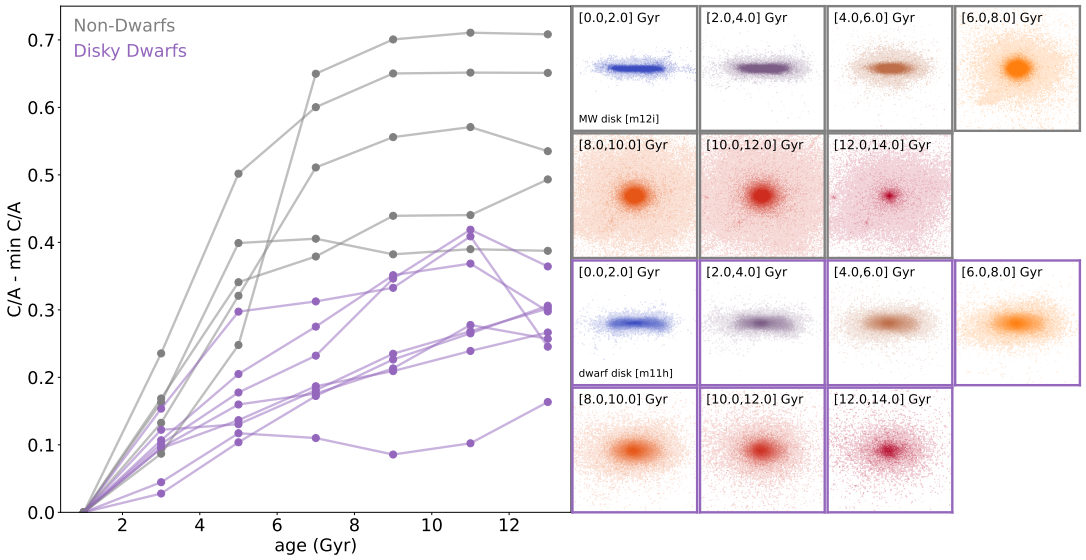

Figure 6.3 *At left:* the change in minor-to-major intrinsic axis ratio C/A as a function of stellar age, in bins of 2 Gyr. We show the change in C/A over the minimum C/A across all age bins (because of the monotonic increase in C/A as a function of age for these galaxies, this is equivalent to the change in C/A over the youngest age bin). Dwarf disks are shown in purple, while high-mass disks are shown in grey. Not only are the old stellar populations of the dwarf disks less spheroidal than their high-mass counterparts, d(C/A)/d(age) is markedly smaller in the dwarfs than the high-mass galaxies. *At right:* the stellar surface density of an example dwarf (top two rows) and massive galaxy (bottom two rows) in bins of 2 Gyr. As at left, while the dwarf stellar population thickens gradually with increasing age, there is a sharp transition between the thin disk and round stellar halo in the more massive galaxy – this contrast is consistent with the differing origin of the dwarf and massive stellar outskirts, wherein dwarf stellar halos are produced via in-situ migration of star particles rather than the accretion of satellites.

6.3.2 The Origin of Dwarf Halo Stars

In Figure 6.5, we show for a selection of galaxies the maximum distance of the star particles from the host halo center since $z \sim 6.2$ as a function of the present-day distance. This figure acts to visualize the contributions to the young (top, blue) and old (bottom, red) stellar populations by in-situ and ex-situ components: in-situ star particles flare out from the 1:1 line, while accreted star particles occupy horizontal bands that correspond to the maximum distance of the progenitor system over the time considered. In the set of panels at left we show the $z = 0$ distances versus maximum distance attained from host center for a disky dwarf (m11h (MHD+)) and non-dwarf

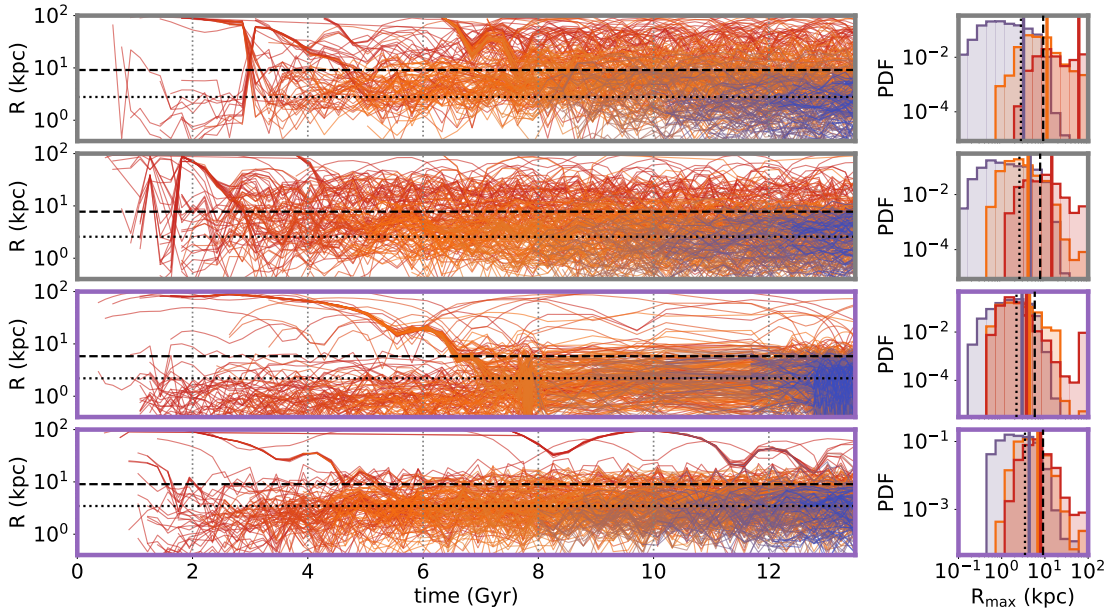

Figure 6.4 *Left:* particle distance from host galaxy center versus time for two high-mass galaxies (m11f (MHD+) and m11g (MHD+), grey-outlined panels) and two disky dwarfs (m11h (MHD+) and m11b , purple-outlined panels), colored by particle age at $z = 0$. The dashed (dotted) black lines show the 3D radius that contains 90% (50%) the stellar mass at $z = 0$. *Right:* distribution over maximum distance from host achieved for star particles younger than 2 Gyr (blue), between 6 and 8 Gyr (orange), and older than 12 Gyr (red). Median values for $R_{\rm max}$ for each age component are shown by the colored vertical lines. The oldest stars in the massive galaxies are dominated by accreted star particles that remain on large-apocenter orbits to $z = 0$.

(m11f (MHD+)), while at right we show the fraction of particles that attain a displacement of greater than 15 kpc (i.e. those particles that lie above the dotted line in the left panels) for the full set of disky dwarfs and massive galaxies. The right panel shows this metric for both the old stars (filled points) and for all particles with a $z = 0$ host distance of greater than $10\% R_{\rm vir}$.

As expected, the young stellar populations in all the galaxies shown in Figure 6.5 are dominated by in-situ contributions. However, the difference in how the dwarfs and the MW-mass galaxy have assembled their old stellar populations is apparent. Whereas the old star particles in the dwarfs (and therefore their stellar halos) are dominated by in-situ star particles, the old stellar population in the MW-mass galaxy is completely dominated by accreted star particles. We find no significant

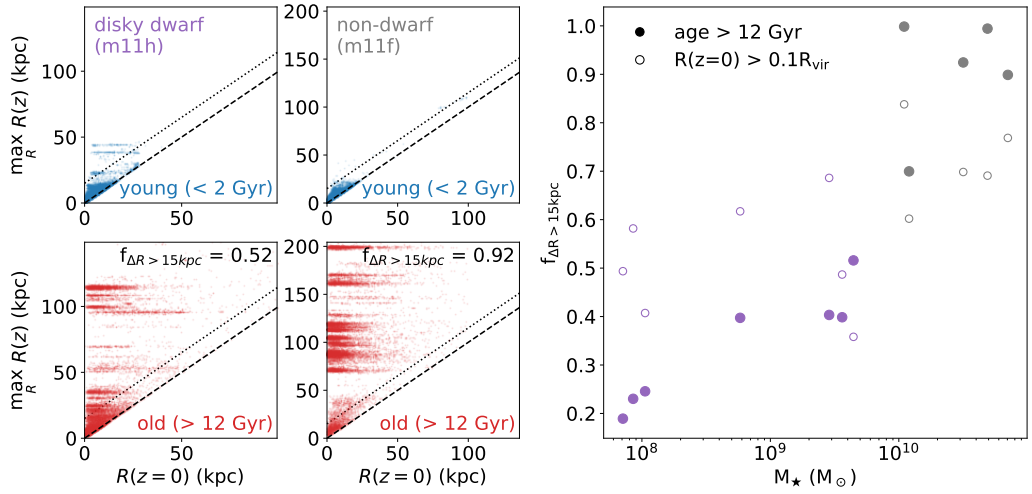

Figure 6.5 *Lefthand panels:* To diagnose the origin of the star particles that populate the stellar halo for the galaxies in this work, we plot the maximum distance between the youngest (ages < 2 Gyr) and oldest (ages > 12 Gyr) star particles and the host center against their $z = 0$ distance. These populations are good tracers of the disk and halo structures, if such structures exist. Star particles with an in-situ origin should flare from the 1:1 line (the dashed black line and physical minimum), while accreted particles populate horizontal bands due to a shared maximum distance that corresponds with the original distance between the main host and progenitor system. As a visual aid, we show a maximum offset of 15 kpc as the dotted grey line. In this space, it is clear that while the massive galaxy (m11f, MHD+), is dominated by an accreted stellar halo (bottom right panel), the dwarf galaxy (m11h, MHD+), old stellar populations are largely in-situ structures. The x-axis and y-axis limits are set at $2/3$R$_{\rm vir}$ and R$_{\rm vir}$, respectively. *Right panel:* For the full sample of disky dwarfs (m11v (MHD+) is excluded due to a central halo tracking issue at high redshift resulting from an ongoing interaction at $z = 0$) and massive galaxies (M$_\star > 10^{10}$M$_\odot$), the fraction of star particles with a lifetime radial displacement of greater than 15 comoving kpc (ΔR = max$_{\rm R}$ R(z) $-$ R(z = 0)), f$_{\Delta {\rm R}>15{\rm kpc}}$. We show this quantity both for the old star particles (filled circles, ages greater than 12 Gyr) and the star particles with large $z = 0$ distances from host halo center (unfilled circles, R > 15 kpc). Both the old stars and stars in the outskirts show an increasing fraction of high-displacement (likely ex-situ) stars as a function of stellar mass, in agreement with the picture of an increasingly in-situ-dominated stellar halo for dwarf galaxies.

difference between the accreted halo fraction of the non-disky dwarfs and disky dwarfs, though the sample size is too small to straightforwardly extrapolate this behavior to the general dwarf population.

The diagnosis of halo star particle origin that we use in this work is not meant to produce exact

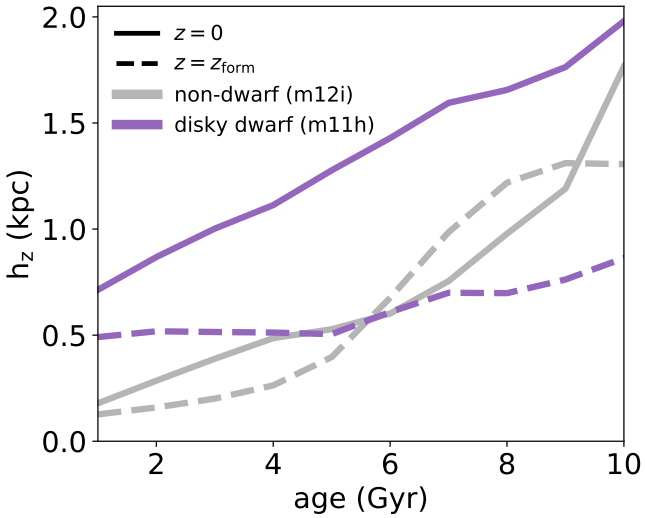

Figure 6.6 For a massive (grey, $M_{halo} \sim 10^{12} M_\odot$) and dwarf (purple, $M_{halo} \sim 10^{11} M_\odot$) disk galaxy, we show the change in the exponential stellar scale height h_z as a function of age. For the star particles with a given age, the solid curves show the current, z = 0 scale height of those star particles, while the dashed curves show the scale height of the same single-aged population at $z = z_{form} = z(t_{lb} = \text{age})$. We exclude stars older than 10 Gyr, as in the massive galaxy they are likely to be dominated by ex-situ stars which should not be well-described by an exponential distribution at birth. Whereas the stars in the massive galaxy show a negligible change in vertical scale, the dwarf stars are consistently more extended at current times than they were at their formation time. This is consistent with the picture in which the dwarf stellar outskirts are populated by stars that have been heated to larger radii after their formation. In contrast, the massive galaxy FIRE-2 thick disks are formed due to an overall change in the configuration of star formation as a function of cosmic time (see Yu et al. 2021).

ex-situ fractions, but is instead aimed to identify bulk changes in halo formation mechanism. We test our $\Delta R > 15$ comoving kpc threshold against a cut in formation distance, which has been used in prior work with the FIRE-2 simulations to track ex-situ contributions [Sanderson et al., 2018] and has been showed to produce accreted fractions in agreement with subhalo tracking from merger trees for MW-like galaxies in FIRE-2 [Necib et al., 2019]. We compare these two ex-situ flagging methods for the disky dwarf m11h (Hydro+, MD) and the high mass galaxy m12i (Hydro+, no MD), and find that our ΔR cut produces accreted fractions consistent to within 10% of those based on a cut on formation distance. We also consider the effect that our choice of a threshold cut at

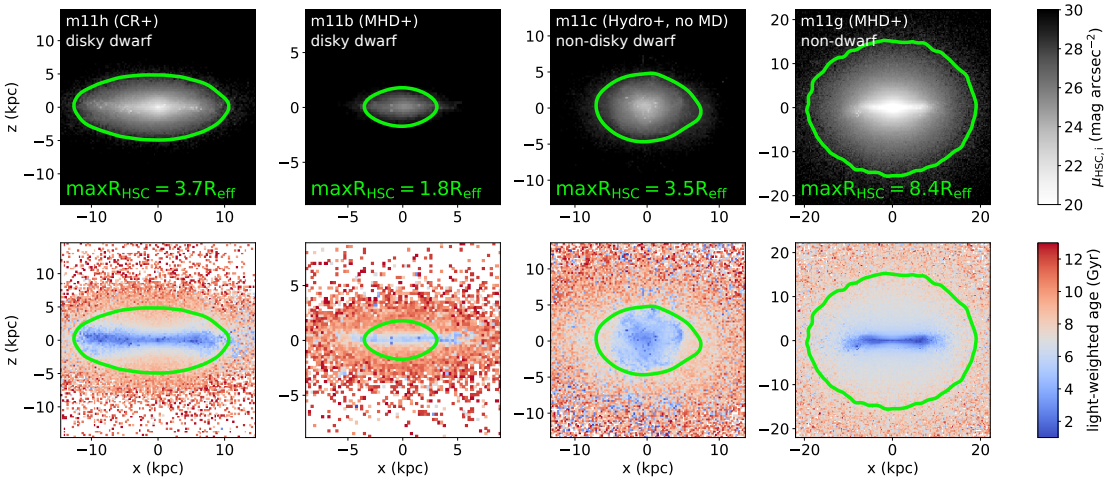

Figure 6.7 Mock HSC-i band surface brightness maps (top row) and HSC-i light-weighted age maps (bottom row) for an example set of galaxies which span the mass and morphologies studied in this work. From left to right, we show: m11h (CR+), a disky dwarf at the high end of the dwarf stellar mass range ($M_{\star,90} = 3 \times 10^9 M_\odot$), m11b (MHD+), a disky dwarf at the low end of the dwarf stellar mass range ($M_{\star,90} = 7 \times 10^7 M_\odot$), m11c (Hydro+, no MD), a non-disky dwarf, and m11g (MHD+), a massive galaxy ($M_{\star,90} = 5 \times 10^{10} M_\odot$). The lime contour in each panel is an isophote at $\mu_i = 28.5$ mag arcsec^{-2}, the approximate surface brightness limit of the HSC-SSP i-band for galaxy outskirts. The values written in lime at the bottom of the top row of panels show the approximate maximum radius that HSC-SSP observations would be able to reach for each galaxy, as a function of the i-band effective radius of the galaxy (as determined by a single two-dimensional Sérsic fit).

$\Delta R = 15$ kpc plays on our estimated ex-situ fractions, and find that a cut of $\Delta R = 30$ kpc ($\Delta R = 7$ kpc) changes the estimated ex-situ fractions by no more than 12% (5.7%), and does not affect the trend with stellar mass shown in Figure 6.5. We also find that this trend holds when we consider all stars in the outskirts, regardless of age ($R(z = 0) > 0.1 R_{vir}$, open points in Figure 6.5). Indeed, the divergent behavior seen in Figure 6.5 between the dwarf and massive galaxy stellar halos is consistent with the supposition that the stellar halos of massive galaxies are dominated by ex-situ stars, while the dwarf stellar halos are largely in-situ structures.

The thick and in-situ nature of the dwarf stellar outskirts in FIRE-2 also draws a clear structural similarity to the thick disks in more massive galaxies. Though the origin, existence, and nature of thick disks in the Milky Way and beyond is still a matter of significant debate [see, e.g. Yoachim

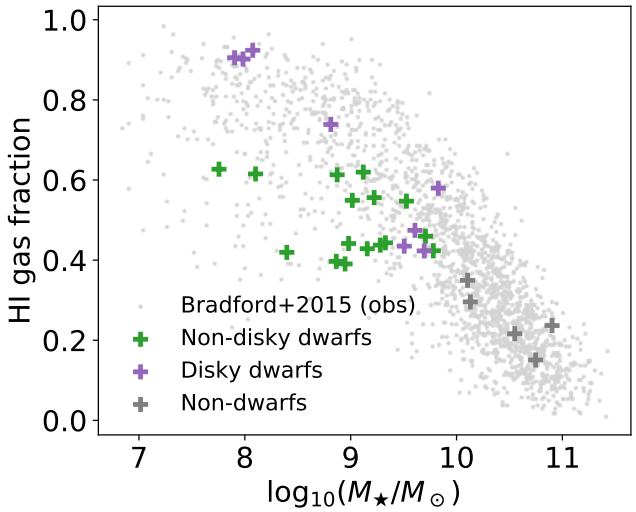

Figure 6.8 The HI gas fraction $M_{\rm HI}/(M_\star + M_{\rm HI})$ versus stellar mass for the simulated FIRE-2 galaxies (marked as crosses) and the observed sample of [Bradford et al., 2015, light grey scatter]. The FIRE-2 galaxies are colored by morphology, as indicated. The FIRE-2 dwarfs tend to be overly HI-depleted compared to observed galaxies [see also El-Badry et al., 2018a], so the gas rich end of the FIRE-2 dwarfs are the most consistent with observations. In particular, the galaxies that successfully form disks have HI gas fractions consistent with the observed relation, while the non-disky dwarfs are systematically gas depleted relative to the Bradford et al. [2015] sample.

and Dalcanton, 2006, Bovy et al., 2012, Belokurov et al., 2020, Agertz et al., 2021, Park et al., 2021], it is straightforward to make an internal comparison between the dwarf stellar outskirts and massive thick disks within the context of the FIRE-2 simulations. It has been demonstrated that the thickened shape of the thick disks in the more massive FIRE-2 galaxies is caused by star formation characterized by larger vertical scale heights during bursty phases of star formation at lookback times of $t_{\rm lb} \gtrsim 5$ Gyr [Yu et al., 2021]. It is thus of interest to examine whether the shape of the FIRE-2 dwarf stellar populations are set by stellar migration or by a change in the star formation configuration as a function of cosmic time. To address this, we show in Figure 6.6 the difference in the scale height of the star particles in bins of age at $z = 0$ and at $z = z_{\rm form}$, where $z_{\rm form}$ is the formation redshift (i.e. the lookback time equivalent to the $z = 0$ age of the star particle population), of star particles in a disky dwarf galaxy (m11h) and a massive galaxy

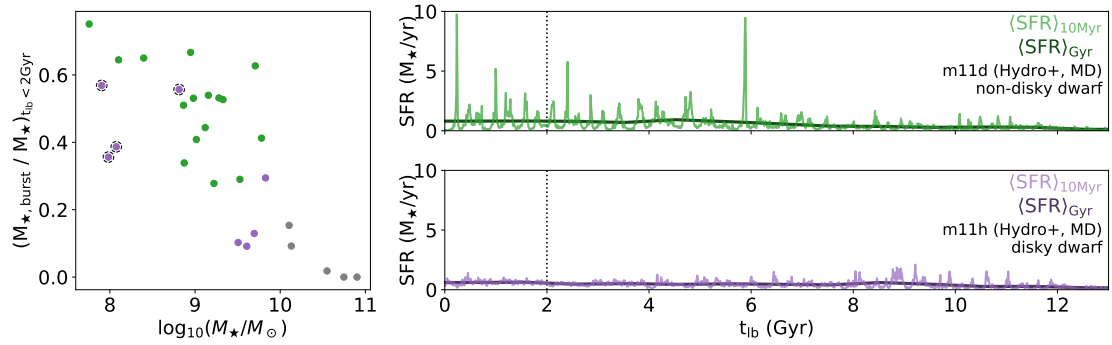

Figure 6.9 At left, the fraction of stellar mass built up in bursts (defined as time periods where $\langle \mathrm{SFR} \rangle_{10\mathrm{Myr}} / \langle \mathrm{SFR} \rangle_{\mathrm{Gyr}} > 1.5$) versus stellar mass for the sample of FIRE-2 dwarfs. The purple points show disky dwarfs, while the green points show the non-disky dwarfs, and the grey points show the non-dwarfs. The low-mass dwarfs that have HI gas fractions of greater than $(M_{\mathrm{HI}}/(M_{\star}+M_{\mathrm{HI}}) = 0.7$ are shown with a dashed outline. We find that the dwarfs that are able to form a young stellar disk have either particularly quiescent (non-bursty) recent star formation histories, or are particularly gas rich relative to the other simulated galaxies. At right we show the star formation history for a non-disky dwarf (top, m11d (Hydro+, MD)) and a disky dwarf (bottom, m11h (Hydro+, MD)). In each panel we show the 10 Myr-averaged and Gyr-averaged star formation rates as the light and dark curves, respectively. We also show vertical lines at $\mathrm{t_{lb}} = 2$ Gyr, the time period over which the burst mass fraction is computed.

(m12i) as a function of star particle age. We compute scale heights from an exponential fit to the vertical stellar surface density in age bins spaced by 1 Gyr with widths of 2 Gyr, and exclude star particles with ages greater than 10 Gyr for the massive galaxy in this figure, as the massive galaxies are expected to be dominated by ex-situ stars at this age (see Figure 6.5) and the majority of the massive FIRE-2 thick disks are assembled at times more recent than 10 Gyr [Yu et al., 2021].

We first consider the massive FIRE-2 galaxy; Figure 6.6 demonstrates that the star particles in this galaxy show a negligible change in vertical scale height between $\mathrm{z} = \mathrm{z_{form}}$ and $\mathrm{z} = 0$. This lack of scale height evolution is consistent with the results of Yu et al. [2021], who find that the thick disks in these massive galaxies are formed as thick disks from birth, rather than from stellar displacement after formation. If, however, we turn our attention to the dwarf disk, we see that the $z = 0$ vertical scale height is consistently higher than the vertical scale height at formation. This evolution is instead consistent with the picture of El-Badry et al. [2016], where the stellar

outskirts are indeed formed from the displacement of stars after formation. This implies that the dwarf stellar outskirts in FIRE-2 are distinct in formation mechanism from both the mechanisms that create massive stellar halos and massive stellar thick disks in the FIRE-2 simulations.

6.3.3 The Observability of the FIRE-2 Dwarf Stellar Halos

As discussed in Section 6.2.2, the way in which we measure the intrinsic shape of the FIRE-2 dwarfs is significantly different than the measurement methods applied to observations in Kado-Fong et al. [2020b]. Thus, it is of interest to quantify the extent to which the stellar halos around the FIRE-2 dwarfs would be observable in Hyper Suprime-Cam Subaru Strategic Program (HSC-SSP), the imaging survey used by Kado-Fong et al. [2020b]. This test will help to understand the extent to which the FIRE-2 dwarf stellar halos and observed dwarf stellar outskirts track the same physical structure.

In order to quantify the observability of the FIRE-2 dwarf stellar halos, we generate mock observations of the sample in this work using the Flexible Population Synthesis (FSPS) package [Conroy et al., 2009b, Conroy and Gunn, 2010] to generate simple stellar populations over a grid of stellar ages (between 10^5 and $10^{10.3}$ yr) and metallicities (in the range $-4 < \log_{10}(Z/Z_\odot) < 1$). We then compute the stellar mass-to-light ratio in the HSC i-band for each model spectrum. Each star particle in the simulated dwarfs is then assigned an HSC i-band mass-to-light ratio based on its age and metallicity via linear interpolation of the model grid; this process allows us to compute surface brightness and light-weighted age maps for each galaxy in our sample. Following Sanderson et al. [2018], we construct these maps via a simple binning of star particles with a box size of 0.25 kpc on a side.

We show these surface brightness and light-weighted age maps in Figure 6.7 for a set of galaxies that span the stellar masses and morphologies of the sample at hand. Each panel shows the isophote at the nominal HSC i-band surface brightness limit for galaxy profiles ($\mu_\mathrm{i} = 28.5$ mag arcsec^{-2}) as a lime green contour. In order to best quantify the ability of HSC to detect the old, round stellar outskirts of the FIRE-2 galaxies, we project each galaxy along the y-axis. We also compute an

effective radius in the HSC i-band using this projection via a two-dimensional, single-component Sérsic fit; in each panel, we note the maximum radial distance of the $\mu_{\rm i} = 28.5$ mag arcsec^{-2} isophote in terms of the HSC i-band effective radius, which we will denote as $\max {\rm R}_{\rm HSC,obs}$.

Naturally, we find that the value of $\max {\rm R}_{\rm HSC,obs}$ increases as a function of stellar mass; adopting the stellar mass bins used in Kado-Fong et al. [2020b], we find that the FIRE-2 galaxies with stellar masses of ${\rm M}_\star < 10^{8.5}{\rm M}_\odot$ have a mean (standard deviation of) $\max {\rm R}_{\rm HSC,obs}$ of 2.0 (0.2) ${\rm R}_{\rm eff,HSC-i}$, while the galaxies with stellar masses of $10^{8.5} < {\rm M}_\star < 10^{9}{\rm M}_\odot$ have a mean (standard deviation of) $\max {\rm R}_{\rm HSC,obs}$ of 3.6 (0.8) ${\rm R}_{\rm eff,HSC-i}$, and the galaxies with stellar masses of $10^{9} < {\rm M}_\star < 10^{9.6}{\rm M}_\odot$ have a mean (standard deviation of) $\max {\rm R}_{\rm HSC,obs}$ of 4.1 (1.7) ${\rm R}_{\rm eff,HSC-i}$. These values are consistent with the spatial limit of the HSC imaging for the dwarfs in Kado-Fong et al. [2020b].

As shown in Figure 6.7, in the cases where a young stellar disk is formed (i.e. excluding the non-disky dwarfs due to the lack of an analogous population in the observations), the mock HSC observations extend beyond the young stellar disk into the rounder and older stellar outskirts. This finding supports our initial assertion in Section 6.2.2 that the age-separated intrinsic shape measurements in the simulated galaxies and the radially-separated intrinsic shapes inferred from the observed dwarf population are tracing the same physical structure.

6.3.4 Properties of the Disky and Non-Disky Dwarfs

Though diagnosing, in detail, the formation path of non-disky dwarfs is not the main aim of this paper, it is informative to compare their global properties to those of the disky FIRE-2 dwarfs and to observed dwarf galaxies.

It is known that the dwarfs in FIRE-2 are, on average, somewhat lower in their HI gas fractions as compared to observed dwarfs [El-Badry et al., 2018b]. Here we expand upon this trend to demonstrate that the gas content of the FIRE-2 dwarfs are also linked to their three dimensional structure. To do so, we compare the HI gas content[4] of the FIRE-2 simulations to that of the observed sample of Bradford et al. [2015]. We compute the HI and stellar masses within 200 kpc

[4]The ionized fraction of hydrogen is calculated self-consistently from the cooling routines implemented in FIRE-2 – a succinct description of the cooling function and radiative feedback processes included in FIRE-2 can be found in appendices B and E of Hopkins et al. [2018], respectively.

of the galaxy center to derive the HI gas fractions of the FIRE-2 galaxies (though we note that a choice of 50 kpc from galaxy center would change the HI gas fractions by a few percent at most, and generally much less). Drawn from Sloan Digital Sky Survey (SDSS) spectroscopically confirmed targets with Arecibo Legacy Fast ALFA (ALFALFA) 21cm observations, this sample consists of isolated galaxies with stellar masses $10^7 \lesssim M_\star/M_\odot \lesssim 10^{11}$. We compare this isolated HI sample to the FIRE-2 galaxies in Figure 6.8; the observed galaxies are shown in grey scatter, while the simulated galaxies are shown by the crosses (colored by morphology, as indicated). Notably, while the disky dwarfs lie on the main relation found by Bradford et al. [2015], the non-disky dwarfs are systematically more gas-poor at fixed stellar mass than the observed galaxies.

Next, we contrast the star formation histories (SFH) of the non-disky and disky dwarfs. In Figure 6.9, we show at left the fraction of stellar mass built in starbursts over the last 2 Gyr versus the galaxy's stellar mass. We define a starburst as the snapshots for which

$$\frac{\langle \mathrm{SFR} \rangle_{10\mathrm{Myr}}}{\langle \mathrm{SFR} \rangle_{1\mathrm{Gyr}}} > 1.5. \tag{6.4}$$

We find that the FIRE-2 dwarfs that succeed in forming disks are those that are either particularly gas rich (as seen in Figure 6.9; for easy comparison we outline the galaxies where the HI gas fraction exceed 0.7 with a dashed circle) or have particularly non-bursty recent star formation histories for their stellar mass. To visualize the difference in star formation histories, we show the SFH for a non-disky dwarf at top (green), and a disky dwarf with a low burst fraction at bottom (purple). Though both are highly bursty at high redshift, the disky dwarf becomes significantly less bursty at low redshift.

6.4 Discussion

In the previous section, we showed that the FIRE-2 dwarfs host stellar outskirts that are assembled from in-situ star particles, a distinctly different formation pathway than the stellar halos of more massive galaxies. Here, we place our results into the context of simulations of dwarf galaxies at

large, and compare the simulated dwarf properties to those of observed dwarf galaxies.

6.4.1 Comparison to Other Simulations

As the FIRE-2 simulation suite are a set of cosmological zooms, we will first contextualize our results via comparison to similar studies done on cosmological and non-cosmological simulations.

Because of the high resolution necessary to study the stellar outskirts of low-mass halos, there are relatively few cosmological simulations that make similar structural measurements on dwarf galaxies to which we can compare. Pillepich et al. [2019] use TNG50, the highest resolution volume of the IllustrisTNG simulations [Pillepich et al., 2018], to present mass-weighted intrinsic shape measurements made in an ellipsoidal aperture at twice the half-mass radius, $2\mathrm{R}_{1/2,\mathrm{mass}}$, with a thickness of $0.4\mathrm{R}_{1/2,\mathrm{mass}}$. TNG50 reaches a baryonic mass resolution of $8.5 \times 10^4 M_\odot$ and a DM mass resolution of $4.5 \times 10^5 \mathrm{M}_\odot$ (about an order of magnitude lower resolution in both baryons and dark matter than the galaxies studied in this work) and a minimum gravitational force softening of 74 pc for the gas (compared to ~ 2 pc for the galaxies in this work). TNG50 contains approximately ~ 5500 dwarf galaxies with stellar masses in the range $10^8 < M_\star/M_\odot < 10^{10}$. The intrinsic shape of the dwarf galaxies in TNG50 show a strong dependence on stellar mass, with the $10^9 < M_\star/M_\odot < 10^{10}$ galaxies characterized by thick disks and the $10^8 < M_\star/M_\odot < 10^9$ dwarfs significantly more spheroidal. We see no such trend with mass in the FIRE-2 simulation suite. It is of interest that the high-mass TNG50 dwarfs form thick disks, even in the old stellar population. This is in contrast to the FIRE-2 dwarfs that succeed in forming thick disks; the FIRE-2 stellar disks are dominated by young stars, while the old stellar populations that dominate the stellar mass budget maintain largely spheroidal shapes at all radii (for cumulative measurements). Observations indicate that high-mass dwarfs should generically host stellar disks, as they do in TNG50 [Kado-Fong et al., 2020b], but also find morphological differences as a function of age in resolved star studies, as is seen in FIRE-2 [Zaritsky et al., 2000, Aparicio and Tikhonov, 2000, Aparicio et al., 2000, Hidalgo et al., 2003, Demers et al., 2006, Bernard et al., 2007, Stinson et al., 2009, Strader et al., 2012, Nidever et al., 2019, Pucha et al., 2019].

It is also informative to compare to higher resolution, non-cosmological simulations of dwarf

galaxies. In particular, Smith et al. [2020] examine the effect of photoionization and photoelectric heating from young stars on the efficacy of supernova feedback and the resultant impact on the SFH and disk structure. They find that the inclusion of photoionization significantly dampens the burstiness of the simulated dwarf SFH, and that runs that include only SNe feedback result in superbubbles that significantly disrupt the gaseous disk. It is important to note that the galaxy studied in Smith et al. [2020] is initialized with both a stellar and gas disk, and is significantly lower in stellar mass ($M_\star \sim 10^7 M_\odot$) than the galaxies studied in this work; it is observationally uncertain whether galaxies in this mass range are generally disky [Kado-Fong et al., 2020b, Carlsten et al., 2021]. However, their finding that over-vigorous star formation feedback can disrupt the disk is in line with our finding that it is the bursty and gas poor FIRE-2 dwarfs that do not form young stellar disks.

Finally, it has been noted that dark matter particles may induce numerical heating in the stellar component of simulated galaxies. We do not expect this numerical heating to significantly affect our results – the resolution of the FIRE-2 dwarfs surpasses the dark matter particle mass limit estimated by Ludlow et al. [2021] at which numerical heating accounts for no more than 10% that of the virial velocity ($\mathrm{m_{DM}} \lesssim 4.5 \times 10^4 \mathrm{M_\odot}$; the maximum particle mass of the FIRE-2 dwarfs is $\mathrm{m_{DM}} = 3.8 \times 10^4 \mathrm{M_\odot}$). Indeed, for the massive FIRE-2 galaxy m12i, Ludlow et al. [2021] estimates that the change in scale height attributable to numerical heating is only 70 parsec, which is much smaller than the change in scale height observed in the FIRE dwarfs (see Figure 6.6). Additionally, a study of the somewhat smaller ($\mathrm{M_{halo}} \sim 10^{10} \mathrm{M_\odot}$) FIRE-2 galaxies run at $30 \mathrm{M_\odot}$ resolution showed that structural measurements in dwarfs at fiducial FIRE-2 resolution are robust to resolution effects [Wheeler et al., 2019].

6.4.2 A Divergent Path of Low-mass Stellar Halo Formation

Due to the steepening stellar-to-halo mass relation at low masses, it has long been thought unlikely for dwarf galaxies to assemble a significant stellar halo population via the accretion of satellite galaxies. Thus, the observed presence of extended old [Lin and Faber, 1983, Minniti and Zijlstra, 1996, Minniti et al., 1999, Zaritsky et al., 2000, Aparicio and Tikhonov, 2000, Aparicio et al., 2000,

Hidalgo et al., 2003, Demers et al., 2006, Bernard et al., 2007, Stinson et al., 2009, Strader et al., 2012, Nidever et al., 2019, Pucha et al., 2019] and round [Kado-Fong et al., 2020b] stellar outskirts around dwarf galaxies points to a different mode of stellar halo formation at low masses.

In this work, we have shown that the FIRE-2 dwarf galaxies are capable of producing an extended old and round stellar population in conjunction with a young stellar disk, and we find that the stellar outskirts of the FIRE-2 dwarfs reproduce several key qualities of observed high-mass dwarf stellar halos. However, FIRE-2 also produces a large contingent of non-disky dwarfs whose structural and gas properties are at odds with the observed population. Nevertheless, it is informative to consider the mechanism through which the high resolution and cosmological dwarfs simulated in FIRE-2 form disk-halo systems, and to consider the plausibility of such a mechanism in the context of our knowledge of the observed dwarf population.

First, in a marked contrast to the ex-situ stellar halos of massive galaxies, these dwarf stellar halo populations are dominated by in-situ stars that occupy an increasingly spheroidal component as a function of age. This behavior explains the apparent ubiquity of round stellar outskirts around high-mass dwarfs ($M_\star > 10^{8.5} M_\odot$), as feedback should be a generic process in all galaxies that proceeds regardless of accretion history or environment. The existence of an old, in-situ population in the outskirts of the FIRE-2 dwarfs is not surprising, as it has been shown that the radial migration of stars due to baryon-driven potential fluctuations operates most strongly in FIRE-2 dwarfs in this mass range [El-Badry et al., 2016, Graus et al., 2019]. This feedback-driven migration has previously been suggested as a formation mechanism for in-situ stellar halos [Stinson et al., 2009, Maxwell et al., 2012]. Star formation feedback-driven size fluctuations have also recently been found via correlations between size and star formation rate in both the FIRE-2 dwarfs and a sample of nearby dwarfs from the Local Volume Legacy Survey [Emami et al., 2021].

Furthermore, the old stellar population of the FIRE-2 dwarfs, though largely spheroidal compared to the young stellar disk populations, are significantly more flattened (a lower minor-to-major intrinsic axis ratio C/A) than are the halos of the higher mass FIRE-2 galaxies. This is again due to their in-situ formation mechanism, wherein the disk gradually thickens into the halo as the stars age. These preferentially flatter dwarf stellar halos are in good agreement with observations of

dwarf stellar outskirts, which find that dwarf stellar outskirts at 4 effective radii are preferentially flatter than the Milky Way at the same distance. Indeed, the mean C/A of the young stellar population of disky dwarfs in FIRE ($\langle \mathrm{C/A} \rangle = 0.21 \pm 0.03$, where $\langle\rangle$ denotes the sample mean, see Table 6.2) is similar to the maximum a posteriori estimate of the mean C/A of the massive dwarf population inferred by Kado-Fong et al. [2020b] ($\langle \mathrm{C/A} \rangle = 0.30 \pm 0.01$ for dwarfs of stellar mass $10^9 < \mathrm{M_\star/M_\odot} < 10^{9.6}$ and $\langle \mathrm{C/A} \rangle = 0.32 \pm 0.02$ for dwarfs of stellar mass $10^{8.5} < \mathrm{M_\star/M_\odot} < 10^9$, see Table 1 of Kado-Fong et al. 2020b). However, we stress that because of the differences in the intrinsic shape measurement method (differential versus cumulative) and the exact stellar populations being measured (i-band light-weighted versus age-separated), we are not emphasizing here the apparent agreement in the numerical value of $\langle \mathrm{C/A} \rangle$ between the observed and simulated dwarfs. Rather, we point to the difference in $\langle C/A \rangle$ of the simulated (observed) dwarfs and simulated (observed) high-mass galaxies as the key observational constraint on the difference in the assembly mode of their stellar halos.

Before continuing on from this point, we stress again that the FIRE-2 simulation suite consists of a relatively small number of initial conditions, and that the isolated dwarfs in the simulation suite are biased towards conditions that are more isolated than the typical field dwarf. Due to the small number of initial conditions and the selection of these initial conditions, it is key to remember that the FIRE-2 dwarfs should not be treated as a dwarf population study. Furthermore, of these relatively small number of initial conditions, the FIRE-2 suite produces a large number of non-disky dwarfs that are inconsistent with average observed dwarf galaxies in both their stellar structure and gas content. We thus emphasize that our goal is not to validate the ability of the FIRE-2 simulations to reproduce the overall dwarf population, but to demonstrate that the in-situ mode of dwarf stellar halo creation that has been suggested from observational results can indeed be naturally produced by contemporary cosmological hydrodynamical simulations.

6.4.3 The Non-Disky Dwarfs

Although the FIRE-2 simulations succeed in producing dwarfs with a disk-halo structure that well-reflects the observations, it must be noted that these disky dwarfs are not the dominant mode of

dwarf stellar structure in the FIRE-2 simulations. Indeed, most of the dwarfs in the sample have significantly lower values of B/A than observed dwarfs, and do not host a clear young stellar disk. To better understand this discrepancy, we suggest three possibilities below.

First, the production of non-disky dwarfs at $z = 0$ could stem from the implemented physics of the FIRE-2 simulations. That the non-disky dwarfs tend to be gas-poor with a bursty recent SFH (see Figure 6.9) suggests that the star formation feedback prescription in FIRE-2 may be preventing the formation of both stellar and gaseous disks in these non-disky dwarfs [see also El-Badry et al., 2018c]. It is also notable that observed high redshift dwarfs lack a well-defined disk; Zhang et al. [2019] found that high-z, high-mass dwarfs are characterized by triaxial prolate ellipsoids at high redshift ($z \gtrsim 1$) and transition to thick-disk structures at low-z [see also Ceverino et al., 2015, for a similar transition in simulated dwarfs]. It is thus possible that the FIRE-2 dwarfs are failing to undergo this transition at the appropriate cosmic time. At the same time, the existence of the disky dwarfs, which also host in-situ stellar halos, indicates that it is possible to form disk-halo structures with this feedback prescription. Interestingly, El-Badry et al. [2018b] also showed that the low-mass FIRE-2 galaxies tend to be overly dispersion-supported due to inefficient accretion of high angular momentum gas, with the same trend that rotation-supported gas disks occupy galaxies with less bursty recent star formation histories. This interplay between the gaseous structure, stellar structure, and recent star formation history of the FIRE-2 dwarfs point to a link between the way in which star formation proceeds in these dwarfs and their ability to form a young stellar disk. Indeed, the idea that star formation feedback can significantly influence dwarf structure is well-established in regards to both the baryonic morphology [see, e.g. Governato et al., 2007, Smith et al., 2019, 2020] and in the dark matter halo [the core-cusp problem; see, e.g. Peñarrubia et al., 2012, Pontzen and Governato, 2012]. Indeed, as the most easily observable leg of this set, the stellar structure of galaxies in the dwarf mass regime could prove to be a powerful tool to constrain the feedback prescriptions in conjunction with requirements for cored/cuspy dark matter profiles.

Second, it is possible that observations are missing a significant population of non-disky dwarfs due primarily to surface brightness sensitivity limits. We find that the non-disky dwarfs are not systematically lower in stellar surface density (within the stellar half-light radius) than the disky

dwarfs. However, there is evidence that the FIRE-2 dwarfs with more bursty star formation also have lower surface brightnesses [Chan et al., 2018]. It is thus plausible that observed samples preferentially include disky dwarfs.

Explaining the lack of observational analogues to non-disky dwarfs in FIRE-2 as being due to observational incompleteness would also necessitate the existence of a substantial and likely dominant population of low surface brightness dwarfs at $10^8 \lesssim M_\star/M_\odot \lesssim 10^{10}$. A forthcoming probe of the distance and stellar mass distribution of a sample of low surface brightness galaxies will help to directly address this question (Greco et al., in preparation). However, observational studies of the intrinsic shapes of low surface brightness galaxies [Kado-Fong et al., 2021] and ultra diffuse galaxies in clusters [Burkert, 2017, Rong et al., 2020] indicate that although LSBGs are relatively round, they do not show significantly lower values of B/A than spectroscopic dwarf samples, as is the case for the non-disky dwarfs. We thus find it unlikely that the non-disky dwarfs represent a dominant low surface brightness population that are undetected in current generation surveys. Similarly, because the non-disky galaxies lack a disk at all stellar age bins considered, we find it unlikely that the difference in observed and simulated intrinsic shape distributions originates from a difference between light-weighted differential and age-binned, mass-weighted cumulative shapes. We note that some of the non-disky dwarfs are consistent with previous inferred shapes for cluster ultra diffuse galaxies [Rong et al., 2020][5]. It is of interest, but beyond the scope of this work, to ask whether these galaxies differ from the general set of non-disky dwarfs.

A last possibility is that, because the FIRE-2 suite represents a relatively small number of dwarf galaxies, non-disky dwarfs may be a smaller proportion of the total dwarf population than is reflected in the FIRE-2 suite. Part of this discrepancy could be due to bias in the dwarfs chosen for the suite. Galaxies in FIRE-2 zooms are selected to be isolated, and to have small Lagrangian regions, and so it is possible that there is some systematic bias in the sample that causes them to be more non-disky. However, observational results do not indicate that non-isolated dwarfs are more non-disky [Kado-Fong et al., 2020b]; further investigation into the behavior of the FIRE-2 zoom suite as a function

[5] Though the results of Burkert [2017] appear to be in good agreement with the non-disky dwarf population, we caution that Burkert [2017] did not allow for triaxiality in their model, and their results are therefore constrained to either B/A=C/A or B/A=1.

of environment would be enlightening, but is outside the scope of this work. To place a limit on the sensitivity of the observational methods of Kado-Fong et al. [2020b] to a morphologically distinct non-disky population, we construct a toy model wherein we simulate a mock galaxy population composed of a disky and non-disky population and rerun our observational analysis, as detailed in Section 6.6. We find that the hypothetical presence of a small minority ($\lesssim 10\%$) of galaxies with non-disky shapes would not affect the observationally inferred intrinsic shape parameters. However, the fraction of non-disky galaxies in FIRE-2 greatly exceeds this 10% threshold. Thus, we find that the over-representation of non-disky dwarfs in the simulated sample is unlikely to be explained by observational uncertainties or by Poisson fluctuations ($\mathrm{N_{non-disky}} = 10 \pm 3$).

6.5 Conclusions

In this work, we have shown that the FIRE-2 simulation suite is capable of reproducing the young, thick stellar disk and old, round stellar halo observed to be the dominant structural configuration of high-mass ($10^{8.5} < \mathrm{M_\star/M_\odot} < 10^{9.6}$) dwarf galaxies. These dwarf halos bear an observational resemblance to the accreted stellar halos of higher mass galaxies, but as we show in Section 6.3.2, the dwarf stellar halos in FIRE-2 are built up by the migration of in-situ stars. The FIRE-2 galaxies that succeed in forming a disk-stellar halo system also succeed in reproducing a number of characteristics of observed dwarfs: their stellar halos are more flattened (lower C/A) than the stellar halos of the higher mass galaxies in FIRE-2 (see Figure 6.2), appear ubiquitously around dwarfs that form disks, and have HI gas fractions in good agreement with observed galaxies (see Figure 6.8). These dwarfs demonstrate that dwarf stellar halo formation via the heating of disk stars is able to reproduce several properties of observed dwarf galaxies – such an in-situ pathway appears necessary to explain the commonality of dwarf stellar halos in observational samples.

However, the majority of the dwarfs in FIRE-2 are not disk-halo systems. The rest of the dwarfs in this work are instead "non-disky" systems, here meaning that the dwarf is significantly non-disky in shape ($A \not\sim B \not\sim C$), without a clear disk-halo transition (see Figure 6.2). We find that these non-disky dwarfs tend to be depleted in HI for their stellar mass or have highly bursty recent star

formation histories compared to the disky dwarfs. These differences may suggest that the galaxies are unable to form a disk due to over-vigorous star formation or star formation feedback.

Given the presence of this non-disky population of dwarfs, we do not claim here that the in-situ method of dwarf stellar halo assembly seen in the disky FIRE-2 dwarfs is the definitive method by which stellar halos form around low mass galaxies in the real Universe. However, we have demonstrated in this work that when in-situ stellar outskirts are formed in FIRE-2, they succeed in reproducing many of the structural properties of observed dwarfs. Indeed, both classes of FIRE-2 dwarfs demonstrate that intrinsic shapes are a useful tool to understand whether simulations are able to produce realistic galaxy structures. This is particularly important for low-mass galaxies where the details of the star formation history, star formation feedback, and gas accretion are expected to play a significant role in shaping the overall stellar content and structure (both due to the shallower potential well and the lower fractional contribution by accreted stars).

Future observational works targeting the low surface brightness universe will be able to determine whether there exists a counterpart to the non-disky dwarfs in FIRE-2 that has been out of reach of previous observational studies (Greco et al., in preparation). Indeed, a great deal of theoretical and observational work remains necessary to understand the population of low mass galaxies beyond the Local Universe; among other open questions, the details of their star formation histories [Chan et al., 2015], their capacity to self-quench [Geha et al., 2012, Dickey et al., 2020], and the emergence of ultra diffuse galaxies [Chan et al., 2018, Greco et al., 2018c, Wright et al., 2021, Kado-Fong et al., 2021] remain areas of active study for both observational and theoretical efforts. All three of these questions are tied intrinsically to the morphology (and more generally, the structure) of the dwarf population – future observational studies of the intrinsic shape of the dwarf population and other structural parameters will thus help to shed light on a number of open questions in dwarf evolution and stellar assembly.

6.6 Appendix: Placing Limits on the Presence of a Non-Disky Minority Population

In the FIRE-2 simulations, we find two distinct morphological classes of dwarf galaxies – those that are able to form young stellar disks and a round old stellar halo, and those that are characterized by highly non-disky shapes at all ages. In the observational analysis of Kado-Fong et al. [2020b], the intrinsic shape population was modeled as a single multivariate Gaussian. It is thus of interest to make an estimate of the maximum fraction of non-disky galaxies that could be present in a dwarf sample without affecting the inferred observational intrinsic shape distribution. Here, we present mock trials to argue that no more than 10% of a non-disky population drawn from the FIRE-2 non-disky dwarfs could exist in a disky population dominated by the FIRE-2 disky dwarfs without changing the results of the observational inference method used in Kado-Fong et al. [2020b].

To do so, we first briefly summarize the observational inference method; a full explanation can be found in Section 4 of Kado-Fong et al. [2020b]. As was demonstrated by Simonneau et al. [1998], it can be shown that the projected axis ratio b/a of an ellipsoid is an analytic function of its intrinsic axes ratios, B/A and C/A, and the observer's viewing angle (θ, ϕ). A given intrinsic axis ratio distribution can then be quickly turned into a distribution of projected ellipticities, assuming that the viewing angle is distributed uniformly over a sphere. This ellipticity distribution can then be used, in conjunction with adopted flat priors over the relevant shape parameters, to infer the distribution of intrinsic shapes for a galaxy sample given a chosen functional form for that distribution via Markov Chain Monte Carlo sampling [MCMC via emcee, Foreman-Mackey et al., 2013]. Kado-Fong et al. [2020b] adopted a multivariate Gaussian for the inference with parameters $\vec{\alpha} = \{\mu_{\rm B}, \mu_{\rm C}, \sigma_{\rm B}, \sigma_{\rm C}\}$, where $\mu_{\rm X}$ and $\sigma_{\rm X}$ are the mean and standard deviation of the Gaussian characterizing the axis ratio X/A distribution, respectively. This choice enforces a singly-peaked distribution in intrinsic shape space.

To investigate the impact of a minority population of non-disky galaxies, we invoke the following toy model. First, to characterize our two underlying intrinsic shape distributions, we measure the mean and covariance matrices of the non-disky and disky FIRE-2 dwarfs separately. Then,

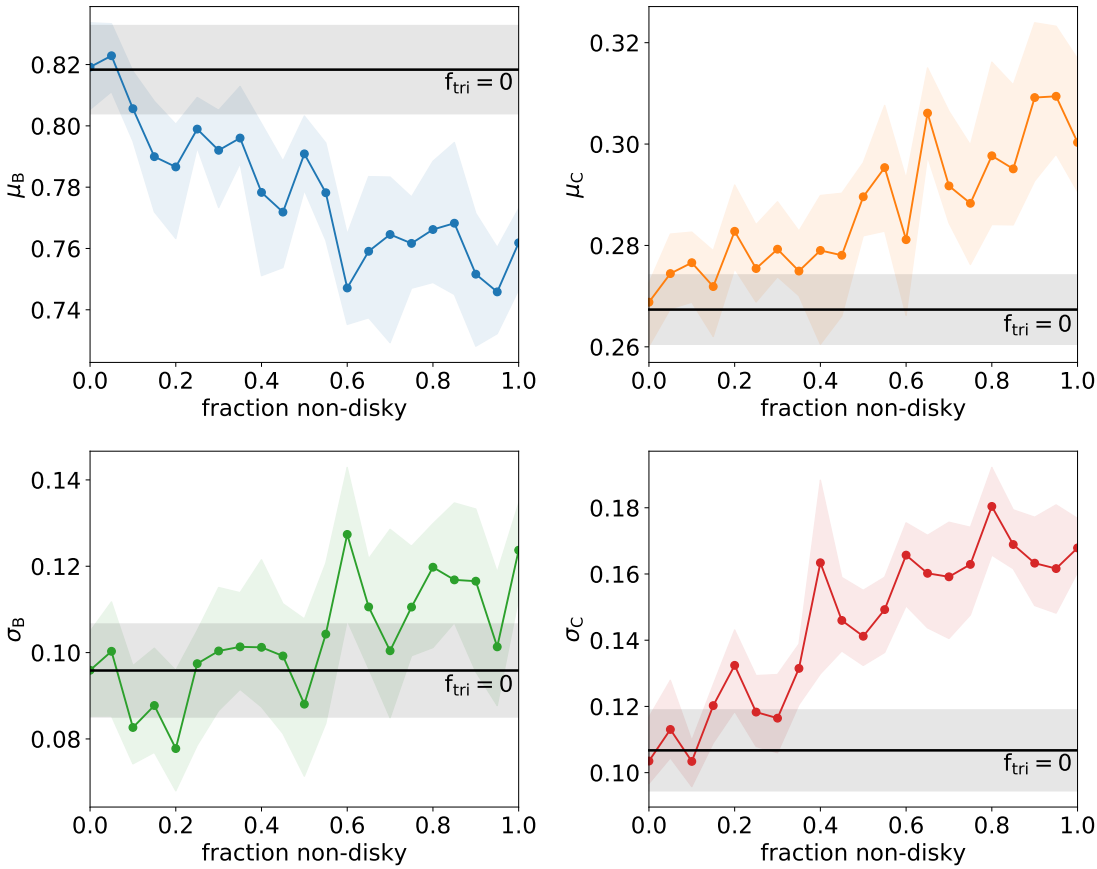

Figure 6.10 The maximum a posteriori (solid curves) and standard deviation (shaded regions) estimates of the observational intrinsic shape parameters as a function of the fraction of the mock sample that is drawn from the non-disky galaxy distribution. The solid black line (region) in each panel shows the maximum a posteriori estimate (standard deviation) of the $f_{non-disky} = 0$ sample. Clockwise from top left, we show: μ_B, the mean axis ratio B/A, μ_C, the mean axis ratio C/A, σ_B, the standard deviation of B/A, and σ_C, the standard deviation of C/A. As the non-disky fraction increases, the mean B/A decreases and mean C/A increases, consistent with a more non-disky shape overall.

we generate a sample from those shape distributions with a given fraction of non-disky galaxies ranging between 0 and 1, and infer the intrinsic shapes of the resulting ellipticity distribution using the same framework as Kado-Fong et al. [2020b]. The mock samples are of size N=4600, selected to be approximately equal to the largest mass bin of Kado-Fong et al. [2020b]. Figure 6.10

shows the evolution of the inferred shape parameters as a function of the non-disky fraction in the mock sample. As expected, we find that the mean B/A decreases and mean C/A increases as the non-disky fraction increases. Interestingly, although the inferred mean shapes of the pure disk population are in good agreement with the true values of the FIRE-2 sample, the inferred mean shapes of the pure non-disky population are somewhat less non-disky than the true values of the FIRE-2 sample. This is likely due to a significant covariance between B/A and C/A in the non-disky sample that is not captured by the model.

To quantify the non-disky fraction at which the mock observational inference changes significantly from the results for a pure disk ($f_{non-disky} = 0$) sample, we compute the ℓ_2 norm between the mean values of each sample and the pure disk sample. The uncertainty σ_{ℓ_2} is the propagation of errors where we adopt the standard deviation of the MCMC chains as the uncertainty on the estimates of the shape parameters. We show the results of this analysis in Figure 6.11 – we find that the inferred parameters change significantly when the non-disky fraction exceeds $f_{non-disky} = 0.1$. Thus, though it is possible for a sub-population of morphologically distinct galaxies to exist undetected within a generally disky population, this possible fraction is much smaller than the realized $\sim 60\%$ non-disky fraction seen in the FIRE-2 galaxies.

6.7 Appendix: A comparison between direct cumulative and inferred differential shape measurements

As discussed in the main text of this work, the methodology that we use to measure the intrinsic shapes of the FIRE-2 galaxies differs significantly from the methodology used to infer the shape distribution of the observed dwarf sample in Kado-Fong et al. [2020b] (see Section 6.2.2). The observational methodology is fundamentally unsuitable for an analysis of the FIRE-2 dwarfs for three main reasons. First, our sample includes only nine independent initial conditions (i.e. not considering runs with different physics as separate), which is not sufficient to fully sample the underlying distribution of three-dimensional shapes. This runs counter to the assumption of a well-sampled population made in the observational inversion technique of Kado-Fong et al. [2020b];

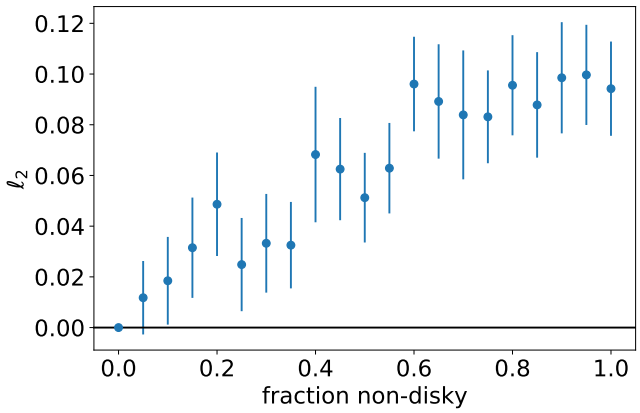

Figure 6.11 The L2-norm, ℓ_2, calculated between the inferred shape parameters of the mock observational sample as a function of the mock sample that is drawn from the non-disky galaxy distribution. The errors reflect the propagation of errors using the standard deviation of the MCMC chains as the uncertainty on the inferred shape parameters.

even though the simulated galaxies may be projected at an unlimited number of viewing angles to generate a smooth distribution in ellipticity, the joint ellipticity distribution of the projected FIRE-2 dwarfs would still be generated from a very low number of unique three-dimensional shapes. Second, as mentioned in the main text, we choose to use cumulative shapes to prevent instability in the shape measurements due to a low number of star particles in the outskirts [see also Allgood et al., 2006]. Because this inference method adds no new additional information, it is likely to suffer from the same instability. Finally, the simulations offer a more direct method to compute the three-dimensional galaxy shapes; using the observational inference method will work to add noise to our measurements, but, as we have detailed above, not contribute significant insight.

Nevertheless, we believe that it is informative to the reader to show that the age-separated, cumulative shape measurements for a single galaxy trace the radial differential measurements one would have derived for that same single galaxy. To do so, we compute 1000 images in the HSC i-band of the relatively massive and disky dwarf m11h (CR+) at a random set of viewing angles distributed isotropically over the unit sphere. We then use the same isophotal fitting technique of Kado-Fong et al. [2020b] to compute the ellipticity distribution of these projected images from

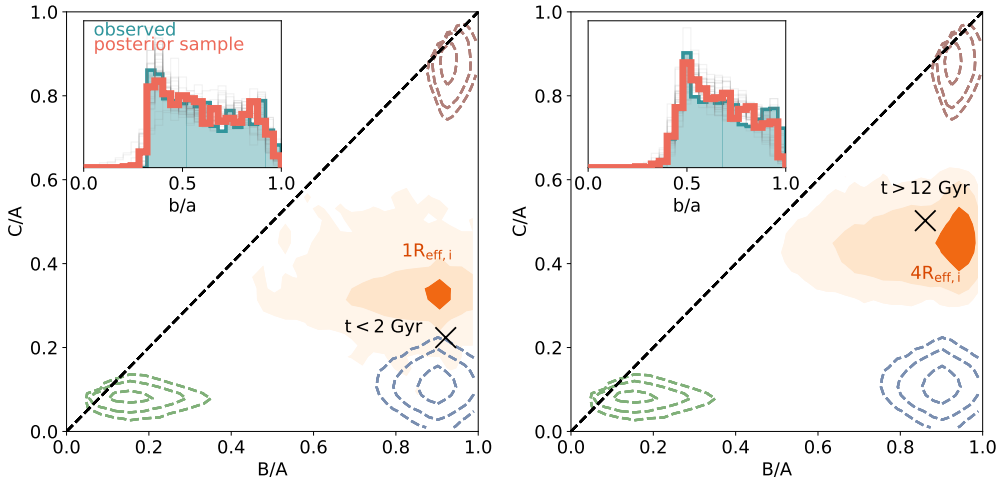

Figure 6.12 *Left:* the results of the mock observational inference for m11h (CR+) at one effective radius. The inset panel shows the distribution of the projected axis ratio b/a for 1000 instances of random projections of the FIRE-2 dwarf in green; the orange curve shows the model output from the inference machinery (600 steps with 300 burn-in; walker convergence is checked manually). Light grey curves show individual draws from the posterior. The main panel shows the same model in intrinsic axis ratio space; the direct cumulative measurement for the young (age < 2 Gyr) star particles is shown by the black X. The colored, dashed contours show results for toy models of a disk (blue), spheroid (red) and prolate (green) galaxy under HSC wide imaging conditions. *Right:* the same, but for differential measurements at four effective radii and cumulative measurements of old (age > 12 Gyr) star particles. In both cases, the differential and cumulative shape measurements well-trace each other.

one to four effective radii. We show the results of this test in Figure 6.12. We find that the age separation approach well-traces the results of the radial inference, though we again emphasize that these approaches are not expected to yield identical results. We thus confirm in a more direct way that the measurements from the age-separated cumulative shapes can be meaningfully compared to the differential shape measurements from Kado-Fong et al. [2020b].

6.8 Appendix: Projection Gallery of Disky and non-Disky Dwarfs

To give the reader a wider sense of the morphologies spanned by the FIRE-2 dwarfs, we show the $z = 0$ projections of young stars, old stars, and HI in the same format as Figure 6.1 for the disky dwarf m11b (Hydro+, no MD) in Figure 6.13 and the non-disky dwarf m11c (Hydro+, no MD) in Figure 6.14.

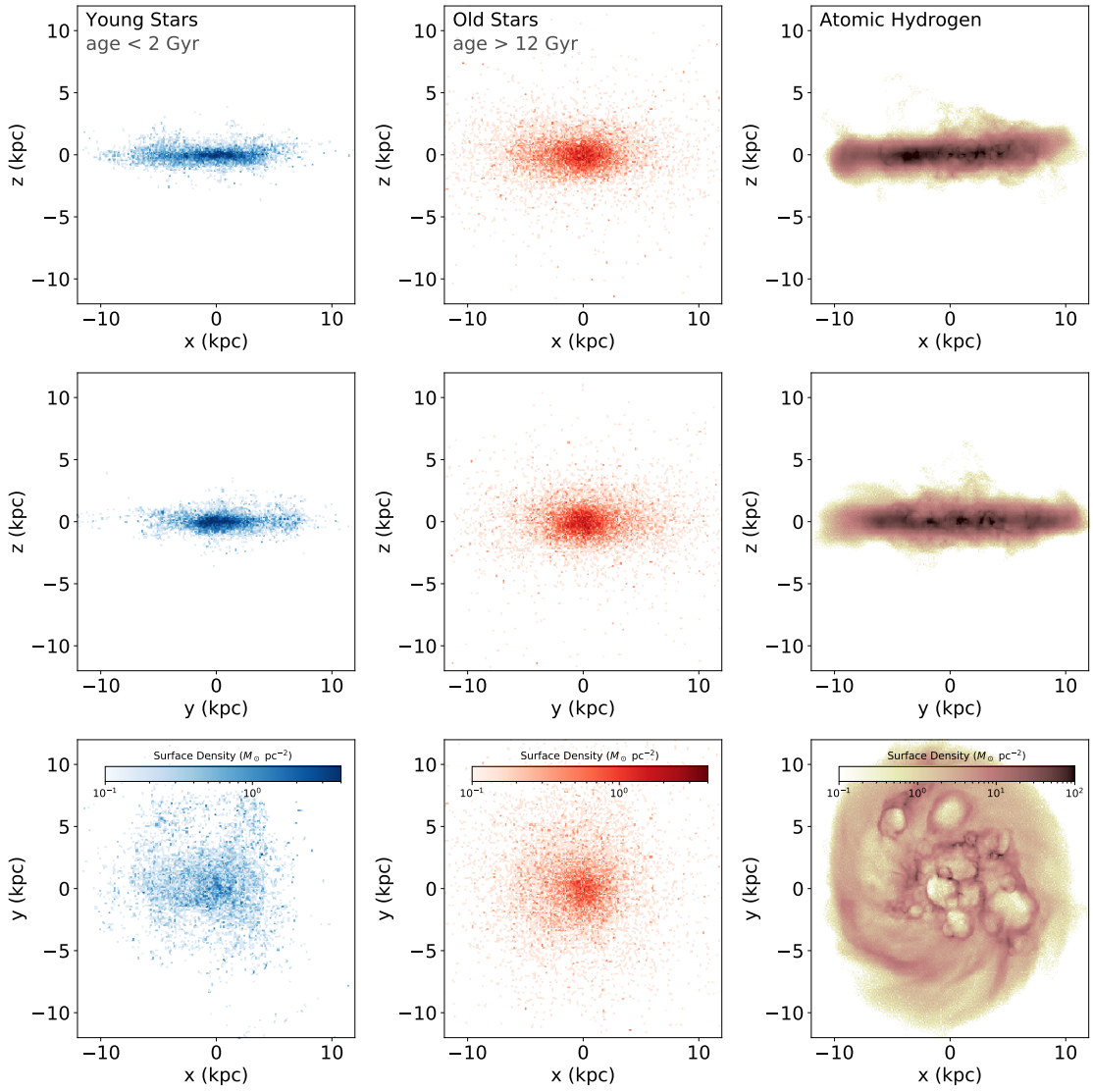

Figure 6.13 Projections of young stars (left), old stars (middle), and HI gas (right) for the disky dwarf m11b (Hydro+, no MD) in the same format as Figure 6.1.

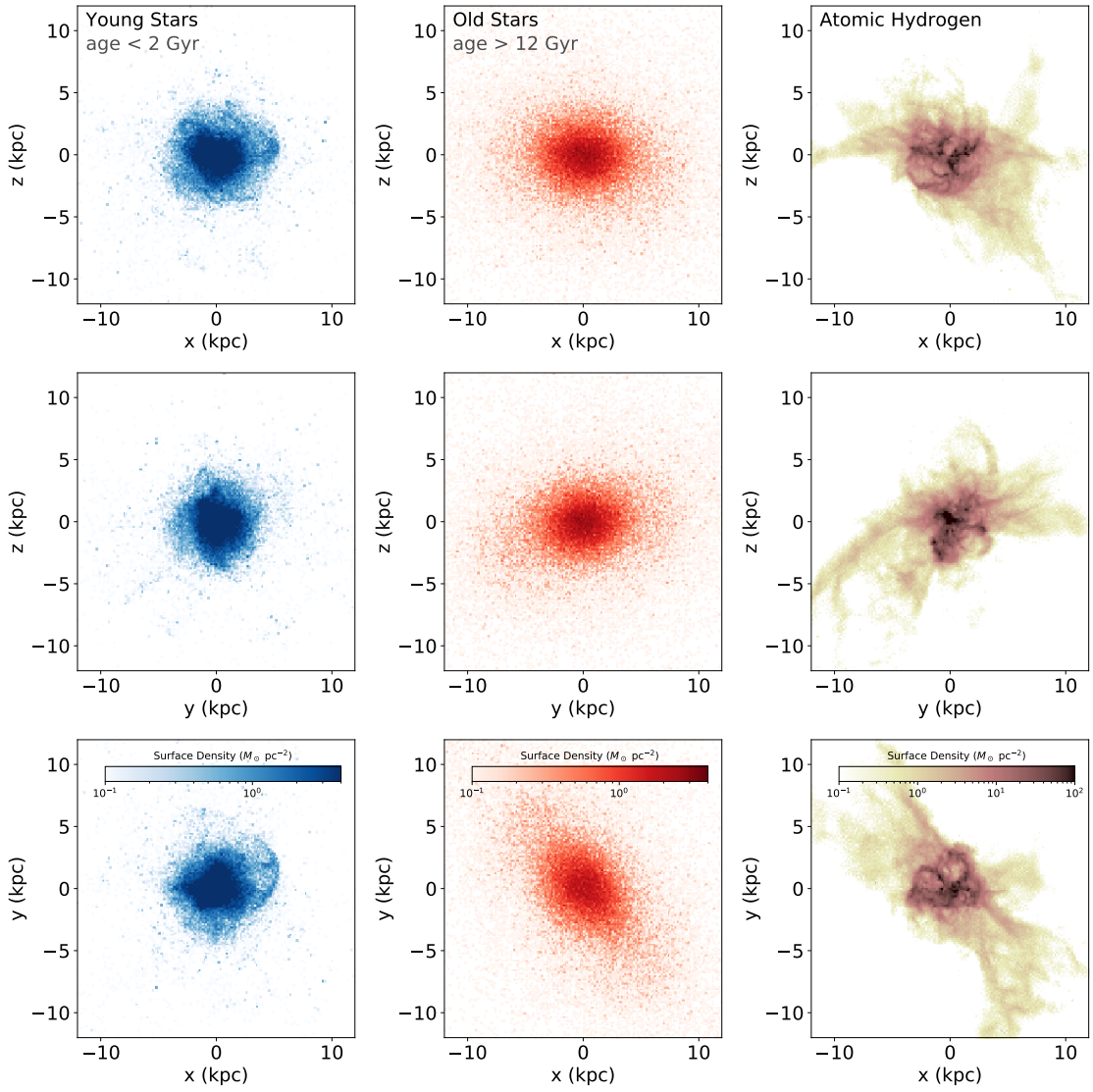

Figure 6.14 Projections of young stars (left), old stars (middle), and HI gas (right) for the non-disky dwarf m11c (Hydro+, no MD) in the same format as Figure 6.1.

Chapter 7

Observational Constraints on the Star Formation Efficiency of Ultra-Diffuse Galaxies

7.1 Introduction

Ultra-diffuse galaxies (UDGs) are dwarf galaxies that are characterized by large stellar sizes ($R_{eff}>$ 1.5 kpc) and low surface brightnesses ($\mu_{0,g} > 24$ mag arcsec^{-2}, though exact definitions vary; see Van Nest et al. 2022 for an overview). These diffuse systems are extreme in two senses: they lie far above the mass-size relation, making them extreme products of galaxy evolution, but they are also extreme environments for star formation due to their low stellar surface densities.

UDGs as extreme products of galaxy evolution is a well-trodden topic both observationally [see, e.g. Sandage and Binggeli, 1984, McGaugh et al., 1995, Dalcanton et al., 1997, van Dokkum et al., 2015, Beasley and Trujillo, 2016a,b, Peng and Lim, 2016, Yagi et al., 2016, Leisman et al., 2017, van Dokkum et al., 2018, Danieli et al., 2019, Janowiecki et al., 2019, van Dokkum et al., 2019, Danieli et al., 2021, Gault et al., 2021] and theoretically [e.g. Amorisco and Loeb, 2016, Di Cintio et al.,

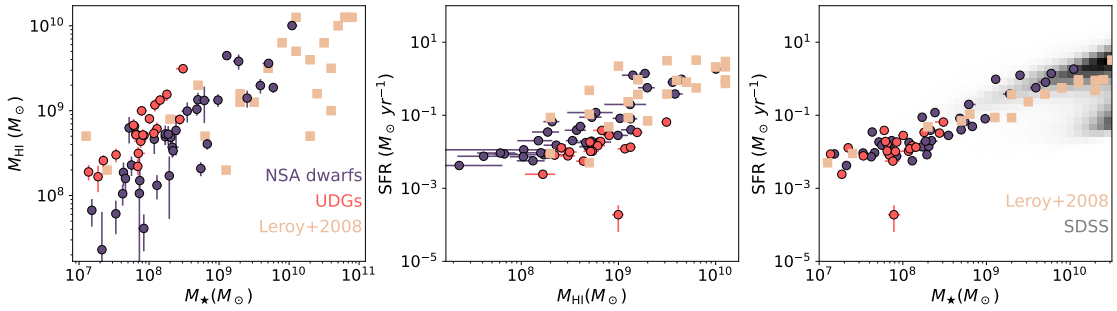

Figure 7.1 A comparison of the integrated properties of the samples derived in this work against the directly measured result of Leroy et al. [2008] (beige points). In all panels, the red points show UDGs and the purple points show NSA dwarfs. From left, we show the relationship between stellar mass and HI mass, the relationship between HI mass and SFR, and the star-forming main sequence (SFMS). In the SFMS panel, we also show the results of the SDSS DR7 MPA-JHU added-value catalogs in greyscale [Kauffmann et al., 2003, Brinchmann et al., 2004, Salim et al., 2007]. We find a good agreement between our results and those from the literature. Although the UDGs have high HI masses for their stellar mass (left panel), they have relatively little SFR for their HI mass (middle panel).

2017, Chan et al., 2018, Greco et al., 2018c,b, Jiang et al., 2019, Liao et al., 2019, Wright et al., 2021, Van Nest et al., 2022, Zaritsky et al., 2022]. However, the formation of the UDG population remains an open question. Several mechanisms have been proposed to form UDGs in the field, including stellar expansion from star formation feedback [El-Badry et al., 2016, Di Cintio et al., 2017, Chan et al., 2018], early mergers that trigger radial expansion of star formation [Wright et al., 2021], and preferential UDG formation in the high-spin tail of the halo distribution [Dalcanton et al., 1997, Liao et al., 2019].

It is observationally challenging to measure robust distances to UDGs due to their low surface brightnesses; as a result, the majority of UDGs with known distances are in clusters or groups. To understand the full breadth of the UDG population, of course, it is necessary to sample this population across a range of environments. Observational works continue to place new constraints on such mechanisms [see, e.g. Leisman et al., 2017, Greco et al., 2018c,b, Janowiecki et al., 2019, Martín-Navarro et al., 2019, Gault et al., 2021, Kado-Fong et al., 2021, E Greene et al., 2022, Villaume et al., 2022], but as of yet there has not been a clear convergence in the literature towards

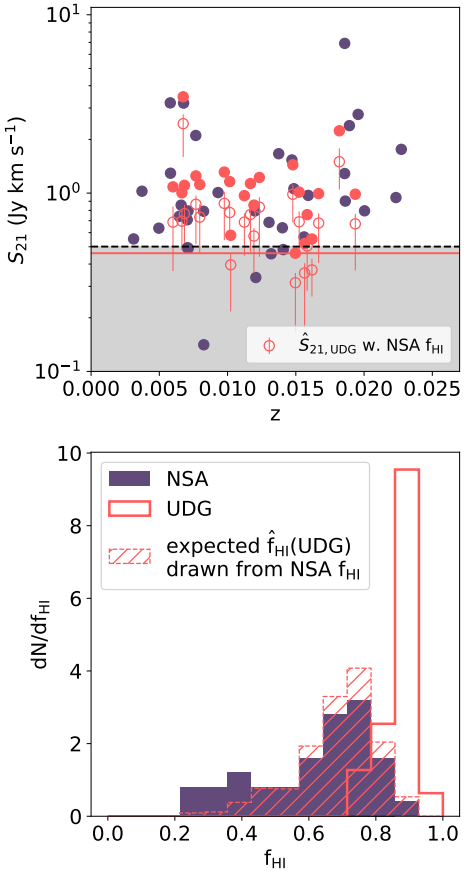

Figure 7.2 *Top:* 21 cm line flux (S_{21}) versus redshift for the NSA (purple) and UDG (red) samples. The nominal ALFALFA flux limit is shown by the dashed black line, while the minimum S_{21} of the UDG sample is shown in red. The unfilled symbols show the expected S_{21} of each of the galaxies in the UDG sample *if* we assume that the distribution over HI fraction of the underlying UDG population is identical to that of the NSA dwarfs. *Bottom:* the distribution over observed HI fractions for the NSA (filled purple histogram) and UDG (unfilled red histogram) samples. The hatched red histogram shows the distribution of HI fractions that we would *expect* to see from the UDG sample if the distribution over HI fractions is identical between the UDG population and NSA sample. We thus conclude that the UDG sample is inconsistent with having the same distribution over f_{HI} as the NSA sample.

one path – of course, it is also not necessarily the case that all UDGs are formed via the same mechanism. Towards this end, there has been a push to use HI to detect and/or measure distances to UDGs [Leisman et al., 2017, Janowiecki et al., 2019, Karunakaran et al., 2020, Gault et al., 2021] – this allows for distance determinations in a sample of UDGs that tend towards low density environments.

It has been shown that although HI-selected UDGs lie on the star-forming main sequence and HI mass-size relation [Gault et al., 2021], they tend to have high HI masses [Leisman et al., 2017] – that is, the UDGs are, in an integrated sense, low in their star formation efficiency as a function of atomic gas, or SFE(HI). This in and of itself is not surprising – it has been demonstrated observationally that stellar mass surface density affects the position of dwarf galaxies with respect to the Kennicutt-

Schmidt relation [Schmidt, 1959, Kennicutt, 1989] in that lower stellar mass surface density dwarfs lie below the main relation [de los Reyes and Kennicutt, 2019]. What has not yet been ascertained, however, is whether the apparently low SFE(HI) of the UDGs is a product of their selection, the distribution of their star formation, or a true physical suppression of SFE(HI).

In order to understand the origin of the low SFE(HI) of the UDGs, we introduce a joint SED fitting method that utilizes the spatial resolution of the optical Hyper Suprime-Cam Subaru Strategic Program (HSC-SSP) and the crucial UV coverage of *GALEX*. We use this method to derive stellar mass and SFR maps of a sample of HI-selected UDGs from Janowiecki et al. [2019] and a reference sample of HI-detected galaxies from the NASA Sloan Atlas [Bradford et al., 2015]. We then use these maps, along with estimated HI radial profiles, to probe the star formation efficiency of these dwarfs down to 500 pc scales. In this work, our main focus will be on characterizing the properties of the HI-selected UDGs with respect to the "normal" NSA dwarf sample through a lens aimed largely at galaxy evolution. In Kado-Fong et al. [2022b] (hereafter Paper II) we will shift our focus towards understanding star formation in HI-rich UDGs, with a particular focus on the role of UDG structure in the pressure-regulated, feedback-modulated model of star formation [Ostriker et al., 2010, Kim et al., 2011, Ostriker and Shetty, 2011, Kim et al., 2013, Kim and Ostriker, 2015, Kim et al., 2017].

7.2 Datasets

Our dwarf sample consists of two main branches: a high surface brightness, "normal" dwarf sample drawn from the HI catalog of Bradford et al. [2015] – hereafter the NSA sample, and an ultra-diffuse galaxy sample with known distances from the HI catalog of Janowiecki et al. [2019]. The UDG sample is selected to have a maximum distance of $d = 120$ Mpc; we enforce the same limit on the NSA sample. We note that in this work we will refer to the "normal" galaxy sample as the NSA sample, as these galaxies were not specifically chosen to exclude low surface brightness galaxies. Rather, their relatively high surface brightnesses are a result of the observational selection which lead to their inclusion in the NSA.

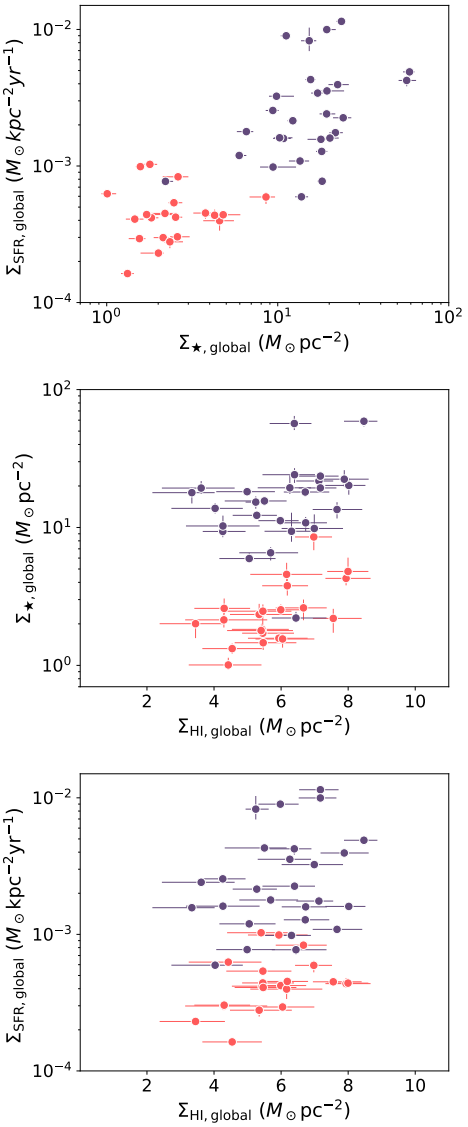

Figure 7.3 Estimates of the SFR, stellar mass, and HI surface densities in a globally averaged sense; i.e., the ratio between the integrated measurement and the isophotal size of the galaxy. UDGs are shown in red and NSA dwarfs in purple for all cases. In this figure, we exclude all NSA dwarfs with stellar masses exceeding $M_\star = 10^9 M_\odot$.

7.2.1 Sample Overview

Here we detail the basic physical properties of the UDG and NSA samples. The sample consists of 58 galaxies at distances less than 120 Mpc; 22 are UDGs from Janowiecki et al. [2019] and 35 are NSA galaxies from Bradford et al. [2015]. All sources are required to have clean 5-band HSC imaging, and all sources have measured HI masses and redshifts due to their selection method. The

sample of Janowiecki et al. [2019] is not explicitly chosen to be in the field (in contrast to Leisman et al. 2017), but they find that the properties of their HI-selected UDGs are largely unchanged by environment. We find that one UDG in our sample, AGC227965, is quenched (SFR$< 10^{-3}$ $M_\odot$ yr^{-1}) due to being a close satellite of MRK1324. We leave this galaxy in our analysis as it still yields a significant HI detection, but note that our discussion of the field UDG formation pathways does not apply to this system.

In Figure 7.1 we show our sample galaxies in stellar mass versus HI mass (left), SFR versus HI mass (center), and the star-forming main sequence (SFMS, right). These results are from a customized SED fitting method that we describe in detail in Section 7.3, but can be thought of as standard SED fitting results for the purposes of the figures in this section. In this figure and all subsequent figures, we show the NSA sample in purple and the UDG sample in red. The NSA sample reaches higher stellar masses and lower HI masses than does the UDG sample; when noted, we compare only NSA galaxies with stellar masses within the observed range of the UDG sample. The results of the Leroy et al. [2008] sample of nearby galaxies and SDSS spectroscopic value-added catalog [Kauffmann et al., 2003, Brinchmann et al., 2004, Salim et al., 2007] are shown in beige and grey, respectively. We see that the UDGs have high HI masses for their stellar masses and that they have low SFRs for their HI masses – conversely, the UDGs lie directly on the SFMS.

A clear question arises from this initial analysis: are the HI-selected UDGs truly drawn from a more HI-rich population than the NSA dwarfs, or are the higher HI masses simply an effect of observational selection? To test this, we consider what our expected distribution of UDG HI fractions, $f_{HI} = M_{HI}/(M_\star + M_{HI})$, would be given the 21cm flux limit of the UDG sample if the f_{HI} distribution of the UDGs were the same as the NSA sample. To put it another way, we ask the following question: if the UDG population had the same distribution of HI fractions as the NSA dwarf sample, what is the distribution of f_{HI} that we would expect to see from an HI-selected sample?

We show the results of this test in Figure 7.2. The top panel shows the observed 21 cm line fluxes in solid points (as always, purple for the NSA sample and red for UDGs), while the unfilled red points show the expected 21 cm flux for each UDG in the sample if the HI fraction were

drawn from the NSA dwarf distribution over f_{HI}. The errorbars in this panel are generated via bootstrap resampling from the NSA distribution. We estimate the detection limit of the UDG sample in two ways: first, from the stated completeness limit of the ALFALFA survey for sources with $1.65 < \log_{10}(W_{50}/[\text{km s}^{-1}]) < 1.7$ [Haynes et al., 2011, black dashed line], and second, from the lowest 21 cm flux of the UDG sample (red solid line). These limits are in good agreement with one another, and we adopt the minimum 21 cm line flux of the UDG sample as our detection limit for this exercise. The bottom panel of Figure 7.2 shows the distribution of observed HI fractions for the NSA (solid purple histogram) and UDG (unfilled red histogram) samples, as well as the UDG sample that we would expect to have detected if the UDG distribution over f_{HI} were the same as that of the NSA sample (hatched dashed red histogram). Indeed, we find that we would expect to detect a significant number of $f_{HI} \lesssim 0.75$ UDGs, should they exist. Rather, the marked HI richness of the UDG sample cannot simply be attributed to observational limits.

We extend this positioning of HI-rich UDGs as unusual star-forming environments by considering a globally averaged stellar mass, HI, and SFR surface density in Figure 7.3. In this figure, we compute $\Sigma_{HI,global}$ using the total HI mass and the total area (as defined by the global elliptical HSC-g aperture, which we will describe Section 7.3). One can immediately see that, as expected from their definition, the UDGs have significantly lower SFR and stellar mass surface densities than the NSA sample. Intriguingly, however, the UDGs do *not* also show signs of lower HI surface densities. Indeed, their HI surface densities span the same range as their spectroscopic counterparts.

The main thrust of this paper will be to root out the physical culprits of this apparently lowered SFE(HI). From globally averaged measurements alone, it is unclear whether the low average star formation rate surface density is a result of a truly lower SFE(HI), or whether the spatial distribution of star formation in UDGs differs from normal dwarfs (e.g. a low globally averaged Σ_{SFR} could arise from an old stellar population that is significantly more extended than the star-forming regions). In order to distinguish between these two scenarios, we must build an SED fitting method to constrain local (500 pc scale) SFR and stellar mass surface densities (Section 7.3) – we will return to this narrative of star formation efficiency in Section 7.5.

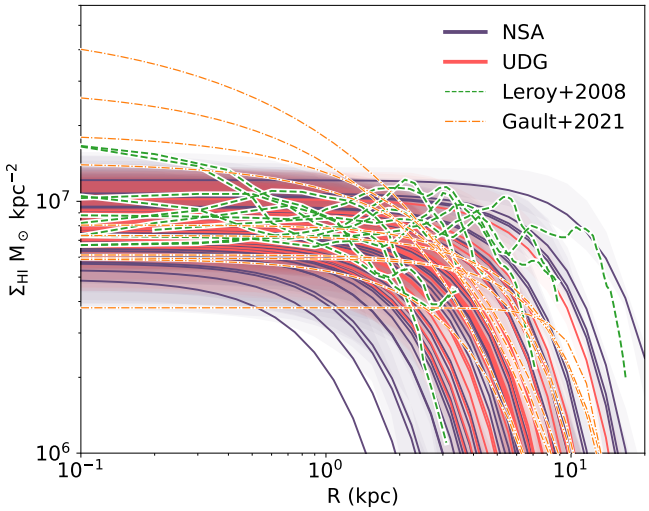

Figure 7.4 A comparison between our estimates of the HI surface density radial profiles for the UDG (red solid curves) and NSA (purple solid curves) samples against spatially resolved HI measurements of dwarfs from the literature. We show the direct radial profiles of Leroy et al. [2008] in green, and Sérsic fits inferred for a sample of HI-rich UDGs from the HI spatial distribution metrics provided by Gault et al. [2021] in orange. We find that our radial profile estimates are in good agreement with these direct literature measurements.

7.2.2 UV-Optical Imaging

HSC-SSP. The HSC-SSP imaging boasts wide spatial coverage, high sensitivity (a point source depth of $i_{\rm HSC} \sim 26$ in its shallowest "Wide" layer), and high spatial resolution (the worst-seeing band, $g_{\rm HSC}$, has an average seeing of 0.77").

For this work, we use the internal data release S21A, which covers 670 deg^2 in 5 optical bands. The HSC-SSP data products include two options for the background subtraction – a local subtraction suited for small, high redshift sources, and a global subtraction suited for nearby galaxies. We use the coadd/bg versions of the co-added HSC images, which uses the "global" background subtraction of the S18A and PDR2 data releases (for an in-depth discussion of the HSC global background subtraction scheme, see Section 4.1 of Aihara et al. 2019 and Li et al. 2021). The data have been shown to reach surface brightness limits of $i_{\rm HSC} \sim 28.5$ mag arcsec^{-2} for radially averaged measurements around a known target [Huang et al., 2018d, Kado-Fong et al., 2020b].

GALEX. To complement the deep and high resolution optical imaging of the HSC imaging, we draw upon archival *GALEX* imaging to measure global UV photometry of our galaxies. We use the package astroquery to query the Barbara A. Mikulski Archive for Space Telescopes (MAST) for *GALEX* FUV and NUV observations that cover the position of each galaxy. We adopt the average *GALEX* PSFs in this work; the FUV and NUV PSFs have full widths at half maximum (FWHM) of 4.2" and 4.9", respectively[1]. We measure our *GALEX* photometry on the background-subtracted intensity maps provided by the *GALEX* pipeline, and estimate uncertainties assuming Poisson noise for the counts.

For targets with more than one *GALEX* archival image, we prefer the data product with a longer total exposure time. Two NSA galaxies (NSA ID 5109 and 30738) do not have FUV imaging; all galaxies have NUV imaging. Of our sample with FUV imaging, 13 galaxies are drawn from the *GALEX* All-Sky Imaging Survey (AIS, $m_{AB} = 20.5$) and 35 from the Medium Imaging Survey [MIS, $m_{AB} = 23.5$, Martin et al., 2005]. 13 are drawn from guest investigator (GI) programs; we make an estimate the depth of the GI programs by measuring the standard deviation of random apertures of apertures the size of the average *GALEX* FWHM. The GI imaging is somewhat deeper than the MIS imaging, with a mean 5σ depth of $m_{AB} = 24.3$. Similarly, 6 galaxies in our sample have NUV AIS imaging, 40 have MIS imaging, and 9 have GI imaging. We repeat the same procedure to estimate the depth of the GI imaging and find a mean 5σ depth of $m_{AB} = 23.4$. We note that the depths estimated here are not used in the analysis, and are simply meant to contextualize the *GALEX* imaging sources for the reader.

7.2.3 HI Measurements

All of the galaxies in the present work have integrated HI measurements from Janowiecki et al. [2019, UDGs] or Bradford et al. [2015, NSA galaxies]. However, resolved HI measurements exist only for a small subset of the UDGs identified by Janowiecki et al. [2019] – 12 from Gault et al. [2021], 3 from Leisman et al. [2017].

To estimate the radial profiles of the HI in our UDG and NSA dwarf samples, we leverage the

[1] http://www.galex.caltech.edu/researcher/techdoc-ch5.html

empirical result that UDGs and "normal" dwarfs are similar in their HI structure – that is, UDGs lie on the HI mass-size relation and have typical average HI surface densities [Gault et al., 2021]. We use this result to estimate Sérsic profile parameters for our sample via a parameter estimation from the spatially resolved measurements of Hunter et al. [2021] (who report Sérsic parameter fits for their sample), as well as the spatially resolved measurements of the UDGs in Gault et al. [2021][2]. We perform a least squares fit to the Sérsic index, n, central surface density, $\Sigma_{0,\mathrm{HI}}$ and effective radius, $\mathrm{R_{eff,HI}}$, of the literature samples as a function of HI mass; only $\mathrm{R_{eff,HI}}$ shows a significant correlation with HI mass (i.e. the HI mass-size relation). This allows us to estimate Sérsic parameters for our galaxies as a function of their HI mass. As these structural measures are not well-constrained, we will account for the uncertainties induced by our estimated HI profiles to demonstrate to the reader that these estimates are indeed reasonable.

First, although the Sérsic profile has three free parameters, our knowledge of the total HI mass allows us to determine the value of one of these parameters given estimates for the other two. We therefore choose to fix the HI central surface density via the analytic solution for the total HI mass of a 1D Sérsic profile, i.e.:

$$\begin{aligned} \mathrm{M_{HI}} &= 2\pi \int_0^\infty \Sigma_{\mathrm{HI}}(R) R dR \\ &= 2\pi \Sigma_0 n ((\frac{1}{h})^{1/n})^{-2n} \Gamma(2n). \end{aligned} \tag{7.1}$$

We thus eliminate the need to estimate Σ_0 from the relations fit to the literature data.

Second, to account for the substantial uncertainty induced by our lack of spatially resolved HI, we include an uncertainty in the parameter estimation of the Sérsic profiles equivalent to the standard deviation of the literature parameter values for reference (literature) galaxies within 0.5 dex of that of the target (NSA/UDG) galaxy in total HI mass. If no galaxies are sufficiently close in HI mass, we increase the tolerance from 0.5 dex to up to 0.9 dex, but note that because the reference sample of Hunter et al. [2021] is systematically lower mass than our sample, this only affects the most massive ($\log_{10} \mathrm{M_{HI}} > 10$) galaxies in our sample. We then estimate the uncertainty

[2]here we solve for the Sérsic parameters of their galaxies using the given measures of HI structure

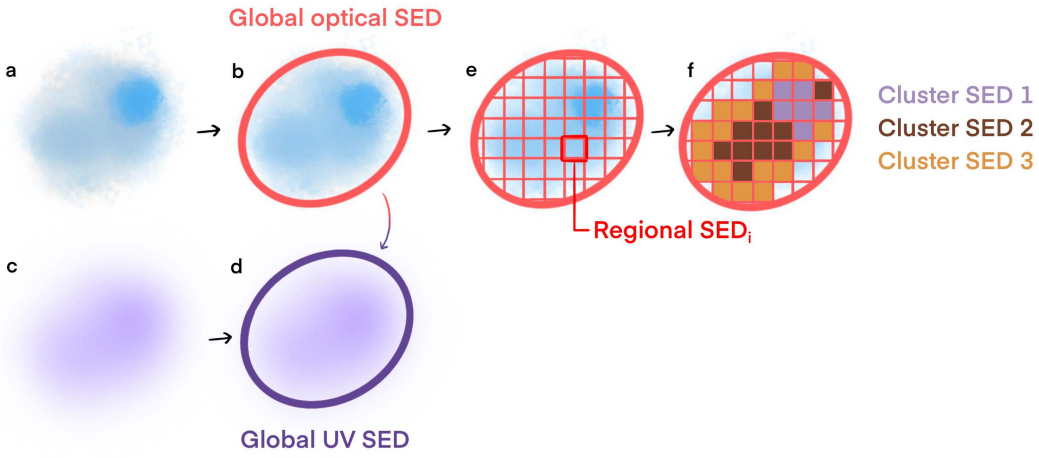

Figure 7.5 A schematic layout of the fitting technique used in this work. At left, we represent the high-resolution optical data and low-resolution UV data (panels *a* and *c*, respectively). Panels *b* and *d* represent the global fit between the optical and UV data; in this step, the apertures are matched between the optical and UV data. Panel *e* shows the spatial division of the optical data into regions in which regional SEDs are measured. Panel *f* shows the clustering of these spatial regions into three representative clusters; these cluster SEDs will be fit jointly with the global UV photometry (panel *d*).

on the radial HI surface density profile via Monte Carlo resampling assuming that the uncertainties are well-describe by normal distributions.

The resulting HI surface density profiles are shown in Figure 7.4; as above, red curves indicate UDGs and purple curves indicate NSA galaxies. The shaded regions span the 16th to 84th percentiles of the Monte Carlo simulation result for each galaxy. The directly measured HI profiles of Leroy et al. [2008] are shown in green, while the Sérsic profiles inferred from the structural measurements of Gault et al. [2021] are shown in orange. We find that our inferred profiles are in good agreement with the shape, normalization, and scatter of the directly measured profiles, with the exception of one UDG (AGC238764, which is not a part of our sample) that has an anomalously high Sérsic index ($n = 1.98$; almost all dwarfs in this mass range are characterized with sub-exponential Sérsic indices, see Hunter et al. 2021).

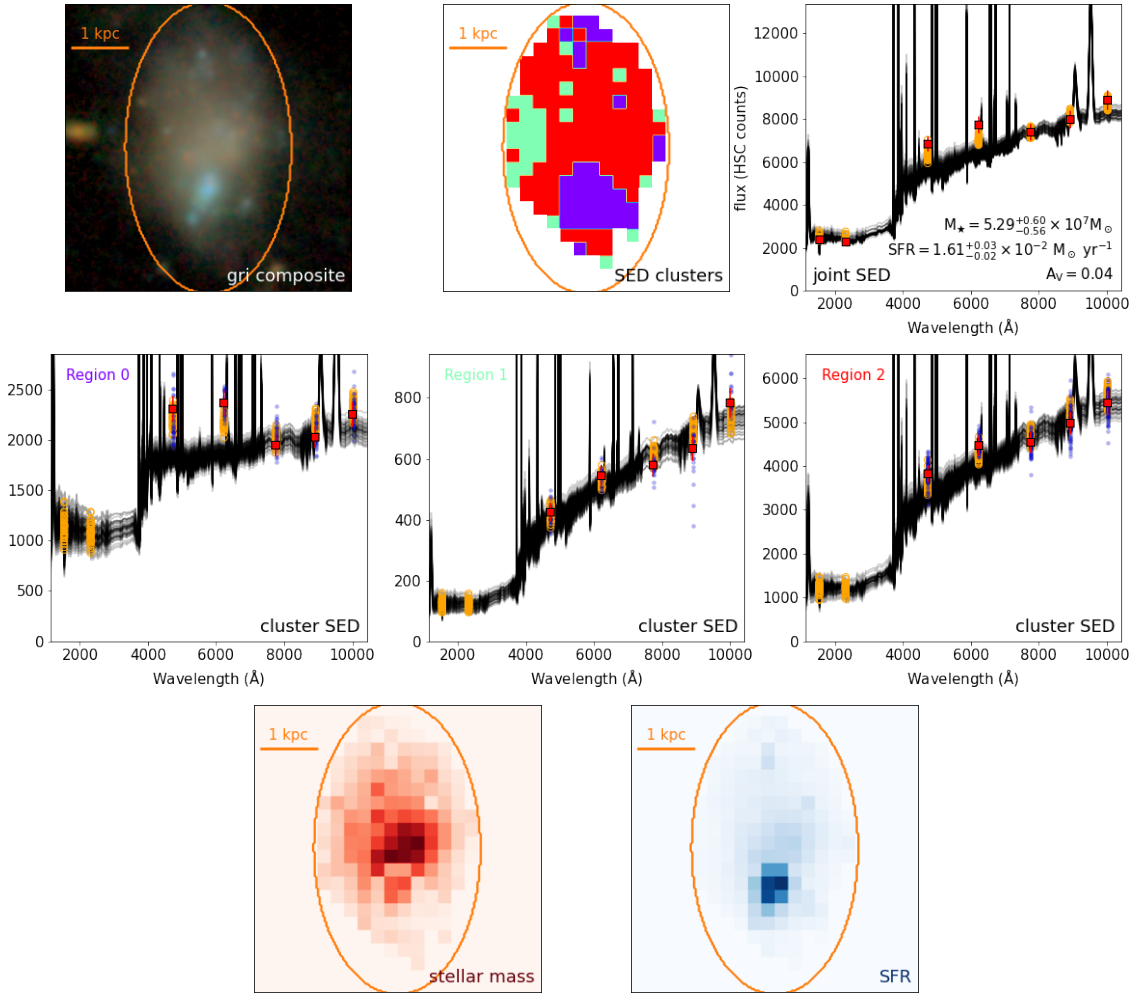

Figure 7.6 An example of the fitting process for one of the NSA galaxies (NSA ID 5449). *Top row:* from left, the HSC *gri*-composite image, the SED cluster map (analogous to panel *f* of Figure 7.5), and the joint UV-optical SED fit. The joint model SED is the result of fitting the spatially resolved (cluster) optical photometry and global UV photometry. The black curves show the model spectra, while the orange points show the model photometry for each filter. The red points show the global UV-optical photometry. The model fitting and figure fluxes are computed as HSC counts. *Middle row:* optical-only results for the individual cluster SEDs. The color of the title text corresponds to the color of the region in the top middle panel; the format is equivalent to the joint SED fit (top right), with the addition of the SEDs measured in individual spatial regions as blue points. *Bottom row:* the resultant stellar mass (left) and SFR (right) maps.

7.3 SED Fitting

The key technical challenge of this work is inferring the star formation and stellar mass properties of the dwarf sample at sub-galactic scales. We accomplish this by modeling the high spatial resolution HSC optical data in conjunction with the UV *GALEX* measurements to constrain star formation activity in a consistent way with the UV data.

The novelty of our approach is to leverage both the high spatial resolution of HSC and the expanded wavelength coverage of *GALEX* to infer local star formation surface density properties of our dwarfs via a joint fit to localized optical photometry and global UV photometry. Here, we detail the fitting process employed in this work.

7.3.1 Stellar Population Models

We use the Flexible Stellar Population Synthesis (FSPS) models [Conroy et al., 2009b, Conroy and Gunn, 2010] with a fixed stellar and gas-phase metallicity of $Z = 0.004$ along with a Kroupa [2001] initial mass function to generate our synthetic spectra. The library includes nebular emission, which may contribute significantly to the broadband flux of the dwarf galaxies in our sample. We adopt an exponentially declining star formation history

$$\mathrm{SFR}(t) \propto e^{-(t-t_0)/\tau}; \tag{7.2}$$

We choose this relatively rigid star formation history (two free parameters, the onset of star formation t_0 and the timescale of decay τ) in order to achieve reasonable computation times when the number of regions to be fit is high. Such a rigid choice of the SFH functional form has the potential to bias SFH recovery, and so we note that the main goal of our analysis is to diagnose the relative change in star formation surface density and star formation efficiency between normal, high surface brightness dwarfs and ultra diffuse galaxies, not to provide comprehensive stellar population synthesis properties for the UDGs. We will return to this point more comprehensively in Section 7.4 when we consider validation tests for this method.

The composite stellar population (CSP) model library spans ages between 2 Myr and 12 Gyr

and timescales (τ) between 0.3 Gyr and 10 Gyr. Each axis consists of 50 logarithmically spaced values. We pre-compute both the UV-optical spectra and the fluxes through the *GALEX* and HSC bands for each model in the library. During fitting, we linearly interpolate between pre-computed library fluxes to obtain the predicted *GALEX* and HSC fluxes for arbitrary choices of t_0 and τ. Because we use pre-computed library fluxes at a fixed distance of 10 Mpc, this induces a small k-correction error in the galaxy sample. However, the most distant galaxies in our sample are at 120 Mpc, and so the k-correction error induced is negligible.

7.3.2 Defining Global, Regional, and Cluster SEDs

The first step to executing a joint fit between the optical and UV photometry is to establish the apertures in which we measure the optical and UV photometry. To obtain consistent optical photometry, we PSF match the HSC imaging with the worst seeing. To do so, we use the Fourier transform-based implementation of photutils with a cosine bell window function ($\alpha = 3$) to compute matching kernels between the other optical bands and the band to which we will match the PSF. We model the PSFs measured by the HSC pipeline (which produces PSF postage stamps with spatial extents of about 7") as two-dimensional Moffat functions. We choose to simplify the PSF model to Moffat functions in order to prevent the emergence of imaging artifacts during the matching process caused by high frequency features in the original pipeline-produced PSFs. We additionally correct for galactic extinction in all UV and optical photometry presented in this work using the measurements of Schlafly and Finkbeiner [2011] via the associated online service [IRSA, 2022].[3]

We then define the global aperture of the galaxy using sep, a python implementation of the segmentation algorithm used in SExtractor [Bertin and Arnouts, 1996]. In all cases, we use the HSC-g band as the detection band, with a detection threshold of 5σ over the variance image supplied by the HSC pipeline. We define the elliptical global aperture as

$$c_{xx}(x-\bar{x})^2 + c_{yy}(y-\bar{y})^2 + c_{xy}(x-\bar{x})(y-\bar{y}) = 3^2, \tag{7.3}$$

[3]Galactic extinction measurements were accessed via https://irsa.ipac.caltech.edu/applications/DUST/

where $\bar{x}$ and $\bar{y}$ are the light-weighted central coordinates of the galaxy and c_{xx}, c_{yy}, and c_{xy} are the standard SExtractor ellipse parameters

$$\begin{aligned} c_{xx} &= \frac{\cos^2\theta}{a^2} + \frac{\sin^2\theta}{b^2} \\ c_{yy} &= \frac{\sin^2\theta}{a^2} + \frac{\cos^2\theta}{b^2} \\ c_{xy} &= 2\cos\theta\sin\theta(\frac{1}{a^2} - \frac{1}{b^2}), \end{aligned} \tag{7.4}$$

where a and b are the semi-major and semi-minor axes, respectively, and θ is the position angle of the galaxy measured counterclockwise from the horizontal (in image coordinates). This global aperture step is shown visually in step b of Figure 7.5 – the global aperture defined in step b using the optical data is then applied to the UV imaging to derive the global UV SED (step d). We choose not to PSF match the optical data to the UV data to maintain the spatial resolution of the optical data in order to hold the input images consistent between the global and spatially resolved SED fitting. If we did perform PSF matching to the *GALEX* imaging to compute the global optical photometry, we have verified that the changes would be negligible, with a mean fractional deviation in flux of 0.03 and a standard deviation of -0.02.

Next, to define the regional boundaries for the optical photometry, we lay a grid of fixed size over the cutout image, as shown in step e of Figure 7.5. The box length of this grid is set to be no less than twice the FWHM of the PSF-matched images, and is increased iteratively until the median SNR of the SEDs measured in the regions is at least 3. To remove regions where a reliable SED cannot be measured at the required spatial scales, we remove the bottom 5% faintest regions. We also mask regions with $(g-i) > 0.8$ and generate additional masks for the UDGs, whose diffuse structure and large on-sky sizes make standard deblending routines unreliable. We verify that this pruning does not affect the total inferred mass and star formation rate in Section 7.4.

Because the size of the regions is small compared to the size of the galaxy, it is unsurprising to note that many of the regional SEDs are identical to each other to within their photometric errors. To decrease the number of parameters to fit, and to increase the SNR of the SEDs that we fit, we group the regions (step e) into clusters of similar SEDs (step f). We group the regions into clusters

using K-means clustering, initially with 3 clusters. If any cluster has a SNR< 10, we combine the low-SNR cluster with the closest high-SNR cluster (here defining closeness by the ℓ^2 norm[4] over the optical SEDs). Next, we must verify that the cluster SEDs adequately represent their input regional SEDs. We use the metric $z^j_{b,i} = |f_{b,i} - \bar{f}^j_b|/\sqrt{\sigma^2_{f_{b,i}} + \sigma^2_{\bar{f}^j_b}}$, where $f_{b,i}$ is the flux in band b measured in region i, while $\bar{f}^j_b$ is the flux in band b measured in cluster j. $\sigma^2_{f_{b,i}}$ and $\sigma^2_{\bar{f}^j_b}$ refer to the uncertainty on the respective flux measurement. We impose the condition $z_{b,i} < 2$ for all bands $b \in \{\mathrm{g}, \mathrm{r}, \mathrm{i}, \mathrm{z}, \mathrm{y}\}$ and all regions i assigned to cluster j for each cluster in the galaxy. If the clustering result fails this verification, we rerun the clustering process with an additional cluster at the K-means step. We allow up to five clusters, at which point the clustering assignment is accepted regardless of verification status. In practice, only one galaxy (the UDG AGC223246) is fit with the maximum five clusters.

7.3.3 SED Fitting

With our PSF-matched photometry and apertures in hand, we are now ready to begin the SED fitting. For all of our fitting, we use the Markov Chain Monte Carlo implementation of emcee [Foreman-Mackey et al., 2013]. We adopt a flat prior over positive values for the amplitude of each cluster SED, a flat prior between 0 and 13.6 Gyr for τ (see Equation 7.3.1), and a log-normal prior over A_V distributed as $\log_{10}(A_V) \sim \mathcal{N}(0, 0.1)$. In our joint fitting step, where multiple amplitudes and τ values are being inferred, the prior is the same for each individual parameter.

We first perform a global SED fit using both the optical and UV photometry to constrain the reddening, A_V, and to provide an estimate of the total stellar mass and star formation rate. We adopt a Gaussian likelihood, defined as:

$$\log \mathcal{L} \propto -\frac{1}{2} \sum_b^M \frac{(f_b - \hat{f}_b)^2}{\sigma^2_{f_b}} + \log(\sigma^2_{f_b}) \tag{7.5}$$

where f_b refers to the flux of the bth band out of M bands ($M = 7$ for our fiducial case), $\hat{f}_b$ is the

[4]Where the ℓ^2-norm is the difference between the SED flux and reference flux $\sqrt{\sum_k^K |f_k - f_{\mathrm{ref}}|^2}$ over the K optical bands

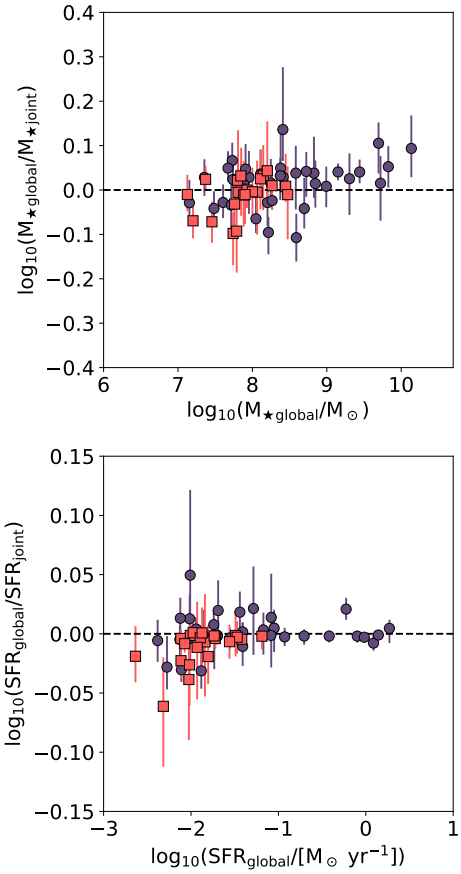

Figure 7.7 *Top:* a comparison between the best-fit stellar masses of the NSA (purple) and UDG (red) samples using the global photometry (y-axis) and the spatially-resolved optical photometry (x-axis). *Bottom:* the same as above, but for SFR.

predicted model flux, and σ_{f_b} is the uncertainty in the $b^{\rm th}$ band. We measure σ_{f_b} directly from the variance images of HSC-SSP added in quadrature to an extra uncertainty of $0.05 f_b$. In this step we run emcee for 1500 iterations with 32 walkers, discarding the first 400 steps. The only parameter from this fit that survives as a final result is the reddening, which is used to the joint fit as a fixed parameter. We find no difference in the A_V estimated for the UDGs and the NSA galaxies at $M_\star < 10^9 M_\odot$: the $50^{\rm th}$ ($16^{\rm th}$ and $84^{\rm th}$) percentile of the A_V distribution is $A_V = 0.17$ (0.04, 0.37) for the UDGs and $A_V = 0.18$ (0.05, 0.38) for the NSA dwarfs at $M_\star < 10^9 M_\odot$. Unsurprisingly, the NSA galaxies at higher stellar mass have systematically higher estimated reddening – $A_V = 0.67$ (0.55, 0.99).

Next, we compute the flux in the N SED clusters defined as above. At this stage, the model

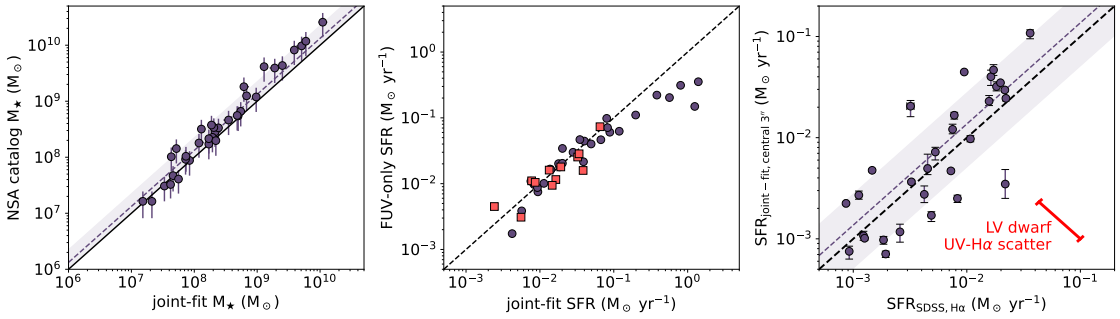

Figure 7.8 *Left:* a comparison between the stellar masses of the galaxies in this work (x-axis) and their catalog NSA stellar masses. The dashed line and shaded regions show the median, and range between the 16$^{\rm th}$ and 84$^{\rm th}$ percentiles of the deviation $\log_{10}(\mathrm{M}_\star/\mathrm{M}_\odot) - \log_{10}(\mathrm{M}_{\star,\mathrm{NSA}}/\mathrm{M}_\odot)$. *Middle:* the same, but for SED fitting-derived SFRs and FUV-only SFRs as computed from the catalog *GALEX* measurements using the SFR(FUV) prescription of Kennicutt [1998]. *Right:* a comparison between SFRs derived from the Hα fluxes measured from SDSS 3" fiber fibers (x-axis) and the total SFR within the central 3" of our SED fits (y-axis, red). The dashed black line denotes a 1:1 relation. As in the left panel, the dashed purple line and shaded purple regions show the median, and range between the 16$^{\rm th}$ and 84$^{\rm th}$ percentiles. SFRs derived from Hα measure star formation over a shorter timescale ($\sim$ 10 Myr) than our SED fits (100 Myr), and some physical scatter is expected as a result; we show the standard deviation (in logarithmic space) of the difference between Hα-derived and FUV-derived SFRs for a set of Local Volume dwarfs from Karachentsev et al. [2021] as a visual aid to the reader in gauging the scatter.

consists of a set of N models across M bands. The likelihood is computed as follows:

$$\begin{aligned}\log \mathcal{L} \propto &-\frac{1}{2}\sum_{i\in UV}\frac{(\sum_j^N f_{i,j} - \sum_j^N \hat{f}_{i,j})^2}{\sum_j^N \sigma^2_{f_{i,j}}} + \log(\sum_j^N \sigma^2_{f_{i,j}}) \\ &+ -\frac{1}{2}\sum_j^N \sum_{i\in Opt}\frac{(f_{i,j} - \hat{f}_{i,j})^2}{\sigma^2_{f_{i,j}}} + \log(\sigma^2_{f_{i,j}}),\end{aligned} \tag{7.6}$$

where i refers to the bandpass index and j refers to the cluster index. In other words, we retain a Gaussian likelihood wherein the UV bands (FUV and NUV) are compared against the sum of the regional models, whereas the optical bands (*Opt* in Equation 7.6; g,r,i,z, and y) are compared against the appropriate regional models. In this step, the walkers are initialized with the positions drawn from the posterior of the global SED fit; the amplitude of each cluster SED is additionally

multiplied by the mean ratio between the flux in the cluster SED and the global SED over the optical bands. In this step, we run emcee for 20000 iterations with at least 32 or $2N + 1$ walkers, discarding the first 5000 steps.

From this process we estimate the total stellar mass and star formation rate for each cluster SED. We then convert these to stellar mass and star formation rate surface densities assigned to each regional SED by multiplying by the ratio of the flux in the regional SED and the flux in its corresponding cluster SED, and dividing by the physical area subtended by the region. We opt to not implement inclination corrections for our sample because the stellar disks are not thin and because empirical results suggest that there is significant variation in the three-dimensional shapes and thicknesses of the dwarf stellar disks [Kado-Fong et al., 2020b, Carlsten et al., 2021]; however, we compute inclination estimates using the mean disk height-to-length ratio following Holmberg [1958] and find that our results would not qualitatively change if we did implement such an inclination correction. Nevertheless, because our sample is ill-matched to the assumptions of a thin, axisymmetric disk, we believe that the inclination correction has a strong potential to bias our measurements.

We show an example of the fitting procedure for the galaxy NSA 5449 in Figure 7.6. We also show an abbreviated gallery of fitting results in Section 7.8 for a set of galaxies that span the morphologies seen in the NSA and UDG samples.

7.4 Method Validation

In order to apply the framework constructed in the previous section to our galaxy samples, we must first take the necessary step of validating that our method is able to accurately deliver the quantities of interest to this study – namely, maps of the star formation and stellar mass surface densities down to the spatial resolution of HSC.

An equally important step is to lay out the quantities that we are *not* attempting to constrain with this modeling. The age, stellar metallicity, and detailed (flexible) star formation history of the galaxies are all parameters that may be estimated from SED fitting. However, it has been

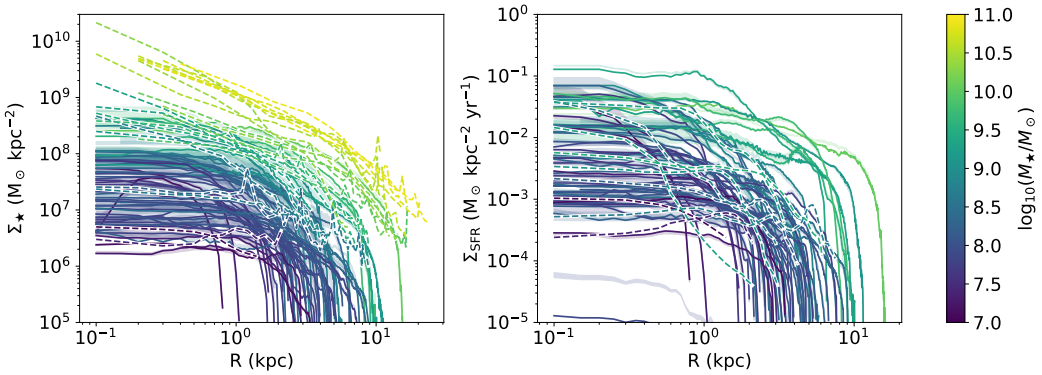

Figure 7.9 A comparison between radial profiles in stellar mass surface density (left) and star formation rate surface density (right) from our SED fitting method (solid curves) as compared to direct measurements from [Leroy et al., 2008, dashed curves]. The color of the curves show the integrated stellar mass of the galaxy in all cases. We find that there is good agreement between our radial profiles and the directly measured profiles in both amplitude and extent.

shown that the exponentially declining tau model is an imperfect model of star formation histories at large, both due to its overall rigidity and that it, by definition, ties early and late star formation [Simha et al., 2014, Carnall et al., 2019]. Thus, we stress that our main goals, and the subjects of our verification tests, will be the estimation of the star formation rate and stellar mass surface densities, and not a detailed interrogation of the star formation history and enrichment of the galaxies in our sample.

7.4.1 Intra-sample Comparisons

We first consider an internal comparison between the star formation rate and stellar masses measured from the global UV+optical SED fitting (step b and step d of Figure 7.5) and the integrated star formation rate and stellar masses obtained by summing the properties inferred from the cluster SED fitting (step f). In Figure 7.7, we show the integrated estimates of stellar mass (top) and star formation rate (bottom) for the UDGs (red) and NSA galaxies (purple). In all cases, we find good internal consistency between the initial SED fit on the global photometry and the final model SED of the spatially resolved method.

We additionally compare the stellar mass and SFR estimates obtained from our spatially resolved SED fitting method to the catalog NSA stellar masses and FUV-only SFRs in Figure 7.8. The FUV-only SFRs are computed from the catalog *GALEX* measurements using the prescription of Kennicutt [1998], i.e.

$$\mathrm{SFR}(L_{FUV}) = 1.4 \times 10^{-28} \frac{L_{FUV}}{\mathrm{erg\ s^{-1}\ Hz}}. \tag{7.7}$$

Both the catalog stellar mass estimates and the FUV-only SFRs are also in good agreement with the results of our spatially resolved fit.

Although we lack truly spatially-resolved spectroscopic measurements for the galaxies in our sample, we do have access to one quasi-resolved measurement for the NSA sample – the SDSS 3" fiber spectra. Because our galaxies exceed the SDSS fiber size, the SDSS spectroscopic measurements do contain information about the spatial distribution of star formation within the galaxy, albeit in a very limited capacity. In the right panel of Figure 7.8 we show a comparison between SFRs derived from the SDSS fiber spectroscopy of the NSA galaxies and SFRs we compute by integrating our SFR maps over SDSS-like apertures. The SDSS spectroscopy we reference are 3" diameter fiber spectra; we use the NSA catalog line fluxes in this comparison. In particular, we use the catalog Hα flux to compute Hα-derived star formation rates within the SDSS aperture following Calzetti [2013] with a Kroupa [2001] IMF:

$$\mathrm{SFR}(L_{H\alpha}) = 5.5 \times 10^{-42} \frac{L_{H\alpha}}{\mathrm{erg\ s^{-1}}}. \tag{7.8}$$

Although the 100 Myr averaged SFRs we produce via our SED fitting are not completely analogous to the Hα SFRs derived from the SDSS spectra (which probe timescales closer to $\lesssim$ 10 Myr), we expect that the two should be well-correlated. Indeed, we find that the star formation rates we compute from the central three arcseconds of our star formation rate maps are in good agreement with the SDSS spectroscopic measurements, with a scatter on the same order as the physical variation between UV and Hα SFRs measured from Local Volume dwarfs [Karachentsev et al., 2021, red line in right panel].

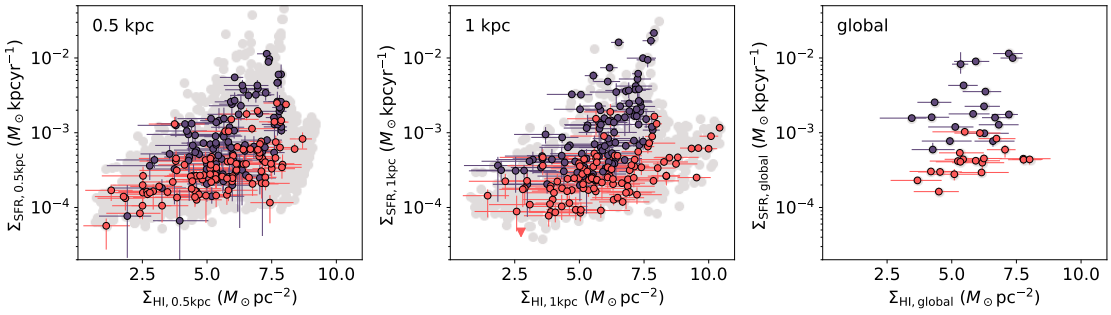

Figure 7.10 A comparison between HI surface density estimates and SFR surface density measurements averaged over 500 pc, 1 kpc, and global scales. In all panels, we only show NSA galaxies that are within the stellar mass range of the UDG sample (i.e. $M_\star < 3 \times 10^8$ $M_\odot$). For visual clarify, we show a random subset of (at most) 70 points for each sample with individual errorbars and colored by sample source; we show the full sample as the underlying grey scatter. Here, we demonstrate that the low SFE(HI) that characterizes the globally averaged properties of the UDGs persists down to sub-kpc scales.

7.4.2 Inter-sample Comparisons to the Literature

We also find good agreement between our results and literature measures of the integrated stellar mass, SFR, and A_V for the two low surface brightness galaxies presented in Greco et al. [2018b], though we do not include these galaxies in this work because they lack HI measurements.

Finally, we compare to spatially resolved measurements of stellar mass, SFR, and HI in nearby samples of dwarfs from the literature. In Figure 7.9, we show a comparison between radial profiles of stellar mass surface density (left) and SFR surface density (right) as derived from our SED fitting method as compared to the directly measured results of Leroy et al. [2008]. Our results are shown as solid curves, the Leroy et al. [2008] profiles are shown as dashed curves; all curves are colored by total stellar mass. Encouragingly, we find good agreement in both the shape and normalization between our inferred radial profiles and the directly measured results of Leroy et al. [2008], indicating that our method is able to recover not just the total amount of stellar mass and SFR, but the distribution of these quantities.

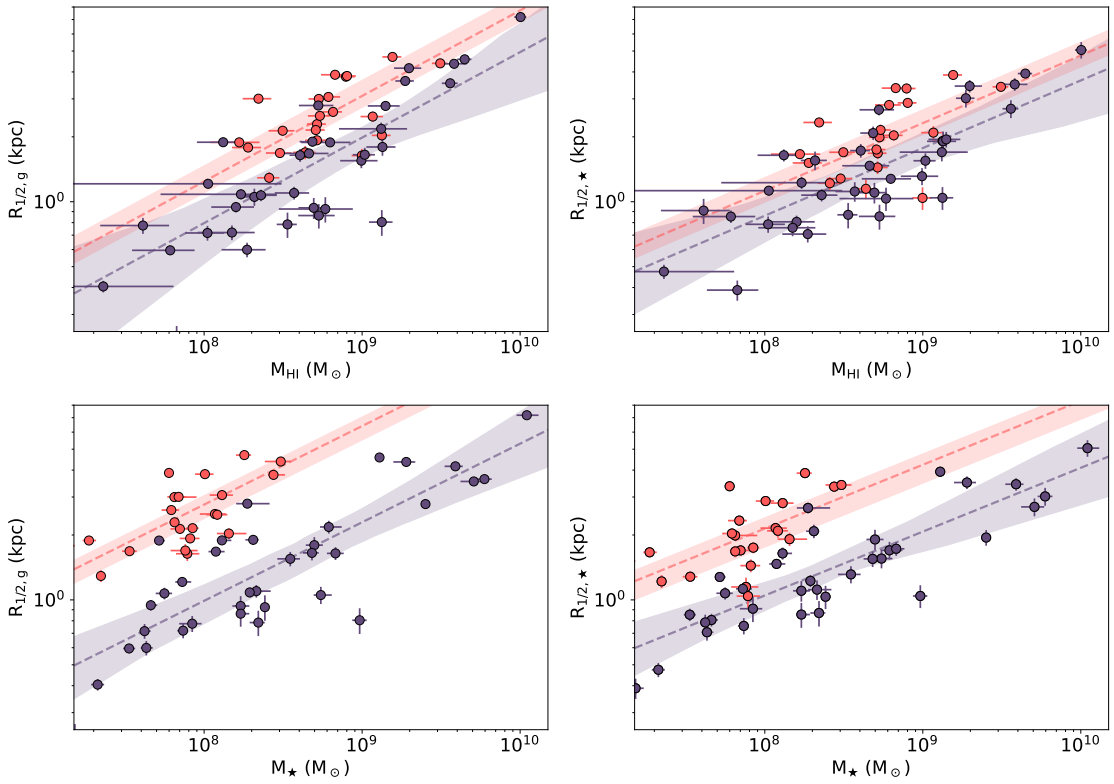

Figure 7.11 A comparison between various measures of galaxy mass and galaxy size; the top row shows size as a function of HI mass, while the bottom row shows size as a function of stellar mass. The left column shows size as measured by the HSC-g band half-light radius, while the right column shows size as measured by the half stellar mass radius. In each panel, the purple dashed line shows the least squares power law fit to the NSA galaxies. The red dashed line shows the least squares fit to the UDG sample when the index of the power law is held fixed to that of the NSA dwarf fit. The shaded regions span the 16th to 84th percentiles as estimated from bootstrap resampling. As one expects, the UDG sample is large in size for their stellar masses. However, their half-stellar mass radii are unremarkable for their HI masses.

7.5 Results

With our methodology in hand, we may now return our focus to the physical question at hand. In Section 7.2.1, we demonstrated that although the UDGs have low globally averaged stellar mass and SFR surface densities, their HI surface densities are comparable to those of the NSA galaxies. Now, we can consider the cause of the low SFE(HI) of the UDGs – and in particular whether this

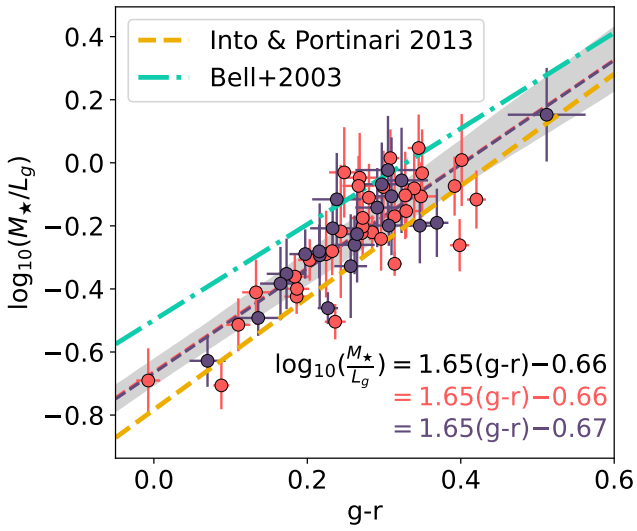

Figure 7.12 Optical color versus stellar mass-to-light ratios in the HSC-g band computed for our UDG (red) and NSA (purple) samples. We find no significant difference in the color-mass relation between the two samples, and additionally find the samples to be reasonably well-described by color-mass relations from the literature (Into and Portinari 2013 as the dashed line, Bell et al. 2003 as the dotted line).

inefficiency persists to sub-kpc scales – as well as the relationship between UDG structure and HI content.

7.5.1 The Efficiency and Distribution of Star Formation in UDGs

In the top row f Figure 7.10, we show the relation between the estimated $\Sigma_{\rm HI}$ and $\Sigma_{\rm SFR}$ at 500 pc, 1 kpc, and global scales from left to right (we note that, for reasons of visual continuity, the bottom right panel of Figure 7.10 is identical in content to the bottom panel of Figure 7.3). We compute 1 kpc and 500 pc average stellar mass surface density and SFR surface density maps by placing a grid of length 1 kpc or 500 pc (at the distance of the galaxy) over the stellar mass and SFR maps produced via SED fitting. We do not compute average quantities over length scales less than the regional SED box size for each galaxy. For the 1 kpc and 500 pc regions, the HI surface density is estimated using the central position of the region and the Sérsic profile estimated for the

galaxy as described in Section 7.2.3. From this figure, the reader may immediately notice that the shift in $\Sigma_{\rm SFR}$ persists down to 500 pc; there are no regions in the area-weighted census of the UDG distribution of SFR surface density that match the vigorously star-forming SFR surface densities observed in the NSA dwarfs.

The persistence of the discrepancy of star formation activity outcomes as a function of HI surface density indicates that it is not simply a matter of the distribution of star formation that drives the apparently low star formation efficiency (as a function of atomic gas) in the UDG sample. Rather, it appears to be a generic property of star formation in our sample of UDGs. The question, then, of whether a more comprehensive understanding of star formation can explain this low star formation efficiency will naturally arise to the reader. This question is the central topic of Paper II, in which we will examine the impact of the UDGs' peculiar stellar structure on their star formation activity within the framework of pressure-regulated, feedback-modulated star formation [Ostriker et al., 2010, Kim et al., 2011, Ostriker and Shetty, 2011, Kim et al., 2013, Kim and Ostriker, 2015, Kim et al., 2017].

We note that the minimum region size over which we can measure $\Sigma_{\rm SFR}$ and $\Sigma_\star$ is set by the distance of the galaxy and the angular scale over which we measure our regional SEDs (panel e, Figure 7.5). In particular, the galaxies for which we are able to measure 500 pc averages tend to be the closest galaxies in our samples, and are thus skewed towards lower stellar masses. However, we find that this effect does not impact the results presented here, as the majority of galaxies affected are more massive than the UDGs in this sample. In particular, there are five galaxies within the stellar mass range of the UDGs that are affected. Four are themselves UDGs (AGC 227965, AGC 322019, AGC 198543, and AGC 238961), and one is a NSA dwarf (NSA ID 17750).

7.5.2 The HI Properties of the UDG Sample

In addition to their star formation efficiency, it is of interest to understand the relationship between the stellar structure of these HI-rich UDGs and their integrated gas properites. In Figure 7.11, we show the mass-size relation of the UDG and NSA samples for two definitions of "mass" and "size" (i.e. four total combinations). The left column shows sizes measured as g-band half-light radii,

while the right column shows sizes measured as half-mass radii, where we refer to the radius that contains half the *stellar* mass of the galaxy as the half-mass radius. The half-light, half-mass, and half-SFR radii reported in this work are measured over the same area of the galaxy as our derived stellar mass and SFR maps (i.e. only in pixels where the stellar mass surface density is nonzero). We use the PSF-matched HSC images with the same machinery as the half-mass and half-SFR radius measurement. The half-light radii reported in this work are thus not completely analogous to effective radii measured using other methods (e.g. Sersic fitting). In particular, though there is no systematic offset between the two methods ($\bar{\Delta}R/R = -0.05$ for the full sample, and -0.06 (-0.04) for the NSA (UDG) subset), there is significant scatter ($\Sigma_{\Delta R/R} = 0.15$ for the full sample, and 0.13 (0.19) for the NSA (UDG) subset). We estimate the uncertainty in our half-mass and half-light radius measurements by adding in quadrature the physical size of the PSF FWHM and the standard deviation of the radii due to the uncertainty in the stellar mass fits/photometry, respectively. The top row shows HI mass, while the bottom shows stellar mass. In essence, one can think of the bottom left panel as the "canonical" mass-size relation (stellar mass versus light-weighted size).

When one considers the size of the UDGs as a function of their integrated stellar mass, it is immediately apparent that they are systematically larger than the NSA sample in both their light-weighted and mass-weighted sizes. This is unsurprising, of course, given that UDGs are selected for their low surface brightnesses and large physical sizes. When one considers the UDGs as a function of their integrated HI mass, however, the picture changes. In particular, we see no significant difference in the relation between the HI masses and half-mass (stellar) radii of the UDG and NSA samples. There is, however, some evidence that the half-light radii of the UDGs remain elevated with respect to the NSA sample at fixed HI mass.

7.5.3 The Color-Mass Relation of UDGs

Though not the main focus of this work, we are able to directly compare the color-mass relation of gas-rich UDGs and "normal" dwarfs as a byproduct of the SPS fitting presented above. Standard color-mass relations [e.g. Bell et al., 2003, Into and Portinari, 2013] have been assumed in the literature for color-based estimates of UDG stellar mass [cf Mancera Piña et al., 2019a, Karunakaran

et al., 2020, Marleau et al., 2021], but it has not been directly shown that these optical color relations are applicable to the UDG population. In particular, the canonical color-mass relations are typically calibrated for and tested on largely massive galaxies; it is thus of practical importance for both the UDG community and general dwarf galaxy community to test the applicability of these relations on the extreme pockets of the dwarf population (e.g. UDGs, Blue Compact Dwarfs, etc.).

In Figure 7.12 we show the global (i.e. light-weighted) g-band mass-to-light relations of the dwarfs in this work (as usual, red points indicate the UDG sample while purple points indicate the spectroscopic dwarf sample). We calculate stellar mass-to-light ratios by computing the $g_{\rm HSC}$ luminosity and stellar mass from the global optical SED of each galaxy (panel b in Figure 7.5). The $g_{\rm HSC} - r_{\rm HSC}$ colors are measured using the same SED used to derive the stellar mass-to-light ratio.

We find that there is no offset between the HI-selected UDG sample and the NSA dwarf sample, and that the samples are well-described by a relation that lies between the Into and Portinari [2013] and Bell et al. [2003] color-mass relations. For completeness, we list our ordinary least squares parameters and standard errors here, where we define $\eta \equiv (M_\star/L_g)(L_\odot/M_\odot)$. We avoid the standard choice of Υ as it is reserved for a parameter linking star formation and midplane pressure in Paper II.

$$\begin{aligned} \log_{10}\eta_{\rm all} &= 1.59 \pm 0.14(g-r) - 0.65 \pm 0.04 \\ \log_{10}\eta_{\rm UDG} &= 1.65 \pm 0.21(g-r) - 0.66 \pm 0.06 \\ \log_{10}\eta_{\rm NSA} &= 1.55 \pm 0.20(g-r) - 0.64 \pm 0.06, \end{aligned} \tag{7.9}$$

the exact calibration of this relation is, of course, dependent on both the photometric bands used and IMF assumptions. We in particular note that Into and Portinari [2013] and Bell et al. [2003] are calibrated for SDSS g and r bands, which are similar but not identical to HSC g and r bands). Regardless, we have demonstrated that the UDGs do not lie systematically off of the color-mass relation of the NSA dwarfs, and that both samples are in relatively good agreement with previous relations from the literature.

7.6 Discussion

Taken altogether, we find that our sample of HI-rich UDGs are characterized by low star formation efficiencies (where SFE(HI) $\equiv \Sigma_{\rm SFR}/\Sigma_{\rm HI}$) down to sub-kpc scales, and that the UDGs are generally incapable of supporting the vigorous star formation seen in the "normal" NSA dwarfs. Intriguingly, although the UDGs are large in light-weighted size for their total stellar mass, their stellar mass-weighted sizes are typical for their HI masses. Finally, the stellar mass-to-light ratios of the UDGs appear consistent with those of the NSA dwarf sample.

7.6.1 Implications for UDG Formation

The results presented in this work suggest that the HI-rich Ultra-Diffuse Galaxies are unable to efficiently convert gas to stars or host vigorous star formation. Such low star formation rate surface densities indicate that UDGs will continue to trail behind the stellar mass build-up of the general dwarf population. This finding, however, does not alone answer the question of *why* certain galaxies fail to trigger vigorous star formation. Several mechanisms have been put forth in the literature to explain the population of field UDGs. For each formation model, we will first discuss the points in which our observations agree with the model predictions before turning towards points of potential conflict.

Feedback-driven expansion. We first consider the picture in which field UDGs are formed via starburst-driven outflows which cause potential fluctuations that in turn lead to net expansion of the stellar population [El-Badry et al., 2016, Di Cintio et al., 2017, Chan et al., 2018]. We note to the reader that in this section we deal with results from both the Feedback In Realistic Environments (FIRE) and Numerical Investigation of a Hundred Astrophysical Objects (NIHAO) simulations; though both simulations point to feedback-driven expansion as the culprit of UDG formation, the feedback implementation between the two simulations is not identical.

In the NIHAO simulation, such UDGs are expected to retain systematically higher HI fractions with respect to "normal" dwarfs, in good agreement with our results [Di Cintio et al., 2017]. However, two points of potential conflict emerge. First, the radial expansion of the UDG stellar

population should enforce a radial age gradient; that is, the older stars should experience more expansion due to having gone through a larger number of inflow/outflow cycles. This picture suggest a relatively centrally concentrated distribution of star formation in UDGs, where the stars experience net expansion while the gas goes through cyclical phases of inflow and outflow. Such behavior is in qualitative conflict with the observation that UDG star formation is both consistently lower than and more radially extended than star formation in the NSA dwarfs (see lower panels of Figure 7.9). However, to our knowledge a detailed study of the star formation extendedness and efficiency has not been done for UDGs created by feedback-driven expansion. Further analysis is necessary to confirm that feedback-driven expansion cannot reproduce this effect (via, e.g. the substantial expansion of stars within 100 Myr of formation).

However, another point of conflict exists between our observations and the feedback-driven expansion picture. Namely, in both FIRE and NIHAO the marked expansion of the UDGs is driven by particularly prolonged and bursty star formation histories [Di Cintio et al., 2017, Chan et al., 2018]. In this work, we have shown that the lack of vigorous star formation in UDGs is linked to their low stellar mass surface densities; that is, their low SFR surface densities are explainable by their stellar and gaseous structure. Conversely, then, the structure of the UDGs makes it difficult to envision a scenario in which they are able to power frequent and vigorous bursts of star formation at late times.

Early mergers. Another proposed mechanism for field UDG formation is the result of an early merger (more than 8 Gyr ago) that caused an increase in total spin as well as a decrease in central SFR and a redistribution of star formation to large radii [Wright et al., 2021]. Like our observed galaxies, the galaxies in the ROMULUS25 simulation are HI-rich for their stellar mass and lie on the integrated star-forming main sequence. However, we do not find the lower central specific star formation that Wright et al. [2021] cite as a significant observable manifestation of this formation channel; indeed, the distribution of sSFR of the UDGs in our sample is not statistically different than that of the NSA sample at any radius.

High-spin halos. Finally, we consider the proposal that UDGs are formed out of the high spin tail of the halo distribution [see, e.g. Dalcanton et al., 1997, Liao et al., 2019]. This formation

scenario predicts that UDGs will host ordered HI disks, in line with resolved measurements from the literature [Mancera Piña et al., 2019a, 2020, Gault et al., 2021]. However, this formation scenario also predicts that, at fixed stellar mass, UDGs should have generally lower gas densities than high surface brightness galaxies. This is seemingly at odds with our results, though a comparison to HI (rather than total gas) properties is necessary to quantitatively demonstrate such a conflict. However, we note that neither the early merger scenario nor the high-spin halo scenario are in conflict with the most salient point of our analysis – that UDGs, once set on a path towards low-efficiency star formation, are likely to continue to fall behind the stellar mass build-up of the general dwarf population.

7.6.2 The Stellar Structure of Dwarfs at fixed M_{HI}

In addition to a comparison with established theoretical models, it is informative to consider what fully empirical statement we may make about the relationship between the HI-rich UDGs and "normal" NSA dwarfs. In the preceding sections, we have demonstrated that the stellar half-mass radii of the UDGs are typical for their HI masses (see Figure 7.11) – that is, the UDGs are not offset from the mass-size plane for a particular casting of mass (HI mass) and size (stellar half-mass radius). This is contrasted, naturally, to the offset in the normal mass-size plane (stellar mass and half light radii) by which UDGs are definitionally characterized.

A concordance in the HI-mass-stellar-size relation would naturally arise if the UDGs were forming stars normally with respect to the spatial distribution of gas, but at decreased star forming efficiency. To illustrate this idea, let us presume that the spatial distribution of HI in UDGs is normal with respect to high surface brightness galaxies, as has been shown for a number of the UDGs in our sample by Gault et al. [2021]. As hinted to in the introduction, the driving mechanism behind the low star formation efficiency of the UDGs will be further explored in Paper II.

In this picture, a galaxy that will become a UDG will form stars over the same spatial distribution as a galaxy that will become a high surface brightness galaxy, but at lower Σ_{SFR} – thus becoming a galaxy with a lower total stellar mass. The concordance of the UDG and NSA samples in the HI mass-stellar size plane is then a natural consequence of the comparatively lower star formation

efficiency of the UDGs. Thus, one mechanism by which to generate the "normal" sizes of the UDGs with respect to their HI masses is for present-day UDGs to have assembled most of their stellar mass via the low SFE(HI) star formation that characterizes their behavior at $z = 0$.

7.7 Conclusions

Due to their large sizes and low stellar mass surface densities, UDGs are both an extreme outcome of galaxy formation and an extreme environment for star formation. HI-selected UDGs are systematically more gas-rich than their "normal" dwarf analogs (see Figure 7.2), and there is evidence that some UDGs have assembled the majority of their stars from extremely dense clumps [Danieli et al., 2021]. Understanding the way in which star formation proceeds in UDGs is thus of key interest to both the galaxy evolution and star formation communities.

In this work, we have presented a method that allows us to compute star formation rate and stellar mass surface density maps over galaxies with known distances using spatially resolved optical data and global UV photometry. We use this method to explore the star formation activity in a sample of nearby (d $<$ 120 Mpc) HI-detected ultra-diffuse galaxies dwarf galaxies from Janowiecki et al. [2019], along with a NASA Sloan Atlas reference sample of "normal" dwarfs with HI measurements from Bradford et al. [2015]. The samples in this work allow us to compare and contrast the star formation behavior of the UDGs against the NSA dwarfs, providing new clues to the evolutionary pathway of these HI-rich UDGs as well as new tests for star formation theory in extreme (low density) environments that we will explore in Paper II.

We find that the globally averaged SFR surface densities of the UDGs are low compared to their globally averaged HI surface densities (see Figure 7.3); this offset could be explained either by a truly lower SFE(HI) in the UDGs, or by a difference in the relationship between the distribution of the UDGs' stellar mass and SFR. Our results indicate that the SFE(HI) of the UDGs remains lower than the NSA dwarfs down to 500 pc scales (see Figure 7.10 and Section 7.5.1) – the UDGs are indeed less efficient at converting atomic gas (to molecular gas) to stars. In the second paper of this series, Kado-Fong et al. [2022b], we will consider the role of the galactic structure of the UDGs on

their star formation. Indeed, we find that the diffuse structure of the UDGs can naturally explain their low star formation rate surface densities and efficiencies. When the structure of the UDGs is considered (rather than the gas content alone), we find that their star formation is quantitatively consistent with star formation in both the NSA sample and in more massive galaxies. As such, we direct the interested reader to Paper II of this paper series.

Returning to the results at immediate hand, we also consider the relationship between the stellar size and HI mass of the UDGs, as compared to the NSA galaxies (Section 7.5.2). We find that although the UDGs have large stellar sizes (both light-weighted and mass-weighted) for their total stellar mass, their stellar sizes are largely unremarkable as a function of their HI mass. This superficially surprisingly result can be explained naturally when we consider the previous conclusions of this work: the UDGs have fairly normal HI structure and properties, and so the spatial distribution of their star formation is set by those normal gas properties. However, because they form stars at a significantly lower SFE(HI), they form fewer stars overall and thus become large for their total stellar mass.

The low efficiency and low star formation rate surface densities of the UDGs indicate that the UDGs will continue to lag behind the general dwarf population in their stellar mass build-up, and thus remain diffuse relative to "normal" dwarfs. However, this does not answer the question of *why* present-day UDGs first entered the evolutionary path to become UDGs at $z = 0$. While this work alone cannot provide a definitive answer to this question, we may consider the implications of our results on contemporary ideas of UDG formation. The spatially extended star formation of the UDGs and apparent inability to power vigorous star formation (high SFR surface densities) are in conflict with the idea of UDG formation via the feedback-driven radial expansion of stars. Formation mechanisms which set certain halos down the path towards UDG formation at early times (e.g. the high spin halo scenario or early merger scenario) can more naturally explain the low SFE(HI) cycle seen in the sample of UDGs presented in this work.

A natural extension of this work will be to obtain a larger number of spatially resolved HI measurements of the UDGs in this sample, with a particular focus on the most nearby galaxies in the sample (such that we may maximize the physical spatial resolution). Higher resolution UV-

optical data will also allow us to directly probe the physical scales relevant to star formation and cluster populations in these galaxies. A further exploration into the star formation and ISM of these UDGs is crucial to further our understanding of UDGs as an extreme environment for star formation, as well as our understanding of how these extreme objects form.

7.8 Fitting Gallery

Here we include an abbreviated gallery of fitting results for the NSA and UDG samples. We choose three galaxies from each sample with their median star formation rate surface density and median stellar mass surface density maps; these galaxies are chosen to roughly span the morphologies seen in the samples.

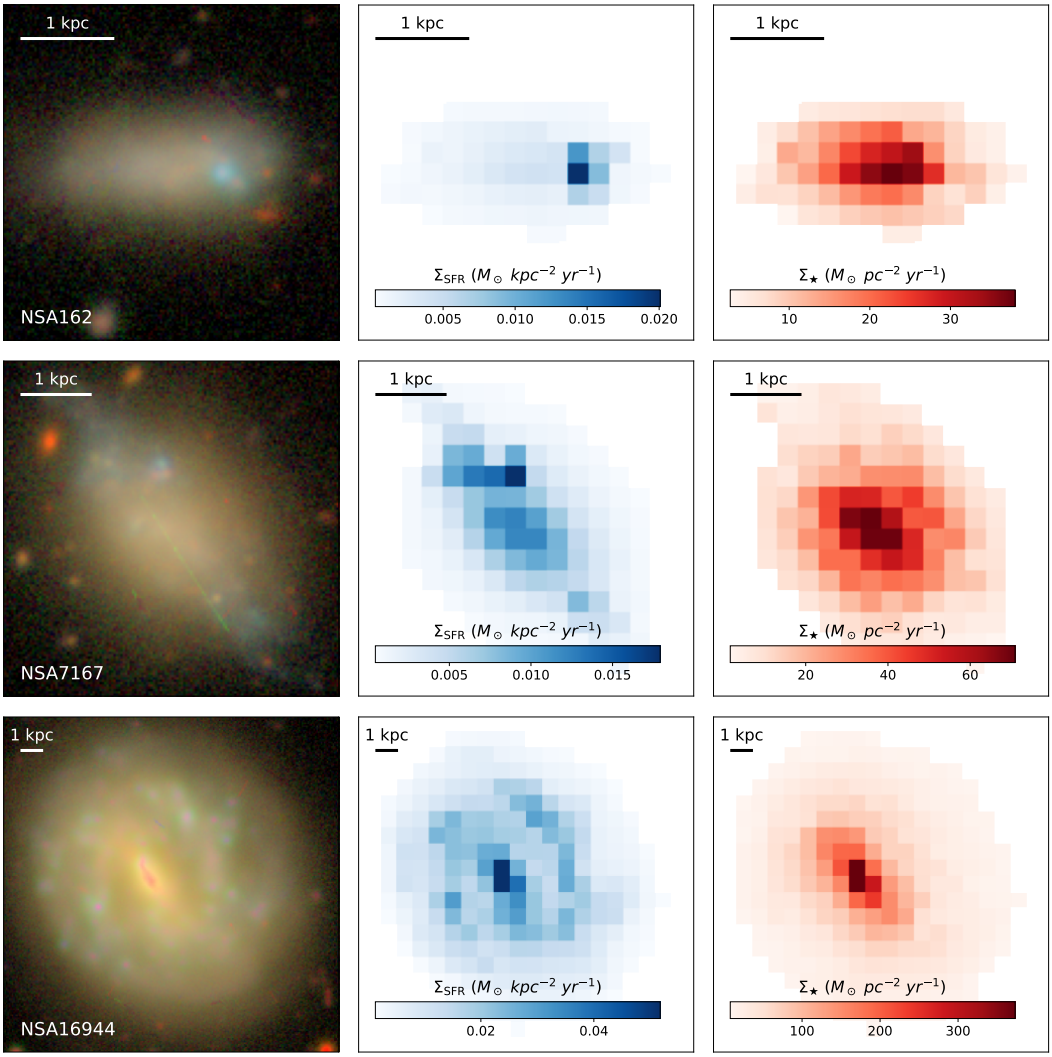

Figure 7.13 A sample of three example galaxies from the NSA sample, as labeled. From left, we show the HSC-SSP gri-composite RGB image, the median star formation rate surface density map, and the median stellar mass surface density map. These galaxies are chosen to span the range of morphologies present in the sample.

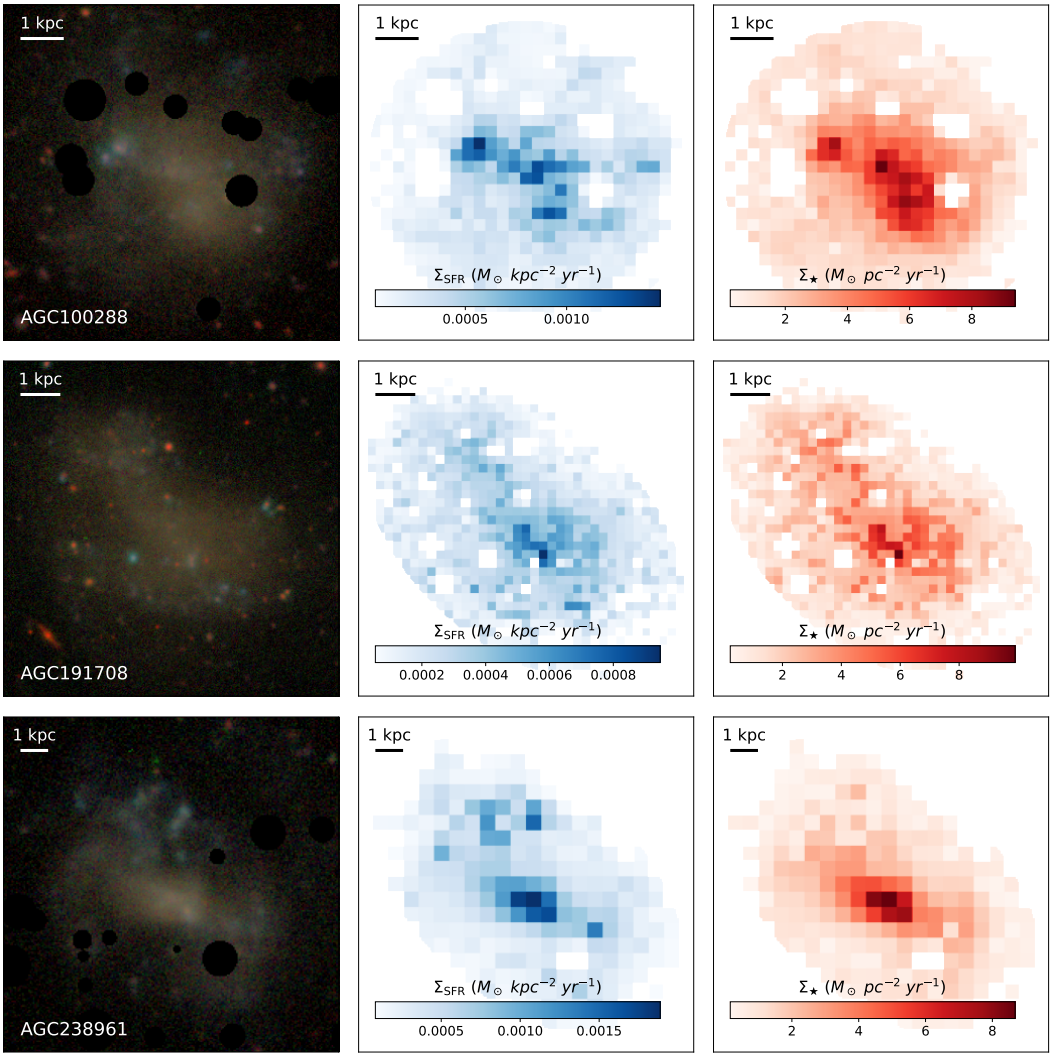

Figure 7.14 A sample of three example galaxies from the UDG sample, as labeled. From left, we show the HSC-SSP gri-composite RGB image, the median star formation rate surface density map, and the median stellar mass surface density map. These galaxies are chosen to span the range of morphologies present in the sample.

Chapter 8

Star Formation of Dwarfs in the Pressure-Regulated, Feedback-Modulated Theory of Star Formation

8.1 Introduction

Star formation and galaxy evolution are intrinsically linked processes; a full understanding of one is not possible in the absence of a theory of the other. In addition to the most definitional link – that star formation grows stellar mass while consuming gas – the resulting feedback from star formation also has a direct impact on the structure of the galaxy's interstellar medium (ISM) via processes including supernovae, UV radiation, and stellar winds [see, e.g. Kim et al., 2013, 2017, Girichidis et al., 2018, Kannan et al., 2019, Kim et al., 2021, Lancaster et al., 2021]. Simply put, in order to understand how and why galaxies evolve the way that they do – especially at the low-mass

end, where star formation feedback is expected to play an outsized role [see, e.g. Silk, 1997, Dekel and Silk, 1986, El-Badry et al., 2016, Behroozi et al., 2019, Hu, 2019, Dashyan and Dubois, 2020, Smith et al., 2020] – we must understand the self-regulatory process of star formation. Likewise, to understand the environments in which star formation proceeds, we must understand the arc of galaxy evolution through cosmic time.

In both the fields of star formation and galaxy evolution, we seek out "extreme" cases in order to best test and stretch our understanding of the underlying physical processes at work. Ultra-diffuse galaxies (UDGs) are dwarf galaxies characterized by large stellar sizes and low surface brightnesses. Though exact definitions vary, UDGs are typically required to have effective radii greater than 1.5 kpc and central surface brightnesses fainter than 24 mag arcsec^{-2} (see Van Nest et al. 2022 for an overview of UDG definitions). These diffuse galaxies are extreme as both a product of galaxy evolution and as an environment in which stars form. Indeed, the study of UDGs as an extreme sector of the dwarf galaxy population has enjoyed both extensive observational [see, e.g. Sandage and Binggeli, 1984, McGaugh et al., 1995, Dalcanton et al., 1997, van Dokkum et al., 2015, Beasley and Trujillo, 2016a,b, Peng and Lim, 2016, Yagi et al., 2016, Leisman et al., 2017, Greco et al., 2018c,b, van Dokkum et al., 2018, Danieli et al., 2019, Janowiecki et al., 2019, van Dokkum et al., 2019, Danieli et al., 2021, Gault et al., 2021, E Greene et al., 2022] and theoretical [e.g. Amorisco and Loeb, 2016, Di Cintio et al., 2017, Chan et al., 2018, Jiang et al., 2019, Liao et al., 2019, Wright et al., 2021, Van Nest et al., 2022] study. However, less work has been devoted to their study as extreme star forming environments.

UDGs are extreme environments for star formation due to their presumably low stellar mass surface densities and likely shallow potential wells (for UDGs in the field, see, for example, Leisman et al. [2017] and Kong et al. [2022] – typical halo masses for UDGs in clusters are a topic of significant debate, see van Dokkum et al. 2015, Beasley and Trujillo 2016a). These conditions are a marked departure from Solar Neighborhood-like or even outer (Milky Way) disk-like conditions that serve as the fiducial environment for many models of star formation [Krumholz et al., 2009, Ostriker et al., 2010]. Mapping out the star formation activity in UDGs thus serves as a test of the extensibility of these star formation models to new and extreme diffuse conditions.

In the first paper of this series [Kado-Fong et al., 2022a, hereafter referred to as Paper I] we demonstrated that UDGs form stars inefficiently relative to their HI surface densities (where SFE(HI)$\equiv \Sigma_{\rm SFR}/\Sigma_{\rm HI}$) on scales down to 500 pc. However, a study of the atomic gas alone is insufficient to understand whether this low SFE(HI) is unexpected given the diffuse structure of the UDGs. In Paper I we demonstrated that the star formation in UDGs is different from normal dwarfs, but in this paper we will consider whether that difference in star formation can be explained by our understanding of the physical processes that drive and modulate star formation.

Towards this end, we turn to the pressure-regulated, feedback-modulated model of star formation that has been developed over a series of works [Ostriker et al., 2010, Kim et al., 2011, Ostriker and Shetty, 2011, Kim et al., 2013, Kim and Ostriker, 2015] and most recently condensed into Ostriker & Kim (2022, in preparation). This theory establishes a link between star formation rate surface density and weight ($\mathcal{W}$) by considering the role of star formation feedback in maintaining the structure of the ISM. This physical relationship provides us with a method that links the two notable features of the UDGs in this work – their unusual structure and their low star formation rate surface density. With this framework in hand, we will endeavour to explain the surprising – or perhaps expected – nature of the star formation in HI-rich UDGs.

We will structure the paper as follows, and note that readers familiar with either Paper I or PRFM star formation may feel free to skip certain sections. We refer the reader to the previous chapter of this work to understand the creation of the data products used in this work. We will then give an abbreviated overview of PRFM star formation theory in Section 8.3, before moving onto a discussion of its application to the dwarfs at hand in Section 8.4. Finally, we will discuss the implications of the analysis on our understanding of the structure and star formation of UDGs in Section 8.5

8.2 Datasets

Readers familiar with Paper I of this series (Chapter 7) will find that this content has been covered in greater detail in Paper I. Here we provide only notes on changes in the sample between Paper I

(Chapter 7) and the present work.

Our dwarf sample consists of two main branches: a high surface brightness, "normal" dwarf sample drawn from the HI catalog of Bradford et al. [2015] – hereafter the NSA sample, and an ultra-diffuse galaxy sample with known distances from the HI catalog of Janowiecki et al. [2019]. The NSA sample is drawn from the NASA Sloan-Atlas, a catalog of nearby galaxies re-analyzed from the Sloan Digitial Sky Survey DR8 [Aihara et al., 2011]. The UDG sample was selected to have a maximum distance of $d = 120$ Mpc; we enforce the same limit on the NSA sample. We note that in this work we will refer to the "normal" galaxy sample as the NSA sample, as these galaxies were not specifically chosen to exclude low surface brightness galaxies. Rather, their relatively high surface brightnesses are a result of the observational selection which lead to their inclusion in the NSA.

In order to make a fair assessment of the star formation activity of the UDGs, we also draw a reference sample of 32 NASA-Sloan Atlas (NSA) dwarfs at $d < 120$ Mpc with HI measurements from Bradford et al. [2015] to act as a "normal" dwarf reference sample. For this work, we consider the 21 NSA dwarfs with stellar masses no greater than $M_\star = 3 \times 10^8$ $M_\odot$ (the maximum stellar mass covered by the UDG sample). This results in a median stellar mass of $\langle \log_{10}(M_\star/M_\odot) \rangle_{50} = 8.0$ for the NSA sample and $\langle \log_{10}(M_\star/M_\odot) \rangle_{50} = 7.9$ for the UDG sample.

After computing stellar mass and SFR maps via SED fitting (see Section 7.3), we compute the average stellar mass density and star formation rate surface density over 500 pc, 1 kpc, and global scales. In this step, we require that the averaging scale is larger than the scale of the regions in which we measure the region SEDs (panel e of Figure 7.5). In practice, this primarily affects galaxies included in Paper I and excluded from the current work due to their high stellar mass. There are five galaxies in the present sample that are affected: four are UDGs (AGC 227965, AGC 322019, AGC 198543, and AGC 238961), and one is a NSA dwarf (NSA ID 17750). The results of these galaxies are thus shown on 1 kpc and global scales, but not on 500 pc scales – their exclusion at 500 pc does not constitute a statistically significant impact on our analysis.

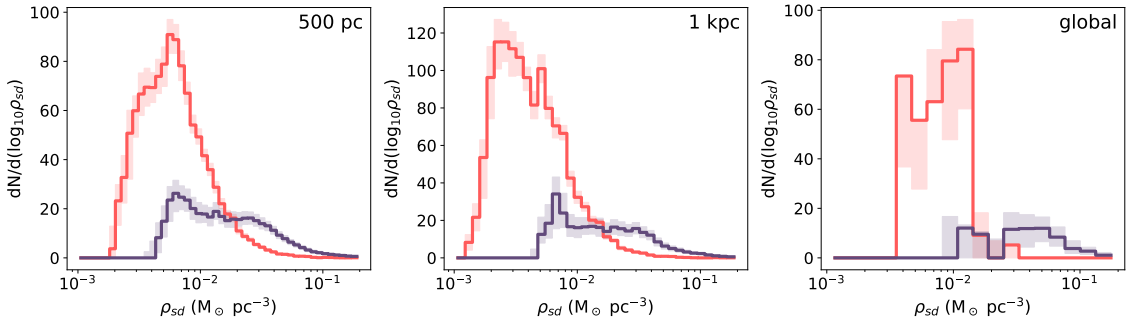

Figure 8.1 The distribution over ρ_{sd} for our fiducial dark matter halo assumptions (see text) for the NSA dwarfs (purple) and UDGs (red) at 500 pc, 1 kpc, and global scales from left to right. The shaded regions are bounded by the 16th to 84th percentiles of the distribution. The NSA dwarfs are characterized by systematically higher stellar+dark matter densities, which is unsurprising given that the UDGs are characterized by low stellar surface densities.

8.3 Background on PRFM theory

We will summarize the basic points of pressure-regulated, feedback-modulated (PRFM) star formation, but direct the reader to Ostriker & Kim (2022, in preparation) for an in-depth discussion of the theory. The reader already familiar with this framework may proceed directly to Section 8.4, though they should take note that we compute dynamical equilibrium pressure using HI measurements only.

For a galaxy disk in vertical dynamical equilibrium or in a quasi-steady state, the weight (per unit area) of the ISM should be balanced by the pressure difference between the midplane and the top of the gas layer. Since the pressure is generally decreasing rapidly along the z-axis (perpendicular to the disk plane), the midplane pressure must match the overlying weight. The weight of the ISM, $\mathcal{W}$, is a sum of the contribution by the gas and by the external components (stars, dark matter),

$$\begin{aligned} \mathcal{W} &= \int_0^{z_{\max}} dz\ \rho(g_{\rm gas} + g_{\rm ext}) \\ &= \mathcal{W}_{\rm gas} + \mathcal{W}_{\rm ext}, \end{aligned} \tag{8.1}$$

where $z_{\max}$ refers to the vertical confine of the disk, $g_{\rm gas}$ and $g_{\rm ext}$ are the vertical components of

the gravitational field due to the gas and the external gravitational potential, and $\mathcal{W}_{\rm gas}$ and $\mathcal{W}_{\rm ext}$ are the corresponding weight components.

Assuming slab geometry, it can be shown that the weight from the gas gravity is $\mathcal{W}_{\rm gas} = (\pi G \Sigma_{\rm gas}^2)/2$, where $\Sigma_{\rm gas}$ is the total gas surface density. If the external gravity dominates, we can approximate the weight as $\mathcal{W}_{\rm ext} = \Sigma_{\rm gas}\sqrt{2G\rho_{\rm sd}}\sigma_{\rm eff}$, where $\rho_{\rm sd}$ is the combined density of stars and dark matter and $\sigma_{\rm eff}$ is the effective vertical velocity dispersion of the gas. This effective velocity dispersion includes the turbulent, thermal, and magnetic contributions. To estimate the weight from observables, we take a simplified form called the dynamical equilibrium pressure $P_{\rm DE}$ that is obtained by combining the two weight contributions as introduced in Ostriker & Kim 2022, in preparation as

$$\begin{aligned} \mathcal{W} &= \mathcal{W}_{\rm gas} + \mathcal{W}_{\rm ext} \\ \mathcal{W} &\approx P_{\rm DE} = \frac{\pi G \Sigma_{\rm HI}^2}{2} + \Sigma_{\rm HI}\sqrt{2G\rho_{sd}}\sigma_{\rm eff}. \end{aligned} \tag{8.2}$$

This approximation is good to within $\approx 20\%$ (see Ostriker & Kim 2022, in preparation for a more complete derivation of the full weight expression), and has been adopted in the literature to estimate the total weight from observable quantities [see, e.g. Sun et al., 2020]. where the reader will note that we have made a notable change to the construction of $\mathcal{W}$. We do not have molecular gas estimates for our samples, and thus take the base assumption that these galaxies are HI-dominated and that the molecular gas is a minor contributor to the total gas mass of the ISM. That is, we assume $\Sigma_{\rm gas} \approx \Sigma_{\rm HI}$. We assume a $\sigma_{\rm eff} = 10$ km s^{-1}, as in previous works [see, e.g. Sun et al., 2020]. This assumption is reasonable for the dwarf samples at hand as $\sigma_{\rm eff}$ is likely dominated by the warm gas sound speed.

Having laid out an observational estimate of the weight (that is, the dynamical equilibrium pressure), which is an estimate of the total midplane pressure, we now want to make a connection between the total pressure and star formation activity. Total pressure here is defined as the sum of contributions from thermal pressure, turbulent pressure (vertical Reynolds stress), and vertical Maxwell stress as $P_{\rm tot} = P_{\rm th} + P_{\rm turb} + \Pi_{\rm mag}$. Each of these pressure terms is expected to be

linked to star formation activity: thermal pressure scales largely with the mean FUV field intensity, turbulent pressure is sourced by momentum injection from supernovae, and magnetic pressure – though relatively less well understood – is thought to scale to some degree with turbulent kinetic pressure via galactic dynamo.

A great deal of work has been devoted to quantifying the relationship between these pressure terms and star formation activity. The key parameter quantifying this relation is the "feedback yield", defined as

$$\Upsilon_{\rm X} \equiv \frac{P_{\rm X}}{\Sigma_{\rm SFR}} \tag{8.3}$$

where X refers to a given pressure component. In particular, Ostriker and Shetty [2011] showed that the turbulent pressure is related to SFR surface density as $P_{\rm turb} = p_\star/(4m_\star)\Sigma_{\rm SFR}$, where $p_\star$ is the spherical momentum injection per supernova and $m_\star$ is the total mass of stars formed per star that will become a supernova. Recently, 3D supernova-driven bubble expansion simulations have converged to a characteristic value of $p_\star/m_\star \sim 1000 - 3000$ km s^{-1}. This value is insensitive to the background density and metallicity [e.g. Kim and Ostriker, 2015, Kim et al., 2017, Martizzi et al., 2015, Iffrig and Hennebelle, 2015, Fielding et al., 2018, Oku et al., 2022]

Likewise, Ostriker et al. [2010] showed that for solar neighborhood-like conditions one arrives at $\Upsilon_{\rm th} \approx 240$ km s^{-1} for solar neighborhood-like conditions [see Equation 15 of Ostriker et al., 2010, or, equivalently, Equation 12 of Ostriker & Kim 2022, in preparation]. However, the feedback yield $\Upsilon_{\rm th}$ should scale with the FUV field intensity, which is sensitive to both $\Sigma_{\rm SFR}$ and attenuation from the ISM. In particular, a scaling relation can be written for $\Upsilon_{\rm th}$ with respect to solar neighborhood conditions as:

$$\Upsilon_{\rm th}(f_\tau, \Sigma_{\rm HI}, Z'_d) = 240 \text{ km s}^{-1} \frac{4.1 f_\tau / f_{\tau,\odot}}{1 + 3.1 \left(\frac{\Sigma_{\rm HI} Z'_d f_\tau / f_{\tau,\odot}}{10 \text{ M}_\odot \text{ pc}^{-2}} \right)^{0.4}}, \tag{8.4}$$

where we assume a dust metallicity of $Z'_d = Z/Z_\odot = 1/3$, in line with our SED fitting assumptions. We also introduce f_τ, which is proportional to the FUV radiation field under the assumption of

slab geometry. This quantity is defined as

$$f_\tau \equiv \frac{1 - E_2(\tau_{\rm FUV}/2)}{\tau_{\rm FUV}}, \tag{8.5}$$

where $E_2(n)$ is the second exponential integral. We estimate the FUV optical depth, $\tau_{\rm FUV}$ for our galaxies by computing $A_{\rm FUV}$ assuming a Calzetti [2013] extinction curve and the A_V inferred from our global SED fits.

The magnetic stress component, though less well understood due to the open questions in dynamo theory, is predicted to be $\Upsilon_{\rm mag} \sim 0.5 - 1.0\Upsilon_{\rm turb}$ [Kim and Ostriker, 2015]. In this work, we adopt a fiducial $\Upsilon_{\rm turb} = 500$ km s^{-1} and a scaling of $\Upsilon_{\rm mag} = 0.75\Upsilon_{\rm turb}$. We thus arrive at a theoretical PRFM prediction of

$$\Upsilon_{\rm tot} = \frac{P_{\rm tot}}{\Sigma_{\rm SFR}} \sim 875 \text{ km s}^{-1} + \Upsilon_{\rm th}(f_\tau, \Sigma_{\rm HI}) \tag{8.6}$$

Numerical results from the TIGRESS[1] framework [Kim and Ostriker, 2017] suggest that $\Upsilon_{\rm tot}$ varies with $P_{\rm DE}$ as (Ostriker & Kim 2022, in preparation, Equation 25c):

$$\log_{10}\left(\frac{\Upsilon_{\rm tot}}{\text{km s}^{-1}}\right) = -0.212 \log_{10}\left(\frac{P_{\rm DE}}{k_B \text{ cm}^{-3} \text{ K}}\right) + 3.86. \tag{8.7}$$

With an adopted $\Upsilon_{\rm tot}$, the PRFM prediction for SFR surface density is

$$\Sigma_{\rm SFR} = \frac{P_{\rm DE}}{\Upsilon_{\rm tot}}, \tag{8.8}$$

where the right hand is composed of our observable quantity ($P_{\rm DE}$) and the the theoretical/numerical prediction ($\Upsilon_{\rm tot}$).

From here, we will consider whether the markedly low SFE(HI) of our observed UDG sample can be explained within the framework of PRFM star formation.

[1]Three-phase Interstellar medium in Galaxies Resolving Evolution with Star formation and Supernova feedback

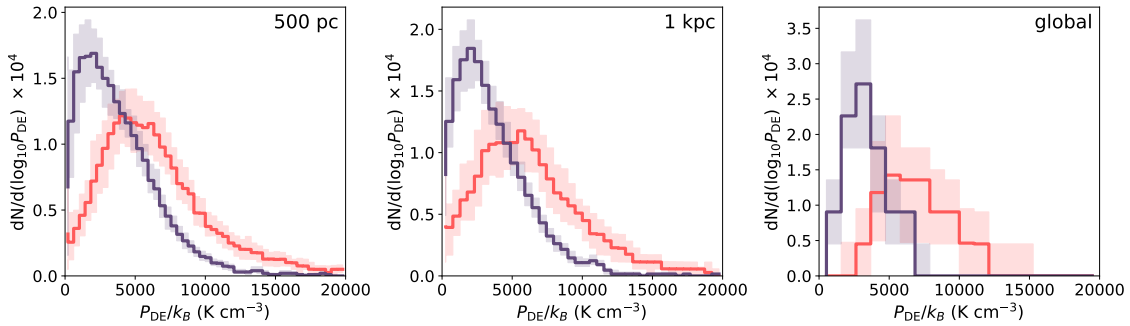

Figure 8.2 The distribution over $P_{\rm DE}$ for the NSA dwarfs (purple) and UDGs (red) at 500 pc, 1 kpc, and global scales from left to right. The shaded regions at 500 pc and 1 kpc are bounded by the $16^{\rm th}$ to $84^{\rm th}$ percentiles of the distribution. We find no significant variation in $P_{\rm DE}$ as a function of spatial scale, but find that the NSA dwarfs have systematically higher dynamical equilibrium pressures than the UDG dwarfs.

8.4 Results

Having provided the reader a brief introduction to PRFM theory, we may now proceed to the application of this framework to the present sample. Before we jump headlong into the computation, however, it is of substantial importance to first justify that the PRFM theory of star formation is applicable to our dwarf samples, and how we will go about estimating the parameters necessary to predict star formation within the model framework.

8.4.1 The validity of PRFM assumptions in the present sample

An obvious preliminary question that we must first address before applying the PRFM model to the sample at hand is whether the equilibrium assumptions that lie at the heart of the theory are satisfied in our low-mass systems.

There is substantial evidence from HI rotation curves that dwarfs (including UDGs) in this mass range do host HI disks [Hunter et al., 2012, Greco et al., 2018b, Mancera Piña et al., 2019a, 2020, Gault et al., 2021]. There are, to the authors' knowledge, no published analyses of the stellar kinematics of field UDGs, but there is evidence that UDGs in the field are "puffy" but largely axisymmetric systems characterized by a mean disk thickness of $\sim 0.5 R_{\rm d}$ where $R_{\rm d}$ is the disk

length [Kado-Fong et al., 2021]. We thus generally find long-lived disks for the galaxies in our sample and that the dynamical equilibrium assumption of PRFM is reasonable for the present work.

The thermal equilibrium assumption of the PRFM model may also be disrupted by ongoing expansion or contraction of gas, driven for example by bursts of star formation [El-Badry et al., 2016]. This assumption must be considered especially carefully due to proposals that dwarfs have generally bursty star formation histories, and that UDGs in particular may be formed via particularly bursty histories [Chan et al., 2018, Di Cintio et al., 2017]. We can estimate over what timescale bursts of star formation may impact the validity of the thermal equilibrium assumption by computing an approximate cooling time for these dwarfs. In particular, let us write the cooling time of warm gas as:

$$t_{\rm cool} = \frac{P_w}{n^2 \Lambda} = \frac{P_w}{L_{\rm cool}}, \tag{8.9}$$

where $P_w/k_B \sim 1000$ K cm^{-3} and $L_{\rm cool} \sim 10^{-27}$ erg cm^{-3} s^{-1} [Wolfire et al., 2003]. This results in a cooling time of $t_{\rm cool} \sim 5$ Myr. This cooling time is significantly shorter than the timescale over which we measure our star-formation rates (100 Myr) – thus, any starbursts that happened within a factor of a few of the cooling time of the warm neutral medium should also be reflected in our measurement of the star formation rate. Our galaxies do not lie above the locus of the star-forming main sequence (see right panel of Figure 7.1), so we conclude that it is reasonable to assume that the galaxies in our sample are in both thermal and dynamical equilibrium.

8.4.2 Estimating $\rho_{\rm sd}$

Having addressed these assumptions, we now proceed to the sample at hand. In order to estimate $P_{\rm DE}$ (Equation 8.2), we will need an estimate for the midplane density of stars and dark matter, $\rho_{\rm sd}$. We estimate the stellar mass density at the midplane as $\rho_\star = \Sigma_\star/(2H_\star)$, where $H_\star$ is the disk scale height and $\Sigma_\star$ is the stellar mass under the assumption of an exponential density profile. We opt to not implement inclination corrections for our sample because the stellar disks are not thin and because empirical results suggest that there is significant variation in the three-dimensional

shapes and thicknesses of the dwarf stellar disks [Kado-Fong et al., 2020b, Carlsten et al., 2021]; however, we compute inclination estimates using the mean disk height-to-length ratio following Holmberg [1958] and find that our results would not qualitatively change if we did implement such an inclination correction. Nevertheless, because our sample is ill-matched to the assumptions of a thin, axisymmetric disk, we believe that the inclination correction has a strong potential to bias our measurements. In order to use this estimate for $\rho_\star$, we also require an estimate of $H_\star$: we do so statistically by using the measured scale lengths of our galaxies in conjunction with the three-dimensional shape distributions inferred by Carlsten et al. [2021] for the NSA dwarf sample and by Kado-Fong et al. [2021] for the UDG sample. We use the Carlsten et al. [2021] 3D shapes because of the overlap in stellar mass between the two samples, but we note that their sample is comprised only of satellite galaxies. We therefore also compute SFR predictions using the 3D intrinsic shape distribution of Kado-Fong et al. [2020b], which is incomplete at the relevant stellar masses but includes field galaxies, and find no significant difference in the SFR predictions between the assumptions of intrinsic shape distribution. We assume in both cases that the three-dimensional shape distribution of the galaxy sample measured at one effective radius is the same as the distribution measured at the scale length $l_\star$. Both the UDGs [Kado-Fong et al., 2021] and the "normal" dwarfs [Kado-Fong et al., 2020b] are well-characterized by exponential surface brightness profiles, meaning that $\mathrm{R_{eff}} \approx 0.6 l_\star$ assuming a constant stellar mass-to-light ratio. We can then estimate the probability distribution function of $H_\star$ as:

$$\Pr[H_\star] = (2\pi\sigma^2_{C/A})^{-1/2} \exp\left[\frac{-(H_\star/l_\star - \mu_{C/A})^2}{(2\sigma^2_{C/A})}\right] \tag{8.10}$$

where C/A indicates the ratio between the smallest and largest principle axes of the ellipsoid that describes the galaxy shape distribution at one effective radius, and $\mu_{C/A}$ and σ_C/A are the inferred mean and standard deviation of the bivariate Gaussian used to describe that intrinsic shape distribution in Carlsten et al. [2021] and Kado-Fong et al. [2021].

We now move on to the estimation of the dark matter density, ρ_{dm}. Here, we must adopt a dark matter halo profile for each galaxy. This component is by far the most uncertain ingredient in the

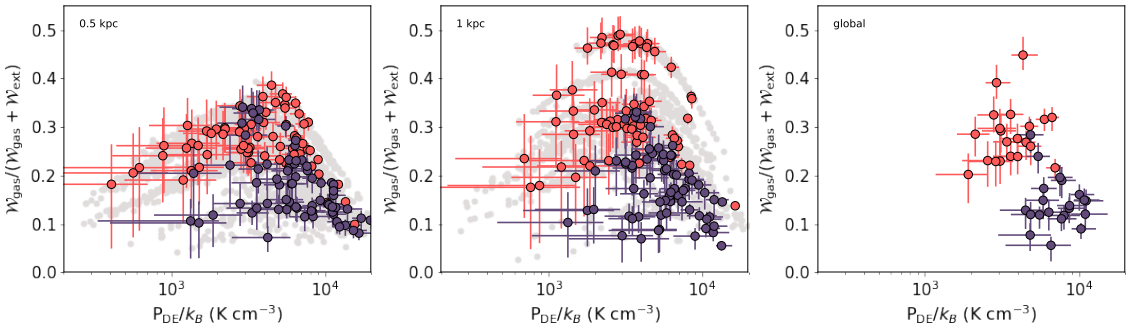

Figure 8.3 The contribution of self-gravity to the total midplane weight ($\mathcal{W}_{\rm gas}/\mathcal{W}$) as a function of dynamical equilibrium pressure ($P_{\rm DE}$) as a function of spatial scale (500 pc to global average, from left to right). We show individual errorbars for a random sample of regions from the UDG sample (red) and the NSA sample (purple); the full sample is shown in grey. Note that the tracks visible in the left and middle panels are a result of the median assumed HI profiles; the uncertainty in the HI profiles result in a larger dispersion in $\mathcal{W}_{\rm gas}/\mathcal{W}$ than is implied by the tracks alone (as is shown by the errorbars of the colored points). We find that the external weight ($\mathcal{W}_{\rm ext}$) is relatively less important in the UDGs as compared to the NSA dwarfs.

star formation prescription – not only do we not have any constraint on the individual dark matter halos in which these galaxies live, the overall stellar-to-halo mass relation is highly uncertain for low-mass galaxies. In order to take into account the scatter and uncertainty in the stellar-to-halo mass relation at these masses, we compute the predicted star formation rate using three different dark matter halos: a best guess halo mass using the stellar-to-halo mass relation of the FIRE-2 simulations [which predicts halo masses between 1.6×10^{10} and 3.3×10^{11} M$_\odot$, Hopkins et al., 2018], a halo with $M_h = 10^{12} M_\odot$, and a halo with $M_h = 10^{9} M_\odot$. We assume a NFW profile for all dark matter halos in this work [Navarro et al., 1997]. We assign a concentration based on the concentration-mass relation of Child et al. [2018]. We assign the uncertainty due to the dark matter density to be the difference between ρ_{dm} estimated for a very massive ($M_h = 10^{12} M_\odot$) and very low-mass ($M_h = 10^{9} M_\odot$) halos, as it is unlikely that any of our galaxies are living in halos with a stellar-to-halo mass ratio more extreme than 0.1 (in the case of the extreme low-mass halo) or 0.0001 (in the case of the extreme high-mass halo).

We show the distribution over ρ_{sd} for our fiducial dark matter halo assumption in Figure 8.1. We find that the NSA dwarfs are characterized by systematically higher values of ρ_{sd}, which is

unsurprising given that the UDGs are characterized by relatively low stellar surface densities.

8.4.3 $P_{\rm DE}$ Estimates

Having estimated both $\Sigma_{\rm HI}$ and ρ_{sd}, we may now arrive at an estimate of the dynamical equilibrium pressure ($P_{\rm DE}$). We compute this quantity following Equation 8.2.

Before considering the full PRFM prediction, it is of interest to first consider how $P_{\rm DE}$ varies between the NSA and UDG samples. We show the overall distribution of $P_{\rm DE}$ at each spatial scale used in this work (500 pc, 1 kpc, and global) for each sample in Figure 8.2. We find that there is no significant variation in $P_{\rm DE}$ distribution as a function of spatial scale, but that the UDGs tend to have lower dynamical equilibrium pressures than do the NSA dwarfs. This result is as expected due to the low ρ_{sd} values of the UDGs (see Figure 8.1). The relatively low stellar+dark matter densities (and relatively similar HI surface densities) of the UDGs also imply that $\mathcal{W}_{\rm gas}$ is a larger contributor to $\mathcal{W}$ in the UDGs than it is in the NSA dwarfs.

We show $\mathcal{W}_{\rm gas}/\mathcal{W}$ in Figure 8.3 as computed from Equation 8.2 where $\mathcal{W} \sim P_{\rm DE}$ and $\mathcal{W}_{\rm gas} \sim (\pi G \Sigma_{\rm HI}^2)/2$. Each panel shows the dynamical equilibrium pressure (recall that we approximate $\mathcal{W} \approx P_{\rm DE}$, see Equation 8.2) versus the fraction of $\mathcal{W}$ contributed by $\mathcal{W}_{\rm gas}$. From left to right, the panels show measurements at 500 pc, 1 kpc, and global scales. For visual clarify, we only show errorbars for a random subset of the regions measured in this work. The colored points show a random sample of UDG regions (red) and NSA regions (purple) with their errorbars included; the full sample is shown by the grey scatter. The tracks visible in the left and middle panels are a result of the median HI profiles we assume for the galaxies; the uncertainty in these profiles result in a wider dispersion than is implied by the tracks (as shown by the vertical extent of the errorbars). Indeed, we find that $\mathcal{W}_{\rm gas}$ accounts for a larger fraction of the total weight in the UDGs than it does in the NSA dwarfs. This difference also indicates that the UDG samples should be relatively more sensitive to the unaccounted-for contribution of molecular hydrogen to the total weight.

8.4.4 PRFM predictions

With the assumptions validated and parameters estimated, we may now move on to predicting $\Sigma_{\rm SFR}$ from the PRFM framework for our observed galaxies. We base our predictions upon the numerically estimated form of $\Upsilon_{\rm tot}$ presented by Ostriker & Kim (2022, in preparation) using the TIGRESS simulations, as discussed in Equation 8.7.

In the top row of Figure 8.4, we show the relationship between $\Sigma_{\rm SFR}$ and HI surface density for our NSA dwarfs (purple) and UDGs (orange) averaging over 500 pc regions, 1 kpc regions, and the full area of the galaxy. As was shown in more detail in Paper I, the UDGs form stars at consistently lower efficiencies (relative to their HI content) relative to the NSA dwarfs.

We then show the relation between the observed and predicted star formation rate surface densities in the bottom row of Figure 8.4 for 500 pc, 1 kpc, and global averages. We find that the PRFM prescription succeeds in reproducing the star formation rate surface density measurements of the UDGs at all spatial scales probed, which we will explore quantitatively via a comparison between the predicted and measured values of $\Upsilon_{\rm tot}$ in the following section. The prescription under-predicts $\Sigma_{\rm SFR}$ for the most vigorously star-forming regions of the NSA sample – this under-prediction can be understood if one considers that the NSA dwarfs may have considerable stores of molecular hydrogen [see, e.g. Leroy et al., 2008, de los Reyes and Kennicutt, 2019]. The discrepancy is most obvious in the globally averaged estimates, which is due to the global averages acting as a $\Sigma_{\rm SFR}$-weighted average (where the most vigorously star-forming regions dominate the total mean signal). We also see that the HI-only PRFM predictions perform best for the NSA dwarfs at 500 pc scales, which is consistent with the picture where much of the galaxy is dominated by atomic hydrogen (over molecular hydrogen as has been suggested previously in, e.g. Leroy et al. 2008). Nonetheless, we find that PRFM theory well-describes the majority of the regions within both galaxy samples and thus naturally predicts the low SFE(HI) of the HI-rich UDGs as a consequence of their low ISM weight.

8.4.5 Empirical estimates of $\Upsilon_{\rm tot}$

Finally, though we have adopted $\Upsilon_{\rm tot}$ as a way to predict $\Sigma_{\rm SFR}$, it is also informative to re-frame the computation as a comparison between the theoretically predicted values for $\Upsilon_{\rm tot}$ (Equation 8.6 and Equation 8.7) and empirically-derived $\Upsilon_{\rm tot}$ as the ratio between our observed $\Sigma_{\rm SFR}$ measurements and $P_{\rm DE}$ estimates. Because the theoretical $\Upsilon_{\rm tot}$ depends explicitly upon $\tau_{\rm FUV}$ (Equation 8.5), we compute a running median predicted $\Upsilon_{\rm tot}$ for our sample as a function of $P_{\rm DE}$ in bins of width 0.1 dex. The shaded region in each panel spans the $16^{\rm th}$ to $84^{\rm th}$ percentiles of the theoretical $\Upsilon_{\rm tot}$ prediction over the same domain.

We show such a comparison in Figure 8.5. At left, we show $\Sigma_{\rm SFR}$ versus $P_{\rm DE}$ at 500 pc, 1 kpc, and global scales with the predictions for $\Upsilon_{\rm tot}$ over-plotted (Equation 8.6 dashed, Equation 8.7 solid). At right we show the empirical estimate for $\Upsilon_{\rm tot}$ as a function of $P_{\rm DE}$, again with both the theoretical and numerical predictions for $\Upsilon_{\rm tot}$ shown in brown. Here we show the median value of $\Upsilon_{\rm tot}$ for the UDG and NSA samples as the red and purple points, respectively, and depict the range between the $16^{\rm th}$ and $84^{\rm th}$ percentiles in both $P_{\rm DE}$ and $\Upsilon_{\rm tot}$ as solid unfilled rectangles of the same color. For the reader's convenience, we tabulate these values in Table 8.4.5. For comparison, we also show empirical $\Upsilon_{\rm tot}$ estimates inferred from the literature results of PHANGS [orange dot-dashed box, Sun et al., 2020], EDGE-CALIFA [blue dot-dashed box, Barrera-Ballesteros et al., 2021], and KINGFISH [green dot-dashed box, Herrera-Camus et al., 2017]. We show the same literature results in each panel, but note that these measurements are taken on the scale of ~ 1 kpc. We also note that the literature measurements take H_2 into account in their computation of $P_{\rm DE}$.

Directing the reader's attention first to the top and middle rows (500 pc scales and kiloparsec scales, respectively), we see that both the empirically-derived $\Upsilon_{\rm tot}$ measured from the UDG sample and NSA sample are in good agreement with the predictions of Ostriker & Kim (2022, in preparation). We moreover see that the empirically-derived $\Upsilon_{\rm tot}$ of both dwarf samples at kiloparsec and lower scales are in good agreement with the measured $\Upsilon_{\rm tot}$ values of the literature samples of more massive galaxies (which do have H_2 incorporated in their $P_{\rm DE}$ estimates). This is to say that, as quantitatively measured by $\Upsilon_{\rm tot}$, star formation appears to be proceeding in fundamentally the

Table 8.1. 16th, $\mathbf{50}^{\text{th}}$, and 84th percentile values of P_{DE} and Υ_{tot} for the UDG and NSA samples at 500 pc, 1 kpc, and global scales.

Sample	Scale	P_{DE}^{16} $\left[\frac{10^3 \text{K}}{\text{k}_\text{B}\ \text{cm}^3}\right]$	$\mathbf{P}_{\text{DE}}^{\mathbf{50}}$ $\left[\frac{10^3 \text{K}}{\text{k}_\text{B}\ \text{cm}^3}\right]$	P_{DE}^{84} $\left[\frac{10^3 \text{K}}{\text{k}_\text{B}\ \text{cm}^3}\right]$	$\Upsilon_{\text{tot}}^{16}$ $\left[10^3 \frac{\text{km}}{\text{s}}\right]$	$\boldsymbol{\Upsilon}_{\text{tot}}^{\mathbf{50}}$ $\left[10^3 \frac{\text{km}}{\text{s}}\right]$	$\Upsilon_{\text{tot}}^{84}$ $\left[10^3 \frac{\text{km}}{\text{s}}\right]$
UDGs	500 pc	$1.32^{+0.18}_{-0.30}$	$3.42^{+0.28}_{-0.22}$	$6.60^{+0.23}_{-0.22}$	$1.01^{+0.12}_{-0.18}$	$2.13^{+0.17}_{-0.14}$	$4.02^{+0.33}_{-0.26}$
	1 kpc	$1.38^{+0.12}_{-0.26}$	$3.26^{+0.21}_{-0.18}$	$6.29^{+0.20}_{-0.17}$	$1.17^{+0.13}_{-0.20}$	$2.38^{+0.11}_{-0.13}$	$4.27^{+0.28}_{-0.24}$
	global	$2.46^{+0.29}_{-0.33}$	$3.69^{+0.27}_{-0.31}$	$5.36^{+0.39}_{-0.37}$	$1.08^{+0.13}_{-0.15}$	$1.79^{+0.16}_{-0.16}$	$2.75^{+0.26}_{-0.26}$
NSA dwarfs	500 pc	$3.03^{+0.37}_{-0.43}$	$6.06^{+0.33}_{-0.28}$	$10.55^{+0.86}_{-0.66}$	$0.57^{+0.06}_{-0.07}$	$1.44^{+0.12}_{-0.10}$	$3.16^{+0.35}_{-0.27}$
	1 kpc	$2.86^{+0.45}_{-0.53}$	$6.02^{+0.34}_{-0.31}$	$10.42^{+0.76}_{-0.55}$	$0.48^{+0.06}_{-0.07}$	$1.27^{+0.11}_{-0.11}$	$2.86^{+0.30}_{-0.27}$
	global	$4.94^{+0.52}_{-0.54}$	$7.37^{+0.58}_{-0.58}$	$10.65^{+1.26}_{-0.83}$	$0.29^{+0.07}_{-0.06}$	$0.73^{+0.10}_{-0.08}$	$1.33^{+0.18}_{-0.15}$

same way between "extreme" (low density) dwarfs, "normal" dwarfs, and their much more massive counterparts. When we consider globally-averaged values, we find that the median empirical Υ_{tot} measured for the NSA dwarfs drops significantly – this may be suggestive of a significant store of H_2 in these NSA dwarfs, which we will discuss further in Section 8.5.2.

Encouragingly, we find that the empirically-measured Υ_{tot} values derived from the dwarf samples on *leq*1 kpc scales are in good agreement with both the theoretical and numerical predictions for Υ_{tot} presented in Ostriker and Kim [2022]. We find that, in contrast to the numerical results of Ostriker and Kim [2022], the theoretical prediction of Υ_{tot} produces a roughly constant value that is independent of P_{DE}. There is some suggestion that the median empirical Υ_{tot} is dropping as a function of P_{DE} when considering the median Υ_{tot} measured in our samples and in Herrera-Camus et al. [2017] (red, purple, and green points in the right column of Figure 8.5). However, the power-law fits to the two massive galaxy samples (PHANGS and EDGE-CALIFA) indicate a spread in Υ_{tot} that is large compared to the change in the numerical prediction over the same range in P_{DE}. Indeed, a unified analysis of a sample that includes high P_{DE} regions ($P_{\text{DE}} \sim 10^5/k_B$ K cm^{-3}) would be necessary to expand quantitatively upon the suggestion of a P_{DE} dependence in the simple literature comparison.

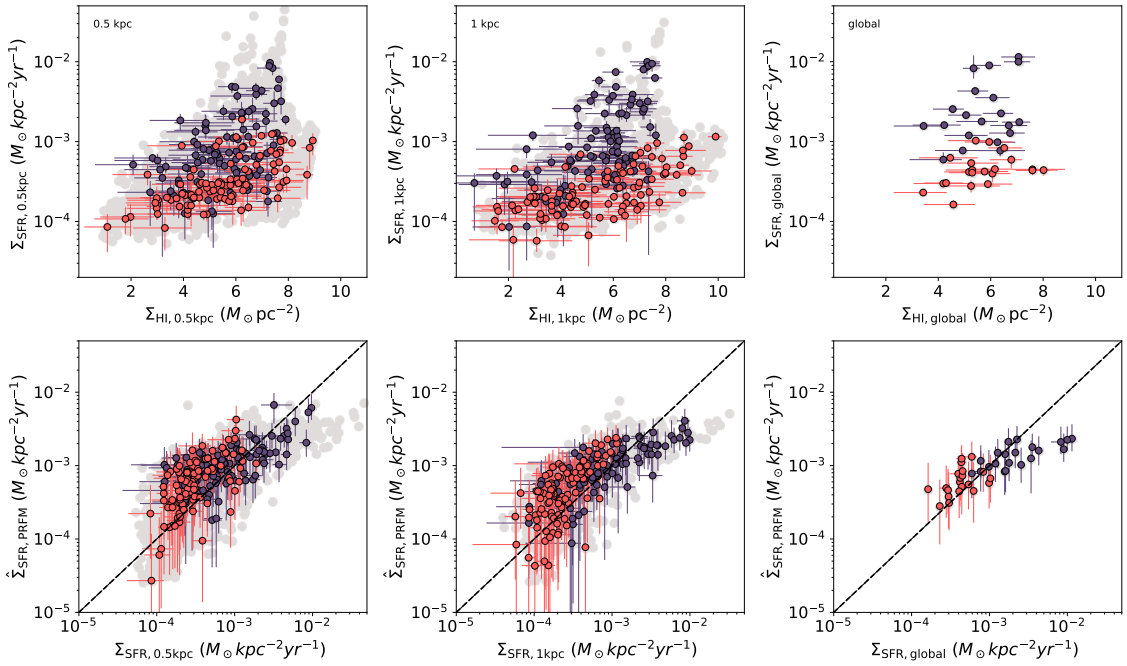

Figure 8.4 *Top Row:* a comparison between HI surface density estimates and SFR surface density measurements at 500 pc (left column), 1 kpc (middle column), and global scales (right column). In all panels, we only show NSA galaxies that are within the stellar mass range of the UDG sample. For visual clarity, we show a random subset of (at most) 70 points for each sample with individual errorbars and colored by sample source; we show the full sample as the underlying grey scatter. *Bottom row:* a comparison between the observed SFR surface densities and the PRFM predictions. Again, red points show UDGs while purple points show NSA dwarfs.

8.5 Discussion

8.5.1 Star Formation Efficiency in UDGs

In Paper I, we demonstrated that UDGs host relatively low star formation rate surface densities given their apparent HI surface densities. In this work, we have gone on to consider whether this low efficiency star formation is surprising in the context of contemporary theories of galactic star formation. As we have detailed in the preceding section, we find that the pressure-regulated, feedback-modulated (PRFM) theory of star formation is remarkably successful at predicting the low Σ_{SFR} and SFE(HI) of the UDGs. These extreme galaxies, then, are forming stars in the

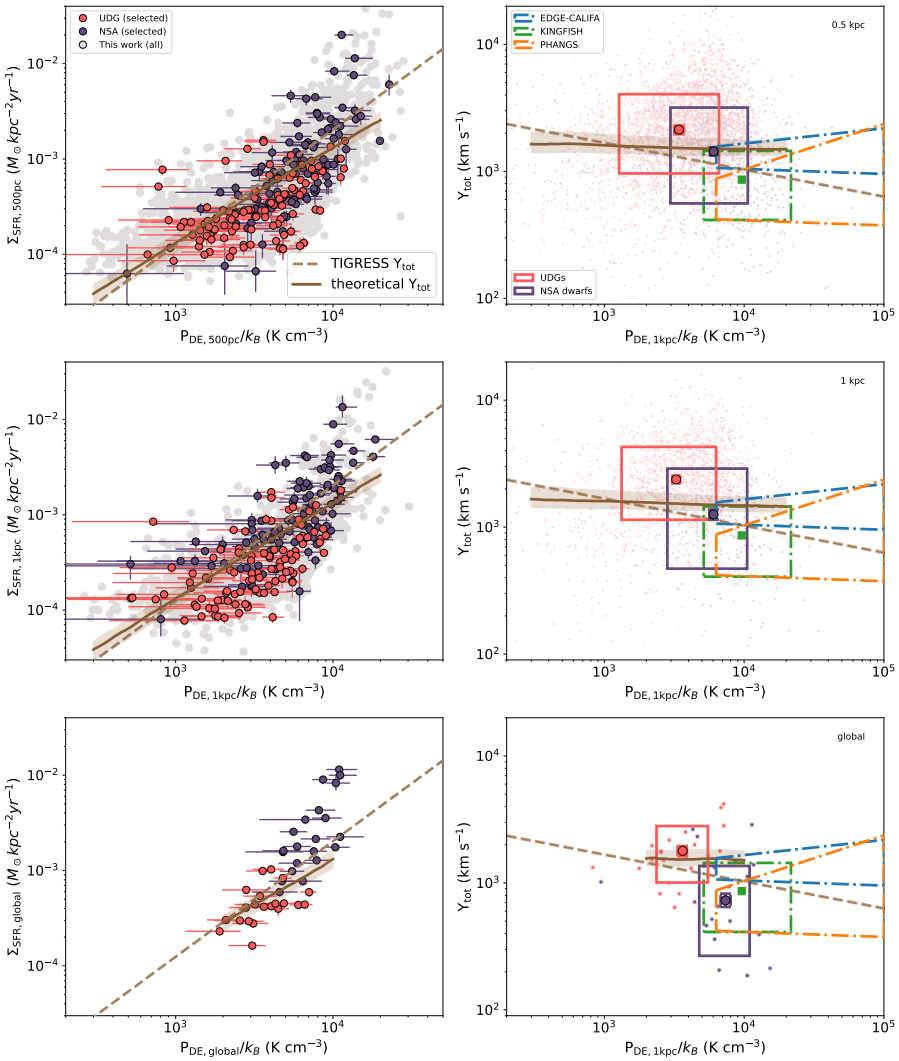

Figure 8.5 *Left:* an estimate of the dynamical equilibrium pressure (P_{DE}) for our sample. We overplot the theoretical (Equation 8.6) and numerical (Equation 8.7) predictions of Ostriker & Kim (2022, in preparation) as the dashed and solid lines, respectively. *Right:* an empirical estimate of $\Upsilon_{\rm tot}$ as a function of $P_{\rm DE}$. We compare to kpc-scale observations from PHANGS [orange dot-dashed, Sun et al., 2020], EDGE-CALIFA [blue dot-dashed, Barrera-Ballesteros et al., 2021], and KINGFISH [green dot-dashed, Herrera-Camus et al., 2017], as well as to the predictions of Ostriker & Kim (2022, in preparation).

same way as "normal" dwarfs or even much more massive galaxies – the difference in their star formation behavior can be quantitatively attributed to the shallower gravitational potential due to

the characteristically diffuse stellar structure of the UDGs.

The bottom panels of Figure 8.4 demonstrate that the PRFM model is highly successful at reproducing the star formation rate surface densities of the UDGs, even without considering the surface density contribution of molecular gas. Furthermore, Figure 8.5 shows that the NSA dwarfs and UDGs lie on the same relation between $P_{\rm DE}$ (dynamical equilibrium pressure) and $\Sigma_{\rm SFR}$ as do massive galaxies. These successes indicate that HI-rich UDGs, which are largely in low-density environments, need not be forming stars in an exotic manner, as has been suggested for globular cluster-rich UDGs in high-density environments [Danieli et al., 2021].

Instead, we have shown that the star formation in these HI-rich UDGs is regulated in the same way as is star formation in the "normal" NSA dwarfs and in more massive galaxies, as evidenced by the concordance between our empirical estimates of $\Upsilon_{\rm tot}$. Despite the apparent oddity of the low $\Sigma_{\rm SFR}$ of the UDGs when considering total gas (HI) availability, contemporary theories of star formation that explicitly include local galactic structure are able to naturally account for the low star formation efficiency of HI-rich UDGs. Notably, this is despite the fact that these theories have been validated and tested largely for more massive, higher density systems quite unlike the diffuse conditions of the dwarfs in our sample.

8.5.2 Molecular Hydrogen in UDGs

In this work we have shown that the PRFM model of star formation does a remarkably good job of accounting for the star formation rate surface density of the UDGs, despite the fact that we assume that the contribution of molecular hydrogen to the overall weight of the system is negligible. In general and quite separate from the discussion of UDGs, galaxies in this mass range are thought to be relatively poor in H_2 overall – a recent study suggests that nearby dwarfs with stellar masses less than $\log_{10}(M_\star/M_\odot) = 8.5$ have a median H_2 fraction of $f_{H_2} \equiv \Sigma_{H_2}/(\Sigma_{H_2} + \Sigma_{\rm HI}) = 0.15$ [de los Reyes and Kennicutt, 2019]. Despite their overall small H_2 content, dwarfs are also thought to preferentially host their molecular gas at small radii, allowing H_2 to contribute significantly to or even dominate the weight of the ISM near the center of the galaxy [Leroy et al., 2008].

In order to understand what we may say about the H_2 content in UDGs, we first consider the

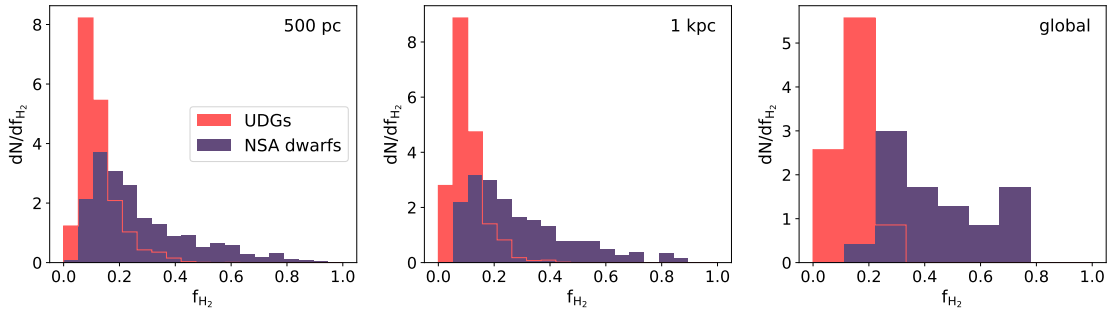

Figure 8.6 The estimated H_2 fraction (where $f_{H_2} = \Sigma_{H_2}/[\Sigma_{H_2} + \Sigma_{HI}]$) for the regions in our sample at 500 pc (left), 1 kpc (middle), and global scales (right) when we assume a constant H_2 depletion time of $\tau_{dep} = \Sigma_{H_2}/\Sigma_{SFR} = 1.8$ Gyr. The red histograms shows the UDGs, while the purple histograms show the NSA dwarfs. We find that while the distribution in f_{H_2} peaks at $f_{H_2} < 0.2$ for both the UDGs and NSA galaxies, the NSA dwarfs are characterized by a tail to high molecular gas fractions. This finding is consistent with the under-prediction of the HI-only PRFM estimate for the highly star-forming regions of the NSA galaxies (as shown in Figure 8.4).

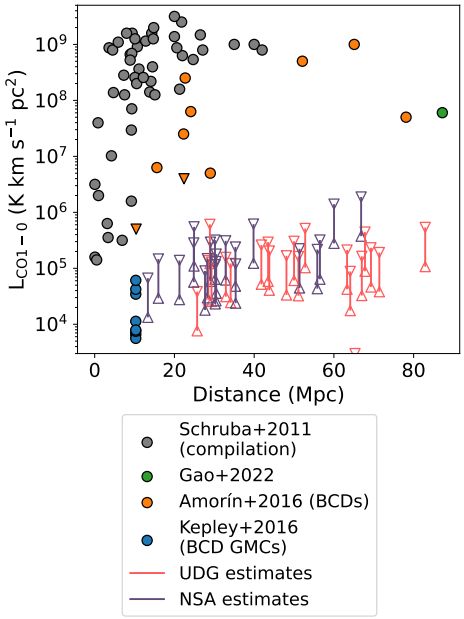

Figure 8.7 A comparison between the expected CO (1-0) luminosities of our NSA (purple) and UDG (red) dwarf samples and real measurements from the literature. We estimate L_{CO1-0} by assuming a constant H_2 depletion time of $\tau_{dep} = 1.8$ Gyr and bounding our estimates from α_{CO} measurements of the LMC and SMC [Schruba et al., 2011]. We find that the expected CO luminosities of the galaxies in the present sample are comparable to measurements made of galaxies at lower distances, but lie well below literature measurements of galaxies at similar distances.

impact of our HI-only approach on the NSA sample. In Figure 8.4, we see that the HI-only PRFM model significantly under-predicts Σ_{SFR} for the NSA dwarfs, particularly when we consider the

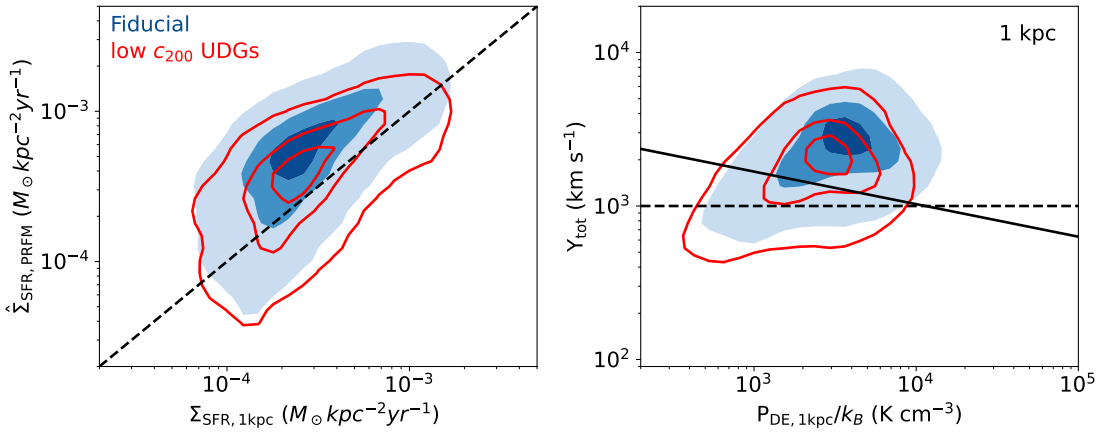

Figure 8.8 *Left:* The observed versus estimated $\Sigma_{\rm SFR}$ for our UDGs under our fiducial assumptions about their dark matter halos (blue filled contour) and for low concentration halos (unfilled red contour). For this demonstration, we hold the halo mass constant between the fiducial and low-concentration predictions. *Right:* A comparison between our fiducial and low concentration results in the dynamical pressure versus empirical $\Upsilon_{\rm tot}$ plane. We show the Ostriker & Kim (2022, in preparation) theoretical and simulation-driven predictions by the dashed and solid black lines.

star formation rate surface density averaged over kiloparsec or larger scales. At 500 pc scales, the bulk of the regions are well-represented by their PRFM predictions, though a tail towards under-predicted $\Sigma_{\rm SFR}$ at high $P_{\rm DE}$ remains. This can be understood if one considers that the average $\Sigma_{\rm SFR}$ measured within any given region of 500 pc, 1000 pc, or greater size is essentially a SFR-weighted average. At global scales, the most vigorously star-forming regions dominate the average $\Sigma_{\rm SFR}$. At 500 pc, these vigorously star-forming regions are siloed into a relatively small number of points. This transition from a roughly SFR-weighted to a roughly area-weighted scheme can also be seen in the behavior of the median $\Upsilon_{\rm tot}$ estimated for the NSA galaxies as a function of region spatial scale in the right column of Figure 8.5. At 500 pc, the median empirical $\Upsilon_{\rm tot}$ computed from the NSA dwarfs is in good agreement with the prediction from the TIGRESS simulations of Ostriker & Kim (2022, in preparation). When we consider the global averages, however, the median empirical $\Upsilon_{\rm tot}$ lies well below the simulation prediction.

Having established the possible impact on neglecting the H_2 contribution in the NSA dwarfs,

we may now consider the UDGs. First, unlike the NSA dwarfs, the PRFM prediction tends to slightly over-predict the star formation rate surface densities of the UDGs as a function of $P_{\rm DE}$. This implies that, holding the dark matter halo properties constant (a point we will return to in the following section), the absence of the weight from the H_2 component does not strongly affect the $\Sigma_{\rm SFR}$ predictions for the UDGs. This is despite the fact that, as shown in Figure 8.3, the self-gravity of the ISM comprises a larger component of the total midplane weight of the UDGs. The UDGs should thus be relatively more sensitive to the effect of neglecting H_2 gas, as the $\mathcal{W}_{\rm gas}$ scales as the square of the gas surface density (as opposed to $\mathcal{W}_{\rm ext}$, which scales linearly with the gas surface density). Thus, we find that unlike the NSA dwarfs, the UDGs in our sample are unlikely to host large molecular gas stores.

One simple exercise we can undertake to test the idea that H_2 is a less important contributor to $P_{\rm DE}$ in UDGs than in the NSA galaxies is by a direct estimate of M_{H_2} from the star formation rate via an assumed depletion time $\tau_{\rm dep}$. Observational support for a constant H_2 depletion time of $\tau_{\rm dep} \sim 1-3$ Gyr has emerged from observational work [see, e.g. Bigiel et al., 2008, Leroy et al., 2008, Bigiel et al., 2011, Schruba et al., 2011, 2012, Leroy et al., 2021], though there is evidence for variation within that range as a function of environment [Utomo et al., 2017]. For this test we will assume a constant depletion time of $\tau_{\rm dep} \equiv \Sigma_{H_2}/\Sigma_{\rm SFR} = 1.8$ Gyr.

Using this assumed H_2 depletion time, we may directly estimate the expected H_2 surface density from our measured star formation rate surface densities. We can then compute the molecular gas fraction in each region, where the H_2 fraction is defined as $f_{H_2} = \Sigma_{H_2}/(\Sigma_{H_2} + \Sigma_{\rm HI})$. We indeed find that the UDG expected H_2 fractions are quite low, with a median expected molecular gas fraction of $f_{H_2} = 0.09$ and a $99^{\rm th}$ percentile expected fraction of $f_{H_2} = 0.31$. Conversely, although the median NSA dwarf region has a relatively low expected H_2 fraction ($f_{H_2} = 0.24$), there is a significant tail to H_2-dominated regions – the $99^{\rm th}$ percentile expected fraction of the NSA sample is $f_{H_2} = 0.83$.

Using these H_2 surface density estimates within the PRFM prediction framework would clearly be circular, as the quantity of interest ($\Sigma_{\rm SFR}$) is the very quantity that we use to estimate Σ_{H_2}. However, this exercise does provide a separate (though we note, not entirely independent) consistency check with our previous claim that the molecular gas stores of the UDGs are a subdominant

contributor to the overall gas surface density.

Outlooks on H_2 Detection

Clearly, a direct estimation of the H_2 content of the UDGs in our sample would be immensely powerful in determining whether they are H_2-depleted, and whether their SFE(H_2) is consistent with that of "normal" galaxies. There are two substantial technical hurdles to gain such an estimation: first, the previously-discussed low predicted H_2 masses of the UDGs, and second, the substantial uncertainty in converting between a direct measurement (e.g. of CO(1-0)) and H_2 mass in a UDG-like environment.

Given a depletion time $\tau_{\rm dep}$, the relation between the CO (1-0) luminosity and H_2 mass can be written as

$$\alpha_{\rm CO(1-0)} = \frac{M_{\rm H_2}}{\rm L_{CO(1-0)}} = \tau_{\rm dep}\frac{\rm SFR}{\rm L_{CO(1-0)}}. \tag{8.11}$$

As above, we assume an H_2 depletion time of 1.8 Gyr. It is both observed and theoretically expected that $\alpha_{\rm CO}$ should be sensitive to environmental factors such as (but not necessarily limited to) metallicity, with $\alpha_{\rm CO}$ increasing with decreasing metallicity [e.g. Schruba et al., 2011, Bolatto et al., 2013, Gong et al., 2020]. Even if a CO detection can be made, it is therefore also necessary to spectroscopically determine the metallicity in order to obtain an estimate of the H_2 mass, which is in itself observationally difficult given the low surface brightnesses and on-sky sparsity of the UDGs. Previous exercises with similar samples have required moderate (1 hr) integration times with wide (2") slits on the 8.1m Gemini South telescope in order to yield gas-phase metallicity measurements [Greco et al., 2018b].

In the absence of a gas-phase metallicity measurement, we can make a simple estimate of the expected CO (1-0) luminosity using existing $\alpha_{\rm CO}$ measurements of our most nearby massive dwarfs, the Large and Small Magellanic Clouds (LMC and SMC, respectively). We adopt the $\alpha_{\rm CO}$ measurements of the LMC and SMC of Schruba et al. [2011] – as the more metal-rich system, adopting the $\alpha_{\rm CO}$ measured for the LMC results in higher CO (1-0) luminosities than does adopting the value measured from the SMC. In Figure 8.7, we show the expected CO (1-0) luminosities of the

galaxies in our sample as a function of luminosity distances given the assumptions detailed above. We additionally show a selection of observed CO (1-0) measurements from the literature for a selection of samples that include low-mass and low-metallicity objects [Schruba et al., 2011, Amorín et al., 2016, Kepley et al., 2016, Gao et al., 2022]. We find that although the predicted CO (1-0) luminosities are comparable to L_{CO1-0} measurements of nearby dwarfs, the predicted luminosities are significantly lower than literature measurements at the distance range of the sample.

An alternative approach is to measure the dust mass via SED fitting in the FIR, where emission may be modeled as a modified blackbody with the dust mass, temperature, and emissivity index as free parameters [see, e.g. Kennicutt et al., 2011, Cigan et al., 2021, Shivaei et al., 2022]. Due to the distance and mass of the UDGs, it is likely that stacking would be necessary to obtain a robust measurement [Shivaei et al., 2022]. The dust mass can then be used to infer to the total gas mass via an assumed dust-to-gas ratio, which can then in turn be used to estimate the H_2 mass given a measured HI mass. However, like α_{CO}, the dust-to-gas ratio is naturally expected to depend on metallicity; measured dust-to-gas ratios at low metallicities also exhibit substantial scatter [see Figure 11 of Cigan et al., 2021].

8.5.3 If UDGs Live in Special Halos

A rather significant uncertainty in our analysis is the unknown nature of the dark matter halos in which our HI-rich UDGs live. A recent work has shed some light on this topic by estimating halo profile parameters for a sample of HI-rich UDGs [Kong et al., 2022]. In this work, the authors suggest that UDGs live in unusually low concentration dark matter halos. Thus, having assumed "normal" dark matter halos for the UDGs – keeping in mind that "normal" is itself an uncertain term for the dwarf population – we may now consider how low concentration halos could impact our results.

There is unfortunately only one galaxy, AGC 242019, which is in both our sample and the sample of Kong et al. [2022]. As an exercise, however, we estimate the change in the Σ_{SFR} predicted by the PRFM TIGRESS model if we were to adopt the median halo concentration measured by Kong et al. [2022] of $c = 2.62$. We show the impact of this change in both the observed-to-predicted star

formation rate and $P_{\rm DE}$-to-$\Upsilon_{\rm tot}$ planes in Figure 8.8. We do find that assuming a lower concentration halo brings the UDGs closer in line with theoretical results. However, for the singular galaxy that does constitute the overlap between the samples, we find that assuming the halo profile reported by Kong et al. [2022] actually causes a greater difference between our observed and predicted $\Sigma_{\rm SFR}$. There thus yet remains significant work to be done in order to reduce the uncertainty of the impact of the UDGs' dark matter halos.

8.6 Conclusions

In this series, we have used spatially-resolved SED fitting to explore the star formation activity in a sample of nearby (d $<$ 120 Mpc) HI-detected ultra-diffuse dwarf galaxies from Janowiecki et al. [2019], along with a NASA Sloan Atlas reference sample of "normal" dwarfs with HI measurements from Bradford et al. [2015]. The samples in this work allow us to compare and contrast the star formation behavior of the UDGs against the NSA dwarfs, providing new tests for star formation theory in extreme (low density) environments, as well as new clues to the evolutionary pathway of these HI-rich UDGs (see Paper I).

As established in the first paper of this series, the UDGs are characterized by low star formation rate surface densities and star formation efficiencies (as a function of their atomic gas surface densities) down to 500 pc scales. In this work, we ask whether the UDGs' lower SFE(HI) is expected in the context of contemporary models of star formation.

We consider the framework of pressure-regulated, feedback-modulated star formation (PRFM), which directly connects star formation and galaxy structure for disks in equilibrium, in Section 8.4. We indeed find that the lower SFR surface densities and lower SFE(HI) seen in the UDGs are well-predicted by the PRFM model; that is, the relationship between midplane pressure and star formation rate surface density ($\Upsilon_{\rm tot}$) is the same for the UDGs in our sample as it is for the NSA dwarfs, or indeed even much more massive galaxies.

This holds true for the UDGs despite the fact that we neglect any weight contributions from H_2 in this analysis. We find that at globally averaged scales (which one can think of as the SFR-

weighted limit), HI-only predictions underestimate star formation in the NSA dwarfs, but that the same HI-only predictions are in good agreement with the NSA dwarfs at 500 pc scales (which one may roughly think of as approaching an area-weighted average). This implies that H_2 is an important contributor to the weight in the regions of the most vigorous star formation, but is a minority component at large – a suggestion that is in agreement with previous results [see, e.g. Leroy et al., 2008, de los Reyes and Kennicutt, 2019]. Star formation in the UDGs, however, is well-described or even somewhat overestimated by the HI-only PRFM predictions at all spatial scales, suggesting that the UDGs may be H_2-poor even compared to similarly (stellar) massive "normal" dwarfs.

As referenced in Paper I, a clear extension of this work will be to measure spatially resolved HI in a larger sample of field UDGs. In this work, we have also considered routes to estimate H_2 mass in the UDGs, but note that obtaining a detection via either CO or FIR dust emission will likely be resource-intensive due to the low predicted H_2 fractions and likely low metallicities of the UDGs. The uncertainty in the X_{CO} factor and/or gas-to-dust ratio in these galaxies further increases the uncertainty in obtaining a H_2 mass from such a detection. Nevertheless, a greater understanding of the ISM in UDGs is a key path towards understanding the landscape of star formation in these unusual objects, as well as towards understanding their utility as laboratories in which to study extreme low-density star formation.

Software used in this work: Astropy [Astropy Collaboration et al., 2013, Price-Whelan et al., 2018], matplotlib [Hunter, 2007], SciPy [jon, 2001], the IPython package [Pérez and Granger, 2007], NumPy [Van Der Walt et al., 2011], pandas [McKinney, 2010, 2011], Astroquery [Ginsburg et al., 2019], extinction [Barbary, 2021]

Chapter 9

Towards a Census of Star-Forming Dwarfs

In the preceding eight chapters, we have demonstrated the novel and significant power that modern era wide-field imaging surveys have to explore the low-mass galaxy population in detail out to intermediate redshift. However, there is still currently inaccessible scientific potential in these surveys – as the reader may have noticed, many of the works in this dissertation rely upon spectroscopic samples drawn from previous wide-field spectroscopic surveys. These spectroscopic surveys are complete at low masses over only a relatively small volume; due to their low luminosities, distance determination for dwarfs remains a key issue.

Although our understanding of the dwarf population beyond the Local Universe has expanded greatly over the last few decades, the low-mass galaxy community still lacks the type of large and complete samples that have proved to be remarkably powerful tools in constraining the nature of the massive galaxy population. Current and upcoming wide-field imaging surveys now have the breadth, depth, and resolution necessary to study large samples of dwarfs at substantial distances – analogous surveys with the capability to make distance determinations for dwarfs (e.g. spectroscopic, narrow-band, or medium-band surveys) are now coming online that will make it possible to assemble these

samples. This advancement signals a fundamental shift in the type of science that can be done for samples of dwarf galaxies outside of the nearby Universe, and is opening up a new, statistical avenue for low-mass galaxy studies. In the final chapter of this dissertation, I will briefly discuss the outlook for two such surveys with which I have been involved during my dissertation work.

9.1 The Merian Survey

As established above, the community still lacks a complete sample of low-mass ($M_\star < 10^9 M_\odot$) galaxies outside the nearby Universe (tens of Mpc from the Milky Way). Merian is a purpose-built medium-band survey designed to produce a sample of star-forming dwarfs that is mass complete down to $M_\star \sim 10^8 M_\odot$ at $0.05 < z < 0.1$.

The Merian survey has been allotted 62 nights with the Dark Energy Camera (DECam) at the Cerro Tololo Inter-American Observatory; observations began in 2020B, and data collection is set to conclude in 2023A. The survey consists of two medium-bands that cover Hα (N708) and [OIII] + Hβ (N540) at $0.05 < z < 0.1$; combined with an on-sky coverage of $\sim$ 860 deg^2, we estimate that we will assemble a sample of more than 100,000 dwarfs in the target stellar mass ($10^8 < M_\star/M_\odot < 10^9$) and redshift range. Such a sample will allow our team to make the first direct constraint of the dwarf stellar-to-halo mass relation, and the scatter around this relation, via galaxy-galaxy lensing, clustering, and number density measurements. Combined with deep and high-resolution imaging data from the Hyper Suprime-Cam Subaru Strategic Program (HSC-SSP), Merian will deliver directly measured star formation maps on the scale of $\sim$ 1 kpc from DECam and stellar light maps on the scale of $\sim$ 0.7 kpc from HSC (at $z = 0.05$). Taken all together, the Merian survey will provide an unprecedentedly comprehensive view of the stellar, dark matter, and star formation content of the low-mass galaxy population.

To illustrate the nature of the Merian for the reader, we show in Figure 9.1 a preliminary continuum subtraction of a $M_\star \sim 10^8$ $M_\odot$ galaxy at $z_{\rm spec} = 0.092$ in the survey. This dwarf is drawn from a complementary spectroscopic survey targeting low-mass galaxies with photometric redshifts that place them within the Merian redshift range using 30-band photometric redshifts

from the COSMOS2015 catalog [Lange et al., 2015]; the redshift, stellar mass, and strong emission line equivalent widths are therefore known for this target.

Because the two medium-bands in the Merian survey lie between the HSC broad bands, for this preliminary continuum subtraction we simply take the average of the bluer and redder broad-bands. These are $r_{\rm HSC}$ and $i_{\rm HSC}$ for the Hα (N708) filter, and $g_{\rm HSC}$ and $r_{\rm HSC}$ for the [OIII]+Hβ (N540) filter. We show these averaged broad-band images in the left column of Figure 9.1, along with the medium-band images in the middle column. At right we show the difference between the medium-band and averaged broad-band images; here, positive values indicate an excess in the medium-band over the nominal expectation from the broad-band images. The purpose of this figure is for visualization only – for excess flux measurements, we will take into account both the shape of the continuum SED in the medium-band (rather than using a geometric mean) and will correct for the difference in the point spread function between the broad-band HSC images and medium-band DECam images. Nevertheless, in this figure we show that even a preliminary subtraction treatment is successful in isolating the star-forming knot at the center of the target galaxy.

One initial and key measurement to be made using the Merian survey is a constraint on the dwarf mass-size relation. Due to their shallow potential wells, dwarf galaxies are more sensitive to the effects of star formation feedback, and their stellar structure is thus more strongly tied to the details of star formation feedback – reproducing the array of dwarf sizes and shapes has been a continuing issue in galaxy formation simulations [El-Badry et al., 2018a, Pillepich et al., 2019, Kado-Fong et al., 2022c]. Composite studies which combine multiple surveys suggest that there may be a flattening in the mass-size relation at stellar masses of $10^8 \lesssim M_\star/M_\odot \lesssim 10^9$. However, this flattening coincides with an observational gap between the mass-size relations measured in the nearby Universe and those at $z > 0$ [Lange et al., 2015, Eigenthaler et al., 2018]. A mass-complete sample of dwarfs in this "sweet spot" is necessary if we hope to not only constrain the mean behavior of the mass-size relation, but also to constrain the physical processes that drive the large diversity of sizes that are observed in dwarf galaxies. We show the predicted mass-size relation that we will measure from the Merian survey in Figure 9.2. Here, the underlying mass-size relation is derived from the COSMOS2015 30-band photometric redshift catalog of Lange et al. [2015]. The

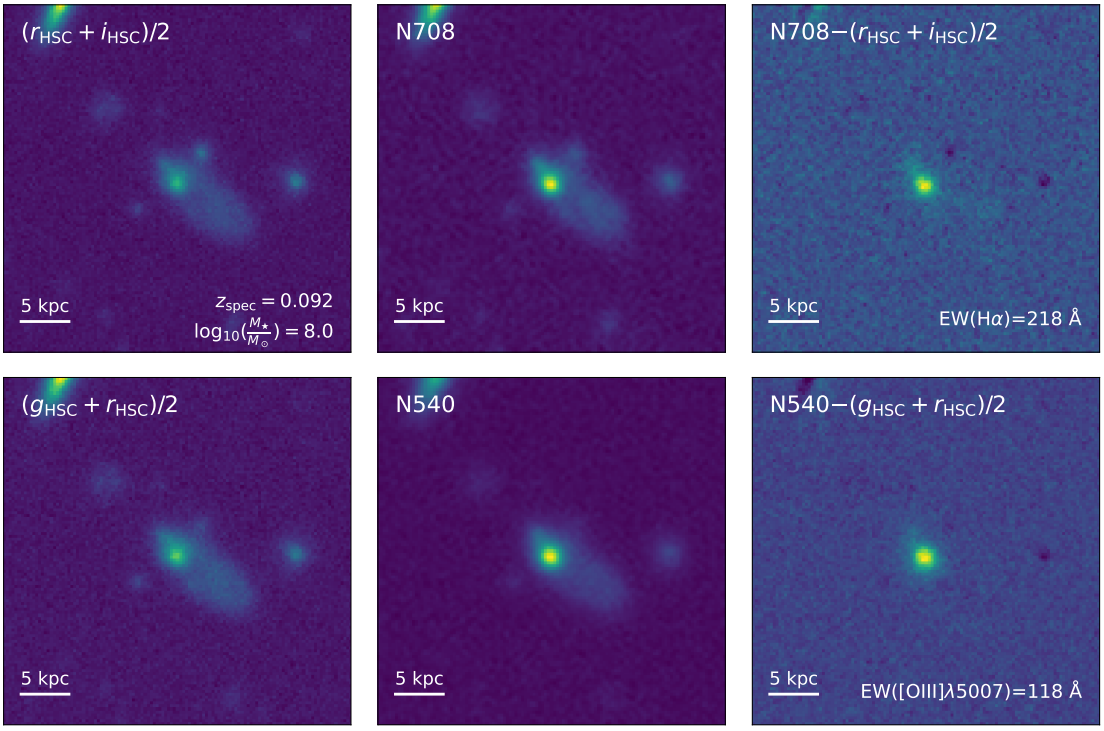

Figure 9.1 A preliminary demonstration of the continuum subtraction for the Merian survey for a $M_\star \sim 10^8$ $M_\odot$ galaxy at $z_{spec} = 0.092$. The top row shows the subtraction for the Hα filter (N708), while the bottom shows the same for the [OIII]+Hβ filter (N540). In each row, the left panel shows the average of the nearest two broad-bands (r_{HSC} and i_{HSC} at top, g_{HSC} and r_{HSC} at bottom), the middle panel shows the medium-band image, and the right panel shows the difference between the medium-band and composite broad-band images. This figure is intended for visualization purposes only, and does not include a correction between the HSC and DECam point spread functions.

blue points show galaxies in which a 7-band photometric redshift is expected to correctly place the galaxy at $0.058 < z < 0.1$; grey points show galaxies within this redshift range whose 7-band photometric redshift estimates lie outside this range (i.e. false negatives). The red points show analogous detections from the GAMA survey where the number of detections is scaled to the ratio between the Merian and GAMA survey volumes over the redshift range in which GAMA is complete down to $M_\star \sim 10^9$ $M_\odot$.

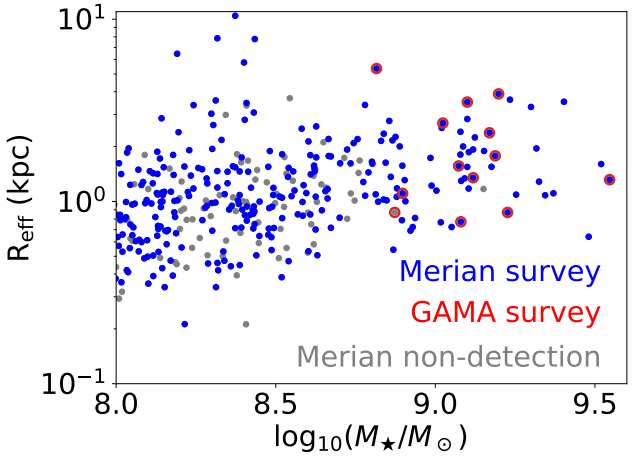

Figure 9.2 The predicted, volume-scaled mass-size relation predicted by the Merian survey (blue points) as compared to the GAMA survey (red). Merian non-detections are shown in grey points. Merian reaches lower stellar masses than GAMA over a larger volume (GAMA is mass-complete to $M_\star = 10^9 M_\odot$ at $z = 0.05$, roughly 5.5% of the Merian volume).

9.2 The Prime Focus Spectrograph Subaru Strategic Program

In addition to specialized imaging programs such as Merian, the increasing sensitivity and surveying power of ongoing and upcoming wide-field spectroscopic efforts will provide significant new spectroscopic insights into the dwarf galaxy population. Ongoing spectroscopic efforts with significant dwarf samples include the Satellites Around Galactic Analogs [SAGA, Geha et al., 2017, Mao et al., 2021, Wu et al., 2022], the Sydney-AAO Multi-object Integral-field spectrograph (SAMI) Galaxy Survey [Bryant et al., 2015, Scott et al., 2018], and the DESI (Dark Energy Spectroscopic Instrument) Experiment [DESI Collaboration et al., 2016].

The dwarf galaxy science objectives of the efforts detailed above focus mainly on the low-redshift dwarf population, as has the bulk of this dissertation thus far. However, wide-field spectroscopic survey instruments such as DESI and the Prime Focus Spectrograph (PFS) on the Subaru Telescope will, for the first time, be able to characterize large samples of dwarfs at significant redshift. These

capabilities will allow the community to directly study the change in the low-mass galaxy population as a function of redshift, and to better understand the nature of dwarfs across cosmic time.

The PFS-SSP galaxy evolution spectroscopic campaign will target galaxies at $0.7 \lesssim z \lesssim 1.7$, with a projected 90% mass completeness of $M_\star \sim 3 \times 10^9 M_\odot$ at the low-redshift end of its target range. The galaxy evolution effort is expected to generate around 68,000 spectra in total; we will account for the increased incompleteness at lower stellar masses by using deeper photometric samples available over smaller areas, namely the COSMOS 30-band photometric catalogs of Ilbert et al. [2009] and the 3DHST grism and photometric catalogs of Skelton et al. [2014]. PFS will cover Hα up to $z \sim 0.8$: for the low-redshift end of the galaxy evolution target sample, we will cover key emission line diagnostics such as Hα and Hβ (to measure star formation and probe extinction), as well as direct or indirect measures of the gas phase metallicity via either [OIII]λ4363 or strong line proxies. These measurements will allow for the first ever direct probe of the progression of chemical enrichment of the low-mass galaxy population over cosmic time.

Bibliography

SciPy: Open source scientific tools for python, 2001. URL `http://www.scipy.org/`.

Mario G. Abadi, Julio F. Navarro, and Matthias Steinmetz. Stars beyond galaxies: the origin of extended luminous haloes around galaxies. *MNRAS*, 365(3):747–758, January 2006. doi: 10.1111/j.1365-2966.2005.09789.x.

Kevork Abazajian, Jennifer K. Adelman-McCarthy, Marcel A. Agüeros, Sahar S. Allam, Kurt Anderson, Scott F. Anderson, James Annis, Neta A. Bahcall, Ivan K. Baldry, Steven Bastian, Andreas Berlind, Mariangela Bernardi, Michael R. Blanton, Jr. Bochanski, John J., William N. Boroski, John W. Briggs, J. Brinkmann, Robert J. Brunner, Tamás Budavári, Larry N. Carey, Samuel Carliles, Francisco J. Castander, A. J. Connolly, István Csabai, Mamoru Doi, Feng Dong, Daniel J. Eisenstein, Michael L. Evans, Xiaohui Fan, Douglas P. Finkbeiner, Scott D. Friedman, Joshua A. Frieman, Masataka Fukugita, Roy R. Gal, Bruce Gillespie, Karl Glazebrook, Jim Gray, Eva K. Grebel, James E. Gunn, Vijay K. Gurbani, Patrick B. Hall, Masaru Hamabe, Frederick H. Harris, Hugh C. Harris, Michael Harvanek, Timothy M. Heckman, John S. Hendry, Gregory S. Hennessy, Robert B. Hindsley, Craig J. Hogan, David W. Hogg, Donald J. Holmgren, Shin-ichi Ichikawa, Takashi Ichikawa, Željko Ivezić, Sebastian Jester, David E. Johnston, Anders M. Jorgensen, Stephen M. Kent, S. J. Kleinman, G. R. Knapp, Alexei Yu. Kniazev, Richard G. Kron, Jurek Krzesinski, Peter Z. Kunszt, Nickolai Kuropatkin, Donald Q. Lamb, Hubert Lampeitl, Brian C. Lee, R. French Leger, Nolan Li, Huan Lin, Yeong-Shang Loh, Daniel C. Long, Jon Loveday, Robert H. Lupton, Tanu Malik, Bruce Margon, Takahiko Matsubara, Peregrine M.

McGehee, Timothy A. McKay, Avery Meiksin, Jeffrey A. Munn, Reiko Nakajima, Thomas Nash, Jr. Neilsen, Eric H., Heidi Jo Newberg, Peter R. Newman, Robert C. Nichol, Tom Nicinski, Maria Nieto-Santisteban, Atsuko Nitta, Sadanori Okamura, William O'Mullane, Jeremiah P. Ostriker, Russell Owen, Nikhil Padmanabhan, John Peoples, Jeffrey R. Pier, Adrian C. Pope, Thomas R. Quinn, Gordon T. Richards, Michael W. Richmond, Hans-Walter Rix, Constance M. Rockosi, David J. Schlegel, Donald P. Schneider, Ryan Scranton, Maki Sekiguchi, Uros Seljak, Gary Sergey, Branimir Sesar, Erin Sheldon, Kazu Shimasaku, Walter A. Siegmund, Nicole M. Silvestri, J. Allyn Smith, Vernesa Smolčić, Stephanie A. Snedden, Albert Stebbins, Chris Stoughton, Michael A. Strauss, Mark SubbaRao, Alexander S. Szalay, István Szapudi, Paula Szkody, Gyula P. Szokoly, Max Tegmark, Luis Teodoro, Aniruddha R. Thakar, Christy Tremonti, Douglas L. Tucker, Alan Uomoto, Daniel E. Vanden Berk, Jan Vandenberg, Michael S. Vogeley, Wolfgang Voges, Nicole P. Vogt, Lucianne M. Walkowicz, Shu-i. Wang, David H. Weinberg, Andrew A. West, Simon D. M. White, Brian C. Wilhite, Yongzhong Xu, Brian Yanny, Naoki Yasuda, Ching-Wa Yip, D. R. Yocum, Donald G. York, Idit Zehavi, Stefano Zibetti, and Daniel B. Zucker. The Second Data Release of the Sloan Digital Sky Survey. *AJ*, 128(1):502–512, July 2004. doi: 10.1086/421365.

A. Adamo, L. J. Smith, J. S. Gallagher, N. Bastian, J. Ryon, M. S. Westmoquette, I. S. Konstantopoulos, E. Zackrisson, S. S. Larsen, E. Silva-Villa, J. C. Charlton, and D. R. Weisz. Revealing a ring-like cluster complex in a tidal tail of the starburst galaxy NGC 2146. *MNRAS*, 426: 1185–1194, October 2012. doi: 10.1111/j.1365-2966.2012.21384.x.

S. M. Adams, D. Zaritsky, D. J. Sand, M. L. Graham, C. Bildfell, H. Hoekstra, and C. Pritchet. The Environmental Dependence of the Incidence of Galactic Tidal Features. *AJ*, 144:128, November 2012. doi: 10.1088/0004-6256/144/5/128.

Oscar Agertz, Florent Renaud, Sofia Feltzing, Justin I. Read, Nils Ryde, Eric P. Andersson, Martin P. Rey, Thomas Bensby, and Diane K. Feuillet. VINTERGATAN - I. The origins of chemically, kinematically, and structurally distinct discs in a simulated Milky Way-mass galaxy. *MNRAS*, 503(4):5826–5845, June 2021. doi: 10.1093/mnras/stab322.

Romina Ahumada, Carlos Allende Prieto, Andres Almeida, Friedrich Anders, Scott F. Anderson,

Brett H. Andrews, Borja Anguiano, Riccardo Arcodia, Eric Armengaud, Marie Aubert, Santiago Avila, Vladimir Avila-Reese, Carles Badenes, Christophe Balland, Kat Barger, Jorge K. Barrera-Ballesteros, Sarbani Basu, Julian Bautista, Rachael L. Beaton, Timothy C. Beers, B. Izamar T. Benavides, Chad F. Bender, Mariangela Bernardi, Matthew Bershady, Florian Beutler, Christian Moni Bidin, Jonathan Bird, Dmitry Bizyaev, Guillermo A. Blanc, Michael R. Blanton, Mederic Boquien, Jura Borissova, Jo Bovy, W. N. Brandt, Jonathan Brinkmann, Joel R. Brownstein, Kevin Bundy, Martin Bureau, Adam Burgasser, Etienne Burtin, Mariana Cano-Diaz, Raffaella Capasso, Michele Cappellari, Ricardo Carrera, Solene Chabanier, William Chaplin, Michael Chapman, Brian Cherinka, Cristina Chiappini, Peter Doohyun Choi, S. Drew Chojnowski, Haeun Chung, Nicolas Clerc, Damien Coffey, Julia M. Comerford, Johan Comparat, Luiz da Costa, Marie-Claude Cousinou, Kevin Covey, Jeffrey D. Crane, Katia Cunha, Gabriele da Silva Ilha, Yu Sophia Dai, Sanna B. Damsted, Jeremy Darling, Danny Horta Darrington, Jr. Davidson, James W., Roger Davies, Kyle Dawson, Nikhil De, Axel de la Macorra, Nathan De Lee, Anna Barbara de Andrade Queiroz, Alice Deconto Machado, Sylvain de la Torre, Flavia Dell'Agli, Helion du Mas des Bourboux, Aleksandar M. Diamond-Stanic, Sean Dillon, John Donor, Niv Drory, Chris Duckworth, Tom Dwelly, Garrett Ebelke, Sarah Eftekharzadeh, Arthur Davis Eigenbrot, Yvonne P. Elsworth, Mike Eracleous, Ghazaleh Erfanianfar, Stephanie Escoffier, Xiaohui Fan, Emily Farr, Jose G. Fernandez-Trincado, Diane Feuillet, Alexis Finoguenov, Patricia Fofie, Amelia Fraser-McKelvie, Peter M. Frinchaboy, Sebastien Fromenteau, Hai Fu, Lluis Galbany, Rafael A. Garcia, D. A. Garcia-Hernandez, Luis Alberto Garma Oehmichen, Junqiang Ge, Marcio Antonio Geimba Maia, Doug Geisler, Joseph Gelfand , Julian Goddy, Jean-Marc Le Goff, Violeta Gonzalez-Perez, Kathleen Grabowski, Paul Green, Catherine J. Grier, Hong Guo, Julien Guy, Paul Harding, Sten Hasselquist, Adam James Hawken, Christian R. Hayes, Fred Hearty, S. Hekker, David W. Hogg, Jon Holtzman, Jiamin Hou, Bau-Ching Hsieh, Daniel Huber, Jason A. S. Hunt, J. Ider Chitham, Julie Imig, Mariana Jaber, Camilo Eduardo Jimenez Angel, Jennifer A. Johnson, Amy M. Jones, Henrik Jonsson, Eric Jullo, Yerim Kim, Karen Kinemuchi, IV Kirkpatrick, Charles C., George W. Kite, Mark Klaene, Jean-Paul Kneib, Juna A. Kollmeier, Hui Kong, Marina Kounkel, Dhanesh Krishnarao, Ivan Lacerna, Ting-Wen Lan, Richard R. Lane,

David R. Law, Henry W. Leung, Hannah Lewis, Cheng Li, Jianhui Lian, Lihwai Lin, Dan Long, Penelope Longa-Pena, Britt Lundgren, Brad W. Lyke, J. Ted Mackereth, Chelsea L. MacLeod, Steven R. Majewski, Arturo Manchado, Claudia Maraston, Paul Martini, Thomas Masseron, Karen L. Masters, Savita Mathur, Richard M. McDermid, Andrea Merloni, Michael Merrifield, Szabolcs Meszaros, Andrea Miglio, Dante Minniti, Rebecca Minsley, Takamitsu Miyaji, Faizan Gohar Mohammad, Benoit Mosser, Eva-Maria Mueller, Demitri Muna, Andrea Munoz-Gutierrez, Adam D. Myers, Seshadri Nadathur, Preethi Nair, Janaina Correa do Nascimento, Rebecca Jean Nevin, Jeffrey A. Newman, David L. Nidever, Christian Nitschelm, Pasquier Noterdaeme, Julia E. O'Connell, Matthew D Olmstead, Daniel Oravetz, Audrey Oravetz, Yeisson Osorio, Zachary J. Pace, Nelson Padilla, Nathalie Palanque-Delabrouille, Pedro A. Palicio, Hsi-An Pan, Kaike Pan, James Parker, Romain Paviot, Sebastien Peirani, Karla Pena Ramrez, Samantha Penny, Will J. Percival, Ismael Perez-Fournon, Ignasi Perez-Rafols, Patrick Petitjean, Matthew M. Pieri, Marc Pinsonneault, Vijith Jacob Poovelil, Joshua Tyler Povick, Abhishek Prakash, Adrian M. Price-Whelan, M. Jordan Raddick, Anand Raichoor, Amy Ray, Sandro Barboza Rembold, Mehdi Rezaie, Rogemar A. Riffel, Rogerio Riffel, Hans-Walter Rix, Annie C. Robin, A. Roman-Lopes, Carlos Roman-Zuniga, Benjamin Rose, Ashley J. Ross, Graziano Rossi, Kate Rowlands, Kate H. R. Rubin, Mara Salvato, Ariel G. Sanchez, Laura Sanchez-Menguiano, Jose R. Sanchez-Gallego, Conor Sayres, Adam Schaefer, Ricardo P. Schiavon, Jaderson S. Schimoia, Edward Schlafly, David Schlegel, Donald P. Schneider, Mathias Schultheis, Axel Schwope, Hee-Jong Seo, Aldo Serenelli, Arman Shafieloo, Shoaib Jamal Shamsi, Zhengyi Shao, Shiyin Shen, Matthew Shetrone, Raphael Shirley, Victor Silva Aguirre, Joshua D. Simon, M. F. Skrutskie, Anze Slosar, Rebecca Smethurst, Jennifer Sobeck, Bernardo Cervantes Sodi, Diogo Souto, David V. Stark, Keivan G. Stassun, Matthias Steinmetz, Dennis Stello, Julianna Stermer, Thaisa Storchi-Bergmann, Alina Streblyanska, Guy S. Stringfellow, Amelia Stutz, Genaro Suarez, Jing Sun, Manuchehr Taghizadeh-Popp, Michael S. Talbot, Jamie Tayar, Aniruddha R. Thakar, Riley Theriault, Daniel Thomas, Zak C. Thomas, Jeremy Tinker, Rita Tojeiro, Hector Hernandez Toledo, Christy A. Tremonti, Nicholas W. Troup, Sarah Tuttle, Eduardo Unda-Sanzana, Marica Valentini, Jaime Vargas-Gonzalez, Mariana Vargas-Magana, Jose Antonio Vazquez-Mata,

M. Vivek, David Wake, Yuting Wang, Benjamin Alan Weaver, Anne-Marie Weijmans, Vivienne Wild, John C. Wilson, Robert F. Wilson, Nathan Wolthuis, W. M. Wood-Vasey, Renbin Yan, Meng Yang, Christophe Yeche, Olga Zamora, Pauline Zarrouk, Gail Zasowski, Kai Zhang, Cheng Zhao, Gongbo Zhao, Zheng Zheng, Zheng Zheng, Guangtun Zhu, and Hu Zou. The Sixteenth Data Release of the Sloan Digital Sky Surveys: First Release from the APOGEE-2 Southern Survey and Full Release of eBOSS Spectra. *arXiv e-prints*, art. arXiv:1912.02905, December 2019.

H. Aihara, N. Arimoto, R. Armstrong, S. Arnouts, N. A. Bahcall, S. Bickerton, J. Bosch, K. Bundy, P. L. Capak, J. H. H. Chan, M. Chiba, J. Coupon, E. Egami, M. Enoki, F. Finet, H. Fujimori, S. Fujimoto, H. Furusawa, J. Furusawa, T. Goto, A. Goulding, J. P. Greco, J. E. Greene, J. E. Gunn, T. Hamana, Y. Harikane, Y. Hashimoto, T. Hattori, M. Hayashi, Y. Hayashi, K. G. Hełminiak, R. Higuchi, C. Hikage, P. T. P. Ho, B.-C. Hsieh, K. Huang, S. Huang, H. Ikeda, M. Imanishi, A. K. Inoue, K. Iwasawa, I. Iwata, A. T. Jaelani, H.-Y. Jian, Y. Kamata, H. Karoji, N. Kashikawa, N. Katayama, S. Kawanomoto, I. Kayo, J. Koda, M. Koike, T. Kojima, Y. Komiyama, A. Konno, S. Koshida, Y. Koyama, H. Kusakabe, A. Leauthaud, C.-H. Lee, L. Lin, Y.-T. Lin, R. H. Lupton, R. Mandelbaum, Y. Matsuoka, E. Medezinski, S. Mineo, S. Miyama, H. Miyatake, S. Miyazaki, R. Momose, A. More, S. More, Y. Moritani, T. J. Moriya, T. Morokuma, S. Mukae, R. Murata, H. Murayama, T. Nagao, F. Nakata, M. Niida, H. Niikura, A. J. Nishizawa, Y. Obuchi, M. Oguri, Y. Oishi, N. Okabe, S. Okamoto, Y. Okura, Y. Ono, M. Onodera, M. Onoue, K. Osato, M. Ouchi, P. A. Price, T.-S. Pyo, M. Sako, M. Sawicki, T. Shibuya, K. Shimasaku, A. Shimono, M. Shirasaki, J. D. Silverman, M. Simet, J. Speagle, D. N. Spergel, M. A. Strauss, Y. Sugahara, N. Sugiyama, Y. Suto, S. H. Suyu, N. Suzuki, P. J. Tait, M. Takada, T. Takata, N. Tamura, M. M. Tanaka, M. Tanaka, M. Tanaka, Y. Tanaka, T. Terai, Y. Terashima, Y. Toba, N. Tominaga, J. Toshikawa, E. L. Turner, T. Uchida, H. Uchiyama, K. Umetsu, F. Uraguchi, Y. Urata, T. Usuda, Y. Utsumi, S.-Y. Wang, W.-H. Wang, K. C. Wong, K. Yabe, Y. Yamada, H. Yamanoi, N. Yasuda, S. Yeh, A. Yonehara, and S. Yuma. The Hyper Suprime-Cam SSP Survey: Overview and survey design. *PASJ*, 70:S4, January 2018a. doi: 10.1093/pasj/psx066.

H. Aihara, R. Armstrong, S. Bickerton, J. Bosch, J. Coupon, H. Furusawa, Y. Hayashi, H. Ikeda, Y. Kamata, H. Karoji, S. Kawanomoto, M. Koike, Y. Komiyama, D. Lang, R. H. Lupton, S. Mineo, H. Miyatake, S. Miyazaki, T. Morokuma, Y. Obuchi, Y. Oishi, Y. Okura, P. A. Price, T. Takata, M. M. Tanaka, M. Tanaka, Y. Tanaka, T. Uchida, F. Uraguchi, Y. Utsumi, S.-Y. Wang, Y. Yamada, H. Yamanoi, N. Yasuda, N. Arimoto, M. Chiba, F. Finet, H. Fujimori, S. Fujimoto, J. Furusawa, T. Goto, A. Goulding, J. E. Gunn, Y. Harikane, T. Hattori, M. Hayashi, K. G. Hełminiak, R. Higuchi, C. Hikage, P. T. P. Ho, B.-C. Hsieh, K. Huang, S. Huang, M. Imanishi, I. Iwata, A. T. Jaelani, H.-Y. Jian, N. Kashikawa, N. Katayama, T. Kojima, A. Konno, S. Koshida, H. Kusakabe, A. Leauthaud, C.-H. Lee, L. Lin, Y.-T. Lin, R. Mandelbaum, Y. Matsuoka, E. Medezinski, S. Miyama, R. Momose, A. More, S. More, S. Mukae, R. Murata, H. Murayama, T. Nagao, F. Nakata, M. Niida, H. Niikura, A. J. Nishizawa, M. Oguri, N. Okabe, Y. Ono, M. Onodera, M. Onoue, M. Ouchi, T.-S. Pyo, T. Shibuya, K. Shimasaku, M. Simet, J. Speagle, D. N. Spergel, M. A. Strauss, Y. Sugahara, N. Sugiyama, Y. Suto, N. Suzuki, P. J. Tait, M. Takada, T. Terai, Y. Toba, E. L. Turner, H. Uchiyama, K. Umetsu, Y. Urata, T. Usuda, S. Yeh, and S. Yuma. First data release of the Hyper Suprime-Cam Subaru Strategic Program. *PASJ*, 70:S8, January 2018b. doi: 10.1093/pasj/psx081.

Hiroaki Aihara, Carlos Allende Prieto, Deokkeun An, Scott F. Anderson, Éric Aubourg, Eduardo Balbinot, Timothy C. Beers, Andreas A. Berlind, Steven J. Bickerton, Dmitry Bizyaev, Michael R. Blanton, John J. Bochanski, Adam S. Bolton, Jo Bovy, W. N. Brandt, J. Brinkmann, Peter J. Brown, Joel R. Brownstein, Nicolas G. Busca, Heather Campbell, Michael A. Carr, Yanmei Chen, Cristina Chiappini, Johan Comparat, Natalia Connolly, Marina Cortes, Rupert A. C. Croft, Antonio J. Cuesta, Luiz N. da Costa, James R. A. Davenport, Kyle Dawson, Saurav Dhital, Anne Ealet, Garrett L. Ebelke, Edward M. Edmondson, Daniel J. Eisenstein, Stephanie Escoffier, Massimiliano Esposito, Michael L. Evans, Xiaohui Fan, Bruno Femenía Castellá, Andreu Font-Ribera, Peter M. Frinchaboy, Jian Ge, Bruce A. Gillespie, G. Gilmore, Jonay I. González Hernández, J. Richard Gott, Andrew Gould, Eva K. Grebel, James E. Gunn, Jean-Christophe Hamilton, Paul Harding, David W. Harris, Suzanne L. Hawley, Frederick R. Hearty, Shirley Ho, David W. Hogg, Jon A. Holtzman, Klaus Honscheid, Naohisa Inada, Inese I. Ivans, Linhua Jiang, Jennifer A.

Johnson, Cathy Jordan, Wendell P. Jordan, Eyal A. Kazin, David Kirkby, Mark A. Klaene, G. R. Knapp, Jean-Paul Kneib, C. S. Kochanek, Lars Koesterke, Juna A. Kollmeier, Richard G. Kron, Hubert Lampeitl, Dustin Lang, Jean-Marc Le Goff, Young Sun Lee, Yen-Ting Lin, Daniel C. Long, Craig P. Loomis, Sara Lucatello, Britt Lundgren, Robert H. Lupton, Zhibo Ma, Nicholas MacDonald, Suvrath Mahadevan, Marcio A. G. Maia, Martin Makler, Elena Malanushenko, Viktor Malanushenko, Rachel Mandelbaum, Claudia Maraston, Daniel Margala, Karen L. Masters, Cameron K. McBride, Peregrine M. McGehee, Ian D. McGreer, Brice Ménard, Jordi Miralda-Escudé, Heather L. Morrison, F. Mullally, Demitri Muna, Jeffrey A. Munn, Hitoshi Murayama, Adam D. Myers, Tracy Naugle, Angelo Fausti Neto, Duy Cuong Nguyen, Robert C. Nichol, Robert W. O'Connell, Ricardo L. C. Ogando, Matthew D. Olmstead, Daniel J. Oravetz, Nikhil Padmanabhan, Nathalie Palanque-Delabrouille, Kaike Pan, Parul Pandey, Isabelle Pâris, Will J. Percival, Patrick Petitjean, Robert Pfaffenberger, Janine Pforr, Stefanie Phleps, Christophe Pichon, Matthew M. Pieri, Francisco Prada, Adrian M. Price-Whelan, M. Jordan Raddick, Beatriz H. F. Ramos, Céline Reylé, James Rich, Gordon T. Richards, Hans-Walter Rix, Annie C. Robin, Helio J. Rocha-Pinto, Constance M. Rockosi, Natalie A. Roe, Emmanuel Rollinde, Ashley J. Ross, Nicholas P. Ross, Bruno M. Rossetto, Ariel G. Sánchez, Conor Sayres, David J. Schlegel, Katharine J. Schlesinger, Sarah J. Schmidt, Donald P. Schneider, Erin Sheldon, Yiping Shu, Jennifer Simmerer, Audrey E. Simmons, Thirupathi Sivarani, Stephanie A. Snedden, Jennifer S. Sobeck, Matthias Steinmetz, Michael A. Strauss, Alexander S. Szalay, Masayuki Tanaka, Aniruddha R. Thakar, Daniel Thomas, Jeremy L. Tinker, Benjamin M. Tofflemire, Rita Tojeiro, Christy A. Tremonti, Jan Vandenberg, M. Vargas Magaña, Licia Verde, Nicole P. Vogt, David A. Wake, Ji Wang, Benjamin A. Weaver, David H. Weinberg, Martin White, Simon D. M. White, Brian Yanny, Naoki Yasuda, Christophe Yeche, and Idit Zehavi. The Eighth Data Release of the Sloan Digital Sky Survey: First Data from SDSS-III. *ApJS*, 193(2):29, April 2011. doi: 10.1088/0067-0049/193/2/29.

Hiroaki Aihara, Yusra AlSayyad, Makoto Ando, Robert Armstrong, James Bosch, Eiichi Egami, Hisanori Furusawa, Junko Furusawa, Andy Goulding, Yuichi Harikane, Chiaki Hikage, Paul T. P. Ho, Bau-Ching Hsieh, Song Huang, Hiroyuki Ikeda, Masatoshi Imanishi, Kei Ito, Ikuru Iwata, An-

ton T. Jaelani, Ryota Kakuma, Kojiro Kawana, Satoshi Kikuta, Umi Kobayashi, Michitaro Koike, Yutaka Komiyama, Xiangchong Li, Yongming Liang, Yen-Ting Lin, Wentao Luo, Robert Lupton, Nate B. Lust, Lauren A. MacArthur, Yoshiki Matsuoka, Sogo Mineo, Hironao Miyatake, Satoshi Miyazaki, Surhud More, Ryoma Murata, Shigeru V. Namiki, Atsushi J. Nishizawa, Masamune Oguri, Nobuhiro Okabe, Sakurako Okamoto, Yuki Okura, Yoshiaki Ono, Masato Onodera, Masafusa Onoue, Ken Osato, Masami Ouchi, Takatoshi Shibuya, Michael A. Strauss, Naoshi Sugiyama, Yasushi Suto, Masahiro Takada, Yuhei Takagi, Tadafumi Takata, Satoshi Takita, Masayuki Tanaka, Tsuyoshi Terai, Yoshiki Toba, Hisakazu Uchiyama, Yousuke Utsumi, Shiang-Yu Wang, Wenting Wang, and Yoshihiko Yamada. Second data release of the Hyper Suprime-Cam Subaru Strategic Program. *PASJ*, 71(6):114, December 2019. doi: 10.1093/pasj/psz103.

Adebusola B. Alabi, Aaron J. Romanowsky, Duncan A. Forbes, Jean P. Brodie, and Nobuhiro Okabe. An expanded catalogue of low surface brightness galaxies in the Coma cluster using Subaru/Suprime-Cam. *MNRAS*, 496(3):3182–3197, August 2020. doi: 10.1093/mnras/staa1763.

S. Alam, F. D. Albareti, C. Allende Prieto, F. Anders, S. F. Anderson, T. Anderton, B. H. Andrews, E. Armengaud, É. Aubourg, S. Bailey, and et al. The Eleventh and Twelfth Data Releases of the Sloan Digital Sky Survey: Final Data from SDSS-III. *ApJS*, 219:12, July 2015. doi: 10.1088/0067-0049/219/1/12.

Brandon Allgood, Ricardo A. Flores, Joel R. Primack, Andrey V. Kravtsov, Risa H. Wechsler, Andreas Faltenbacher, and James S. Bullock. The shape of dark matter haloes: dependence on mass, redshift, radius and formation. *MNRAS*, 367(4):1781–1796, April 2006. doi: 10.1111/j.1365-2966.2006.10094.x.

A. Aloisi, G. Clementini, M. Tosi, F. Annibali, R. Contreras, G. Fiorentino, J. Mack, M. Marconi, I. Musella, A. Saha, M. Sirianni, and R. P. van der Marel. I Zw 18 Revisited with HST ACS and Cepheids: New Distance and Age. *ApJ*, 667:L151–L154, October 2007. doi: 10.1086/522368.

R. Amorín, C. Muñoz-Tuñón, J. A. L. Aguerri, and P. Planesas. Molecular gas in low-metallicity

starburst galaxies:. Scaling relations and the CO-to-H_2 conversion factor. *A&A*, 588:A23, April 2016. doi: 10.1051/0004-6361/201526397.

N. C. Amorisco. On feathers, bifurcations and shells: the dynamics of tidal streams across the mass scale. *MNRAS*, 450:575–591, June 2015. doi: 10.1093/mnras/stv648.

N. C. Amorisco. Contributions to the accreted stellar halo: an atlas of stellar deposition. *MNRAS*, 464(3):2882–2895, January 2017. doi: 10.1093/mnras/stw2229.

N. C. Amorisco and A. Loeb. Ultradiffuse galaxies: the high-spin tail of the abundant dwarf galaxy population. *MNRAS*, 459(1):L51–L55, June 2016. doi: 10.1093/mnrasl/slw055.

Daniel Anglés-Alcázar, Claude-André Faucher-Giguère, Dušan Kereš, Philip F. Hopkins, Eliot Quataert, and Norman Murray. The cosmic baryon cycle and galaxy mass assembly in the FIRE simulations. *MNRAS*, 470(4):4698–4719, October 2017. doi: 10.1093/mnras/stx1517.

Hong Bae Ann. Morphology of Dwarf Galaxies in Isolated Satellite Systems. *Journal of Korean Astronomical Society*, 50(4):111–124, August 2017. doi: 10.5303/JKAS.2017.50.4.111.

F. Annibali, M. Cignoni, M. Tosi, R. P. van der Marel, A. Aloisi, G. Clementini, R. Contreras Ramos, G. Fiorentino, M. Marconi, and I. Musella. The Star Formation History of the Very Metal-poor Blue Compact Dwarf I Zw 18 from HST/ACS Data. *AJ*, 146:144, December 2013. doi: 10.1088/0004-6256/146/6/144.

F. Annibali, M. Bellazzini, M. Correnti, E. Sacchi, M. Tosi, M. Cignoni, A. Aloisi, D. Calzetti, L. Ciotti, and F. Cusano. HST resolves stars in a tiny body falling on the dwarf galaxy DDO 68. *arXiv e-prints*, art. arXiv:1904.01986, Apr 2019.

Francesca Annibali, Carlo Nipoti, Luca Ciotti, Monica Tosi, Alessandra Aloisi, Michele Bellazzini, Michele Cignoni, Felice Cusano, Diego Paris, and Elena Sacchi. Ddo 68: A flea with smaller fleas that on him prey. *The Astrophysical Journal Letters*, 826(2):L27, 2016. URL `http://stacks.iop.org/2041-8205/826/i=2/a=L27`.

A. Aparicio and N. Tikhonov. The Spatial and Age Distribution of Stellar Populations in DDO 190. *AJ*, 119(5):2183–2193, May 2000. doi: 10.1086/301360.

Antonio Aparicio, Nikolay Tikhonov, and Igor Karachentsev. DDO 187: Do Dwarf Galaxies Have Extended, Old Halos? *AJ*, 119(1):177–187, January 2000. doi: 10.1086/301157.

Astropy Collaboration, T. P. Robitaille, E. J. Tollerud, P. Greenfield, M. Droettboom, E. Bray, T. Aldcroft, M. Davis, A. Ginsburg, A. M. Price-Whelan, W. E. Kerzendorf, A. Conley, N. Crighton, K. Barbary, D. Muna, H. Ferguson, F. Grollier, M. M. Parikh, P. H. Nair, H. M. Unther, C. Deil, J. Woillez, S. Conseil, R. Kramer, J. E. H. Turner, L. Singer, R. Fox, B. A. Weaver, V. Zabalza, Z. I. Edwards, K. Azalee Bostroem, D. J. Burke, A. R. Casey, S. M. Crawford, N. Dencheva, J. Ely, T. Jenness, K. Labrie, P. L. Lim, F. Pierfederici, A. Pontzen, A. Ptak, B. Refsdal, M. Servillat, and O. Streicher. Astropy: A community Python package for astronomy. *A&A*, 558:A33, October 2013. doi: 10.1051/0004-6361/201322068.

A. M. Atkinson, R. G. Abraham, and A. M. N. Ferguson. Faint Tidal Features in Galaxies within the Canada-France-Hawaii Telescope Legacy Survey Wide Fields. *ApJ*, 765:28, March 2013. doi: 10.1088/0004-637X/765/1/28.

I. K. Baldry, S. P. Driver, J. Loveday, E. N. Taylor, L. S. Kelvin, J. Liske, P. Norberg, A. S. G. Robotham, S. Brough, A. M. Hopkins, S. P. Bamford, J. A. Peacock, J. Bland-Hawthorn, C. J. Conselice, S. M. Croom, D. H. Jones, H. R. Parkinson, C. C. Popescu, M. Prescott, R. G. Sharp, and R. J. Tuffs. Galaxy And Mass Assembly (GAMA): the galaxy stellar mass function at z ¡ 0.06. *MNRAS*, 421(1):621–634, March 2012. doi: 10.1111/j.1365-2966.2012.20340.x.

I. K. Baldry, J. Liske, M. J. I. Brown, A. S. G. Robotham, S. P. Driver, L. Dunne, M. Alpaslan, S. Brough, M. E. Cluver, E. Eardley, D. J. Farrow, C. Heymans, H. Hildebrandt, A. M. Hopkins, L. S. Kelvin, J. Loveday, A. J. Moffett, P. Norberg, M. S. Owers, E. N. Taylor, A. H. Wright, S. P. Bamford, J. Bland-Hawthorn, N. Bourne, M. N. Bremer, M. Colless, C. J. Conselice, S. M. Croom, L. J. M. Davies, C. Foster, M. W. Grootes, B. W. Holwerda, D. H. Jones, P. R. Kafle, K. Kuijken, M. A. Lara-Lopez, Á. R. López-Sánchez, M. J. Meyer, S. Phillipps, W. J.

Sutherland, E. van Kampen, and S. M. Wilkins. Galaxy And Mass Assembly: the G02 field, Herschel-ATLAS target selection and data release 3. *MNRAS*, 474:3875–3888, March 2018. doi: 10.1093/mnras/stx3042.

Kyle Barbary. SEP: Source Extractor as a library. *The Journal of Open Source Software*, 1(6):58, October 2016. doi: 10.21105/joss.00058.

Kyle Barbary. extinction: Dust extinction laws. Astrophysics Source Code Library, record ascl:2102.026, February 2021.

C. E. Barbosa, D. Zaritsky, R. Donnerstein, H. Zhang, A. Dey, C. Mendes de Oliveira, L. Sampedro, A. Molino, M. V. Costa-Duarte, P. Coelho, A. Cortesi, F. R. Herpich, J. A. Hernandez-Jimenez, T. Santos-Silva, E. Pereira, A. Werle, R. A. Overzier, R. Cid Fernandes, A. V. Smith Castelli, T. Ribeiro, W. Schoenell, and A. Kanaan. One Hundred SMUDGes in S-PLUS: Ultra-diffuse Galaxies Flourish in the Field. *ApJS*, 247(2):46, April 2020. doi: 10.3847/1538-4365/ab7660.

J. K. Barrera-Ballesteros, S. F. Sánchez, T. Heckman, T. Wong, A. Bolatto, E. Ostriker, E. Rosolowsky, L. Carigi, S. Vogel, R. C. Levy, D. Colombo, Yufeng Luo, and Yixian Cao. The EDGE-CALIFA survey: self-regulation of star formation at kpc scales. *MNRAS*, 503(3): 3643–3659, May 2021. doi: 10.1093/mnras/stab755.

K. Bartošková, B. Jungwiert, I. Ebrová, L. Jílková, and M. Křížek. Simulations of Shell Galaxies with GADGET-2: Multi-Generation Shell Systems. *Astrophysics and Space Science Proceedings*, 27:195, 2011. doi: 10.1007/978-3-642-20285-8_39.

Michael A. Beasley and Ignacio Trujillo. Globular Clusters Indicate That Ultra-diffuse Galaxies Are Dwarfs. *ApJ*, 830(1):23, October 2016a. doi: 10.3847/0004-637X/830/1/23.

Michael A. Beasley and Ignacio Trujillo. Globular Clusters Indicate That Ultra-diffuse Galaxies Are Dwarfs. *ApJ*, 830(1):23, October 2016b. doi: 10.3847/0004-637X/830/1/23.

R. L. Beaton, D. Martínez-Delgado, S. R. Majewski, E. D'Onghia, S. Zibetti, R. J. Gabany, K. E. Johnson, M. Blanton, and A. Verbiscer. Cannibalization and Rebirth in the NGC 5387 System.

I. The Stellar Stream and Star-forming Region. *ApJ*, 790:117, August 2014. doi: 10.1088/0004-637X/790/2/117.

Peter Behroozi, Risa H. Wechsler, Andrew P. Hearin, and Charlie Conroy. UNIVERSEMACHINE: The correlation between galaxy growth and dark matter halo assembly from z = 0-10. *MNRAS*, 488(3):3143–3194, September 2019. doi: 10.1093/mnras/stz1182.

Kenji Bekki. Unequal-Mass Galaxy Mergers and the Creation of Cluster S0 Galaxies. *ApJL*, 502 (2):L133–L137, Aug 1998. doi: 10.1086/311508.

Kenji Bekki. Formation of blue compact dwarf galaxies from merging and interacting gas-rich dwarfs. *MNRAS*, 388(1):L10–L14, Jul 2008a. doi: 10.1111/j.1745-3933.2008.00489.x.

Kenji Bekki. Origin of Dwarf Irregular Galaxies with Outer Early-Type Structures. *ApJL*, 680(1): L29, June 2008b. doi: 10.1086/589770.

Eric F. Bell, Daniel H. McIntosh, Neal Katz, and Martin D. Weinberg. The Optical and Near-Infrared Properties of Galaxies. I. Luminosity and Stellar Mass Functions. *ApJS*, 149(2):289–312, December 2003. doi: 10.1086/378847.

M. Bellazzini, V. Belokurov, L. Magrini, F. Fraternali, V. Testa, G. Beccari, A. Marchetti, and R. Carini. Redshift, metallicity and size of two extended dwarf Irregular galaxies: a link between dwarf Irregulars and ultra diffuse galaxies? *MNRAS*, 467(3):3751–3758, May 2017. doi: 10.1093/mnras/stx236.

V. Belokurov, D. Erkal, A. J. Deason, S. E. Koposov, F. De Angeli, D. W. Evans, F. Fraternali, and D. Mackey. Clouds, Streams and Bridges. Redrawing the blueprint of the Magellanic System with Gaia DR1. *MNRAS*, 466:4711–4730, April 2017. doi: 10.1093/mnras/stw3357.

Vasily Belokurov, Jason L. Sanders, Azadeh Fattahi, Martin C. Smith, Alis J. Deason, N. Wyn Evans, and Robert J. J. Grand. The biggest splash. *MNRAS*, 494(3):3880–3898, May 2020. doi: 10.1093/mnras/staa876.

Samantha M. Benincasa, Sarah R. Loebman, Andrew Wetzel, Philip F. Hopkins, Norman Murray, Matthew A. Bellardini, Claude-André Faucher-Giguère, Dávid Guszejnov, and Matthew Orr. Live fast, die young: GMC lifetimes in the FIRE cosmological simulations of Milky Way mass galaxies. *MNRAS*, 497(3):3993–3999, September 2020. doi: 10.1093/mnras/staa2116.

A. J. Benson. Orbital parameters of infalling dark matter substructures. *MNRAS*, 358:551–562, April 2005. doi: 10.1111/j.1365-2966.2005.08788.x.

Edouard J. Bernard, Antonio Aparicio, Carme Gallart, Carmen P. Padilla-Torres, and Maurizio Panniello. Stellar Content and Recent Star Formation History of the Local Group Dwarf Irregular Galaxy IC 1613. *AJ*, 134(3):1124–1132, September 2007. doi: 10.1086/520805.

E. Bertin and S. Arnouts. SExtractor: Software for source extraction. **??***jnlA&AS*, 117:393–404, June 1996. doi: 10.1051/aas:1996164.

Gurtina Besla. The Orbits and Total Mass of the Magellanic Clouds. *arXiv e-prints*, art. arXiv:1511.03346, November 2015.

Gurtina Besla, David R. Patton, Sabrina Stierwalt, Vicente Rodriguez-Gomez, Ekta Patel, Nitya J. Kallivayalil, Kelsey E. Johnson, Sarah Pearson, George C. Privon, and Mary E. Putman. The frequency of dwarf galaxy multiples at low redshift in SDSS versus cosmological expectations. *MNRAS*, 480(3):3376–3396, November 2018. doi: 10.1093/mnras/sty2041.

F. Bigiel, A. Leroy, F. Walter, E. Brinks, W. J. G. de Blok, B. Madore, and M. D. Thornley. The Star Formation Law in Nearby Galaxies on Sub-Kpc Scales. *AJ*, 136(6):2846–2871, December 2008. doi: 10.1088/0004-6256/136/6/2846.

F. Bigiel, A. K. Leroy, F. Walter, E. Brinks, W. J. G. de Blok, C. Kramer, H. W. Rix, A. Schruba, K. F. Schuster, A. Usero, and H. W. Wiesemeyer. A Constant Molecular Gas Depletion Time in Nearby Disk Galaxies. *ApJL*, 730(2):L13, April 2011. doi: 10.1088/2041-8205/730/2/L13.

Bruno Binggeli, Allan Sandage, and G. A. Tammann. The luminosity function of galaxies. *AR&AA*, 26:509–560, Jan 1988. doi: 10.1146/annurev.aa.26.090188.002453.

James Binney and Scott Tremaine. *Galactic Dynamics: Second Edition*. 2008.

Michael R. Blanton, Eyal Kazin, Demitri Muna, Benjamin A. Weaver, and Adrian Price-Whelan. Improved Background Subtraction for the Sloan Digital Sky Survey Images. *AJ*, 142(1):31, July 2011. doi: 10.1088/0004-6256/142/1/31.

Alberto D. Bolatto, Mark Wolfire, and Adam K. Leroy. The CO-to-H_2 Conversion Factor. *AR&AA*, 51(1):207–268, August 2013. doi: 10.1146/annurev-astro-082812-140944.

James Bosch, Robert Armstrong, Steven Bickerton, Hisanori Furusawa, Hiroyuki Ikeda, Michitaro Koike, Robert Lupton, Sogo Mineo, Paul Price, Tadafumi Takata, Masayuki Tanaka, Naoki Yasuda, Yusra AlSayyad, Andrew C. Becker, William Coulton, Jean Coupon, Jose Garmilla, Song Huang, K. Simon Krughoff, Dustin Lang, Alexie Leauthaud, Kian-Tat Lim, Nate B. Lust, Lauren A. MacArthur, Rachel Mandelbaum, Hironao Miyatake, Satoshi Miyazaki, Ryoma Murata, Surhud More, Yuki Okura, Russell Owen, John D. Swinbank, Michael A. Strauss, Yoshihiko Yamada, and Hitomi Yamanoi. The Hyper Suprime-Cam software pipeline. *PASJ*, 70:S5, January 2018. doi: 10.1093/pasj/psx080.

O. Boulade, X. Charlot, P. Abbon, S. Aune, P. Borgeaud, P.-H. Carton, M. Carty, J. Da Costa, H. Deschamps, D. Desforge, D. Eppellé, P. Gallais, L. Gosset, R. Granelli, M. Gros, J. de Kat, D. Loiseau, J.-. Ritou, J. Y. Roussé, P. Starzynski, N. Vignal, and L. G. Vigroux. MegaCam: the new Canada-France-Hawaii Telescope wide-field imaging camera. In M. Iye and A. F. M. Moorwood, editors, *Instrument Design and Performance for Optical/Infrared Ground-based Telescopes*, volume 4841 of **??***jnlProc. SPIE*, pages 72–81, March 2003. doi: 10.1117/12.459890.

Mia S. Bovill and Massimo Ricotti. Pre-Reionization Fossils, Ultra-Faint Dwarfs, and the Missing Galactic Satellite Problem. *ApJ*, 693(2):1859–1870, March 2009. doi: 10.1088/0004-637X/693/2/1859.

Jo Bovy, Hans-Walter Rix, and David W. Hogg. The Milky Way Has No Distinct Thick Disk. *ApJ*, 751(2):131, June 2012. doi: 10.1088/0004-637X/751/2/131.

Michael Boylan-Kolchin, Daniel R. Weisz, Benjamin D. Johnson, James S. Bullock, Charlie Conroy, and Alex Fitts. The Local Group as a time machine: studying the high-redshift Universe with nearby galaxies. *MNRAS*, 453(2):1503–1512, October 2015. doi: 10.1093/mnras/stv1736.

Jeremy D. Bradford, Marla C. Geha, and Michael R. Blanton. A Study in Blue: The Baryon Content of Isolated Low-mass Galaxies. *ApJ*, 809(2):146, August 2015. doi: 10.1088/0004-637X/809/2/146.

Jarle Brinchmann, Stephane Charlot, Timothy M. Heckman, Guinevere Kauffmann, Christy Tremonti, and Simon D. M. White. Stellar masses, star formation rates, metallicities and AGN properties for 200,000 galaxies in the SDSS Data Release Two (DR2). *arXiv e-prints*, art. astro-ph/0406220, June 2004.

C. B. Brook, A. Di Cintio, A. Knebe, S. Gottlöber, Y. Hoffman, G. Yepes, and S. Garrison-Kimmel. The Stellar-to-halo Mass Relation for Local Group Galaxies. *ApJL*, 784(1):L14, March 2014. doi: 10.1088/2041-8205/784/1/L14.

Alyson M. Brooks and Adi Zolotov. Why Baryons Matter: The Kinematics of Dwarf Spheroidal Satellites. *ApJ*, 786(2):87, May 2014. doi: 10.1088/0004-637X/786/2/87.

G. Bruzual and S. Charlot. Stellar population synthesis at the resolution of 2003. *MNRAS*, 344:1000–1028, October 2003. doi: 10.1046/j.1365-8711.2003.06897.x.

Greg L. Bryan and Michael L. Norman. Statistical Properties of X-Ray Clusters: Analytic and Numerical Comparisons. *ApJ*, 495(1):80–99, March 1998. doi: 10.1086/305262.

J. J. Bryant, M. S. Owers, A. S. G. Robotham, S. M. Croom, S. P. Driver, M. J. Drinkwater, N. P. F. Lorente, L. Cortese, N. Scott, M. Colless, A. Schaefer, E. N. Taylor, I. S. Konstantopoulos, J. T. Allen, I. Baldry, L. Barnes, A. E. Bauer, J. Bland-Hawthorn, J. V. Bloom, A. M. Brooks, S. Brough, G. Cecil, W. Couch, D. Croton, R. Davies, S. Ellis, L. M. R. Fogarty, C. Foster, K. Glazebrook, M. Goodwin, A. Green, M. L. Gunawardhana, E. Hampton, I. T. Ho, A. M. Hopkins, L. Kewley, J. S. Lawrence, S. G. Leon-Saval, S. Leslie, R. McElroy, G. Lewis,

J. Liske, Á. R. López-Sánchez, S. Mahajan, A. M. Medling, N. Metcalfe, M. Meyer, J. Mould, D. Obreschkow, S. O'Toole, M. Pracy, S. N. Richards, T. Shanks, R. Sharp, S. M. Sweet, A. D. Thomas, C. Tonini, and C. J. Walcher. The SAMI Galaxy Survey: instrument specification and target selection. *MNRAS*, 447(3):2857–2879, March 2015. doi: 10.1093/mnras/stu2635.

James S. Bullock and Michael Boylan-Kolchin. Small-Scale Challenges to the ΛCDM Paradigm. *AR&AA*, 55(1):343–387, August 2017. doi: 10.1146/annurev-astro-091916-055313.

James S. Bullock and Kathryn V. Johnston. Tracing Galaxy Formation with Stellar Halos. I. Methods. *ApJ*, 635(2):931–949, December 2005. doi: 10.1086/497422.

A. Burkert. The Geometry and Origin of Ultra-diffuse Ghost Galaxies. *ApJ*, 838(2):93, April 2017. doi: 10.3847/1538-4357/aa671c.

Daniela Calzetti. Star Formation Rate Indicators. In Jesús Falcón-Barroso and Johan H. Knapen, editors, *Secular Evolution of Galaxies*, page 419. 2013.

Salvador Cardona-Barrero, Arianna Di Cintio, Christopher B. A. Brook, Tomas Ruiz-Lara, Michael A. Beasley, Jesus Falcón-Barroso, and Andrea V. Macciò. NIHAO XXIV: rotation- or pressure-supported systems? Simulated Ultra Diffuse Galaxies show a broad distribution in their stellar kinematics. *MNRAS*, 497(4):4282–4292, October 2020. doi: 10.1093/mnras/staa2094.

S. G. Carlsten, G. K. T. Hau, and A. Zenteno. Stellar populations of shell galaxies. *MNRAS*, 472: 2889–2905, December 2017. doi: 10.1093/mnras/stx2182.

Scott G. Carlsten, Jenny E. Greene, Johnny P. Greco, Rachael L. Beaton, and Erin Kado-Fong. Structures of Dwarf Satellites of Milky Way-like Galaxies: Morphology, Scaling Relations, and Intrinsic Shapes. *ApJ*, 922(2):267, December 2021. doi: 10.3847/1538-4357/ac2581.

Adam C. Carnall, Joel Leja, Benjamin D. Johnson, Ross J. McLure, James S. Dunlop, and Charlie Conroy. How to Measure Galaxy Star Formation Histories. I. Parametric Models. *ApJ*, 873(1): 44, March 2019. doi: 10.3847/1538-4357/ab04a2.

Daniel Ceverino, Joel Primack, and Avishai Dekel. Formation of elongated galaxies with low masses at high redshift. *MNRAS*, 453(1):408–413, October 2015. doi: 10.1093/mnras/stv1603.

G. Chabrier. Galactic Stellar and Substellar Initial Mass Function. *PASP*, 115:763–795, July 2003a. doi: 10.1086/376392.

G. Chabrier. The Galactic Disk Mass Function: Reconciliation of the Hubble Space Telescope and Nearby Determinations. *ApJL*, 586:L133–L136, April 2003b. doi: 10.1086/374879.

T. K. Chan, D. Kereš, J. Oñorbe, P. F. Hopkins, A. L. Muratov, C. A. Faucher-Giguère, and E. Quataert. The impact of baryonic physics on the structure of dark matter haloes: the view from the FIRE cosmological simulations. *MNRAS*, 454(3):2981–3001, December 2015. doi: 10.1093/mnras/stv2165.

T. K. Chan, D. Kereš, A. Wetzel, P. F. Hopkins, C. A. Faucher-Giguère, K. El-Badry, S. Garrison-Kimmel, and M. Boylan-Kolchin. The origin of ultra diffuse galaxies: stellar feedback and quenching. *MNRAS*, 478(1):906–925, July 2018. doi: 10.1093/mnras/sty1153.

T. K. Chan, D. Kereš, P. F. Hopkins, E. Quataert, K. Y. Su, C. C. Hayward, and C. A. Faucher-Giguère. Cosmic ray feedback in the FIRE simulations: constraining cosmic ray propagation with GeV γ-ray emission. *MNRAS*, 488(3):3716–3744, September 2019. doi: 10.1093/mnras/stz1895.

Y.-M. Chen, G. Kauffmann, C. A. Tremonti, S. White, T. M. Heckman, K. Kovač, K. Bundy, J. Chisholm, C. Maraston, D. P. Schneider, A. S. Bolton, B. A. Weaver, and J. Brinkmann. Evolution of the most massive galaxies to z= 0.6 - I. A new method for physical parameter estimation. *MNRAS*, 421:314–332, March 2012. doi: 10.1111/j.1365-2966.2011.20306.x.

Hillary L. Child, Salman Habib, Katrin Heitmann, Nicholas Frontiere, Hal Finkel, Adrian Pope, and Vitali Morozov. Halo Profiles and the Concentration-Mass Relation for a ΛCDM Universe. *ApJ*, 859(1):55, May 2018. doi: 10.3847/1538-4357/aabf95.

Phil Cigan, Lisa M. Young, Haley L. Gomez, Suzanne C. Madden, Pieter De Vis, Deidre A. Hunter, Bruce G. Elmegreen, Elias Brinks, and LITTLE THINGS Team. Herschel Photomet-

ric Observations of LITTLE THINGS Dwarf Galaxies. *AJ*, 162(3):83, September 2021. doi: 10.3847/1538-3881/abfd2e.

P. Compère, M. López-Corredoira, and F. Garzón. Three-dimensional decomposition of galaxies with bulge and long bar. *A&A*, 571:A98, November 2014. doi: 10.1051/0004-6361/201424572.

Charlie Conroy and James E. Gunn. The Propagation of Uncertainties in Stellar Population Synthesis Modeling. III. Model Calibration, Comparison, and Evaluation. *ApJ*, 712(2):833–857, April 2010. doi: 10.1088/0004-637X/712/2/833.

Charlie Conroy, James E. Gunn, and Martin White. The Propagation of Uncertainties in Stellar Population Synthesis Modeling. I. The Relevance of Uncertain Aspects of Stellar Evolution and the Initial Mass Function to the Derived Physical Properties of Galaxies. *ApJ*, 699:486–506, July 2009a. doi: 10.1088/0004-637X/699/1/486.

Charlie Conroy, James E. Gunn, and Martin White. The Propagation of Uncertainties in Stellar Population Synthesis Modeling. I. The Relevance of Uncertain Aspects of Stellar Evolution and the Initial Mass Function to the Derived Physical Properties of Galaxies. *ApJ*, 699(1):486–506, July 2009b. doi: 10.1088/0004-637X/699/1/486.

L. Costantin, J. Méndez-Abreu, E. M. Corsini, M. C. Eliche-Moral, T. Tapia, L. Morelli, E. Dalla Bontà, and A. Pizzella. The intrinsic shape of bulges in the CALIFA survey. *A&A*, 609:A132, February 2018. doi: 10.1051/0004-6361/201731823.

J. Coupon, N. Czakon, J. Bosch, Y. Komiyama, E. Medezinski, S. Miyazaki, and M. Oguri. The bright-star masks for the HSC-SSP survey. *PASJ*, 70:S7, January 2018. doi: 10.1093/pasj/psx047.

Julianne J. Dalcanton, David N. Spergel, James E. Gunn, Maarten Schmidt, and Donald P. Schneider. The Number Density of Low-Surface Brightness Galaxies with 23 ¡ mu_0 ¡ 25 V Mag/arcsec$\hat{2}$. *AJ*, 114:635–654, August 1997. doi: 10.1086/118499.

Shany Danieli and Pieter van Dokkum. Revisiting the Size-Luminosity Relation in the Era of Ultra Diffuse Galaxies. *ApJ*, 875(2):155, April 2019. doi: 10.3847/1538-4357/ab14f3.

Shany Danieli, Pieter van Dokkum, and Charlie Conroy. Hunting Faint Dwarf Galaxies in the Field Using Integrated Light Surveys. *ApJ*, 856(1):69, March 2018. doi: 10.3847/1538-4357/aaadfb.

Shany Danieli, Pieter van Dokkum, Charlie Conroy, Roberto Abraham, and Aaron J. Romanowsky. Still Missing Dark Matter: KCWI High-resolution Stellar Kinematics of NGC1052-DF2. *ApJL*, 874(2):L12, April 2019. doi: 10.3847/2041-8213/ab0e8c.

Shany Danieli, Deborah Lokhorst, Jielai Zhang, Allison Merritt, Pieter van Dokkum, Roberto Abraham, Charlie Conroy, Colleen Gilhuly, Johnny Greco, Steven Janssens, Jiaxuan Li, Qing Liu, Tim B. Miller, and Lamiya Mowla. The Dragonfly Wide Field Survey. I. Telescope, Survey Design, and Data Characterization. *ApJ*, 894(2):119, May 2020. doi: 10.3847/1538-4357/ab88a8.

Shany Danieli, Pieter van Dokkum, Sebastian Trujillo-Gomez, J. M. Diederik Kruijssen, Aaron J. Romanowsky, Scott Carlsten, Zili Shen, Jiaxuan Li, Roberto Abraham, Jean Brodie, Charlie Conroy, Jonah S. Gannon, and Johnny Greco. NGC5846-UDG1: A galaxy formed mostly by star formation in massive, extremely dense clumps of gas. *arXiv e-prints*, art. arXiv:2111.14851, November 2021.

Payel Das and James Binney. Characterizing stellar halo populations - I. An extended distribution function for halo K giants. *MNRAS*, 460(2):1725–1738, August 2016. doi: 10.1093/mnras/stw744.

Gohar Dashyan and Yohan Dubois. Cosmic ray feedback from supernovae in dwarf galaxies. *arXiv e-prints*, art. arXiv:2003.09900, March 2020.

K. S. Dawson, D. J. Schlegel, C. P. Ahn, S. F. Anderson, É. Aubourg, S. Bailey, R. H. Barkhouser, J. E. Bautista, A. Beifiori, A. A. Berlind, V. Bhardwaj, D. Bizyaev, C. H. Blake, M. R. Blanton, M. Blomqvist, A. S. Bolton, A. Borde, J. Bovy, W. N. Brandt, H. Brewington, J. Brinkmann, P. J. Brown, J. R. Brownstein, K. Bundy, N. G. Busca, W. Carithers, A. R. Carnero, M. A. Carr, Y. Chen, J. Comparat, N. Connolly, F. Cope, R. A. C. Croft, A. J. Cuesta, L. N. da Costa, J. R. A. Davenport, T. Delubac, R. de Putter, S. Dhital, A. Ealet, G. L. Ebelke, D. J. Eisenstein, S. Escoffier, X. Fan, N. Filiz Ak, H. Finley, A. Font-Ribera, R. Génova-Santos, J. E. Gunn, H. Guo, D. Haggard, P. B. Hall, J.-C. Hamilton, B. Harris, D. W. Harris, S. Ho, D. W. Hogg, D. Holder,

K. Honscheid, J. Huehnerhoff, B. Jordan, W. P. Jordan, G. Kauffmann, E. A. Kazin, D. Kirkby, M. A. Klaene, J.-P. Kneib, J.-M. Le Goff, K.-G. Lee, D. C. Long, C. P. Loomis, B. Lundgren, R. H. Lupton, M. A. G. Maia, M. Makler, E. Malanushenko, V. Malanushenko, R. Mandelbaum, M. Manera, C. Maraston, D. Margala, K. L. Masters, C. K. McBride, P. McDonald, I. D. McGreer, R. G. McMahon, O. Mena, J. Miralda-Escudé, A. D. Montero-Dorta, F. Montesano, D. Muna, A. D. Myers, T. Naugle, R. C. Nichol, P. Noterdaeme, S. E. Nuza, M. D. Olmstead, A. Oravetz, D. J. Oravetz, R. Owen, N. Padmanabhan, N. Palanque-Delabrouille, K. Pan, J. K. Parejko, I. Pâris, W. J. Percival, I. Pérez-Fournon, I. Pérez-Ràfols, P. Petitjean, R. Pfaffenberger, J. Pforr, M. M. Pieri, F. Prada, A. M. Price-Whelan, M. J. Raddick, R. Rebolo, J. Rich, G. T. Richards, C. M. Rockosi, N. A. Roe, A. J. Ross, N. P. Ross, G. Rossi, J. A. Rubiño-Martin, L. Samushia, A. G. Sánchez, C. Sayres, S. J. Schmidt, D. P. Schneider, C. G. Scóccola, H.-J. Seo, A. Shelden, E. Sheldon, Y. Shen, Y. Shu, A. Slosar, S. A. Smee, S. A. Snedden, F. Stauffer, O. Steele, M. A. Strauss, A. Streblyanska, N. Suzuki, M. E. C. Swanson, T. Tal, M. Tanaka, D. Thomas, J. L. Tinker, R. Tojeiro, C. A. Tremonti, M. Vargas Magaña, L. Verde, M. Viel, D. A. Wake, M. Watson, B. A. Weaver, D. H. Weinberg, B. J. Weiner, A. A. West, M. White, W. M. Wood-Vasey, C. Yeche, I. Zehavi, G.-B. Zhao, and Z. Zheng. The Baryon Oscillation Spectroscopic Survey of SDSS-III. *AJ*, 145:10, January 2013. doi: 10.1088/0004-6256/145/1/10.

Mithi A. C. de los Reyes and Jr. Kennicutt, Robert C. Revisiting the Integrated Star Formation Law. I. Non-starbursting Galaxies. *ApJ*, 872(1):16, February 2019. doi: 10.3847/1538-4357/aafa82.

Alis Deason, Andrew Wetzel, and Shea Garrison-Kimmel. Satellite Dwarf Galaxies in a Hierarchical Universe: The Prevalence of Dwarf-Dwarf Major Mergers. *ApJ*, 794(2):115, October 2014. doi: 10.1088/0004-637X/794/2/115.

A. Dekel and J. Silk. The Origin of Dwarf Galaxies, Cold Dark Matter, and Biased Galaxy Formation. *ApJ*, 303:39, April 1986. doi: 10.1086/164050.

Avishai Dekel and Yuval Birnboim. Galaxy bimodality due to cold flows and shock heating. *MNRAS*, 368:2–20, May 2006. doi: 10.1111/j.1365-2966.2006.10145.x.

S. Demers, P. Battinelli, and E. Artigau. Carbon stars in the outer spheroid of NGC 6822. *A&A*, 456(3):905–910, September 2006. doi: 10.1051/0004-6361:20065507.

DESI Collaboration, Amir Aghamousa, Jessica Aguilar, Steve Ahlen, Shadab Alam, Lori E. Allen, Carlos Allende Prieto, James Annis, Stephen Bailey, Christophe Balland, Otger Ballester, Charles Baltay, Lucas Beaufore, Chris Bebek, Timothy C. Beers, Eric F. Bell, José Luis Bernal, Robert Besuner, Florian Beutler, Chris Blake, Hannes Bleuler, Michael Blomqvist, Robert Blum, Adam S. Bolton, Cesar Briceno, David Brooks, Joel R. Brownstein, Elizabeth Buckley-Geer, Angela Burden, Etienne Burtin, Nicolas G. Busca, Robert N. Cahn, Yan-Chuan Cai, Laia Cardiel-Sas, Raymond G. Carlberg, Pierre-Henri Carton, Ricard Casas, Francisco J. Castander, Jorge L. Cervantes-Cota, Todd M. Claybaugh, Madeline Close, Carl T. Coker, Shaun Cole, Johan Comparat, Andrew P. Cooper, M. C. Cousinou, Martin Crocce, Jean-Gabriel Cuby, Daniel P. Cunningham, Tamara M. Davis, Kyle S. Dawson, Axel de la Macorra, Juan De Vicente, Timothée Delubac, Mark Derwent, Arjun Dey, Govinda Dhungana, Zhejie Ding, Peter Doel, Yutong T. Duan, Anne Ealet, Jerry Edelstein, Sarah Eftekharzadeh, Daniel J. Eisenstein, Ann Elliott, Stéphanie Escoffier, Matthew Evatt, Parker Fagrelius, Xiaohui Fan, Kevin Fanning, Arya Farahi, Jay Farihi, Ginevra Favole, Yu Feng, Enrique Fernandez, Joseph R. Findlay, Douglas P. Finkbeiner, Michael J. Fitzpatrick, Brenna Flaugher, Samuel Flender, Andreu Font-Ribera, Jaime E. Forero-Romero, Pablo Fosalba, Carlos S. Frenk, Michele Fumagalli, Boris T. Gaensicke, Giuseppe Gallo, Juan Garcia-Bellido, Enrique Gaztanaga, Nicola Pietro Gentile Fusillo, Terry Gerard, Irena Gershkovich, Tommaso Giannantonio, Denis Gillet, Guillermo Gonzalez-de-Rivera, Violeta Gonzalez-Perez, Shelby Gott, Or Graur, Gaston Gutierrez, Julien Guy, Salman Habib, Henry Heetderks, Ian Heetderks, Katrin Heitmann, Wojciech A. Hellwing, David A. Herrera, Shirley Ho, Stephen Holland, Klaus Honscheid, Eric Huff, Timothy A. Hutchinson, Dragan Huterer, Ho Seong Hwang, Joseph Maria Illa Laguna, Yuzo Ishikawa, Dianna Jacobs, Niall Jeffrey, Patrick Jelinsky, Elise Jennings, Linhua Jiang, Jorge Jimenez, Jennifer Johnson, Richard Joyce, Eric Jullo, Stéphanie Juneau, Sami Kama, Armin Karcher, Sonia Karkar, Robert Kehoe, Noble Kennamer, Stephen Kent, Martin Kilbinger, Alex G. Kim, David Kirkby, Theodore Kisner, Ellie Kitanidis, Jean-Paul Kneib, Sergey Koposov, Eve Kovacs, Kazuya Koyama, Anthony Kremin,

Richard Kron, Luzius Kronig, Andrea Kueter-Young, Cedric G. Lacey, Robin Lafever, Ofer Lahav, Andrew Lambert, Michael Lampton, Martin Landriau, Dustin Lang, Tod R. Lauer, Jean-Marc Le Goff, Laurent Le Guillou, Auguste Le Van Suu, Jae Hyeon Lee, Su-Jeong Lee, Daniela Leitner, Michael Lesser, Michael E. Levi, Benjamin L'Huillier, Baojiu Li, Ming Liang, Huan Lin, Eric Linder, Sarah R. Loebman, Zarija Lukić, Jun Ma, Niall MacCrann, Christophe Magneville, Laleh Makarem, Marc Manera, Christopher J. Manser, Robert Marshall, Paul Martini, Richard Massey, Thomas Matheson, Jeremy McCauley, Patrick McDonald, Ian D. McGreer, Aaron Meisner, Nigel Metcalfe, Timothy N. Miller, Ramon Miquel, John Moustakas, Adam Myers, Milind Naik, Jeffrey A. Newman, Robert C. Nichol, Andrina Nicola, Luiz Nicolati da Costa, Jundan Nie, Gustavo Niz, Peder Norberg, Brian Nord, Dara Norman, Peter Nugent, Thomas O'Brien, Minji Oh, Knut A. G. Olsen, Cristobal Padilla, Hamsa Padmanabhan, Nikhil Padmanabhan, Nathalie Palanque-Delabrouille, Antonella Palmese, Daniel Pappalardo, Isabelle Pâris, Changbom Park, Anna Patej, John A. Peacock, Hiranya V. Peiris, Xiyan Peng, Will J. Percival, Sandrine Perruchot, Matthew M. Pieri, Richard Pogge, Jennifer E. Pollack, Claire Poppett, Francisco Prada, Abhishek Prakash, Ronald G. Probst, David Rabinowitz, Anand Raichoor, Chang Hee Ree, Alexandre Refregier, Xavier Regal, Beth Reid, Kevin Reil, Mehdi Rezaie, Constance M. Rockosi, Natalie Roe, Samuel Ronayette, Aaron Roodman, Ashley J. Ross, Nicholas P. Ross, Graziano Rossi, Eduardo Rozo, Vanina Ruhlmann-Kleider, Eli S. Rykoff, Cristiano Sabiu, Lado Samushia, Eusebio Sanchez, Javier Sanchez, David J. Schlegel, Michael Schneider, Michael Schubnell, Aurélia Secroun, Uros Seljak, Hee-Jong Seo, Santiago Serrano, Arman Shafieloo, Huanyuan Shan, Ray Sharples, Michael J. Sholl, William V. Shourt, Joseph H. Silber, David R. Silva, Martin M. Sirk, Anze Slosar, Alex Smith, George F. Smoot, Debopam Som, Yong-Seon Song, David Sprayberry, Ryan Staten, Andy Stefanik, Gregory Tarle, Suk Sien Tie, Jeremy L. Tinker, Rita Tojeiro, Francisco Valdes, Octavio Valenzuela, Monica Valluri, Mariana Vargas-Magana, Licia Verde, Alistair R. Walker, Jiali Wang, Yuting Wang, Benjamin A. Weaver, Curtis Weaverdyck, Risa H. Wechsler, David H. Weinberg, Martin White, Qian Yang, Christophe Yeche, Tianmeng Zhang, Gong-Bo Zhao, Yi Zheng, Xu Zhou, Zhimin Zhou, Yaling Zhu, Hu Zou, and Ying Zu. The DESI Experiment Part I: Science,Targeting, and Survey Design. *arXiv e-prints*, art. arXiv:1611.00036,

October 2016.

Arjun Dey, David J. Schlegel, Dustin Lang, Robert Blum, Kaylan Burleigh, Xiaohui Fan, Joseph R. Findlay, Doug Finkbeiner, David Herrera, Stéphanie Juneau, Martin Landriau, Michael Levi, Ian McGreer, Aaron Meisner, Adam D. Myers, John Moustakas, Peter Nugent, Anna Patej, Edward F. Schlafly, Alistair R. Walker, Francisco Valdes, Benjamin A. Weaver, Christophe Yèche, Hu Zou, Xu Zhou, Behzad Abareshi, T. M. C. Abbott, Bela Abolfathi, C. Aguilera, Shadab Alam, Lori Allen, A. Alvarez, James Annis, Behzad Ansarinejad, Marie Aubert, Jacqueline Beechert, Eric F. Bell, Segev Y. BenZvi, Florian Beutler, Richard M. Bielby, Adam S. Bolton, César Briceño, Elizabeth J. Buckley-Geer, Karen Butler, Annalisa Calamida, Raymond G. Carlberg, Paul Carter, Ricard Casas, Francisco J. Castander, Yumi Choi, Johan Comparat, Elena Cukanovaite, Timothée Delubac, Kaitlin DeVries, Sharmila Dey, Govinda Dhungana, Mark Dickinson, Zhejie Ding, John B. Donaldson, Yutong Duan, Christopher J. Duckworth, Sarah Eftekharzadeh, Daniel J. Eisenstein, Thomas Etourneau, Parker A. Fagrelius, Jay Farihi, Mike Fitzpatrick, Andreu Font-Ribera, Leah Fulmer, Boris T. Gänsicke, Enrique Gaztanaga, Koshy George, David W. Gerdes, Satya Gontcho A. Gontcho, Claudio Gorgoni, Gregory Green, Julien Guy, Diane Harmer, M. Hernandez, Klaus Honscheid, Lijuan Wendy Huang, David J. James, Buell T. Jannuzi, Linhua Jiang, Richard Joyce, Armin Karcher, Sonia Karkar, Robert Kehoe, Jean-Paul Kneib, Andrea Kueter-Young, Ting-Wen Lan, Tod R. Lauer, Laurent Le Guillou, Auguste Le Van Suu, Jae Hyeon Lee, Michael Lesser, Laurence Perreault Levasseur, Ting S. Li, Justin L. Mann, Robert Marshall, C. E. Martínez-Vázquez, Paul Martini, Hélion du Mas des Bourboux, Sean McManus, Tobias Gabriel Meier, Brice Ménard, Nigel Metcalfe, Andrea Muñoz-Gutiérrez, Joan Najita, Kevin Napier, Gautham Narayan, Jeffrey A. Newman, Jundan Nie, Brian Nord, Dara J. Norman, Knut A. G. Olsen, Anthony Paat, Nathalie Palanque-Delabrouille, Xiyan Peng, Claire L. Poppett, Megan R. Poremba, Abhishek Prakash, David Rabinowitz, Anand Raichoor, Mehdi Rezaie, A. N. Robertson, Natalie A. Roe, Ashley J. Ross, Nicholas P. Ross, Gregory Rudnick, Sasha Safonova, Abhijit Saha, F. Javier Sánchez, Elodie Savary, Heidi Schweiker, Adam Scott, Hee-Jong Seo, Huanyuan Shan, David R. Silva, Zachary Slepian, Christian Soto, David Sprayberry, Ryan Staten, Coley M. Stillman, Robert J. Stupak, David L. Summers, Suk Sien

Tie, H. Tirado, Mariana Vargas-Magaña, A. Katherina Vivas, Risa H. Wechsler, Doug Williams, Jinyi Yang, Qian Yang, Tolga Yapici, Dennis Zaritsky, A. Zenteno, Kai Zhang, Tianmeng Zhang, Rongpu Zhou, and Zhimin Zhou. Overview of the DESI Legacy Imaging Surveys. *AJ*, 157(5): 168, May 2019. doi: 10.3847/1538-3881/ab089d.

Arianna Di Cintio, Chris B. Brook, Aaron A. Dutton, Andrea V. Macciò, Aura Obreja, and Avishai Dekel. NIHAO - XI. Formation of ultra-diffuse galaxies by outflows. *MNRAS*, 466(1):L1–L6, March 2017. doi: 10.1093/mnrasl/slw210.

Claire M Dickey, Tjitske K Starkenburg, Marla Geha, ChangHoon Hahn, Daniel Anglés-Alcázar, Ena Choi, Romeel Davé, Shy Genel, Kartheik G Iyer, Ariyeh H Maller, Nir Mandelker, Rachel S Somerville, and L Y Aaron Yung. IQ Collaboratory II: The Quiescent Fraction of Isolated, Low Mass Galaxies Across Simulations and Observations. *arXiv e-prints*, art. arXiv:2010.01132, October 2020.

S. G. Djorgovski, R. R. Gal, S. C. Odewahn, R. R. de Carvalho, R. Brunner, G. Longo, and R. Scaramella. The Palomar Digital Sky Survey (DPOSS). In Stephane Colombi, Yannick Mellier, and Brigitte Raban, editors, *Wide Field Surveys in Cosmology*, volume 14, page 89, January 1998.

Mamoru Doi, Masayuki Tanaka, Masataka Fukugita, James E. Gunn, Naoki Yasuda, Željko Ivezić, Jon Brinkmann, Ernst de Haars, S. J. Kleinman, Jurek Krzesinski, and R. French Leger. Photometric Response Functions of the Sloan Digital Sky Survey Imager. *AJ*, 139(4):1628–1648, April 2010. doi: 10.1088/0004-6256/139/4/1628.

A. Dressler. Galaxy morphology in rich clusters: implications for the formation and evolution of galaxies. *ApJ*, 236:351–365, March 1980. doi: 10.1086/157753.

R. D'Souza, G. Kauffman, J. Wang, and S. Vegetti. Parametrizing the stellar haloes of galaxies. *MNRAS*, 443:1433–1450, September 2014. doi: 10.1093/mnras/stu1194.

C. Dupraz and F. Combes. Shells around galaxies - Testing the mass distribution and the 3-D shape of ellipticals. *A&A*, 166:53–74, September 1986.

Jenny E Greene, Johnny P. Greco, Andy D. Goulding, Song Huang, Erin Kado-Fong, Shany Danieli, Jiaxuan Li, Ji Hoon Kim, Yutaka Komiyama, Alexie Leauthaud, Lauren A. MacArthur, and Cristobal Sifon. The Nature of Low Surface Brightness Galaxies in the Hyper Suprime-Cam Survey. *arXiv e-prints*, art. arXiv:2204.11883, April 2022.

Paul Eigenthaler, Thomas H. Puzia, Matthew A. Taylor, Yasna Ordenes-Briceño, Roberto P. Muñoz, Karen X. Ribbeck, Karla A. Alamo-Martínez, Hongxin Zhang, Simón Ángel, Massimo Capaccioli, Patrick Côté, Laura Ferrarese, Gaspar Galaz, Eva K. Grebel, Maren Hempel, Michael Hilker, Ariane Lançon, Steffen Mieske, Bryan Miller, Maurizio Paolillo, Mathieu Powalka, Tom Richtler, Joel Roediger, Yu Rong, Ruben Sánchez-Janssen, and Chelsea Spengler. The Next Generation Fornax Survey (NGFS). II. The Central Dwarf Galaxy Population. *ApJ*, 855(2):142, March 2018. doi: 10.3847/1538-4357/aaab60.

Kareem El-Badry, Andrew Wetzel, Marla Geha, Philip F. Hopkins, Dusan Kereš, T. K. Chan, and Claude-André Faucher-Giguère. Breathing FIRE: How Stellar Feedback Drives Radial Migration, Rapid Size Fluctuations, and Population Gradients in Low-mass Galaxies. *ApJ*, 820(2):131, April 2016. doi: 10.3847/0004-637X/820/2/131.

Kareem El-Badry, Jeremy Bradford, Eliot Quataert, Marla Geha, Michael Boylan-Kolchin, Daniel R. Weisz, Andrew Wetzel, Philip F. Hopkins, T. K. Chan, Alex Fitts, Dušan Kereš, and Claude-André Faucher-Giguère. Gas kinematics in FIRE simulated galaxies compared to spatially unresolved H I observations. *MNRAS*, 477(2):1536–1548, June 2018a. doi: 10.1093/mnras/sty730.

Kareem El-Badry, Jeremy Bradford, Eliot Quataert, Marla Geha, Michael Boylan-Kolchin, Daniel R. Weisz, Andrew Wetzel, Philip F. Hopkins, T. K. Chan, Alex Fitts, Dušan Kereš, and Claude-André Faucher-Giguère. Gas kinematics in FIRE simulated galaxies compared to spatially unresolved H I observations. *MNRAS*, 477(2):1536–1548, June 2018b. doi: 10.1093/mnras/sty730.

Kareem El-Badry, Eliot Quataert, Andrew Wetzel, Philip F. Hopkins, Daniel R. Weisz, T. K. Chan, Alex Fitts, Michael Boylan-Kolchin, Dušan Kereš, Claude-André Faucher-Giguère, and Shea

Garrison-Kimmel. Gas kinematics, morphology and angular momentum in the FIRE simulations. *MNRAS*, 473(2):1930–1955, January 2018c. doi: 10.1093/mnras/stx2482.

Sara L. Ellison, Barbara Catinella, and Luca Cortese. Enhanced atomic gas fractions in recently merged galaxies: quenching is not a result of post-merger gas exhaustion. *MNRAS*, 478(3): 3447–3466, Aug 2018. doi: 10.1093/mnras/sty1247.

Bruce G. Elmegreen, Hong-Xin Zhang, and Deidre A. Hunter. In-spiraling Clumps in Blue Compact Dwarf Galaxies. *ApJ*, 747(2):105, Mar 2012. doi: 10.1088/0004-637X/747/2/105.

Najmeh Emami, Brian Siana, Kareem El-Badry, David Cook, Xiangcheng Ma, Daniel Weisz, Joobin Gharibshah, Sara Alaee, Claudia Scarlata, and Evan Skillman. Testing the Relationship Between Bursty Star Formation and Size Fluctuations of Local Dwarf Galaxies. *arXiv e-prints*, art. arXiv:2108.08857, August 2021.

Peter Erwin. IMFIT: A Fast, Flexible New Program for Astronomical Image Fitting. *ApJ*, 799(2): 226, February 2015. doi: 10.1088/0004-637X/799/2/226.

Ivanna Escala, Andrew Wetzel, Evan N. Kirby, Philip F. Hopkins, Xiangcheng Ma, Coral Wheeler, Dušan Kereš, Claude-André Faucher-Giguère, and Eliot Quataert. Modelling chemical abundance distributions for dwarf galaxies in the Local Group: the impact of turbulent metal diffusion. *MNRAS*, 474(2):2194–2211, February 2018. doi: 10.1093/mnras/stx2858.

Claude-André Faucher-Giguère. A model for the origin of bursty star formation in galaxies. *MNRAS*, 473(3):3717–3731, January 2018. doi: 10.1093/mnras/stx2595.

Claude-André Faucher-Giguère, Adam Lidz, Matias Zaldarriaga, and Lars Hernquist. A New Calculation of the Ionizing Background Spectrum and the Effects of He II Reionization. *ApJ*, 703 (2):1416–1443, October 2009. doi: 10.1088/0004-637X/703/2/1416.

R. Feldmann, L. Mayer, and C. M. Carollo. Tidal Debris in Elliptical Galaxies as Tracers of Mergers with Disks. *ApJ*, 684:1062-1074, September 2008. doi: 10.1086/590235.

Drummond Fielding, Eliot Quataert, and Davide Martizzi. Clustered supernovae drive powerful galactic winds after superbubble breakout. *MNRAS*, 481(3):3325–3347, December 2018. doi: 10.1093/mnras/sty2466.

M. D. Filipovic, G. L. White, P. A. Jones, R. F. Haynes, W. N. Pietsch, R. Wielebinski, and U. Klein. The Magellanic Clouds: Overview of their History, Structure, Chemical Composition and Surveys. In A. Burkert, D. H. Hartmann, and S. A. Majewski, editors, *The History of the Milky Way and Its Satellite System*, volume 112 of *Astronomical Society of the Pacific Conference Series*, page 91, January 1996.

Alex Fitts, Michael Boylan-Kolchin, Oliver D. Elbert, James S. Bullock, Philip F. Hopkins, Jose Oñorbe, Andrew Wetzel, Coral Wheeler, Claude-André Faucher-Giguère, Dušan Kereš, Evan D. Skillman, and Daniel R. Weisz. fire in the field: simulating the threshold of galaxy formation. *MNRAS*, 471(3):3547–3562, November 2017. doi: 10.1093/mnras/stx1757.

Alex Fitts, Michael Boylan-Kolchin, James S. Bullock, Daniel R. Weisz, Kareem El-Badry, Coral Wheeler, Claude-André Faucher-Giguère, Eliot Quataert, Philip F. Hopkins, Dušan Kereš, Andrew Wetzel, and Christopher C. Hayward. No assembly required: mergers are mostly irrelevant for the growth of low-mass dwarf galaxies. *MNRAS*, 479(1):319–331, September 2018. doi: 10.1093/mnras/sty1488.

José A. Flores Velázquez, Alexander B. Gurvich, Claude-André Faucher-Giguère, James S. Bullock, Tjitske K. Starkenburg, Jorge Moreno, Alexandres Lazar, Francisco J. Mercado, Jonathan Stern, Martin Sparre, Christopher C. Hayward, Andrew Wetzel, and Kareem El-Badry. The time-scales probed by star formation rate indicators for realistic, bursty star formation histories from the FIRE simulations. *MNRAS*, 501(4):4812–4824, March 2021. doi: 10.1093/mnras/staa3893.

Daniel Foreman-Mackey, David W. Hogg, Dustin Lang, and Jonathan Goodman. emcee: The MCMC Hammer. *PASP*, 125(925):306, March 2013. doi: 10.1086/670067.

B. P. Fort, J.-L. Prieur, D. Carter, S. J. Meatheringham, and L. Vigroux. Surface photometry of shell galaxies. *ApJ*, 306:110–121, July 1986. doi: 10.1086/164324.

C. Foster, H. Lux, A. J. Romanowsky, D. Martínez-Delgado, S. Zibetti, J. A. Arnold, J. P. Brodie, R. Ciardullo, R. J. GaBany, M. R. Merrifield, N. Singh, and J. Strader. Kinematics and simulations of the stellar stream in the halo of the Umbrella Galaxy. *MNRAS*, 442:3544–3564, August 2014. doi: 10.1093/mnras/stu1074.

T. K. Fritz, G. Battaglia, M. S. Pawlowski, N. Kallivayalil, R. van der Marel, S. T. Sohn, C. Brook, and G. Besla. Gaia DR2 proper motions of dwarf galaxies within 420 kpc. Orbits, Milky Way mass, tidal influences, planar alignments, and group infall. *A&A*, 619:A103, November 2018. doi: 10.1051/0004-6361/201833343.

H. Furusawa, M. Koike, T. Takata, Y. Okura, H. Miyatake, R. H. Lupton, S. Bickerton, P. A. Price, J. Bosch, N. Yasuda, S. Mineo, Y. Yamada, S. Miyazaki, F. Nakata, S. Koshida, Y. Komiyama, Y. Utsumi, S. Kawanomoto, E. Jeschke, J. Noumaru, K. Schubert, I. Iwata, F. Finet, T. Fujiyoshi, A. Tajitsu, T. Terai, and C.-H. Lee. The on-site quality-assurance system for Hyper Suprime-Cam: OSQAH. *PASJ*, 70:S3, January 2018. doi: 10.1093/pasj/psx079.

J. M. Gabor and R. Davé. The growth of red sequence galaxies in a cosmological hydrodynamic simulation. *MNRAS*, 427:1816–1829, December 2012. doi: 10.1111/j.1365-2966.2012.21640.x.

A. Gallazzi, S. Charlot, J. Brinchmann, and S. D. M. White. Ages and metallicities of early-type galaxies in the Sloan Digital Sky Survey: new insight into the physical origin of the colour-magnitude and the Mg_2-σ_V relations. *MNRAS*, 370:1106–1124, August 2006. doi: 10.1111/j.1365-2966.2006.10548.x.

Yulong Gao, Qiusheng Gu, Yong Shi, Luwenjia Zhou, Min Bao, Xiaoling Yu, Zhi-Yu Zhang, Tao Wang, Suzanne C. Madden, Matthew Hayes, Shiying Lu, and Ke Xu. The molecular gas resolved by ALMA in the low-metallicity merging dwarf galaxy Haro 11. *A&A*, 661:A136, May 2022. doi: 10.1051/0004-6361/202142309.

Shea Garrison-Kimmel, Andrew Wetzel, Philip F. Hopkins, Robyn Sanderson, Kareem El-Badry, Andrew Graus, T. K. Chan, Robert Feldmann, Michael Boylan-Kolchin, Christopher C. Hayward, James S. Bullock, Alex Fitts, Jenna Samuel, Coral Wheeler, Dušan Kereš, and Claude-André

Faucher-Giguère. Star formation histories of dwarf galaxies in the FIRE simulations: dependence on mass and Local Group environment. *MNRAS*, 489(4):4574–4588, November 2019. doi: 10.1093/mnras/stz2507.

Lexi Gault, Lukas Leisman, Elizabeth A. K. Adams, Pavel E. Mancera Piña, Kameron Reiter, Nicholas Smith, Michael Battipaglia, John M. Cannon, Filippo Fraternali, Martha P. Haynes, Elizabeth McAllan, Hannah J. Pagel, Katherine L. Rhode, John J. Salzer, and Quinton Singer. VLA Imaging of H I-bearing Ultra-diffuse Galaxies from the ALFALFA Survey. *ApJ*, 909(1):19, March 2021. doi: 10.3847/1538-4357/abd79d.

M. Geha, M. R. Blanton, R. Yan, and J. L. Tinker. A Stellar Mass Threshold for Quenching of Field Galaxies. *ApJ*, 757(1):85, September 2012. doi: 10.1088/0004-637X/757/1/85.

Marla Geha, Risa H. Wechsler, Yao-Yuan Mao, Erik J. Tollerud, Benjamin Weiner, Rebecca Bernstein, Ben Hoyle, Sebastian Marchi, Phil J. Marshall, Ricardo Muñoz, and Yu Lu. The SAGA Survey. I. Satellite Galaxy Populations around Eight Milky Way Analogs. *ApJ*, 847(1):4, September 2017. doi: 10.3847/1538-4357/aa8626.

Adam Ginsburg, Brigitta M. Sipőcz, C. E. Brasseur, Philip S. Cowperthwaite, Matthew W. Craig, Christoph Deil, James Guillochon, Giannina Guzman, Simon Liedtke, Pey Lian Lim, Kelly E. Lockhart, Michael Mommert, Brett M. Morris, Henrik Norman, Madhura Parikh, Magnus V. Persson, Thomas P. Robitaille, Juan-Carlos Segovia, Leo P. Singer, Erik J. Tollerud, Miguel de Val-Borro, Ivan Valtchanov, Julien Woillez, Astroquery Collaboration, and a subset of astropy Collaboration. astroquery: An Astronomical Web-querying Package in Python. *AJ*, 157(3):98, March 2019. doi: 10.3847/1538-3881/aafc33.

Riccardo Giovanelli, Martha P. Haynes, Brian R. Kent, Philip Perillat, Amelie Saintonge, Noah Brosch, Barbara Catinella, G. Lyle Hoffman, Sabrina Stierwalt, Kristine Spekkens, Mikael S. Lerner, Karen L. Masters, Emmanuel Momjian, Jessica L. Rosenberg, Christopher M. Springob, Alessandro Boselli, Vassilis Charmandaris, Jeremy K. Darling, Jonathan Davies, Diego Garcia Lambas, Giuseppe Gavazzi, Carlo Giovanardi, Eduardo Hardy, Leslie K. Hunt, Angela Iovino,

Igor D. Karachentsev, Valentina E. Karachentseva, Rebecca A. Koopmann, Christian Marinoni, Robert Minchin, Erik Muller, Mary Putman, Carmen Pantoja, John J. Salzer, Marco Scodeggio, Evan Skillman, Jose M. Solanes, Carlos Valotto, Wim van Driel, and Liese van Zee. The Arecibo Legacy Fast ALFA Survey. I. Science Goals, Survey Design, and Strategy. *AJ*, 130(6):2598–2612, December 2005. doi: 10.1086/497431.

Philipp Girichidis, Thorsten Naab, Michał Hanasz, and Stefanie Walch. Cooler and smoother - the impact of cosmic rays on the phase structure of galactic outflows. *MNRAS*, 479(3):3042–3067, September 2018. doi: 10.1093/mnras/sty1653.

Munan Gong, Eve C. Ostriker, Chang-Goo Kim, and Jeong-Gyu Kim. The Environmental Dependence of the X_{CO} Conversion Factor. *ApJ*, 903(2):142, November 2020. doi: 10.3847/1538-4357/abbdab.

Andy D. Goulding, Jenny E. Greene, Rachel Bezanson, Johnny Greco, Sean Johnson, Alexie Leauthaud, Yoshiki Matsuoka, Elinor Medezinski, and Adrian M. Price-Whelan. Galaxy interactions trigger rapid black hole growth: An unprecedented view from the Hyper Suprime-Cam survey. *Publications of the Astronomical Society of Japan*, 70:S37, January 2018. doi: 10.1093/pasj/psx135.

F. Governato, B. Willman, L. Mayer, A. Brooks, G. Stinson, O. Valenzuela, J. Wadsley, and T. Quinn. Forming disc galaxies in ΛCDM simulations. *MNRAS*, 374(4):1479–1494, February 2007. doi: 10.1111/j.1365-2966.2006.11266.x.

Andrew S. Graus, James S. Bullock, Alex Fitts, Michael C. Cooper, Michael Boylan-Kolchin, Daniel R. Weisz, Andrew Wetzel, Robert Feldmann, Claude-André Faucher-Giguère, Eliot Quataert, Philip F. Hopkins, and Dušan Kereš. A predicted correlation between age gradient and star formation history in FIRE dwarf galaxies. *MNRAS*, 490(1):1186–1201, November 2019. doi: 10.1093/mnras/stz2649.

E. K. Grebel. Evolutionary Histories of Dwarf Galaxies in the Local Group. In Patricia Whitelock

and Russell Cannon, editors, *The Stellar Content of Local Group Galaxies*, volume 192 of *IAU Symposium*, page 17, January 1999.

J. P. Greco, J. E. Greene, A. M. Price-Whelan, A. Leauthaud, S. Huang, A. D. Goulding, M. A. Strauss, Y. Komiyama, R. H. Lupton, S. Miyazaki, M. Takada, M. Tanaka, and T. Usuda. Sumo Puff: Tidal debris or disturbed ultra-diffuse galaxy? *PASJ*, 70:S19, January 2018a. doi: 10.1093/pasj/psx051.

Johnny P. Greco. *Hidden in Plain Sight: Illuminating Low Surface Brightness Galaxies with the Hyper Suprime-Cam*. PhD thesis, 2018. URL `https://www.proquest.com/dissertations-theses/hidden-plain-sight-illuminating-low-surface/docview/2128052158/se-2?accountid=13314`. Copyright - Database copyright ProQuest LLC; ProQuest does not claim copyright in the individual underlying works; Last updated - 2021-05-25.

Johnny P. Greco, Andy D. Goulding, Jenny E. Greene, Michael A. Strauss, Song Huang, Ji Hoon Kim, and Yutaka Komiyama. A Study of Two Diffuse Dwarf Galaxies in the Field. *ApJ*, 866(2): 112, October 2018b. doi: 10.3847/1538-4357/aae0f4.

Johnny P. Greco, Jenny E. Greene, Michael A. Strauss, Lauren A. Macarthur, Xzavier Flowers, Andy D. Goulding, Song Huang, Ji Hoon Kim, Yutaka Komiyama, Alexie Leauthaud, Lukas Leisman, Robert H. Lupton, Cristóbal Sifón, and Shiang-Yu Wang. Illuminating Low Surface Brightness Galaxies with the Hyper Suprime-Cam Survey. *ApJ*, 857(2):104, April 2018c. doi: 10.3847/1538-4357/aab842.

M. Gu, L. C. Ho, C. Y. Peng, and S. Huang. A Novel Approach to Constrain the Mass Ratio of Minor Mergers in Elliptical Galaxies: Application to NGC 4889, the Brightest Cluster Galaxy in Coma. *ApJ*, 773:34, August 2013. doi: 10.1088/0004-637X/773/1/34.

James E. Gunn and III Gott, J. Richard. On the Infall of Matter Into Clusters of Galaxies and Some Effects on Their Evolution. *ApJ*, 176:1, August 1972. doi: 10.1086/151605.

Sarah M. Hansen, Erin S. Sheldon, Risa H. Wechsler, and Benjamin P. Koester. The Galaxy Content

of SDSS Clusters and Groups. *ApJ*, 699:1333–1353, July 2009. doi: 10.1088/0004-637X/699/2/1333.

J. R. Hargis, S. Albers, D. Crnojević, D. J. Sand , D. R. Weisz, J. L. Carlin, K. Spekkens, B. Willman, A. H. G. Peter, C. J. Grillmair, and A. E. Dolphin. Hubble Space Telescope Imaging of Antlia B: Star Formation History and a New Tip of the Red Giant Branch Distance. *ApJ*, 888 (1):31, January 2020. doi: 10.3847/1538-4357/ab58d2.

Martha P. Haynes, Riccardo Giovanelli, Ann M. Martin, Kelley M. Hess, Amélie Saintonge, Elizabeth A. K. Adams, Gregory Hallenbeck, G. Lyle Hoffman, Shan Huang, Brian R. Kent, Rebecca A. Koopmann, Emmanouil Papastergis, Sabrina Stierwalt, Thomas J. Balonek, David W. Craig, Sarah J. U. Higdon, David A. Kornreich, Jeffrey R. Miller, Aileen A. O'Donoghue, Ronald P. Olowin, Jessica L. Rosenberg, Kristine Spekkens, Parker Troischt, and Eric M. Wilcots. The Arecibo Legacy Fast ALFA Survey: The α.40 H I Source Catalog, Its Characteristics and Their Impact on the Derivation of the H I Mass Function. *AJ*, 142(5):170, November 2011. doi: 10.1088/0004-6256/142/5/170.

Raymond Haynes, Roslynn D. Haynes, David Malin, and Richard McGee. *Explorers of the Southern Sky*. 2010.

David Hendel and Kathryn V. Johnston. Tidal debris morphology and the orbits of satellite galaxies. *MNRAS*, 454(3):2472–2485, Dec 2015. doi: 10.1093/mnras/stv2035.

L. Hernquist and P. J. Quinn. Formation of shell galaxies. II - Nonspherical potentials. *ApJ*, 342: 1–16, July 1989. doi: 10.1086/167571.

L. Hernquist and D. N. Spergel. Formation of shells in major mergers. *ApJL*, 399:L117–L120, November 1992. doi: 10.1086/186621.

Lars Hernquist and P. J. Quinn. Shells and Dark Matter in Elliptical Galaxies. *ApJ*, 312:1, January 1987. doi: 10.1086/164844.

Lars Hernquist and P. J. Quinn. Formation of Shell Galaxies. I. Spherical Potentials. *ApJ*, 331: 682, August 1988. doi: 10.1086/166592.

R. Herrera-Camus, A. Bolatto, M. Wolfire, E. Ostriker, B. Draine, A. Leroy, K. Sandstrom, L. Hunt, R. Kennicutt, D. Calzetti, J. D. Smith, K. Croxall, M. Galametz, I. de Looze, D. Dale, A. Crocker, and B. Groves. Thermal Pressure in the Cold Neutral Medium of Nearby Galaxies. *ApJ*, 835(2): 201, February 2017. doi: 10.3847/1538-4357/835/2/201.

S. L. Hidalgo, A. Marín-Franch, and A. Aparicio. Spatial Distribution of Stellar Populations in the Dwarf Irregular Galaxies DDO 165 and DDO 181. *AJ*, 125(3):1247–1260, March 2003. doi: 10.1086/367779.

S. J. U. Higdon, J. L. Higdon, B. J. Smith, and M. Hancock. Star Formation and the Interstellar Medium in Nearby Tidal Streams (SAINTS): Spitzer Mid-infrared spectroscopy and Imaging of Intergalactic Star-forming Objects. *ApJ*, 787:103, June 2014. doi: 10.1088/0004-637X/787/2/103.

Michael Hilz, Thorsten Naab, and J. P. Ostriker. How do minor mergers promote inside-out growth of ellipticals, transforming the size, density profile and dark matter fraction? *MNRAS*, 429: 2924–2933, March 2013. doi: 10.1093/mnras/sts501.

E. Holmberg. A photographic photometry of extragalactic nebulae. *Meddelanden fran Lunds Astronomiska Observatorium Serie II*, 136:1, January 1958.

Callie E. Hood, Sheila J. Kannappan, David V. Stark, Ian P. Dell'Antonio, Amanda J. Moffett, Kathleen D. Eckert, Mark A. Norris, and David Hendel. The Origin of Faint Tidal Features around Galaxies in the RESOLVE Survey. *ApJ*, 857:144, April 2018. doi: 10.3847/1538-4357/aab719.

Philip F. Hopkins. A new class of accurate, mesh-free hydrodynamic simulation methods. *MNRAS*, 450(1):53–110, June 2015. doi: 10.1093/mnras/stv195.

Philip F. Hopkins. A constrained-gradient method to control divergence errors in numerical MHD. *MNRAS*, 462(1):576–587, October 2016. doi: 10.1093/mnras/stw1578.

Philip F. Hopkins. Anisotropic diffusion in mesh-free numerical magnetohydrodynamics. *MNRAS*, 466(3):3387–3405, April 2017. doi: 10.1093/mnras/stw3306.

Philip F. Hopkins and Matthias J. Raives. Accurate, meshless methods for magnetohydrodynamics. *MNRAS*, 455(1):51–88, January 2016. doi: 10.1093/mnras/stv2180.

Philip F. Hopkins, Lars Hernquist, Thomas J. Cox, and Dušan Kereš. A Cosmological Framework for the Co-Evolution of Quasars, Supermassive Black Holes, and Elliptical Galaxies. I. Galaxy Mergers and Quasar Activity. *ApJS*, 175(2):356–389, Apr 2008. doi: 10.1086/524362.

Philip F. Hopkins, Desika Narayanan, and Norman Murray. The meaning and consequences of star formation criteria in galaxy models with resolved stellar feedback. *MNRAS*, 432(4):2647–2653, July 2013. doi: 10.1093/mnras/stt723.

Philip F. Hopkins, Andrew Wetzel, Dušan Kereš, Claude-André Faucher-Giguère, Eliot Quataert, Michael Boylan-Kolchin, Norman Murray, Christopher C. Hayward, Shea Garrison-Kimmel, Cameron Hummels, Robert Feldmann, Paul Torrey, Xiangcheng Ma, Daniel Anglés-Alcázar, Kung-Yi Su, Matthew Orr, Denise Schmitz, Ivanna Escala, Robyn Sanderson, Michael Y. Grudić, Zachary Hafen, Ji-Hoon Kim, Alex Fitts, James S. Bullock, Coral Wheeler, T. K. Chan, Oliver D. Elbert, and Desika Narayanan. FIRE-2 simulations: physics versus numerics in galaxy formation. *MNRAS*, 480(1):800–863, October 2018. doi: 10.1093/mnras/sty1690.

Philip F. Hopkins, T. K. Chan, Shea Garrison-Kimmel, Suoqing Ji, Kung-Yi Su, Cameron B. Hummels, Dušan Kereš, Eliot Quataert, and Claude-André Faucher-Giguère. But what about...: cosmic rays, magnetic fields, conduction, and viscosity in galaxy formation. *MNRAS*, 492(3): 3465–3498, March 2020a. doi: 10.1093/mnras/stz3321.

Philip F. Hopkins, Michael Y. Grudić, Andrew Wetzel, Dušan Kereš, Claude-André Faucher-Giguère, Xiangcheng Ma, Norman Murray, and Nathan Butcher. Radiative stellar feedback in galaxy formation: Methods and physics. *MNRAS*, 491(3):3702–3729, January 2020b. doi: 10.1093/mnras/stz3129.

Chia-Yu Hu. Supernova-driven winds in simulated dwarf galaxies. *MNRAS*, 483(3):3363–3381, March 2019. doi: 10.1093/mnras/sty3252.

Chia-Yu Hu, Thorsten Naab, Stefanie Walch, Simon C. O. Glover, and Paul C. Clark. Star formation and molecular hydrogen in dwarf galaxies: a non-equilibrium view. *MNRAS*, 458(4):3528–3553, June 2016. doi: 10.1093/mnras/stw544.

S. Huang, L. C. Ho, C. Y. Peng, Z.-Y. Li, and A. J. Barth. The Carnegie-Irvine Galaxy Survey. IV. A Method to Determine the Average Mass Ratio of Mergers That Built Massive Elliptical Galaxies. *ApJ*, 821:114, April 2016. doi: 10.3847/0004-637X/821/2/114.

S. Huang, A. Leauthaud, J. Greene, K. Bundy, Y.-T. Lin, M. Tanaka, R. Mandelbaum, S. Miyazaki, and Y. Komiyama. A Detection of the Environmental Dependence of the Sizes and Stellar Haloes of Massive Central Galaxies. *ArXiv e-prints*, March 2018a.

S. Huang, A. Leauthaud, J. E. Greene, K. Bundy, Y.-T. Lin, M. Tanaka, S. Miyazaki, and Y. Komiyama. Individual stellar haloes of massive galaxies measured to 100 kpc at $0.3 < z < 0.5$ using Hyper Suprime-Cam. *MNRAS*, 475:3348–3368, April 2018b. doi: 10.1093/mnras/stx3200.

S. Huang, A. Leauthaud, R. Murata, J. Bosch, P. Price, R. Lupton, R. Mandelbaum, C. Lackner, S. Bickerton, S. Miyazaki, J. Coupon, and M. Tanaka. Characterization and photometric performance of the Hyper Suprime-Cam Software Pipeline. *PASJ*, 70:S6, January 2018c. doi: 10.1093/pasj/psx126.

Song Huang, Alexie Leauthaud, Jenny E. Greene, Kevin Bundy, Yen-Ting Lin, Masayuki Tanaka, Satoshi Miyazaki, and Yutaka Komiyama. Individual stellar haloes of massive galaxies measured to 100 kpc at 0.3 ¡ z ¡ 0.5 using Hyper Suprime-Cam. *MNRAS*, 475(3):3348–3368, April 2018d. doi: 10.1093/mnras/stx3200.

Song Huang, Alexie Leauthaud, Jenny E. Greene, Kevin Bundy, Yen-Ting Lin, Masayuki Tanaka, Satoshi Miyazaki, and Yutaka Komiyama. Individual stellar haloes of massive galaxies measured to 100 kpc at 0.3 < z < 0.5 using Hyper Suprime-Cam. *MNRAS*, 475(3):3348–3368, April 2018e. doi: 10.1093/mnras/stx3200.

E. P. Hubble. Extragalactic nebulae. *ApJ*, 64:321–369, December 1926. doi: 10.1086/143018.

Deidre A. Hunter, Dana Ficut-Vicas, Trisha Ashley, Elias Brinks, Phil Cigan, Bruce G. Elmegreen, Volker Heesen, Kimberly A. Herrmann, Megan Johnson, Se-Heon Oh, Michael P. Rupen, Andreas Schruba, Caroline E. Simpson, Fabian Walter, David J. Westpfahl, Lisa M. Young, and Hong-Xin Zhang. Little Things. *AJ*, 144(5):134, November 2012. doi: 10.1088/0004-6256/144/5/134.

Deidre A. Hunter, Bruce G. Elmegreen, Esther Goldberger, Hannah Taylor, Anton I. Ermakov, Kimberly A. Herrmann, Se-Heon Oh, Bradley Malko, Brian Barandi, and Ryan Jundt. Relationships between the Stellar, Gaseous, and Star Formation Disks in LITTLE THINGS Dwarf Irregular Galaxies: Indirect Evidence for Substantial Fractions of Dark Molecular Gas. *AJ*, 161 (2):71, February 2021. doi: 10.3847/1538-3881/abd089.

J. D. Hunter. Matplotlib: A 2d graphics environment. *Computing in Science & Engineering*, 9(3): 90–95, 2007. doi: 10.1109/MCSE.2007.55.

Olivier Iffrig and Patrick Hennebelle. Mutual influence of supernovae and molecular clouds. *A&A*, 576:A95, April 2015. doi: 10.1051/0004-6361/201424556.

O. Ilbert, P. Capak, M. Salvato, H. Aussel, H. J. McCracken, D. B. Sanders, N. Scoville, J. Kartaltepe, S. Arnouts, E. Le Floc'h, B. Mobasher, Y. Taniguchi, F. Lamareille, A. Leauthaud, S. Sasaki, D. Thompson, M. Zamojski, G. Zamorani, S. Bardelli, M. Bolzonella, A. Bongiorno, M. Brusa, K. I. Caputi, C. M. Carollo, T. Contini, R. Cook, G. Coppa, O. Cucciati, S. de la Torre, L. de Ravel, P. Franzetti, B. Garilli, G. Hasinger, A. Iovino, P. Kampczyk, J. P. Kneib, C. Knobel, K. Kovac, J. F. Le Borgne, V. Le Brun, O. Le Fèvre, S. Lilly, D. Looper, C. Maier, V. Mainieri, Y. Mellier, M. Mignoli, T. Murayama, R. Pellò, Y. Peng, E. Pérez-Montero, A. Renzini, E. Ricciardelli, D. Schiminovich, M. Scodeggio, Y. Shioya, J. Silverman, J. Surace, M. Tanaka, L. Tasca, L. Tresse, D. Vergani, and E. Zucca. Cosmos Photometric Redshifts with 30-Bands for 2-deg^2. *ApJ*, 690(2):1236–1249, January 2009. doi: 10.1088/0004-637X/690/2/1236.

Tom Into and Laura Portinari. New colour-mass-to-light relations: the role of the asymptotic giant

branch phase and of interstellar dust. *MNRAS*, 430(4):2715–2731, April 2013. doi: 10.1093/mnras/stt071.

G. Iorio, V. Belokurov, D. Erkal, S. E. Koposov, C. Nipoti, and F. Fraternali. The first all-sky view of the Milky Way stellar halo with Gaia+2MASS RR Lyrae. *MNRAS*, 474(2):2142–2166, February 2018. doi: 10.1093/mnras/stx2819.

Giuliano Iorio and Vasily Belokurov. The shape of the Galactic halo with Gaia DR2 RR Lyrae. Anatomy of an ancient major merger. *MNRAS*, 482(3):3868–3879, January 2019. doi: 10.1093/mnras/sty2806.

IRSA. Galactic dust reddening and extinction, 2022. URL `https://catcopy.ipac.caltech.edu/dois/doi.php?id=10.26131/IRSA537`.

Ethan D. Jahn, Laura V. Sales, Andrew Wetzel, Michael Boylan-Kolchin, T. K. Chan, Kareem El-Badry, Alexandres Lazar, and James S. Bullock. Dark and luminous satellites of LMC-mass galaxies in the FIRE simulations. *MNRAS*, 489(4):5348–5364, November 2019. doi: 10.1093/mnras/stz2457.

Steven Janowiecki and John J. Salzer. The Unique Structural Parameters of the Underlying Host Galaxies in Blue Compact Dwarfs. *ApJ*, 793:109, October 2014. doi: 10.1088/0004-637X/793/2/109.

Steven Janowiecki, Michael G. Jones, Lukas Leisman, and Andrew Webb. The environment of H I-bearing ultra-diffuse galaxies in the ALFALFA survey. *MNRAS*, 490(1):566–577, November 2019. doi: 10.1093/mnras/stz1868.

Robert I. Jedrzejewski. CCD surface photometry of elliptical galaxies - I. Observations, reduction and results. *MNRAS*, 226:747–768, June 1987. doi: 10.1093/mnras/226.4.747.

Suoqing Ji, T. K. Chan, Cameron B. Hummels, Philip F. Hopkins, Jonathan Stern, Dušan Kereš, Eliot Quataert, Claude-André Faucher-Giguère, and Norman Murray. Properties of the circum-

galactic medium in cosmic ray-dominated galaxy haloes. *MNRAS*, 496(4):4221–4238, August 2020. doi: 10.1093/mnras/staa1849.

Fangzhou Jiang, Avishai Dekel, Jonathan Freundlich, Aaron J. Romanowsky, Aaron A. Dutton, Andrea V. Macciò, and Arianna Di Cintio. Formation of ultra-diffuse galaxies in the field and in galaxy groups. *MNRAS*, 487(4):5272–5290, August 2019. doi: 10.1093/mnras/stz1499.

L. Jiang, S. Cole, T. Sawala, and C. S. Frenk. Orbital parameters of infalling satellite haloes in the hierarchical ΛCDM model. *MNRAS*, 448:1674–1686, April 2015. doi: 10.1093/mnras/stv053.

Kathryn V. Johnston, Penny D. Sackett, and James S. Bullock. Interpreting Debris from Satellite Disruption in External Galaxies. *ApJ*, 557(1):137–149, Aug 2001. doi: 10.1086/321644.

Kathryn V. Johnston, James S. Bullock, Sanjib Sharma, Andreea Font, Brant E. Robertson, and Samuel N. Leitner. Tracing Galaxy Formation with Stellar Halos. II. Relating Substructure in Phase and Abundance Space to Accretion Histories. *ApJ*, 689(2):936–957, December 2008. doi: 10.1086/592228.

E. Kado-Fong, J. E. Greene, D. Hendel, A. M. Price-Whelan, J. P. Greco, A. D. Goulding, S. Huang, K. V. Johnston, Y. Komiyama, C. H. Lee, N. B. Lust, M. A. Strauss, and M. Tanaka. Tidal Features at 0.05 < z < 0.45 in the Hyper Suprime-Cam Subaru Strategic Program: Properties and Formation Channels. *ApJ*, 866(2):103, October 2018. doi: 10.3847/1538-4357/aae0f0.

Erin Kado-Fong, Jenny E. Greene, Johnny P. Greco, Rachael Beaton, Andy D. Goulding, Sean D. Johnson, and Yutaka Komiyama. Star Formation in Isolated Dwarf Galaxies Hosting Tidal Debris: Extending the Dwarf-Dwarf Merger Sequence. *AJ*, 159(3):103, March 2020a. doi: 10.3847/1538-3881/ab6ef3.

Erin Kado-Fong, Jenny E. Greene, Song Huang, Rachael Beaton, Andy D. Goulding, and Yutaka Komiyama. Tracing the Intrinsic Shapes of Dwarf Galaxies Out to Four Effective Radii: Clues to Low-mass Stellar Halo Formation. *ApJ*, 900(2):163, September 2020b. doi: 10.3847/1538-4357/abacc2.

Erin Kado-Fong, Mihai Petrescu, Majid Mohammad, Johnny Greco, Jenny E. Greene, Elizabeth A. K. Adams, Song Huang, Lukas Leisman, Ferah Munshi, Dimitrios Tanoglidis, and Jordan Van Nest. The Intrinsic Shapes of Low Surface Brightness Galaxies (LSBGs): A Discriminant of LSBG Galaxy Formation Mechanisms. *ApJ*, 920(2):72, October 2021. doi: 10.3847/1538-4357/ac15f0.

Erin Kado-Fong, Jenny E. Greene, Song Huang, and Andy Goulding. Ultra-Diffuse Galaxies as Extreme Star-forming Environments I: Mapping Star Formation in HI-Rich UDGs. 2022a.

Erin Kado-Fong, Jenny E. Greene, Chang-Goo Kim, and Lachlan Lancaster. Ultra-Diffuse Galaxies as Extreme Star-forming Environments II: Star Formation and Pressure Balance in HI-Rich UDGs. 2022b.

Erin Kado-Fong, Robyn E. Sanderson, Jenny E. Greene, Emily C. Cunningham, Coral Wheeler, T. K. Chan, Kareem El-Badry, Philip F. Hopkins, Andrew Wetzel, Michael Boylan-Kolchin, Claude-André Faucher-Giguère, Song Huang, Eliot Quataert, and Tjitske Starkenburg. The In Situ Origins of Dwarf Stellar Outskirts in FIRE-2. *ApJ*, 931(2):152, June 2022c. doi: 10.3847/1538-4357/ac6c88.

Rahul Kannan, Mark Vogelsberger, Federico Marinacci, Ryan McKinnon, Rüdiger Pakmor, and Volker Springel. AREPO-RT: radiation hydrodynamics on a moving mesh. *MNRAS*, 485(1):117–149, May 2019. doi: 10.1093/mnras/stz287.

I. D. Karachentsev, E. I. Kaisina, and S. S. Kaisin. Local Volume late-type galaxies with an extreme ratio of H α-to-FUV SFRs. *MNRAS*, 506(1):1346–1354, September 2021. doi: 10.1093/mnras/stab1402.

Ananthan Karunakaran, Kristine Spekkens, Dennis Zaritsky, Richard L. Donnerstein, Jennifer Kadowaki, and Arjun Dey. Systematically Measuring Ultradiffuse Galaxies in H I: Results from the Pilot Survey. *ApJ*, 902(1):39, October 2020. doi: 10.3847/1538-4357/abb464.

Guinevere Kauffmann, Timothy M. Heckman, Simon D. M. White, Stéphane Charlot, Christy Tremonti, Jarle Brinchmann, Gustavo Bruzual, Eric W. Peng, Mark Seibert, Mariangela

Bernardi, Michael Blanton, Jon Brinkmann, Francisco Castander, Istvan Csábai, Masataka Fukugita, Zeljko Ivezic, Jeffrey A. Munn, Robert C. Nichol, Nikhil Padmanabhan, Aniruddha R. Thakar, David H. Weinberg, and Donald York. Stellar masses and star formation histories for 10^5 galaxies from the Sloan Digital Sky Survey. *MNRAS*, 341(1):33–53, May 2003. doi: 10.1046/j.1365-8711.2003.06291.x.

S. Kawanomoto, F. Uraguchi, Y. Komiyama, S. Miyazaki, H. Furusawa, F. Finet, T. Hattori, S.-Y. Wang, N. Yasuda, and N. Suzuki. Hyper Suprime-Cam: Filters. *PASJ*, 70:66, August 2018. doi: 10.1093/pasj/psy056.

D. Kawata, J. S. Mulchaey, B. K. Gibson, and P. Sánchez-Blázquez. Are Red Tidal Features Unequivocal Signatures of Major Dry Mergers? *ApJ*, 648:969–975, September 2006. doi: 10.1086/506247.

Jr. Kennicutt, Robert C. The Star Formation Law in Galactic Disks. *ApJ*, 344:685, September 1989. doi: 10.1086/167834.

Jr. Kennicutt, Robert C. Star Formation in Galaxies Along the Hubble Sequence. *AR&AA*, 36: 189–232, January 1998. doi: 10.1146/annurev.astro.36.1.189.

R. C. Kennicutt, D. Calzetti, G. Aniano, P. Appleton, L. Armus, P. Beirão, A. D. Bolatto, B. Brandl, A. Crocker, K. Croxall, D. A. Dale, J. Donovan Meyer, B. T. Draine, C. W. Engelbracht, M. Galametz, K. D. Gordon, B. Groves, C. N. Hao, G. Helou, J. Hinz, L. K. Hunt, B. Johnson, J. Koda, O. Krause, A. K. Leroy, Y. Li, S. Meidt, E. Montiel, E. J. Murphy, N. Rahman, H. W. Rix, H. Roussel, K. Sandstrom, M. Sauvage, E. Schinnerer, R. Skibba, J. D. T. Smith, S. Srinivasan, L. Vigroux, F. Walter, C. D. Wilson, M. Wolfire, and S. Zibetti. KINGFISH—Key Insights on Nearby Galaxies: A Far-Infrared Survey with Herschel: Survey Description and Image Atlas. *PASP*, 123(910):1347, December 2011. doi: 10.1086/663818.

Amanda A. Kepley, Adam K. Leroy, Kelsey E. Johnson, Karin Sandstrom, and C. H. Rosie Chen. The Molecular Clouds Fueling A 1/5 Solar Metallicity Starburst. *ApJ*, 828(1):50, September 2016. doi: 10.3847/0004-637X/828/1/50.

Chang-Goo Kim and Eve C. Ostriker. Vertical Equilibrium, Energetics, and Star Formation Rates in Magnetized Galactic Disks Regulated by Momentum Feedback from Supernovae. *ApJ*, 815(1): 67, December 2015. doi: 10.1088/0004-637X/815/1/67.

Chang-Goo Kim and Eve C. Ostriker. Three-phase Interstellar Medium in Galaxies Resolving Evolution with Star Formation and Supernova Feedback (TIGRESS): Algorithms, Fiducial Model, and Convergence. *ApJ*, 846(2):133, September 2017. doi: 10.3847/1538-4357/aa8599.

Chang-Goo Kim, Woong-Tae Kim, and Eve C. Ostriker. Regulation of Star Formation Rates in Multiphase Galactic Disks: Numerical Tests of the Thermal/Dynamical Equilibrium Model. *ApJ*, 743(1):25, December 2011. doi: 10.1088/0004-637X/743/1/25.

Chang-Goo Kim, Eve C. Ostriker, and Woong-Tae Kim. Three-dimensional Hydrodynamic Simulations of Multiphase Galactic Disks with Star Formation Feedback. I. Regulation of Star Formation Rates. *ApJ*, 776(1):1, October 2013. doi: 10.1088/0004-637X/776/1/1.

Chang-Goo Kim, Eve C. Ostriker, and Roberta Raileanu. Superbubbles in the Multiphase ISM and the Loading of Galactic Winds. *ApJ*, 834(1):25, January 2017. doi: 10.3847/1538-4357/834/1/25.

Jeong-Gyu Kim, Eve C. Ostriker, and Nina Filippova. Star Formation Efficiency and Dispersal of Giant Molecular Clouds with UV Radiation Feedback: Dependence on Gravitational Boundedness and Magnetic Fields. *ApJ*, 911(2):128, April 2021. doi: 10.3847/1538-4357/abe934.

T. Kim, K. Sheth, J. L. Hinz, M. G. Lee, D. Zaritsky, D. A. Gadotti, J. H. Knapen, E. Schinnerer, L. C. Ho, E. Laurikainen, H. Salo, E. Athanassoula, A. Bosma, B. de Swardt, J.-C. Muñoz-Mateos, B. F. Madore, S. Comerón, M. W. Regan, K. Menéndez-Delmestre, A. Gil de Paz, M. Seibert, J. Laine, S. Erroz-Ferrer, and T. Mizusawa. Early-type Galaxies with Tidal Debris and Their Scaling Relations in the Spitzer Survey of Stellar Structure in Galaxies (S^4G). *ApJ*, 753:43, July 2012. doi: 10.1088/0004-637X/753/1/43.

Johan H. Knapen and Ignacio Trujillo. *Ultra-Deep Imaging: Structure of Disks and Haloes*, pages 255–289. Springer International Publishing, Cham, 2017. ISBN 978-3-319-56570-5. doi: 10.1007/978-3-319-56570-5_8. URL `https://doi.org/10.1007/978-3-319-56570-5_8`.

K. Knierman, P. M. Knezek, P. Scowen, R. A. Jansen, and E. Wehner. Tidal Tails of Minor Mergers: Star Formation Efficiency in the Western Tail of NGC 2782. *ApJL*, 749:L1, April 2012. doi: 10.1088/2041-8205/749/1/L1.

K. A. Knierman, P. Scowen, T. Veach, C. Groppi, B. Mullan, I. Konstantopoulos, P. M. Knezek, and J. Charlton. Tidal Tails of Minor Mergers. II. Comparing Star Formation in the Tidal Tails of NGC 2782. *ApJ*, 774:125, September 2013. doi: 10.1088/0004-637X/774/2/125.

Yutaka Komiyama, Yoshiyuki Obuchi, Hidehiko Nakaya, Yukiko Kamata, Satoshi Kawanomoto, Yousuke Utsumi, Satoshi Miyazaki, Fumihiro Uraguchi, Hisanori Furusawa, Tomoki Morokuma, Tomohisa Uchida, Hironao Miyatake, Sogo Mineo, Hiroki Fujimori, Hiroaki Aihara, Hiroshi Karoji, James E. Gunn, and Shiang-Yu Wang. Hyper Suprime-Cam: Camera dewar design. *PASJ*, 70:S2, Jan 2018. doi: 10.1093/pasj/psx069.

Demao Kong, Manoj Kaplinghat, Hai-Bo Yu, Filippo Fraternali, and Pavel E. Mancera Piña. The Odd Dark Matter Halos of Isolated Gas-Rich Ultra-Diffuse Galaxies. *arXiv e-prints*, art. arXiv:2204.05981, April 2022.

John Kormendy and Ralf Bender. A Revised Parallel-sequence Morphological Classification of Galaxies: Structure and Formation of S0 and Spheroidal Galaxies. *ApJS*, 198(1):2, January 2012. doi: 10.1088/0067-0049/198/1/2.

Pavel Kroupa. On the variation of the initial mass function. *MNRAS*, 322(2):231–246, April 2001. doi: 10.1046/j.1365-8711.2001.04022.x.

Mark R. Krumholz and Nickolay Y. Gnedin. A Comparison of Methods for Determining the Molecular Content of Model Galaxies. *ApJ*, 729(1):36, March 2011. doi: 10.1088/0004-637X/729/1/36.

Mark R. Krumholz, Christopher F. McKee, and Jason Tumlinson. The Star Formation Law in Atomic and Molecular Gas. *ApJ*, 699(1):850–856, July 2009. doi: 10.1088/0004-637X/699/1/850.

Lachlan Lancaster, Eve C. Ostriker, Jeong-Gyu Kim, and Chang-Goo Kim. Star Formation Regulation and Self-pollution by Stellar Wind Feedback. *ApJL*, 922(1):L3, November 2021. doi: 10.3847/2041-8213/ac3333.

Rebecca Lange, Simon P. Driver, Aaron S. G. Robotham, Lee S. Kelvin, Alister W. Graham, Mehmet Alpaslan, Stephen K. Andrews, Ivan K. Baldry, Steven Bamford, Joss Bland-Hawthorn, Sarah Brough, Michelle E. Cluver, Christopher J. Conselice, Luke J. M. Davies, Boris Haeussler, Iraklis S. Konstantopoulos, Jon Loveday, Amanda J. Moffett, Peder Norberg, Steven Phillipps, Edward N. Taylor, Ángel R. López-Sánchez, and Stephen M. Wilkins. Galaxy And Mass Assembly (GAMA): mass-size relations of z ¡ 0.1 galaxies subdivided by Sérsic index, colour and morphology. *MNRAS*, 447(3):2603–2630, March 2015. doi: 10.1093/mnras/stu2467.

Barry M. Lasker, Conrad R. Sturch, Brian J. McLean, Jane L. Russell, Helmut Jenkner, and Michael M. Shara. The Guide Star Catalog. I. Astronomical Foundations and Image Processing. *AJ*, 99:2019, June 1990. doi: 10.1086/115483.

Henrietta S. Leavitt and Edward C. Pickering. Periods of 25 Variable Stars in the Small Magellanic Cloud. *Harvard College Observatory Circular*, 173:1–3, March 1912.

J. Lee and S. K. Yi. On the Assembly History of Stellar Components in Massive Galaxies. *ApJ*, 766:38, March 2013. doi: 10.1088/0004-637X/766/1/38.

J. Lee and S. K. Yi. Formation and Assembly History of Stellar Components in Galaxies as a Function of Stellar and Halo Mass. *ApJ*, 836:161, February 2017. doi: 10.3847/1538-4357/aa5b87.

Janice C. Lee, Jr. Kennicutt, Robert C., S. J. José G. Funes, Shoko Sakai, and Sanae Akiyama. Dwarf Galaxy Starburst Statistics in the Local Volume. *ApJ*, 692(2):1305–1320, Feb 2009. doi: 10.1088/0004-637X/692/2/1305.

Myung Gyoon Lee, Jisu Kang, Jeong Hwan Lee, and In Sung Jang. Detection of a Large Population of Ultradiffuse Galaxies in Massive Galaxy Clusters: Abell S1063 and Abell 2744. *ApJ*, 844(2): 157, August 2017. doi: 10.3847/1538-4357/aa78fb.

Lukas Leisman, Martha P. Haynes, Steven Janowiecki, Gregory Hallenbeck, Gyula Józsa, Riccardo Giovanelli, Elizabeth A. K. Adams, David Bernal Neira, John M. Cannon, William F. Janesh, Katherine L. Rhode, and John J. Salzer. (Almost) Dark Galaxies in the ALFALFA Survey: Isolated H I-bearing Ultra-diffuse Galaxies. *ApJ*, 842(2):133, June 2017. doi: 10.3847/1538-4357/aa7575.

Claus Leitherer, Daniel Schaerer, Jeffrey D. Goldader, Rosa M. González Delgado, Carmelle Robert, Denis Foo Kune, Duília F. de Mello, Daniel Devost, and Timothy M. Heckman. Starburst99: Synthesis Models for Galaxies with Active Star Formation. *ApJS*, 123(1):3–40, July 1999. doi: 10.1086/313233.

Federico Lelli, Marc Verheijen, and Filippo Fraternali. The triggering of starbursts in low-mass galaxies. *MNRAS*, 445(2):1694–1712, Dec 2014. doi: 10.1093/mnras/stu1804.

Adam K. Leroy, Fabian Walter, Elias Brinks, Frank Bigiel, W. J. G. de Blok, Barry Madore, and M. D. Thornley. The Star Formation Efficiency in Nearby Galaxies: Measuring Where Gas Forms Stars Effectively. *AJ*, 136(6):2782–2845, December 2008. doi: 10.1088/0004-6256/136/6/2782.

Adam K. Leroy, Eva Schinnerer, Annie Hughes, Erik Rosolowsky, Jérôme Pety, Andreas Schruba, Antonio Usero, Guillermo A. Blanc, Mélanie Chevance, Eric Emsellem, Christopher M. Faesi, Cinthya N. Herrera, Daizhong Liu, Sharon E. Meidt, Miguel Querejeta, Toshiki Saito, Karin M. Sandstrom, Jiayi Sun, Thomas G. Williams, Gagandeep S. Anand, Ashley T. Barnes, Erica A. Behrens, Francesco Belfiore, Samantha M. Benincasa, Ivana Bešlić, Frank Bigiel, Alberto D. Bolatto, Jakob S. den Brok, Yixian Cao, Rupali Chandar, Jérémy Chastenet, I. Da Chiang, Enrico Congiu, Daniel A. Dale, Sinan Deger, Cosima Eibensteiner, Oleg V. Egorov, Axel García-Rodríguez, Simon C. O. Glover, Kathryn Grasha, Jonathan D. Henshaw, I. Ting Ho, Amanda A. Kepley, Jaeyeon Kim, Ralf S. Klessen, Kathryn Kreckel, Eric W. Koch, J. M. Diederik Kruijssen, Kirsten L. Larson, Janice C. Lee, Laura A. Lopez, Josh Machado, Ness Mayker, Rebecca McElroy, Eric J. Murphy, Eve C. Ostriker, Hsi-An Pan, Ismael Pessa, Johannes Puschnig, Alessandro Razza, Patricia Sánchez-Blázquez, Francesco Santoro, Amy Sardone, Fabian Scheuermann, Kazimierz Sliwa, Mattia C. Sormani, Sophia K. Stuber, David A. Thilker, Jordan A.

Turner, Dyas Utomo, Elizabeth J. Watkins, and Bradley Whitmore. PHANGS-ALMA: Arcsecond CO(2-1) Imaging of Nearby Star-forming Galaxies. *ApJS*, 257(2):43, December 2021. doi: 10.3847/1538-4365/ac17f3.

Jiaxuan Li, Song Huang, Alexie Leauthaud, John Moustakas, Shany Danieli, Jenny E. Greene, Roberto Abraham, Felipe Ardila, Erin Kado-Fong, Deborah Lokhorst, Robert Lupton, and Paul Price. Reaching for the Edge I: Probing the Outskirts of Massive Galaxies with HSC, DECaLS, SDSS, and Dragonfly. *arXiv e-prints*, art. arXiv:2111.03557, November 2021.

Shihong Liao, Liang Gao, Carlos S. Frenk, Robert J. J. Grand, Qi Guo, Facundo A. Gómez, Federico Marinacci, Rüdiger Pakmor, Shi Shao, and Volker Springel. Ultra-diffuse galaxies in the Auriga simulations. *MNRAS*, 490(4):5182–5195, December 2019. doi: 10.1093/mnras/stz2969.

D. N. C. Lin and S. M. Faber. Some implications of nonluminous matter in dwarf spheroidal galaxies. *ApJL*, 266:L21–L25, March 1983. doi: 10.1086/183971.

C. Lintott, K. Schawinski, S. Bamford, A. Slosar, K. Land, D. Thomas, E. Edmondson, K. Masters, R. C. Nichol, M. J. Raddick, A. Szalay, D. Andreescu, P. Murray, and J. Vandenberg. Galaxy Zoo 1: data release of morphological classifications for nearly 900 000 galaxies. *MNRAS*, 410: 166–178, January 2011. doi: 10.1111/j.1365-2966.2010.17432.x.

J. Liske, I. K. Baldry, S. P. Driver, R. J. Tuffs, M. Alpaslan, E. Andrae, S. Brough, M. E. Cluver, M. W. Grootes, M. L. P. Gunawardhana, L. S. Kelvin, J. Loveday, A. S. G. Robotham, E. N. Taylor, S. P. Bamford, J. Bland-Hawthorn, M. J. I. Brown, M. J. Drinkwater, A. M. Hopkins, M. J. Meyer, P. Norberg, J. A. Peacock, N. K. Agius, S. K. Andrews, A. E. Bauer, J. H. Y. Ching, M. Colless, C. J. Conselice, S. M. Croom, L. J. M. Davies, R. De Propris, L. Dunne, E. M. Eardley, S. Ellis, C. Foster, C. S. Frenk, B. Häußler, B. W. Holwerda, C. Howlett, H. Ibarra, M. J. Jarvis, D. H. Jones, P. R. Kafle, C. G. Lacey, R. Lange, M. A. Lara-López, Á. R. López-Sánchez, S. Maddox, B. F. Madore, T. McNaught-Roberts, A. J. Moffett, R. C. Nichol, M. S. Owers, D. Palamara, S. J. Penny, S. Phillipps, K. A. Pimbblet, C. C. Popescu, M. Prescott, R. Proctor, E. M. Sadler, A. E. Sansom, M. Seibert, R. Sharp, W. Sutherland, J. A. Vázquez-Mata, E. van

Kampen, S. M. Wilkins, R. Williams, and A. H. Wright. Galaxy And Mass Assembly (GAMA): end of survey report and data release 2. *MNRAS*, 452(2):2087–2126, September 2015. doi: 10.1093/mnras/stv1436.

Aaron D. Ludlow, S. Michael Fall, Joop Schaye, and Danail Obreschkow. Spurious heating of stellar motions in simulated galactic disks by dark matter halo particles. *arXiv e-prints*, art. arXiv:2105.03561, May 2021.

R. Lupton, M. R. Blanton, G. Fekete, D. W. Hogg, W. O'Mullane, A. Szalay, and N. Wherry. Preparing Red-Green-Blue Images from CCD Data. *PASP*, 116:133–137, February 2004. doi: 10.1086/382245.

D. F. Malin. Unsharp masking. *AAS Photo Bulletin*, 16:10–13, 1977.

D. F. Malin and D. Carter. A catalog of elliptical galaxies with shells. *ApJ*, 274:534–540, November 1983. doi: 10.1086/161467.

D. F. Malin, P. J. Quinn, and J. A. Graham. Shell structure in NGC 5128. *ApJL*, 272:L5–L7, September 1983. doi: 10.1086/184106.

Pavel E. Mancera Piña, J. A. L. Aguerri, Reynier F. Peletier, Aku Venhola, Scott Trager, and Nelvy Choque Challapa. The evolution of ultra-diffuse galaxies in nearby galaxy clusters from the Kapteyn IAC WEAVE INT Clusters Survey. *MNRAS*, 485(1):1036–1052, May 2019a. doi: 10.1093/mnras/stz238.

Pavel E. Mancera Piña, Filippo Fraternali, Elizabeth A. K. Adams, Antonino Marasco, Tom Oosterloo, Kyle A. Oman, Lukas Leisman, Enrico M. di Teodoro, Lorenzo Posti, Michael Battipaglia, John M. Cannon, Lexi Gault, Martha P. Haynes, Steven Janowiecki, Elizabeth McAllan, Hannah J. Pagel, Kameron Reiter, Katherine L. Rhode, John J. Salzer, and Nicholas J. Smith. Off the Baryonic Tully-Fisher Relation: A Population of Baryon-dominated Ultra-diffuse Galaxies. *ApJL*, 883(2):L33, October 2019b. doi: 10.3847/2041-8213/ab40c7.

Pavel E. Mancera Piña, Filippo Fraternali, Kyle A. Oman, Elizabeth A. K. Adams, Cecilia Bacchini, Antonino Marasco, Tom Oosterloo, Gabriele Pezzulli, Lorenzo Posti, Lukas Leisman, John M. Cannon, Enrico M. di Teodoro, Lexi Gault, Martha P. Haynes, Kameron Reiter, Katherine L. Rhode, John J. Salzer, and Nicholas J. Smith. Robust H I kinematics of gas-rich ultra-diffuse galaxies: hints of a weak-feedback formation scenario. *MNRAS*, 495(4):3636–3655, July 2020. doi: 10.1093/mnras/staa1256.

R. Mandelbaum, U. Seljak, G. Kauffmann, C. M. Hirata, and J. Brinkmann. Galaxy halo masses and satellite fractions from galaxy-galaxy lensing in the Sloan Digital Sky Survey: stellar mass, luminosity, morphology and environment dependencies. *MNRAS*, 368:715–731, May 2006. doi: 10.1111/j.1365-2966.2006.10156.x.

Yao-Yuan Mao, Marla Geha, Risa H. Wechsler, Benjamin Weiner, Erik J. Tollerud, Ethan O. Nadler, and Nitya Kallivayalil. The SAGA Survey. II. Building a Statistical Sample of Satellite Systems around Milky Way-like Galaxies. *ApJ*, 907(2):85, February 2021. doi: 10.3847/1538-4357/abce58.

Francine R. Marleau, Rebecca Habas, Mélina Poulain, Pierre-Alain Duc, Oliver Müller, Sungsoon Lim, Patrick R. Durrell, Rubén Sánchez-Janssen, Sanjaya Paudel, Syeda Lammim Ahad, Abhishek Chougule, Michal Bílek, and Jérémy Fensch. Ultra diffuse galaxies in the MATLAS low-to-moderate density fields. *A&A*, 654:A105, October 2021. doi: 10.1051/0004-6361/202141432.

D. Christopher Martin, James Fanson, David Schiminovich, Patrick Morrissey, Peter G. Friedman, Tom A. Barlow, Tim Conrow, Robert Grange, Patrick N. Jelinsky, Bruno Milliard, Oswald H. W. Siegmund, Luciana Bianchi, Yong-Ik Byun, Jose Donas, Karl Forster, Timothy M. Heckman, Young-Wook Lee, Barry F. Madore, Roger F. Malina, Susan G. Neff, R. Michael Rich, Todd Small, Frank Surber, Alex S. Szalay, Barry Welsh, and Ted K. Wyder. The Galaxy Evolution Explorer: A Space Ultraviolet Survey Mission. *ApJL*, 619(1):L1–L6, January 2005. doi: 10.1086/426387.

Ignacio Martín-Navarro, Aaron J. Romanowsky, Jean P. Brodie, Anna Ferré-Mateu, Adebusola Alabi, Duncan A. Forbes, Margarita Sharina, Alexa Villaume, Viraj Pandya, and David Martinez-

Delgado. Extreme chemical abundance ratio suggesting an exotic origin for an ultradiffuse galaxy. *MNRAS*, 484(3):3425–3433, April 2019. doi: 10.1093/mnras/stz252.

D. Martínez-Delgado, M. Pohlen, R. J. Gabany, S. R. Majewski, J. Peñarrubia, and C. Palma. Discovery of a Giant Stellar Tidal Stream Around The Disk Galaxy NGC 4013. *ApJ*, 692:955–963, February 2009. doi: 10.1088/0004-637X/692/2/955.

D. Martínez-Delgado, R. J. Gabany, K. Crawford, S. Zibetti, S. R. Majewski, H.-W. Rix, J. Fliri, J. A. Carballo-Bello, D. C. Bardalez-Gagliuffi, J. Peñarrubia, T. S. Chonis, B. Madore, I. Trujillo, M. Schirmer, and D. A. McDavid. Stellar Tidal Streams in Spiral Galaxies of the Local Volume: A Pilot Survey with Modest Aperture Telescopes. *AJ*, 140:962–967, October 2010. doi: 10.1088/0004-6256/140/4/962.

D. Martínez-Delgado, E. D'Onghia, T. S. Chonis, R. L. Beaton, K. Teuwen, R. J. GaBany, E. K. Grebel, and G. Morales. A Stellar Tidal Stream Around the Whale Galaxy, NGC 4631. *AJ*, 150:116, October 2015. doi: 10.1088/0004-6256/150/4/116.

David Martinez-Delgado, Aaron J. Romanowsky, R. Jay Gabany, Francesca Annibali, Jacob A. Arnold, Jrgen Fliri, Stefano Zibetti, Roeland P. van der Marel, Hans-Walter Rix, Taylor S. Chonis, Julio A. Carballo-Bello, Alessandra Aloisi, Andrea V. Macci, J. Gallego-Laborda, Jean P. Brodie, and Michael R. Merrifield. Dwarfs gobbling dwarfs: A stellar tidal stream around ngc4449 and hierarchical galaxy formation on small scales. *The Astrophysical Journal Letters*, 748(2):L24, 2012. URL `http://stacks.iop.org/2041-8205/748/i=2/a=L24`.

David Martínez-Delgado, Ronald Läsker, Margarita Sharina, Elisa Toloba, Jürgen Fliri, Rachael Beaton, David Valls-Gabaud, Igor D. Karachentsev, Taylor S. Chonis, Eva K. Grebel, Duncan A. Forbes, Aaron J. Romanowsky, J. Gallego-Laborda, Karel Teuwen, M. A. Gómez-Flechoso, Jie Wang, Puragra Guhathakurta, Serafim Kaisin, and Nhung Ho. Discovery of an Ultra-diffuse Galaxy in the Pisces–Perseus Supercluster. *AJ*, 151(4):96, April 2016. doi: 10.3847/0004-6256/151/4/96.

Davide Martizzi, Claude-André Faucher-Giguère, and Eliot Quataert. Supernova feedback in an

inhomogeneous interstellar medium. *MNRAS*, 450(1):504–522, June 2015. doi: 10.1093/mnras/stv562.

Aaron J. Maxwell, James Wadsley, H. M. P. Couchman, and Sergey Mashchenko. Building the Stellar Halo through Feedback in Dwarf Galaxies. *ApJL*, 755(2):L35, August 2012. doi: 10.1088/2041-8205/755/2/L35.

Stacy S. McGaugh, Gregory D. Bothun, and James M. Schombert. Galaxy Selection and the Surface Brightness Distribution. *AJ*, 110:573, August 1995. doi: 10.1086/117543.

Wes McKinney. Data structures for statistical computing in python. In Stéfan van der Walt and Jarrod Millman, editors, *Proceedings of the 9th Python in Science Conference*, pages 51 – 56, 2010.

Wes McKinney. pandas: a foundational python library for data analysis and statistics. *Python for High Performance and Scientific Computing*, 14, 2011.

J. Meaburn. The giant and supergiant shells of the Magellanic Clouds. *MNRAS*, 192:365–375, August 1980. doi: 10.1093/mnras/192.3.365.

J. Méndez-Abreu, L. Costantin, J. A. L. Aguerri, A. de Lorenzo-Cáceres, and E. M. Corsini. The intrinsic three-dimensional shape of galactic bars. *MNRAS*, 479(3):4172–4186, September 2018. doi: 10.1093/mnras/sty1694.

Allison Merritt, Pieter van Dokkum, Shany Danieli, Roberto Abraham, Jielai Zhang, I. D. Karachentsev, and L. N. Makarova. The Dragonfly Nearby Galaxies Survey. II. Ultra-Diffuse Galaxies near the Elliptical Galaxy NGC 5485. *ApJ*, 833:168, December 2016. doi: 10.3847/1538-4357/833/2/168.

J. C. Mihos, J. Dubinski, and L. Hernquist. Tidal Tales Two: The Effect of Dark Matter Halos on Tidal Tail Morphology and Kinematics. *ApJ*, 494:183–193, February 1998. doi: 10.1086/305179.

Dante Minniti and Albert A. Zijlstra. Dwarf Galaxies Also Have Stellar Halos. *ApJL*, 467:L13, August 1996. doi: 10.1086/310189.

Dante Minniti, Albert A. Zijlstra, and M. Victoria Alonso. The Stellar Populations of NGC 3109: Another Dwarf Irregular Galaxy with a Population II Stellar Halo. *AJ*, 117(2):881–893, February 1999. doi: 10.1086/300735.

S. Miyazaki, Y. Komiyama, H. Nakaya, Y. Kamata, Y. Doi, T. Hamana, H. Karoji, H. Furusawa, S. Kawanomoto, T. Morokuma, Y. Ishizuka, K. Nariai, Y. Tanaka, F. Uraguchi, Y. Utsumi, Y. Obuchi, Y. Okura, M. Oguri, T. Takata, D. Tomono, T. Kurakami, K. Namikawa, T. Usuda, H. Yamanoi, T. Terai, H. Uekiyo, Y. Yamada, M. Koike, H. Aihara, Y. Fujimori, S. Mineo, H. Miyatake, N. Yasuda, J. Nishizawa, T. Saito, M. Tanaka, T. Uchida, N. Katayama, S.-Y. Wang, H.-Y. Chen, R. Lupton, C. Loomis, S. Bickerton, P. Price, J. Gunn, H. Suzuki, Y. Miyazaki, M. Muramatsu, K. Yamamoto, M. Endo, Y. Ezaki, N. Itoh, Y. Miwa, H. Yokota, T. Matsuda, R. Ebinuma, and K. Takeshi. Hyper Suprime-Cam. In *Ground-based and Airborne Instrumentation for Astronomy IV*, volume 8446 of **??***jnlProc. SPIE*, page 84460Z, September 2012. doi: 10.1117/12.926844.

S. Miyazaki, Y. Komiyama, S. Kawanomoto, Y. Doi, H. Furusawa, T. Hamana, Y. Hayashi, H. Ikeda, Y. Kamata, H. Karoji, M. Koike, T. Kurakami, S. Miyama, T. Morokuma, F. Nakata, K. Namikawa, H. Nakaya, K. Nariai, Y. Obuchi, Y. Oishi, N. Okada, Y. Okura, P. Tait, T. Takata, Y. Tanaka, M. Tanaka, T. Terai, D. Tomono, F. Uraguchi, T. Usuda, Y. Utsumi, Y. Yamada, H. Yamanoi, H. Aihara, H. Fujimori, S. Mineo, H. Miyatake, M. Oguri, T. Uchida, M. M. Tanaka, N. Yasuda, M. Takada, H. Murayama, A. J. Nishizawa, N. Sugiyama, M. Chiba, T. Futamase, S.-Y. Wang, H.-Y. Chen, P. T. P. Ho, E. J. Y. Liaw, C.-F. Chiu, C.-L. Ho, T.-C. Lai, Y.-C. Lee, D.-Z. Jeng, S. Iwamura, R. Armstrong, S. Bickerton, J. Bosch, J. E. Gunn, R. H. Lupton, C. Loomis, P. Price, S. Smith, M. A. Strauss, E. L. Turner, H. Suzuki, Y. Miyazaki, M. Muramatsu, K. Yamamoto, M. Endo, Y. Ezaki, N. Ito, N. Kawaguchi, S. Sofuku, T. Taniike, K. Akutsu, N. Dojo, K. Kasumi, T. Matsuda, K. Imoto, Y. Miwa, M. Suzuki, K. Takeshi, and H. Yokota. Hyper Suprime-Cam: System design and verification of image quality. *PASJ*, 70:S1, January 2018. doi: 10.1093/pasj/psx063.

Gustavo Morales, David Martínez-Delgado, Eva K. Grebel, Andrew P. Cooper, Behnam Ja-

vanmardi, and Arpad Miskolczi. Systematic search for tidal features around nearby galaxies. I. Enhanced SDSS imaging of the Local Volume. *A&A*, 614:A143, June 2018. doi: 10.1051/0004-6361/201732271.

P. Morrissey, T. Conrow, T. A. Barlow, T. Small, M. Seibert, T. K. Wyder, T. Budavári, S. Arnouts, P. G. Friedman, K. Forster, D. C. Martin, S. G. Neff, D. Schiminovich, L. Bianchi, J. Donas, T. M. Heckman, Y.-W. Lee, B. F. Madore, B. Milliard, R. M. Rich, A. S. Szalay, B. Y. Welsh, and S. K. Yi. The Calibration and Data Products of GALEX. *ApJS*, 173:682–697, December 2007. doi: 10.1086/520512.

Benjamin P. Moster, Thorsten Naab, and Simon D. M. White. Galactic star formation and accretion histories from matching galaxies to dark matter haloes. *MNRAS*, 428(4):3121–3138, February 2013. doi: 10.1093/mnras/sts261.

Ferah Munshi, Alyson Brooks, Elaad Applebaum, Charlotte Christensen, Jordan P. Sligh, and T. Quinn. Quantifying scatter in galaxy formation at the lowest masses. *arXiv e-prints*, art. arXiv:2101.05822, January 2021.

Alexander L. Muratov, Dušan Kereš, Claude-André Faucher-Giguère, Philip F. Hopkins, Eliot Quataert, and Norman Murray. Gusty, gaseous flows of FIRE: galactic winds in cosmological simulations with explicit stellar feedback. *MNRAS*, 454(3):2691–2713, December 2015. doi: 10.1093/mnras/stv2126.

Adam Muzzin, Danilo Marchesini, Mauro Stefanon, Marijn Franx, Bo Milvang-Jensen, James S. Dunlop, J. P. U. Fynbo, Gabriel Brammer, Ivo Labbé, and Pieter van Dokkum. A Public K_s -selected Catalog in the COSMOS/ULTRAVISTA Field: Photometry, Photometric Redshifts, and Stellar Population Parameters. *ApJS*, 206(1):8, May 2013. doi: 10.1088/0067-0049/206/1/8.

P. B. Nair and R. G. Abraham. A Catalog of Detailed Visual Morphological Classifications for 14,034 Galaxies in the Sloan Digital Sky Survey. *ApJS*, 186:427–456, February 2010. doi: 10.1088/0067-0049/186/2/427.

Narendra Nath Patra. HI scale height in dwarf galaxies. *arXiv e-prints*, art. arXiv:2005.05979, May 2020.

Julio F. Navarro, Vincent R. Eke, and Carlos S. Frenk. The cores of dwarf galaxy haloes. *MNRAS*, 283(3):L72–L78, December 1996. doi: 10.1093/mnras/283.3.L72.

Julio F. Navarro, Carlos S. Frenk, and Simon D. M. White. A Universal Density Profile from Hierarchical Clustering. *ApJ*, 490(2):493–508, December 1997. doi: 10.1086/304888.

Lina Necib, Mariangela Lisanti, Shea Garrison-Kimmel, Andrew Wetzel, Robyn Sanderson, Philip F. Hopkins, Claude-André Faucher-Giguère, and Dušan Kereš. Under the FIRElight: Stellar Tracers of the Local Dark Matter Velocity Distribution in the Milky Way. *ApJ*, 883(1): 27, September 2019. doi: 10.3847/1538-4357/ab3afc.

David L. Nidever, Knut Olsen, Yumi Choi, Thomas J. L. de Boer, Robert D. Blum, Eric F. Bell, Dennis Zaritsky, Nicolas F. Martin, Abhijit Saha, Blair C. Conn, Gurtina Besla, Roeland P. van der Marel, Noelia E. D. Noël, Antonela Monachesi, Guy S. Stringfellow, Pol Massana, Maria-Rosa L. Cioni, Carme Gallart, Matteo Monelli, David Martinez-Delgado, Ricardo R. Muñoz, Steven R. Majewski, A. Katherina Vivas, Alistair R. Walker, Catherine Kaleida, and You-Hua Chu. Exploring the Very Extended Low-surface-brightness Stellar Populations of the Large Magellanic Cloud with SMASH. *ApJ*, 874(2):118, April 2019. doi: 10.3847/1538-4357/aafaf7.

Masafumi Noguchi. The Secular Evolution of Galactic Disks with a Star Formation Threshold: The Origins of Low Surface Brightness Spirals, Magellanic Irregulars, and Blue Compact Dwarfs. *ApJ*, 555(1):289–300, Jul 2001. doi: 10.1086/321479.

Yuri Oku, Kengo Tomida, Kentaro Nagamine, Ikkoh Shimizu, and Renyue Cen. Osaka Feedback Model II: Modeling Supernova Feedback Based on High-Resolution Simulations. *arXiv e-prints*, art. arXiv:2201.00970, January 2022.

L. Oser, J. P. Ostriker, T. Naab, P. H. Johansson, and A. Burkert. The Two Phases of Galaxy Formation. *ApJ*, 725:2312–2323, December 2010. doi: 10.1088/0004-637X/725/2/2312.

Ludwig Oser, Thorsten Naab, Jeremiah P. Ostriker, and Peter H. Johansson. The Cosmological Size and Velocity Dispersion Evolution of Massive Early-type Galaxies. *ApJ*, 744:63, January 2012. doi: 10.1088/0004-637X/744/1/63.

G. Östlin, P. Amram, N. Bergvall, J. Masegosa, J. Boulesteix, and I. Márquez. Dynamics of blue compact galaxies, as revealed by their Hα velocity fields. II. Mass models and the starburst triggering mechanism. *A&A*, 374:800–823, Aug 2001. doi: 10.1051/0004-6361:20010832.

Eve C. Ostriker and Chang-Goo Kim. Pressure-Regulated, Feedback-Modulated Star Formation In Disk Galaxies. *arXiv e-prints*, art. arXiv:2206.00681, June 2022.

Eve C. Ostriker and Rahul Shetty. Maximally Star-forming Galactic Disks. I. Starburst Regulation Via Feedback-driven Turbulence. *ApJ*, 731(1):41, April 2011. doi: 10.1088/0004-637X/731/1/41.

Eve C. Ostriker, Christopher F. McKee, and Adam K. Leroy. Regulation of Star Formation Rates in Multiphase Galactic Disks: A Thermal/Dynamical Equilibrium Model. *ApJ*, 721(2):975–994, October 2010. doi: 10.1088/0004-637X/721/2/975.

Nelson D. Padilla and Michael A. Strauss. The shapes of galaxies in the Sloan Digital Sky Survey. *MNRAS*, 388(3):1321–1334, Aug 2008. doi: 10.1111/j.1365-2966.2008.13480.x.

Benjamin Panter, Raul Jimenez, Alan F. Heavens, and Stephane Charlot. The star formation histories of galaxies in the Sloan Digital Sky Survey. *MNRAS*, 378(4):1550–1564, July 2007. doi: 10.1111/j.1365-2966.2007.11909.x.

Minjung J. Park, Sukyoung K. Yi, Sebastien Peirani, Christophe Pichon, Yohan Dubois, Hoseung Choi, Julien Devriendt, Sugata Kaviraj, Taysun Kimm, Katarina Kraljic, and Marta Volonteri. Exploring the Origin of Thick Disks Using the NewHorizon and Galactica Simulations. *ApJS*, 254(1):2, May 2021. doi: 10.3847/1538-4365/abe937.

S. Paudel, R. Smith, P.-A. Duc, P. Côté, J.-C. Cuillandre, L. Ferrarese, J. P. Blakeslee, A. Boselli, M. Cantiello, S. D. J. Gwyn, P. Guhathakurta, S. Mei, J. C. Mihos, E. W. Peng, M. Powalka, R. Sánchez-Janssen, E. Toloba, and H. Zhang. The Next Generation Virgo Cluster Survey. XXII.

Shell Feature Early-type Dwarf Galaxies in the Virgo Cluster. *ApJ*, 834:66, January 2017. doi: 10.3847/1538-4357/834/1/66.

Sanjaya Paudel, Rory Smith, Suk Jin Yoon, Paula Calderón-Castillo, and Pierre-Alain Duc. A Catalog of Merging Dwarf Galaxies in the Local Universe. *ApJS*, 237(2):36, Aug 2018. doi: 10.3847/1538-4365/aad555.

Jorge Peñarrubia, Andrew Pontzen, Matthew G. Walker, and Sergey E. Koposov. The Coupling between the Core/Cusp and Missing Satellite Problems. *ApJL*, 759(2):L42, November 2012. doi: 10.1088/2041-8205/759/2/L42.

Chien Y. Peng, Luis C. Ho, Chris D. Impey, and Hans-Walter Rix. Detailed Decomposition of Galaxy Images. II. Beyond Axisymmetric Models. *AJ*, 139(6):2097–2129, June 2010. doi: 10.1088/0004-6256/139/6/2097.

Eric W. Peng and Sungsoon Lim. A Rich Globular Cluster System in Dragonfly 17: Are Ultra-diffuse Galaxies Pure Stellar Halos? *ApJL*, 822(2):L31, May 2016. doi: 10.3847/2041-8205/822/2/L31.

Fernando Pérez and Brian E. Granger. IPython: a system for interactive scientific computing. *Computing in Science and Engineering*, 9(3):21–29, May 2007. ISSN 1521-9615. doi: 10.1109/MCSE.2007.53. URL `http://ipython.org`.

J. Pfleiderer. Gravitationseffekte bei der Begegnung zweier Galaxien. Mit 5 Textabbildungen. *Zeitschrift fur Astrophysik*, 58:12, January 1963.

Annalisa Pillepich, Volker Springel, Dylan Nelson, Shy Genel, Jill Naiman, Rüdiger Pakmor, Lars Hernquist, Paul Torrey, Mark Vogelsberger, Rainer Weinberger, and Federico Marinacci. Simulating galaxy formation with the IllustrisTNG model. *MNRAS*, 473(3):4077–4106, January 2018. doi: 10.1093/mnras/stx2656.

Annalisa Pillepich, Dylan Nelson, Volker Springel, Rüdiger Pakmor, Paul Torrey, Rainer Weinberger, Mark Vogelsberger, Federico Marinacci, Shy Genel, Arjen van der Wel, and Lars Hern-

quist. First results from the TNG50 simulation: the evolution of stellar and gaseous discs across cosmic time. *MNRAS*, 490(3):3196–3233, December 2019. doi: 10.1093/mnras/stz2338.

Planck Collaboration, N. Aghanim, Y. Akrami, M. Ashdown, J. Aumont, C. Baccigalupi, M. Ballardini, A. J. Banday, R. B. Barreiro, N. Bartolo, S. Basak, R. Battye, K. Benabed, J. P. Bernard, M. Bersanelli, P. Bielewicz, J. J. Bock, J. R. Bond, J. Borrill, F. R. Bouchet, F. Boulanger, M. Bucher, C. Burigana, R. C. Butler, E. Calabrese, J. F. Cardoso, J. Carron, A. Challinor, H. C. Chiang, J. Chluba, L. P. L. Colombo, C. Combet, D. Contreras, B. P. Crill, F. Cuttaia, P. de Bernardis, G. de Zotti, J. Delabrouille, J. M. Delouis, E. Di Valentino, J. M. Diego, O. Doré, M. Douspis, A. Ducout, X. Dupac, S. Dusini, G. Efstathiou, F. Elsner, T. A. Enßlin, H. K. Eriksen, Y. Fantaye, M. Farhang, J. Fergusson, R. Fernandez-Cobos, F. Finelli, F. Forastieri, M. Frailis, A. A. Fraisse, E. Franceschi, A. Frolov, S. Galeotta, S. Galli, K. Ganga, R. T. Génova-Santos, M. Gerbino, T. Ghosh, J. González-Nuevo, K. M. Górski, S. Gratton, A. Gruppuso, J. E. Gudmundsson, J. Hamann, W. Handley, F. K. Hansen, D. Herranz, S. R. Hildebrandt, E. Hivon, Z. Huang, A. H. Jaffe, W. C. Jones, A. Karakci, E. Keihänen, R. Keskitalo, K. Kiiveri, J. Kim, T. S. Kisner, L. Knox, N. Krachmalnicoff, M. Kunz, H. Kurki-Suonio, G. Lagache, J. M. Lamarre, A. Lasenby, M. Lattanzi, C. R. Lawrence, M. Le Jeune, P. Lemos, J. Lesgourgues, F. Levrier, A. Lewis, M. Liguori, P. B. Lilje, M. Lilley, V. Lindholm, M. López-Caniego, P. M. Lubin, Y. Z. Ma, J. F. Macías-Pérez, G. Maggio, D. Maino, N. Mandolesi, A. Mangilli, A. Marcos-Caballero, M. Maris, P. G. Martin, M. Martinelli, E. Martínez-González, S. Matarrese, N. Mauri, J. D. McEwen, P. R. Meinhold, A. Melchiorri, A. Mennella, M. Migliaccio, M. Millea, S. Mitra, M. A. Miville-Deschênes, D. Molinari, L. Montier, G. Morgante, A. Moss, P. Natoli, H. U. Nørgaard-Nielsen, L. Pagano, D. Paoletti, B. Partridge, G. Patanchon, H. V. Peiris, F. Perrotta, V. Pettorino, F. Piacentini, L. Polastri, G. Polenta, J. L. Puget, J. P. Rachen, M. Reinecke, M. Remazeilles, A. Renzi, G. Rocha, C. Rosset, G. Roudier, J. A. Rubiño-Martín, B. Ruiz-Granados, L. Salvati, M. Sandri, M. Savelainen, D. Scott, E. P. S. Shellard, C. Sirignano, G. Sirri, L. D. Spencer, R. Sunyaev, A. S. Suur-Uski, J. A. Tauber, D. Tavagnacco, M. Tenti, L. Toffolatti, M. Tomasi, T. Trombetti, L. Valenziano, J. Valiviita, B. Van Tent, L. Vibert, P. Vielva, F. Villa, N. Vittorio, B. D. Wandelt, I. K. Wehus, M. White, S. D. M. White, A. Zac-

chei, and A. Zonca. Planck 2018 results. VI. Cosmological parameters. *A&A*, 641:A6, September 2020. doi: 10.1051/0004-6361/201833910.

Andrew Pontzen and Fabio Governato. How supernova feedback turns dark matter cusps into cores. *MNRAS*, 421(4):3464–3471, April 2012. doi: 10.1111/j.1365-2966.2012.20571.x.

A.-R. Pop, A. Pillepich, N. Amorisco, and L. Hernquist. Galaxies with Shells in the Illustris Simulation: Metallicity Signatures. *Galaxies*, 5:34, August 2017a. doi: 10.3390/galaxies5030034.

A.-R. Pop, A. Pillepich, N. C. Amorisco, and L. Hernquist. Formation and Incidence of Shell Galaxies in the Illustris Simulation. *ArXiv e-prints*, June 2017b.

M. Postman and M. J. Geller. The morphology-density relation - The group connection. *ApJ*, 281: 95–99, June 1984. doi: 10.1086/162078.

Matthew Prescott, I. K. Baldry, P. A. James, S. P. Bamford, J. Bland-Hawthorn, S. Brough, M. J. I. Brown, E. Cameron, C. J. Conselice, S. M. Croom, S. P. Driver, C. S. Frenk, M. Gunawardhana, D. T. Hill, A. M. Hopkins, D. H. Jones, L. S. Kelvin, K. Kuijken, J. Liske, J. Loveday, R. C. Nichol, P. Norberg, H. R. Parkinson, J. A. Peacock, S. Phillipps, K. A. Pimbblet, C. C. Popescu, A. S. G. Robotham, R. G. Sharp, W. J. Sutherland, E. N. Taylor, R. J. Tuffs, E. van Kampen, and D. Wijesinghe. Galaxy and Mass Assembly (GAMA): the red fraction and radial distribution of satellite galaxies. *MNRAS*, 417:1374–1386, October 2011. doi: 10.1111/j.1365-2966.2011.19353.x.

D. J. Price and J. J. Monaghan. An energy-conserving formalism for adaptive gravitational force softening in smoothed particle hydrodynamics and N-body codes. *MNRAS*, 374(4):1347–1358, February 2007. doi: 10.1111/j.1365-2966.2006.11241.x.

A. M. Price-Whelan, B. Sesar, K. V. Johnston, and H.-W. Rix. Spending Too Much Time at the Galactic Bar: Chaotic Fanning of the Ophiuchus Stream. *ApJ*, 824:104, June 2016. doi: 10.3847/0004-637X/824/2/104.

A. M. Price-Whelan, B. M. Sipőcz, H. M. Günther, P. L. Lim, S. M. Crawford, S. Conseil, D. L. Shupe, M. W. Craig, N. Dencheva, A. Ginsburg, J. T. VanderPlas, L. D. Bradley, D. Pérez-Suárez,

M. de Val-Borro, (Primary Paper Contributors, T. L. Aldcroft, K. L. Cruz, T. P. Robitaille, E. J. Tollerud, (Astropy Coordination Committee, C. Ardelean, T. Babej, Y. P. Bach, M. Bachetti, A. V. Bakanov, S. P. Bamford, G. Barentsen, P. Barmby, A. Baumbach, K. L. Berry, F. Biscani, M. Boquien, K. A. Bostroem, L. G. Bouma, G. B. Brammer, E. M. Bray, H. Breytenbach, H. Buddelmeijer, D. J. Burke, G. Calderone, J. L. Cano Rodríguez, M. Cara, J. V. M. Cardoso, S. Cheedella, Y. Copin, L. Corrales, D. Crichton, D. D'Avella, C. Deil, É. Depagne, J. P. Dietrich, A. Donath, M. Droettboom, N. Earl, T. Erben, S. Fabbro, L. A. Ferreira, T. Finethy, R. T. Fox, L. H. Garrison, S. L. J. Gibbons, D. A. Goldstein, R. Gommers, J. P. Greco, P. Greenfield, A. M. Groener, F. Grollier, A. Hagen, P. Hirst, D. Homeier, A. J. Horton, G. Hosseinzadeh, L. Hu, J. S. Hunkeler, Ž. Ivezić, A. Jain, T. Jenness, G. Kanarek, S. Kendrew, N. S. Kern, W. E. Kerzendorf, A. Khvalko, J. King, D. Kirkby, A. M. Kulkarni, A. Kumar, A. Lee, D. Lenz, S. P. Littlefair, Z. Ma, D. M. Macleod, M. Mastropietro, C. McCully, S. Montagnac, B. M. Morris, M. Mueller, S. J. Mumford, D. Muna, N. A. Murphy, S. Nelson, G. H. Nguyen, J. P. Ninan, M. Nöthe, S. Ogaz, S. Oh, J. K. Parejko, N. Parley, S. Pascual, R. Patil, A. A. Patil, A. L. Plunkett, J. X. Prochaska, T. Rastogi, V. Reddy Janga, J. Sabater, P. Sakurikar, M. Seifert, L. E. Sherbert, H. Sherwood-Taylor, A. Y. Shih, J. Sick, M. T. Silbiger, S. Singanamalla, L. P. Singer, P. H. Sladen, K. A. Sooley, S. Sornarajah, O. Streicher, P. Teuben, S. W. Thomas, G. R. Tremblay, J. E. H. Turner, V. Terrón, M. H. van Kerkwijk, A. de la Vega, L. L. Watkins, B. A. Weaver, J. B. Whitmore, J. Woillez, V. Zabalza, and (Astropy Contributors. The Astropy Project: Building an Open-science Project and Status of the v2.0 Core Package. *AJ*, 156:123, September 2018. doi: 10.3847/1538-3881/aabc4f.

J.-L. Prieur. *Status of shell galaxies.*, pages 72–83. International Conference on Dynamics and Interactions of Galaxies, 1990.

G. C. Privon, S. Stierwalt, D. R. Patton, G. Besla, S. Pearson, M. Putman, K. E. Johnson, N. Kallivayalil, S. Liss, and TiNy Titans. A widespread, clumpy starburst in the isolated ongoing dwarf galaxy merger dm1647+21. *The Astrophysical Journal*, 846(1):74, 2017. URL `http://stacks.iop.org/0004-637X/846/i=1/a=74`.

D. J. Prole, R. F. J. van der Burg, M. Hilker, and L. R. Spitler. The quiescent fraction of isolated low surface brightness galaxies: observational constraints. *MNRAS*, 500(2):2049–2062, January 2021. doi: 10.1093/mnras/staa3296.

P. Prugniel and F. Simien. The fundamental plane of early-type galaxies: non-homology of the spatial structure. *A&A*, 321:111–122, May 1997.

Ragadeepika Pucha, Jeffrey L. Carlin, Beth Willman, Jay Strader, David J. Sand, Keith Bechtol, Jean P. Brodie, Denija Crnojević, Duncan A. Forbes, Christopher Garling, Jonathan Hargis, Annika H. G. Peter, and Aaron J. Romanowsky. Hyper Wide Field Imaging of the Local Group Dwarf Irregular Galaxy IC 1613: An Extended Component of Metal-poor Stars. *ApJ*, 880(2): 104, August 2019. doi: 10.3847/1538-4357/ab29fb.

Chris W. Purcell, James S. Bullock, and Andrew R. Zentner. Shredded Galaxies as the Source of Diffuse Intrahalo Light on Varying Scales. *ApJ*, 666(1):20–33, September 2007. doi: 10.1086/519787.

S. A. Pustilnik, A. Y. Kniazev, V. A. Lipovetsky, and A. V. Ugryumov. Environment status of blue compact galaxies and trigger of star formation. *A&A*, 373:24–37, Jul 2001. doi: 10.1051/0004-6361:20010555.

J. Putko, J. Sánchez Almeida, C. Muñoz-Tuñón, A. Asensio Ramos, B. G. Elmegreen, and D. M. Elmegreen. Inferring the 3D Shapes of Extremely Metal-poor Galaxies from Sets of Projected Shapes. *ApJ*, 883(1):10, September 2019. doi: 10.3847/1538-4357/ab365a.

P. J. Quinn. On the formation and dynamics of shells around elliptical galaxies. In E. Athanassoula, editor, *Internal Kinematics and Dynamics of Galaxies*, volume 100 of *IAU Symposium*, page 347, 1983.

P. J. Quinn. On the formation and dynamics of shells around elliptical galaxies. *ApJ*, 279:596–609, April 1984. doi: 10.1086/161924.

J. I. Read and G. Gilmore. Mass loss from dwarf spheroidal galaxies: the origins of shallow dark matter cores and exponential surface brightness profiles. *MNRAS*, 356(1):107–124, January 2005. doi: 10.1111/j.1365-2966.2004.08424.x.

J. I. Read, A. P. Pontzen, and M. Viel. On the formation of dwarf galaxies and stellar haloes. *MNRAS*, 371(2):885–897, September 2006. doi: 10.1111/j.1365-2966.2006.10720.x.

B. Reid, S. Ho, N. Padmanabhan, W. J. Percival, J. Tinker, R. Tojeiro, M. White, D. J. Eisenstein, C. Maraston, A. J. Ross, A. G. Sánchez, D. Schlegel, E. Sheldon, M. A. Strauss, D. Thomas, D. Wake, F. Beutler, D. Bizyaev, A. S. Bolton, J. R. Brownstein, C.-H. Chuang, K. Dawson, P. Harding, F.-S. Kitaura, A. Leauthaud, K. Masters, C. K. McBride, S. More, M. D. Olmstead, D. Oravetz, S. E. Nuza, K. Pan, J. Parejko, J. Pforr, F. Prada, S. Rodríguez-Torres, S. Salazar-Albornoz, L. Samushia, D. P. Schneider, C. G. Scóccola, A. Simmons, and M. Vargas-Magana. SDSS-III Baryon Oscillation Spectroscopic Survey Data Release 12: galaxy target selection and large-scale structure catalogues. *MNRAS*, 455:1553–1573, January 2016. doi: 10.1093/mnras/stv2382.

R. M. Rich, M. L. M. Collins, C. M. Black, F. A. Longstaff, A. Koch, A. Benson, and D. B. Reitzel. A tidally distorted dwarf galaxy near NGC 4449. *Nature*, 482(7384):192–194, Feb 2012. doi: 10.1038/nature10837.

Silvio Rodríguez, Nelson D. Padilla, and Diego García Lambas. The effects of environment on the intrinsic shape of galaxies. *MNRAS*, 456(1):571–577, February 2016. doi: 10.1093/mnras/stv2660.

V. Rodriguez-Gomez, A. Pillepich, L. V. Sales, S. Genel, M. Vogelsberger, Q. Zhu, S. Wellons, D. Nelson, P. Torrey, V. Springel, C.-P. Ma, and L. Hernquist. The stellar mass assembly of galaxies in the Illustris simulation: growth by mergers and the spatial distribution of accreted stars. *MNRAS*, 458:2371–2390, May 2016. doi: 10.1093/mnras/stw456.

M. Rodruck, I. Konstantopoulos, K. Knierman, K. Fedotov, B. Mullan, S. Gallagher, P. Durrell, R. Ciardullo, C. Gronwall, and J. Charlton. A tale of two tails: exploring stellar populations in the tidal tails of NGC 3256. *MNRAS*, 461:36–50, September 2016. doi: 10.1093/mnras/stw1294.

Javier Román and Ignacio Trujillo. Spatial distribution of ultra-diffuse galaxies within large-scale structures. *MNRAS*, 468(1):703–716, June 2017. doi: 10.1093/mnras/stx438.

Javier Román, Michael A. Beasley, Tomás Ruiz-Lara, and David Valls-Gabaud. Discovery of a red ultra-diffuse galaxy in a nearby void based on its globular cluster luminosity function. *MNRAS*, 486(1):823–835, June 2019. doi: 10.1093/mnras/stz835.

Yu Rong, Qi Guo, Liang Gao, Shihong Liao, Lizhi Xie, Thomas H. Puzia, Shuangpeng Sun, and Jun Pan. A Universe of ultradiffuse galaxies: theoretical predictions from ΛCDM simulations. *MNRAS*, 470(4):4231–4240, October 2017. doi: 10.1093/mnras/stx1440.

Yu Rong, Xiao-Yu Dong, Thomas H. Puzia, Gaspar Galaz, Ruben Sánchez-Janssen, Tianwen Cao, Remco F. J. van der Burg, Cristóbal Sifón, Pavel E. Mancera Piña, Mora Marcelo, Giuseppe D'Ago, Hong-Xin Zhang, Evelyn J. Johnston, and Paul Eigenthaler. Intrinsic Morphology of Ultra-diffuse Galaxies. *ApJ*, 899(1):78, August 2020. doi: 10.3847/1538-4357/aba74a.

S. Roychowdhury, J. N. Chengalur, I. D. Karachentsev, and E. I. Kaisina. The intrinsic shapes of dwarf irregular galaxies. *MNRAS*, 436:L104–L108, November 2013. doi: 10.1093/mnrasl/slt123.

L. V. Sales, M. Vogelsberger, S. Genel, P. Torrey, D. Nelson, V. Rodriguez-Gomez, W. Wang, A. Pillepich, D. Sijacki, V. Springel, and L. Hernquist. The colours of satellite galaxies in the Illustris simulation. *MNRAS*, 447:L6–L10, February 2015. doi: 10.1093/mnrasl/slu173.

Laura V. Sales, Wenting Wang, Simon D. M. White, and Julio F. Navarro. Satellites and haloes of dwarf galaxies. *Monthly Notices of the Royal Astronomical Society*, 428(1):573–578, 2013. doi: 10.1093/mnras/sts054. URL `+http://dx.doi.org/10.1093/mnras/sts054`.

Samir Salim, R. Michael Rich, Stéphane Charlot, Jarle Brinchmann, Benjamin D. Johnson, David Schiminovich, Mark Seibert, Ryan Mallery, Timothy M. Heckman, Karl Forster, Peter G. Friedman, D. Christopher Martin, Patrick Morrissey, Susan G. Neff, Todd Small, Ted K. Wyder, Luciana Bianchi, José Donas, Young-Wook Lee, Barry F. Madore, Bruno Milliard, Alex S. Szalay, Barry Y. Welsh, and Sukyoung K. Yi. UV Star Formation Rates in the Local Universe. *ApJS*, 173(2):267–292, December 2007. doi: 10.1086/519218.

R. Sánchez-Janssen, J. Méndez-Abreu, and J. A. L. Aguerri. Thin discs, thick dwarfs and the effects of stellar feedback. *MNRAS*, 406(1):L65–L69, July 2010. doi: 10.1111/j.1745-3933.2010.00883.x.

R. Sánchez-Janssen, T. H. Puzia, L. Ferrarese, P. Côté, P. Eigenthaler, B. Miller, Y. Ordenes-Briceño, E. W. Peng, K. X. Ribbeck, J. Roediger, C. Spengler, and M. A. Taylor. How nucleation and luminosity shape faint dwarf galaxies. *MNRAS*, 486(1):L1–L5, June 2019. doi: 10.1093/mnrasl/slz008.

Rubén Sánchez-Janssen, Laura Ferrarese, Lauren A. MacArthur, Patrick Côté, John P. Blakeslee, Jean-Charles Cuillandre, Pierre-Alain Duc, Patrick Durrell, Stephen Gwyn, Alan W. McConnachie, Alessandro Boselli, Stéphane Courteau, Eric Emsellem, Simona Mei, Eric Peng, Thomas H. Puzia, Joel Roediger, Luc Simard, Fred Boyer, and Matthew Santos. The Next Generation Virgo Cluster Survey. VII. The Intrinsic Shapes of Low-luminosity Galaxies in the Core of the Virgo Cluster, and a Comparison with the Local Group. *ApJ*, 820(1):69, March 2016. doi: 10.3847/0004-637X/820/1/69.

A. Sandage and B. Binggeli. Studies of the Virgo cluster. III. A classification system and an illustrated Atlas of Virgo cluster dwarf galaxies. *AJ*, 89:919–931, July 1984. doi: 10.1086/113588.

Robyn E. Sanderson and Amina Helmi. An analytical phase-space model for tidal caustics. *MNRAS*, 435:378–399, October 2013. doi: 10.1093/mnras/stt1307.

Robyn E. Sanderson, Shea Garrison-Kimmel, Andrew Wetzel, Tsang Keung Chan, Philip F. Hopkins, Dušan Kereš, Ivanna Escala, Claude-André Faucher-Giguère, and Xiangcheng Ma. Reconciling Observed and Simulated Stellar Halo Masses. *ApJ*, 869(1):12, December 2018. doi: 10.3847/1538-4357/aaeb33.

Robyn E. Sanderson, Andrew Wetzel, Sarah Loebman, Sanjib Sharma, Philip F. Hopkins, Shea Garrison-Kimmel, Claude-André Faucher-Giguère, Dušan Kereš, and Eliot Quataert. Synthetic Gaia Surveys from the FIRE Cosmological Simulations of Milky Way-mass Galaxies. *ApJS*, 246 (1):6, January 2020. doi: 10.3847/1538-4365/ab5b9d.

Edward F. Schlafly and Douglas P. Finkbeiner. Measuring Reddening with Sloan Digital Sky Survey Stellar Spectra and Recalibrating SFD. *ApJ*, 737(2):103, August 2011. doi: 10.1088/0004-637X/737/2/103.

Maarten Schmidt. The Rate of Star Formation. *ApJ*, 129:243, March 1959. doi: 10.1086/146614.

Ralph Schönrich and James Binney. Origin and structure of the Galactic disc(s). *MNRAS*, 399(3): 1145–1156, November 2009. doi: 10.1111/j.1365-2966.2009.15365.x.

Andreas Schruba, Adam K. Leroy, Fabian Walter, Frank Bigiel, Elias Brinks, W. J. G. de Blok, Gaelle Dumas, Carsten Kramer, Erik Rosolowsky, Karin Sandstrom, Karl Schuster, Antonio Usero, Axel Weiss, and Helmut Wiesemeyer. A Molecular Star Formation Law in the Atomic-gas-dominated Regime in Nearby Galaxies. *AJ*, 142(2):37, August 2011. doi: 10.1088/0004-6256/142/2/37.

Andreas Schruba, Adam K. Leroy, Fabian Walter, Frank Bigiel, Elias Brinks, W. J. G. de Blok, Carsten Kramer, Erik Rosolowsky, Karin Sandstrom, Karl Schuster, Antonio Usero, Axel Weiss, and Helmut Wiesemeyer. Low CO Luminosities in Dwarf Galaxies. *AJ*, 143(6):138, June 2012. doi: 10.1088/0004-6256/143/6/138.

F. Schweizer and P. Seitzer. Ripples in disk galaxies. *ApJ*, 328:88–92, May 1988. doi: 10.1086/166270.

Nicholas Scott, Jesse van de Sande, Scott M. Croom, Brent Groves, Matt S. Owers, Henry Poetrodjojo, Francesco D'Eugenio, Anne M. Medling, Dilyar Barat, Tania M. Barone, Joss Bland-Hawthorn, Sarah Brough, Julia Bryant, Luca Cortese, Caroline Foster, Andrew W. Green, Sree Oh, Matthew Colless, Michael J. Drinkwater, Simon P. Driver, Michael Goodwin, Madusha L. P. Gunawardhana, Christoph Federrath, Lloyd Harischandra, Yifei Jin, J. S. Lawrence, Nuria P. Lorente, Elizabeth Mannering, Simon O'Toole, Samuel N. Richards, Sebastian F. Sanchez, Adam L. Schaefer, Katrina Sealey, Rob Sharp, Sarah M. Sweet, Dan S. Taranu, and Mathew Varidel. The SAMI Galaxy Survey: Data Release Two with absorption-line physics value-added products. *MNRAS*, 481(2):2299–2319, December 2018. doi: 10.1093/mnras/sty2355.

Y.-K. Sheen, S. K. Yi, C. H. Ree, and J. Lee. Post-merger Signatures of Red-sequence Galaxies in Rich Abell Clusters at z <~ 0.1. *ApJS*, 202:8, September 2012. doi: 10.1088/0067-0049/202/1/8.

Irene Shivaei, Gergö Popping, George Rieke, Naveen Reddy, Alexandra Pope, Robert Kennicutt, Bahram Mobasher, Alison Coil, Yoshinobu Fudamoto, Mariska Kriek, Jianwei Lyu, Pascal Oesch, Ryan Sanders, Alice Shapley, and Brian Siana. IR SED and Dust Masses of Sub-solar Metallicity Galaxies at z~2.3. *arXiv e-prints*, art. arXiv:2201.04270, January 2022.

Joseph Silk. Feedback, Disk Self-Regulation, and Galaxy Formation. *ApJ*, 481(2):703–709, May 1997. doi: 10.1086/304073.

Vimal Simha, David H. Weinberg, Charlie Conroy, Romeel Dave, Mark Fardal, Neal Katz, and Benjamin D. Oppenheimer. Parametrising Star Formation Histories. *arXiv e-prints*, art. arXiv:1404.0402, April 2014.

E. Simonneau, A. M. Varela, and C. Munoz-Tunon. Astronomical observations and synthesis of ellipsoidal triaxial structures. I. Geometrical considerations. *Nuovo Cimento B Serie*, 113B(7): 927–944, Jul 1998.

Christine M. Simpson, Robert J. J. Grand, Facundo A. Gómez, Federico Marinacci, Rüdiger Pakmor, Volker Springel, David J. R. Campbell, and Carlos S. Frenk. Quenching and ram pressure stripping of simulated Milky Way satellite galaxies. *MNRAS*, 478:548–567, July 2018. doi: 10.1093/mnras/sty774.

Rosalind E. Skelton, Eric F. Bell, and Rachel S. Somerville. The Effect of Dry Mergers on the Color-Magnitude Relation of Early-Type Galaxies. *ApJ*, 699:L9–L12, July 2009. doi: 10.1088/0004-637X/699/1/L9.

Rosalind E. Skelton, Katherine E. Whitaker, Ivelina G. Momcheva, Gabriel B. Brammer, Pieter G. van Dokkum, Ivo Labbé, Marijn Franx, Arjen van der Wel, Rachel Bezanson, Elisabete Da Cunha, Mattia Fumagalli, Natascha Förster Schreiber, Mariska Kriek, Joel Leja, Britt F. Lundgren, Daniel Magee, Danilo Marchesini, Michael V. Maseda, Erica J. Nelson, Pascal Oesch, Camilla

Pacifici, Shannon G. Patel, Sedona Price, Hans-Walter Rix, Tomer Tal, David A. Wake, and Stijn Wuyts. 3D-HST WFC3-selected Photometric Catalogs in the Five CANDELS/3D-HST Fields: Photometry, Photometric Redshifts, and Stellar Masses. *ApJS*, 214(2):24, October 2014. doi: 10.1088/0067-0049/214/2/24.

Matthew C. Smith, Debora Sijacki, and Sijing Shen. Cosmological simulations of dwarfs: the need for ISM physics beyond SN feedback alone. *MNRAS*, 485(3):3317–3333, May 2019. doi: 10.1093/mnras/stz599.

Matthew C. Smith, Greg L. Bryan, Rachel S. Somerville, Chia-Yu Hu, Romain Teyssier, Blakesley Burkhart, and Lars Hernquist. Efficient early stellar feedback can suppress galactic outflows by reducing supernova clustering. *arXiv e-prints*, art. arXiv:2009.11309, September 2020.

Alessandro Sonnenfeld, James H. H. Chan, Yiping Shu, Anupreeta More, Masamune Oguri, Sherry H. Suyu, Kenneth C. Wong, Chien-Hsiu Lee, Jean Coupon, Atsunori Yonehara, Adam S. Bolton, Anton T. Jaelani, Masayuki Tanaka, Satoshi Miyazaki, and Yutaka Komiyama. Survey of Gravitationally-lensed Objects in HSC Imaging (SuGOHI). I. Automatic search for galaxy-scale strong lenses. *PASJ*, 70:S29, January 2018. doi: 10.1093/pasj/psx062.

Martin Sparre, Christopher C. Hayward, Robert Feldmann, Claude-André Faucher-Giguère, Alexander L. Muratov, Dušan Kereš, and Philip F. Hopkins. (Star)bursts of FIRE: observational signatures of bursty star formation in galaxies. *MNRAS*, 466(1):88–104, April 2017. doi: 10.1093/mnras/stw3011.

Volker Springel. The cosmological simulation code GADGET-2. *MNRAS*, 364(4):1105–1134, December 2005. doi: 10.1111/j.1365-2966.2005.09655.x.

J. L. Starck, J. Fadili, and F. Murtagh. The undecimated wavelet decomposition and its reconstruction. *IEEE Transactions on Image Processing*, 16(2):297–309, Feb 2007. ISSN 1057-7149. doi: 10.1109/TIP.2006.887733.

Jean-Luc Starck, Fionn Murtagh, and Mario Bertero. *Starlet Transform in Astronomical Data*

Processing, pages 2053–2098. Springer New York, New York, NY, 2015. ISBN 978-1-4939-0790-8. doi: 10.1007/978-1-4939-0790-8_34. URL https://doi.org/10.1007/978-1-4939-0790-8_34.

T. K. Starkenburg and A. Helmi. Dark influences: imprints of dark satellites on dwarf galaxies. *A&A*, 575:A59, March 2015. doi: 10.1051/0004-6361/201425082.

T. K. Starkenburg, A. Helmi, and L. V. Sales. Dark influences II. Gas and star formation in minor mergers of dwarf galaxies with dark satellites. *A&A*, 587:A24, March 2016a. doi: 10.1051/0004-6361/201527247.

T. K. Starkenburg, A. Helmi, and L. V. Sales. Dark influences. III. Structural characterization of minor mergers of dwarf galaxies with dark satellites. *A&A*, 595:A56, Oct 2016b. doi: 10.1051/0004-6361/201528066.

S. Stierwalt, G. Besla, D. Patton, K. Johnson, N. Kallivayalil, M. Putman, G. Privon, and G. Ross. Tiny titans: The role of dwarfdwarf interactions in low-mass galaxy evolution. *The Astrophysical Journal*, 805(1):2, 2015. URL http://stacks.iop.org/0004-637X/805/i=1/a=2.

S. Stierwalt, S. E. Liss, K. E. Johnson, D. R. Patton, G. C. Privon, G. Besla, N. Kallivayalil, and M. Putman. Direct evidence of hierarchical assembly at low masses from isolated dwarf galaxy groups. *Nature Astronomy*, 1:0025, January 2017. doi: 10.1038/s41550-016-0025.

G. S. Stinson, J. J. Dalcanton, T. Quinn, S. M. Gogarten, T. Kaufmann, and J. Wadsley. Feedback and the formation of dwarf galaxy stellar haloes. *MNRAS*, 395(3):1455–1466, May 2009. doi: 10.1111/j.1365-2966.2009.14555.x.

Jay Strader, Anil C. Seth, and Nelson Caldwell. Old Massive Globular Clusters and the Stellar Halo of the Dwarf Starburst Galaxy NGC 4449. *AJ*, 143(2):52, February 2012. doi: 10.1088/0004-6256/143/2/52.

Iskra Strateva, Željko Ivezić, Gillian R. Knapp, Vijay K. Narayanan, Michael A. Strauss, James E. Gunn, Robert H. Lupton, David Schlegel, Neta A. Bahcall, Jon Brinkmann, Robert J. Brunner, Tamás Budavári, István Csabai, Francisco Javier Castander, Mamoru Doi, Masataka Fukugita,

Zsuzsanna Győry, Masaru Hamabe, Greg Hennessy, Takashi Ichikawa, Peter Z. Kunszt, Don Q. Lamb, Timothy A. McKay, Sadanori Okamura, Judith Racusin, Maki Sekiguchi, Donald P. Schneider, Kazuhiro Shimasaku, and Donald York. Color Separation of Galaxy Types in the Sloan Digital Sky Survey Imaging Data. *AJ*, 122:1861–1874, October 2001. doi: 10.1086/323301.

Michael A. Strauss, David H. Weinberg, Robert H. Lupton, Vijay K. Narayanan, James Annis, Mariangela Bernardi, Michael Blanton, Scott Burles, A. J. Connolly, Julianne Dalcanton, Mamoru Doi, Daniel Eisenstein, Joshua A. Frieman, Masataka Fukugita, James E. Gunn, Željko Ivezić, Stephen Kent, Rita S. J. Kim, G. R. Knapp, Richard G. Kron, Jeffrey A. Munn, Heidi Jo Newberg, R. C. Nichol, Sadanori Okamura, Thomas R. Quinn, Michael W. Richmond, David J. Schlegel, Kazuhiro Shimasaku, Mark SubbaRao, Alexander S. Szalay, Dan Vanden Berk, Michael S. Vogeley, Brian Yanny, Naoki Yasuda, Donald G. York, and Idit Zehavi. Spectroscopic Target Selection in the Sloan Digital Sky Survey: The Main Galaxy Sample. *AJ*, 124(3):1810–1824, September 2002. doi: 10.1086/342343.

Kung-Yi Su, Philip F. Hopkins, Christopher C. Hayward, Claude-André Faucher-Giguère, Dušan Kereš, Xiangcheng Ma, and Victor H. Robles. Feedback first: the surprisingly weak effects of magnetic fields, viscosity, conduction and metal diffusion on sub-L* galaxy formation. *MNRAS*, 471(1):144–166, October 2017. doi: 10.1093/mnras/stx1463.

Jiayi Sun, Adam K. Leroy, Eve C. Ostriker, Annie Hughes, Erik Rosolowsky, Andreas Schruba, Eva Schinnerer, Guillermo A. Blanc, Christopher Faesi, J. M. Diederik Kruijssen, Sharon Meidt, Dyas Utomo, Frank Bigiel, Alberto D. Bolatto, Mélanie Chevance, I-Da Chiang, Daniel Dale, Eric Emsellem, Simon C. O. Glover, Kathryn Grasha, Jonathan Henshaw, Cinthya N. Herrera, Maria Jesus Jimenez-Donaire, Janice C. Lee, Jérôme Pety, Miguel Querejeta, Toshiki Saito, Karin Sandstrom, and Antonio Usero. Dynamical Equilibrium in the Molecular ISM in 28 Nearby Star-forming Galaxies. *ApJ*, 892(2):148, April 2020. doi: 10.3847/1538-4357/ab781c.

T. Tal, P. G. van Dokkum, J. Nelan, and R. Bezanson. The Frequency of Tidal Features Associated with Nearby Luminous Elliptical Galaxies From a Statistically Complete Sample. *AJ*, 138:1417–1427, November 2009. doi: 10.1088/0004-6256/138/5/1417.

D. Tanoglidis, A. Drlica-Wagner, K. Wei, T. S. Li, J. Sánchez, Y. Zhang, A. H. G. Peter, A. Feldmeier-Krause, J. Prat, K. Casey, A. Palmese, C. Sánchez, J. DeRose, C. Conselice, L. Gagnon, T. M. C. Abbott, M. Aguena, S. Allam, S. Avila, K. Bechtol, E. Bertin, S. Bhargava, D. Brooks, D. L. Burke, A. Carnero Rosell, M. Carrasco Kind, J. Carretero, C. Chang, M. Costanzi, L. N. da Costa, J. De Vicente, S. Desai, H. T. Diehl, P. Doel, T. F. Eifler, S. Everett, A. E. Evrard, B. Flaugher, J. Frieman, J. García-Bellido, D. W. Gerdes, R. A. Gruendl, J. Gschwend, G. Gutierrez, W. G. Hartley, D. L. Hollowood, D. Huterer, D. J. James, E. Krause, K. Kuehn, N. Kuropatkin, M. A. G. Maia, M. March, J. L. Marshall, F. Menanteau, R. Miquel, R. L. C. Ogando, F. Paz-Chinchón, A. K. Romer, A. Roodman, E. Sanchez, V. Scarpine, S. Serrano, I. Sevilla-Noarbe, M. Smith, E. Suchyta, G. Tarle, D. Thomas, D. L. Tucker, A. R. Walker, and DES Collaboration. Shadows in the Dark: Low-surface-brightness Galaxies Discovered in the Dark Energy Survey. *ApJS*, 252(2):18, February 2021. doi: 10.3847/1538-4365/abca89.

E. N. Taylor, A. M. Hopkins, I. K. Baldry, M. J. I. Brown, S. P. Driver, L. S. Kelvin, D. T. Hill, A. S. G. Robotham, J. Bland-Hawthorn, D. H. Jones, R. G. Sharp, D. Thomas, J. Liske, J. Loveday, P. Norberg, J. A. Peacock, S. P. Bamford, S. Brough, M. Colless, E. Cameron, C. J. Conselice, S. M. Croom, C. S. Frenk, M. Gunawardhana, K. Kuijken, R. C. Nichol, H. R. Parkinson, S. Phillipps, K. A. Pimbblet, C. C. Popescu, M. Prescott, W. J. Sutherland, R. J. Tuffs, E. van Kampen, and D. Wijesinghe. Galaxy And Mass Assembly (GAMA): stellar mass estimates. *MNRAS*, 418:1587–1620, December 2011. doi: 10.1111/j.1365-2966.2011.19536.x.

The Astropy Collaboration, A. M. Price-Whelan, B. M. Sipócz, H. M. Günther, P. L. Lim, S. M. Crawford, S. Conseil, D. L. Shupe, M. W. Craig, N. Dencheva, A. Ginsburg, J. T. VanderPlas, L. D. Bradley, D. Pérez- Suárez, M. de Val-Borro, T. L. Aldcroft, K. L. Cruz, T. P. Robitaille, E. J. Tollerud, C. Ardelean, T. Babej, M. Bachetti, A. V. Bakanov, S. P. Bamford, G. Barentsen, P. Barmby, A. Baumbach, K. L. Berry, F. Biscani, M. Boquien, K. A. Bostroem, L. G. Bouma, G. B. Brammer, E. M. Bray, H. Breytenbach, H. Buddelmeijer, D. J. Burke, G. Calderone, J. L. Cano Rodríguez, M. Cara, J. V. M. Cardoso, S. Cheedella, Y. Copin, D. Crichton, D. DÁvella, C. Deil, É. Depagne, J. P. Dietrich, A. Donath, M. Droettboom, N. Earl, T. Erben, S. Fabbro,

L. A. Ferreira, T. Finethy, R. T. Fox, L. H. Garrison, S. L. J. Gibbons, D. A. Goldstein, R. Gommers, J. P. Greco, P. Greenfield, A. M. Groener, F. Grollier, A. Hagen, P. Hirst, D. Homeier, A. J. Horton, G. Hosseinzadeh, L. Hu, J. S. Hunkeler, Ž. Ivezić, A. Jain, T. Jenness, G. Kanarek, S. Kendrew, N. S. Kern, W. E. Kerzendorf, A. Khvalko, J. King, D. Kirkby, A. M. Kulkarni, A. Kumar, A. Lee, D. Lenz, S. P. Littlefair, Z. Ma, D. M. Macleod, M. Mastropietro, C. McCully, S. Montagnac, B. M. Morris, M. Mueller, S. J. Mumford, D. Muna, N. A. Murphy, S. Nelson, G. H. Nguyen, J. P. Ninan, M. Nöthe, S. Ogaz, S. Oh, J. K. Parejko, N. Parley, S. Pascual, R. Patil, A. A. Patil, A. L. Plunkett, J. X. Prochaska, T. Rastogi, V. Reddy Janga, J. Sabater, P. Sakurikar, M. Seifert, L. E. Sherbert, H. Sherwood-Taylor, A. Y. Shih, J. Sick, M. T. Silbiger, S. Singanamalla, L. P. Singer, P. H. Sladen, K. A. Sooley, S. Sornarajah, O. Streicher, P. Teuben, S. W. Thomas, G. R. Tremblay, J. E. H. Turner, V. Terrón, M. H. van Kerkwijk, A. de la Vega, L. L. Watkins, B. A. Weaver, J. B. Whitmore, J. Woillez, and V. Zabalza. The Astropy Project: Building an inclusive, open-science project and status of the v2.0 core package. *ArXiv e-prints*, January 2018.

A. Toomre. Mergers and Some Consequences. In B. M. Tinsley and R. B. G. Larson, D. Campbell, editors, *Evolution of Galaxies and Stellar Populations*, page 401, 1977.

A. Toomre and J. Toomre. Galactic Bridges and Tails. *ApJ*, 178:623–666, December 1972. doi: 10.1086/151823.

M. Tremmel, M. Karcher, F. Governato, M. Volonteri, T. R. Quinn, A. Pontzen, L. Anderson, and J. Bellovary. The Romulus cosmological simulations: a physical approach to the formation, dynamics and accretion models of SMBHs. *MNRAS*, 470(1):1121–1139, September 2017. doi: 10.1093/mnras/stx1160.

M. Tremmel, T. R. Quinn, A. Ricarte, A. Babul, U. Chadayammuri, P. Natarajan, D. Nagai, A. Pontzen, and M. Volonteri. Introducing ROMULUSC: a cosmological simulation of a galaxy cluster with an unprecedented resolution. *MNRAS*, 483(3):3336–3362, March 2019. doi: 10.1093/mnras/sty3336.

M. Tremmel, A. C. Wright, A. M. Brooks, F. Munshi, D. Nagai, and T. R. Quinn. The formation of ultradiffuse galaxies in the RomulusC galaxy cluster simulation. *MNRAS*, 497(3):2786–2810, July 2020. doi: 10.1093/mnras/staa2015.

Ignacio Trujillo and Jüergen Fliri. Beyond 31 mag arcsec^{-2}: The Frontier of Low Surface Brightness Imaging with the Largest Optical Telescopes. *ApJ*, 823(2):123, June 2016. doi: 10.3847/0004-637X/823/2/123.

Dyas Utomo, Alberto D. Bolatto, Tony Wong, Eve C. Ostriker, Leo Blitz, Sebastian F. Sanchez, Dario Colombo, Adam K. Leroy, Yixian Cao, Helmut Dannerbauer, Ruben Garcia-Benito, Bernd Husemann, Veselina Kalinova, Rebecca C. Levy, Damian Mast, Erik Rosolowsky, and Stuart N. Vogel. The EDGE-CALIFA Survey: Variations in the Molecular Gas Depletion Time in Local Galaxies. *ApJ*, 849(1):26, November 2017. doi: 10.3847/1538-4357/aa88c0.

Remco F. J. van der Burg, Adam Muzzin, and Henk Hoekstra. The abundance and spatial distribution of ultra-diffuse galaxies in nearby galaxy clusters. *A&A*, 590:A20, May 2016. doi: 10.1051/0004-6361/201628222.

Roeland P. van der Marel. The Large Magellanic Cloud: structure and kinematics. In Mario Livio and Thomas M. Brown, editors, *The Local Group as an Astrophysical Laboratory*, volume 17, pages 47–71, January 2006.

Stefan Van Der Walt, S Chris Colbert, and Gael Varoquaux. The numpy array: a structure for efficient numerical computation. *Computing in Science & Engineering*, 13(2):22–30, 2011.

A. van der Wel, Yu-Yen Chang, E. F. Bell, B. P. Holden, H. C. Ferguson, M. Giavalisco, H. W. Rix, R. Skelton, K. Whitaker, I. Momcheva, G. Brammer, S. A. Kassin, M. Martig, A. Dekel, D. Ceverino, D. C. Koo, M. Mozena, P. G. van Dokkum, M. Franx, S. M. Faber, and J. Primack. Geometry of Star-forming Galaxies from SDSS, 3D-HST, and CANDELS. *ApJL*, 792(1):L6, September 2014. doi: 10.1088/2041-8205/792/1/L6.

P. G. van Dokkum. The Recent and Continuing Assembly of Field Elliptical Galaxies by Red Mergers. *AJ*, 130:2647–2665, December 2005. doi: 10.1086/497593.

Pieter van Dokkum, Shany Danieli, Yotam Cohen, Allison Merritt, Aaron J. Romanowsky, Roberto Abraham, Jean Brodie, Charlie Conroy, Deborah Lokhorst, Lamiya Mowla, Ewan O'Sullivan, and Jielai Zhang. A galaxy lacking dark matter. *Nature*, 555(7698):629–632, March 2018. doi: 10.1038/nature25767.

Pieter van Dokkum, Asher Wasserman, Shany Danieli, Roberto Abraham, Jean Brodie, Charlie Conroy, Duncan A. Forbes, Christopher Martin, Matt Matuszewski, Aaron J. Romanowsky, and Alexa Villaume. Spatially Resolved Stellar Kinematics of the Ultra-diffuse Galaxy Dragonfly 44. I. Observations, Kinematics, and Cold Dark Matter Halo Fits. *ApJ*, 880(2):91, August 2019. doi: 10.3847/1538-4357/ab2914.

Pieter G. van Dokkum, Roberto Abraham, Allison Merritt, Jielai Zhang, Marla Geha, and Charlie Conroy. Forty-seven Milky Way-sized, Extremely Diffuse Galaxies in the Coma Cluster. *ApJL*, 798(2):L45, January 2015. doi: 10.1088/2041-8205/798/2/L45.

Jordan D. Van Nest, F. Munshi, A. C. Wright, M. Tremmel, A. M. Brooks, D. Nagai, and T. Quinn. What's in a Name? Quantifying the Interplay between the Definition, Orientation, and Shape of Ultra-diffuse Galaxies Using the Romulus Simulations. *ApJ*, 926(1):92, February 2022. doi: 10.3847/1538-4357/ac43b7.

Vladas Vansevičius, Nobuo Arimoto, Takashi Hasegawa, Chisato Ikuta, Pascale Jablonka, Donatas Narbutis, Kouji Ohta, Rima Stonkutė, Naoyuki Tamura, Valdas Vansevičius, and Yoshihiko Yamada. The Full-fledged Dwarf Irregular Galaxy Leo A. *ApJL*, 611(2):L93–L96, August 2004. doi: 10.1086/423802.

Alexa Villaume, Aaron J. Romanowsky, Jean Brodie, Pieter van Dokkum, Charlie Conroy, Duncan A. Forbes, Shany Danieli, Christopher Martin, and Matt Matuszewski. Spatially Resolved Stellar Spectroscopy of the Ultra-diffuse Galaxy Dragonfly 44. III. Evidence for an Unexpected Star Formation History under Conventional Galaxy Evolution Processes. *ApJ*, 924(1):32, January 2022. doi: 10.3847/1538-4357/ac341e.

M. Vogelsberger, S. Genel, V. Springel, P. Torrey, D. Sijacki, D. Xu, G. Snyder, S. Bird, D. Nelson,

and L. Hernquist. Properties of galaxies reproduced by a hydrodynamic simulation. *Nature*, 509: 177–182, May 2014. doi: 10.1038/nature13316.

H. Y. Wang, Y. P. Jing, S. Mao, and X. Kang. The phase-space distribution of infalling dark matter subhaloes. *MNRAS*, 364:424–432, December 2005. doi: 10.1111/j.1365-2966.2005.09543.x.

Wenting Wang, Laura V. Sales, Bruno M. B. Henriques, and Simon D. M. White. Satellite abundances around bright isolated galaxies - II. Radial distribution and environmental effects. *MNRAS*, 442:1363–1378, August 2014. doi: 10.1093/mnras/stu988.

Wenting Wang, Jiaxin Han, Alessandro Sonnenfeld, Naoki Yasuda, Xiangchong Li, Yipeng Jing, Surhud More, Paul A. Price, Robert Lupton, Eli S. Rykoff, David V. Stark, Ting-Wen Lan, Masahiro Takada, Song Huang, Wentao Luo, Neta A. Bahcall, and Yutaka Komiyama. The stellar halo of isolated central galaxies in the Hyper Suprime-Cam imaging survey. *MNRAS*, 487 (2):1580–1606, August 2019. doi: 10.1093/mnras/stz1339.

Simone M. Weinmann, Frank C. van den Bosch, Xiaohu Yang, and H. J. Mo. Properties of galaxy groups in the Sloan Digital Sky Survey - I. The dependence of colour, star formation and morphology on halo mass. *MNRAS*, 366(1):2–28, February 2006. doi: 10.1111/j.1365-2966.2005.09865.x.

Daniel R. Weisz and Michael Boylan-Kolchin. Local Group ultra-faint dwarf galaxies in the reionization era. *MNRAS*, 469(1):L83–L88, July 2017. doi: 10.1093/mnrasl/slx043.

Andrew R. Wetzel, Jeremy L. Tinker, and Charlie Conroy. Galaxy evolution in groups and clusters: star formation rates, red sequence fractions and the persistent bimodality. *MNRAS*, 424:232–243, July 2012. doi: 10.1111/j.1365-2966.2012.21188.x.

Andrew R. Wetzel, Philip F. Hopkins, Ji-hoon Kim, Claude-André Faucher-Giguère, Dušan Kereš, and Eliot Quataert. Reconciling Dwarf Galaxies with ΛCDM Cosmology: Simulating a Realistic Population of Satellites around a Milky Way-mass Galaxy. *ApJL*, 827(2):L23, August 2016. doi: 10.3847/2041-8205/827/2/L23.

Coral Wheeler, Andrew B. Pace, James S. Bullock, Michael Boylan-Kolchin, Jose Oñorbe, Oliver D. Elbert, Alex Fitts, Philip F. Hopkins, and Dušan Kereš. The no-spin zone: rotation versus dispersion support in observed and simulated dwarf galaxies. *MNRAS*, 465(2):2420–2431, February 2017. doi: 10.1093/mnras/stw2583.

Coral Wheeler, Philip F. Hopkins, Andrew B. Pace, Shea Garrison-Kimmel, Michael Boylan-Kolchin, Andrew Wetzel, James S. Bullock, Dušan Kereš, Claude-André Faucher-Giguère, and Eliot Quataert. Be it therefore resolved: cosmological simulations of dwarf galaxies with 30 solar mass resolution. *MNRAS*, 490(3):4447–4463, December 2019. doi: 10.1093/mnras/stz2887.

S. D. M. White and C. S. Frenk. Galaxy formation through hierarchical clustering. *ApJ*, 379:52–79, September 1991. doi: 10.1086/170483.

S. D. M. White and M. J. Rees. Core condensation in heavy halos - A two-stage theory for galaxy formation and clustering. *MNRAS*, 183:341–358, May 1978. doi: 10.1093/mnras/183.3.341.

Mark G. Wolfire, Christopher F. McKee, David Hollenbach, and A. G. G. M. Tielens. Neutral Atomic Phases of the Interstellar Medium in the Galaxy. *ApJ*, 587(1):278–311, April 2003. doi: 10.1086/368016.

A. H. Wright, A. S. G. Robotham, S. P. Driver, M. Alpaslan, S. K. Andrews, I. K. Baldry, J. Bland -Hawthorn, S. Brough, M. J. I. Brown, M. Colless, E. da Cunha, L. J. M. Davies, Alister W. Graham, B. W. Holwerda, A. M. Hopkins, P. R. Kafle, L. S. Kelvin, J. Loveday, S. J. Maddox, M. J. Meyer, A. J. Moffett, P. Norberg, S. Phillipps, K. Rowlands, E. N. Taylor, L. Wang, and S. M. Wilkins. Galaxy And Mass Assembly (GAMA): the galaxy stellar mass function to z = 0.1 from the r-band selected equatorial regions. *MNRAS*, 470(1):283–302, September 2017. doi: 10.1093/mnras/stx1149.

Anna C. Wright, Michael Tremmel, Alyson M. Brooks, Ferah Munshi, Daisuke Nagai, Ray S. Sharma, and Thomas R. Quinn. The formation of isolated ultradiffuse galaxies in ROMULUS25. *MNRAS*, 502(4):5370–5389, April 2021. doi: 10.1093/mnras/stab081.

John F. Wu, J. E. G. Peek, Erik J. Tollerud, Yao-Yuan Mao, Ethan O. Nadler, Marla Geha, Risa H. Wechsler, Nitya Kallivayalil, and Benjamin J. Weiner. Extending the SAGA Survey (xSAGA). I. Satellite Radial Profiles as a Function of Host-galaxy Properties. *ApJ*, 927(1):121, March 2022. doi: 10.3847/1538-4357/ac4eea.

Masafumi Yagi, Jin Koda, Yutaka Komiyama, and Hitomo Yamanoi. Catalog of Ultra-diffuse Galaxies in the Coma Clusters from Subaru Imaging Data. *ApJS*, 225(1):11, July 2016. doi: 10.3847/0067-0049/225/1/11.

Peter Yoachim and Julianne J. Dalcanton. Structural Parameters of Thin and Thick Disks in Edge-on Disk Galaxies. *AJ*, 131(1):226–249, January 2006. doi: 10.1086/497970.

Donald G. York, J. Adelman, Jr. Anderson, John E., Scott F. Anderson, James Annis, Neta A. Bahcall, J. A. Bakken, Robert Barkhouser, Steven Bastian, Eileen Berman, William N. Boroski, Steve Bracker, Charlie Briegel, John W. Briggs, J. Brinkmann, Robert Brunner, Scott Burles, Larry Carey, Michael A. Carr, Francisco J. Castander, Bing Chen, Patrick L. Colestock, A. J. Connolly, J. H. Crocker, István Csabai, Paul C. Czarapata, John Eric Davis, Mamoru Doi, Tom Dombeck, Daniel Eisenstein, Nancy Ellman, Brian R. Elms, Michael L. Evans, Xiaohui Fan, Glenn R. Federwitz, Larry Fiscelli, Scott Friedman, Joshua A. Frieman, Masataka Fukugita, Bruce Gillespie, James E. Gunn, Vijay K. Gurbani, Ernst de Haas, Merle Haldeman, Frederick H. Harris, J. Hayes, Timothy M. Heckman, G. S. Hennessy, Robert B. Hindsley, Scott Holm, Donald J. Holmgren, Chi-hao Huang, Charles Hull, Don Husby, Shin-Ichi Ichikawa, Takashi Ichikawa, Željko Ivezić, Stephen Kent, Rita S. J. Kim, E. Kinney, Mark Klaene, A. N. Kleinman, S. Kleinman, G. R. Knapp, John Korienek, Richard G. Kron, Peter Z. Kunszt, D. Q. Lamb, B. Lee, R. French Leger, Siriluk Limmongkol, Carl Lindenmeyer, Daniel C. Long, Craig Loomis, Jon Loveday, Rich Lucinio, Robert H. Lupton, Bryan MacKinnon, Edward J. Mannery, P. M. Mantsch, Bruce Margon, Peregrine McGehee, Timothy A. McKay, Avery Meiksin, Aronne Merelli, David G. Monet, Jeffrey A. Munn, Vijay K. Narayanan, Thomas Nash, Eric Neilsen, Rich Neswold, Heidi Jo Newberg, R. C. Nichol, Tom Nicinski, Mario Nonino, Norio Okada, Sadanori Okamura, Jeremiah P. Ostriker, Russell Owen, A. George Pauls, John Peoples, R. L.

Peterson, Donald Petravick, Jeffrey R. Pier, Adrian Pope, Ruth Pordes, Angela Prosapio, Ron Rechenmacher, Thomas R. Quinn, Gordon T. Richards, Michael W. Richmond, Claudio H. Rivetta, Constance M. Rockosi, Kurt Ruthmansdorfer, Dale Sandford, David J. Schlegel, Donald P. Schneider, Maki Sekiguchi, Gary Sergey, Kazuhiro Shimasaku, Walter A. Siegmund, Stephen Smee, J. Allyn Smith, S. Snedden, R. Stone, Chris Stoughton, Michael A. Strauss, Christopher Stubbs, Mark SubbaRao, Alexander S. Szalay, Istvan Szapudi, Gyula P. Szokoly, Anirudda R. Thakar, Christy Tremonti, Douglas L. Tucker, Alan Uomoto, Dan Vanden Berk, Michael S. Vogeley, Patrick Waddell, Shu-i. Wang, Masaru Watanabe, David H. Weinberg, Brian Yanny, Naoki Yasuda, and SDSS Collaboration. The Sloan Digital Sky Survey: Technical Summary. *AJ*, 120 (3):1579–1587, September 2000. doi: 10.1086/301513.

Sijie Yu, James S. Bullock, Courtney Klein, Jonathan Stern, Andrew Wetzel, Xiangcheng Ma, Jorge Moreno, Zachary Hafen, Alexander B. Gurvich, Philip F. Hopkins, Dušan Kereš, Claude-André Faucher-Giguère, Robert Feldmann, and Eliot Quataert. The bursty origin of the Milky Way thick disc. *arXiv e-prints*, art. arXiv:2103.03888, March 2021.

Dennis Zaritsky, Jason Harris, Eva K. Grebel, and Ian B. Thompson. The Morphologies of the Small Magellanic Cloud. *ApJL*, 534(1):L53–L56, May 2000. doi: 10.1086/312649.

Dennis Zaritsky, Richard Donnerstein, Arjun Dey, Jennifer Kadowaki, Huanian Zhang, Ananthan Karunakaran, David Martínez-Delgado, Mubdi Rahman, and Kristine Spekkens. Systematically Measuring Ultra-diffuse Galaxies (SMUDGes). I. Survey Description and First Results in the Coma Galaxy Cluster and Environs. *ApJS*, 240(1):1, January 2019. doi: 10.3847/1538-4365/aaefe9.

Dennis Zaritsky, Richard Donnerstein, Ananthan Karunakaran, C. E. Barbosa, Arjun Dey, Jennifer Kadowaki, Kristine Spekkens, and Huanian Zhang. Systematically Measuring Ultra-Diffuse Galaxies (SMUDGes). III. The Southern SMUDGes Catalog. *arXiv e-prints*, art. arXiv:2205.02193, May 2022.

Haowen Zhang, Joel R. Primack, S. M. Faber, David C. Koo, Avishai Dekel, Zhu Chen, Daniel

Ceverino, Yu-Yen Chang, Jerome J. Fang, Yicheng Guo, Lin Lin, and Arjen van der Wel. The evolution of galaxy shapes in CANDELS: from prolate to discy. *MNRAS*, 484(4):5170–5191, April 2019. doi: 10.1093/mnras/stz339.